

# Scalable Methods for Deterministic Integration of Quantum Emitters in Photonic Crystal Cavities

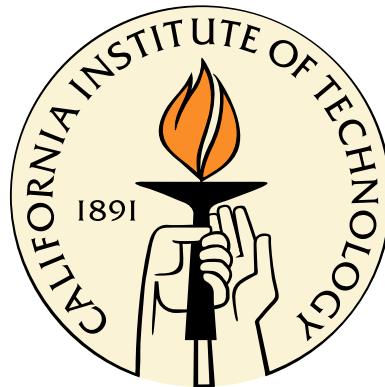
Thesis by

Andrew P. Homyk

In Partial Fulfillment of the Requirements

for the Degree of

Doctor of Philosophy



California Institute of Technology

Pasadena, California

2015

(Defended June 4, 2015)

© 2015

Andrew P. Homyk

All Rights Reserved

*To my amazing wife, Kelsey, who both inspires me to soar  
and gives me the foundation on which to land.*

# Acknowledgements

I am deeply indebted to quite an amazing group of people for all of their love, support, advice, inspiration (and often, commiseration), without which I could never have been successful. I must first thank my advisor, Prof. Axel Scherer, for providing one of the most incredible opportunities of my life. You managed to cultivate the most remarkable intellectual playground I can imagine, confidently supporting all of our crazy ideas, guiding us with calm reassurance, and responding to our failures with infinite patience. I cannot express how fortunate I feel to have worked with someone so exceptionally creative, and from whose wisdom I could learn so much about both science and life.

To other members of my committees — Amnon Yariv, Oskar Painter, Changhui Yang, Hyuck Choo and Sameer Walavalkar — thank you all for your guidance and inspiration throughout my graduate career. My work was inspired by lectures and discussions with you, and I remain humbled and honored to have worked with such a brilliant group of scientists.

To Prof. Tom Tombrello, who truly embodies the spirit of science, I thank you for your guidance, mentorship and example throughout my graduate career. I fondly remember our morning discussions over coffee and tea and the occasions when I was fortunate enough to sit in during Ph11 course, where topics would continuously evolve, jump and dance along the wildest directions, seemingly unrelated and yet somehow woven into an intricate, coherent intellectual blanket. I cannot recall a single subject on which you were unable to hold a deeper discussion than anyone in your company, and am gratifyingly amazed by the depth of both your passion and your brilliance.

To the many members of the Scherer group with whom I was fortunate to share this experience, I thank you all for your support, inspiration, wisdom, laughter and trickery (equally applied to fixing a fab process or pulling one over on Kate). To Mike and Tom, for getting me started and imparting

a career's worth of advice into a summer's worth of collaboration; to Se-Heon, Uday and Mike for many insightful tips and conversations; to Jingqing, whose perspective — whether about science, food or fun — was extraordinarily sharp, amusingly playful, and always appreciated; to Max, who openly shared a refreshing (often amusing) perspective on everything, expressed the most admirable humility I have ever known (“mistakes were made...”), exhibited boundless resilience when faced with a challenge, and who was as successful at getting you to think deeply about a problem as anyone could be (“No, that can't be right, Max” “How can I explain this to him,” “There certainly isn't going to be any magic”); to Pawel and Claudia, two of the most focused and brilliant students I have ever met, who set the bar way too high and then somehow blow away all expectations; and to Akram, Ben, Chris, Dvin, Erika, Guangxi, Jeebs, Jeff, Joyce, Mladen, William, Xio, Zhenyu, and the many other amazing people I've had the pleasure of interacting with over my time in the group.

To Kate, who kept us all happy, healthy and generally in one piece (Aditya may no longer own a pocket knife), I thank you for everything you did organizing us, corralling us, feeding us, reorganizing us, and generally putting up with anything and everything we threw your way. I greatly enjoyed our many conversations whether about science, acting, life or girl scout cookies, and admire your drive, enthusiasm and curiosity.

To Profs. Gibbs and Khitrova and Josh Hendrickson, Ben Richards, JD Olitzky, Mike Gehl, Ricky Gibson at UA, to Prof. Huffaker and Ping-Show Wong at UCLA, to Prof. Li and Wei-Ting Lai at NCU Taiwan, Prof. Honkanen and Antti Säynätjoki at Aalto and Prof. Lee at KAIST, I very much enjoyed our collaborations and look forward to future opportunities to work with all of you.

To Alex Krausse, Amir Safavi-Naeini, Carrie Hofmann, Christos Santis, Dan Turner-Evans, Dave Brown, Derrick Chi, Imogen Pryce, Jeff Hill, Jim Fakonas, Justin Cohen, Karl Yee, Ken Diest, Marcus Teague, Matt Dicken, Matt Eichenfield, Michael Burek, Raviv Perahia, Richard Norte, Ryan Briggs, Scott Steger, Stanley Burgos, Xinchang Zhang, and the many other fellow grads and cleanroom residents I have been fortunate to study and work with, I thank you for countless new ideas, experiences, perspectives and endless assistance.

To Guy, Melissa, Nils, Bophan, Carol and Mary, thank you for everything you've done to support

the KNI, for countless hours helping train me on nearly every piece of equipment in the cleanroom, and for the infinite patience helping me fix equipment, fix processes and once in awhile, fix an errant user who wants to put Au in the DRIE or evaporate the evaporator.

To Tanya and Linda, for always being there to help, even when you only had the last minute to do so.

To the ARCS foundation, who ensured I could still put food on the table and make sure my kids had a childhood as rich and colorful as my own, and without whom we would never have lasted through my graduate career.

To Ernie, who kept me in enough of a food coma during the entire experience to forget any hardship, and who tolerated *most* of my ridiculous requests (still waiting on that jaws chimichanga con carnitas), thank you.

To Vik, Juhwan and Sarah for all of your advice, encouragement and patience throughout the entire process.

To Al, Linh, Euni, Byron, Kaushik and Sohini for barbecues, pool parties, camping trips, and really being our family there. Linh, thank you for being so inclusive and really keeping us balanced when we started juggling more than we could have done on our own.

To Mike and Anya, who quickly surpassed my knowledge of LA, food, and food in LA, but were equally quick to share all of it. Thank you for so many amazing dinner parties (although you've basically ruined these for anyone who tries to follow), beach trips and insider tips. You really rolled out the Red Carpet (or at least explained it!) and made us feel at home here.

To Aditya, whose continuous stream of escapades, HAT tricks, ill-advised competitiveness (what other lactose intolerant person challenges someone to a calzone-eating contest?) and mix tapes provided a perpetual source of amusement, but who simultaneously *attempts* to hide an unmatched brilliance behind a naïve exterior, thank you for your endless enthusiasm, encouragement and amusement. You have more heart than anyone I've met, and you shoot straight from it.

To Dave and Shay, for fascinating science, fantastic food and an immense amount of support both in- and out-of-the lab, thank you. You took me under your wing from the start, whether

showing me around a cleanroom or showing me the ropes for a SCUBA dive. Through both your leadership and your barbecues, you brought the group together and really defined the culture that made it such an amazing place. I had a blast working, conversing and just hanging out with you and very much look forward to our next chance to meet up.

To Sameer, your knowledge of physics was matched only by your knowledge of The Simpsons, both of which came in surprisingly useful. Your creativity in the lab spans an incomparable range from elegant solutions to borderline deranged; I honestly can't say if I've more shocked by your max-power proposals or the fact that they worked. For all of the ridiculous food, ridiculous bets, ridiculous tautological arguments, and ridiculous pranks, I couldn't have had a better partner in crime; I certainly wouldn't have enjoyed it as much and absolutely wouldn't have gotten through it without you there. On that note, thank you for serving on my committee and signing off on my defense, even though it means you owe me dinner at Gyu Kaku now.

To Rick and Kyle, for all of the support you've been for my family, for all of the faith, encouragement and patience you've shown me, and for loads of hikes, feasts and fun we've shared all over the country, thank you. I'm very fortunate to be a part of your family, and to have you both in my life.

To my brothers, John and David, for having put up with a lifetime of me, for senseless fun and heartfelt love, for limitless support and encouragement, and for continuing to be examples of who I want to be, thank you.

To my parents, for a lifetime of love, support and inspiration. My fascination of science began when you took me into your labs, and on every conceivable level, I know that I'm here because of everything you've done. Your creativity, devotion, spirit and unconditional love have been the guiding example for me as a scientist, spouse and parent. Words fail to capture any of this, but I love you is as close as I can come.

To my kids, Natalie and Ashton, whose boundless curiosity, unabashed inquisitiveness, and unmatched creativity are the best example a scientist could ever have. I'm continuously amazed as I watch you grow, learn and achieve so many things I could never have done. I believe I will always

be running to catch up, and while I'm certainly not in any rush to see you get there, I'm incredibly excited to see all of the marvelous things you'll do and the wonderful people you're becoming. Your fascination, energy and support have been an inspiration to me throughout this, and I thank you for it. I love you.

To my wife, Kelsey, who encouraged me to jump head first into this in the first place and then stood by it the whole time, who supported me through late nights, early mornings, and long years, whose hard work and sacrifice and dedication enabled all of my exploration, who is without a doubt the most insightful person I have ever met and an inspiration both at work and at home, and whose care and compassion and unwavering love are what define the very center of my life, thank you for everything. I love you.

# Abstract

We investigated four unique methods for achieving scalable, deterministic integration of quantum emitters into ultra-high  $Q/V$  photonic crystal cavities, including selective area heteroepitaxy, engineered photoemission from silicon nanostructures, wafer bonding and dimensional reduction of III-V quantum wells, and cavity-enhanced optical trapping. In these areas, we were able to demonstrate site-selective heteroepitaxy, size-tunable photoluminescence from silicon nanostructures, Purcell modification of QW emission spectra, and limits of cavity-enhanced optical trapping designs which exceed any reports in the literature and suggest the feasibility of capturing and detecting nanostructures with dimensions below 10 nm. In addition to process scalability and the requirement for achieving accurate spectral and spatial overlap between the emitter and cavity, these techniques paid specific attention to the ability to separate the cavity and emitter material systems in order to allow optimal selection of these independently, and eventually enable monolithic integration with other photonic and electronic circuitry.

We also developed an analytic photonic crystal design process yielding optimized cavity tapers with minimal computational effort, and reported on a general cavity modification which exhibits improved fabrication tolerance by relying exclusively on positional rather than dimensional tapering. We compared several experimental coupling techniques for device characterization. Significant efforts were devoted to optimizing cavity fabrication (including the use of atomic layer deposition to improve surface quality), exploration into factors affecting the design fracturing, and automated analysis of SEM images. Using optimized fabrication procedures, we experimentally demonstrated 1D photonic crystal nanobeam cavities exhibiting the highest  $Q/V$  reported on substrate. Finally, we analyzed the bistable behavior of the devices to quantify the nonlinear optical response of our cavities.

# Contents

<b>Acknowledgements</b>	<b>iv</b>
<b>Abstract</b>	<b>ix</b>
<b>1 Introduction</b>	<b>1</b>
<b>2 Emitter Integration</b>	<b>4</b>
2.1 Emitter characteristics . . . . .	4
2.2 Emitter types . . . . .	10
2.3 Existing integration methods . . . . .	19
2.4 Development of deterministic coupling techniques . . . . .	23
2.4.1 Semiconductor heterogrowth . . . . .	24
2.4.1.1 Directed growth . . . . .	24
2.4.1.2 Aperture fabrication process . . . . .	27
2.4.1.3 Growth results and characterization . . . . .	42
2.4.1.4 SiGe detectors . . . . .	61
2.4.2 Silicon quantum wires and dots . . . . .	72
2.4.2.1 Silicon nanowire photoluminescence . . . . .	72
2.4.2.2 Influence of strain . . . . .	78
2.4.2.3 Lifetime measurements . . . . .	82
2.4.2.4 Etch modulation and three dimensional confinement . . . . .	85
2.4.2.5 Silicon quantum dot photoluminescence . . . . .	92

2.4.2.6	Geometric band gap engineering . . . . .	100
2.4.3	Wafer bonding . . . . .	118
2.4.4	Cavity-enhanced optical trapping . . . . .	129
2.4.4.1	Optical trapping, gradient forces and cavity enhancement . . . . .	131
2.4.4.2	Optical trapping metrics - depth, stiffness and sensitivity . . . . .	139
2.4.4.3	Cavity-enhanced optical trapping with silicon photonic crystal nanobeams	149
2.4.4.4	Emitters . . . . .	166
2.4.4.5	Particle delivery, detection and fixation . . . . .	169
2.4.5	Comparisons . . . . .	171
<b>3</b>	<b>Cavity Design</b>	<b>175</b>
3.1	Cavity Structures . . . . .	175
3.2	Photonic Crystals . . . . .	177
3.2.1	Band structure computation . . . . .	180
3.2.2	Gap characteristics . . . . .	191
3.2.3	Mode characteristics . . . . .	199
3.2.4	Defects . . . . .	200
3.2.5	Tapers . . . . .	204
3.2.6	Coupling . . . . .	206
3.2.7	Design methodologies . . . . .	211
3.2.8	1D, 2D, 3D . . . . .	215
3.3	Photonic Crystal Nanobeam Cavities . . . . .	218
3.3.1	Mirror optimization . . . . .	219
3.3.2	Defects, tapers, losses . . . . .	226
3.3.2.1	Initial design . . . . .	229
3.3.2.2	Expanded parameter design . . . . .	232
3.3.2.3	Analytic design . . . . .	236
3.3.3	Comparison . . . . .	243

3.3.4	Coupling . . . . .	246
3.4	Cavity Fabrication, Testing, and Optimization . . . . .	247
3.4.1	Fabrication . . . . .	247
3.4.2	Fiber loop and resonant scattering . . . . .	251
3.4.3	ALD passivation . . . . .	255
3.4.4	Further improvements - expanded parameters, fracturing, PEC . . . . .	260
3.4.5	SEM feedback, fabrication robustness, and constant radius designs . . . . .	267
3.4.6	Optical bistability . . . . .	282
<b>4</b>	<b>Conclusions and Outlook</b>	<b>290</b>
	<b>Bibliography</b>	<b>293</b>

# List of Figures

2.1	Photon correlation ( $g^{(2)}$ ) measurements. . . . .	6
2.2	Common colloidal quantum dots. . . . .	14
2.3	Self-assembled quantum dots and growth modes. . . . .	16
2.4	One of the first solid-state cQED systems. From [390]. . . . .	20
2.5	Existing methods for deterministic emitter integration. . . . .	21
2.6	Equilibrium diagram showing the critical radius as a function of lattice mismatch for maintaining coherent nanowire growth. From [82]. . . . .	27
2.7	Illustrations for additive and subtractive processes to reduce aperture dimensions after lithography. . . . .	28
2.8	Pillar fabrication process. . . . .	30
2.9	EDAX spectrum for the sputter deposited alumina on silicon, showing 2:3 stoichiomet- ric ratio of aluminum to oxygen. . . . .	31
2.10	SEMs of as-etched silicon nanopillars, showing our ability to produce large arrays of highly uniform, high aspect ratio devices. . . . .	34
2.11	Dry oxidation of (100) silicon in the thin film regime, following [235, 234, 233, 232]. . . . .	36
2.12	Self-terminating oxidation at 875°C. $d_i$ corresponds to the original (in parts b,c), unoxidized diameter, and $r$ the radius (part a). Note the terminal core size reached after $\approx 5$ hr. Consistent with the core behavior, the pillar oxide also terminates after $\approx 5$ hr. Also note that the initial oxidation is <i>faster</i> than the planar surface, but eventually terminates whereas the field oxide continues to grow. The schematic in (d) depicts the theory proposed by Cui <i>et al.</i> [62]. . . . .	38

2.13	Use of initial diameter and oxidation temperature to tune the final core size. Data points show the measured core sizes for 35 nm and 50 nm initial pillar diameters. For comparison, the solid curves show the oxidative trends reported by Liu <i>et al.</i> [207]. . .	40
2.14	TEM imaging and contrast of oxidized silicon nanopillars. . . . .	40
2.15	TEM images showing a range of oxidized silicon nanopillar cores suitable for heteroepitaxy. . . . .	41
2.16	Heteroepitaxy of GaP/InGaP and GaP on silicon using oxidized silicon nanopillar growth templates. . . . .	44
2.17	Wide array of growth templates from cleaving oxidized silicon nanopillars. . . . .	45
2.18	Schematics of the nanopillar cleaving process and potential issues. . . . .	45
2.19	InAs heteroepitaxy onto silicon nanowire templates at 630°C. . . . .	46
2.20	InAs QD growth on 35 nm silicon templates. . . . .	47
2.21	InAs heteroepitaxy onto silicon nanowire templates at 630°C. . . . .	48
2.22	InAs heteroepitaxy onto silicon nanowire templates at 660°C. . . . .	50
2.23	Detailed SEM images of InAs heteroepitaxy onto silicon nanowire templates at 660°C. . . . .	51
2.24	Cross-sectional TEMs of InAs nanowires grown on oxidized silicon nanowire templates. The core diameter at the interface is 32 nm. . . . .	52
2.25	Energy dispersive x-ray analysis of a heteroepitaxial InAs nanowire grown on an oxidized silicon nanowire template. The core diameter at the interface is 32 nm. . . . .	53
2.26	Use of a planarization layer to improve exposure of the oxidized silicon nanowire growth aperture. . . . .	55
2.27	InAs QD growth onto oxidized silicon nanowire apertures at 630°. These devices used the revised planarization and cleaving process. . . . .	57
2.28	SEMs showing TEM cross-section preparation in the FIB. This sample contained InAs QDs grown at 650°C onto oxidized silicon nanowires templates. The pre- and post-oxidation core diameters were $\approx 100$ nm and 16 nm, respectively. . . . .	58

2.29	TEMs showing InAs QDs grown on our silicon growth templates at 630°C. The starting diameter of the pillars was 80 nm. In this orientation, the silicon substrate is at the top, and the base of the pillars can be seen projecting downwards. The apparent distance between the silicon tip and the growth area arises from a deliberate miscut in the sample preparation. . . . .	59
2.30	InAs QD growth onto oxidized silicon nanowire apertures at 650°. These devices showed improved uniformity when compared to the process at 630°C (Figure 2.27), but decreased coverage over larger cores. . . . .	59
2.31	InAs QD growth onto oxidized silicon nanowire apertures, with a reduced V-III ratio of 5. The reduction in As flow enables greater In diffusion, resulting in more uniform growth and larger crystals than the process at 650°C (Figure 2.30). . . . .	60
2.32	Growth of InSb dots at 515°C on the oxidized silicon nanowire growth templates. . .	60
2.33	Large arrays of uniform, oxidized nanopillars for SiGe quantum dot growth. Start diameters ranged from 40 nm - 100 nm. . . . .	63
2.34	TEM sample preparation of SiGe quantum dots grown on oxidized silicon nanopillar templates. . . . .	64
2.35	Cross-sectional TEMs of SiGe quantum dots grown on oxidized silicon nanowire templates. . . . .	65
2.36	SiGe QD devices grown on Si nanopillars. . . . .	67
2.37	Electrical behavior of the SiGe QD detectors. . . . .	68
2.38	Schematic of the SiGe QD band structure and reverse-bias operation. . . . .	70
2.40	Schematics of the PL testing setup. . . . .	77
2.41	Normalized PL from eight SiNW samples with varying diameters, obtained by controlling the oxidation temperature. Diameter measurements reflect the average size measured by TEM. Dotted lines represent pillars with 50 nm pre-oxidation diameters, and continuous lines with 35 nm initial diameters. . . . .	77

2.42	(a) Peak PL emission as a function of terminal core diameter. Continuous lines represent three different theoretical explanations for the blue-shifted emission energy. Error bars in the $x$ -direction represent standard deviation in pillar size and in the $y$ -direction the FWHM of the measured PL. (b) Magnified view of peak emission for pillars between 2 - 4 nm. (c) Finite element strain model used to calculate the strain in the nanowires after oxidation. Shown is the strain in the radial and circumferential direction; the strain in the $z$ -direction is negligible. . . . .	78
2.43	Peak SiNW PL emission before and after annealing, illustrating the effect of oxidative strain on the emission properties. The red diamonds represent the pre-annealed measurements, while the green squares show measurements after annealing. The solid line is the simulated emission peak for the annealed pillars, based on a TBM. . . . .	80
2.44	Identification of PL peak associated with silica double bond defects. . . . .	81
2.45	Lifetime measurements for changing silicon core diameters. Error bars indicate uncertainty in the fit of the exponential decay time. Inset shows example of PL lifetime measurement with fitting curve in black. . . . .	83
2.46	Band-structure (in eV) of a TBM simulation of a strained and unstrained 2.5 nm diameter silicon nanowire. The dotted line shows the relative conduction band edge for the unstrained wire while the two insets show the axial and transverse structure of the nanowire. . . . .	84
2.47	Suspended structures possible through modulated etching. (a) A schematic of an etch mask to create a suspended beam. (b) Resulting etched structure, with a thin, electron-transparent membrane. Scale bar is 500 nm. (c) Set of fully-undercut beams. Scale bar is 500 nm. (d) Suspended beam, 100 nm wide and 50 $\mu\text{m}$ long, which was etched and suspended with a single step. The image is taken from a foreshortened angle to fit the entire beam. Scale bar is 2 $\mu\text{m}$ . (e) Three-dimensional silicon mesh created with a single etch step. Scale bar is 1 $\mu\text{m}$ . Inset shows a single silicon wire-frame cube. Scale bar is 250 nm. . . . .	86

2.48	Modulated etch process development . . . . .	87
2.49	SEM images of vertical silicon structures under progressive etch modulation conditions	88
2.50	Etch recipe for a single notch in a silicon nanopillar. (a) An array of silicon pillars with a 15 nm notch in a 75 nm diameter pillar. Scale bar is 200 nm. (b) Schematic of a pillar with the various etch steps highlighted; the conditions are described in the table.	89
2.51	Etch recipe for a 500 nm long, extended notch in a silicon nanopillar. (a) An array of silicon pillars with a 35 nm diameter stem on a 75 nm diameter pillar. Scale bar is 500 nm. (b) Schematic of a pillar with the various etch steps highlighted and the conditions described in the table. . . . .	90
2.52	The combination of multiple notch steps results in a ‘bow-tie’ structure, with a single bulge in the center of the pillar. . . . .	91
2.53	SEM images of corrugated nanopillars, showing both uniform and varied bead sizes. .	92
2.54	TEMs of SiQDs embedded in an SiO <sub>2</sub> matrix. . . . .	94
2.55	PL spectra of three samples of etched and oxidized quantum dots with different initial corrugation diameters. The leftmost curve (centered at 600 nm) corresponds to pillars in frame (a), the middle curve (centered at 640 nm) corresponds to the pillars in frame (b), and the right-most curve (entered at 810 nm) corresponds to the pillars in frame (c). The preoxidation size is 30 nm, 37 nm, and 45 nm for the (a) black, (b) blue, and (c) green samples, respectively. Note that the larger the preoxidation size, the longer the peak emission wavelength. Scale bars are 200 nm in each frame. . . . .	95
2.56	Comparison between PL spectra for uniform SiQD arrays and tapered arrays with multiple SiQD sizes in each pillar. . . . .	97
2.57	TEM images and energy band schematics illustrating the concept of geometric band using corrugated silicon nanopillars. . . . .	101

2.58	Illustrations of electron scattering and detection in a TEM. Just as the elastic scattering (diffraction) contains important structural information, including atomic spacing and crystal symmetry, the inelastic components are rich in electronic information and may be used to probe band structure or for elemental mapping. Images from [187]. . . . .	102
2.59	Illustration of typical EELS spectrum and information contained in different regions. From [187]. . . . .	103
2.60	Elemental identification using EELS spectra. From [187]. . . . .	104
2.61	Normalized EELS spectra as a function of Si particle diameter. The spectra were modeled by sets of parabolic band edges corresponding to final states at $\Delta_1$ , $L_1$ , and $L_3$ . Below 50 Å, the edge shape changes to a single parabolic component and shifts upwards in energy. From [26]. . . . .	105
2.62	Hyperspectral EELS data can be recorded either as full spectra from a single point which is scanned over the surface, or as complete images by scanning the energy filter. Schematic from [187]. . . . .	106
2.63	Bright field TEM images of a silicon nanopillar with a uniform constriction. These devices were fabricated to enable independent EELS measurements over the bulk-like core and narrowed regions. This particular device had a narrowed section with $\approx 16$ nm diameter, which is too large to modify the electronic band structure. . . . .	107
2.64	TEM images of the pillar used for EELS studies. The pre-oxidation diameter was $\approx 58$ nm around the head, and $\approx 30.7$ nm at the constriction. After oxidation, these dimensions narrowed to $\approx 22$ nm and $\approx 7.4$ nm, respectively. . . . .	110
2.65	Raw EELS spectra showing the near-edge fine structure for the head and tail region of the tapered nanopillar in Figure 2.64. Curves are normalized and offset vertically for clarity. . . . .	112
2.66	Reference EELS spectra and near-edge fine structure features for Si and SiO <sub>2</sub> . . . . .	113
2.67	Fabrication and schematic of double tunnel junction device. From [363]. . . . .	116

2.68	Differential conductance of a double tunnel junction device at 300K and 77K. Plot was numerically computed from measured I-V data. Note that the 77K data are scaled by a factor of 10. Periodic peaks can be seen with a spacing of 0.452V. From [363]. . . .	117
2.69	Self-aligned quantum nanostructures embedded in 2D PhCs by selective wet etching. From [270]. . . . .	120
2.70	Schematic of process flows for fabricating bonded/etched quantum dots in 1D photonic crystal nanobeams using aligned lithography (left) or self-aligned wet etching (right).	123
2.71	Characterization of our QW sample. . . . .	124
2.72	Photonic band structures of bonded 1D nanobeams, showing the collapse of the lowest-order band gap for thick buffers. . . . .	126
2.73	Electric-field energy ( $\epsilon \vec{E} ^2$ ) for a bonded nanobeam cavity with 50 nm InAlAs buffer layer. . . . .	127
2.74	Comparison of normalized photoluminescence spectra from $\text{In}_{0.53}\text{Ga}_{0.47}\text{As}$ QWs when coupled to a 1D nanobeam cavity, bonded, and unbonded. The peak unbonded PL was greater by a factor of $\approx 700$ . The large red-shift between bonded and unbonded is due to measurements at different temperatures. The sharp edge and discrete peaks in the on-cavity spectrum are consistent with the semiconductor band-edge and presence of acceptor modes within the photonic band gap. . . . .	127
2.75	Illustrations of the optical trapping setup and diagram of the proposed model from Ashkin's first demonstration in 1970 [8]. . . . .	131
2.76	Schematic of a single Gaussian beam optical trap. Transverse gradient forces dominate near the focus and draw the particle towards the optical axis. Precisely at the focus, however, the symmetric axial profile results in a zero gradient force, but a net radiation pressure. Thus, a stable trapping position is found just beyond the focus, where the backwards-oriented axial gradient opposes the forward scattering forces. Far from the focus, the scattering forces again dominate. . . . .	134

2.77	Expected trapping sensitivity for our system. Both plots correspond to trapping a $\varnothing_0 = 7.75$ nm PbS quantum dot with our 1D nanobeam photonic crystal resonator, and are evaluated for $Q = 1 \times 10^5$ . . . . .	146
2.78	Effective index method for estimating the effective index and field profile for a 2D waveguide. This method was used to determine the functional form of the trapping field, allowing more accurate estimation of trapping forces as well as informing ultimate limits which could be achieved in a dielectric 1D nanobeam cavity. . . . .	152
2.79	Cross-sections of the 1D nanobeam cavity mode from a 3D FDTD simulation, and fits to the functional forms derived from an effective index model of the 2D waveguide cross-section. Solid vertical lines in the $\hat{z}$ cross-section show the material boundaries, while the dashed line shows the offset to the particle location. By this point, the field has decayed by a factor of 0.436 from its peak. The curvatures from these fits were used to calculate trapping metrics. . . . .	153
2.80	Illustration showing the expected trapping depth for our 1D nanobeam cavity, assuming $Q = 100k$ and $P = 1.454$ mW, matching the stable trapping threshold for this device. . . . .	157
2.81	Cross-sections of air mode field (through center of beam) and corresponding FFTs ( $\lambda/4$ in substrate). Note that the $\vec{E}$ -field confinement in the holes and the $\vec{H}$ confinement within the dielectric are the opposite of what we find for the semiconductor mode (Figure 2.82). The FFT circles indicate the light cones for air (inner) and oxide (outer). The significant overlap within the oxide light-cone indicates heavy leakage for the mode, resulting in poor confinement and low $Q$ . The extent of the mode into the cladding can also be readily seen in the vertical cross-section. Compare to the semiconductor mode shown in Figure 2.82. . . . .	160

2.82	Cross-sections of semiconductor-mode field (through center of beam) and corresponding FFTs ( $\lambda/4$ in substrate). The FFT circles indicate the light cones for air (inner) and oxide (outer). Compared to the air mode resonance in Figure 2.81, the field here shows much tighter confinement (smaller $V$ ) and significantly less overlap with the light cone (higher $Q$ ). . . . .	161
2.83	Introduction of nanoslots or nanoholes can reduce mode volume, enhance the electric field, and improve access to the field maximum. . . . .	162
2.84	Effective index method for estimating the effective index and field profile for a 2D slotted waveguide. A large field enhancement is observed within the slot region, but the gradient and curvature are relatively small due to the cosh functional form within this region. . . . .	163
2.85	Dependence of $V^{-1}$ and force enhancement on gap width for a 1D slotted waveguide. These are calculated using an analytic solution for the field dependence, with numerical solutions for the characteristic equation to derive the propagation constant. . . . .	164
2.86	TEM images of the colloidal PbS QDs used in our studies, showing a typical diameter $\approx 7.75$ nm. . . . .	167
2.87	Room temperature photoluminescence spectrum for an ensemble of colloidal PbS QD dots, showing peak emission in the communications S band. . . . .	168
3.1	Comparison between TE and TM photonic band structures in a 1D nanobeam. A large (30%) band gap exists between the lowest TE bands, while a more complex TM band structure eliminates gaps between the lowest bands, and shows only small gaps between higher modes (with smaller $k$ -space margin). The lowest TE bands have nearly twice the difference in E-field confinement factor as the lowest TM, indicative of the energy splitting between these pairs. The lack of large, overlapping band gaps makes TE-TM coupling (due to fabrication imperfections or asymmetries) a problem for maintaining confinement and quality factor. . . . .	201
3.2	Loss mechanisms in temporal coupled mode theory. . . . .	208

3.3	Examples of photonic crystals with 1D, 2D, and 3D periodicity. . . . .	216
3.4	SEM of a 1D nanobeam cavity fabricated in SOI, illustrating the geometric parameters used to describe the device. . . . .	222
3.5	Dependence of TE band gap dependence 1D nanobeam geometry parameters. The thickness has been fixed to 220 nm to match the SOI substrate, while geometric combinations have been constrained to yield a mid-gap wavelength of $\lambda = 1550$ nm. A peak gap of $\approx 435$ nm occurs for $w1.42a \approx 645$ nm, $r = 0.35a \approx 160$ nm, and $t = 0.48a$ .	223
3.6	Combinations of normalized mirror geometry parameters which produce a mid-gap wavelength of $\lambda = 1550$ nm and match a 220 nm SOI device layer. . . . .	224
3.7	Extent of the band gap at in $k$ -space at the mid-gap wavelength of $\lambda = 1550$ nm. Thickness has been constrained to 220 nm, to match the substrate. . . . .	224
3.8	Combined metric showing the gap area for a 1D nanobeam geometry, defined as the product of the size of the energy gap ( $\Delta\omega$ ) and the extent in $k$ -space ( $\Delta k$ ). Values have been normalized to the peak. The thickness is fixed to 220 nm; geometry combinations yield a mid-gap wavelength of $\lambda = 1550$ nm. . . . .	225
3.9	FEM simulations an abrupt cavity, showing cross-sections of the fields (through center of beam) and corresponding FFTs ( $\lambda/4$ in substrate). The FFT circles indicate the light cones for air (inner) and oxide (outer). Geometry parameters were selected to be similar to our nanobeam devices and produce a resonance near 1550 nm, but the cavity is constructed by abruptly introducing the mirror section, without a taper region. Although the light appears to be well-confined, FFTs reveal significant scattering into radiative modes. . . . .	227
3.10	FEM simulations of our initial beam design, showing cross-sections of the fields (through center of beam) and corresponding FFTs ( $\lambda/4$ in substrate). The FFT circles indicate the light cones for air (inner) and oxide (outer). . . . .	231

3.11	Results of FEM simulations used to optimize the 1D nanobeam geometry with an expanded parameter range. These values correspond to a device layer thickness of $T = 220$ nm, with a resonance wavelength of $\lambda = 1550$ nm. . . . .	233
3.12	FEM simulations of our expanded beam design, showing cross-sections of the fields (through center of beam) and corresponding FFTs ( $\lambda/4$ in substrate). The FFT circles indicate the light cones for air (inner) and oxide (outer). Although the overall pattern appears similar, we note the use of <i>smaller</i> holes and a wider beam. While this decreases the mirror strength and results in a somewhat larger mode volume, this is outweighed by the $Q$ improvement resulting from a more gentle confinement. Practically, the wider beam also results in less field interaction with edge roughness. . . . .	235
3.13	Schematic illustrating the analytic design process. Solid and dashed curves correspond to real and imaginary $k$ components from the Brillouin zone edge; the solid black line highlights the resonance frequency, which matches the semiconductor band edge of the inner-most taper. Combinations of beam are chosen such that this resonance occurs at $\lambda = 1550$ nm. These parameters are scaled up by $[taperdepth]^{-1}$ to reveal the outer mirror segments. Geometry parameters yielding the maximum band gap are selected. . . . .	238
3.14	Analytic design band structures and corresponding $k$ components along the taper. . . . .	239
3.15	Results of FEM simulations characterizing analytically-designed 1D nanobeam cavities. The quality factor and $Q/V$ show $>400\%$ improvement over the expanded design results. Due to the deterministic design process, each depth and period combination produces a single, optimized cavity geometry which operates at the intended wavelength without excessive parameter sweeps to simultaneously tune resonance, quality, and mode volume. . . . .	241

3.16	FEM simulations of our analytic beam design, showing cross-sections of the fields (through center of beam) and corresponding FFTs ( $\lambda/4$ in substrate). The FFT circles indicate the light cones for air (inner) and oxide (outer). This design has a slightly more gentle confinement than the expanded design, resulting in a marginally higher $V$ but significant $Q$ improvements. . . . .	242
3.17	SEMs of our initial nanobeam devices, showing an array with different lattice constants and a single device. The hole tapering is visible at the center of the cavity. These devices were designed to be tested by tapered fiber loops and cross-polarized resonant scattering setups. Large buffer regions were included to avoid coupling to slab modes.	248
3.18	Effect of piranha treatment on 1D photonic crystal nanobeam cavities. All devices showed a significant increase in $Q$ after treatment. A more pronounced effect (in both relative and absolute change) is observed as the number of cavity periods increased, due to the greater sensitivity of high- $Q$ devices to surface quality. Over the entire set, the mean $Q$ increased by a factor of 2.75. Devices also blue-shifted by an average of 5.45 nm. Despite similar resonant wavelengths across devices, clear trends in resonance <i>shift</i> are observed for the geometries due to differences in their field components at the surface. . . . .	250
3.19	The first generation of our nanobeam devices, which were tested using a tapered fiber loop and resonant scattering. . . . .	251
3.20	Schematics describing the experimental setups for characterizing our 1D nanobeams. .	252
3.21	Fiber loop transmission spectra of a typical nanobeam cavity at $45^\circ$ , comparing the effects for center and edge contact positions. The red curve in (a) shows the spectrum directly from the laser. Note the red-shift induced for the center contact position due to higher dielectric loading, as well as the deeper resonant dip. In contrast, the spectra taken from the edge exhibits a higher quality factor. . . . .	253

3.22	Fiber loop transmission measurements as a function of position on a typical nanobeam cavity at $45^\circ$ (center of the nanobeam corresponds to $0 \mu\text{m}$ and the attached edges to $\pm 6 \mu\text{m}$ ), showing cavity resonant wavelength (black squares) and $Q$ (red circles). . . . .	253
3.23	Comparison of spectra recorded from the same cavity using the fiber loop setup and cross-polarized resonant scattering technique. Black curves show raw data for the cavity; red curves show laser spectra; the blue curve in (b) shows the fitted Fano lineshape. Note the red-shift and drop in $Q$ induced by the fiber loop due to dielectric loading and the introduction of an additional loss channel. . . . .	254
3.24	SEM images comparing the cavity region of a silicon nanobeam before and after ALD.	256
3.25	Comparison of cavity $Q$ s before and after ALD. The solid lines have a slope of 1 and represent no change in $Q$ , while the dotted lines represent the average change. For $\text{Al}_2\text{O}_3$ deposition, cavity quality increased by an average of 38%, while $\text{TiO}_2$ deposition led to an average decrease of 1.3%. . . . .	257
3.26	Crossed polarizer resonant scattering measurements of a cavity before and after 20 nm $\text{Al}_2\text{O}_3$ ALD. Before the deposition, the cavity resonance exhibited a $Q$ of 107,000; this increased to 212,000 after ALD. . . . .	257
3.27	Dependence of nanobeam quality on hole radius offset. Based on FDTD simulations, a peak is expected for an offset of 0 nm. Experimentally, we did not observe the peak, but rather a consistent trend indicating the starting holes were too large. . . . .	258
3.28	Plots showing the changes in cavity behavior due to the ALD process as a function of the hole radius. . . . .	259
3.29	SEMs showing a complete grating-coupled 1D nanobeam device, as well as detailed views of the grating region. . . . .	260
3.30	SEMs comparing end-fired and evanescently-coupled nanobeams. . . . .	261

3.31	<p>Typical transmission spectral for an expanded parameter 1D nanobeam at low and high excitation. The same device is represented in both curves, with black dots corresponding to experimental data and the blue line showing a Lorentzian fit. The powers listed correspond to output from the laser; powers coupled into the nanobeam were lower due to additional propagation and coupling losses. At high powers, the lineshape no longer follows a Lorentzian profile, but instead exhibits a triangular profile with a sudden, sharp drop, characteristic of optical bistability. . . . .</p>	261
3.32	<p>SEMs showing a stitching error at the field boundary between a manual cavity field and the connecting waveguide. The thin line below the cavity is due to a misalignment between the low- and high-current beams. . . . .</p>	262
3.33	<p>Distributions of the quality factors for several design iterations, sampled at a laser power of 0 dBm. The averages for the initial, expanded, and improved fracturing were 21,187.1, 25,674.8, and 30,823.3, respectively. Both the expanded and revised fracturing showed consistent improvements over the initial design. While higher <math>Q</math>s were observed at lower power, the data for earlier devices was more complete at moderate powers. Note that the expanded design and revised fracturing used identical device geometries, and show similar distributions. In this case, the gains came primarily from an increase in fabrication reliability, including a few higher quality beams and the elimination of low-quality devices. . . . .</p>	263
3.34	<p>Monte Carlo simulations of electron propagation and resist exposure, calculated using PENELOPE[21]. . . . .</p>	264

- 3.35 Empirical derivation of exposure parameters and proximity effects using dose sensors. Images in the left column show base dose patterns, surrounded by 50% filled patterns to determine optimal exposure level. Scale bars are  $2 \mu\text{m}$ . Note the disconnected corners in the over-dosed pattern, the connected corners and channel debris in the under-exposed pattern, and the square features in the base dose. The right columns show mid-range dose sensors used to determine proximity effects from nearby features, and their simulated equivalents. Sizes denote checkerboard square lengths. Note the similarity of corner rounding and feature blurring between the measured and simulated patterns. . . . . 266
- 3.36 1D photonic crystal nanobeam which has been segmented to identify the device regions (Si, red) and etched areas ( $\text{SiO}_2$ , blue). These regions could then be further analyzed to extract device geometry, including beam width, hole location, and radius. This geometry utilized local hole tapering, which tracked the tapering of the lattice constant. 267
- 3.37 Illustration of sub-pixel hole-edge finding. Beginning from the centroid of each hole, radial traces are examined as a function of angle. The location of the hole-edge can be found from intersection with the mid-point intensity. . . . . 268
- 3.38 Comparison of the designed and measured location and spacing of holes in a 1D photonic crystal nanobeam with tapered holes. Hole number is relative to the cavity center. The solid line shows the expected position, while circular points show the position as determined from SEM analysis. The spacing reflects the difference between neighboring hole locations, corresponding to the cavity taper and local lattice constant. Excellent agreement is observed over both short- and long-range, reflecting the ability to achieve extremely high positional accuracy with electron-beam lithography. . . . . 269
- 3.39 Comparison of designed and measured hole sizes for a 1D photonic crystal nanobeam with tapered holes. Hole number is relative to the cavity center. Here, the complete hole-edge profiles have been fit to ellipses, with  $\hat{x}$  corresponding to the cavity axis and  $\hat{y}$  the transverse direction. . . . . 270

3.40	Fracturing results for fixed-radius and tapered-hole nanobeam cavities. Note the slight differences in patterns between the larger edge holes and tapered center holes. These changes can inadvertently introduce non-systematic errors in hole dimensions, whereas the fixed-radius holes have nominally identical write processes. . . . .	271
3.41	Results of FEM simulations used to optimize the fixed-radius 1D nanobeam geometry. The design followed a similar process to the one used for the expanded parameter range devices. These values correspond to a device layer thickness of $T = 220$ nm, with a resonance wavelength of $\lambda = 1550$ nm. . . . .	273
3.42	FEM simulations of our fixed-radius beam design, showing cross-sections of the fields (through center of beam) and corresponding FFTs ( $\lambda/4$ in substrate). The FFT circles indicate the light cones for air (inner) and oxide (outer). Although this design shows slightly more theoretical leakage than the equivalent design with tapered holes, the fabrication tolerance outweighs this from a practical standpoint. . . . .	274
3.43	Comparison between $Q$ distributions for the expanded parameter design (with fixed fracturing) and fixed-radius devices. Both sets correspond to devices sampled at a laser power of 0 dBm. Despite significantly lower theoretical quality factors, the fixed-radius devices significantly out-performed the tapered devices. . . . .	275
3.44	Ultra-high $Q$ spectrum from a fixed-radius, 1D photonic crystal nanobeam on substrate.	275
3.45	Fixed-radius, 1D photonic crystal nanobeam which has been segmented to identify the device regions (Si, red) and etched areas ( $\text{SiO}_2$ , blue). . . . .	276
3.46	Comparison of the designed and measured location and spacing of holes in a fixed-radius, 1D photonic crystal nanobeam. Hole number is relative to the cavity center. The solid line shows the expected position, while circular points show the position as determined from SEM analysis. The spacing reflects the difference between neighboring hole locations, corresponding to the cavity taper and local lattice constant. Excellent agreement is observed over both short- and long-range, reflecting the ability to achieve extremely high positional accuracy with electron-beam lithography. . . . .	277

3.47	Comparison of designed and measured hole sizes for a fixed-radius, 1D photonic crystal nanobeam. Hole number is relative to the cavity center. Here, the complete hole-edge profiles have been fit to ellipses, with $\hat{x}$ corresponding to the cavity axis and $\hat{y}$ the transverse direction. . . . .	278
3.48	Tolerance of tapered-hole and fixed-radius nanobeam cavities to random perturbations in beam width, hole position, and hole radius. . . . .	278
3.49	Results of FEM simulations characterizing fixed-radius, analytically-designed 1D nanobeam cavities. The quality factor and $Q/V$ show remarkable improvements over the basic fixed-radius design, including a theoretical $Q$ of $7.8 \times 10^6$ which is nearly as high as that for the tapered radius cavities. Due to the deterministic design process, each depth and period combination produces a single, optimized cavity geometry which operates at the intended wavelength without excessive parameter sweeps to simultaneously tune resonance, quality, and mode volume. . . . .	280
3.50	FEM simulations of our fixed-radius, analytic beam design, showing cross-sections of the fields (through center of beam) and corresponding FFTs ( $\lambda/4$ in substrate). The FFT circles indicate the light cones for air (inner) and oxide (outer). This device represents a significant improvement over the fixed-radius, expanded beam design with a much more appropriately designed taper. Although the theoretical performance does not quite reach that of the tapered design, practical improvements in fabrication tolerance would likely significantly outweigh these concerns. . . . .	281
3.51	Wavelength and power sweeps of a 1D photonic crystal nanobeam exhibiting bistable characteristics. At higher powers, the lineshape changes dramatically, exhibiting a red-shift of the peak and an abrupt drop for long wavelengths. Higher excitation powers also show a decrease in the normalized power transmitted through the device, as increasing energy is lost to nonlinear absorptive effects. In the power sweeps, the bistability results in a hysteretic response. . . . .	282
3.52	Nonlinear optical transmission spectra. . . . .	286

- 3.53 Normalized transmission spectra for a fixed-radius, 1D nanobeam cavity (colored dots) and corresponding simulated spectra (solid lines). Labeled powers correspond to the laser output, before coupling and propagation losses. Excellent agreement for both the lineshape variation and bistable thresholds are reproduced over a wide range of input powers. The dashed line shows the simulated  $(\Delta\omega_0, \Delta T)$  trend of the critical point, with star symbols to mark the values corresponding to the laser inputs. . . . . 287

# List of Tables

2.1	Information contained in different EELS spectral ranges . . . . .	103
2.2	Comparison of normalized trapping parameters . . . . .	156
2.3	Absolute trapping performance for a 7.75 nm PbS quantum dot. The stability, stiffness, and displacement are evaluated at $P=1.454$ mW, corresponding to the stable trapping threshold for our $Q = 100k$ device. . . . .	158
2.4	Comparison between emitter-cavity integration techniques . . . . .	174
3.1	Geometric parameters and performance metrics for different cavity designs. All devices used 15 mirror periods (including taper region) on each side of the cavity center. . . . .	244
3.2	Comparisons of electric and magnetic fields for different cavity designs. Horizontal sections are taken through the beam center, and FFTs are taken $\lambda/4$ below the beam (in the substrate). The FFT circles indicate the light cones for air (inner) and oxide (outer). While the field patterns between the three tapered cavities reveal only subtle differences, the energy content within the light cones shows a dramatic reduction at each stage, explaining the progressive improvement in quality factor. . . . .	245
3.3	Material and computed constants for calculating bistable optical response of our 1D photonic crystal nanobeams. . . . .	285
3.4	Parameters to model optical bistability in 1D nanobeam, extracted from nonlinear optimization. . . . .	288

# Chapter 1

## Introduction

As the size of a particle shrinks to nanometer dimensions, increasingly quantum behavior emerges, exhibiting discrete energy levels rather than continuous spectra. At the smallest sizes, we begin to find resonances at optical frequencies, not only in atoms, but molecules, semiconductor nanocrystals, and even defect states in larger systems. In optically active materials, light fields which are tuned to appropriate level spacings can excite these resonances between energy states, which can be further enhanced by embedding the quantum emitter into a resonant optical cavity. The strong interactions possible between light and matter in this configuration can result in anything from modified emission rates to quantum entanglement, where the photon and emitter states can no longer be independently described. This regime of cavity quantum electrodynamics (cQED) serves as one of the most significant, fundamental test beds of quantum mechanics. And beyond experimental verification of scientifically interesting phenomena — such as photon anti-bunching, squeezed states, entanglement, and state teleportation — cQED systems are an important platform for both classical and quantum information processing, computation, and communication.

The pioneering cavity QED experiments were performed with atoms in free space, interacting with micron-scale cavities composed of very-high-reflectivity mirrors. This arrangement presents significant challenges in localizing a single atom to the field anti-node and maintaining its position over timescales long enough to conduct experiments. In spite of successes using atom traps, extending these systems to more complex configurations — where multiple cavities can be reliably coupled simultaneously — will require significant advancements.

Fortunately, our technological capabilities have evolved to a stage where we may directly construct many of these systems entirely in the solid state. Pioneering work in the last decade has shown the potential for such systems, with demonstrations of Purcell enhancement, Rabi splitting, and cavities whose response is controlled by the state of a quantum emitter. However, many of these continue to rely on probabilistic integration, where cavities are fabricated around arrays of randomly-dispersed emitters and devices, of which some fraction happen to align well enough to produce functioning systems. Several more recent efforts have begun exploring deterministic integration techniques, where spectral and spatial overlap is achieved by design. While these methods exhibit excellent coupling characteristics, they too face severe challenges in scaling, due to the significant manual efforts required for assembly or the need to redesign individual cavities and circuits to match emitter locations on a given substrate.

In this work, we explore several new techniques to integrate quantum emitters into ultra-high  $Q/V$  photonic crystal cavities. Not only were these methods designed to enable *deterministic* integration, they have been specifically developed in manners which are *extensible* to larger systems, beyond single cavities. Because the emitters are fixed in the cavity, these systems can be repeatably probed and exploit passive photonic components to couple multiple cavities on-chip in more complex configurations. This scalability is a critical element towards the creation of longer-lived, more complex quantum optics systems which realize the potential of integrated cavity quantum electrodynamics.

This thesis is organized into two main parts. In Chapter 2, we describe the development of four methods to enable scalable, deterministic emitter integration, including selective area heteroepitaxy, engineered emission from silicon nanostructures, wafer bonding and dimensional reduction of III-V quantum wells, and cavity-enhanced optical trapping. Chapter 3 reports the design, optimization, fabrication, and testing of our 1D nanobeam photonic crystal cavities. Although the cavity and emitter are inevitably coupled, we intentionally present these elements as independently as possible, emphasizing opportunities to optimize these elements individually when possible (using separate material systems, for example).

Between these efforts, we describe a method of producing selective area heteroepitaxy apertures with dimensions down to 2.5 nm, widely mismatched heteroepitaxial growth, lithographically-determined, size-tunable photoluminescence in silicon nanowires and quantum dots, and Purcell modification of wafer-bonded III-V spectra. We derive normalized metrics for cavity-enhanced optical trapping and introduce a parameter to understand the system's ability to discriminate particle sizes. These are cast in terms of common parameters used to describe cQED systems, and used to quantitatively compare our cavity system to a wide variety of existing trapping methods. We describe the influence of these parameters on cavity design and the ultimate limits achievable with dielectric cavities, and show performance metrics with our 1D nanobeam which greatly exceed anything currently reported in the literature. The process of 1D nanobeam photonic crystal cavity design and optimization is described in detail, including a method for automatically selecting mirror and taper parameters in 1D nanobeams to maximize cavity performance while providing deterministic control over resonance frequency. This allows rapid design of cavities in new material systems or while applying new constraints (device layer thickness, presence of substrate) without requiring excessive simulation of full cavities. Experimentally, we observe the highest reported  $Q/V$  for a cavity on substrate, and describe methods to tune the fabrication process and ensure robustness. Along the way, we also include some ancillary development, including heteroepitaxial growth of high-sensitivity, SiGe quantum dot photodetectors, and explorations into geometric engineering of the silicon band-gap, which shows the potential to develop quantum electronic devices directly in silicon.

# Chapter 2

## Emitter Integration

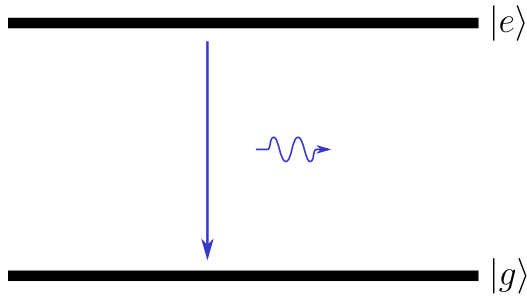
### 2.1 Emitter characteristics

The most basic means of obtaining single photons is from a strongly attenuated laser. Using standard laser pulses and calibrated attenuators to reach an average photon number much less than one, one can easily approximate the single photon Fock state using a classical device. Being significantly cheaper and more convenient than a true single photon source, faint laser pulses are still used in the vast majority of quantum cryptography experiments [218]. Moreover, specific protocols have been developed to achieve high key rates for quantum key distribution (QKD) using weak laser pulses. At least for certain applications, this might call into question the need for a truly quantum light source in the first place [310]. Upon further consideration, however, those authors show that such protocols are not inherently secure, but rather highly dependent on the source itself. As such, the system becomes subject to weakness based on manufacturer negligence, intentional tampering, or operator ignorance.

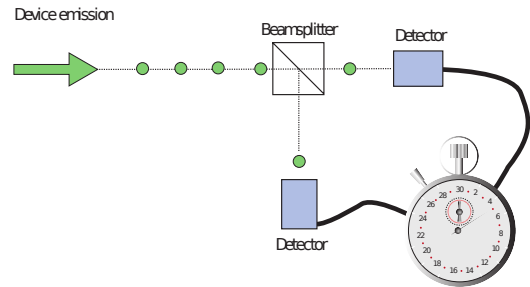
As a coherent state, lasers obey Poissonian statistics. The emission of each photon is random, resulting in a Gaussian noise known as shot noise. While the shot noise of a laser is the absolute minimum of any macroscopic source [218], the unknown arrival time of each photon can cause experimental difficulties. In order to adequately suppress multi-photon emission, the laser must be very strongly attenuated until the average photon number is much less than one, resulting in potentially large dead times between events and increased detector dark counts. For many

applications (including QKD), sources capable of generating entangled *pairs* of photons offer significant advantages. Here, the arrival of one photon from the pair can be used to herald the emission of the other, triggering the second detector only when a photon is available. Besides enabling improved macroscopic sources of single photons, entangled photon pairs have themselves proven an invaluable resource to quantum applications. Using pairs generated by atomic cascades, such states were used in the first tests of Bell's inequalities [95, 57, 11]. More recently, spontaneous parametric down-conversion (SPDC) has been used to generate entangled photon pairs. Here, a high-energy photon is converted into two lower energy photons using the the  $\chi^{(2)}$  nonlinearity of crystals such as KDP, BBO, LBO, or LiNbO<sub>3</sub> [323]. Despite the inefficiency of the pair creation process ( $\approx 10^{-7} - 10^{-11}$ , [218]), these sources show improved brightness over atomic cascades. Additionally, SPDC sources show retention of polarization correlation, broader operating wavelengths, ease of coupling, and generally less experimental complexity, and have become the preferred source of correlated photon pairs. Even today, these remain the workhorses of quantum-optics experiments [218, 324].

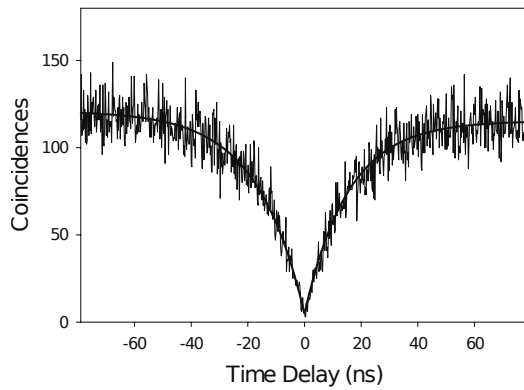
Like the attenuated lasers, however, photon emission from macroscopic parametric sources is still subject to Poissonian statistics. These must be similarly attenuated to reduce the probability for multiple pair emission, thereby limiting the rate and reliability of single photon emission. Even then, there remains a finite probability of obtaining multiple emission events, no matter how much the source is attenuated. By contrast, photon emission from single *nanometric* objects is inherently far from Poissonian. We can often model atom and atom-like emitters as two-level systems, with a single ground and excited state. The system emits a photon when it decays from the excited state, but cannot emit any additional photons until it has been excited again. This process imposes a delay between emission events, resulting in anti-bunching of the photons. Anti-bunching is verified by measuring the second-order correlations between photons. This method, developed by Hanbury Brown and Twiss for measuring coherence from astronomical sources [121], circumvents the dead time of the detectors by using a beam splitter to send the photons to two separate detectors. When a photon arrival is measured on one detector, a counter begins recording the time until a photon is



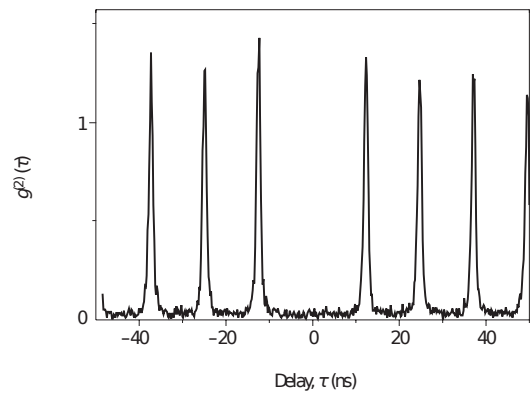
(a) Schematic of a two-level atom.



(b) Schematic of a photon-correlation measurement setup, from [29].



(c) Continuous correlation measurement, from [216].



(d) Pulsed correlation measurement, from [29].

Figure 2.1: Photon correlation ( $g^{(2)}$ ) measurements.

found at the second detector. After correcting for the path lengths of the different beam paths, the resulting distribution  $g^{(2)}(\tau) = \frac{\langle I(t+\tau)I(t) \rangle}{\langle I(t) \rangle^2}$  is recorded as a function of the time delay,  $\tau$ . At zero delay,  $g^{(2)}(0)$  gives a quantitative measurement of the probability of multi photon emission. For a thermal source, photon emission is bunched and  $g^{(2)}(0) = 2$ . A coherent source, such as a laser, will show  $g^{(2)} = 1$ . For a source exhibiting anti-bunching, however, a characteristic dip will be observed at  $g^{(2)}(0)$ . When  $g^{(2)} < 1$ , only a single photon could have passed through the beam splitter at a time. This dip is therefore the signature of a true single photon source. For  $g^{(2)}(0) < 1/2$ , the measurement corresponds to the  $n=1$  Fock state, indicating the presence of only a single quantum emitter. A minimal  $g^{(2)}(0)$  is therefore one of the most important metrics for any single photon source [45, 324].

In order to achieve strong anti-bunching, several qualities of the system are immediately apparent. Clearly, the source should exhibit low background fluorescence or quenching from the substrate or other nearby structures. Additionally, a strongly anharmonic energy structure allows for the filtering of multi photon output or unintended excitation and emission of other energy levels.

However, an ideal single photon source requires much more than anti-bunching [218]. In most applications, there is a strong preference for a source capable of producing single photons on-demand, which requires an emission quantum yield near unity and the ability to prepare the excited state with certainty. Beyond the actual generation of photons, achieving a high efficiency implies effective collection of the photons and channeling the emission into a well-defined spatial mode. All-optical quantum computing, for example, could require an efficiency  $> 99\%$  [170] (although this can be relaxed somewhat, if all of the other elements in the system are perfect, [355]), while higher efficiency and lower error rates translate directly into more secure communication for QKD [45].

Along with efficient generation, the speed of generation would directly affect the bit rate for applications in quantum communication or quantum information processing. This rate is primarily determined by the spontaneous emission rate of the emitter, although it is possible to decrease this by coupling to an optical cavity. For QKD, speeds of at least 1-10Gbps are desirable. For more complex applications requiring high numbered Fock states, the time taken to prepare an N-

photon entangled state from single photons increases a  $t^N$  [45]. Recent observations of 8-photon entanglement occurred at a rate of nine events per hour [387]; any practical implementations will clearly require significant improvements.

Another major challenge lies in achieving interference from photons emitted at different times or separate sources, a feature required by applications in linear-optics quantum computation (LOQC), quantum information processing (QIP), and quantum repeaters [45]. This, in turn, requires that the individual photons must be indistinguishable. Indistinguishability is generally measured using a Hong-Ou-Mandel experiment [132], where two photons simultaneously strike a beamsplitter. If the photons are indistinguishable, they will emerge from the same port, resulting in a dip in the coincidence counts for detectors monitoring both outputs. For such interference to occur, the photons must be described by the same coherent wavepacket. This implies that the sources be perfectly tuned and free from spectral diffusion or dephasing, at least within the time frame between the different emission events [312].

Perfectly reproducible energy levels and Fourier-limited linewidths are inherent features of atomic sources, essentially guaranteeing indistinguishability. For solid state emitters, however, sensitivity to the environment due to excess charges on the surface or in wetting layers, defect states, or multi-exciton states can greatly influence the spectra; isolation from such influences is critical for operation in the solid state. Additionally, timing jitter of the emission events due to incoherent pumping can further broaden the emission spectrum and prevent reaching a lifetime-limited linewidth [218].

Beyond electronic influences, thermal broadening due to interactions with phonons can cause exciton lines to overlap in solid state emitters, leading to a loss of single photon characteristics or even luminescence altogether [45]. Even for those sources which have demonstrated room temperature single photon emission, significant linewidth broadening has been observed [245, 34, 217, 89]. While an ideal source would support room temperature operation, even operation at liquid nitrogen temperatures would be a great improvement over a system requiring liquid helium cryostats. Exactly how far this can be pushed will depend upon the application; higher temperature operation may be suitable for QKD, but lack the indistinguishability needed for LOQC or QIP.

Although not strictly necessary, broad wavelength tunability of the emitter is also highly desirable. The ability to precisely control the emission energy could help accommodate fabrication errors (ensuring spectral alignment between different emitters or cavities), correct for spectral diffusion, or dynamically control interaction between different sources. To date, broad tunability has not been achieved in any practical source, [45], although narrowband tuning of various emitters has been accomplished using temperature [86], electric fields [87], Zeeman effect [119], strain [319], free carrier injection [99], photorefractive effect [85], and gas condensation [256, 124]. Additionally, significant progress has been made in wavelength conversion at the single photon level (*cf.* [45] and references therein).

Our ideal source, then, would be a microscopic emitter providing a repeatable, strongly anharmonic energy structure, single photon emission exhibiting clear anti-bunching and a minimal  $g^{(2)}(0)$ , near-unity quantum yield, a narrow, lifetime-limited linewidth, long coherence time, fast emission rate, efficient collection, low sensitivity to environmental factors or drift, a broadly tunable resonance, and high temperature operation. Practically, not all of these will be achievable with a single source, but many of these aspects can be significantly improved by coupling the emitter to a microcavity. Not only can a cavity enhance the spontaneous emission rate of the emitter through the Purcell effect (and thus increase repetition rate and device speed), the cavity can also improve collection efficiency and utilization by channeling emission into a well-defined spatial mode and polarization, enable coupling to other optical elements, and restrict the spectral range of emission, which serves both to filter out unwanted spectral lines as well as increase the indistinguishability of emitted photons. Effective coupling requires a high  $Q/V$  cavity, accurate spatial overlap between the emitter and the anti-node of the cavity mode, and precise spectral alignment of the cavity resonance to the emitter's transition energy; scalability requires a deterministic method to accomplish these objectives. Such a deterministic technique represents a critical element in maximizing the potential of single photon devices.

## 2.2 Emitter types

At this stage, we are primarily concerned with developing a *platform* for emitter integration rather than a specific device. Without any specific requirements for properties such as operating wavelength or emission rate, we will therefore consider the generally properties for different *classes* of emitters, rather than selecting a specific individual material.

Single atomic emitters are perhaps the most obvious single photon source and one of the most ideal. The discrete electronic transitions in atoms provide well-known, perfectly reproducible energy levels. Multi-photon emission can be readily excluded due to the strongly anharmonic level spacing, allowing strongly anti-bunched emission from single atoms or ions; the first demonstration of photon anti-bunching was conducted using an atomic sodium beam, excited by a tunable dye laser [168]. Atomic linewidths are quite narrow, on order  $\approx$  MHz, as well as lifetime-limited, enabling perfectly indistinguishable photons. Due to the absence of other non-radiative channels, the radiative yield is essentially unity and the entirety of the oscillator strength lies in a single transition, making them very efficient sources, although the speed is limited by moderately long radiative lifetimes  $\approx$  30 ns. Finally, atoms and ions are stable under illumination, and do not suffer from photobleaching or long-lived dark states. In nearly all ways, atoms and ions make ideal single photon sources. Unfortunately, the isolation and trapping of atoms requires complex instrumentation, employing several high-resolution stabilized lasers and ultrahigh vacuum systems. The operating time of atomic single photon sources is determined by the dwell time of the atom; even with advanced far-off-resonance traps (FORT), this limits the number of generated photons to  $\approx 10^4$  [240]. While excellent for demonstrations, this complexity greatly restricts the scalability of atomic single photon systems.

The first observations of anti-bunching in condensed-matter utilized organic molecules [23], which were also one of the first systems to exhibit room-temperature single photon emission [217]. Due to coupling with molecular vibrations, the emission peaks of molecules are significantly broadened as compared to atomic lines. At room temperature, only very broad absorption and emission bands appear, although the fluorescence quantum yield can remain above 90%. As the system approaches cryogenic temperatures, individual bands become apparent, with fluorescence showing deep anti-

bunching and damped Rabi oscillations [23]. In particular, the zero phonon line (ZPL) becomes discernible below  $\approx 50\text{K}$  in soft molecular matrices. This band, corresponding to a transition between the ground vibrational states of the ground and excited electronic levels, has a narrower width determined by the long lifetime of the excited state ( $\approx \text{ns}$ ) rather than short vibronic lifetimes (typically in the ps range). At the lowest temperatures, the ZPL is often lifetime-limited, making it the only line capable of producing indistinguishable photons [218]. Unfortunately, while molecules often show high overall fluorescent efficiencies, only a small portion of the emission comes from the ZPL. The Debye-Waller factor, which compares the ZPL intensity to the total absorption spectrum, is typically around 0.1 at liquid He temperatures and quickly decreases as the temperature rises, while the ZPL width continues to broaden [218]. Despite the potential as a room temperature single photons source, obtaining indistinguishable requires cryogenic temperatures, while filtering the emission to include only the ZPL results in a loss of 80-90% of the fluorescence.

Besides the emission bands, molecular emitters have complex upper vibronic levels. These higher singlet levels undergo rapid relaxation ( $\approx \text{ps}$ ) to the lowest singlet state, but do not emit photons. Under conditions of off-resonant pumping or the absorption of multiple photons, this rapid decay process results in the emission of only a single photon. While this enables incoherent pumping for single photon emission from molecules, such a system could not be used for QIP, which requires a reversible process [45].

Perhaps the most severe limitation of molecular emitters is poor photostability. As a consequence of the higher vibronic levels, many highly excited molecular states are accessible. Not only can these excite long-lasting metastable dark states during which emission is suppressed [401], but the higher molecular levels can trigger photochemical processes which result in the irreversible destruction of the molecule. Under optimal conditions, molecular lifetime can reach hours. This requires protection from atmospheric oxygen by embedding the molecule within a crystalline host, as well as liquid helium temperatures. At room temperature, thermal fluctuations can excite the photochemical processes, exacerbating problems with dark states and greatly reducing lifetime. Even within a crystalline host, molecular lifetime at room temperature can be reduced to minutes [92, 186], while

dyes in a polymer matrix may only last seconds under typical excitation intensities. A potential alternative is the use of multichromophoric systems. Here, many individual chromophores can each absorb the excitation pulse, but the system still only emits a single photon due to a similar rapid decay process and singlet-singlet annihilation. While these systems are susceptible to the same photobleaching processes as the single molecular emitters, neighboring fluorophores can continue emission after one of them is photobleached, as long as the bleached fluorophore does not act as a quencher. The lifetime of such assemblies can therefore be greatly extended due to the number of available emitters; durations of hours have been observed for single polymer molecules on glass slides [193].

For scalability, the source must not only have excellent emission properties, but must also be readily integrated and highly stable. Consequently, neither single atoms nor single molecules are suitable emitters. Instead, we consider several other solid state emitters based on crystalline materials. Broadly speaking, these fall into three categories: color centers, colloidal quantum dots (often referred to as “semiconductor nanocrystals”), and self-assembled quantum dots (often “epitaxial quantum dots,” “semiconductor quantum dots,” or simply, “quantum dots”).

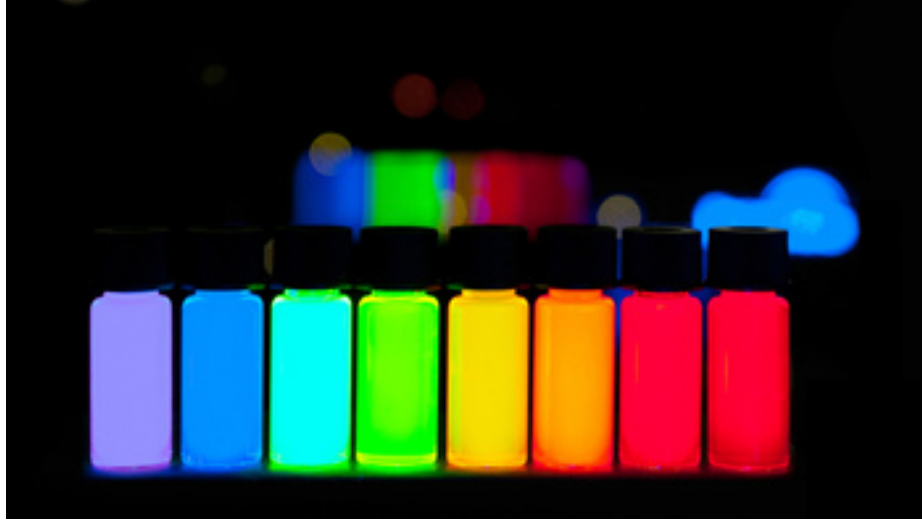
Color centers are formed by introducing certain defects into inorganic crystals. The defects, which can be interstitial atoms, substitutional impurities, or vacancies, create localized electronic states which can often exhibit fluorescence. Some such defects have been found to yield discrete fluorescence bands with properties suitable for single photon generation. In general, these have photophysical properties which are similar to organic molecules, but with lower broadening due to the stiffness of the crystalline matrix. As with molecules, color centers exhibit blinking and can suffer from long lived dark states. Proximity to surface charges or defects can also damage the luminescence properties or modify lifetimes. As compared to molecules, the primary advantage of color centers is the excellent photostability provided by the protection from oxygen or other environmental factors which can degrade the molecule [218, 45].

The nitrogen-vacancy (NV) center in diamond was the first single color center discovered [115] and has also become the most widely studied. This defect contains a trapped electron, and is

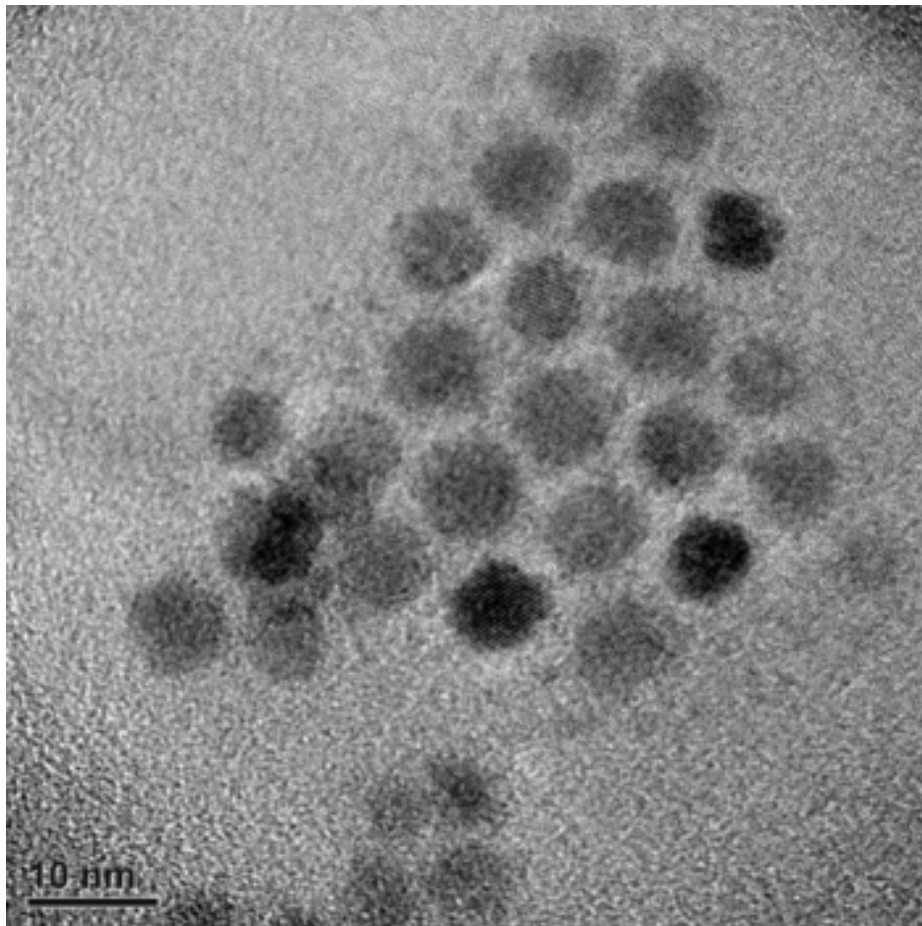
formed by a substitutional nitrogen atom adjacent to a carbon vacancy in the diamond lattice. NV centers have a spontaneous emission lifetime is 12 ns, with a weak ZPL at 637 nm alongside a broad phonon sideband spanning 637 nm - 720 nm. The photostability is excellent and because the ZPL is still visible at room temperature, the defect is capable of producing single photons under ambient conditions [115]. Although diamond is difficult to fabricate and the luminescence is sensitive to etch damage and other surface defects, there has been some success integrating diamond nanocrystals into other resonators [17, 81, 313] and directly fabricating structures in diamond [84, 124]. In spite of this success, however, the ZPL has a linewidth of  $50 \text{ cm}^{-1}$ , making the emission very far from lifetime-limited. As such, NV centers are not capable of producing indistinguishable photons.

The task remains to find an ideal color center suitable for fast, indistinguishable single photon generation, but there are numerous possibilities. Currently, over 500 color centers have been documented in diamond alone [394], while many researchers are turning to other materials such as SiC [174]. Other donor impurities in semiconductors have shown atom-like homogeneity and coherence. Utilizing excitons bound to isolated fluorine impurities in a ZnSe/ZnMgSe quantum-well, [308] reported an indistinguishability of 65% for photon emission between two independent impurities at 6K. The individual defects exhibited  $g^{(2)}(0) = 0.41$  and 0.25, consistent with single quantum emitters, and maintained spectral alignment within the resolution of their spectrometer. Combined with a lifetime below 100 ps, these provide a very compelling combination of atomic and solid-state properties.

Colloidal quantum dots (or semiconductor nanocrystals) are discrete crystalline particles a few nanometers in diameter. The basic electronic and optical properties develop from that of the bulk electronic band structure. As dimensions decrease below that of the Bohr exciton radius, however, quantum confinement induces the emergence of discrete exciton energies. For decreasing sizes, excitation energies are blue shifted while the oscillator strength is concentrated into fewer transitions [5]. Dubbed “artificial atoms,” the discrete spectra of colloidal quantum dots resemble those of molecules, with a ZPL and a weak phonon sideband, but can be tuned by varying the size and composition of the structure. The most highly studied examples are II-VI semiconductors such as



(a) ZnCdSe alloyed quantum dots are highly luminescent and available over a broad wavelength range. Because the emission spectrum is tunable by varying alloy and particle dimension, these artificial atoms could enable highly flexible cQED systems. From [280].



(b) TEM of PbS QDs dispersed on a holey carbon grid.

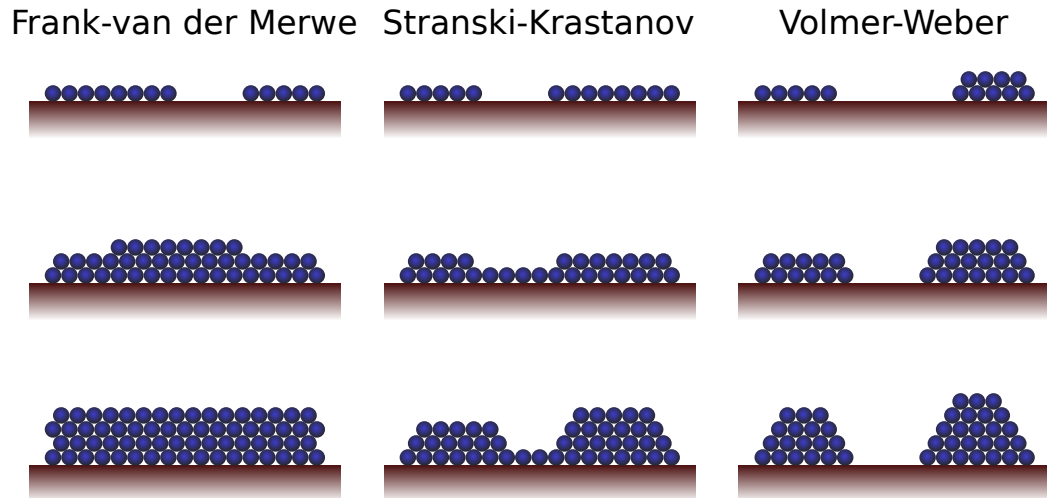
Figure 2.2: Common colloidal quantum dots.

CdSe which produce visible spectra, although emission wavelengths spanning the visible and near-IR communication bands are now available.

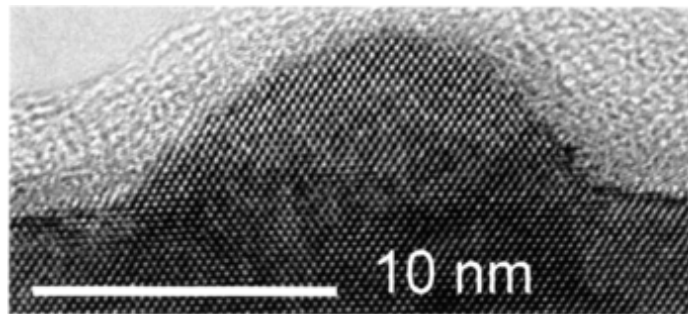
Anti-bunching in colloidal quantum dots was first observed in 2000 using CdSe/ZnS core/shell dots at room temperature [245, 216]. This is at first surprising; in contrast to atoms, molecules, and color centers, the luminescence from nanocrystals involves a large number of optically active electrons. While these could lead to multi-exciton states in principle, higher excitations are effectively quenched by Auger recombination, occurring over time scales of  $\approx 20$  ps compared to a luminescence lifetime  $\approx 20$  ns at room temperature [216]. The broad absorption bands therefore support radiative quantum yields near unity, allowing for efficient single photon generation even under incoherent excitation.

Unfortunately, colloidal quantum dots suffer several major challenges. While they exhibit excellent photostability, they are much more susceptible to blinking than organic molecules due to the occasional transfer of charge carriers out of the device. The remnant free charge quenches further excitations, and can remain for long durations [218]. Additionally, colloidal quantum dots are extremely susceptible to dephasing and spectral diffusion. Spontaneous fluctuations and charge reorganization in the local electrostatic environment lead to persistent diffusion [111, 90, 77]. At room temperature, ZPL linewidths are typically several hundred  $\text{cm}^{-1}$ . Although this reduces to  $\approx 1 \text{ cm}^{-1}$  at cryogenic temperatures, the emission is still quite far from Fourier-limited. So far, this has precluded the generation of indistinguishable photons from colloidal quantum dots. Spectral measurements, however, typically require integration times on order seconds to minutes, during which significant diffusion can occur. Recent work [206] suggests that the linewidth of CdSe/CdZnS core/shell quantum dots reaches an asymptotic limit of  $12 \mu\text{eV}$ , or  $\approx 0.1 \text{ cm}^{-1}$ ; other authors have measured linewidths as low as  $400 \text{ MHz}$  ( $1.65 \mu\text{eV}$ ,  $0.013 \text{ cm}^{-1}$ ) with fast scans [90]. Combined with recent efforts to reduce blinking [228], greater environmental isolation, and strong Purcell enhancement through efficient cavity coupling, this could enable indistinguishable photon generation using colloidal quantum dots, at least over short timescales.

To date, the most promising candidates for solid state quantum light sources are self-assembled



(a) Illustration of different epitaxial growth modes. As adatoms diffuse across the surface, they settle at different locations depending on the relative adhesion between the surface and other adatoms. In Frank-van der Merwe growth, the adhesion to the surface dominates, resulting in smooth, layer-by-layer growth. At the other extreme, Volmer-Weber growth proceeds by droplet formation and agglomeration. Stranski-Krastanov, which lies in between these extremes, begins by the formation of a wetting layer. As the wetting layer thickness, a misfit strain accumulates due to lattice mismatch. Beyond a critical thickness, the strain is relieved by the formation of islands.



(b) Cross-sectional TEM of an uncapped InAs-GaAs self-assembled quantum dot. From [96].

Figure 2.3: Self-assembled quantum dots and growth modes.

quantum dots. These are discrete islands of a low band gap semiconductor grown on a higher band gap substrate. These are most commonly formed by Stranski-Krastanov growth, where the dots form spontaneously during hetero-epitaxy. This process occurs when there is a moderate lattice mismatch between the substrate and epitaxial layer. During the first few monolayers, the strain can be accommodated and a uniform wetting layer grows layer-by-layer. Beyond a critical point known as the Stranski-Krastanov instability, however, the incremental energy required to overcome the strain due to mismatch exceeds the increased surface energy necessary to form individual clusters. The elastic energy relaxes by separating into discrete islands, which continue to grow outwards from their nucleation site. The structures are usually protected by subsequent growth of a thick capping layer with a high band gap, which isolates the dot from surface defects and other trapped charges, leading to increased photostability. Epitaxial quantum dots can also be formed by Volmer-Weber growth, which proceeds without a wetting layer under conditions of greater lattice mismatch, or droplet epitaxy, where droplets of group-III material are crystallized by exposure to group-V flux.

Self-assembled QDs exhibit excellent photostability, with only occasional blinking no long-lived dark state. The spontaneous emission rate is much faster than other quantum emitters ( $< 1ns$ ), and Fourier-limited linewidths are possible at cryogenic temperatures (5-10K), where quantum yield is thought to be near unity. At higher temperatures, excitons can escape towards the wetting layer, reducing the emission efficiency. Indistinguishability  $> 80\%$  has been demonstrated for photons from a single dot [312, 30, 356, 190], and more recently, from two individual, remote quantum dots [274, 91]. Unlike atoms and molecules, individual quantum dots can vary slightly in size, composition, and environment, all of which can affect their emission characteristics. Achieving interference between photons from two distinct quantum dots therefore represents a significant achievement. Besides these achievements, epitaxial quantum dots have been utilized for QKD [246, 144], a single photon laser [263], as well as high-temperature, electrically pumped single photon sources operating up to 80K [290].

Unlike the luminescence from organic molecules, color centers, and colloidal quantum dots, the spectra of self-assembled quantum dots do not show significant phonon sidebands, and often exhibit

multiple discrete exciton lines [244]. This is likely a result of the higher purity and better crystal quality of grown QDs compared to nanocrystals, as well as a consequence of decreased Coulomb interaction between carriers and excitons due to larger sizes [218]. For a single photon source, these additional lines must be spectrally filtered, although some work has been done to use both the exciton and bi-exciton emission for correlated photon pairs [31], while the bi-exciton line has also shown anti-bunching [347, 403] and could be a separate source for single photons.

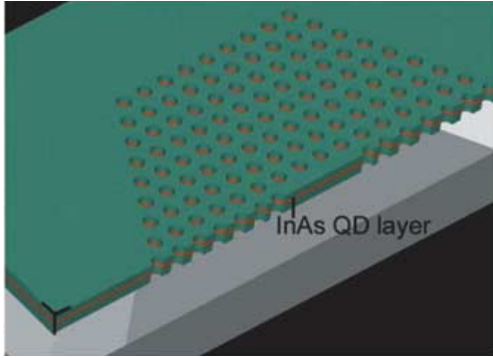
Of the available quantum light sources, epitaxial quantum dots, colloidal quantum dots, and color centers show the greatest potential for integration and scalability. So far, epitaxial quantum dots have exhibited the best emitter characteristics, including Fourier-limited linewidths and rapid spontaneous emission rates. They also benefit from shared fabrication technology with other semiconductors, offering a natural opportunity for integration with photonic structures as well as electrical connectivity. However, these still face challenges. Extending the operating window to higher temperatures is highly desirable for practical devices. Growth uniformity and determinism require substantial improvements to achieve proper spatial and spectral matching on demand. Additionally, current epitaxial processes impose greater constraints on other aspects of the system, including restriction of the substrate material, presence of thick buffer and capping layers, and limitations on thermal budget. While the search for an ideal nanocrystal color center or colloidal quantum dot continues, there remains significant potential for integration techniques which could utilize these emitters. Besides the possibility of higher temperature operation, these could naturally allow for separation of material systems, permitting independent selection of optimal emitter, photonic, and possibly electronic components. The discrete nature of these elements would allow pre-selection of the emitters, which might prove critical to achieving proper spectral overlap between cavities or remote emitters. Additionally, the use of discrete particles encourages an integration process which is not specific to the emitter itself. Depending on the details of the integration process, it has the potential to be readily applied to new emitters as they become available, whereas specifics for the epitaxial process are greatly affected by the exact materials and geometries used.

## 2.3 Existing integration methods

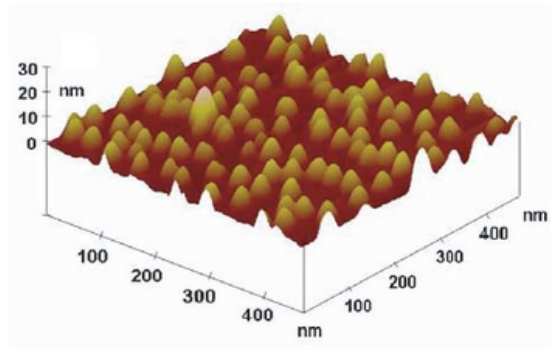
The first demonstrations of cavity coupling with quantum emitters took place in the 1970s, showing Purcell enhancement of molecular complexes on metallic mirrors [185, 48]. This was extended to atomic emitters about a decade later, with the first observation of Purcell enhancement for a single atom taking place in 1983 [110]. Nearly another decade passed before cQED reached the regime of strong coupling, beginning with measurements of optical bistability with  $N = 18$  atoms 1991 [292] and vacuum Rabi splitting with  $N = 1$  atom shortly afterwards [346].

Up to this point, the emitters were obtained from atomic beams, which primarily results in ensemble measurements; measurements on single atoms were difficult to obtain due to the extremely short dwell times within the cavity. Around this same time, however, two major breakthroughs occurred: the development of the magneto-optic trap (MOT) in 1987 [288] followed by the far-off-resonance trap (FORT) in 1993 [247]. These systems enabled the cooling and trapping of neutral atoms, which would profoundly advance atomic cQED systems. Single Cs atoms were observed in an MOT in 1994 [137], after which the system was employed to drop single emitters from an MOT directly into a high-finesse Fabry-Perot resonator in the regime of strong coupling [227]. It was not long before a FORT was integrated which could trap the atom directly in the cavity anti-node [389], enabling atomic dwell times of nearly  $30ms$ . A flurry of demonstrations continued over the next decade, including *single photon* atom traps [279], the *deterministic* emission of single photons from a single atom using a stimulated Raman transition [184], a single atom laser [239], *deterministic* single photon emission from a single *trapped* atom [240], and photon blockade from a single trapped atom [37]. As further improvements to the high-finesse Fabry-Perot mirrors began to face significant technical challenges [135], more recent experiments have begun exploring the strong coupling of atomic emitters to lithographic cavities, beginning with ultrahigh-quality toroidal resonators [6], and more recently, schemes to utilize photonic crystal nanobeams [140, 391].

While significant advances in atom trapping eventually led to lifetimes of several seconds [241], all of these schemes suffer from the finite dwell time of the atom in the cavity, and greater scalability is further impeded by the substantial experimental complexity required for even a single trap. Fueled



(a) Schematic of a solid state cQED system comprising a 2D slab photonic crystal with embedded InAs QDs.



(b) AFM showing the distribution of InAs QDs within the active layer. The scan was performed on the InAs QD layer prior to growth of the capping layer.

Figure 2.4: One of the first solid-state cQED systems. From [390].

by the tremendous successes in atomic cQED, researchers began translating the experiments into solid state cQED systems, which would enable indefinite probing of the same emitter and potentially scale to large, coupled systems. The developmental sequence followed a similar path, beginning with enhanced and suppressed spontaneous emission from quantum wells which were weakly coupled to micropillar cavities [383, 151]. Purcell enhancement of quantum dot ensembles was demonstrated in 1998 [105], followed shortly by single quantum dots [328, 327, 362] and cavity-enhanced single photon emission from single quantum dots [275]. In 2004, strong coupling in the solid state was finally achieved, with simultaneous reports of Rabi splitting for single self-assembled quantum dots in 2D photonic crystal slabs [390] (see Figure 2.4) and micropillar [291] cavities. Within a few years, strong coupling with self-assembled quantum dots was also observed in microdisk resonators [334] and 1D photonic crystal nanobeams [272]. During the same period, experiments were reported of other cavity-coupled solid state emitters, including the coupling of colloidal PbS quantum dots suspended in a polymer layer over a 2D photonic crystal slab [98], molecular emitters in a lithographically-defined polymer region [297], and NV centers in etched into monolithic diamond ring resonators [84] and photonic crystal nanobeams [124].

While each of these experiments achieved fixed coupling between the emitter and cavity, none of the integration methods were deterministic and could not be readily scaled. In each case, the emitters were composed of a random distribution, due to either the stochastic nature of SK growth,

arbitrary location of colloidal and molecular emitters within the polymer matrix, or random location of the NV centers. The *likelihood* of overlap between the cavity anti-node and emitter position is a function of the emitter density, and can therefore be controlled to some extent. Beyond a certain point, however, increasing the density also increases the risk of coupling multiple emitters with the same cavity. The optimal density is therefore a compromise between the likelihood of achieving coupling at all and coupling to multiple emitters at once. Producing a functioning device is inherently tedious, requiring the fabrication and testing of many cavities in order to find the one which happens to have reasonable alignment (both spectrally and spatially) of the emitter and cavity. Even aided by automation, the process remains probabilistic at best and far from scalable.

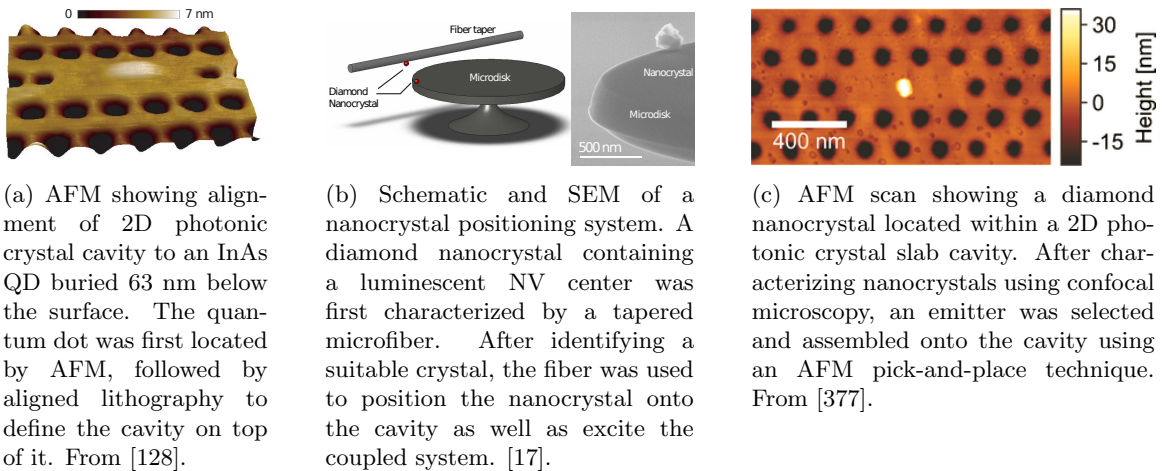


Figure 2.5: Existing methods for deterministic emitter integration.

In response, several groups began developing *deterministic* integration methods. Shortly after the initial demonstrations of strong coupling in the solid state, Badolato *et al.* [14] reported the first deterministic integration technique in 2005. The substrate contained a random distribution of SK-grown semiconductor quantum dots, but rather than a single layer, a total of six dot layers were stacked together. As before, the initial layer consisted of randomly dispersed dots. To distinguish it from subsequent growth, the dot spectra were blue-shifted by an *in situ* anneal while depositing a capping layer. Following this, the subsequent QD layers were grown. Unlike the first, however, their locations were not random. Due to strain correlations in the growth process, the first QD layer acted as a seed layer for subsequent growth, resulting in vertical stacks of quantum dots. While a single

QD could be difficult to locate in an electron microscope, the combined stack was visible, acting as a tracer through which the original dots could be located prior to lithography. After substrate growth was complete, gold markers were lithographically patterned on the surface. By imaging the chip in a scanning electron microscope (SEM), the relative location of the quantum dots was recorded. Using these locations, site-specific cryogenic micro-photoluminescence ( $\mu$ PL) was used to verify the presence of the quantum dot and record its emission spectra. Standard lithographic and etching techniques could then be used to define square-lattice photonic crystal cavities which precisely matched the position and resonance wavelength of the individual quantum dots. Rather than precisely matching, however, cavities were designed with slight red shifts. Following fabrication, these could then be tuned precisely using a digital etching technique, enabling high-accuracy, deterministic integration with simultaneous spectral and spatial overlap. The authors reported a spatial accuracy of approximately 25 nm, and spectral alignment below 1 nm, close enough to permit further tuning by applying magnetic fields or varying temperature. Although they were not able to show evidence of strong coupling, significant Purcell enhancement demonstrated the effectiveness of the technique.

Subsequent efforts were able to achieve strong coupling. Two years after the first report, the same group report strong coupling from a deterministically integrated quantum dot. They used a similar approach, but employed atomic force microscopy (AFM) to locate the quantum dot rather than SEM [128] (see Figure 2.5a). With a higher-quality L3 photonic crystal slab cavity in place of the square lattice cavity, they were able to show photon anti-bunching by second-order correlation measurements, as well as Rabi splitting based on a spectral anti-crossing. More recently, a similar technique was demonstrated which located the dots using a  $\mu$ PL setup [176]. Not only does this provide a more accessible method of finding the QD than SEM or AFM, the spectral characterization is handled simultaneously, offering significant experimental simplicity. The authors report spatial and spectral alignments of  $<50$  nm and 4 nm, respectively, as well as Rabi splitting with a coupling coefficient of  $57.5\mu\text{eV}$  ( $\approx 14$  GHz).

Along with the techniques for aligning cavities to epitaxial quantum dots, various other approaches to deterministic integration were developed for nanocrystalline emitters. Barclay *et al.*

[17] used a fiber taper to probe the spectrum of NV centers in individual diamond nanocrystals, place a single nanocrystal onto a disk resonator, and evanescently couple to the resonator, achieving a position accuracy of  $\approx 100$  nm and coupling rate 28 MHz (Figure 2.5b). Using a confocal microscope to perform second-order correlation measurements, Wolters *et al.* [378] identified diamond nanocrystals with single NV centers. The selected diamonds were then aligned and assembled onto a pre-characterized L3 photonic crystal cavity using an AFM (Figure 2.5c). The system exhibited cavity-enhanced ZPL emission with a Purcell factor of 12.1. A similar report using pre-characterized diamond nanocrystals and an SEM nanomanipulator claimed a Purcell factor of 25 for the ZPL emission [313]. Finally, Englund *et al.* [81] select diamond NV centers embedded in a polymer host using PL. Rather than place these onto the cavity, however, they transfer the cavity to a polymer stamp, and place the cavity itself onto the diamond-doped film. A noteworthy feature of these techniques, as compared to those described above for integrating epitaxial quantum dots, is the separation of material systems between the cavity and emitter, allowing essentially independent and optimal selection of them both. Although none of these techniques have yet to achieve strong coupling, their methods have demonstrated great success in achieving deterministic coupling of individual nanocrystals, and could readily be applied to emitters with more optimal properties as they become available.

## 2.4 Development of deterministic coupling techniques

Deterministic integration techniques have made remarkable strides, yielding extremely accurate spatial and spectral overlaps between a variety of atom-like emitters and cavities, including strong coupling in certain systems. The remaining quality which has yet to be demonstrated, however, is scalability. For the systems employing epitaxial quantum dots, the extension to increasing numbers of cavities has thus far been hindered by the random locations of the emitters, as it would require redesigning the optical circuit for each individual substrate. Although the techniques for integrating nanocrystals could align multiple emitters into pre-designed photonic systems, at least in principle, the selection, characterization, and pick-and-place alignment processes are as yet too laborious for

scalable fabrication. We therefore considered a few potential methods to achieve deterministic integration in a scalable manner, with simultaneous spectral and spatial overlap, while attempting to retain the flexibility of independent cavity and emitter material systems.

## 2.4.1 Semiconductor heterogrowth

### 2.4.1.1 Directed growth

Given the success with SK quantum dots in cQED systems and their excellent properties as emitters, the ability to exercise deterministic control over their growth has been highly sought after. Recent years have shown significant progress in selective-area heteroepitaxy using a wide variety of methods to direct the growth. These generally operate by controlling nucleation of the dots, either by patterning thin amorphous mask layers such as  $\text{Al}_x\text{O}_y$ ,  $\text{SiO}_2$  and  $\text{Si}_x\text{N}_y$  [39, 38, 162, 73, 379, 384, 196] or etching pits into the substrate itself [146, 175, 147, 329, 12]. Under the appropriate growth and masking conditions, these are thought to confine adatom diffusion within the regions of interest, through which the location of the emitter can be determined. Alternatively, organized nanowire arrays have been grown using templated catalyst droplets in vapor-liquid-solid (VLS) processes [226]. In particular, the use of nanowires could provide an interesting way to isolate the emitter from the substrate and embed it within the center of the anti-node, rather than at the cavity surface. Tatebayashi *et al.* [345] recently reported single photon emission from a site-controlled InGaAs/GaAs QD-in-nanowire, exhibiting  $\mu\text{PL}$  linewidths of  $87\mu\text{eV}$ , a second-order correlation  $g^{(2)}(0)$  as low as 0.11, anti-bunching and cascaded bi-exciton emission.

Of these selective-area growth techniques, the methods employing lithographic control show the greatest promise for cQED systems. In addition to precise spatial alignment of the emitter, deterministic growth could potentially be used to define the cavity *in situ*. Scofield *et al.* [318] developed a bottom-up photonic crystal laser, where the cavity and gain material were simultaneously formed by growing GaAs/InGaAs/GaAs nanopillars on GaAs substrates through a thin  $\text{SiO}_2$  mask.

Ideally, the use of patterned substrates would also permit a broader, more independent selection

of materials for the substrate and emitter than typical III-V combinations. Although the influences of crystal symmetry, lattice matching, and band alignment must still be considered, the ability to relieve strain in multiple directions leads to an order-of-magnitude increase in the critical radius for nanowire growth as compared to planar 2D limit [82, 402], resulting in higher quality growth with fewer defects [52, 399, 384, 198]. One of the most appealing combinations is InAs (and similar III-Vs) on Si, which has a very high lattice mismatch of 11.6%. As a platform for passive photonic devices, silicon-on-insulator (SOI) is nearly ideal, providing high index contrast, excellent loss factors, and extremely mature processing technology, making an ideal material system for the cavity fabrication. Additionally, silicon's prevalence in the electronics industry could provide a natural route to large-scale electronic integration. While the indirect band gap is normally a limitation for active photonics applications, in this case it could actually be a benefit due to the lower background emission from the substrate.

Reports of epitaxial growth InAs on Si began with randomly-organized InAs islands and Si capping layers. At optimal conditions, Heitz *et al.* [126] observed the formation of coherent islands with diameters in the range 2 - 4 nm. At cryogenic temperatures, these also produced a broad photoluminescence peak around 1.3  $\mu\text{m}$  as well as several secondary bands at shorter wavelengths. The exact locations depended strongly on the excitation energy, with spacings consistent with phonon-assisted emission. A subsequent report from the same group [395] investigated the diffusion of InAs into the Si capping layer, which they found to be an ordered solution which extended the effective dot size slightly to  $\approx 6$  nm, providing greater carrier confinement which enhanced the photoluminescence. Hansen *et al.* [122] explored larger dots. For fewer than 1.7ML and diameters below  $\approx 30$  nm, progressively longer growth times would primarily produce dots with greater heights, showing little change in diameter, while additional growth above this threshold tended to segregate into increasingly larger islands. This suggests SK growth with a critical diameter, above which coherent growth might no longer be possible. Using different conditions, Zhao *et al.* [400] demonstrated VW mode growth nucleating below 1ML, which also showed diameters in the 10 - 25 nm range.

Suggesting that the poor or negligible optical performance of the previous work was due to high defect density in VW growth, Zhao *et al.* [399] employed patterned substrates to grow GaAs seed layers, onto which InAs dots could be grown with higher quality. Their process used an SiO<sub>2</sub> mask with 250 - 300 nm holes and a fairly thick buffer layer of 400 nm, although the authors mention this was done to improve PL visibility and could be substantially thinner. For apertures this large, multiple dots with slightly varying sizes can grow on the same GaAs pillar. Although dot geometry was not characterized in this study, the same conditions yield QDs with  $\approx 20 - 30$  nm diameters on bulk GaAs substrates. Ensemble photoluminescence measurements revealed a linewidth of 155 meV for measurements up to 130K. A follow-up report explored the effect of hole size and the presence of the oxide mask [125], confirming preferential nucleation within the holes, an absence of growth on the oxide layers, higher quality growth on the masked sample showing multiple resolvable peaks with linewidths down to 50meV, and a transition to 3D growth at smaller aperture sizes. Wang *et al.* [371] used a diblock copolymer mask to create even smaller apertures, down to 20 nm. These produced extremely high quality QDs, with only a single InAs dot for each opening which exhibited coherence and required only a minimal GaAs buffer.

Current developments have shown lasing from random SK InAs QDs grown on Si using thick GaAs buffer layers [370] as well as InGaAs/GaAs heterostructure nanopillars grown monolithically on silicon [50]. Single photon emission has been observed for GaAs dots on silicon substrates [47], albeit with very thick buffer layers, while  $\mu$ PL has very recently been reported for single random InAs dots on silicon [33], showing linewidths down to  $150\mu\text{eV}$  [32].

These investigations have shown the effectiveness of decreasing apertures for achieving strain relaxation and confirmed the ability to achieve high-quality growth on mismatched substrates. Together, the studies suggest an opportunity for InAs QDs on silicon as quantum emitters which provide deterministic control over the location. Beyond spatial alignment, these could potentially enable lithographically-controlled spectral properties as well, assuming one could maintain sufficient accuracy of the size. However, the feature sizes needed to produce apertures suitable for single dots are already pushing e-beam lithography to its limits. For VLS growth of InAs nanowires on Si, a

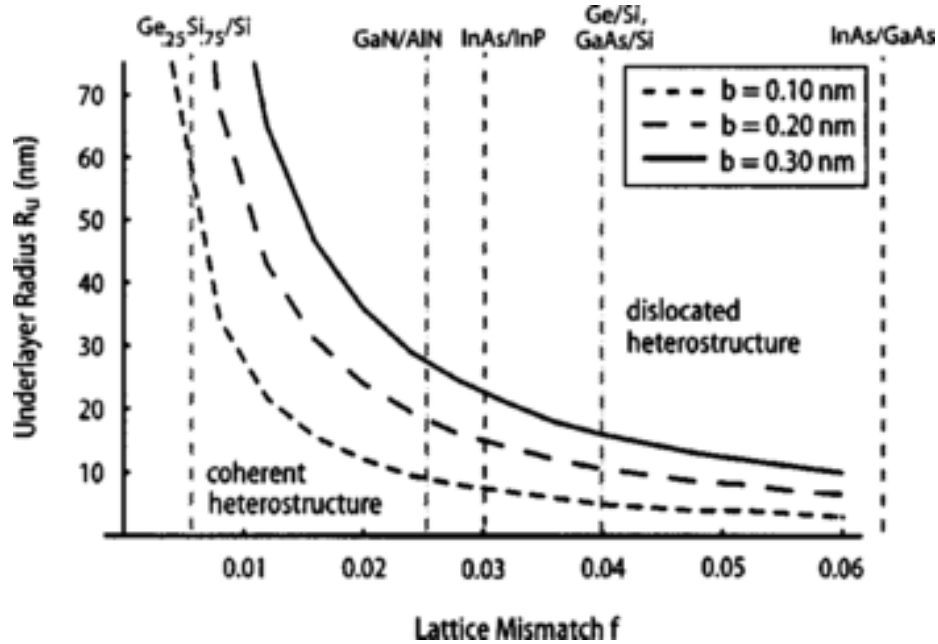


Figure 2.6: Equilibrium diagram showing the critical radius as a function of lattice mismatch for maintaining coherent nanowire growth. From [82].

critical diameter of 26 nm was observed experimentally [55], after which the growth exhibits stacking faults due to twinning between wurtzite and zinc blende crystal structures [253]. This is consistent to the QD dimensions and critical diameters noted previously [122, 400, 399, 371]. For InAs on Si, suitable apertures therefore span the range between the  $\approx 5$  nm originally demonstrated [126, 395] and an upper limit  $\approx 25$  nm.

#### 2.4.1.2 Aperture fabrication process

For the deterministic integration of quantum dots using selective-area heteroepitaxy, our ideal process should combine several features. The growth region must be lithographically defined in order to ensure accurate spatial alignment of the emitters. Background emission must be minimized by selection of a suitable substrate as well as by preventing nucleation outside of the selected area. Besides a low background, the substrate material system should exhibit excellent passive photonic properties for fabrication of the cavity, permitting greater integration with other photonic devices. Finally, the aperture fabrication would ideally enable spectral tuning of the dots as well. For InAs on Si, this implies accurate lithographic control of features between  $\approx 5 - 25$  nm.

# Growth aperture dimension reduction

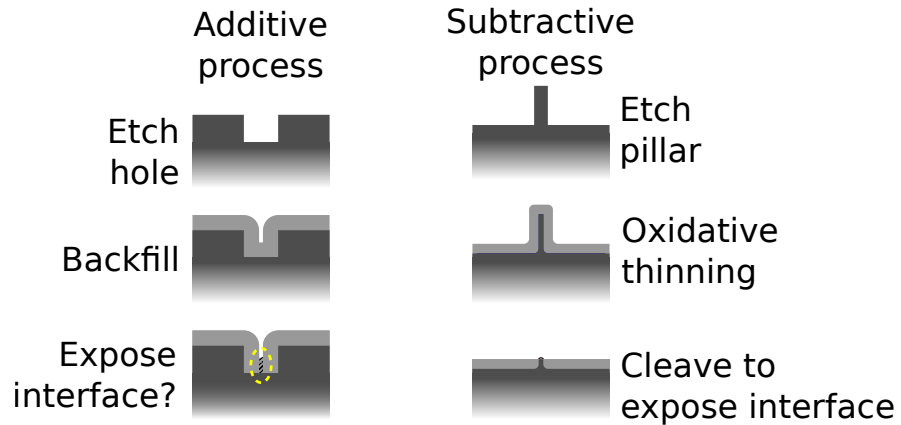


Figure 2.7: Illustrations for additive and subtractive processes to reduce aperture dimensions after lithography.

Creating features of these dimensions is challenging even with modern electron beam lithography, and effectively eliminates any future transition to photolithography for large fabrication. Rather than attempting to directly define sub-10 nm features, we sought methods of shrinking the lithographic features to obtain appropriate growth apertures. In general, these can be grouped into additive or subtractive processes. In an additive process, we would shrink the size of the aperture by the deposition of additional dielectric material to the masking layer, for example using atomic layer deposition (ALD). While such a method could readily achieve the necessary control of the aperture size, these processes are inevitably conformal; coating the aperture sidewalls would simultaneously obscure the crystalline growth template. Highly directional etching could be employed to expose the substrate once more, potentially using the aperture itself as a mask, but this becomes increasingly difficult for smaller diameters, due to the thicker additive layers required to adequately shrink lithographic dimensions and narrower channels which restrict transport of the etchant atoms and products from the deeply recessed core.

As an alternative to additive process, we developed a subtractive method of reducing lithographic

dimensions using thermal oxidation; we described details of this process in [129, 364, 189]. Briefly, nanopillars were etched into bulk silicon substrates using an alumina hard mask and dry etch process. Thermal oxidation reduced the diameters of the silicon cores to 2.5 - 30 nm, while providing a high-quality SiO<sub>2</sub> mask layer over the entire substrate. Immediately before growth, the pillars were mechanically cleaved in order to expose the crystalline core, onto which QD growth was performed using metal organic chemical vapor deposition (MOCVD).

Although we tested a variety of substrates, most of our growth used lightly p-doped <111> silicon. This orientation has been shown to be the preferential growth direction for moderate (10 - 20 nm) Si nanowires [380]. Additionally, <111> is preferred for QD growth due to reduced or eliminated fine splitting by symmetry [345].

In order to maximize our control over the aperture dimensions, we needed to ensure that the nanopillar sidewalls were as smooth and vertical as possible, since edge roughness and sidewall tapers would translate directly into size variation in the core. Because typical polymer masks such as PMMA and ZEP520A do not possess the necessary resilience for such a process, we developed a process to deposit a stoichiometric aluminum oxide (Al<sub>2</sub>O<sub>3</sub>) hard mask in a reactive ion sputtering chamber.

The hard mask was patterned using electron beam lithography and a lift-off process. Because the majority of the surface would be removed during a robust etching process, only a simple cleaning of the substrate with acetone and isopropanol was performed prior to lithography. After cleaning, the wafer was baked on a hot plate 180°C for 3 minutes to dry. Since our lift-off process needed a high-resolution positive resist rather than etch resistance, PMMA was an ideal choice. A thin layer of 2% Microchem PMMA 950k in chlorobenzene (PMMA 950k C2) was deposited by spin coating at 4000 rpm for 60 s with an acceleration of 1330 rpm/s, followed by another 3 minute pre-bake on a hot plate 180°C to drive out solvents in the resist. Reflectometry measurements reported typical resist thicknesses around 103 nm.

Following application of the resist, electron beam lithography was performed in a Leica EBPG 5000+ at 100 kV. Relatively high doses in the range 1100-1200  $\mu\text{C}/\text{cm}^2$  were selected to yield high

contrast development and ensure complete removal of the resist for proper adhesion of the  $\text{Al}_2\text{O}_3$ . Patterns consisted of rectangular and hexagonally-packed arrays of circles, with nominal diameters ranging from 35 nm - 100 nm and typical center-to-center spacings of a several hundred nm. Arrays of pillars were fractured with 2.5 nm beam steps. Given the sparsity of the patterns and lack of sharp corners, proximity error correction was found to yield a negligible difference in pattern accuracy and was generally left out during fracturing. After exposure, samples were developed in a 1:3 mixture of methyl isobutyl ketone (MIBK):isopropanol (IPA) for 30 s, rinsed with IPA for 5 s and dried with nitrogen.

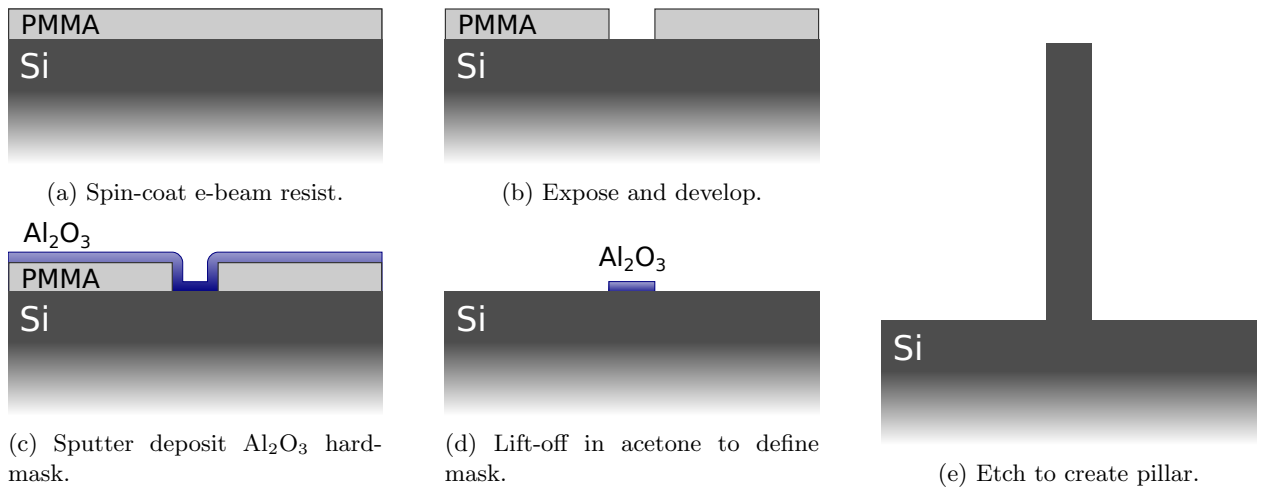


Figure 2.8: Pillar fabrication process.

For the hard mask, we developed a process to deposit stoichiometric aluminum oxide ( $\text{Al}_2\text{O}_3$ , or simply alumina) via reactive ion sputtering [129]. Alumina exhibits extremely high physical and chemical resilience. In particular, the etch product aluminum fluoride is nonvolatile at temperatures below  $1300^\circ\text{C}$  [375], making alumina an ideal etch mask for fluorine-based dry etch processes, even with moderately high accelerating voltages. The use of a highly selective mask permits thinner mask layers, which is critical to achieving accurate nanoscale resolution. In our testing, we found an etch selectivity against silicon of  $\approx 68:1$  in a highly anisotropic mixed-mode  $\text{SF}_6:\text{C}_4\text{F}_8$  process, and  $>5000:1$  in a cryogenic  $\text{SF}_6:\text{O}_2$  process [129].

For the mask deposition, we chose to use DC reactive ion sputtering with a metallic aluminum

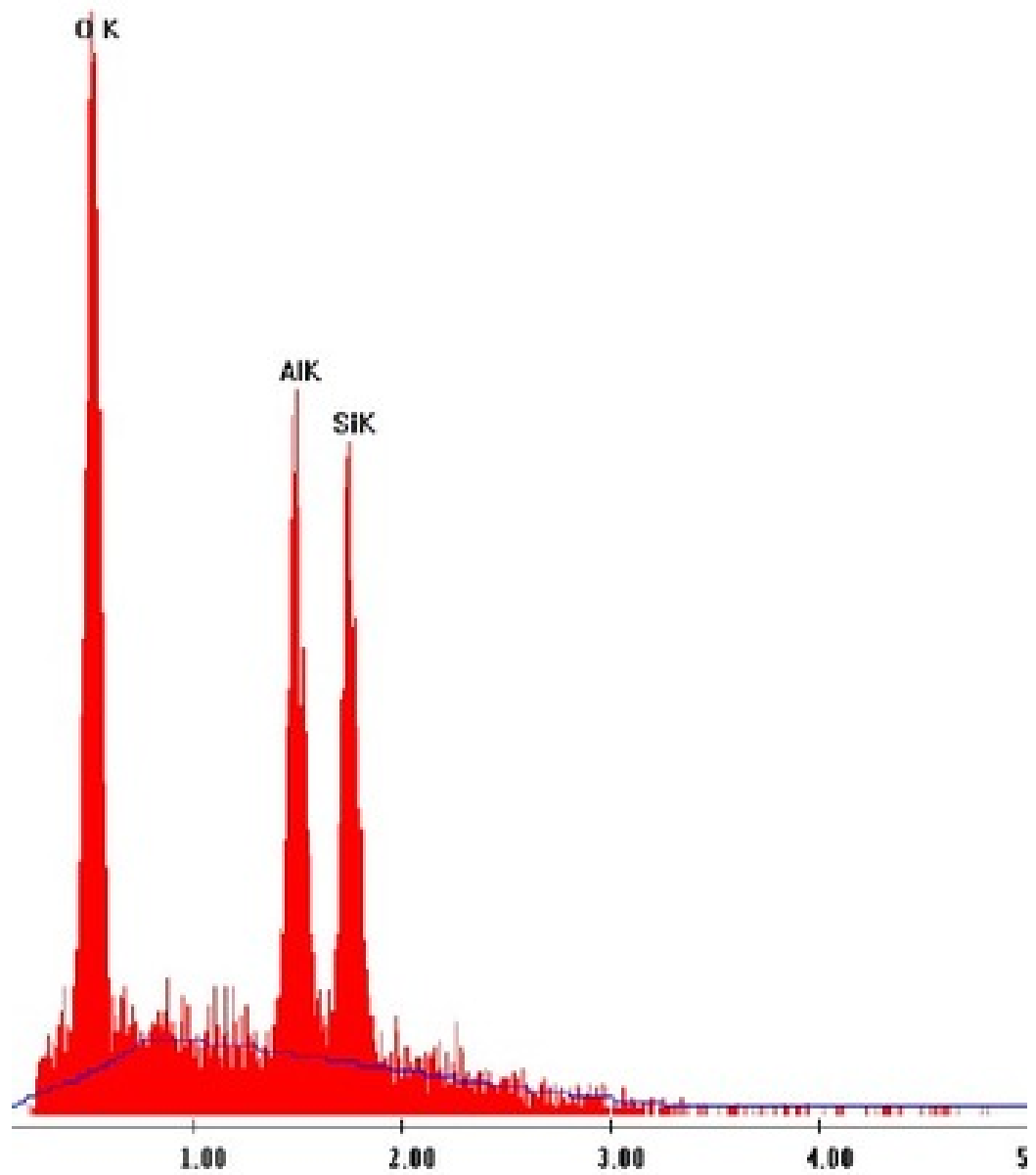


Figure 2.9: EDAX spectrum for the sputter deposited alumina on silicon, showing 2:3 stoichiometric ratio of aluminum to oxygen.

target rather than RF sputtering with a ceramic alumina target and only inert process gas, since the latter tends to produce lower deposition rates. The stoichiometry of the film was controlled by adjusting the ratio of process gas flows. We found a ratio of 5:1 Ar:O<sub>2</sub> to provide suitable results, which we verified with energy dispersive X-ray analysis (EDAX); see Figure 2.9. Care must be taken during such a process to ensure the target surface has not been poisoned by excess oxygen [178]. This results in a hysteretic relationship between the target voltage and oxygen flow rate, requiring that the target be cleaned by an Ar-only plasma to retrace the hysteresis loop and resume alumina deposition. We found the plasma color to provide a valuable indication of the target condition, where a deep cobalt blue signaled the correct deposition, as opposed to the deep purple plasma exhibited by a poisoned target.

After developing the PMMA lift-off layer, 30 nm thick alumina hard mask was deposited in a Tescal BJD-1800 thin film deposition sputtering system. Prior to deposition, a base pressure of  $5 \times 10^{-6}$  Torr was verified to prevent contamination. During deposition, the sample was placed on a stage rotating at 10 rpm to ensure uniformity. Process conditions were held for 30 s prior to opening the shutter, in order to allow plasma stabilization and target cleanliness. Deposition proceeded using a DC power of 400 W, with 100 sccm Ar and 20 sccm O<sub>2</sub>. Chamber pressure was maintained at a moderate 10 mTorr to prevent excess sidewall coverage. An induced target voltage of  $\approx 350$  V was noted. Under these conditions, deposition continued for 3 min at a rate of 10 nm/min, yielding a mask layer of 30 nm.

To transfer the lithographic features into the alumina hard mask, lift-off was performed by briefly immersing the sample in acetone (30-60 s). The absorption of the solvent causes the PMMA resist to swell, fracturing the brittle alumina at its interface with the substrate. We found that the lift-off can greatly benefit from a pulsating acetone spray from a squirt bottle, which is normally all that was required to produce excellent features and achieve complete removal of the excess alumina. If necessary, several rinse/soak cycles were used to ensure complete removal. While the process can be assisted by breaking up the layer with ultrasonication or gentle wiping with a swab, these steps risk damaging the intended pattern and were generally found to be unnecessary. Following the acetone

lift-off, the sample was rinsed with IPA, dipped in chloroform to further clean, rinsed once again in IPA, and dried with N<sub>2</sub>. During development of this process, we discovered the following guidelines to be invaluable. Once the wafer has been exposed to solvent, no part of the sample should be allowed to dry until the process is complete, or suspended alumina debris can become permanently affixed to the surface causing micromasking at unwanted locations. Since many of these solvents are quite volatile, particularly acetone and chloroform, this makes inspection of the sample to ensure completely removal quite difficult to perform during the process. If absolutely necessary, we found this best to perform during an IPA rinse step, since it has slightly lower volatility. Additionally, the use of secondary beakers for subsequent rinse or immersion steps is highly recommended to avoid reintroducing any of the alumina debris during a secondary soaking step. Finally, any transition to chloroform should be preceded and followed by an IPA rinse, due to its incompatibility with acetone. After lift-off, circular alumina pads remained at the location of the mask circles, defining the future locations of the nanopillars.

Etching of the structure was performed using inductively-coupled plasma reactive ion etching (ICP-RIE). In a typical RIE, an RF field driving the capacitively-coupled table electrode accelerates free electrons in the plasma to both the chamber sidewalls and samples surface, while atomic species do not accelerate quickly enough to reach either surface within an RF cycle. Because the table is capacitively coupled, this results in a *net* accumulation of negative charges on the sample surface, creating a *DC* electric field which then accelerates positive ions towards the sample, enabling anisotropic etching. The ion angular distribution (IAD) is also influenced by the chamber pressure, where additional collisions at higher pressures reduce the mean free path of the ions and tend to produce a more isotropic angular distribution. In addition to the capacitively-coupled power source in an RIE, an ICP-RIE uses an inductive coil around the chamber to control plasma density independently from the accelerating potential, providing additional control over the degree of chemical etching and passivation. The final etch parameters, including etch rate, selectivity, and anisotropy, are a complex balance between the sample characteristics, process gas chemistry and flow rate, CCP and ICP powers, chamber pressure, table and chamber temperature, and even the

sidewall conditions.

Our silicon nanopillar etching utilized a mixed mode process with a steady flow of sulfur hexafluoride ( $\text{SF}_6$ ) and octafluorocyclobutane ( $\text{C}_4\text{F}_8$ ). With this chemistry, silicon etching is accomplished when fluorine radicals bind with silicon atoms to form  $\text{SiF}_4$ , which is volatile and exists through the chamber exhaust. Simultaneously, the  $\text{C}_4\text{F}_8$  in the plasma results in a passivating polymer layer which coats the exposed areas and prevents etching by the  $\text{SF}_6$ . The ability to control the thickness of the passivating layer is critical to producing smooth, nanoscale features with vertical sidewalls. In the case of cryogenic silicon etching using  $\text{SF}_6$  and  $\text{O}_2$ , for example, the passivation is a glassy  $\text{SiF}_x\text{O}_y$  compound which is derived from the etch products. Because this layer can some time to establish, this etch often results in undercutting near the top; for our dimensions, this could be enough to lose the mask entirely. By contrast, the passivation in our  $\text{SF}_6/\text{C}_4\text{F}_8$  chemistry is directly deposited from the process gases themselves, eliminating concerns with undercutting. The passivating layer is responsible for etch anisotropy. For a primarily vertical IAD, the acceleration of the ions (particularly  $\text{SF}_5^+$ ) by the DC electric field causes the passivation to be milled away on the exposed horizontal surfaces, while the sidewalls remain protected. Our ability to ensure thick passivating layers enables the use of high accelerating voltages which produce a narrower IAD and better verticality, while maintaining control over the etch rate at a level suitable for nanoscale accuracy. By carefully balancing the passivation rate, milling rate, and IAD, it is also possible to not only control the sidewall angle, but vary it as a function of depth [366, 365]. We will explore this further in a later section.

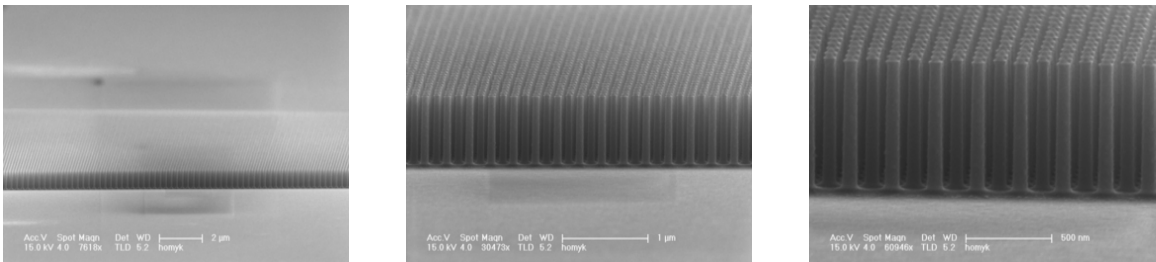


Figure 2.10: SEMs of as-etched silicon nanopillars, showing our ability to produce large arrays of highly uniform, high aspect ratio devices.

ICP-RIE etching was conducted in an Oxford Plasmalab ICP380. Samples were mounted on a

6" silicon carrier wafer; the excess of exposed silicon loads the etch, which serves to slow the etch for controllability as well as ensure process characteristics between different samples (any differences in sample size or exposed area are quite small compared to the carrier area). Chamber sidewalls were held at 40°C, while the table was cooled slightly to 15°C using LN<sub>2</sub>. These temperatures prevent condensation of the C<sub>4</sub>F<sub>8</sub> on the chamber sidewalls (which both consumes the passivation gas and results in dirty sidewalls) while encouraging passivation of the sample. To ensure adequate thermal control over the sample, He was flowed through the table with a back pressure of 10 Torr against the carrier, and the samples were mounted to the carrier using a thin layer of Fomblin oil. After a delay of 30 s to allow the sample to reach thermal equilibrium, gas was injected using 32 sccm SF<sub>6</sub> and 52 sccm C<sub>4</sub>F<sub>8</sub>. A slit valve between the chamber and turbomolecular pump was used to maintain a chamber pressure of 10 mTorr throughout the etch. Once this pressure had stabilized, the ICP and RIE power sources were enabled at 1200 W and 23 W, respectively. These resulted in an overall etch rate of  $\approx$  200-250 nm/min, with extremely vertical sidewalls and extremely smooth features. Etching continued for 4-5 minutes to achieve nanopillar lengths of 800 nm - 1  $\mu$ m. Following the etch, an oxygen plasma was used to remove excess polymer from the sample surfaces, using 100 sccm O<sub>2</sub>, 2000 W ICP, 200 W RIE, and 10 mTorr chamber pressure.

After etching, our nanopillars had diameters between 40 - 100 nm. While these dimensions were quite reasonable for accurate lithographic control, they were still well out of our target range of  $\approx$  5 - 25 nm. The critical element enabling the transition between these domains was a unique, self-terminating oxidation process. In the case of planar oxidation, Deal and Grove proposed a model of silicon oxidation based on Fick's laws [66]; an empirical correction was later applied by Massoud to better model thin oxides [235, 234, 233, 232]. In these models, oxide growth proceeds by transport of the oxygen species to the surface (normally neglected, since the furnace atmosphere can easily be saturated), diffusion through any existing oxide, and finally a chemical reaction at the SiO<sub>2</sub>:Si interface. In general terms, the rate of oxide growth according to the Deal-Grove model [66] is:

$$\frac{\partial x_o}{\partial t} = \frac{F}{N_1} = \frac{C^*/N}{1/k + 1/h + x_o/D}$$

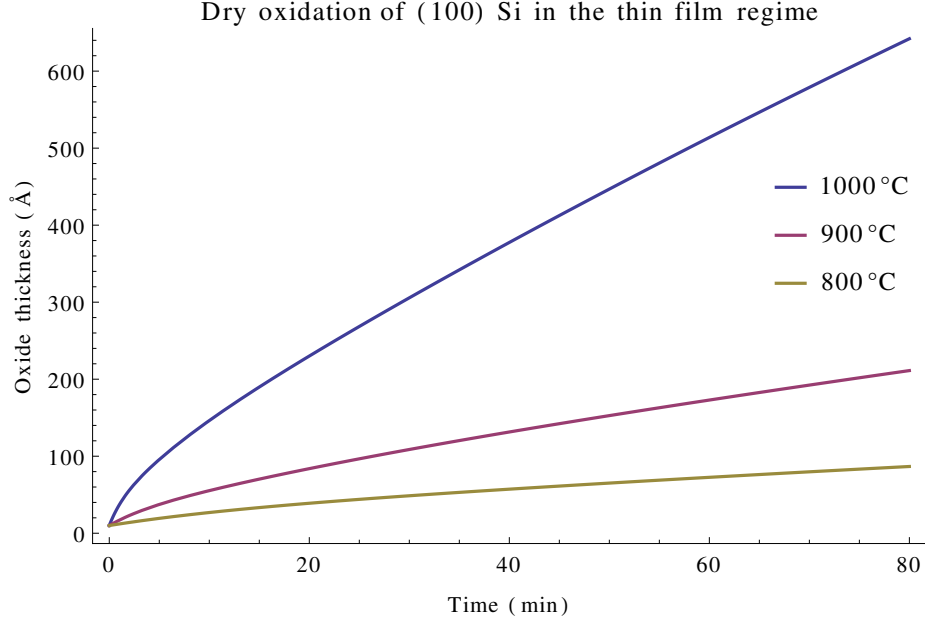


Figure 2.11: Dry oxidation of (100) silicon in the thin film regime, following [235, 234, 233, 232].

where  $x_o$  is the oxide thickness,  $F$  is oxidant flux,  $N$  denotes the oxide density,  $C^*$  is the oxidant solubility in the oxide,  $k$  is the oxidative reaction rate constant,  $h$  is the gas phase transport constant, and  $D$  is the effective diffusion coefficient of the oxidant through the oxide. Assuming an initial oxide thickness  $x_i$  at time  $t = 0$ , the oxide thickness at time  $t$  is:

$$\frac{x_o}{A/2} = \left(1 + \frac{t + \tau}{A^2/4B}\right)^{1/2} - 1$$

where  $A \equiv 2D(1/k + 1/h)$ ,  $B \equiv 2DC^*/N$ , and  $\tau \equiv (x_i^2 + Ax_i)/B$ .

For thin oxide layers, we find that the oxide growth is limited by the reaction kinetics and is essentially linear with time, while thicker oxidation enters a diffusion-limited regime and has a square root dependence. Additionally, we note that oxidation occurs at the  $\text{SiO}_2\text{:Si}$  interface; the oxide at the surface formed first, with deeper oxide developing later, and originating from deeper below the original Si surface.

Using cylindrical coordinates, we can apply these same concepts to a cylindrical structure such as our nanopillar to find [207]:

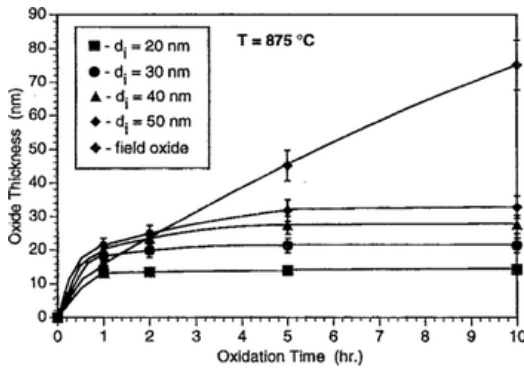
$$\frac{\partial x_o}{\partial t} = \frac{C^*/N}{(1/k + (1/h)(r_c/r_o)) + (r_c/D)\ln(r_o/r_c)}$$

where  $r_c$  and  $r_o$  are the inner core and outer oxide radii, respectively, and  $x_o = r_o - r_c$ . For thin

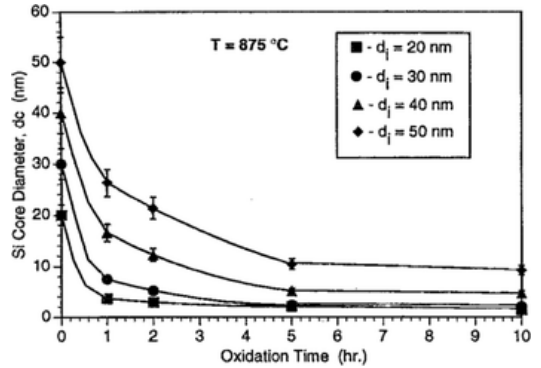
oxides,  $r_o \approx r_c$ ; the diffusive term drops out and we recover the same reaction-rate limited growth. As we consider thicker oxides, however, we notice that the diffusive term for planar growth scales linearly as  $x_o/D$ , while the cylindrical case shows a sublinear dependence diffusion,  $r_c/D \ln(r_o/r_c) = r_c/D \ln(1 + x_o/r_c)$ , since  $r_c$  is *decreasing* during oxidation, and the rate remains primarily reaction limited. Physically, as the oxide radius increases, the additional surface area permits a incoming oxidant flux.

At first glance, we should expect faster oxidation of our convex structure than the planar case. Reported data, however, shows an asymptotic limit on the oxide thickness for silicon nanowires [207]. During initial oxidation, the convex nanowires show more rapid oxide growth than planar surfaces. At sufficient durations, however, oxidation of the nanowires appears to cease entirely. The final thickness depends on the initial pillar diameter and oxidation temperature, but is unaffected by additional oxidation time; see Figure 2.12(a,b). Interestingly, the self-limiting behavior was only observed for oxidation temperatures below 960°C. This temperature corresponds to the viscoelastic reflow point of SiO<sub>2</sub>, below which the oxide is unable to relax by undergoing amorphous flow. This suggests a mechanism which is dependent on the strain accumulated during the process in the oxide layer.

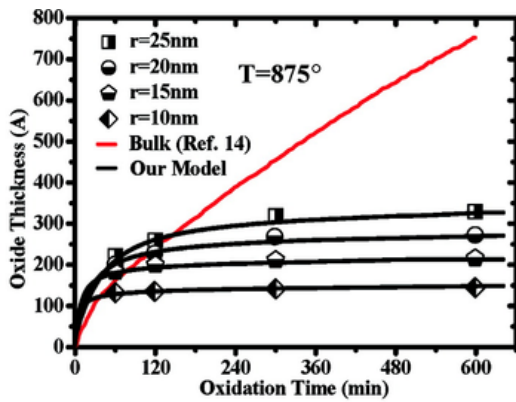
Although the exact mechanism is still unknown, the authors of the first study considered several potential causes [207]. First, they ruled out the possibility of a constrained equilibrium, estimating the upper bound on activation energy required to form an oxide molecule around a 2 nm Si core to be 0.04 eV, which is greater than 2 orders of magnitude lower than the 9 eV released by the exothermic reaction. Similarly, a kinetic equilibrium based on strain-dependent modification of the interface reaction was also examined. Because the interface stress is primarily determined by the inner radius, this would predict only a weak dependence on the outer radius, in contradiction with the data. A third proposal suggested a modification of the oxidant diffusion rate as the dominant mechanism, rather than a dependence on the reaction itself. This explanation seemed to fit the data well, and was consistent with an underlying mechanism related to viscous flow. More recent investigations have further supported this conclusion. Cui *et al.* [62] developed an analytic model



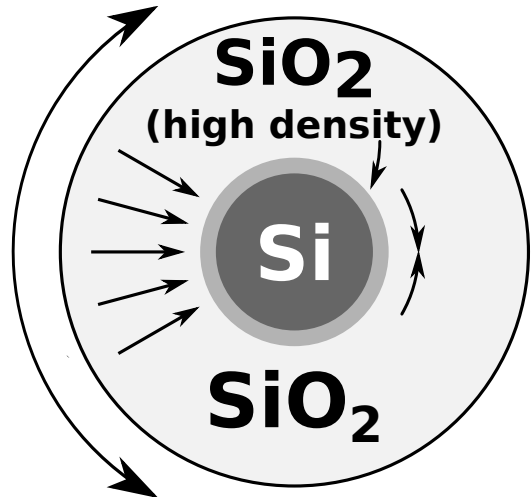
(a) Oxide thickness around the silicon pillar during oxidation, and comparison to planar field oxidation. From [207].



(b) Silicon core diameter during oxidation. From [207].



(c) Comparison between the theoretical model developed by Cui *et al.* [62] (solid curve) and the experimental data from Liu *et al.* [207] (points). Excellent agreement is found. Image from [62].



(d) Schematic of the strain-induced self-terminating oxidation. Because the growth occurs at the inner Si:SiO<sub>2</sub> interface, the existing oxide becomes increasingly stretched as additional as it expands to incorporate additional O<sub>2</sub> into the structure. This creates a *compressive* strain on the inner core. Eventually, this strain results in a high-density region at the interface which prevents further diffusion and terminates the oxidation.

Figure 2.12: Self-terminating oxidation at 875°C.  $d_i$  corresponds to the original (in parts b,c), unoxidized diameter, and  $r$  the radius (part a). Note the terminal core size reached after  $\approx 5$  hr. Consistent with the core behavior, the pillar oxide also terminates after  $\approx 5$  hr. Also note that the initial oxidation is *faster* than the planar surface, but eventually terminates whereas the field oxide continues to grow. The schematic in (d) depicts the theory proposed by Cui *et al.* [62].

to include the effects of strain on the diffusion. As follows from our intuition, the outer layers of oxide become increasingly stretched by the generation of additional oxide at the core, resulting in a highly compressive stress at the oxide-silicon interface. Their study suggests that diffusion becomes limited by a 1 nm thick, high-density oxide region which develops at the oxide-silicon interface as a result of this stress. The model is further supported by molecular dynamics simulations [271] and shows excellent agreement with published data (Figure 2.12c).

We performed dry oxidation of our etched pillars at temperatures ranging from 850°C - 950°C in a 6", three-zone tube furnace (Thermtec Black Max). During oxidation, samples were placed upon either a bare silicon wafer or quartz plate and loaded into the furnace on a quartz boat. The samples remained upwards facing during processing. While ramping up to the intended process temperature, the furnace was purged with a steady flow of N<sub>2</sub> at 2 ft<sup>3</sup>/hr. Once adequate temperature stabilization had been achieved, the flow was switched to a pure O<sub>2</sub> source at 2 ft<sup>3</sup>/hr. Only semiconductor grade, ultrahigh purity (UHP) O<sub>2</sub> was used to ensure oxide quality. Oxidation proceeded for enough time to ensure the asymptotic limit had been reached, typically 6 - 8 hr depending on the temperature [207, 62]. After the oxidation period, the gas flow was switched back to N<sub>2</sub> while ramping the temperature down for sample removal.

To measure and verify final core diameters, the oxidized pillars were imaged using transmission electron microscopy (TEM) in an FEI Tecnai TF20 operating at 200 kV. We utilized both a reflective mode (reflection electron microscopy, or REM) for non-destructive imaging of pillars while they were still attached to the substrate, as well as destructive imaging by transferring them to a holey carbon grid (this enables greater control over pillar orientation and easier imaging). Under appropriate imaging conditions and orientation, diffraction from the crystalline core provides excellent contrast against the surrounding oxide layer, allowing accurate measurements of the remaining silicon core. We measured these diameters to fall between 2.5 nm - 30 nm, spanning the intended range of growth apertures. Additional characterization using photoluminescence and electron energy loss spectroscopy (EELS) will be presented later.

Due to the self-limiting nature of the oxidation process, the final aperture diameters were only a

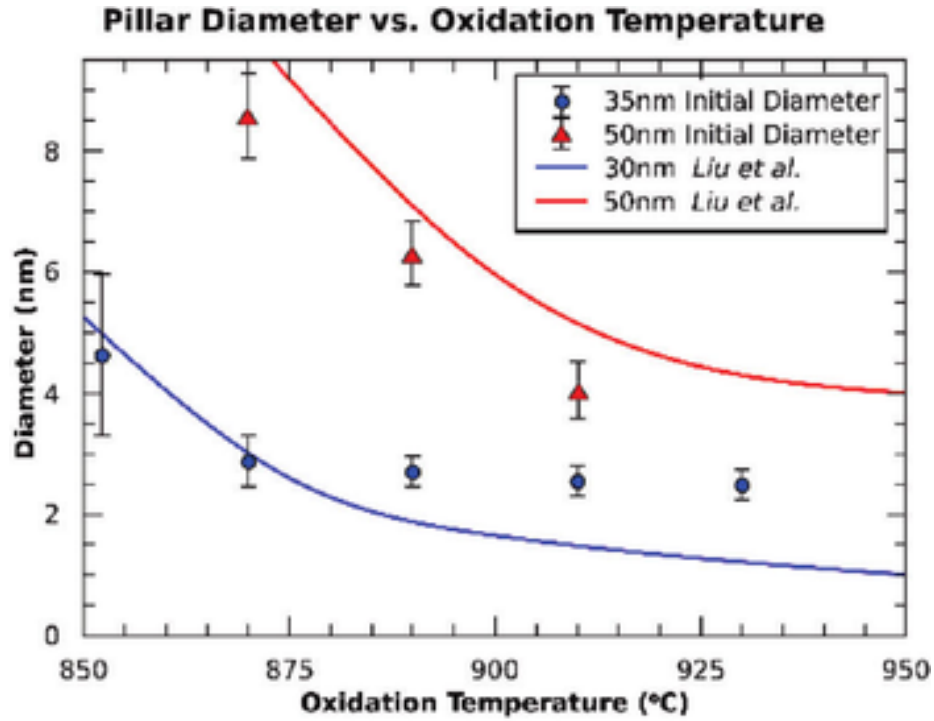
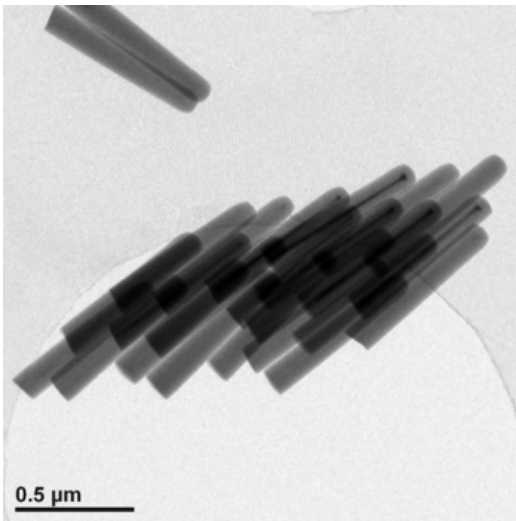
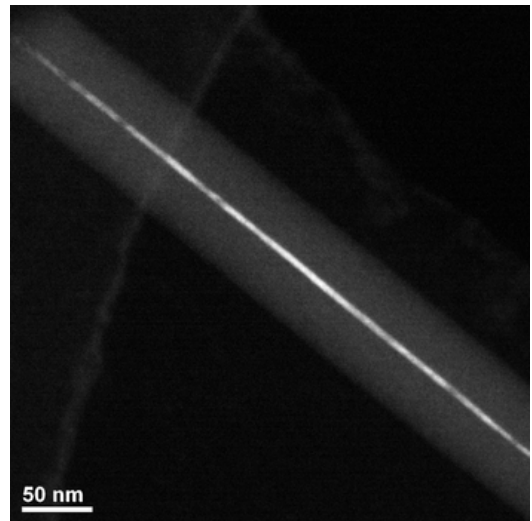


Figure 2.13: Use of initial diameter and oxidation temperature to tune the final core size. Data points show the measured core sizes for 35 nm and 50 nm initial pillar diameters. For comparison, the solid curves show the oxidative trends reported by Liu *et al.* [207].

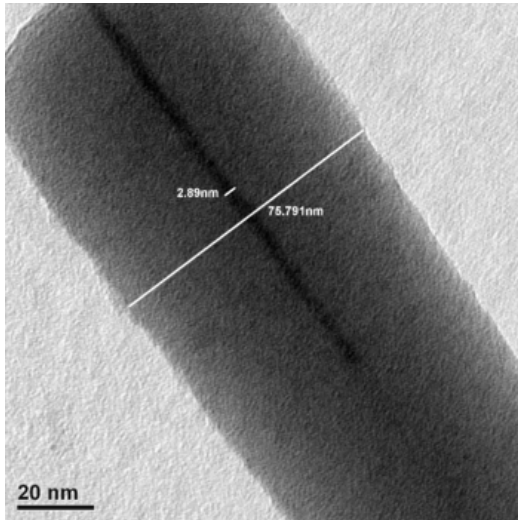


(a) TEM image showing a large bundle of nanowires. The devices show excellent sidewall roughness and diameter uniformity. We note that the crystalline core is visible in some samples and not others. Because of the random crystallographic orientation of the pillars after cleaving, they generally have unique diffraction conditions which maximize contrast.

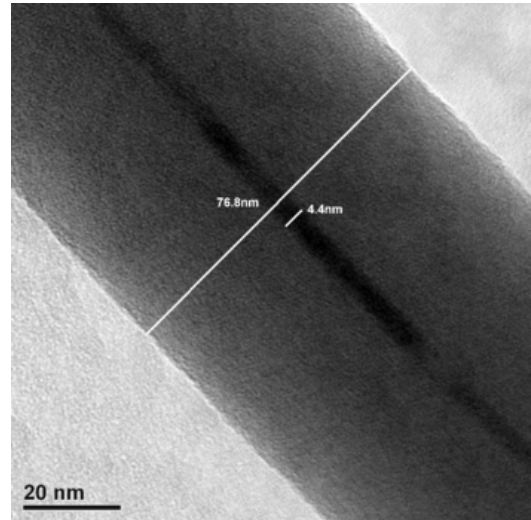


(b) TEM of an oxidized silicon nanopillar, using dark-field diffraction contrast to highlight the crystalline core.

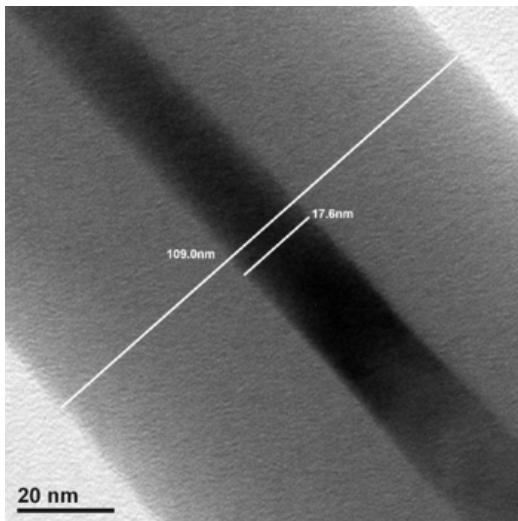
Figure 2.14: TEM imaging and contrast of oxidized silicon nanopillars.



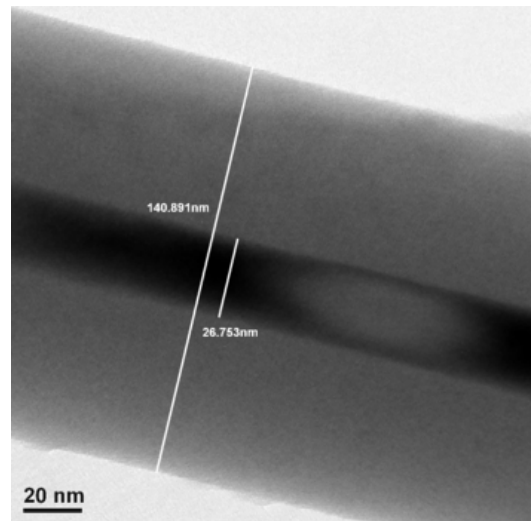
(a) Silicon nanopillar with a 2.9 nm silicon core.



(b) Silicon nanopillar with a 4.4 nm silicon core.



(c) Silicon nanopillar with a 17.6 nm silicon core.



(d) Silicon nanopillar with a 26.8 nm silicon core.

Figure 2.15: TEM images showing a range of oxidized silicon nanopillar cores suitable for heteroepitaxy.

function of the starting diameter and oxidation temperature, but quite insensitive to the oxidation time. This allowed us to utilize larger lithographic dimensions where we could ensure accuracy of the pillar geometry. The time-insensitive nature of the oxidation also permitted long periods of temperature stabilization within the furnace, making the process quite robust in terms of achieving precise temperature control and remaining insensitive to ramp profiles. Together, these qualities proved to be incredibly effective, enabling a controllable method of producing oxide apertures down to 2.5 nm.

### 2.4.1.3 Growth results and characterization

The condition of the growth surface is a critical factor in the success of the epitaxial process. Even the presence of a thin native oxide plays a crucial role, and partial epitaxial coverage can often be traced back to incomplete oxide removal [32]. For this step, most references report not only a chemical oxide removal prior to loading the sample in the chamber, but an additional *in situ* oxygen desorption using elevated temperatures or an H<sub>2</sub> plasma [370, 32, 33, 329, 225, 226, 101, 12]. The quality of the exposed crystalline must also be maintained. Elarde *et al.* [73] suggest that dry etching should be avoided on the exposed surfaces because the process introduces too much damage, while wet etching tends to produce a superior surface quality. Wang *et al.* [371] utilize a dry etch to expose the growth surface, followed by a KOH dip to remove etch damage. Unfortunately, these processes also tend to increase the hole sizes [73, 371] and introduce size variability [12] in the range of 10s of nm — on the order of our target dimensions themselves!

By contrast, the crystalline cores in our apertures had never been exposed to *any* etching. The sidewall interface was formed by oxidation, which also consumes the dry-etch-damaged regions in the outer regions of the oxide. In order to actually expose the core, the pillars were mechanically cleaved immediately prior to growth. Together, these features preserved the crystalline quality of the growth interface as well as maintained the nm-scale control over the aperture size.

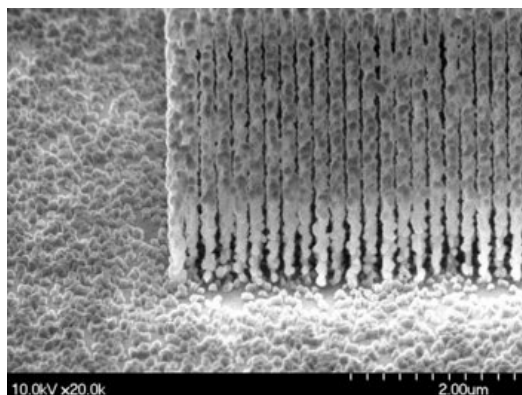
The growth was performed in collaboration with the Huffaker group at UCLA, using metal organic chemical vapor deposition (MOCVD). Immediately prior to loading into the MOCVD

chamber, samples were immersed in IPA and cleaved; performing this step while immersed was important in preventing permanent adhesion of the broken pillars to the substrate by van der Waals forces. The samples were then rinsed briefly in IPA to ensure pillar removal, dried with  $N_2$ , and loaded into the chamber.

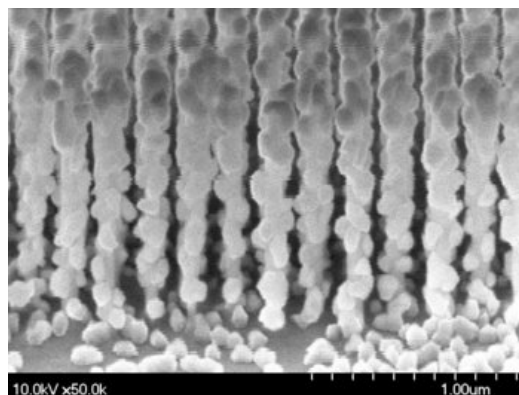
Based on the Huffaker group's previous success with heteroepitaxy on Si, we began with attempts to grow GaP and GaP/InGaP heterostructures [344]. For these first experiments, the cleaving process was performed using sonication. Samples with oxidized nanopillars were immersed in IPA, and the beaker was placed in an ultrasonic bath for up to three minutes. Following sonication, the sample was rinsed again in IPA, dried with  $N_2$ , and loaded into the growth chamber. For the GaP sample, only a single layer was deposited for 1 min. The GaP/InGaP heterostructure utilized 1 min of GaP deposition followed by 1 min each of InGaP-1, InGaP-2, and InGaP-1, where the suffixes indicate different In:Ga flux ratios.

SEM images of the samples are presented in Figure 2.16. On the GaP sample, the ultrasonic process was unsuccessful in cleaving any of the pillars. Interestingly, no nucleation was observed on the oxide-coated substrate or pillar sidewalls; see Figure 2.16d. The GaP/InGaP heterostructure sample was partially cleaved. Unlike the GaP sample, some nucleation occurred on the oxide. In regions where the pillars were not successfully removed, a similar density of quantum dots can be observed on both the substrate and pillar regions, as shown in Figure 2.16(a,b). Where the cores were exposed, however, the growth occurred primarily over the templated area, with only incidental deposition occurring around the planar regions; this behavior can be seen in Figure 2.16c. This effect is consistent with preferential nucleation over the exposed crystalline areas. After initial seeding within the templated area, subsequent adatom diffusion tends to occur towards the existing growth. This results in growth accumulating within the  $SiO_2$  apertures, while depleting deposition in the surrounding planar region [146, 125, 399].

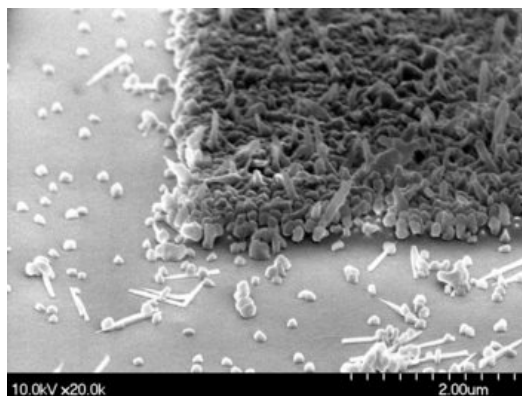
A mechanical cleaving process was developed for the next set of growth. In place of the sonication step, a cleanroom swab was dragged across the surface while the chip was immersed in IPA (Figure 2.18a). The chip was then rinsed in IPA, dried with  $N_2$ , and loaded into the MOCVD as



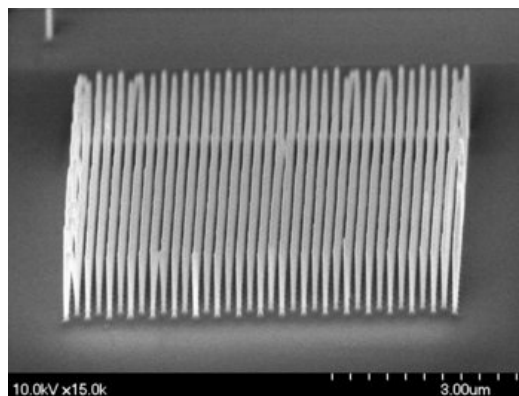
(a) GaP/InGaP growth on oxidized silicon nanopillars. The ultrasonic process failed to cleave the pillars, resulting in non-selective nucleation.



(b) Detail of GaP/InGaP growth on oxidized silicon nanopillars.



(c) Where the cleaving was successful, GaP/InGaP growth occurred preferentially over the exposed silicon cores.



(d) An attempt at heteroepitaxy of GaP on Si. The ultrasonic process failed to cleave the pillars, and no growth was observed. Interestingly, no nucleation was observed on the oxide-coated substrate or pillar sidewalls.

Figure 2.16: Heteroepitaxy of GaP/InGaP and GaP on silicon using oxidized silicon nanopillar growth templates.

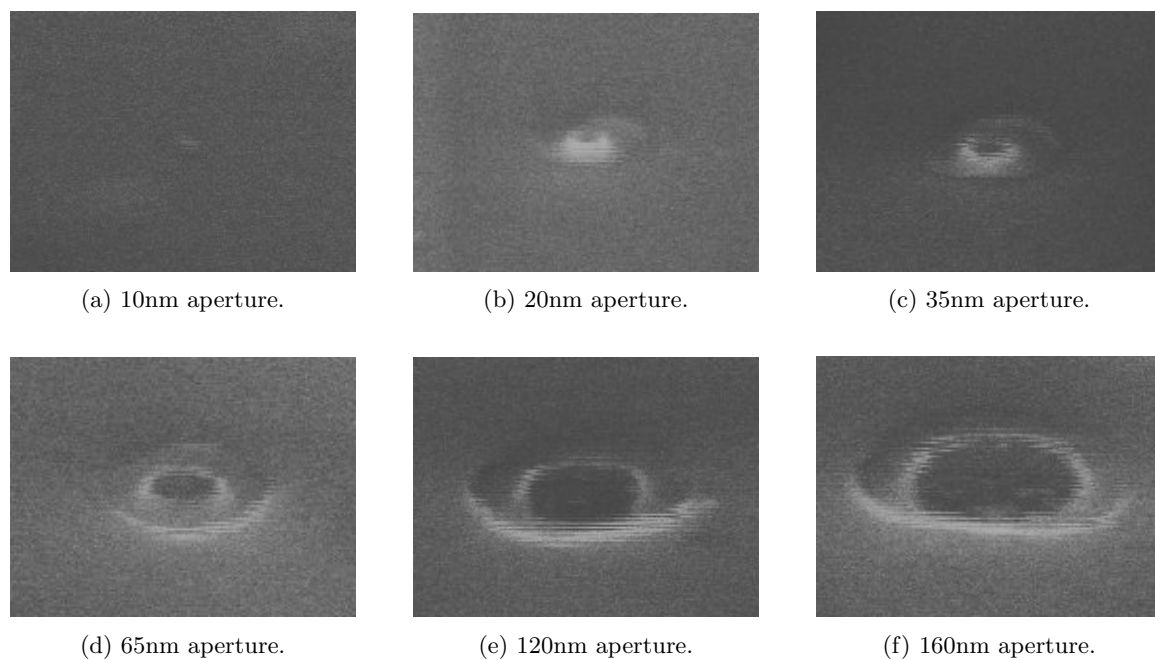


Figure 2.17: Wide array of growth templates from cleaving oxidized silicon nanopillars.

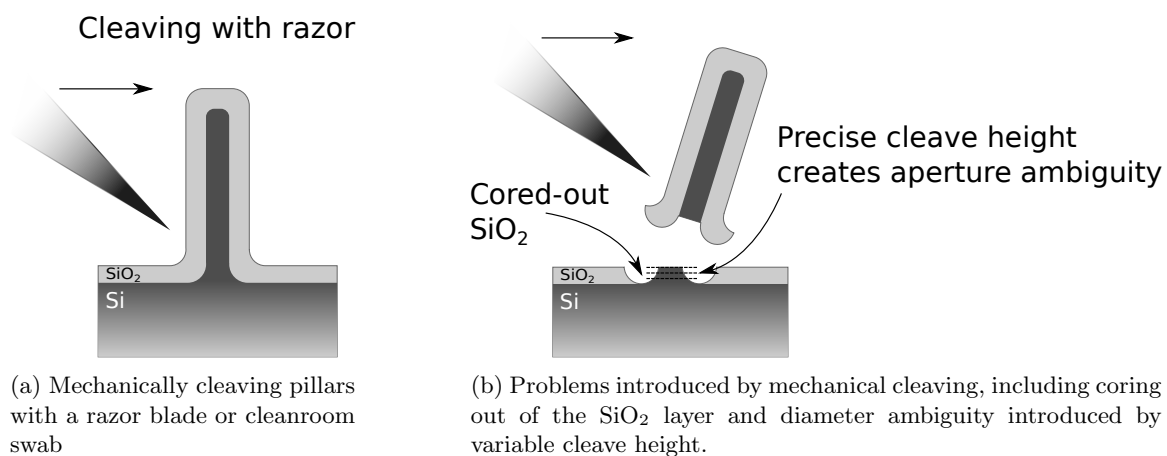
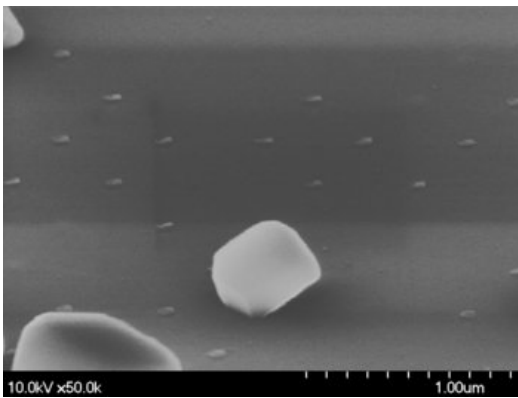
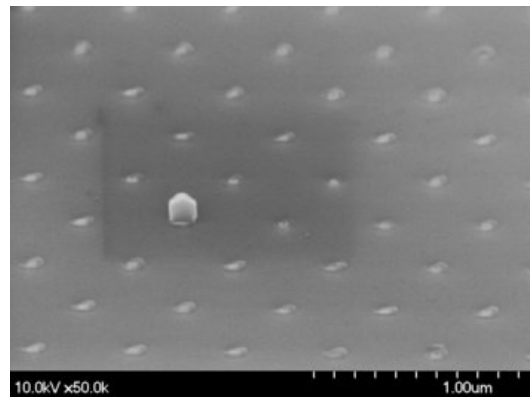


Figure 2.18: Schematics of the nanopillar cleaving process and potential issues.

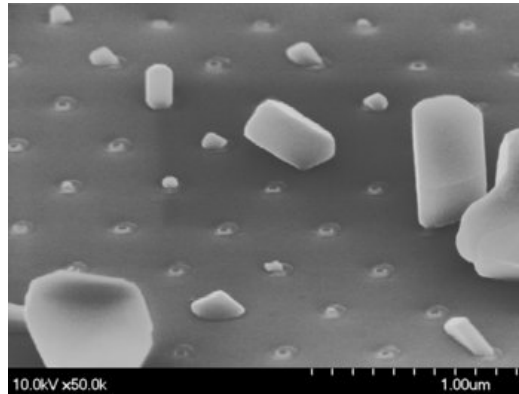
before. This technique greatly improved the removal of pillars and exposure of the growth interface. However, the pillar cleavage tended to happen below the planar oxide surface, while coring out the surrounding oxide. This effect is illustrated in Figure 2.18b, and can be seen in SEMs of the cleaved interfaces shown in Figure 2.17, as well as TEMs presented shortly (Figures 2.24 and 2.25). Because the pillars broke near the base where they begin to taper into the bulk, the uncertainty in the exact height of the break introduced an ambiguity as to the precise core diameter. This prevented our ability to characterize the aperture geometries by imaging the broken pillars in a TEM. Based on the more limited resolution available in the SEM, however, these still appeared to cover a range down to at least 10 nm.



(a) 10 nm apertures.



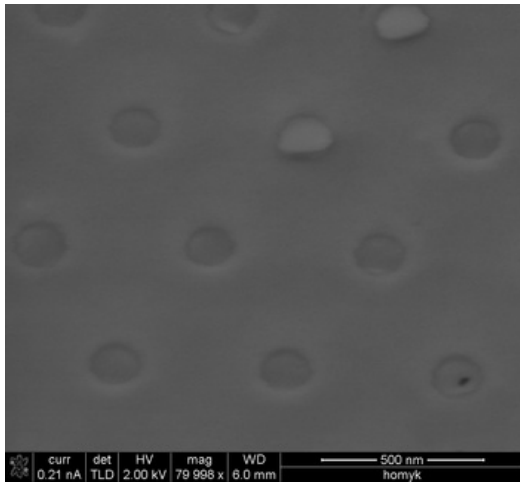
(b) 20 nm apertures.



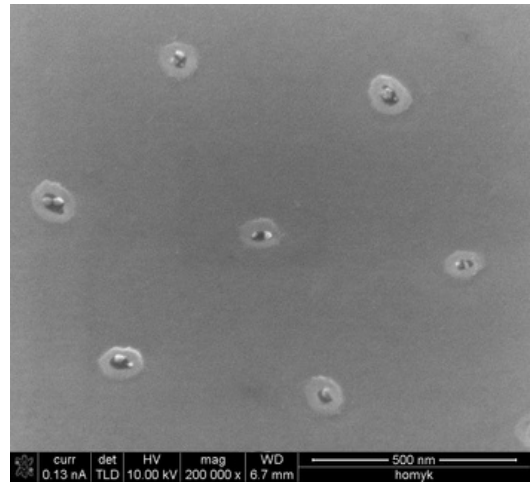
(c) 35 nm apertures.

Figure 2.19: InAs heteroepitaxy onto silicon nanowire templates at 630°C.

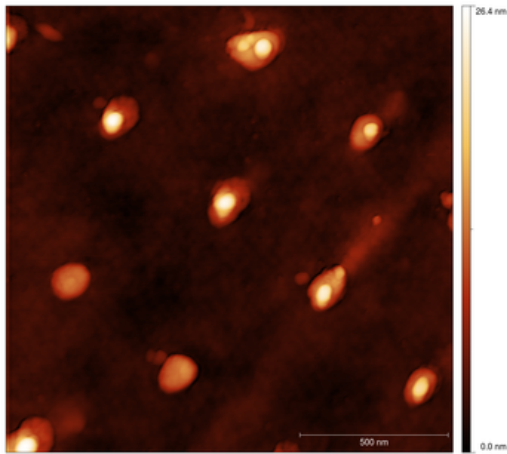
Using this revised method, InAs growth was performed over a variety of temperatures, flux ratios, and aperture diameters (Figure 2.17). The baseline process used a growth temperature of 630°C



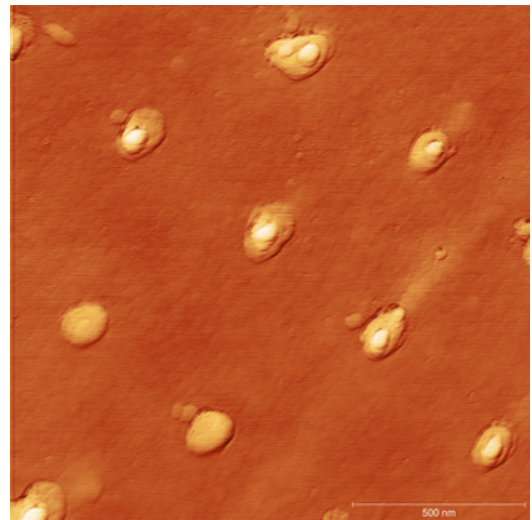
(a) SEM of InAs QD growth, showing complete filling of the cored-out oxide region and buckling.



(b) SEM of InAs QD growth, showing isolated clusters.

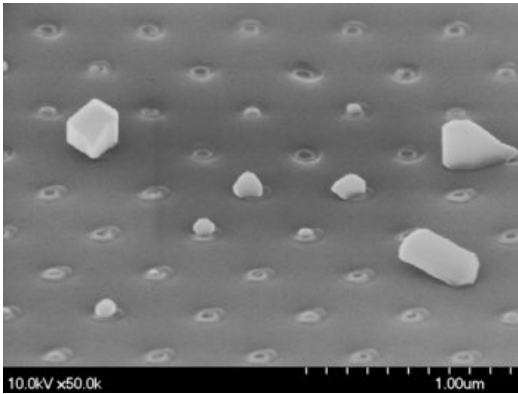


(c) AFM of InAs QD growth on silicon nanowire templates.

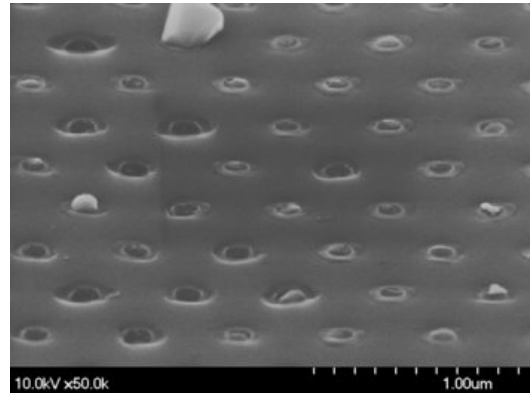


(d) AFM of InAs QD growth, enhanced to show texture.

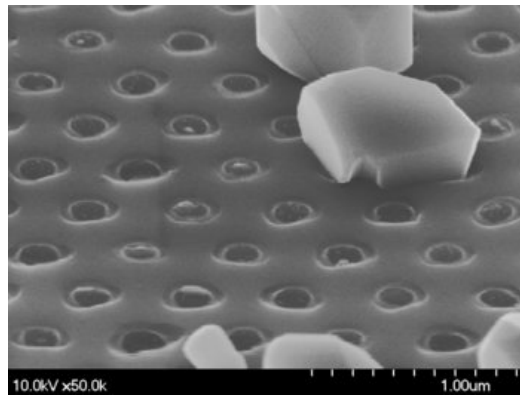
Figure 2.20: InAs QD growth on 35 nm silicon templates.



(a) 65 nm apertures.



(b) 120 nm apertures.



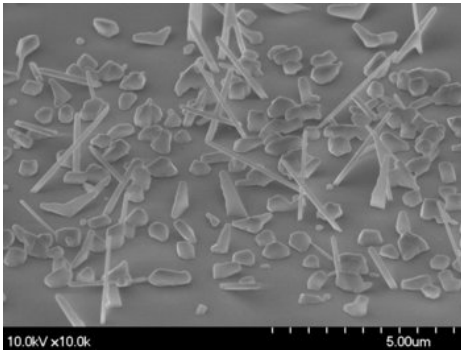
(c) 160 nm apertures.

Figure 2.21: InAs heteroepitaxy onto silicon nanowire templates at 630°C.

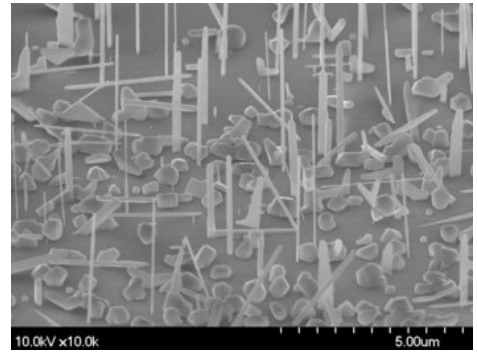
and a V/III flux ratio of 10, corresponding to a planar growth rate of  $\approx 0.5 \text{ \AA/s}$ . Under these growth conditions, we noted two distinct growth regimes based on the aperture size. For smaller diameters ( $\approx 10 \text{ nm} - 35 \text{ nm}$ , by SEM), the growth tended to cover the entire exposed Si surface where nucleation occurred; see Figure 2.19. Often, the growth would fill in the cored out oxide region as well. In some instances, these dots can be seen to buckle out of the holes, as shown in Figure 2.20a. By contrast, growth over larger diameters ( $\gtrsim 35 \text{ nm}$ ) tended to form isolated clusters, as shown in Figure 2.21. For apertures around the transition diameter of  $\approx 35 \text{ nm}$ , both growth regimes can be observed; SEMs and AFM scans of filled apertures, single isolated dots, and multi-dot growth on 35 nm apertures are shown in Figure 2.20. We note that this diameter is roughly in the range of transition diameters previously reported [55, 122, 400, 399, 371]. In all cases, including aperture diameters ranging from  $\approx 10 \text{ nm} - 160 \text{ nm}$ , nucleation over the template was incomplete. Where it did occur, however, growth tended to be preferential to the defined area. The incomplete nucleation could be an indication of a surface oxide which formed while loading the sample [32]. This could have also contributed to the variability in growth characteristics around the transition diameter, although this is more likely due to minor process variation between samples.

At a slightly higher growth temperature of  $660^\circ\text{C}$ , the growth transitioned from the formation of isolated QDs into the production of vertical InAs nanowires. SEMs of the InAs nanowire growth are presented in Figure 2.22 for aperture diameters of  $10 \text{ nm} - 160 \text{ nm}$ . Within this range, growth was most successful for the  $20 \text{ nm}$ ,  $35 \text{ nm}$ , and  $65 \text{ nm}$  apertures (see Figure 2.23). Nucleation of the nanopillars still occurred preferentially within the growth apertures, and tended to occur over only a fraction of the cores. As before, this could have been due to partial surface oxidation while loading the sample. At the higher temperature, another possibility is the increased adatom diffusion, enabling the In atoms to diffuse away before being trapped in the apertures. Once nucleation occurred, however, pillar growth proceeded along the  $\langle 111 \rangle$  direction, consistent with the substrate orientation and typical for pillar diameters  $\gtrsim 10 \text{ nm}$ .

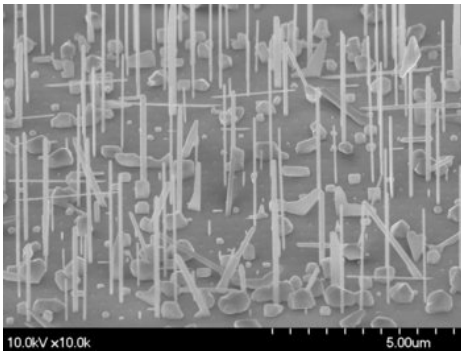
Cross-sectional TEMs of the InAs nanowire growth, presented in Figure 2.24, reveal that the nanowires growth was crystalline, but full of stacking faults. From the images, it is difficult to resolve



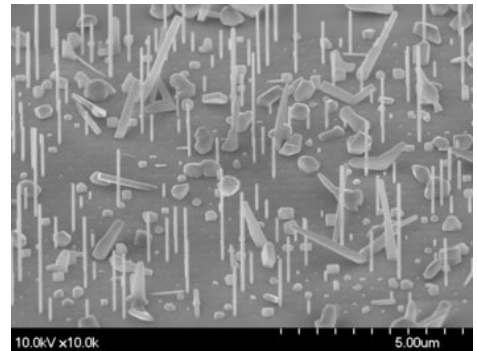
(a) 10 nm apertures.



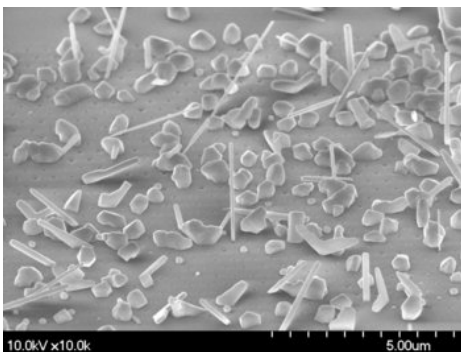
(b) 20 nm apertures.



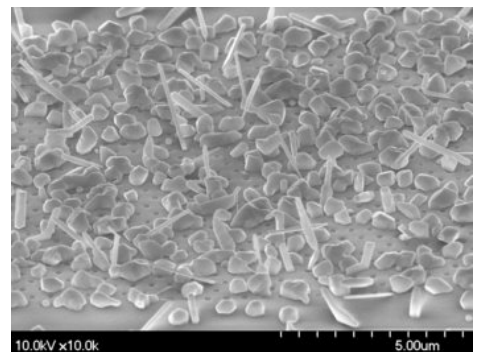
(c) 35 nm apertures.



(d) 65 nm apertures.

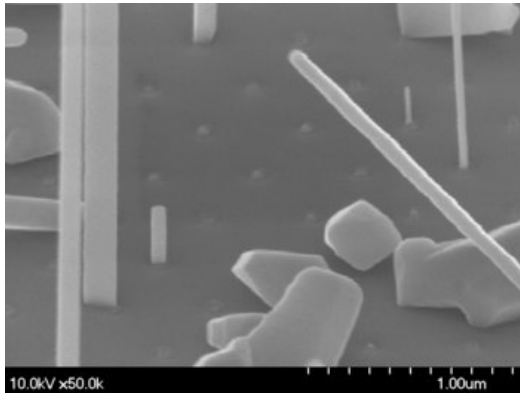


(e) 120 nm apertures.

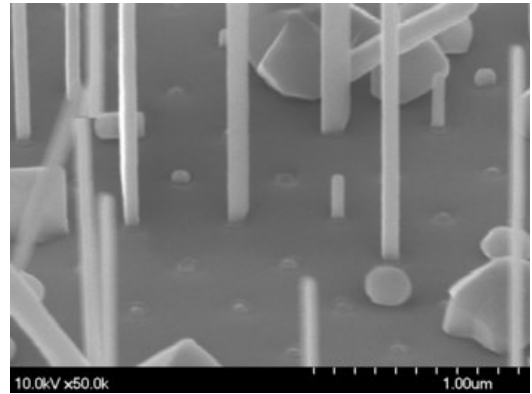


(f) 160 nm apertures.

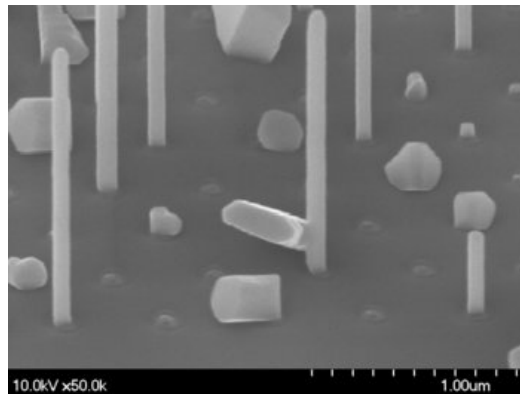
Figure 2.22: InAs heteroepitaxy onto silicon nanowire templates at 660°C.



(a) 20 nm apertures.

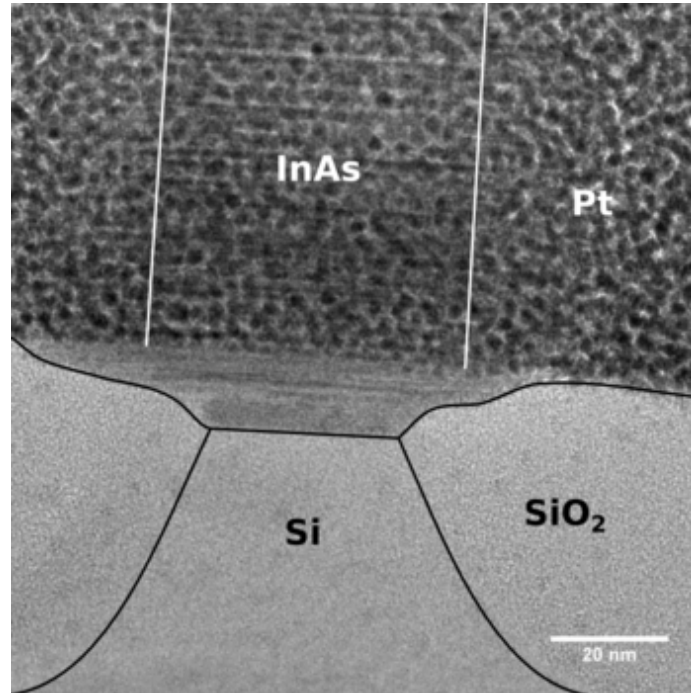


(b) 35 nm apertures.

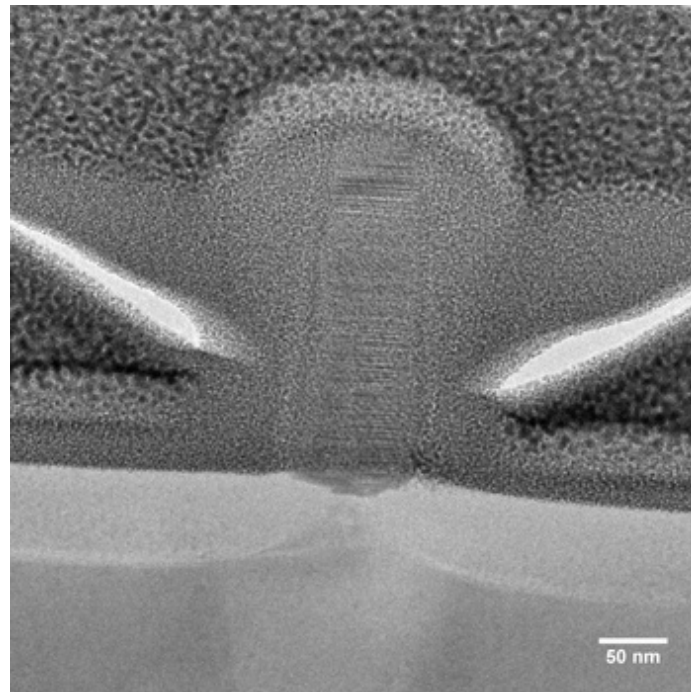


(c) 65 nm apertures.

Figure 2.23: Detailed SEM images of InAs heteroepitaxy onto silicon nanowire templates at 660°C.

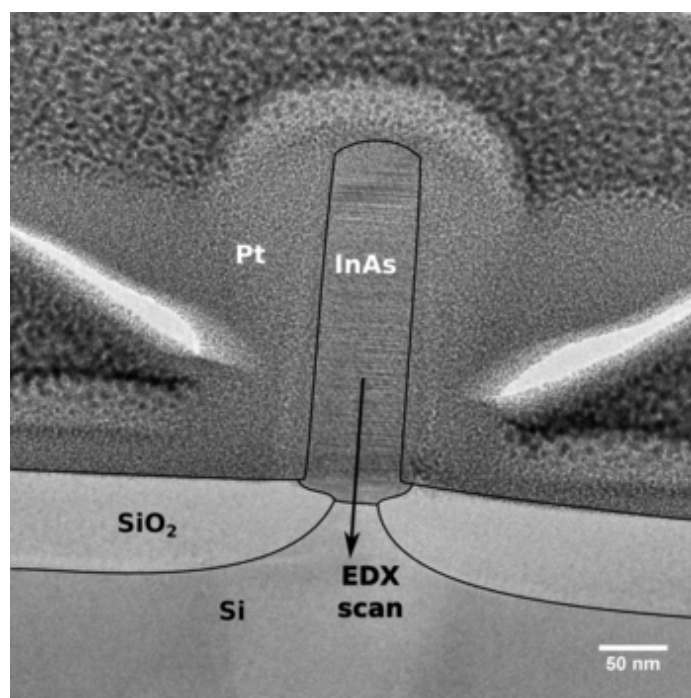


(a) Cross-sectional TEM of InAs nanowire growth. The Pt region is a consequence of the cross-section preparation in the FIB, and would not normally be present on the device.

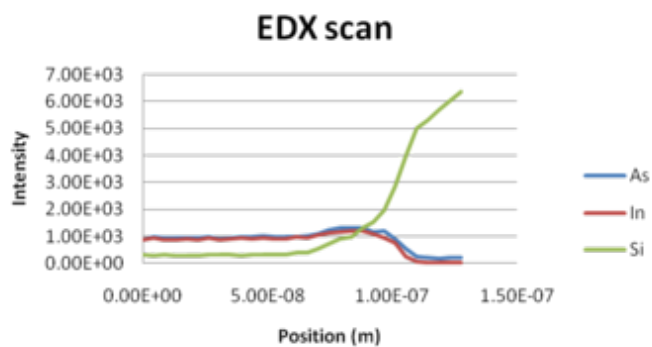


(b) Cross-sectional TEM of InAs nanowire growth. The lattice is visible, indicating crystalline growth; however, a large quantity of stacking faults are present.

Figure 2.24: Cross-sectional TEMs of InAs nanowires grown on oxidized silicon nanowire templates. The core diameter at the interface is 32 nm.



(a) Cross-sectional TEM of InAs nanowire growth, showing location and direction of EDX scan.



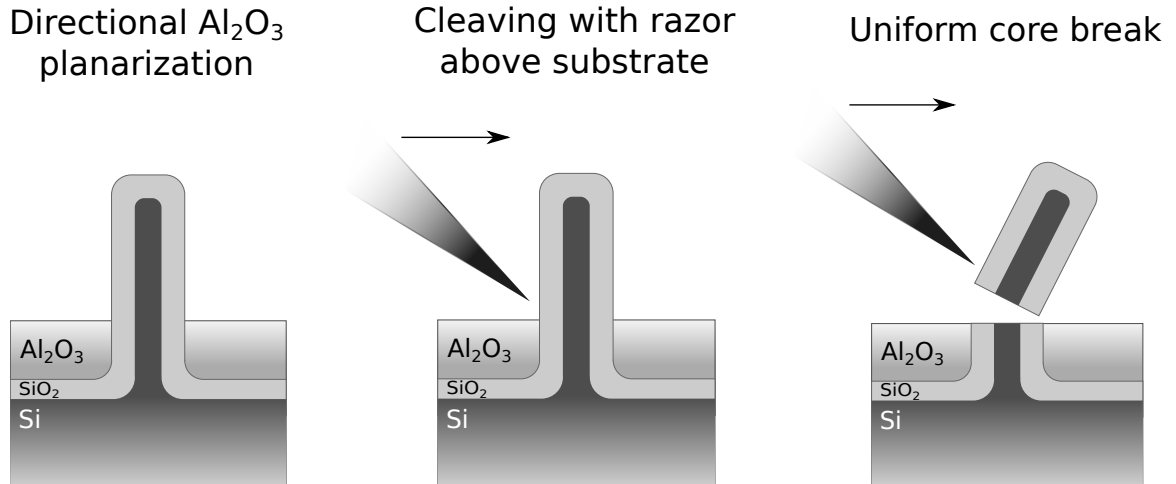
(b) Energy dispersive x-ray data showing elemental composition as a function of position along the nanowire axis. These data show a balanced concentration of In and As atoms in the grown nanowire, before transitioning into the Si substrate.

Figure 2.25: Energy dispersive x-ray analysis of a heteroepitaxial InAs nanowire grown on an oxidized silicon nanowire template. The core diameter at the interface is 32 nm.

if there was any coherency between the InAs lattice and that of the underlying Si substrate. To confirm the nanowire stoichiometry, an energy dispersive x-ray analysis (EDX) scan was performed along the axis of the nanowire into the substrate (Figure 2.25a). These data show a balanced concentration of In and As atoms, before transitioning into the Si substrate (Figure 2.25b).

Another important quality revealed by the TEMs was the complexity of the cleaved interface. As suspected from SEM the images, the silicon core was broken below the planar oxide surface. At this depth, the core diameter is still tapering to its minimal diameter within the pillar. The sub-surface break therefore resulted in both an increase in the effective core size as well as an additional degree of uncertainty in the aperture diameter compared to what could have been achieved within the uniform section of the pillar. Perhaps more significantly, a large region of the oxide itself was also removed during the process. Examining the TEM image in Figure 2.24a, we can see that this created a much broader hole, with a diameter of  $\approx 85$  nm as compared to the 32 nm diameter of the crystalline silicon region (which would have tapered further, had it broken higher in the pillar). Not only did this enlarge the hole, but the oxide removal resulted in a highly irregular growth well, with an asymmetric geometry around the core and stepped sidewalls. These features might greatly complicate the epitaxial process, inducing defects or nucleation at multiple sites within each aperture.

For our next QD growth experiments, we sought to elevate the cleavage point above the planar oxide interface. Besides reducing uncertainty in the core diameter as well as reaching the smaller apertures of the self-terminated region, breaking the pillar at a prescribed height above the substrate would help embed the QD in the center of a cavity to be formed around it while isolating it from the substrate. To accomplish this, we proposed to deposit a planarization layer over the oxidized pillars prior to the cleaving process, effectively raising the height of the cleave. After the epitaxy had been completed, the layer would be removed, leaving QD resting on a pedestal whose height above the oxide surface matched the planarization layer thickness (Figure 2.26). This process has the additional benefit that any growth that happens to nucleate in the surrounding regions will be eliminated when the planarization layer is removed, leaving only the QDs over the intended growth



(a) Deposition of a planarization layer, to raise the effective cleaving surface. The deposition should be mostly directional, as deposition on the sidewalls will widen the effective pillar diameter and exacerbate cleaving. A slight tilt or degree of conformal deposition is desired to avoid shadowing, which would create a void near the pillar.

(b) Pillar cleaving proceeds as before by scraping a razor or cleanroom swab over the surface, but the effective height is offset from the oxide interface.

(c) The uniform pillar diameter at the higher location eliminates ambiguity in the aperture size due to height variation of the cleave.

Figure 2.26: Use of a planarization layer to improve exposure of the oxidized silicon nanowire growth aperture.

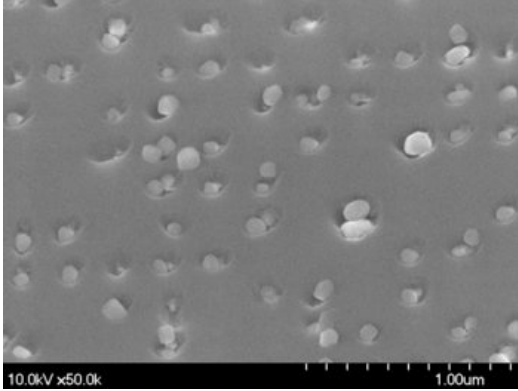
apertures.

The success of this process imposed several requirements. First, we needed a material which was hard enough to withstand the cleaving, stable at the elevated temperatures of the epitaxial process, and possible to remove later without affecting the grown QD or underlying oxide layer. Additionally, the directionality of the deposition was critical. Perfect step coverage was undesirable, as it would increase the pillar diameter by the twice the planarization thickness which might hinder cleavage. Conversely, a perfectly directional deposition could introduce challenges in properly coating the region at the base of the pillar due to shading by the structure itself.

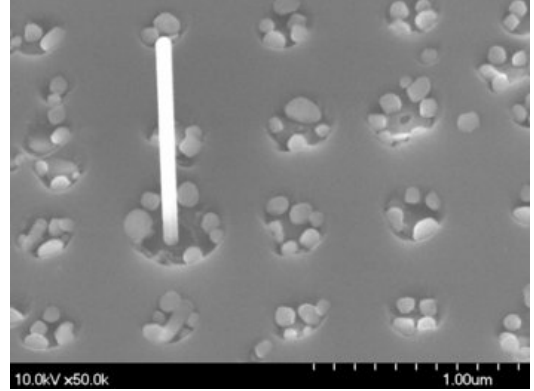
To satisfy these requirements, we chose to use electron-beam evaporation to deposit aluminum oxide. This deposition method allows extremely precise control over layer thickness, while the sidewall step coverage can be varied by performing an angled evaporation and using a rotating stage to ensure conformal layer coverage. As a material, alumina is physically robust and chemically inert. While silicon nitride might also be suitable, the alumina can be more readily removed using a quick ammonium fluoride etch, while  $\text{Si}_3\text{N}_4$  etching typically uses hot phosphoric acid, which needs a reflux condenser to maintain the concentration as it evaporates.

Aluminum oxide was evaporated onto the samples using a Temescal BJD-1800 electron beam evaporator with a source voltage of 10 kV. Samples were mounted on a rotating platform operating at approximately 5 rpm during deposition. After loading, the chamber was evacuated to a base pressure of  $8 \times 10^{-6}$  Torr prior to enabling the electron gun. Soak and predeposition powers were 7% and 12%, respectively; both process steps used 60 s ramp times followed by 90 s of steady power. Deposition rate was controlled by a crystal monitor to maintain 1 Å/s deposition. The final layer thickness on planar regions was  $\approx 100$  nm, as measured by reflectometry and later verified with TEM measurements. Sidewall deposition showed a radial thickness of  $\approx 20$  nm.

Following deposition of the planarization layer, we cleaved the pillars using a cleanroom swab and again performed InAs heteroepitaxy using MOCVD. For the same baseline process (growth temperature of  $630^\circ\text{C}$ , V-III flux ratio of 10), growth occurred preferentially within the apertures. Unlike the previous growth at these conditions, where dot formation was typically restricted to the



(a) 40 nm preoxidation diameters,  $\approx 2.5$  nm core diameters.

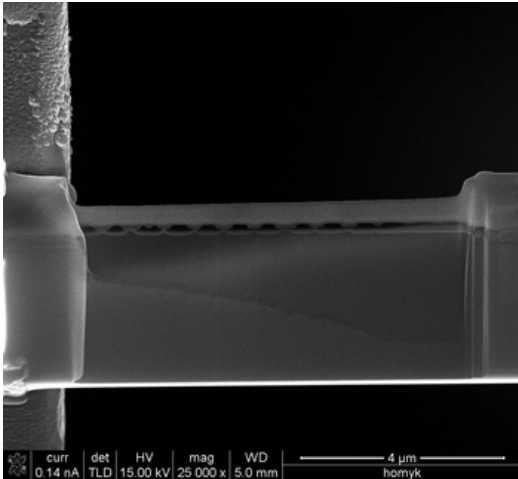


(b) 100 nm preoxidation diameters,  $\approx 16$  nm core diameters.

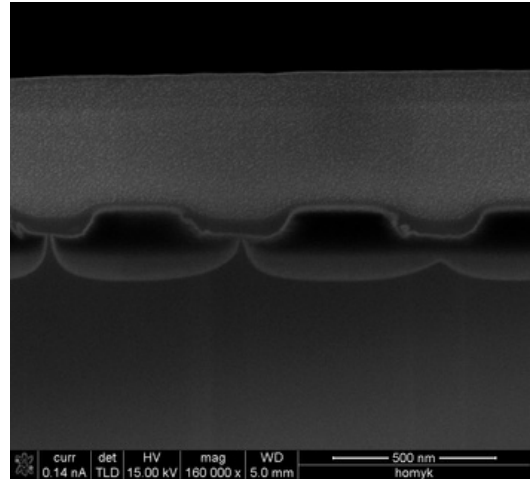
Figure 2.27: InAs QD growth onto oxidized silicon nanowire apertures at  $630^\circ$ . These devices used the revised planarization and cleaving process.

core region, the deposition here tended to form isolated clusters towards the outer edges of the wells within the alumina layer. For smaller lithographic pillar, only single dots were typically found within the alumina recesses, while multiple dots were generally observed as the diameters increased. SEMs for 40 nm and 100 nm starting diameters (corresponding to  $\approx 2.5$  nm and  $\approx 16$  nm cores, respectively) are shown in Figure 2.27.

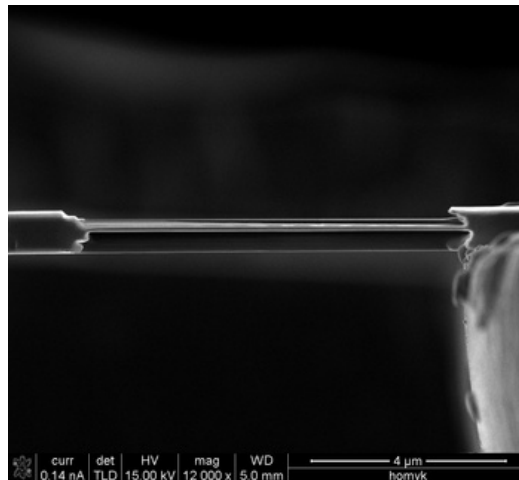
To understand the discrepancy between growth on the planarized sample and the previous runs, we examined cross-sections of the sample using a TEM; several images are presented in Figure 2.29. Although difficult to resolve, pillar cleavage was indeed observed above the planar oxide interface, as intended by the planarization process, but only by a few nm. The presence of the alumina layer did not elevate the break to a point along the bulk of the pillar, but only into the section where the oxide tapers at the pillar base. While this represents a minor improvement in achieving the minimum crystalline growth templates, the alumina was cored out all the way down to the oxide interface. This created a much deeper well than the cored out oxide did in the previous experiments, with a depth of  $\approx 100$  nm compared to the previous  $\approx 13$  nm. Because these higher alumina barriers were even more effective at trapping diffusing adatoms, growth was likely to nucleate anywhere within the aperture, resulting in the isolated clusters we observed on the sample. Based on the TEM cross-sections, these are clearly incoherent and tended to form against the alumina walls rather than over the core region.



(a) A line of pillars is visible in the middle, along with the grid on the left, and wider silicon regions for structural support. In this view, the silicon substrate is at the bottom and the pillars are vertically oriented.

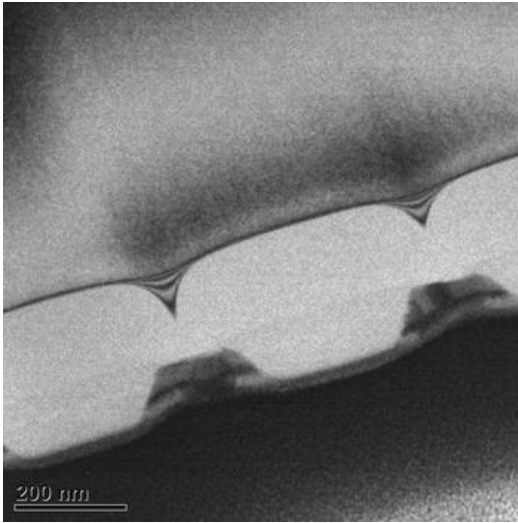


(b) Detail of the pillars. To ensure at least some devices are centered within the cross-section, the sample is intentionally cut at a slight angle relative to the array axis. The apparent variation in core diameter and height is a consequence of this.

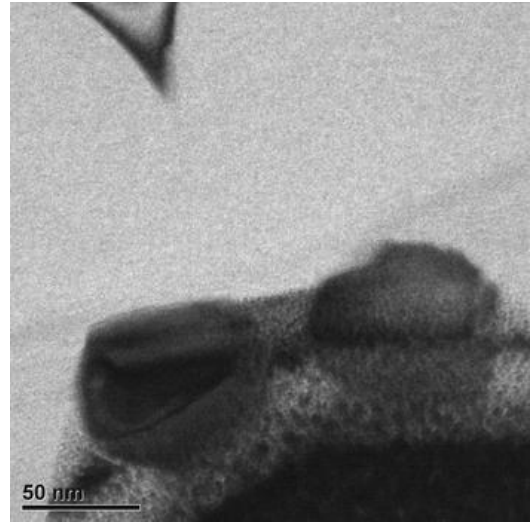


(c) Top-down view of the TEM section. The sample window has been thinned to  $\approx 35$  nm.

Figure 2.28: SEMs showing TEM cross-section preparation in the FIB. This sample contained InAs QDs grown at  $650^\circ\text{C}$  onto oxidized silicon nanowires templates. The pre- and post-oxidation core diameters were  $\approx 100$  nm and 16 nm, respectively.

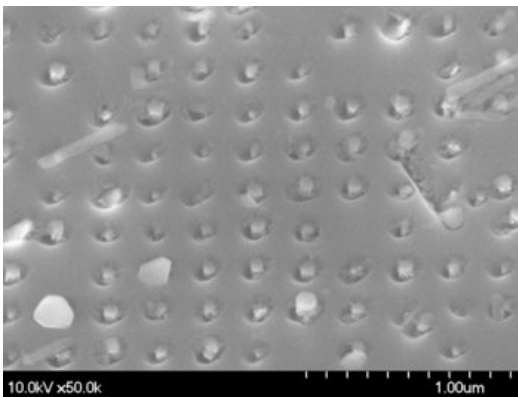


(a) An InAs QD within the growth aperture. The interface between the thermal  $\text{SiO}_2$  and e-beam deposited  $\text{Al}_2\text{O}_3$  is faintly visible (approximately at the depth of the growth aperture), confirming that the pillar cleaved slightly above the planar oxide height. However, the break occurred well below the  $\text{Al}_2\text{O}_3$  surface, creating a large recessed region. An InAs QD is visible within this area, likely the result of adatom trapping within the alumina barrier.

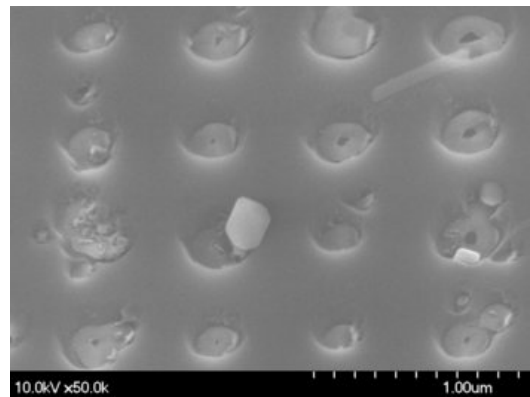


(b) A detailed view showing multiple large InAs QDs within a single growth aperture.

Figure 2.29: TEMs showing InAs QDs grown on our silicon growth templates at  $630^\circ\text{C}$ . The starting diameter of the pillars was 80 nm. In this orientation, the silicon substrate is at the top, and the base of the pillars can be seen projecting downwards. The apparent distance between the silicon tip and the growth area arises from a deliberate miscut in the sample preparation.

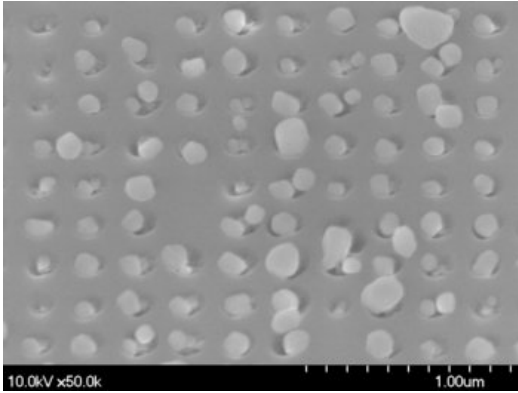


(a) 40 nm preoxidation diameters,  $\approx 2.5$  nm core diameters.

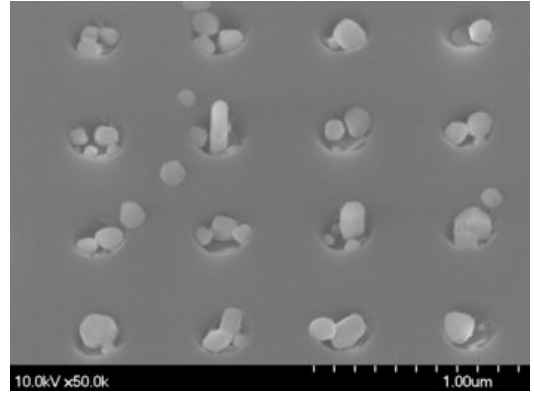


(b) 100 nm preoxidation diameters,  $\approx 16$  nm core diameters.

Figure 2.30: InAs QD growth onto oxidized silicon nanowire apertures at  $650^\circ$ . These devices showed improved uniformity when compared to the process at  $630^\circ\text{C}$  (Figure 2.27), but decreased coverage over larger cores.



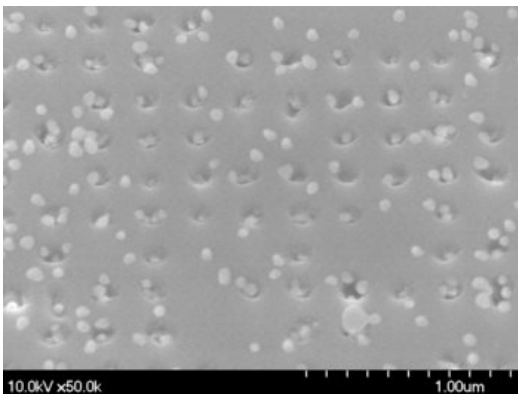
(a) 40 nm preoxidation diameters,  $\approx 2.5$  nm core diameters.



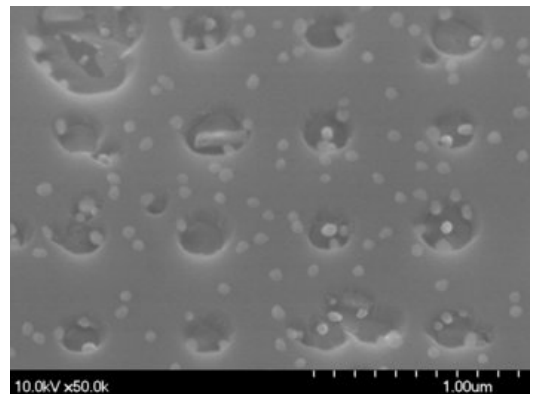
(b) 100 nm preoxidation diameters,  $\approx 16$  nm core diameters.

Figure 2.31: InAs QD growth onto oxidized silicon nanowire apertures, with a reduced V-III ratio of 5. The reduction in As flow enables greater In diffusion, resulting in more uniform growth and larger crystals than the process at  $650^\circ\text{C}$  (Figure 2.30).

On the next samples, we sought to overcome the trapping and nucleation problems by increasing In adatom diffusion. Increasing the temperature to  $650^\circ\text{C}$  successfully reduced the nucleation, resulting in more regular deposition over the smaller apertures but almost no deposition over larger cores; SEMs of growth over the 40 nm and 100 nm pillars (starting diameter) are presented in Figure 2.30. As an alternative to temperature control, the ratio of process gases will also influence the effective adatom diffusion length. By reducing the V-III ratio to 5, increased In diffusion enabled more uniform growth and larger crystals than the  $650^\circ\text{C}$  sample; SEMs for 40 nm and 100 nm starting diameters are shown in Figure 2.31.



(a) 40 nm preoxidation diameters,  $\approx 2.5$  nm core diameters.



(b) 100 nm preoxidation diameters,  $\approx 16$  nm core diameters.

Figure 2.32: Growth of InSb dots at  $515^\circ\text{C}$  on the oxidized silicon nanowire growth templates.

Additional deposition was performed of InSb (Figure 2.32), which behaved similarly to InAs but at lower temperatures and flux ratios. Growth of GaP and GaAs was also attempted, but these materials did not exhibit any nucleation at conditions which have been successful for nanopillar growth (500°C and 660 - 720°C, respectively). Of all of the deposition performed, only the InAs nanopillar growth exhibited coherence with the underlying silicon substrate, but even that contained a significant density of stacking faults. It is therefore unsurprising that no photoluminescence was observed from any sample, as light emission is only expected for sufficient crystal quality and coherent growth [32].

The nanometer-scale silicon structures we developed using self-terminating oxidation remain an exciting platform for heteroepitaxy. We have demonstrated their suitability as growth templates for III-V quantum dots and nanowires on silicon. Future development to improve the planarization and cleaving process, *e.g.*, by employing chemical-mechanical polishing (CMP) and an oxidation removal step, would greatly reduce the inadvertent trapping and nucleation within the amorphous apertures. By enhancing specific growth over the crystalline cores, this could provide the quality improvements necessary to produce high-quality quantum emitters directly on silicon. Precise spatial alignment of the emitter would be achieved with lithographic control over the template's location, along with height control through the polishing process. Additionally, nm-scale dimensional accuracy could enable accurate command over the emitter's spectral properties, while the surrounding oxide layer would naturally serve as both a growth window and self-aligned current aperture for electrical pumping [212, 75, 74]. While we chose to pursue other methods of deterministic integration, we believe that this technique still holds great potential as a platform for the integration of optically active materials on silicon substrates.

#### 2.4.1.4 SiGe detectors

Along with techniques for deterministic integration of quantum emitters, monolithic cQED systems also requires the production of sensitive detectors. Since the passive guiding medium must itself exhibit minimum absorption in order to produce high-quality cavities, the fabrication of detectors

on the same platform presents a similar materials integration challenge as that faced for emitter integration. Beyond possessing a high quantum efficiency, the ideal detector must also produce minimal dark current. This requires a suitable electronic aperture to confine the current source to the intended area and minimize background current through outside channels, as well as high crystalline quality for the detector material, as generation and hopping processes through defect states are major sources of dark current. Since both of these qualities could potentially be improved by the oxide apertures we developed for the InAs QDs, we sought to apply this process to the fabrication of heteroepitaxial photodetectors on silicon.

Among many possible material choices for CMOS-compatible photonics, Ge is particularly attractive as a detector because of its high absorption coefficient and wide band gap engineering possible within the Ge/Si heterostructure system. Much like the growth of III-Vs on Si, layer-by-layer epitaxy of Ge on Si is challenging due to a large mismatch of 4.2%. Many other approaches to reduce defect have been previously explored, including the use of SiGe and oxide buffer layers [224, 307, 64], two-step growth processes [20, 222], and annealing [260, 54]. Although suitable for bulk photodetectors, these techniques are less desirable for integrated nanophotonic applications due to the requirements for thick layers. Ge nanowire growth has also been previously demonstrated [336], but the technique did not possess site controllability, while the use of Au nanoparticle seeds is incompatible with CMOS fabrication. Kozłowski *et al.* [182] reported a selective growth technique of Ge-on-Si nanopillars which is schematically similar to our method; however, no photodetector characterization was reported. Additionally, this report only used pillar diameters down to 50 nm and without further self-terminated oxidative reduction, while theoretical calculations have indicated a critical diameter of 40 nm for this system [402].

Here, we developed high-sensitivity, broadband photodetectors fabricated by selective growth of  $\text{Si}_{0.3}\text{Ge}_{0.7}$  quantum dots over Si nanopillars with self-terminated oxide apertures, as reported in [189]. We began our fabrication as described above, but using highly-doped 60  $\text{m}\Omega\cdot\text{cm}$  p-type  $\langle 111 \rangle$  silicon substrates rather than the lightly-doped wafers used for the InAs QD growth. Electron-beam lithography was used to pattern 40 nm - 100 nm circular holes into PMMA. An aluminum oxide

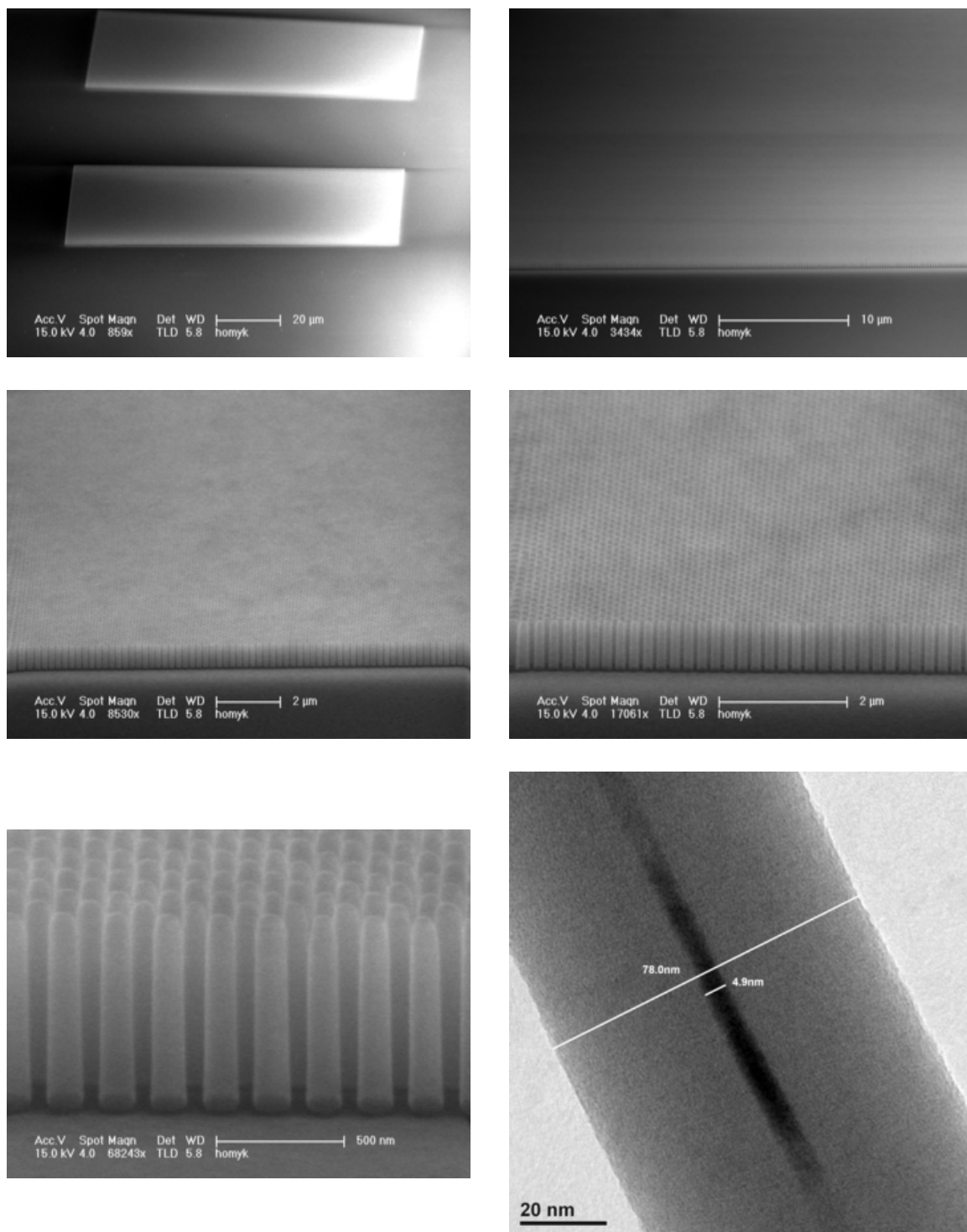


Figure 2.33: Large arrays of uniform, oxidized nanopillars for SiGe quantum dot growth. Start diameters ranged from 40 nm - 100 nm.

hard mask was deposited onto the template using reactive ion sputtering, followed by lift-off in acetone, chloroform and IPA to produce circular alumina masks. Masked samples were etched in an ICP-RIE using an  $\text{SF}_6/\text{C}_4\text{F}_8$  chemistry to produce silicon nanopillars with heights  $\approx 1 \mu\text{m}$ . Pillars were then oxidized in a dry environment at  $900^\circ\text{C}$  until the oxide growth had terminated, yielding core diameters  $\approx 5 \text{ nm} - 30 \text{ nm}$  as measured by TEM. SEM and TEM images of the oxidized pillars are shown in Figure 2.33.

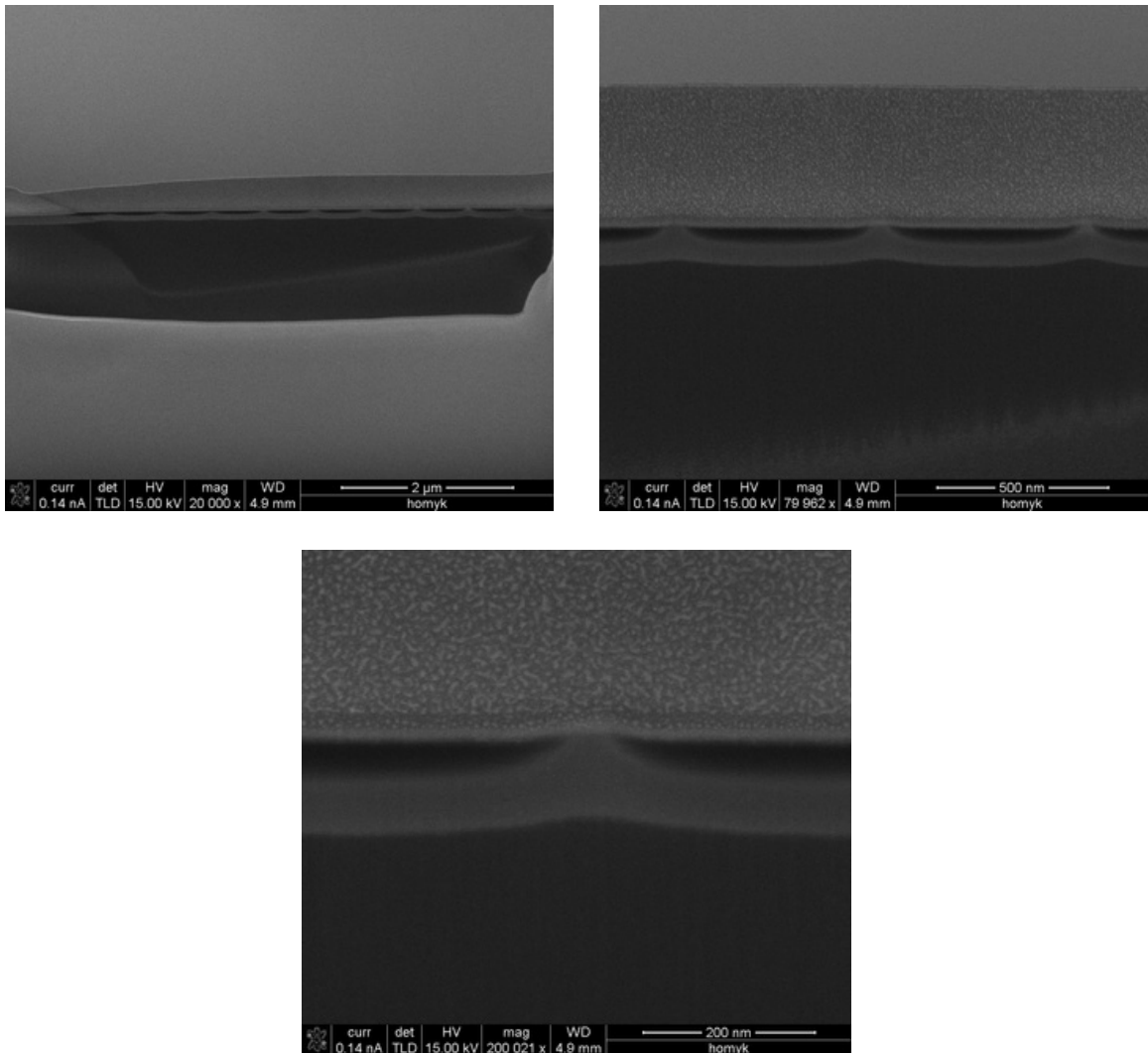


Figure 2.34: TEM sample preparation of SiGe quantum dots grown on oxidized silicon nanopillar templates.

Growth of the  $\text{Si}_{0.3}\text{Ge}_{0.7}$  quantum dots was performed in collaboration with the Li group at the Center for Nanoscience and Technology, National Central University, Taiwan. Just prior to growth,

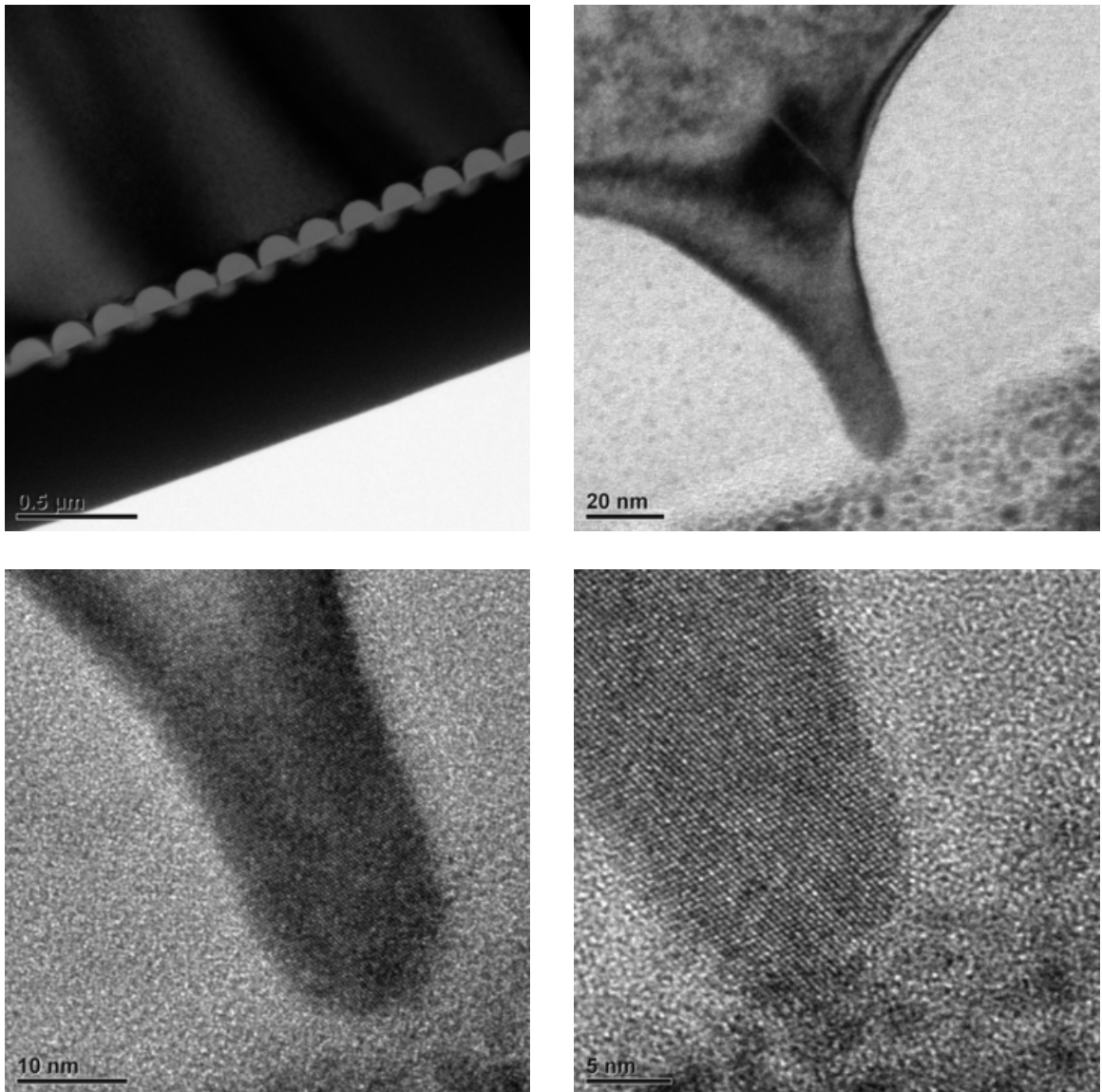
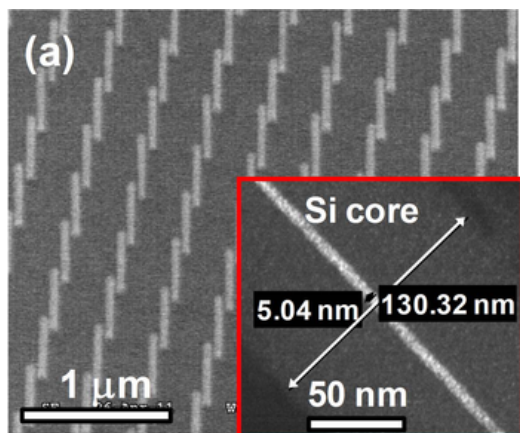


Figure 2.35: Cross-sectional TEMs of SiGe quantum dots grown on oxidized silicon nanowire templates.

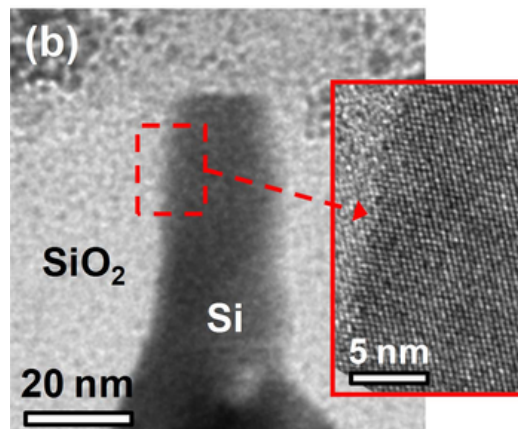
the pillars were cleaved by wiping the surface with a cleanroom swab, followed by an immediate RCA clean, HF dip, and deposition.  $\text{Si}_{0.3}\text{Ge}_{0.7}$  quantum dots were selectively grown over the nanopillar cores using low-pressure chemical vapor deposition (LPCVD) at  $400^\circ\text{C}$  for 15 minutes, corresponding to a nominal planar deposition rate of 0.8 - 1.3 nm/min. No dopants were intentionally introduced during the deposition process. After removal from the chamber, a 30 nm layer of transparent indium tin oxide (ITO) was deposited over the array and patterned to serve as the top electrode, followed by a 500 nm Al layer on the backside of the substrate. For comparison, control samples were also prepared which contained the ITO and Al electrodes, but without the  $\text{Si}_{0.3}\text{Ge}_{0.7}$  QDs.

Figure 2.36a presents an array of pillars after oxidation; their initial diameters were 60 nm. The inset shows shows a cross-sectional TEM in dark-field using diffraction contrast to highlight the 5 nm core. In Figure 2.36b, a cross-sectional TEM displays the Si core of a larger pillar, surrounded by thermal  $\text{SiO}_2$ . A lattice image for a section of the pillar is visible in the inset of Figure 2.36b, indicating the crystalline quality of the pillar after cleaving. The top of the pillar corresponds to the cleaved interface, where the lighter semicircular region above is the SiGe dot, confirmed by EDX analysis. The darker speckles around the top of the image are caused by the Pt deposited as part of the TEM sample preparation. Figure 2.36c shows a plan-view SEM of the grown  $\text{Si}_{0.3}\text{Ge}_{0.7}$  quantum dots. Finally, Figure 2.36d shows a corresponding cross-sectional TEM of the Si: $\text{Si}_{0.3}\text{Ge}_{0.7}$  QD interface; an HRTEM image for a section of this is presented in the inset. Together, these illustrate the successful growth of oblong (26 nm high, 50 nm wide)  $\text{Si}_{0.3}\text{Ge}_{0.7}$  QDs over Si pillars.

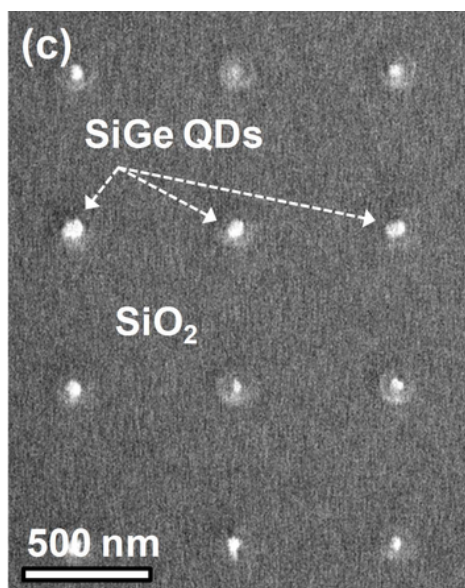
The absence of QDs over the  $\text{SiO}_2$  in the plan-view SEM (Figure 2.36c) indicates highly preferential growth within each aperture, with excellent uniformity and coverage of the dots. As compared to the InAs growth, these improvements could have been enabled by the additional RCA and HF steps performed immediately prior to deposition. Examining the cross-sectional TEM in Figure 2.36d, the dots themselves appear to consist of a mixture of amorphous and polycrystalline SiGe. This is potentially a consequence of microfractures or uneven surfaces created during the cleaving process, resulting in nucleation at multiple points on the core during the initial SiGe deposition. As with the III-V growth, a CMP process might improve the template surface and



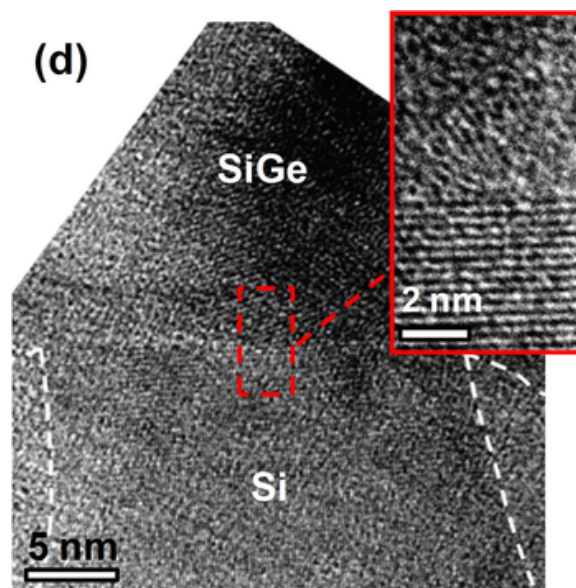
(a) SEM image of Si pillar array after self-terminating oxidation. Inset shows a dark-field TEM image of a 5 nm Si core.



(b) Cross-sectional TEM of a Si pillar. Inset exhibits good single-crystallinity of the Si pillar by HRTEM.



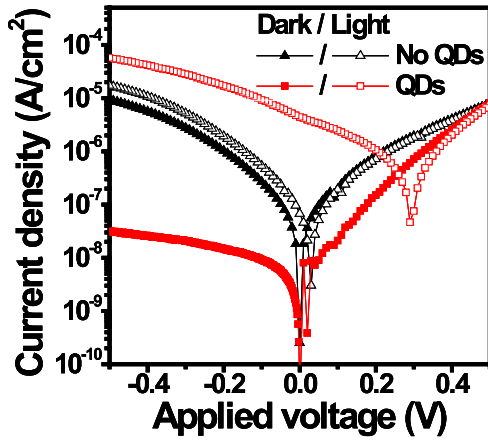
(c) Plan-view SEM image of selective growth of SiGe QDs over Si pillars.



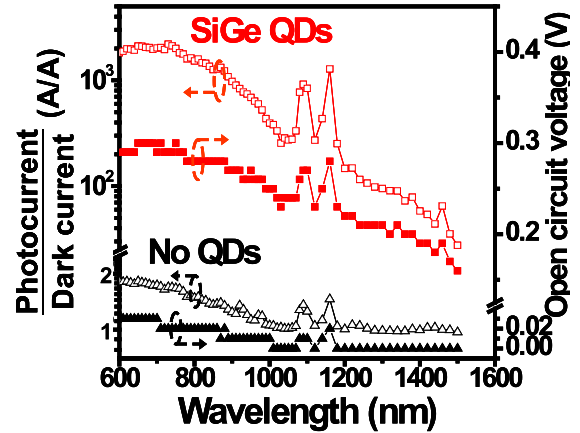
(d) Cross-sectional TEM of the SiGe QDs/Si pillar interface. Inset shows the corresponding HRTEM image.

Figure 2.36: SiGe QD devices grown on Si nanopillars.

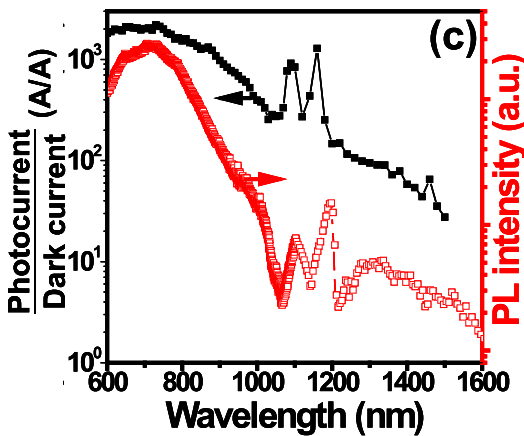
enable single-crystal epitaxial QD growth.



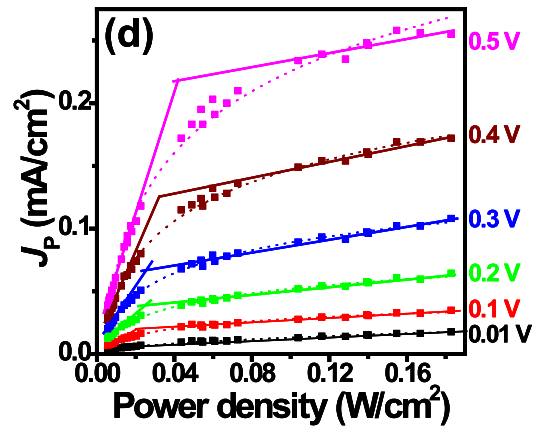
(a) J-V characteristics under dark environment and with 550-800 nm illumination at 9 mW/cm<sup>2</sup>.



(b) Ratio of photocurrent to dark current and open-circuit voltage as a function of incident light wavelength for both diodes with and without SiGe QDs.



(c)  $\mu$ PL spectroscopy of Si<sub>0.3</sub>Ge<sub>0.7</sub> QD/Si pillar array.



(d) Power-dependent photocurrent density under various bias conditions for diodes containing SiGe QDs at the wavelength of 550 nm.

Figure 2.37: Electrical behavior of the SiGe QD detectors.

Despite the amorphous phases, however, the SiGe exhibited a very low current density ( $J_{dark}$ ) of  $3.2 \times 10^{-8}$  A/cm<sup>2</sup>, suggesting that the QDs are of sufficient quality for photodetection. DC responsivity of the diodes was measured using a monochromatic light source in the wavelength range 500 - 1500 nm, over a gate area of 2500  $\mu$ m<sup>2</sup>, including an active area of 8.87  $\mu$ m<sup>2</sup> under the SiGe QDs (where present). Figure 2.37a illustrates the current density-voltage ( $J$ - $V$ ) characteristics of ITO/Si pillar diodes both with and without SiGe QDs, and in both dark environments and under 550-800 nm illumination at 9 mW/cm<sup>2</sup>. The bare ITO/Si diodes possessed a symmetrical

$J$ - $V$  relationship under different bias polarities, both when illuminated and dark. By contrast, the diodes containing  $\text{Si}_{0.3}\text{Ge}_{0.7}$  QDs showed current rectification. For these devices, illumination induced significant current enhancement of the QD diodes under reverse bias, and an open-circuit voltage of +0.3 V. The significant DC photocurrent at zero bias indicates that a built-in electric field was already established within the SiGe QD devices, suggesting good intrinsic SiGe QD material quality [208]. The diodes without QDs showed little variation between the dark and illuminated characteristics, with no appreciable open-circuit voltage and dark currents approximately two orders of magnitude greater than the SiGe devices.

When biased at -0.5 V, the QD-based diodes exhibited a ratio of photocurrent to dark current up to  $\approx 2200$ , 100, and 30 under illumination at  $9 \text{ mW/cm}^2$  for wavelengths in the range 500-800 nm, 1300 nm, and 1550 nm, respectively; these data are shown in Figure 2.37b. The photocurrent-to-dark current ratio and the open-circuit voltage shared similar spectral characteristics, showing fairly wideband operation with noticeable declines for wavelengths longer than 800 nm. Given the limited thickness of the QD layer, this was likely due to the reduced absorption coefficient for Ge in the IR, which drops from  $2 \times 10^5 \text{ cm}^{-1}$  at 500 nm to  $8 \times 10^3 \text{ cm}^{-1}$  and  $3 \times 10^3 \text{ cm}^{-1}$  at 1300 nm and 1500 nm, respectively. By contrast, illumination over similar spectra induced comparatively marginal changes on photocurrent and open-circuit voltage for the ITO/Si pillars containing no QDs (note the different scale in Figure 2.37b). We also note the two satellite peaks around 1100 nm. These occurred in both sets of data, and are likely a consequence of light absorption from the Si substrate. The spectral response of the QD diode also agreed well with microphotoluminescence ( $\mu\text{PL}$ ) spectra measured from the array of  $\text{Si}_{0.3}\text{Ge}_{0.7}$  QDs (Figure 2.37c). This emission was possibly due to a combination of quantum confinement and strain induced in the SiGe nanocrystals, as well as photoluminescence from the Si pillars themselves (to be discussed further in the next section).

Within the peak operating regime between 500 nm to 800 nm, the SiGe QD diodes exhibited an overall photoresponsivity of 6 and 30 mA/W at applied voltages of 0.5 and 3 V, respectively. For  $\lambda=500$  nm, this corresponds to an *external* quantum efficiency of  $\approx 19\%$  at 3 V bias. Given that the measured dark current was only  $3.2 \times 10^{-8} \text{ A/cm}^2$ , this also implies a dark count rate of only  $\approx 10$  Hz

per diode. Already, this is quite comparable to commercial single photon detectors (for comparison, the Thorlabs SPCM20 and SPCM50 single photon Si APDs have max responsivity  $\approx 35\%$  at 500 nm and dark counts of 25 - 150 Hz, albeit with much larger detection areas). Moreover, we note that this experiment utilized only planar illumination over a broad area. The responsivity is expected to be further enhanced by directly coupling the detector to a waveguide and increasing the SiGe QD layer thickness, while the dark counts could potentially be reduced by improving the crystallinity through a CMP process on the template and optimized growth conditions. Finally, the extremely small junction also results in a significantly reduced capacitance compared to broad area detectors, critical to high speed operation.

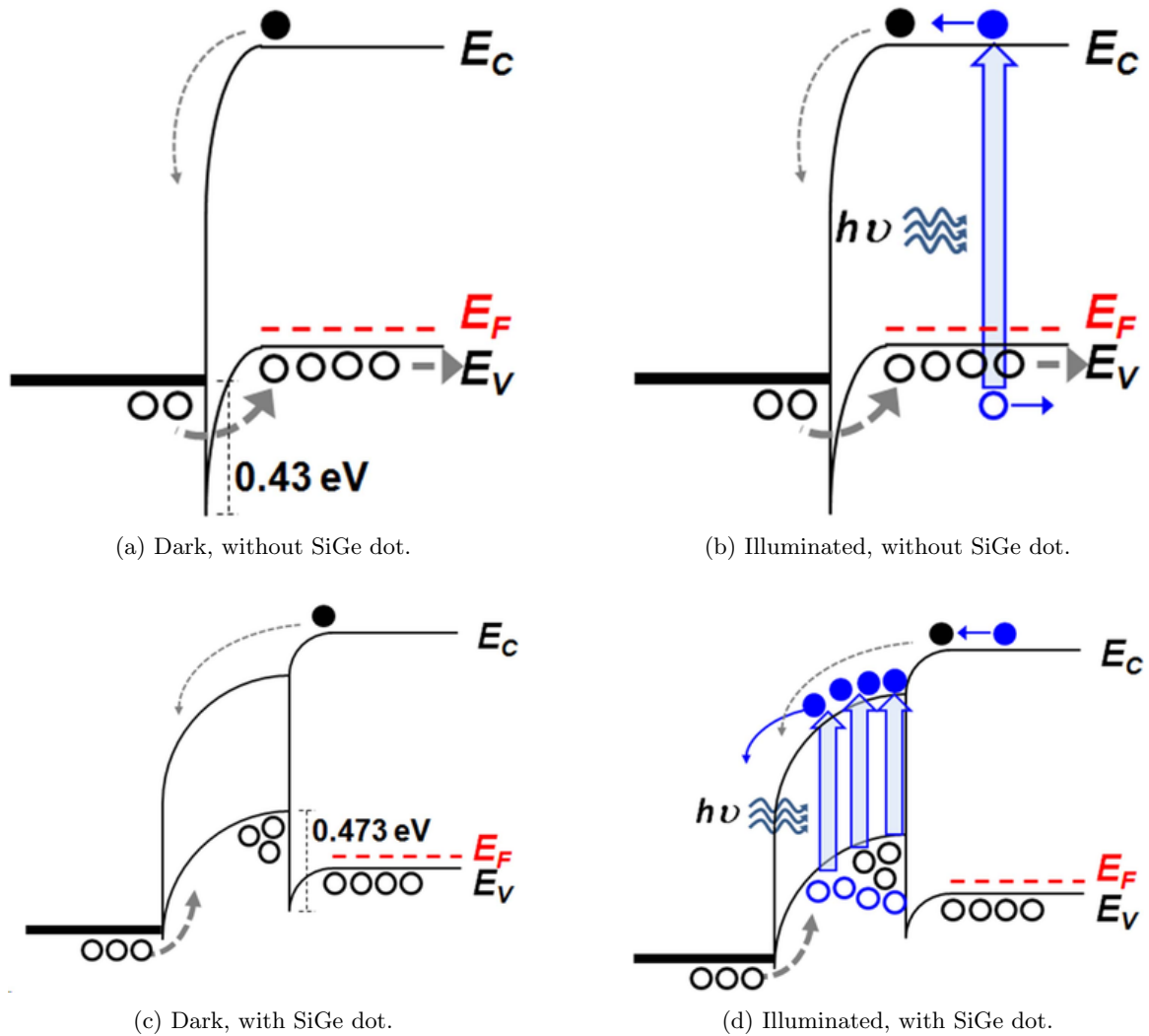


Figure 2.38: Schematic of the SiGe QD band structure and reverse-bias operation.

Figure 2.38 shows schematic energy band diagrams for the diodes under reverse bias. For diodes without QDs (Figure 2.38a), a Schottky barrier with a height of 0.43 eV and 7.3 nm in width was inherently present in the valence band at the ITO/Si pillar interface due to the work function difference between these materials. Such a thin barrier was easily overcome by charge tunneling, leading to quasi-symmetrical current behaviors and an ohmic response, as shown in Figure 2.37a. Under illumination, the poor absorption in the Si contributed negligible exciton generation (Figure 2.38b), resulting in insignificant current enhancement for the ITO/Si pillar diodes. In contrast, for the diodes containing SiGe QDs, holes from the ITO electrode had little chance to surmount the relatively high and thick barrier induced by the valence band offset between the intrinsic SiGe QD and p<sup>+</sup>-Si pillar, leading to effective hole confinement and thus a built-in electric field within the QD (Figure 2.38c). Under illumination, photoexcited electrons in the QD drift toward the ITO electrode under the electric field, producing a significant enhancement of the current by three orders of magnitude.

Considering the power-intensity dependence of the photocurrent, the QD-based photodiodes exhibited a quadratic power density dependence on illumination ( $J_P \approx 4 \times 10^{-5} P^{0.5}$ , where  $J_P$  is the photocurrent density and  $P$  is the incident optical intensity) at low power and low bias voltages ( $\approx 0.01$  V), eventually reaching a saturation around  $P_{sat} \approx 0.075$  W/cm<sup>2</sup> (Figure 2.37d). Hong *et al.* [133] have reported a similar nonlinear power-dependent photocurrent behavior for p-i-n GaAs/AlGaAs multiple quantum well (MQW) diodes as a result of hole-accumulation induced charge recombination [133, 255, 254]. A hole confinement phenomenon also occurs in our SiGe QD diodes, leading to the competition between electron drift and carrier recombination and a nonlinearity in photocurrent density. The nonlinear power dependence of the photocurrent density could be described by  $J_P \approx bP^a$ , as shown in Figure 2.37d, where  $a$  is the fitting coefficient and  $b$  denotes the initial slope of  $J_P$  when  $P$  is less than  $P_{sat}$ , beyond which  $J_P$  becomes saturated. Notably,  $a$  appears to be 0.5 for  $V=0.01$  V, corresponding to Hong's prediction that recombination processes dominate at very small bias voltages [133]. Another interesting conclusion from these power-dependent characteristics is that the fitting coefficients  $b$  and  $P_{sat}$  increase with an increase

in bias voltage. This suggests that the linearity is tunable through the applied bias, which enhances the carrier drift process and suppresses recombination as the voltage increases.

Through the self-terminating oxidation of silicon nanopillars, we have developed a technique to enable selective-area heteroepitaxy of highly-mismatched semiconductor crystals on silicon. Using this method, we successfully demonstrated high-quality deposition of  $\text{Si}_{0.3}\text{Ge}_{0.7}$  quantum dots onto these templates, exhibiting highly preferential growth within the apertures, with superb coverage and uniformity. By characterizing the DC photoresponsivity of these devices, we have shown that they possess both high quantum efficiency and extraordinarily low dark counts with properties rivaling existing commercial technology, making the  $\text{Si}_{0.3}\text{Ge}_{0.7}$  QD diodes extremely attractive as broadband photodetectors in next-generation integrated photonic systems. Future work should seek to improve the growth interface and crystal quality through chemical mechanical polishing, as well as optimize the coupling to waveguides or other integrated photonic circuitry.

## 2.4.2 Silicon quantum wires and dots

### 2.4.2.1 Silicon nanowire photoluminescence

During our development of the Si nanopillar heteroepitaxy templates, photoluminescence was one of the primary methods we used to characterize the self-terminating oxidation process, providing a rapid, non-destructive method of evaluating the core dimensions. Besides the ability to validate the heteroepitaxy aperture sizes, the photoluminescence studies suggested an opportunity to use silicon as the quantum light emitters themselves, offering another appealing option for large-scale integration. Our photoluminescence studies on silicon nanowires were reported in [364].

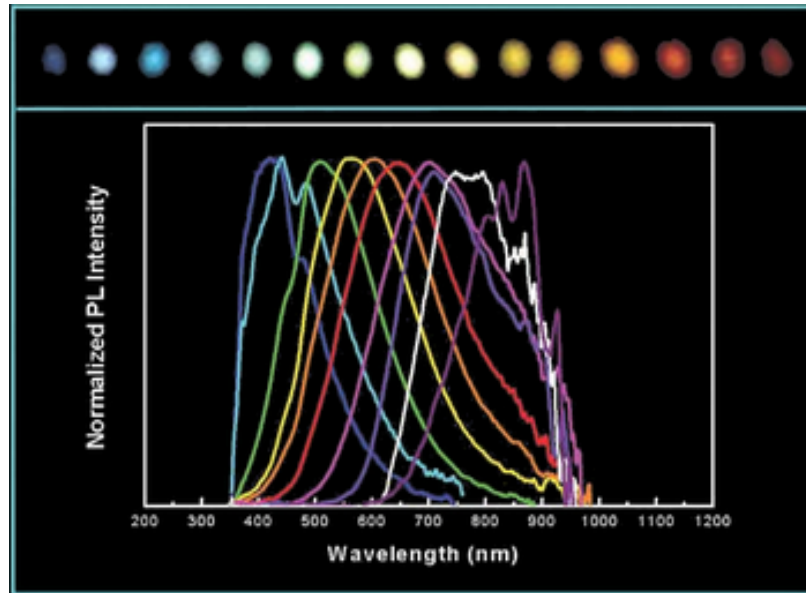
In bulk, silicon possesses an indirect band gap where the valence band maximum and conduction band minimum lie at different points within the Brillouin zone. In order for silicon to emit a photon, momentum conservation requires participation of a phonon. For bulk silicon, radiative recombination is therefore an inefficient, second-order process, making the material a poor light emitter. Technically, it is possible to improve the luminescence by minimizing nonradiative decay. For example, the use of extremely pure material with carefully passivated surfaces can reduce nonradiative recombination

through defects or surface. At best, however, these methods have shown these have only shown luminescence efficiencies up to  $\approx 1\%$  [112].

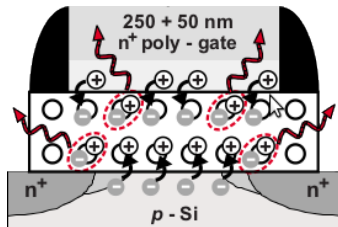
Alternatively, luminescence efficiency can also be improved by increasing the radiative recombination rate. Nanostructures are capable of achieving this in several ways [88]. At length scales on the order of the exciton Bohr radius — approximately 5 nm in silicon [27] — the carrier wavefunctions are significantly affected by the semiconductor boundaries, and the use of bulk band structures is no longer justified. The Brillouin zone effectively folds, potentially resulting in quasi-direct band structures and a competition between no-phonon and phonon-assisted transitions. As confinement energy increases, the ratio between these recombination channels changes by 2 orders of magnitude, eventually leading to radiative transitions which are governed by no-phonon, quasi-direct processes. Even outside this regime, the spatial localization of the electron and hole wavefunctions within the nanostructures corresponds to a spread in momentum space, increasing their overlap in the Brillouin zone [142]. Additionally, crystal imperfections are simply less likely to exist within the limited volume of a nanostructure, or might be annealed to the surface, thereby decreasing competition from nonradiative decay channels.

Excitement over light emission from silicon began when visible light emission was reported from electrochemically-etched porous silicon nanostructures [46, 63]. After etching, the remaining structures consisted of a skeletal framework of interconnecting columns which were still crystalline. TEM analysis showed these primarily had diameters  $>10$  nm, but containing a fraction of threads below  $\approx 3$  nm in diameter. Since the spectra tended to blue shift with decreasing size, consistent with particle-in-a-box calculations, the behavior was attributed to quantum confinement. Although later work indicated the emission may have been due to Si-H complexes rather than confinement [281], interest in silicon light emission continued to grow.

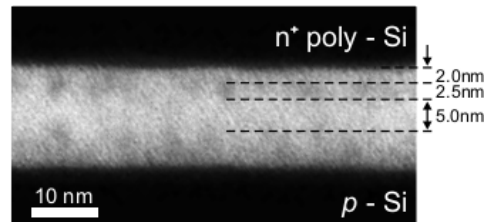
A great deal of work followed to create luminescent silicon nanostructures. Silicon nanocrystals in particular have shown great success [65, 167, 166, 27, 181]. These have nanometer dimensions in all directions and therefore the complete quantum confinement of the excited carriers. This enables the most efficient luminescence and very broad wavelength tuning throughout the visible and near



(a) PL spectra from Si QDs in a  $\text{Si}_3\text{N}_4$  matrix. The peak emission is controlled by varying the QD size. From [167].



(b) Schematic of an electro-luminescent silicon FET using silicon nanocrystals implanted in the gate. From [35]



(c) Cross-sectional EFTEM showing two layers of 2 - 3 nm SiNCs embedded in the gate of an electro-luminescent silicon FET. These emitters were formed by ion irradiation and precipitation during annealing, leading to a broad size and spectral distribution. From [35]

infrared (see Figure 2.39a). A number of methods have been explored to produce these, including implantation of Si into SiO<sub>2</sub> [248], deposition of amorphous Si/SiO<sub>2</sub> [349, 114], or SiO/SiO<sub>2</sub> [393] multilayer stacks, for example by magnetron sputtering, direct CVD of Si-rich SiO<sub>2</sub>, or PECVD of Si-rich SiN<sub>x</sub> [167]. Many of these involve annealing Si-rich dielectric films, causing silicon clusters to form within an amorphous matrix. Having to tunnel electrons through the insulating film creates some challenges to electrical pumping, but this too has been demonstrated [368]. A greater challenge for our purposes is the stochastic nature of the deposition process, which results in a random placement and distribution of nanocrystal dimensions, directly influencing the spectrum. While the size distribution can be controlled to some extent by the stoichiometry of the film or deposition method, a given population can show 20-50% variation from the average [248]. To our knowledge, precise, deterministic control over the size and location of Si nanocrystal emitters has not been reported (outside of our own work, which will be discussed shortly).

Significant effort has also been made with grown [116, 68, 283, 305, 262] and etched [259, 194, 350, 177] nanowires. Nanowire growth often employs a vapor-liquid-solid (VLS) process, in which a catalyst droplet is heated above its eutectic point and subjected to a background flux of Si atoms. As the catalyst becomes supersaturated with silicon, the atoms precipitate out, pushing the catalyst droplet upwards and causing a nanowire to grow underneath. Proper control over the droplet deposition therefore enables command over the nanowire size and location. Au is the most common catalyst for VLS growth of silicon nanowires, but unfortunately results in a deep level trap, resulting in a fast, non-radiative decay channel which hinders efficient photoluminescence [116]. Using TiSi<sub>2</sub> as an alternative catalyst, Guichard *et al.* [116, 117] have demonstrated size-dependent photoluminescence using VLS-grown silicon nanowires; however, this too is inevitably inefficient. Wu *et al.* [380] showed that nanowire growth proceeds along  $\langle 110 \rangle$  or  $\langle 111 \rangle$ , depending on the diameter. Based on density functional theory (DFT) and tight binding method (TBM) simulations, however, wires grown along these axes are not expected to undergo transition to a direct band gap as the diameter is decreased [276], unlike wires grown along the  $\langle 100 \rangle$  direction [13].

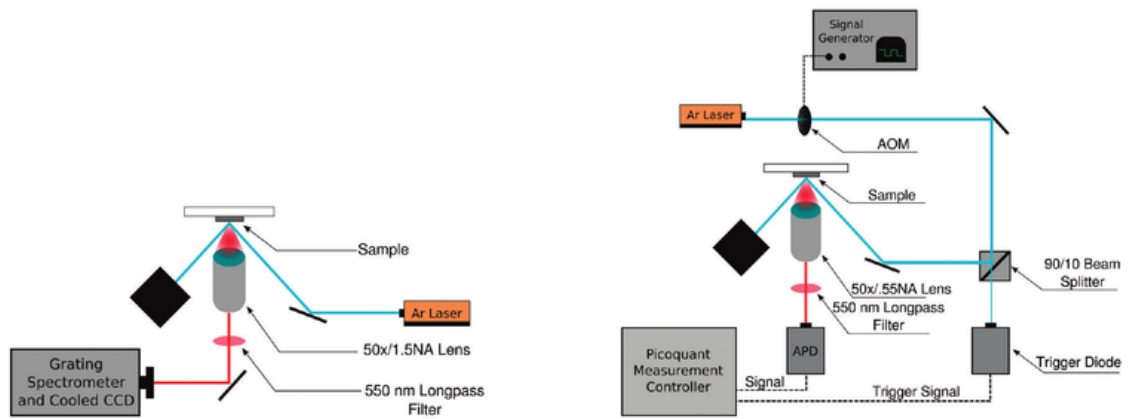
Alternatively, etched nanowires can utilize any substrate orientation, and naturally offer

lithographic control over the size and location. The primary challenges for these systems lie in lithographically defining the sub-10 nm dimensions required to begin observing PL, as well as achieving the necessary etch depth, sidewall roughness, and anisotropy to yield bright, uniform spectra. Previous efforts using etched nanopillars have reported bright PL, but with spectral widths exceeding 1 eV [259, 350]. This spectral broadening was attributed to the distribution of pillar sizes in the etched samples, which was sufficiently large as to obscure the effects of specific pillar sizes on PL characteristics.

Using the self-terminating oxidation process, we had the ability to create large arrays of highly-uniform silicon nanostructures, possessing much tighter size and therefore spectral distributions than these reports. Fabrication of the arrays utilized the same masking, etching, and oxidation processes described above, with the exception that lightly-doped  $\langle 100 \rangle$  wafers were utilized rather than the (potentially highly-doped)  $\langle 111 \rangle$  substrates required for the growth studies. While photoluminescence has been demonstrated for  $\langle 111 \rangle$  silicon nanowires [116, 117], the efficiency could be limited. As noted previously, band structure simulations have revealed that only  $\langle 100 \rangle$  silicon will undergo the transition to a direct band structure as the diameter is decreased [276, 13]. Lithographic diameters of the pillars ranged from 30 nm - 50 nm. Dry oxidation was performed between 850°C - 950°C until terminal oxidation had been achieved, approximately 7 h - 10 h.

Microphotoluminescence was performed in an inverted microscope, using free space excitation from an Ar<sup>+</sup> ion laser at 488 nm. To minimize the amount of reflected laser light entering the spectrometer, samples were mounted downwards with the laser coupling in at a 45° angle. Light was collected by a 50×/0.55 NA objective, passed through a 550 nm long-pass filter to block out excitation light, and coupled into a grating spectrometer with a cryogenically cooled Si CCD array. A schematic of the measurement is shown in Figure 2.40.

Photoluminescence was observed between 600 nm - 800 nm (1.5 eV - 1.9 eV). Figure 2.41 shows normalized spectra for pillars with cores between 2.5 nm and 8.6 nm; the solid lines correspond to pillars with lithographic diameters of 35 nm, while the dotted lines indicate starting diameters of 50 nm. Clearly, the luminescent spectra underwent a strong blue shift with decreasing core diameter.



(a) Setup for photoluminescence spectra. Laser light is coupled at a  $45^\circ$  angle and sent to a beam block, while PL is collected through a microscope, filtered by a 550nm long pass, and recorded by a spectrometer

(b) Lifetime measurement schematic. Laser light is gated by an AOM with a period of  $20\mu\text{s}$  and a 50% duty cycle, split with a 90:10 beam splitter and sent to the sample and a trigger diode. PL from the sample is detected by an APD which is gated by the Picoquant controller to obtain lifetime measurements.

Figure 2.40: Schematics of the PL testing setup.

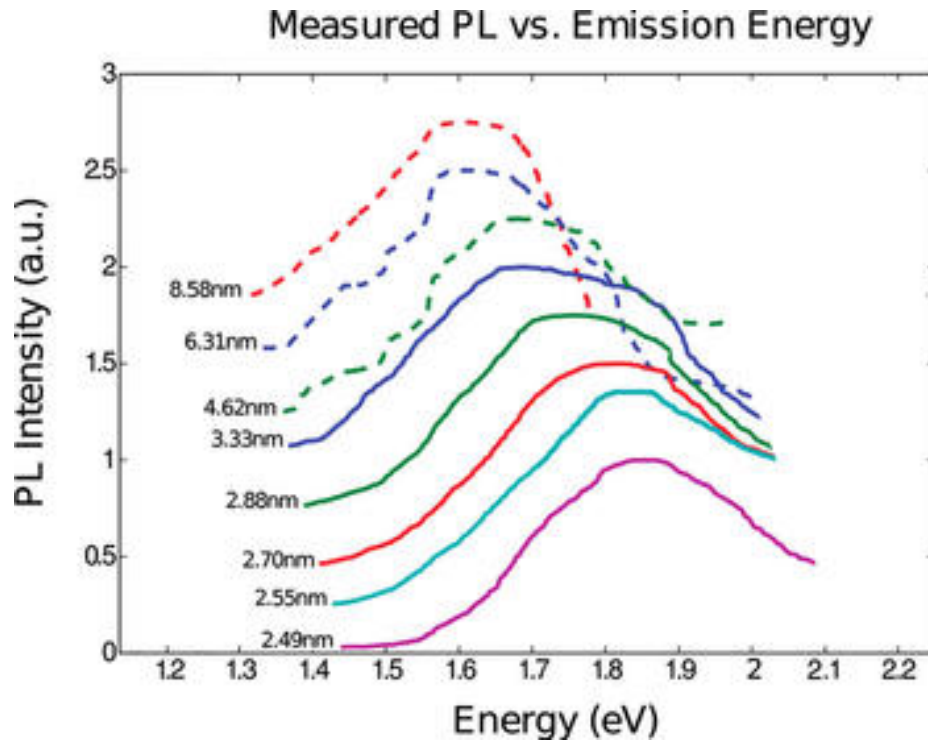


Figure 2.41: Normalized PL from eight SiNW samples with varying diameters, obtained by controlling the oxidation temperature. Diameter measurements reflect the average size measured by TEM. Dotted lines represent pillars with 50 nm pre-oxidation diameters, and continuous lines with 35 nm initial diameters.

This trend is presented further in Figure 2.42(a,b). Here, the peak emission energy (and wavelength) are plotted as a function of core diameter. The  $x$  error bars depict the standard deviation of core diameters, and  $y$  error bars indicate the spectral width of the emission (full width at half-maximum, FWHM). We note that the average FWHM was 240 meV, with most widths at roughly 150 meV or less. This broadening is 30% to 50% narrower than previously reported results [116, 259, 194], indicative of a narrower size distribution of silicon cores within each array. We believe this is due to a combination of greater preoxidation uniformity through our improvements to the masking and etch process, as well as allowing the pillar cores to reach a terminal diameter through a 7 h - 10 h oxidation time.

### 2.4.2.2 Influence of strain

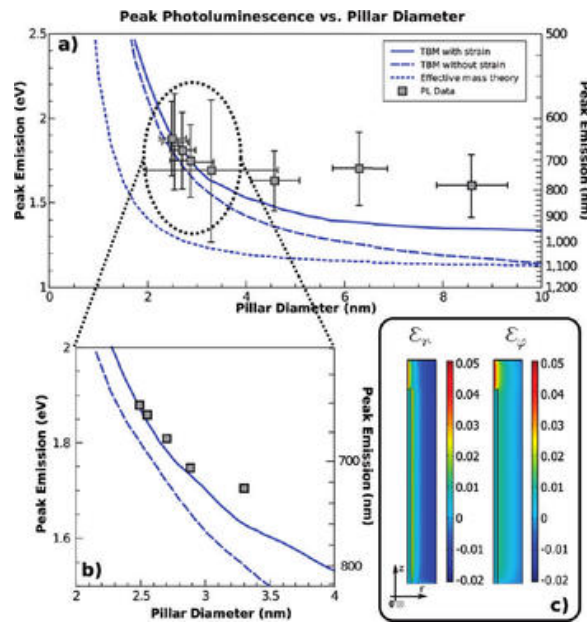


Figure 2.42: (a) Peak PL emission as a function of terminal core diameter. Continuous lines represent three different theoretical explanations for the blue-shifted emission energy. Error bars in the  $x$ -direction represent standard deviation in pillar size and in the  $y$ -direction the FWHM of the measured PL. (b) Magnified view of peak emission for pillars between 2 - 4 nm. (c) Finite element strain model used to calculate the strain in the nanowires after oxidation. Shown is the strain in the radial and circumferential direction; the strain in the  $z$ -direction is negligible.

Several models were investigated to explain the blue shifting of the emission peak, shown in Figure 2.42(a,b) as continuous lines. First, a simple effective mass theory was proposed, shown as

a dotted blue line in Figure 2.42. This assumes the band curvature follows that of the bulk silicon band structure, and includes the effect of quantum confinement in an infinite cylinder, resulting in a spectral trend which is proportional to  $1/d^2$ . As has been previously noted [67], this method underestimates the peak emission energy, implying an invalid application of the bulk band structure for dimensions below 10 nm. To account for potential changes in the band structure at these diameters, a twenty band (ten valence, ten conduction)  $sp^3s^*d^5$  tight binding model [369, 258] was employed to calculate the bands between the  $\Gamma$  and  $X$  symmetry points. These results are plotted as a dashed line in Figure 2.42. Although this model provided a better fit to the data, it also tended to underestimate the emission energy. A final model utilized the same tight binding simulation, but incorporated lattice deformation due to the strain applied by the thermal oxidation process. This strain was calculated using methods described elsewhere [207, 62, 160] and parameters extracted from TEM images, including core diameter and oxide thickness. Additionally, a finite element model (FEM) estimated the additional strain induced when cooling after oxidation due to the mismatch in the coefficients of thermal expansion (CTE) between Si and  $SiO_2$ . Strain along the axial direction was found to be negligible; strain distributions within the pillar in the radial and circumferential directions are shown in Figure 2.42c. The final tight binding model incorporating this in-plane tensile strain provided a better fit to the peak emission data, depicted as a solid line in Figure 2.42(a,b). This suggests that the blue shift in emission wavelength is due to a combination of both strain within the pillar as well as quantum confinement.

Previous theoretical [276] and experimental [116, 13] work has examined the role of strain in the energy and direct/indirect nature of the silicon band gap. While biaxial compressive strain tends to red shift the gap energy, the biaxial tensile strain associated with oxidation [207, 62] produces a blue shift of the band gap [276, 13] due to the bonding nature of the  $d$  orbital that contributes to the conduction band. From theoretical calculations based on [160, 62] to compute the strain applied during oxidation, as well as the FEM analysis of CTE mismatch strain, we concluded that the pillars experience approximately 1.5% tensile strain in the radial and circumferential direction Figure 2.42c, with negligible axial strain. This is because the axially compressive strain associated

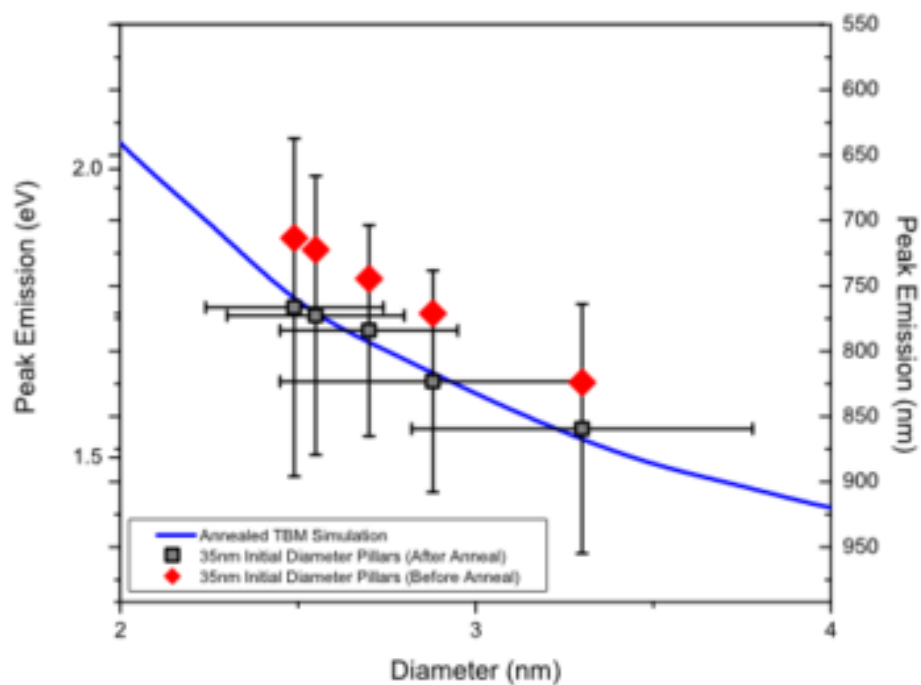


Figure 2.43: Peak SiNW PL emission before and after annealing, illustrating the effect of oxidative strain on the emission properties. The red diamonds represent the pre-annealed measurements, while the green squares show measurements after annealing. The solid line is the simulated emission peak for the annealed pillars, based on a TBM.

with the CTE mismatch during cooling approximately cancels the tensile strain incurred during the oxidation itself.

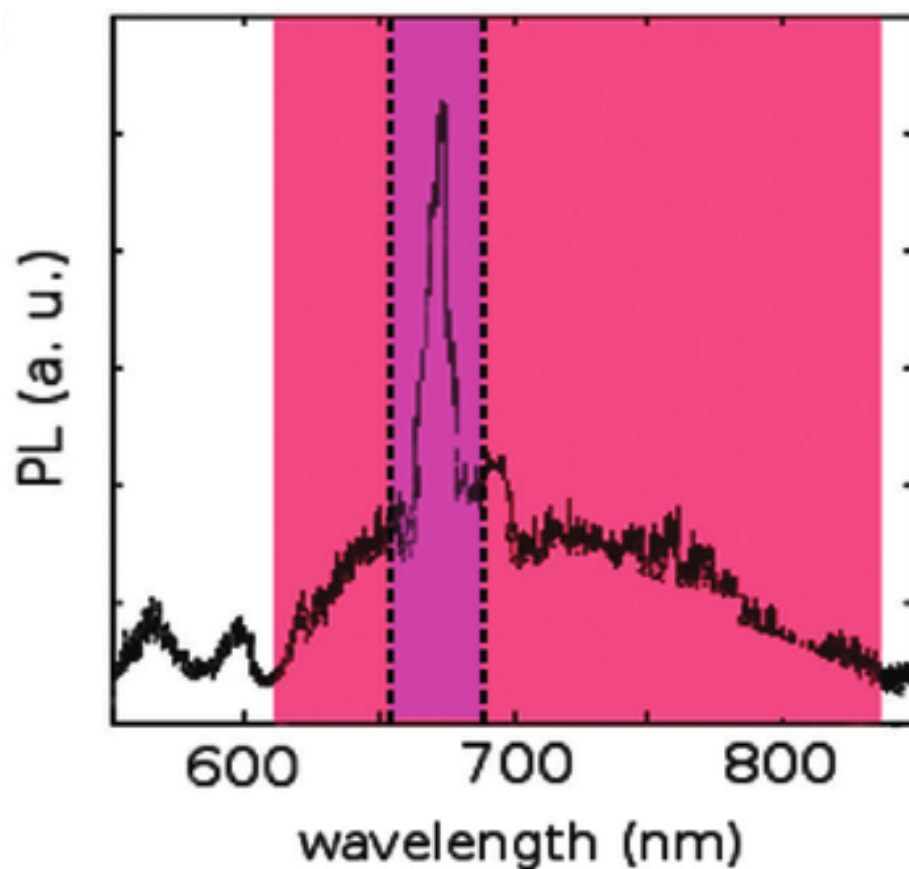


Figure 2.44: Identification of PL peak associated with silica double bond defects.

There has been extensive theoretical and experimental work examining the role of oxidation and the silicon–oxygen bond in determining the band gap and peak emission energy in silicon nanocrystals. Two studies [223, 376] have predicted that the presence of a silicon–oxygen double bond, resulting from the incomplete oxidation at the interface, creates a localized exciton state in nanocrystals with diameters of 2.5 nm or smaller. This state pins the band gap at 2.1 eV with the creation of a fast radiative trap state, effectively halting the band gap energy expansion due to quantum confinement. We believe a variation of this effect was observed when these nanopillars were oxidized and allowed to return to room temperature in a nitrogen or oxygen ambient. In these samples, a sharp peak was consistently observed at 1.85 eV - 1.9 eV (650 nm - 670 nm), along with the wider peak associated with quantum confined PL; an example spectra exhibiting

this behavior is shown in Figure 2.44. While the broad PL spectra shifted as a function of pillar diameter, this sharp peak was found to remain at a fixed energy, regardless of core size. However, the pillar cores examined here were all larger than the 2.5 nm threshold for the oxygen double bond pinning effect, and the longer wavelength emission remained, suggesting an alternative mechanism. Instead, the presence of a non-bridging oxygen hole center, typically found in compressively strained silica matrices [113], could have existed within the layers surrounding the strained pillars. This state can trap holes on isolated oxygen atoms, resulting in fixed photoluminescence at 1.9 eV. But because the defect is contained within the oxide and not the core itself, it is possible to observe PL from the trap state and band-to-band transitions simultaneously. To validate this hypothesis, we attempted to anneal out the defect by terminating the extra oxygen bond with hydrogen. When pillars were cooled to room temperature in forming gas (5% H<sub>2</sub>, 95% N<sub>2</sub>) instead of pure N<sub>2</sub> or O<sub>2</sub>, the peak at 1.9 eV disappeared. This suppression is consistent with protonation and quenching of the non-bridging oxygen hole center [113].

### 2.4.2.3 Lifetime measurements

Lifetime measurements of the photoluminescence were performed by passing the 488 nm Ar<sup>+</sup> laser through an acousto-optic modulator (AOM). This provided a square-wave modulation of the excitation with a 20 μs period and 50% duty cycle. The modulated beam was then passed through 90/10 beam splitter onto the sample and a trigger diode, respectively. PL from the sample was collected by the 50×/0.55 NA lens and 550 nm long-pass filter previously described, but coupled onto an avalanche photodiode (APD) rather than the spectrometer. After being triggered by the trigger diode, the APD signal was monitored using a Picoquant PicoHarp 300, allowing decay times to be extracted from the PL's temporal characteristics.

The lifetime data are presented in Figure 2.45, with an example decay curve for a 2.88 nm core shown in the inset. For the samples tested, we measured decay times  $\approx$  200 ns. These were found to decrease with narrowing core diameter, which was expected for several reasons. First, the smaller volume occupied by the narrower cores decreases the probability of finding defects within narrower

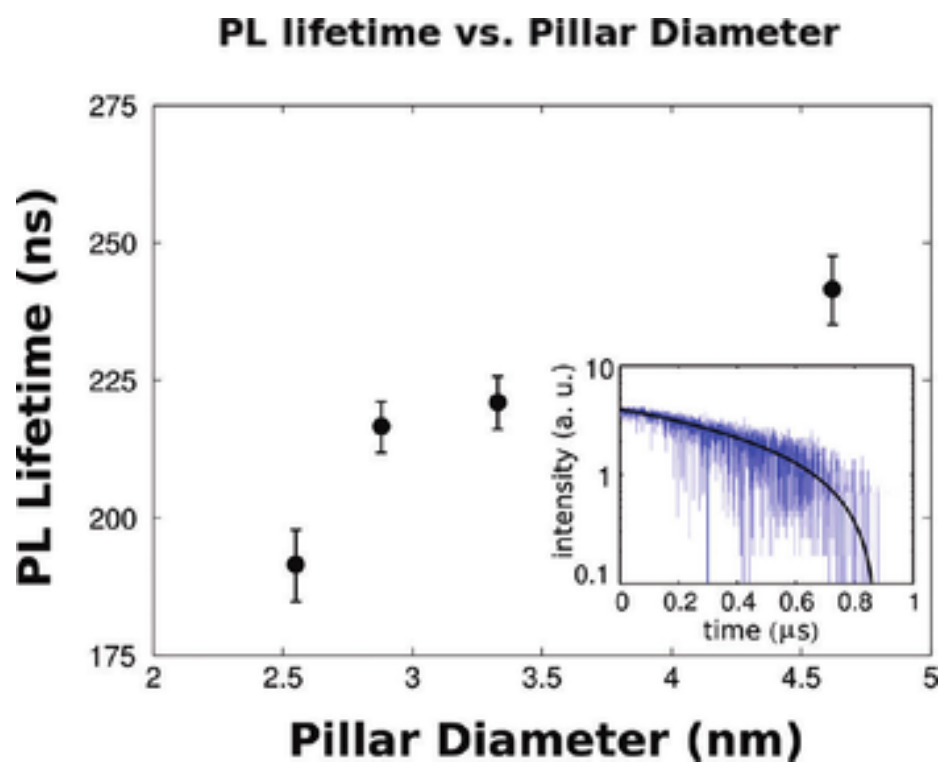


Figure 2.45: Lifetime measurements for changing silicon core diameters. Error bars indicate uncertainty in the fit of the exponential decay time. Inset shows example of PL lifetime measurement with fitting curve in black.

pillars. The pillars were fabricated in Czochralski (CZ) grown silicon wafers, placing an upper bound of  $10^7 \text{ cm}^{-3}$  on the fast midgap nonradiative defect density, corresponding to a nonradiative lifetime of  $\approx 1 \text{ ms}$  [301, 325]. Based on diffraction contrast TEM images, the core material appeared to remain single crystal without, as any damage induced during the etch process was removed from the surface via oxidation (Figure 2.15).

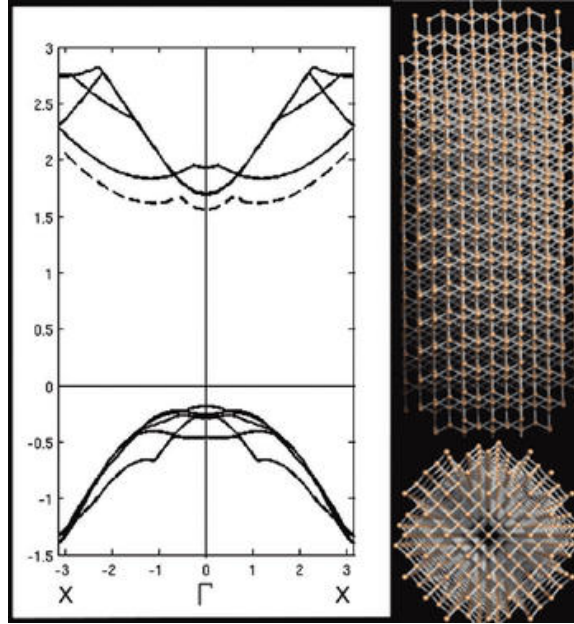


Figure 2.46: Band-structure (in eV) of a TBM simulation of a strained and unstrained 2.5 nm diameter silicon nanowire. The dotted line shows the relative conduction band edge for the unstrained wire while the two insets show the axial and transverse structure of the nanowire.

Additionally, the decrease in lifetime was consistent the expectation that exciton dynamics become increasingly dominated by no-phonon, quasi-direct radiative transitions [88]. The transition to a radiative lifetime limited regime could be related to the magnitude of the splitting between the direct and indirect valleys of the conduction band. Theoretical calculations have found the strain in nanowires to have a significant influence on the splitting, resulting in an increase between the direct  $\Gamma$  conduction band valley and the bulk, indirect valley along the X direction [276, 13]. For pillars with diameters below 10 nm under tensile strain in the radial and circumferential directions, the splitting between these minima is several times the room temperature thermal energy; this is illustrated in Figure 2.46, which shows TBM band structure simulations of strained and unstrained 2.5 nm silicon nanowires. The large splitting enables a higher fraction of excited electrons to sit in

the  $\Gamma$  valley, allowing a faster, direct optical transition. For unstrained or compressively strained pillars (dotted line in Figure 2.46), the splitting between the two valleys is closer to the thermal energy, forcing occupation of both the  $\Gamma$  and X valleys, which require slower, phonon-mediated transitions.

Although the photoluminescence setup we used was not capable of performing cryogenic measurements, it would be interesting to explore the variation of radiative lifetime with temperature in order to elucidate the relative contributions of no-phonon and phonon mediated processes. Guichard *et al.* [117] have shown that the bimolecular bound exciton Auger recombination coefficient of VLS grown nanowires scales with both temperature and exciton density. Since the pillars in our report spanned a range both larger and smaller than the 4.9 nm ground state exciton in silicon [27], it may be possible to see the onset of this effect as the size of the pillars crosses this threshold. We therefore believe future work could utilize the self-terminating oxidized nanopillars as a platform to investigate exciton recombination dynamics as they transition between bulk-like behavior into their 1D counterparts.

#### 2.4.2.4 Etch modulation and three dimensional confinement

The oxidized silicon nanowires exhibited excellent lithographic control over their spatial and spectral characteristics, with widely tunable emission over a broad range of visible and NIR wavelengths. While these features suggest great potential as CMOS-compatible, integrated emitters for a number of classical photonic applications, the silicon nanowires did not possess ideal properties as quantum emitters. The long axial dimensions introduced uncertainty into the precise location of the emission in the vertical direction. Although the spectral uniformity of the arrays we tested was already 30% - 50% narrower than previously reported results, this was still far too broad to yield indistinguishable photons for cQED. While single pillars could have the potential to further reduce the spectral linewidth, any tapering of the sidewall slope along this region would yield a continuum of core diameters even within a single pillar, resulting in a similar spectral uncertainty. Finally, the measured decay times  $\approx 200$  ns were fairly long compared to common emission times in the ns or sub-ns regime.

Instead of 1D quantum structures, the ability to achieve confinement in all three dimensions offers a potential method to address many of these shortcomings. The emitter location would then be fixed along all axes, providing a precise spatial source of emission. Complete quantum confinement would provide common energy levels for all emission, rather than the potentially extended distribution of band gaps resulting from a spatially-extended wire with sidewall variation. Finally, increased exciton confinement forces an increased overlap between the hole and electron wavefunctions, resulting in an increase in the radiative recombination rate ([325], and discussion above).

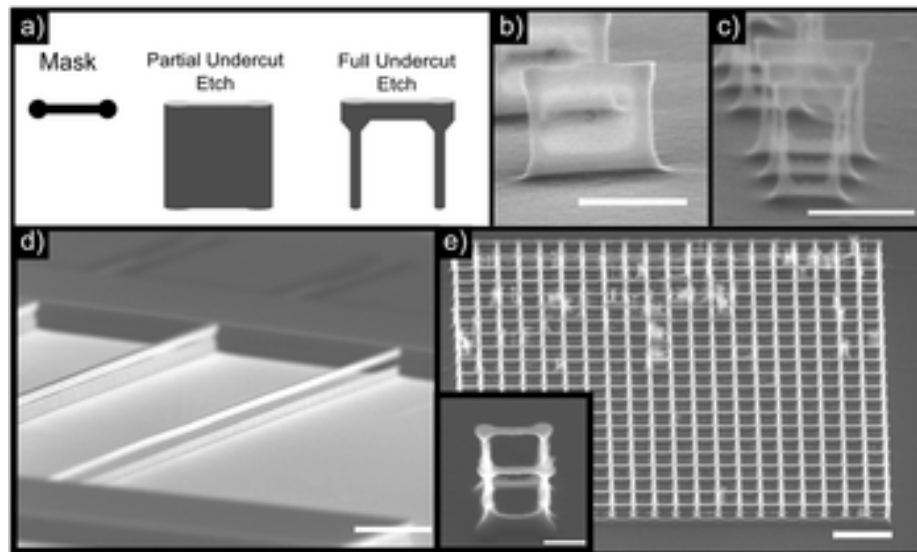


Figure 2.47: Suspended structures possible through modulated etching. (a) A schematic of an etch mask to create a suspended beam. (b) Resulting etched structure, with a thin, electron-transparent membrane. Scale bar is 500 nm. (c) Set of fully-undercut beams. Scale bar is 500 nm. (d) Suspended beam, 100 nm wide and 50  $\mu\text{m}$  long, which was etched and suspended with a single step. The image is taken from a foreshortened angle to fit the entire beam. Scale bar is 2  $\mu\text{m}$ . (e) Three-dimensional silicon mesh created with a single etch step. Scale bar is 1  $\mu\text{m}$ . Inset shows a single silicon wire-frame cube. Scale bar is 250 nm.

With this in mind, we began exploring techniques to achieve top-down fabrication of luminescent, zero-dimensional silicon nanostructures. Having already established methods to achieve nanometer features for in-plane directions through lithography and oxidation, we turned to the etching process to extend control into the third dimension. Not only would three-dimensional etching provide a top-down method of producing silicon quantum dots for our studies, it could enable the fabrication of a wide variety of other devices including vertical multigate transistors, Coulomb blockade devices, and fully suspended structures without the use of sacrificial layers or critical point drying. Further

details of this development are reported in [365].

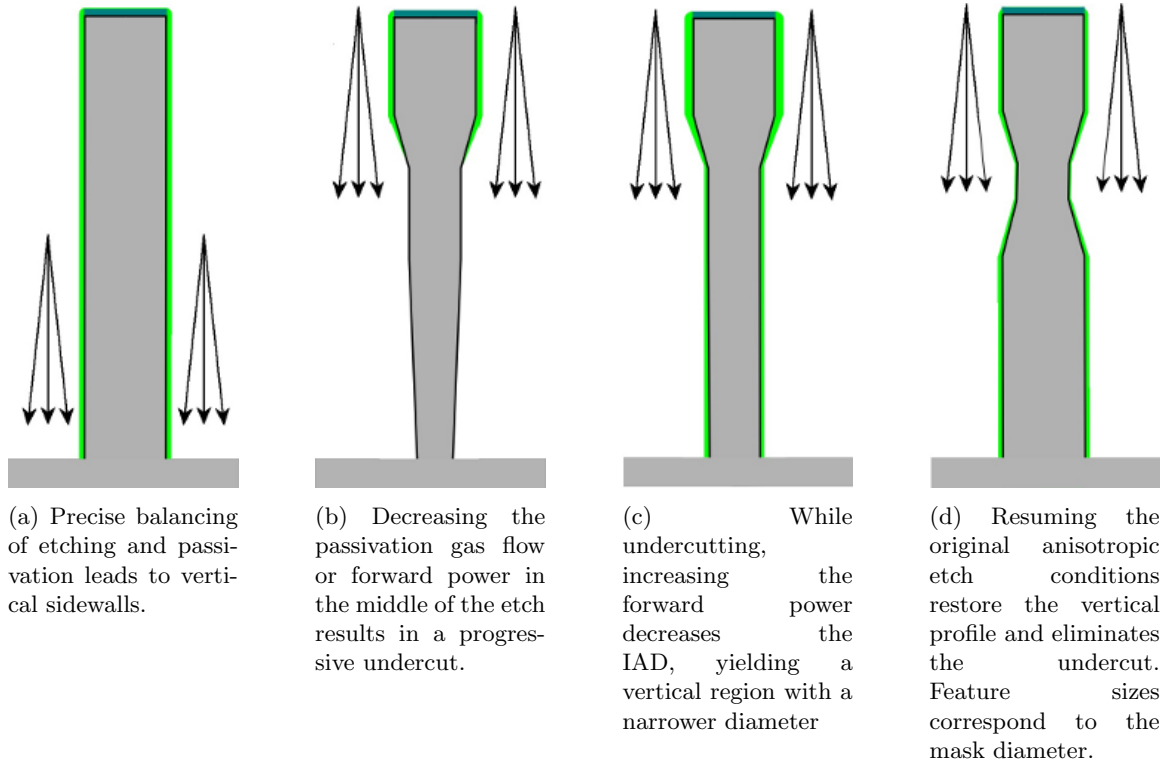


Figure 2.48: Modulated etch process development

Recalling the original etch development for the nanopillars, the critical requirement to producing vertical sidewalls was achieving a careful balance between the ion angular distribution (IAD), physical and chemical etch rates, and deposition of the passivation layer. Ideally, the ions could be accelerated entirely perpendicularly to the surface. In reality, however, ions obtain slight in-plane components to their momentum as a result of collisions with other gases within the plasma. The angular spread is therefore a function of both the accelerating voltage as well as pressure within the chamber. In general, one seeks to improve ion collimation by lowering the pressure or increasing the forward voltage, but this must be balanced by their effects on etch rate and mask lifetime. If the sidewall passivation is inadequate, the main consequence of a broad IAD is a lateral etching underneath the masked regions, known as undercut, which becomes more severe as the etch progresses into the substrate. Conversely, excess passivation under weak acceleration can lead to outward sloping sidewalls. While the lateral etching rate is usually only a small fraction of the vertical etch rate,

the undercut or over-passivation can have a significant effect on the feature size over the course of a deep etch.

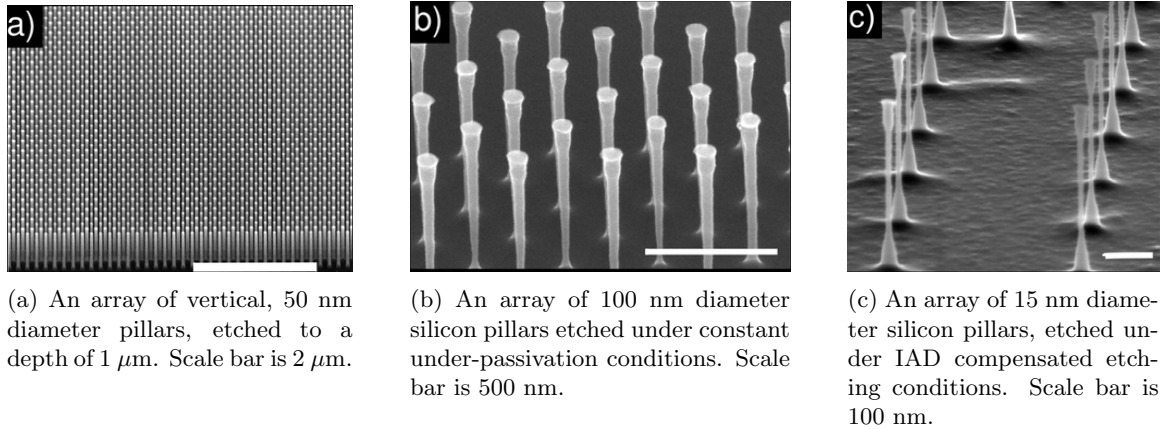


Figure 2.49: SEM images of vertical silicon structures under progressive etch modulation conditions

By modifying the conditions within the chamber during etching, it was possible to sculpt the profile of silicon as the etch progressed into the substrate; a schematic illustration is shown in Figure 2.48, with SEMs presented in Figure 2.49. By simply reducing the flow of passivation gas, for example, the ion bombardment due to the IAD could overcome the deposition of polymer on the sidewalls, causing lateral etching underneath the mask. This undercut became progressively greater as the etch proceeded into the substrate; this effect is shown in Figure 2.49b. In order to make vertically uniform structures, this behavior could later be compensated by reducing the IAD as a function of etch depth. This allowed the etch to progress vertically at a *fixed* undercut for the subsequent portion of the process. Significantly, this served to replicate the masked region at a smaller lateral scale, defined by the reduction in the ratio of passivation to etch gas; an example is shown in Figure 2.49c. This technique transferred challenging lithographic tolerances into easily controlled etch parameters. Rather than attempting to pattern a 15 nm diameter disk to create a 15 nm pillar segment, for example, we defined a 50 nm disk and used the fixed undercut to scale the mask down in size. For applications such as vertical transistors, the wider head and foot region would be critical to improving electrical contact and maintaining mechanical stability.

In order to achieve precise control over the etch profile we performed a sequential investigation, attempting to produce progressively more complicated features. Following characterization of

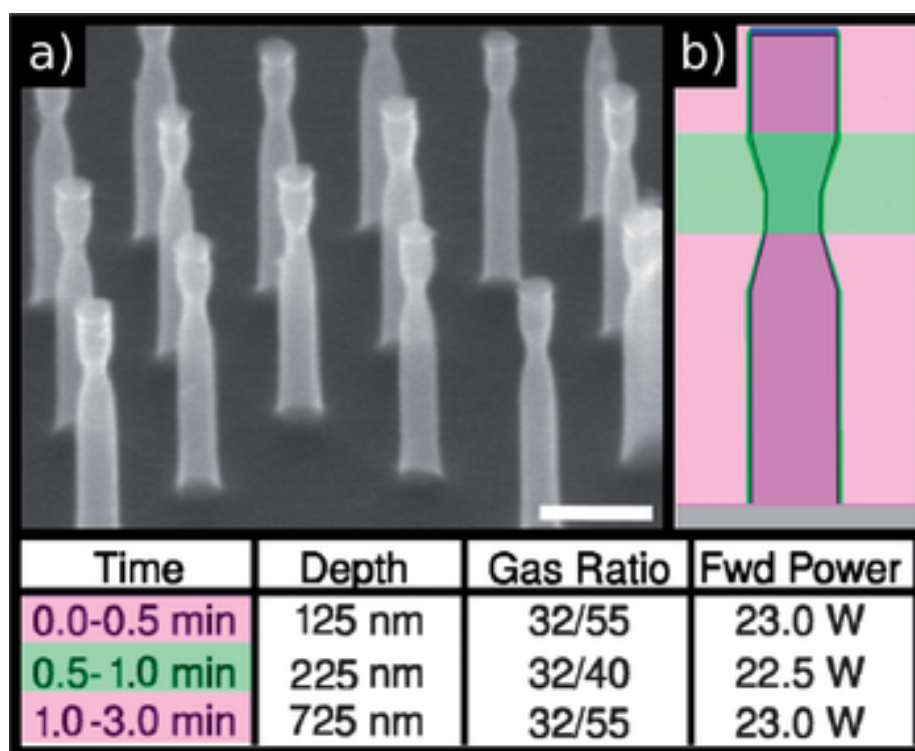


Figure 2.50: Etch recipe for a single notch in a silicon nanopillar. (a) An array of silicon pillars with a 15 nm notch in a 75 nm diameter pillar. Scale bar is 200 nm. (b) Schematic of a pillar with the various etch steps highlighted; the conditions are described in the table.

etches to yield perfectly vertical sidewalls (Figure 2.49a) and progressively undercut structures (Figure 2.49b), we developed a combined process to produce a single notch, as shown in Figure 2.50a. A three step etch procedure was carried out, where the color on the schematic in Figure 2.50b corresponds to the color of the step in the table. The notch itself was created during the second step (shown in green), where both the passivation gas flow and the forward power were reduced. The lowered forward power increased the angular distribution of the etchant ions, taking advantage of the thinner sidewall passivation to carve out the notch. The angled sidewall was created in the time between the start of the etch step with reduced gas flow and the time when the gas concentration stabilized. Following this stabilization, the etch continued vertically until the passivation gas flow was again increased, causing the pillar diameter to widen once more.

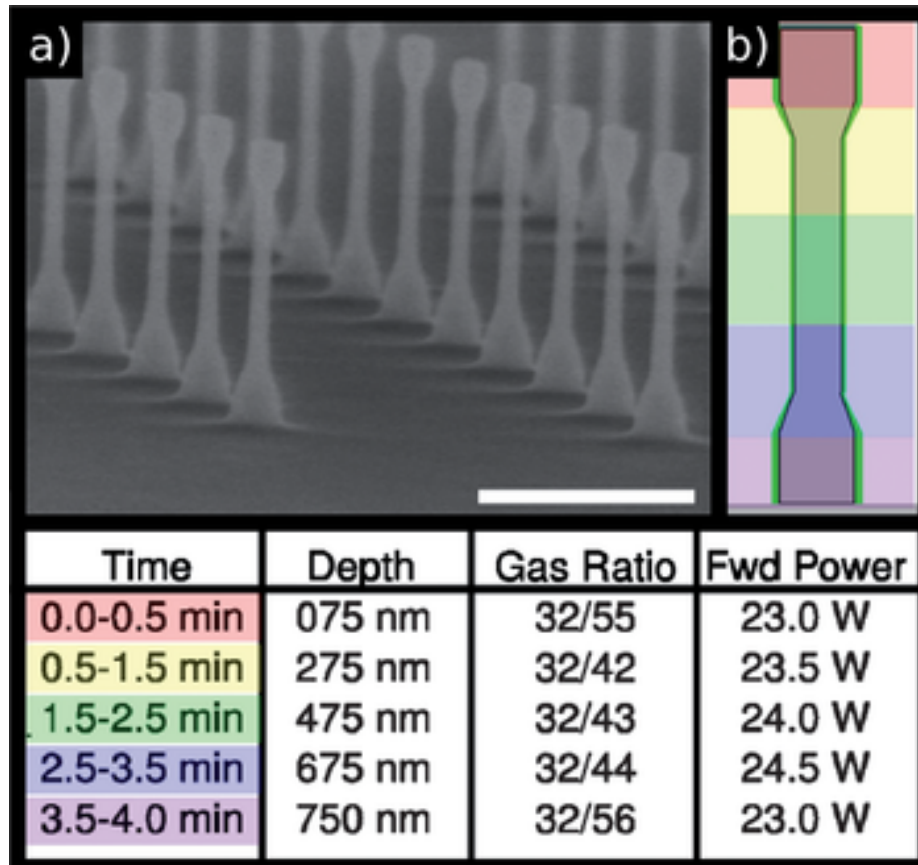


Figure 2.51: Etch recipe for a 500 nm long, extended notch in a silicon nanopillar. (a) An array of silicon pillars with a 35 nm diameter stem on a 75 nm diameter pillar. Scale bar is 500 nm. (b) Schematic of a pillar with the various etch steps highlighted and the conditions described in the table.

The next step was to characterize a vertically-uniform segment, but whose dimensions were narrowed (Figures 2.49c, 2.51a). This process made it possible to uniformly shrink the mask dimensions while etching them vertically into the silicon substrate. In order to maintain straight sidewalls, both the forward power and the passivation gas flow were increased approximately every 200 nm the etch progressed into the substrate. The changes in the etch condition are marked with colors on both the schematic in Figure 2.51b and in the table. Note that the etch maintained a diameter of 35 nm over the course of a  $\approx 500$  nm length of the stem.

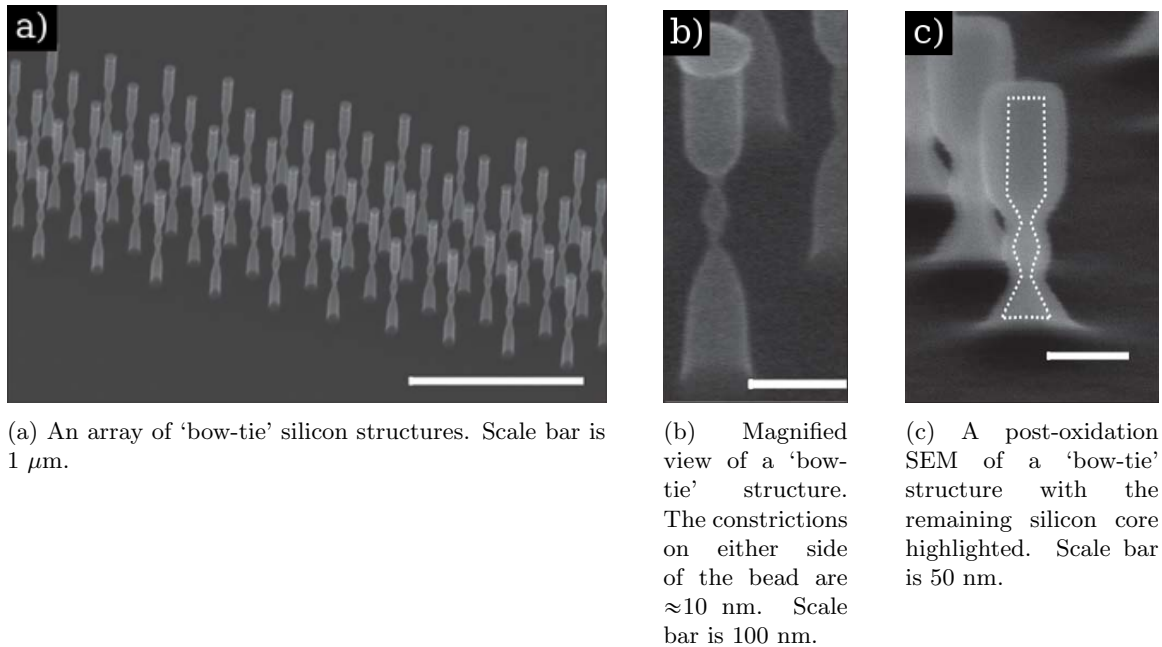
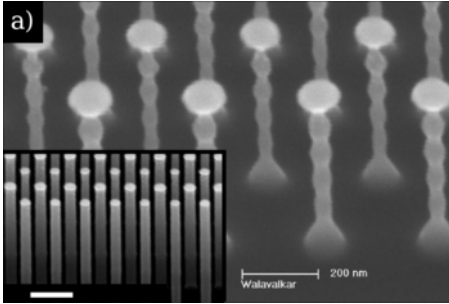


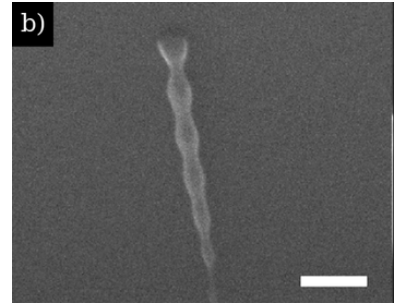
Figure 2.52: The combination of multiple notch steps results in a 'bow-tie' structure, with a single bulge in the center of the pillar.

Combining multiple notch steps within an etch process, we were able to create a single bulge in the center of a pillar, as shown in Figure 2.52. Similarly, a rapid modulation of the etch was used to produce multiply-corrugated nanopillars resembling a string of beads. Precise tuning over the undercut characteristics enabled these to be produced with either uniform corrugation diameters, as shown in Figure 2.53a, or a variety of different diameters within the same pillar, Figure 2.53b. In general, tuning the gas ratio and other etch parameters enabled controllable generation of corrugation profiles with features as small as 30 nm.

These corrugated structures were the key to achieving three-dimensional quantum confinement.



(a) SEM image of an array of corrugated silicon nanopillars immediately after etching. These pillars were fabricated by alternating the etching conditions to controllably undercut and overpassivate the silicon. Note the uniformity of the corrugation. The inset shows an array of nanopillars with vertical sidewalls, etching using constant conditions.



(b) Single silicon nanopillar etched under oscillating conditions to produce periodic surface morphology (pillar is lying down on the substrate). Note the overall taper of the pillar, producing a multitude of bead sizes. Scale bar is 100 nm.

Figure 2.53: SEM images of corrugated nanopillars, showing both uniform and varied bead sizes.

Once oxidized, the corrugations could yield both isolated silicon quantum dots, which were entirely surrounded by oxide, as well as continuous crystalline cores with variable diameters along the axis. Because the band gap itself can be tuned with diameter, this represents a new method of creating heterostructures using *geometry* to manipulate the band structure and confinement rather than inherent material properties. A brief discussion of this geometric band gap engineering will be presented later.

#### 2.4.2.5 Silicon quantum dot photoluminescence

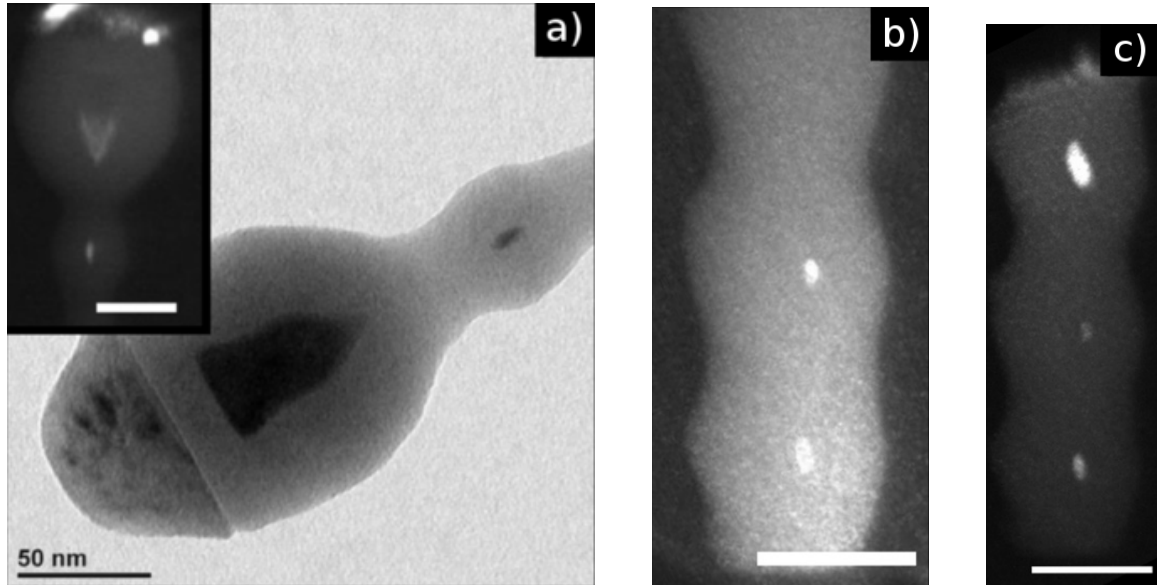
Returning to the prospect of fabricating zero-dimensional structures in silicon, the production of completely isolated silicon regions might at first seem surprising given the self-terminating nature of the oxidation. That behavior, however, relied on the convex geometry of the structure. While it was reasonable to assume the nanopillars behaved as infinite 2D nanostructures with perfect cylindrical symmetry, this approximation was no longer valid for the corrugated pillars. In this case, the tapered regions possessed a *concave* axial geometry, while the wider regions were *convex* in all directions. When oxidized in the self-terminating regime (below the viscoelastic reflow temperature,  $\approx 960^\circ\text{C}$ ), a narrow enough taper would therefore be oxidized completely, while the wider areas would continue

to terminate as before.

This process resulted in oblong islands of crystalline silicon, completely passivated by the surrounding thermal oxide. The height of the dot from the substrate could be readily controlled using the etch step durations, enabling full three-dimensional command over the position. Similarly, precise control of the undercut during etching permitted the use of larger mask diameters for a given feature size, further improving the ease and precision of the fabrication process. Combined with the self-terminating oxidation, the corrugated etching process expanded our ability to achieve nanometer scale, lithographic control into the third dimension.

We reported the fabrication and microphotoluminescence characterization of the corrugated, silicon quantum dot (SiQD) devices in [366]. Processing of the SiQD samples utilized the same electron beam lithography and masking process described earlier. As with the silicon nanowires described in our previous photoluminescence studies [364], lightly-doped  $\langle 100 \rangle$  silicon was chosen for the substrate. An alumina hard mask was patterned using liftoff to create several arrays of disks, with diameters of 80 nm and 100 nm. These features were undercut during the etching process to produce smaller diameters. The corrugation size was varied between samples, but was typically chosen to produce three uniform corrugations per pillar. After etching, the samples were simultaneously oxidized at  $915^\circ\text{C}$  for seven hours, and cooled to room temperature in a forming gas of 5%  $\text{H}_2$  : 95%  $\text{N}_2$ . The presence of elliptical silicon quantum dots was first confirmed nondestructively by RTEM, as well as destructively after PL measurements by transferring the devices onto a TEM grid and viewing the structures in transmission mode.

TEM images showing of vertical stacks of silicon quantum dots are presented in Figure 2.54. The first image shows the morphology around the top of the pillar in both bright-field and dark-field (inset). Diffraction contrast highlights the large acorn-shaped silicon core within the wider head region, while the first quantum dot is also visible. This indicates that the remnant quantum dot maintained similar diffraction characteristics as the larger core region within the pillar head, demonstrating the single crystal nature of the SiQD. The second two frames show the lower corrugations around the middle and base of the pillar. While the narrower regions between dots is



(a) Bright-field TEM image of the head and first quantum dot of a corrugated pillar after oxidation. Inset shows a similar picture with diffraction contrast to highlight the crystalline nature of the remaining silicon nanocrystals.

(b) Dark-field TEM image showing lower SiQDs in the pillar.

(c) Dark-field TEM image showing lower SiQDs in the pillar.

Figure 2.54: TEMs of SiQDs embedded in an  $\text{SiO}_2$  matrix.

oxidized completely, the presence of crystalline silicon dots within the wider areas can be clearly observed.

In Figure 2.55, SEM images of three samples are shown prior to oxidation; the colored frames correspond to the line colors in the photoluminescence spectra plot. Before oxidation, these samples had diameters of 30 nm (a, black), 37 nm (b, blue), and 45 nm (c, green), as measured at the widest portion of the dots. The corrugations of all samples had a vertical period of approximately 60 nm. Micro-PL was performed in an inverted microscope with the laser coupling in at a  $45^\circ$  angle, similar to the setup described for the nanowire photoluminescence studies [364]. Here, a 457 nm free-space argon ion laser was used for excitation. The data collected from three samples of different preoxidation diameter are shown in Figure 2.55, where the line colors match the SEM image frames. We observed a correlation between the original size of the etched corrugations and the peak emission wavelength of the oxidized quantum dot. Peak emission was found to be at roughly 600 nm (2.06 eV), 640 nm (1.94 eV), and 810 nm (1.53 eV) for the samples with initial diameters of 30 nm (black), 37 nm (blue), and 45 nm (green), respectively. A full width at half maximum less

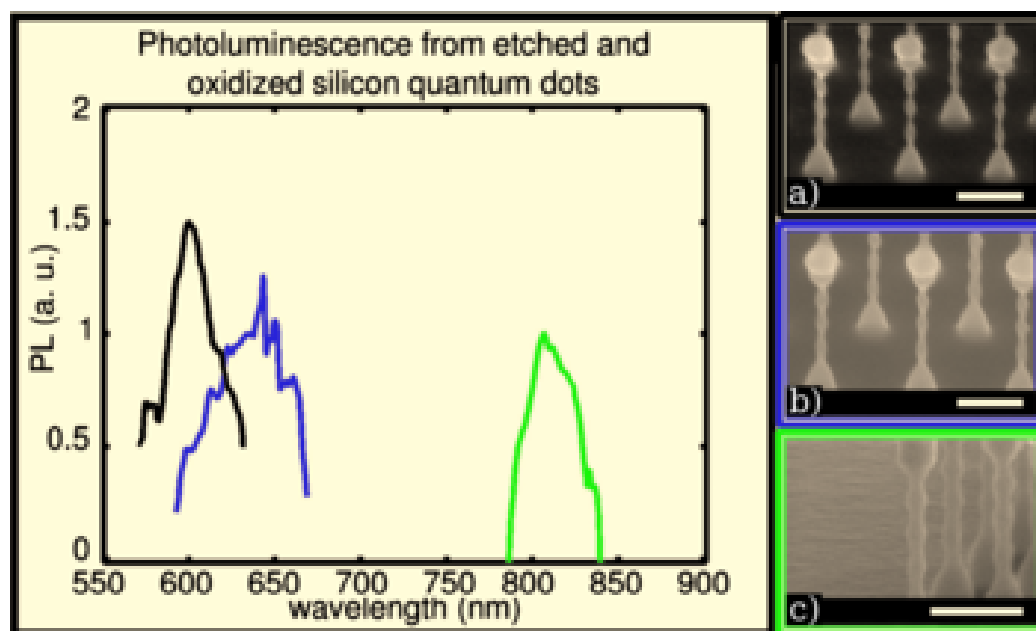


Figure 2.55: PL spectra of three samples of etched and oxidized quantum dots with different initial corrugation diameters. The leftmost curve (centered at 600 nm) corresponds to pillars in frame (a), the middle curve (centered at 640 nm) corresponds to the pillars in frame (b), and the right-most curve (entered at 810 nm) corresponds to the pillars in frame (c). The preoxidation size is 30 nm, 37 nm, and 45 nm for the (a) black, (b) blue, and (c) green samples, respectively. Note that the larger the preoxidation size, the longer the peak emission wavelength. Scale bars are 200 nm in each frame.

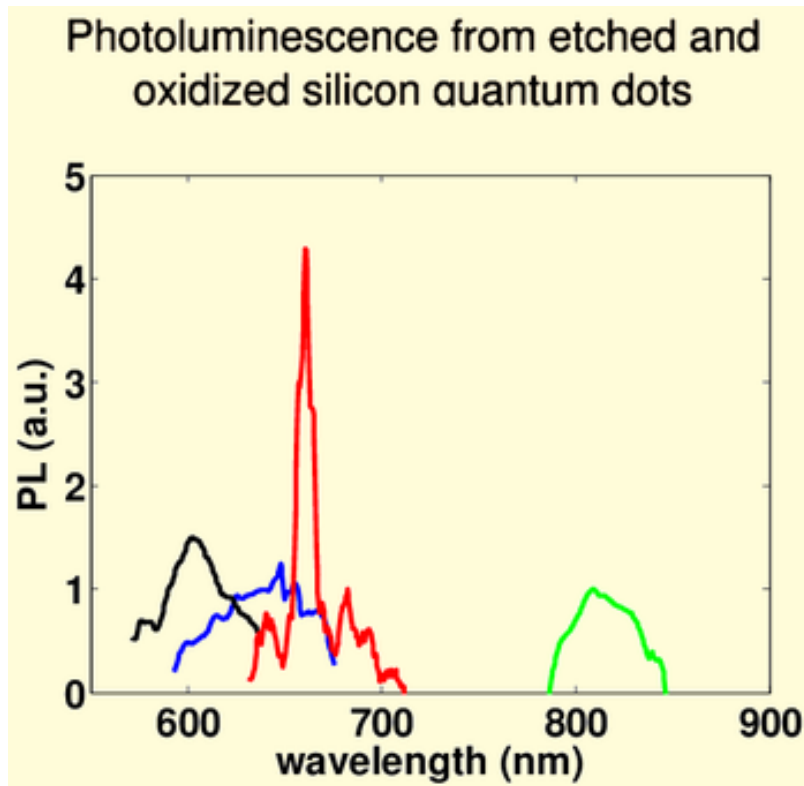
than 150 meV was noted for each sample.

While it is possible to estimate the size of the quantum dots within the oxidized pillars from the dark- and light-field TEM images, the difficulties and distortions caused by imaging through 50 nm - 75 nm of oxide make the error bounds too large for yield meaningful size measurements. Instead, dot sizes were determined by comparing the peak emission energy with the band gaps obtained by previous theoretical and experimental work [376, 103]. It is also critical to note that these dots are embedded in an oxide matrix, which has been found to red-shift the peak emission by as much as 1 eV as compared to bare quantum dots or those with hydrogen terminated surfaces. Based on data presented in [376, 338, 373, 103], we estimate that the measured nanocrystal sizes are centered around 2 nm (black), 2.4 nm (blue), and 5 nm (green) in diameter.

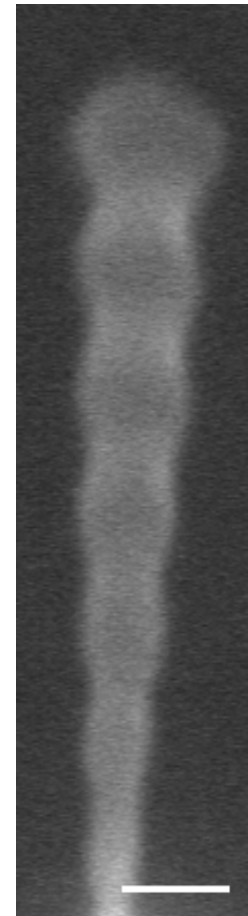
Although careful effort was made to produce quantum dots with diameters that had as narrow a size distribution as possible, the peak emission wavelength is a strong function of dot size [376, 373]; a change as small as 0.25 nm in diameter (about one monolayer of Si) can shift the peak emission energy up to 100 meV (30 nm) [376]. Several causes, including non-circular mask patterning, debris on the wafer, and local etch variation, could have such an impact on the peak emission wavelength. Furthermore, it has been shown [116] that the strain incorporated into thermally oxidized silicon nanostructures can have a significant impact on the band gap, an affect we also observed in our nanowire photoluminescence studies [364]. Here, a shift between 1% compressive and tensile strain can shift the peak emission energy by 200 meV. While the present work assumed that the three stacked quantum dots had the same size and strain conditions, this is not necessarily true; in particular, the strain on the top and bottom quantum dots might show significant influence from the wider head and tail regions, as compared to the middle dot which is surrounded by other narrow structures. These effects might account for the multiply-peaked structure of the emission spectra, which have individual widths comparable to previously measured 100 meV - 130 meV linewidths of single etched quantum dots taken at room temperature [338, 354].

Alternatively, the sharp peaks observed, particularly in the blue curve in Figure 2.55, could also be influenced by the discrete nature of the experiment. The pillar arrays had an aerial density of

$\approx 5 \times 10^9 \text{ cm}^{-2}$ , or roughly three orders of magnitude less dense than coalesced nanoparticles [372]. In our case, the  $50\times$  objective sampled an area of approximately  $5 \mu\text{m} \times 5 \mu\text{m}$ , corresponding to between 300 and 500 pillars. Particularly if certain quantum dots tended to scatter more preferentially into the detectors, any minor variation between individual pillar diameters could be reasonably expected to cause an observable change in the spectral shape, resulting in a relatively discrete spectrum.



(a) Photoluminescence spectra for etched and oxidized SiQDs. The black, blue, and green curves (identical to the data presented in Figure 2.55) correspond to uniform quantum dots with pre-oxidation diameters of 30 nm, 37 nm, and 45 nm, respectively. The red curve shows data for tapered SiQD pillars, possessing multiple discrete QD size which result in distinct spectral peaks between 640 nm and 705 nm. The large emission peak at 660 nm resulted from a non-bridging oxygen hole center which had not been annealed out in this sample.



(b) SEM of a tapered SiQD pillar, possessing multiple discrete QD sizes with distinct emission peaks. The scale bar is 50 nm.

Figure 2.56: Comparison between PL spectra for uniform SiQD arrays and tapered arrays with multiple SiQD sizes in each pillar.

One method to probe this further was to deliberately introduce size variation into the array. A sample of corrugated pillars was fabricated without fully compensating for the undercut. This

resulted in pillars with an overall taper, yielding discrete SiQD sizes within each stack, as shown in Figure 2.56b. When photoluminescence measurements were taken, this sample produced multiple distinct spectral peaks between 640 nm and 705 nm; this data is presented as the red curve in Figure 2.56a, along with the previously discussed spectra for comparison. Having neglected to anneal this particular sample in forming gas, a large emission peak at 660 nm resulted from non-bridging oxygen hole centers as discussed above. For the other peaks, we note that the individual spectral widths fall in the range  $\approx 15$  meV - 30 meV. These individual linewidths are significantly narrower than the overall emission bandwidths of the nominally uniform samples. This suggests that slight, inadvertent tapering within those pillars may have resulted in indistinguishable shifts of each emission peak. When combined, these appeared to yield a single, broader spectra.

Not only were the individual peaks of the tapered sample significantly narrower than the original linewidths, they were also  $\approx 85\%$  narrower than previous room temperature measurements of etched quantum dots [338]. This is particularly surprising, given that our measurements were conducted over ensembles of quantum dots within large arrays, while their report corresponded to measurements of individual dots. The narrower widths we observed could be due to improved fabrication quality or a slight difference in local environment within the oxide. Additionally, our photoluminescence integration occurred over 3 - 5 min, compared to the 30 min required for the spectral acquisition in the single QD study [338]. It is therefore possible that a higher degree of spectral diffusion might have contributed to a greater broadening in their study.

Alternatively, this could indicate a transition to no-phonon dominated processes in our device. Sychugov *et al.* [338] did observe a  $\approx 60$  meV sideband which did not vary with dot size. Having a similar energy to the transverse optical (TO) phonon in silicon (in bulk, 56 meV at the X point, 64 meV at the  $\Gamma$  point), they attributed this to TO phonon involvement. At 80 K, only a fraction of the dots exhibited the sideband, but because the fraction did not appear to depend on dot size, they rejected the hypothesis that the emission would transition to a no-phonon process as the size decreased. However, they reported average emission peaks primarily between 1.7 eV - 1.8 eV, with only a handful of dots exhibiting higher energy, whereas our sample with 30 nm starting diameters

had a peak energy closer to 2 eV, with the narrow peaks of the tapered sample emitting at up to 1.94 eV. Therefore, the narrower linewidths we observed might indicate the onset of this transition.

Future work is needed to quantitatively explain these spectral details. In particular, performing the measurements at cryogenic temperatures could further narrow the linewidths, while spectroscopy of individual quantum dots should also be undertaken to properly assess the limits of these devices. Sychugov *et al.* [338] performed measurements on individual quantum dots at 35 K, reporting sharper peaks down to 2 meV which were distinguishable over a broader background emission. Similar work, resulting in multiply- and sharply-peaked spectra has been reported elsewhere [167, 354].

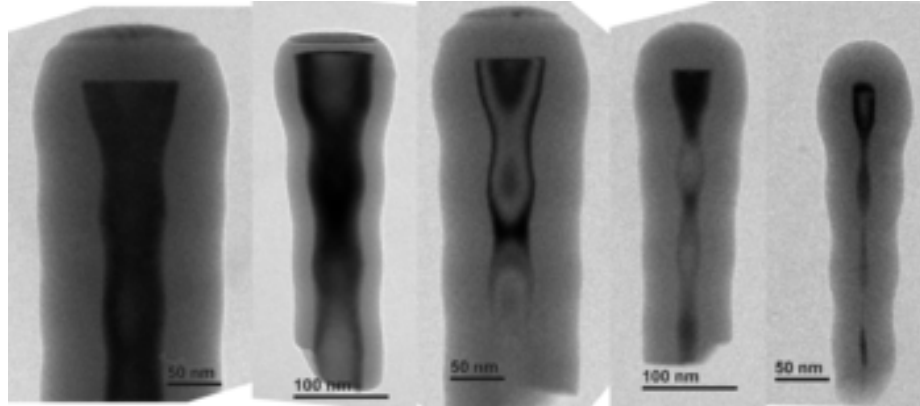
While this suggests linewidths in the range of  $\approx 1$  meV would be possible to generate using our technique, the SiQDs seem unsuitable for integration into optical cQED systems. The long integration times required for spectral acquisition are not promising for the production of bright single photon sources. Attempts to quantify the efficiency of etched SiQDs estimated a maximum QE of  $\approx 35\%$ , with the majority of dots showing QEs between 5% and 20% [354]. Given the long lifetimes we measured in the nanowire photoluminescence studies, it is also unlikely that the radiative transition could be made efficient enough to eliminate the presence of phonon-mediated transitions. As such, we chose to pursue other techniques for deterministic integration.

Overall, the combination of self-terminating oxidation and corrugated etching provided a novel way of integrating quantum nanostructures into silicon wafers, with unmatched 3D spatial localization and dimensional control down to 2 nm. This enabled a modification of the effective carrier dynamics, transitioning from bulk indirect band characteristics into one where the transitions were dominated by quasi-direct transitions with tunable energy gaps. Based on room temperature photoluminescence spectra, the quality and uniformity of the arrays were unparalleled, exhibiting spectral peaks up to 85% narrower than previously reported values. While the persistent effect of phonon-mediated transitions prohibits these devices from acting as effective quantum emitters in cQED systems, we believe these could still find uses as classical on-chip light sources or exotic nanoelectronic devices.

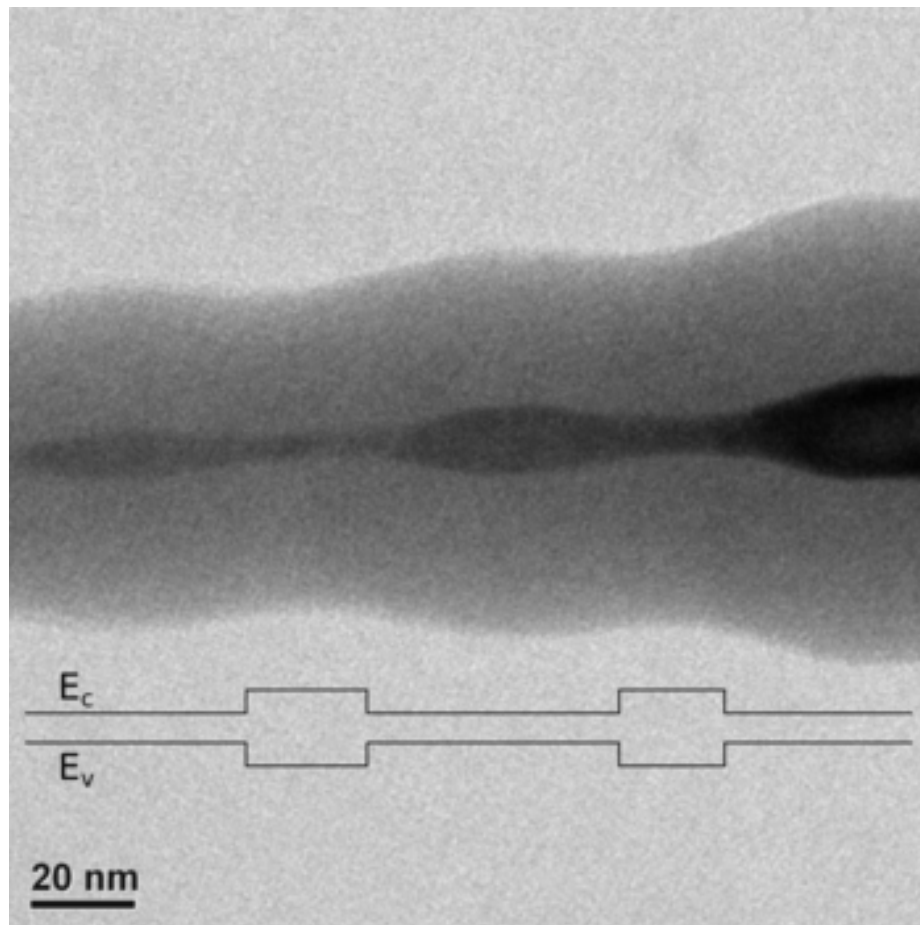
#### 2.4.2.6 Geometric band gap engineering

Through both the silicon nanowire and quantum dot studies, a clear dependence on local diameter and strain had emerged for the effective band gap. In the case of the nanowires, the uniform core gave rise to single, widened band gap with a continuous electronic channel. Conversely, photoluminescence spectra of the tapered quantum dot structures exhibited multiple distinct band gaps, albeit with electronically isolated silicon islands. By careful selection of the diameter and modulation, however, it seemed possible to combine these features to create a single, continuous electronic channel with a spatially-varying band gap. In effect, our technique to modulate the diameter of the core throughout the pillar would enable the ability to create *geometrically engineered band gaps*, mimicking electronic heterojunctions but fabricated out of a uniform bulk material. Having already extended the use of silicon into active photonic applications, the creation of complex electronic junctions in a CMOS process would further propel the material into another previously inaccessible arena which has historically been dominated by III-Vs.

We began by exploring the etch and oxidation parameters necessary to yield channels with constrictions below 10 nm. Because the basic self-terminating oxidation is affected by the convex or concave bend radii, the fabrication is closer to that for the SiQDs (which have both qualities) than the nanowires (which are uniformly convex). In the case of the quantum dots, however, preservation of the narrow channel was not required and the constrictions could be completely oxidized. While we were still able to rely on the self-terminating oxidation, we found that the production of continuous, modulated channels required slightly larger diameters than those used for the quantum dots. This permitted a self-terminated constrictions below 10 nm in diameter (and thus capable of band gap widening), as well as wider, bulk-like regions in between. Using the same techniques as described above for lithography, hardmask processing, modulated etching, and oxidation, we fabricated an array of modulated channels with various starting diameters. After oxidation, samples of the different pillars were transferred onto TEM grids and imaged. Using diffraction contrast in the TEM, the presence of wide, bulk-like regions and continuous, sub-10 nm constrictions was verified. A variety of these structures with decreasing core diameters is shown in Figure 2.57a.



(a) A sequence of TEM images showing the progressive narrowing of corrugated Si nanopillars. Diffraction contrast is used to highlight the crystalline core region. For larger samples, the core remains bulk-like throughout the pillar. As the diameter is further decreased, the core remains continuously connected throughout the pillar, but transitions through regions narrow enough to influence the band gap. These alternating narrow and wide features result in a modulated energy band structure along the pillar axis.



(b) TEM image and schematic illustrating the concept of geometric band gap engineering. Diffraction contrast is used to highlight the crystalline silicon core. At the narrowest regions, the band edges blue-shift due to a combination of quantum confinement and strain, resulting in a spatially-modulated energy structure following the pillar corrugations.

Figure 2.57: TEM images and energy band schematics illustrating the concept of geometric band using corrugated silicon nanopillars.

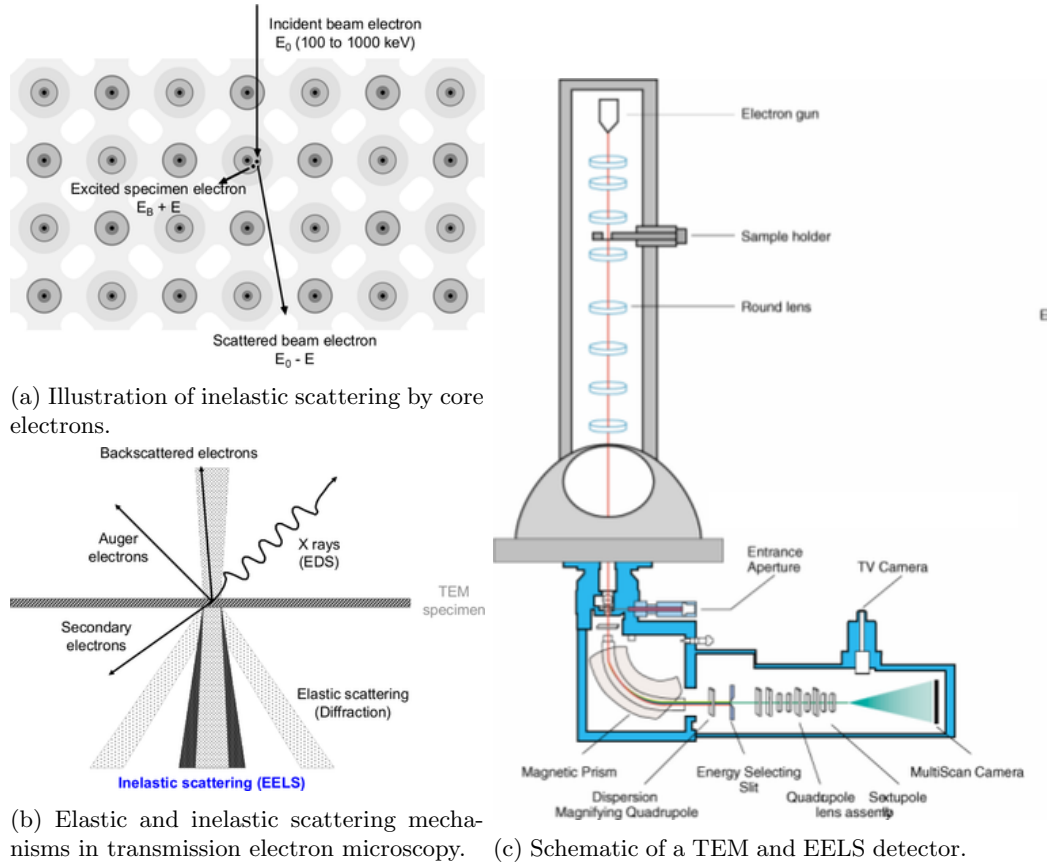


Figure 2.58: Illustrations of electron scattering and detection in a TEM. Just as the elastic scattering (diffraction) contains important structural information, including atomic spacing and crystal symmetry, the inelastic components are rich in electronic information and may be used to probe band structure or for elemental mapping. Images from [187].

Having identified structures with the appropriate core modulation, we sought a method to characterize the band structure throughout the device. Due to the wide distribution of core diameters along the axis, photoluminescence measurements could only provide broadened spectra, making it impossible to distinguish contributions originating from different areas along the device. This was further complicated by the varying luminescence efficiency as a function of the diameter (for example, bulk regions would not provide any luminescence signal at all). As such, our previous photoluminescence characterization was incapable of mapping the band gap throughout the device.

Instead, we attempted to use electron energy loss spectroscopy (EELS) to quantify shifts in the band gap. When imaging structures using TEM, the elastically scattered electrons produce diffraction patterns. These signals are rich with information about the crystalline structure

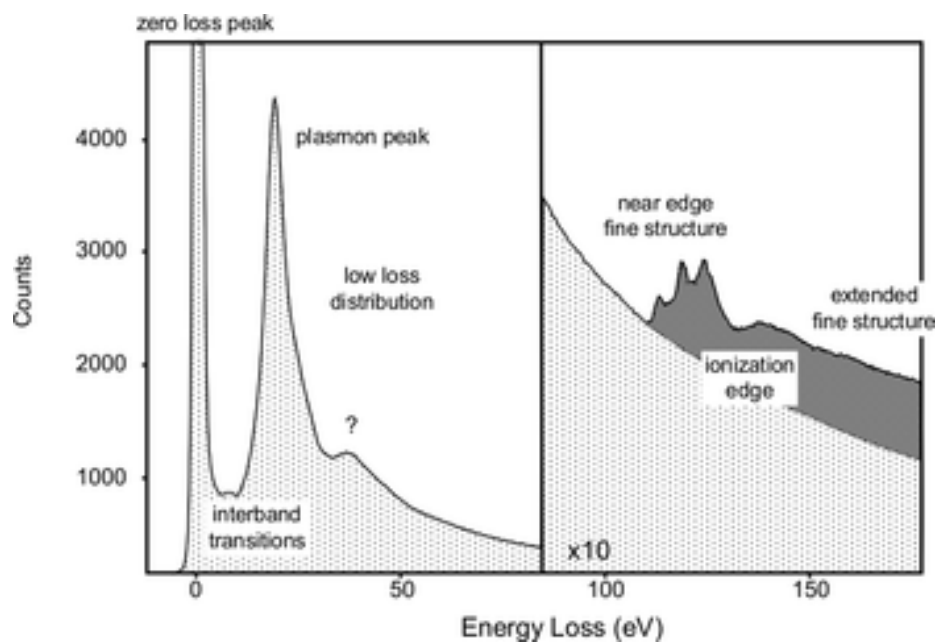
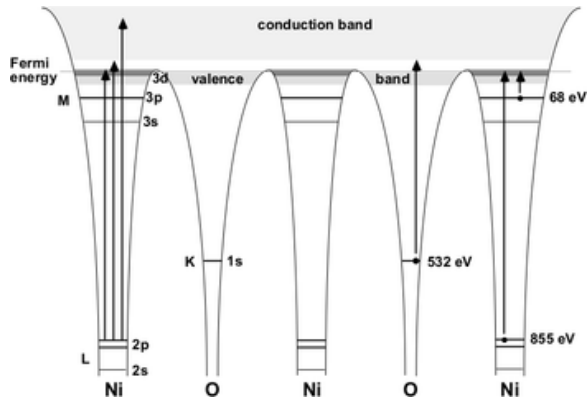


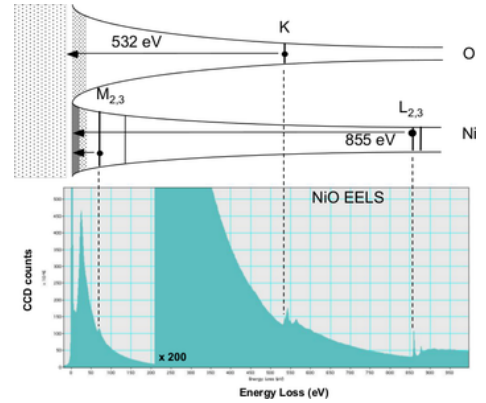
Figure 2.59: Illustration of typical EELS spectrum and information contained in different regions. From [187].

<b>Feature</b>	<b>Information</b>
Zero-loss peak	Thickness
Plasmon peaks	Valence/conductance electron density
Low loss distribution	Complex dielectric
Near zero loss features	Band structure: <i>interband transitions</i>
Core loss edges	Elemental composition
<b>Near edge fine structure</b>	<b>Band structure:</b> <i>density of unoccupied states</i>

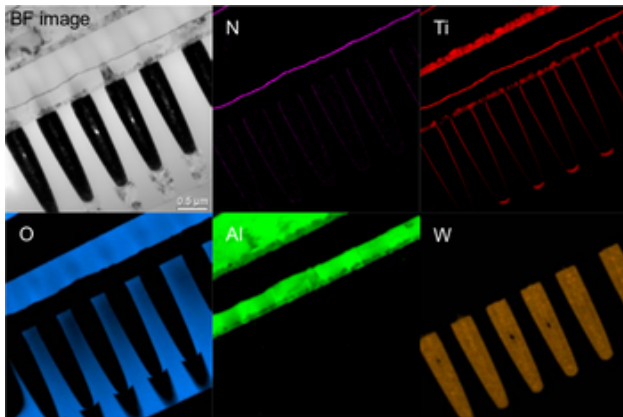
Table 2.1: Information contained in different EELS spectral ranges



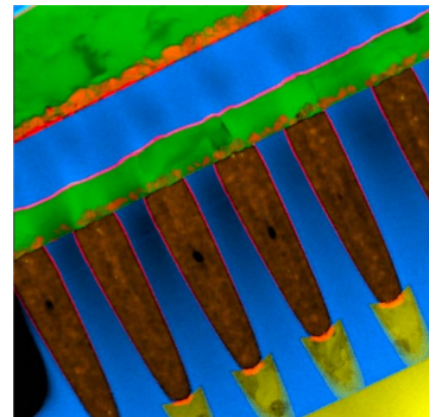
(a) Schematic of core energy levels and their contributions to ionization edge EELS structure. Only transitions to unoccupied levels are permitted.



(b) Correlation of EELS loss edges and elemental ionization energies enables elemental identification.



(c) Unfiltered bright-field TEM image of semiconductor device structure and some elemental maps formed from ionization-edge signals of N-K, Ti-L, O-K, Al-K, and W-M.



(d) Color composite of the elemental maps displayed on the left, clearly showing the construction of the device.

Figure 2.60: Elemental identification using EELS spectra. From [187].

of the sample, producing lattice images, atomic spacings, crystal symmetry, orientation, and characterization of crystalline defects. Simultaneously, a portion of the electrons passing through the sample end up transferring some of their energy to the core electrons, and thus exiting with a lower energy than the primary beam. Because these losses depend upon the electronic behavior of the sample, these inelastically scattered electrons contain a wealth of information about the sample's electronic structure; see Figure 2.58. Resolving the electron loss spectrum in the TEM can therefore yield great insight into the elemental composition, electronic band structure, and complex dielectric properties, as well as provide enhanced contrast and a measurement of sample thickness [187]. These spectral features are summarized in Figure 2.59 and Table 2.1. A description and example of elemental identification are shown in Figure 2.60.

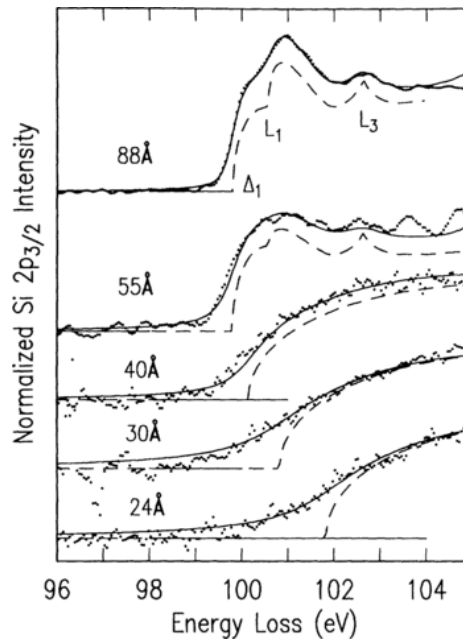


Figure 2.61: Normalized EELS spectra as a function of Si particle diameter. The spectra were modeled by sets of parabolic band edges corresponding to final states at  $\Delta_1$ ,  $L_1$ , and  $L_3$ . Below 50 Å, the edge shape changes to a single parabolic component and shifts upwards in energy. From [26].

In particular, the near edge fine structure, corresponding to losses  $\approx 100 - 150$  eV, contains information related to the density of unoccupied states; see Figure 2.60a. The onset of the conduction band appears as a sharp rise in the EELS spectrum in this region. A blue shift in the conduction band relative to the bulk is manifested as an equivalent shift in the position of this loss peak. This feature

has previously been used to study the quantum confinement-induced band gap widening in isolated silicon quantum dots [26]. These authors examined the EELS spectra  $\approx 100$  eV, corresponding to the  $2p$  core ionization edge, which yields information about the conduction band states near  $\Delta_1$  and  $L_1$  in the Brillouin zone. Measuring hydrogen-terminated QDs immediately after synthesis, the authors reported bulk-like properties for diameters  $\approx 80 - 90$  Å. For diameters below 50 Å, however, the edge changed abruptly to a single parabolic band with a relative shift  $\sim 1/R^2$  (although they could not rule out  $1/R^3$ ); these data are shown in Figure 2.61.

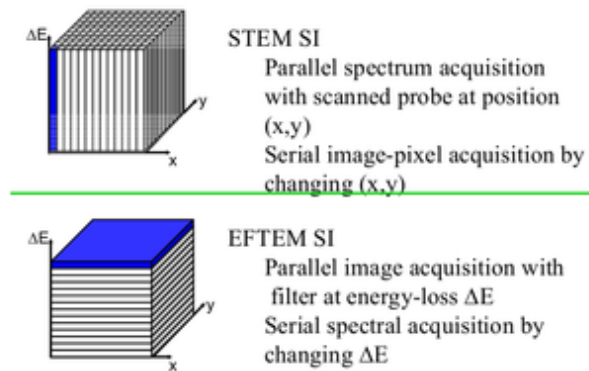


Figure 2.62: Hyperspectral EELS data can be recorded either as full spectra from a single point which is scanned over the surface, or as complete images by scanning the energy filter. Schematic from [187].

Ideally, we would have been able to quantitatively map the blue shifts of the conduction band edge by performing similar measurements along the axis of the pillar. Unlike measurements of isolated QDs where there are no nearby structures to corrupt the spectra, our study was complicated by the continuous core region with varying diameter as well as the presence of the thermal oxide surrounding the structure. Rather than loss spectra taken at single points, this required a means to obtain both spatially- and spectrally-resolved scattering data, ideally at resolutions better than 1 nm and 0.1 eV, respectively. There are two common approaches to taking these data: either performing spectral measurements over an array of points, or alternatively, recording a hyperspectral stack of images; these are illustrated in Figure 2.62. In either case, the conduction band onset can be extracted and spatially mapped to the structure. In the first method, the beam is focused to a nm-scale probe; the inelastically scattered electrons from this location are then dispersed by a magnetic prism and

collected on the CCD as spectra. By raster scanning the probe across the sample in STEM mode (scanning transmission electron microscopy), the unique spectra at each location can thereby be obtained (EELS/STEM). Conversely, a collimated, broad area illumination can be used to image the entire structure, after which a narrowband energy filter serves to select a specific loss window (energy-filtered TEM, or EFTEM). In this case, the filter's energy window is varied, with each spectral point being measured simultaneously across the structure. While these methods produce seemingly equivalent data, each imposes trade-offs affecting the achievable accuracy. The primary challenge in EELS/STEM comes from longer sampling times making the technique more susceptible to drift. Modern tools, however, are capable of compensating for spatial drift by recording reference STEM images at intervals, and similar reference spectra at fixed locations can be used to account for energy drift. Despite the longer overall acquisition duration, however, the total dose delivered to a sample region is *lower* in EELS/STEM. Here, the entire spectra is recorded simultaneously and a given region is only illuminated during this period, while EFTEM must perform multiple sequential exposures at the same location but ends up rejecting the majority of inelastic electrons as they lay outside of the current filter window. Perhaps most significantly, the energy resolution achievable EELS/STEM is limited by the dispersive element ( $<0.1$  eV), which is typically much greater than the achievable filter widths limiting EFTEM ( $\approx 1$  eV); spatial resolution is generally comparable between the two (0.2 - 1 nm).

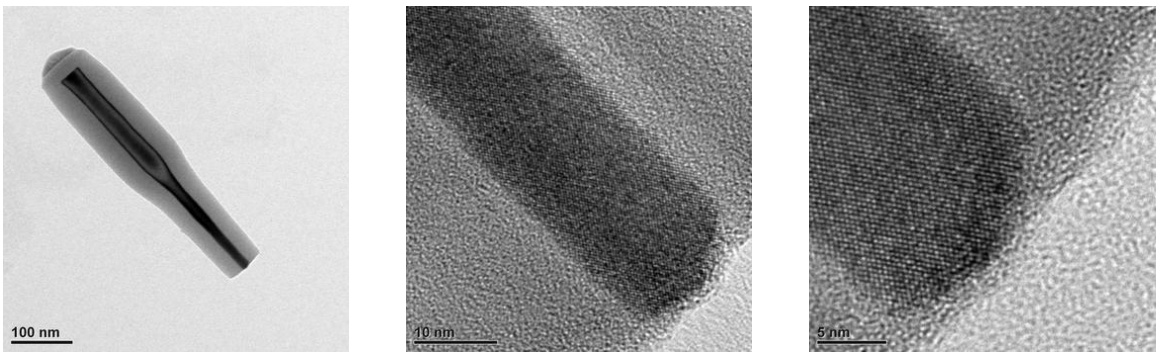


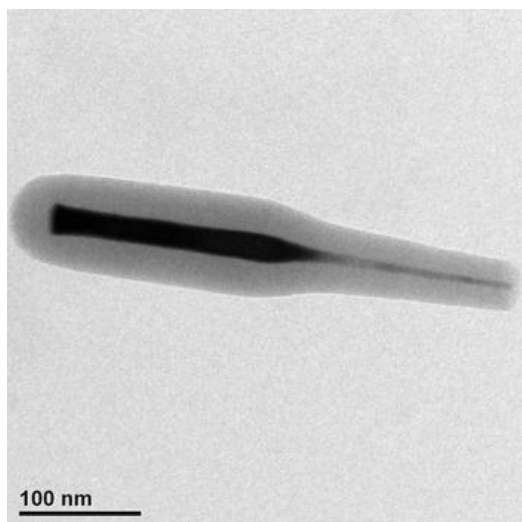
Figure 2.63: Bright field TEM images of a silicon nanopillar with a uniform constriction. These devices were fabricated to enable independent EELS measurements over the bulk-like core and narrowed regions. This particular device had a narrowed section with  $\approx 16$  nm diameter, which is too large to modify the electronic band structure.

Given that we were hoping to measure energy shifts  $\approx 0.1 - 1$  eV, recording the data spectrally with EELS rather than EFTEM was imperative. While the available TEM (FEI Tecnai TF20 Super Twin, operating at 100 kV) had the capabilities of both STEM imaging and EELS individually, the particular tool was unfortunately incapable of performing coordinated STEM/EELS analysis. Because EFTEM was unable to achieve the necessary energy resolution, we instead attempted to manually emulate the STEM/EELS analysis by taking EELS spectra with a nm probe and manually sampling discrete points. While this lacked the desired spatial resolution and is not suitable for mapping the energy structure over the entire pillar, it was sufficient for a proof of concept. To make this easier, we prepared sets of pillars with two uniform, extended regions: a wide diameter, bulk-like region near the top, and a narrow core at the bottom. Bright field images of a sample with a  $\approx 16$  nm constriction are presented in Figure 2.63 to illustrate the structure; given a diameter  $> 10$  nm, this sample was not expected to exhibit any band shift.

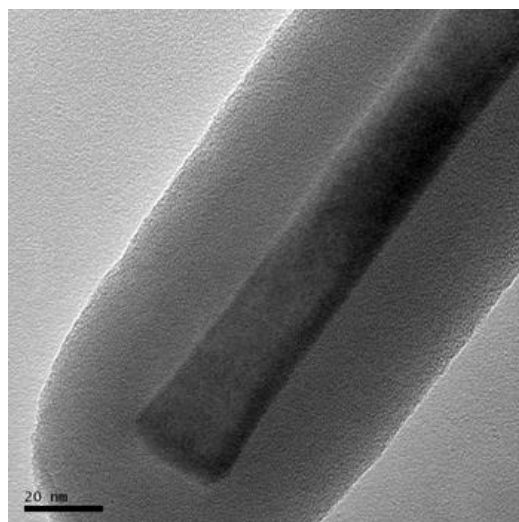
Using suitably smaller pillars, we initially attempted to probe the bulk and quantum-confined regions using automated movements between the two. Several stage positions were recorded, corresponding to the beam being centered at the bulk-like head region, the constricted tail region, and a completely empty region (without any substrate membrane on the grid) to be used for spectrometer calibration. After verifying that the system appeared to move reliably between the points, the beam was focused to a  $\approx 1$  nm probe. From this point, the beam parameters were held constant in order to avoid introducing any shifts to the ZLP or other miscalibrations of the EELS spectrometer. Calibration of the EELS spectrometer was performed over the empty region several times over a period of several minutes so that system drift could be included in the compensation. After calibration, the head and tail regions were moved into focus using the automated stage positioning. EELS spectra were taken using integration times between 0.2 - 5 s, with a spectral step size of 0.2 eV (the limit of the machine; although the machine is capable of taking spectra with step sizes of 0.05 eV and 0.1 eV, these settings offer little improvement due to inherent energy distribution in the beam and are not recommended by the manufacturer). Because the beam alignment could not be verified visually (without broadening the beam and introducing spectral miscalibrations), the measurements

were repeated several times while alternating between the regions in order to ensure repeatability. Unfortunately, the automated stage movements were unable to provide sufficient alignment accuracy to probe the tapered core. While spectra from the head regions showed characteristics of the silicon core, the tail region only exhibited peaks reflecting the oxide presence, likely an indication of misalignment.

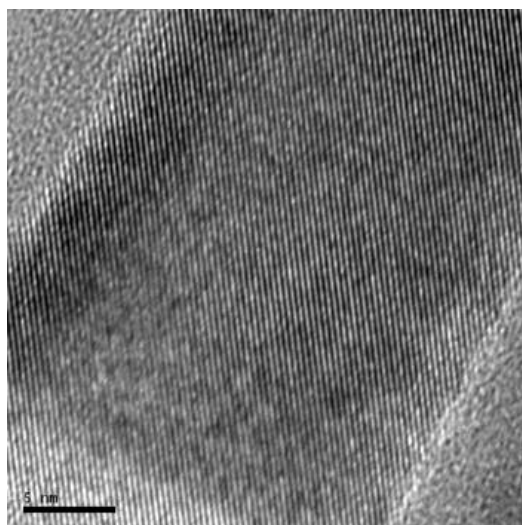
A final attempt was made to quantify the band gap variation by manually positioning the beam at the head and tail regions. Because this required modifying the beam parameters between each measurement, the absolute calibration of the spectra was somewhat uncertain. But even though the beam parameters were not identical they were likely to remain quite similar, making it possible to correct small drifts in EELS data by aligning other peaks in the spectra. For this study, we located a pillar which had a starting diameter of  $\approx 58$  nm and a taper down to 30.7 nm, yielding a 22 nm core at the head and constriction down to 7.4 nm; a bright-field image using diffraction contrast to highlight the core is presented in Figure 2.64a, as well as several detailed views taken with EFTEM to illustrate the crystalline quality of the core; see Figures 2.64(b-d).



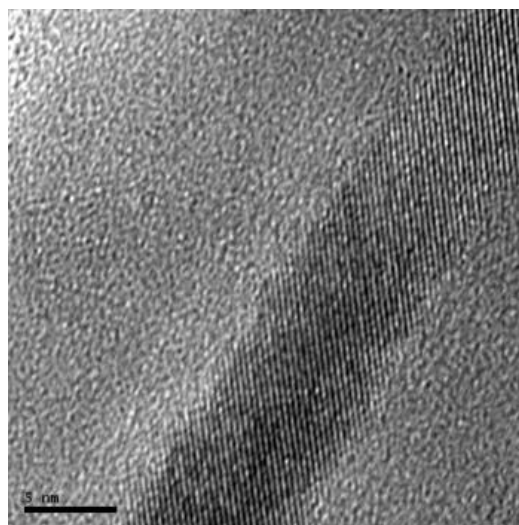
(a) Bright-field TEM image, using diffraction contrast to highlight the core.



(b) Detail of the pillar head region taken using EFTEM.

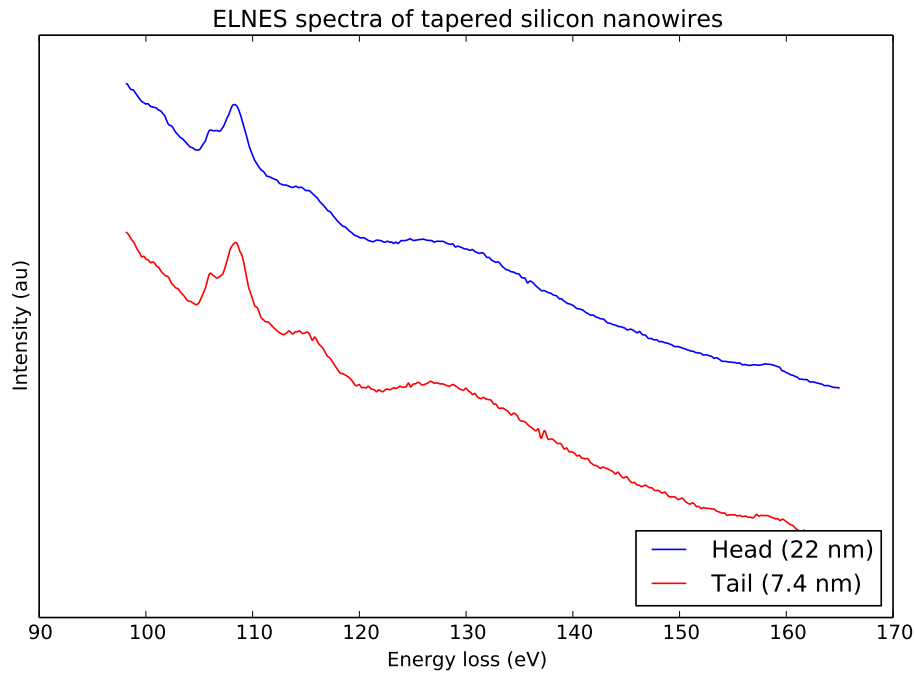


(c) Lattice image of the pillar head region from EFTEM. The core diameter in this region is  $\approx 22$  nm.

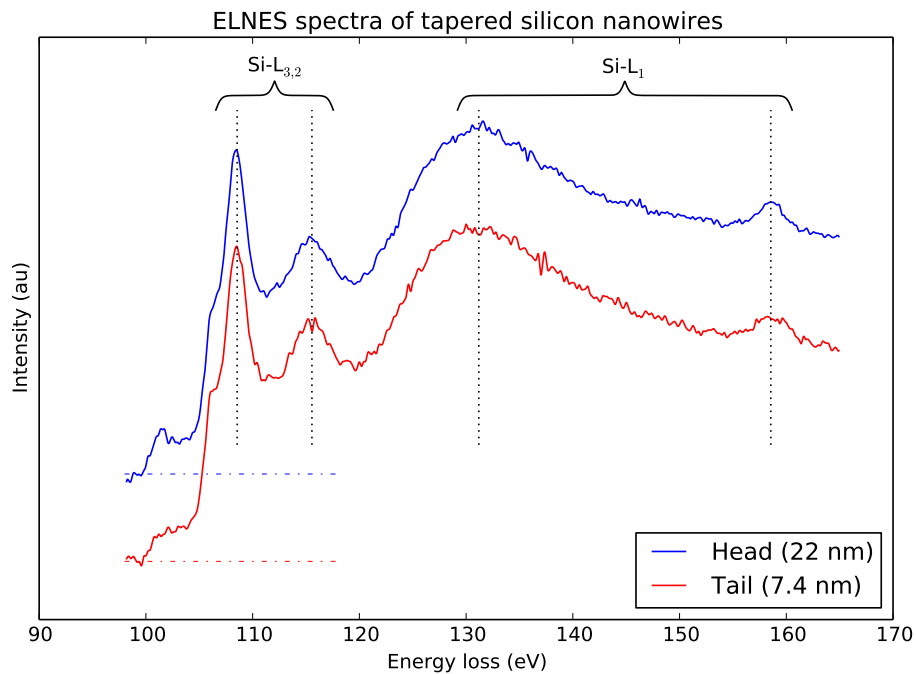


(d) Lattice image of the tail region from EFTEM. The core diameter in this region is  $\approx 7.4$  nm.

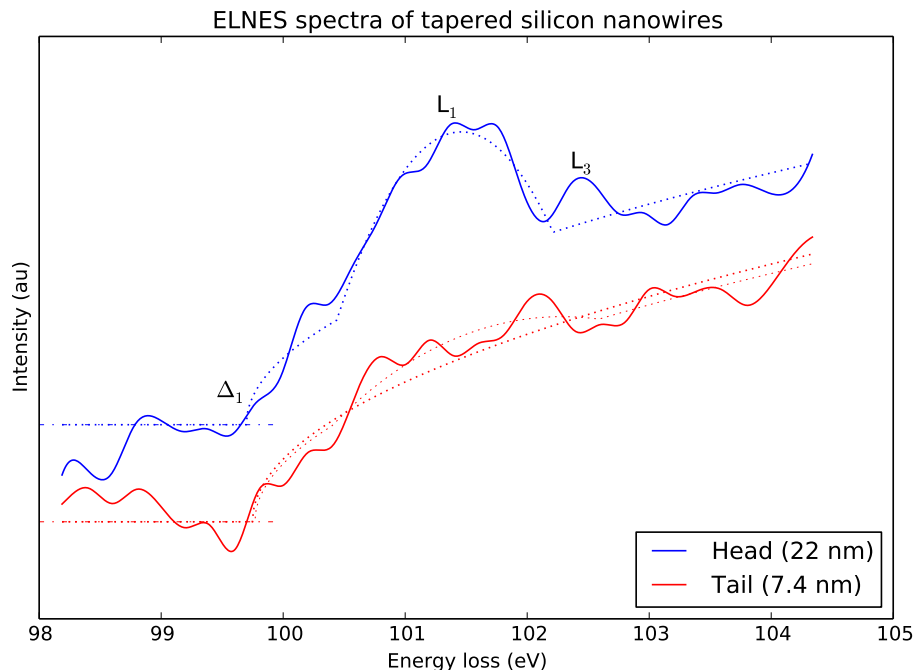
Figure 2.64: TEM images of the pillar used for EELS studies. The pre-oxidation diameter was  $\approx 58$  nm around the head, and  $\approx 30.7$  nm at the constriction. After oxidation, these dimensions narrowed to  $\approx 22$  nm and  $\approx 7.4$  nm, respectively.



(a) Raw EELS spectra showing the near-edge fine structure for the head and tail region of the tapered nanopillar in Figure 2.64.



(b) EELS spectra after background subtraction. The peaks arising from the Si-L<sub>3,2</sub> and Si-L<sub>1</sub> edges in the SiO<sub>2</sub> matrix are clearly visible. Dotted vertical lines indicate the features used to align the head and tail spectra.

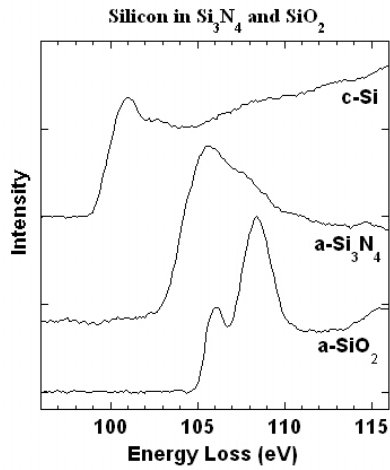


(c) Detailed EELS spectra showing Si features below the  $\text{SiO}_2$  edge. DOS fits similar to [26] are shown as dotted lines. The head region exhibits a clear  $\Delta_1$  onset and distinct  $L_1$  and  $L_3$  peaks, while the constricted tail region lacks the sharp  $L_1$  peak and mostly resembles a single parabolic band. Both a single parabolic fit and the complete fit are shown for comparison.

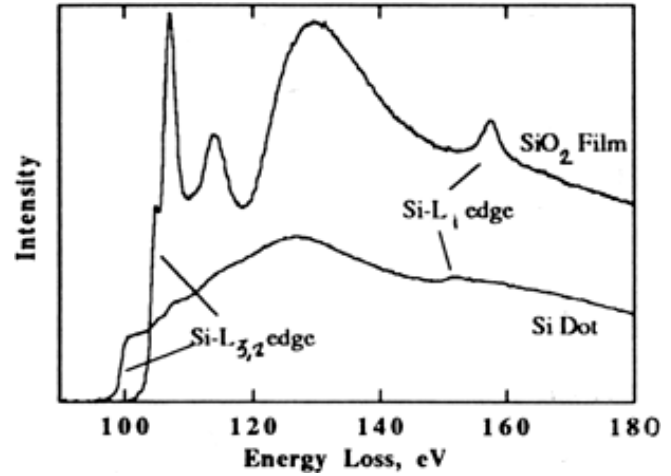
Figure 2.65: Raw EELS spectra showing the near-edge fine structure for the head and tail region of the tapered nanopillar in Figure 2.64. Curves are normalized and offset vertically for clarity.

Similar stage positions were recorded to allow rapid alignment to the head, tail, and empty regions. Immediately prior to acquiring the EELS spectra, the beam was focused to a  $\approx 1$  nm probe over an empty area of the sample. After calibration of the spectrometer, the tail region of the pillar was moved into focus, expanding the beam just enough to enable visual confirmation of the alignment. With the tail constriction properly centered under the beam, the probe was reduced back to a 1 nm spot, and the EELS spectrum was acquired from 70 eV to 274.6 eV in steps of 0.2 eV; the broad range allowed subtraction of the background and identification of multiple peaks for spectral alignment. This process was repeated to acquire a spectrum of the head region. After subtracting the background, the  $\text{SiO}_2$  peaks at 108 eV, 114 eV, 132 eV, and 157 eV were used to align the two spectra.

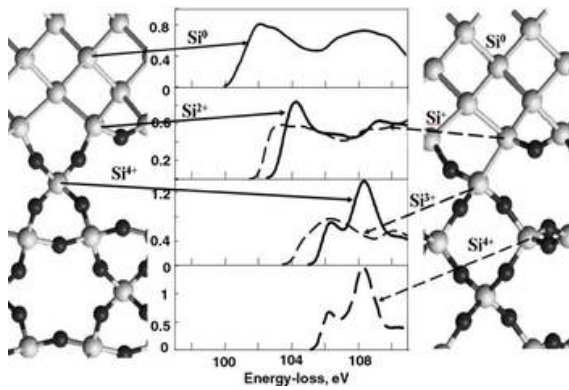
The raw spectra, corrected and aligned spectra, and a detail around the Si- $L_{3,2}$  edge are presented



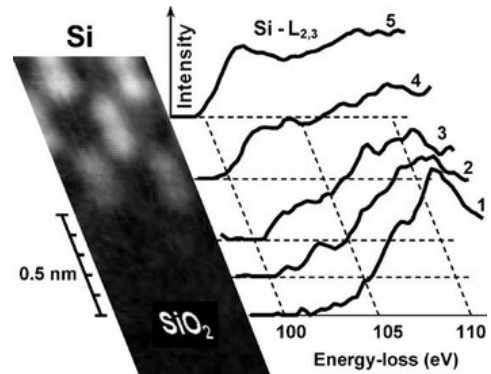
(a) EELS spectra for crystalline Si, amorphous  $\text{Si}_3\text{N}_4$  and amorphous  $\text{SiO}_2$ . Note the features exhibited by c-Si below the  $\text{SiO}_2$  band edge. From [392].



(b) EELS spectra for an Si QD and  $\text{SiO}_2$  film. Note the Si features below the  $\text{SiO}_2$  onset, as well as the  $\text{SiO}_2$  peaks at  $\approx 108$  eV, 114 eV, 130 eV, and 157 eV, and the inflection at 106 eV. From [304].



(c) Schematic illustrating the origins of near edge fine structure features for EELS spectra of Si/ $\text{SiO}_2$  interfaces. From [374]



(d) Line scan over an Si: $\text{SiO}_2$  interface showing EELS spectra of the Si- $L_{3,2}$  ionization edge. From [374].

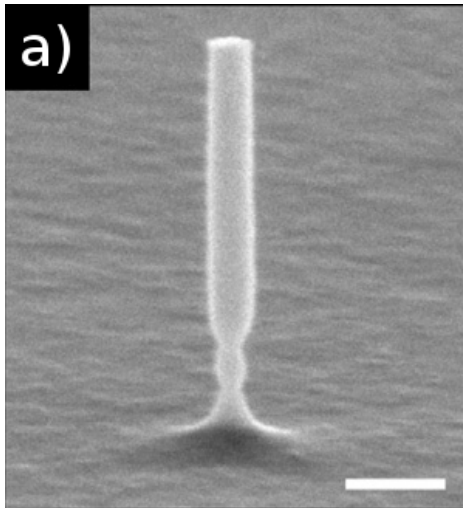
Figure 2.66: Reference EELS spectra and near-edge fine structure features for Si and  $\text{SiO}_2$ .

in Figure 2.65. Both spectra showed significant contributions from the  $\text{SiO}_2$  surrounding the core, with a subtle inflection at 106 eV and pronounced peaks at 108 eV and 114 eV arising from the Si-L<sub>3,2</sub> edge of the  $\text{Si}^{4+}$  oxidation state in the  $\text{SiO}_2$  matrix (see Figure 2.66c), as well as the broad peak at 132 eV and smaller peak at 157 eV corresponding to the Si-L<sub>1</sub> edge in  $\text{SiO}_2$  [304, 374]. While these features are shared with  $\text{SiO}_2$  films, the sharp rise between 100 eV - 104 eV is unique to the elemental Si-L<sub>3,2</sub> edge, and not found in  $\text{SiO}_2$  or  $\text{Si}_3\text{N}_4$  (see Figure 2.66(a,b)) [304, 392]. Because this loss regime precedes the  $\text{SiO}_2$  onset, we were still able to resolve spectral features resulting from the core without these being obscured by the  $\text{SiO}_2$  background.

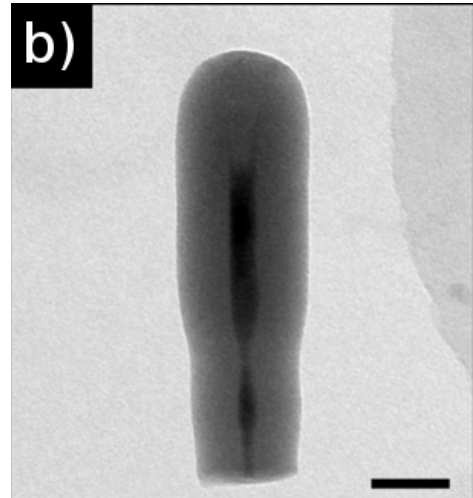
Examining the detail below the  $\text{SiO}_2$  edge (Figure 2.65c), we found the head region to exhibit characteristics matching bulk silicon, including the  $\Delta_1$  onset, distinct L<sub>1</sub> peak, and the smaller L<sub>3</sub> peak. By contrast, the spectrum taken in the 7.4 nm tail region lacked the sharp L<sub>1</sub> peak and assumed the form of a single parabolic band. In both cases, we note that these characteristics are similar to those reported by Batson and Heath [26] for Si QDs (see Figure 2.61). Our data measured at the constricted region aligns quite well with the 40 Å Si QDs, which is significantly smaller than the diameter of the nanowire. The earlier onset we observed to this band modification could be a result of the oxidation-imposed strain in the pillar, which we know to induce a blue shift of the band gap (see discussion above); such an affect would not have been observed in their study, which utilized isolated, bare quantum dots. Similarly, our observations in the head region reflect the bulk-like spectra of larger, 88 Å Si QDs, although the prominent L<sub>1</sub> peak in our case appears blue-shifted by  $\approx 0.35$  eV compared to the bulk location. Interestingly, the two smaller peaks at  $\approx 102 - 103$  eV appear to have equivalent features in the tail spectra with the same  $\approx 0.35$  eV shift. If this offset were accurate — due to a miscalibration introduced while adjusting the beam, perhaps — a similar data fit to extract the band edge [25, 26, 24] would imply a total blue shift of  $\approx 0.55$  eV between the 7.4 nm tail and bulk-like head region. This value is quite consistent with energy shift we observed from  $\mu\text{PL}$  measurements of similar diameter pillars, as described earlier. Unfortunately, the EELS data are not clear enough to draw firm conclusions, given the uncertainty in energy introduced during the alignment steps. In particular, we cannot rule out the influence of the  $\text{SiO}_2$  or Si-SiO<sub>2</sub>

interface, which could also have contributed to the measured intensity in the 100 - 104 eV region. While pure SiO<sub>2</sub> produces negligible loss here, the presence of additional Si<sup>1+</sup> and Si<sup>2+</sup> oxidation states at the interface could be responsible. Windl *et al.* [374] both modeled and recorded EELS data across the Si-SiO<sub>2</sub> interface and found intermediate behavior resembling the spectra from our nanowire (see Figure 2.66(c,d)). Alternatively, line shapes with similar characteristics have also been reported from SiO<sub>2</sub> films after excess electron beam exposure initiated the formation of silicon nanoparticles in the layer (see Figure 2.66b, from [304]).

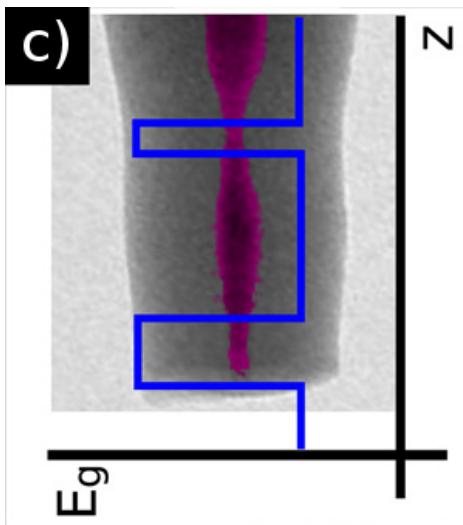
Despite the challenges associated with directly measuring the band gap fluctuations, several collaborators applied the geometric band gap engineering technique to the creation of quantum electronic devices in silicon nanopillars and successfully demonstrated Coulomb blockade using the effect [363]. In this work, pillars were fabricated with two notches with slightly different axial lengths. After oxidation, these constrictions were narrowed to sub-10 nm dimensions, producing a quantum-confined blue-shift of the local band structure. Aligned lithography was used to remove the oxide only at the top of the pillar, after which electrodes were fabricated on top of the conduction channel, with an additional electrical contact on the backside of the wafer; schematics, SEM, and TEM images are shown in Figure 2.67. In the final structure, the tapered sections acted as high band gap barriers through which the carriers must tunnel, surrounding a bulk-like quantum dot. Due to their different lengths, however, one of these barriers was significantly more electron transparent than the other, forming an asymmetric double barrier tunnel junction. Because carriers could more easily tunnel through the shorter barrier, they began to accumulate against the within quantum dot against the longer barrier. This created a Coulomb blockade, requiring an additional voltage  $V_t \sim e/(2C_j)$  to transfer another electron onto the island, where  $e$  denotes the electron charge and  $C_j$  reflects the junction capacitance impeded additional carrier injection. The overall device current was limited to the exponential tunneling current through the wider barrier, which was proportional to the number of charges within the dot,  $I \sim I_0(n, V) \exp(V_a/k_b T)$ . At discrete steps of  $V_t$ , however, the transfer of an additional electron onto the island provided a discrete increase in  $I_0$ , resulting in a staircase-like  $I - V$  relationship. This behavior was observed at moderate temperatures (77K)



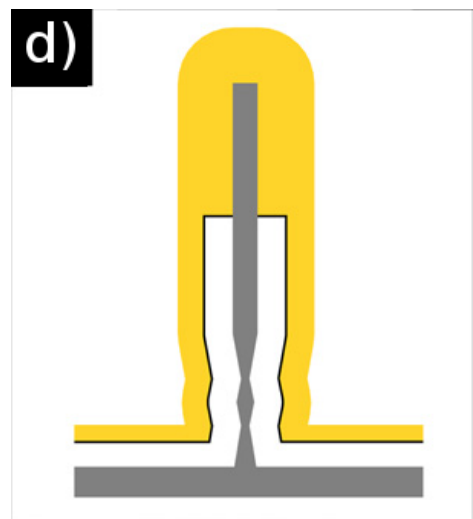
(a) SEM of as-etched, sculpted, silicon nanopillar. Scale bar is 100 nm.



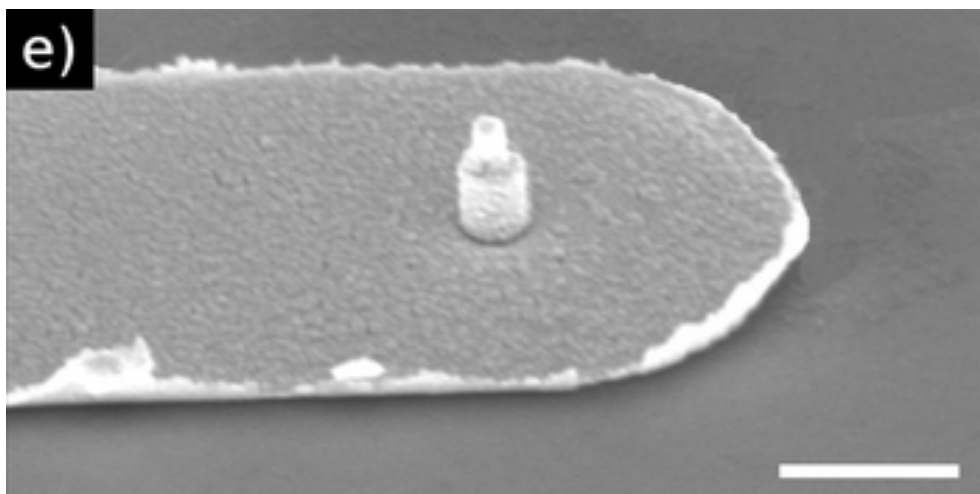
(b) TEM of oxidized double tunnel junction pillar after removal from the substrate. Scale bar is 50 nm.



(c) Schematic placed over the TEM image showing regions of widened silicon band gap after oxidation.



(d) Schematic of the completed device.



(e) SEM of the completed device. Scale bar is 500 nm.

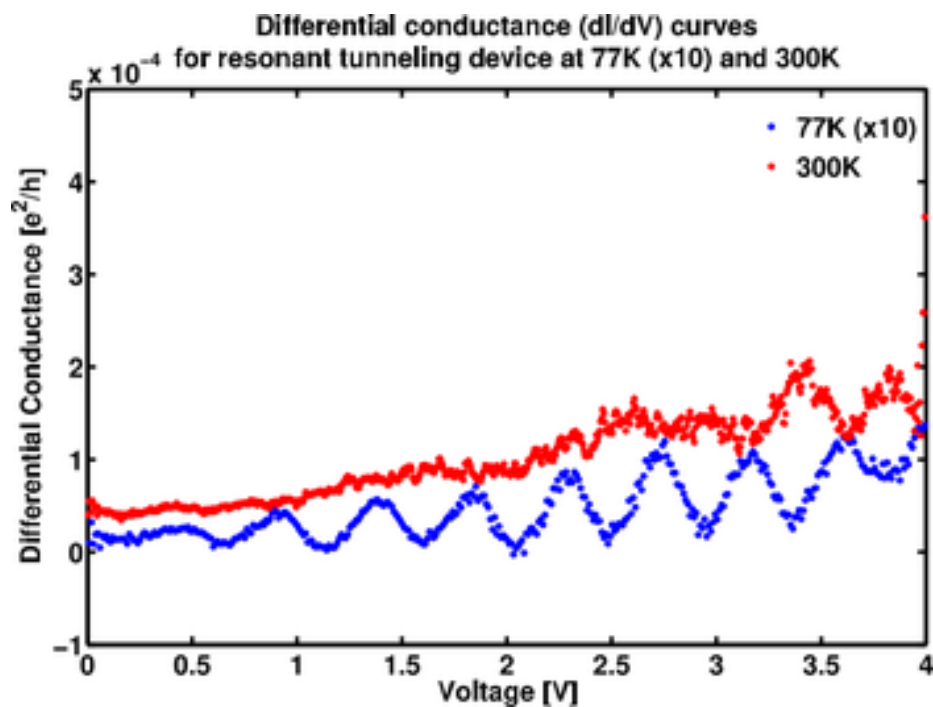


Figure 2.68: Differential conductance of a double tunnel junction device at 300K and 77K. Plot was numerically computed from measured I-V data. Note that the 77K data are scaled by a factor of 10. Periodic peaks can be seen with a spacing of 0.452V. From [363].

for a threshold voltage of  $V_t=0.452$  V, corresponding to a capacitance of 0.356 aF; these curves are shown in Figure 2.68.

While we were unable to definitively map the band structure along our nanowires, the EELS spectra we obtained clearly reflected a change in band characteristics between the bulk and quantum confined regimes. Additionally, the technique of geometric band gap engineering has been successfully applied to the development of Coulomb blockade devices using asymmetric double barrier tunnel junctions fabricated from a bulk material. Future work should continue to explore such structures with geometrically engineered band gaps, potentially employing STEM/EELS to extract accurate quantitative maps of the electronic band structure, along with the development of gated structures and sharper junctions to yield more elaborate control of the electron behavior.

### 2.4.3 Wafer bonding

In addition to the directed growth techniques described above, we considered subtractive methods to achieve deterministic placement of III-V quantum dots. While it might be possible to isolate individual quantum dots grown by Stranski-Krastanov growth [14, 128] and eliminate the excess surrounding material by etching, the random location of these structures would still require unique lithographic patterning for each device, imposing severe limits on the scalability of the process. Instead, we proposed to start with planar semiconductor quantum wells, from which isolated regions could be lithographically defined and etched. This method provides the necessary deterministic control over both the dot location and dimensions. Additionally, the capping layers are preserved over the majority of the dot's surface area (only the thin edges are exposed during etching), which should maintain carrier confinement within the quantum dot and prevent excess recombination at surface states. Finally, for an appropriate cavity design, this method offers the tantalizing possibility of creating dots which are self-aligned to the cavity anti-node using a single lithographic process.

Contrary to initial expectations, early investigations into lithographically-defined quantum dots reported extremely efficient photoluminescence [161, 317]. In these studies, electron beam lithography was used to define quantum wires and disks with dimensions down to 40 nm. Using RIE, these features were transferred into the substrate containing GaAs/Al<sub>0.3</sub>Ga<sub>0.7</sub>As multiple quantum well (MQW) structures. Not only did the excitation spectra exhibit different characteristics than the bulk, the overall excitation efficiency *increased* by as much as 50-100 times per unit volume. Given dimensions well below those to produce an optical resonance at the excitation frequencies, the effect could not be attributed to resonant coupling into the structures. Similarly, the dimensions were too large to produce significant lateral confinement and substantially alter Coulomb attraction within the structure. Consequently, the high luminescence efficiency and altered spectra were attributed to inhibition of nonradiative recombination due to reduced numbers of defects likely to be present within the dots as compared to bulk structures. Surprisingly, the free surfaces created by the etching procedure did not function as efficient recombination centers.

As dot dimensions increase, so does the effective dipole. When observing vacuum Rabi splitting

(VRS), this produces a more impressive splitting-to-linewidth ratio. But at large dimensions, a question arises as to the quantum nature of emission from these structures: at what point does the emission no longer reflect effects of quantized fields, and instead exhibit semiclassical behavior? Khitrova *et al.* [163] studied saturation absorption from quantum wells with various excitation beam diameters and cavity apertures. For a beam diameter of 50  $\mu\text{m}$ , 200,000 photons were required to saturate a single QW and appreciably alter the VRS; with a 2  $\mu\text{m}$  oxide aperture, the saturation limit was reduced to 300 photons. Using several additional apertures, the number extrapolated to  $\approx 90$  photons/ $\mu\text{m}^2$ . Although additional nonlinear experiments would be required to verify that such structures can truly reach the regime of strong coupling, this analysis provides a rough upper limit, and suggests that quantum effects may appear for dimensions below  $\approx 100$  nm.

More recently, Verma *et al.* [358] examined lithographically-defined QDs which had been wet etched from a single  $\text{In}_{0.2}\text{Ga}_{0.8}\text{As}$  QW. The emission spectra for dots showed a clear blue-shift with decreasing size, likely due to a combination of quantum confinement and strain. For 35 nm diameter dots, photon antibunching was observed for the single exciton peak at 888.6 nm. Coincidence measurements revealed a second-order correlation of  $g^{(2)}(0) = 0.314$ , consistent with emission from a single emitter. The behavior from individual dots showed single exciton emission with linewidths down to 250  $\mu\text{eV}$ . Lifetime measurements indicated very rapid emission following a biexponential decay with a fast component at 470 ps as well as a slower contribution at 2.1 ns. The measured linewidth is significantly larger than those typically measured for self-assembled QDs and far from lifetime limited. Although this makes these dots incapable of producing indistinguishable photons, it confirms the ability of such etched quantum dots to act as true single photon sources with size-tunable spectra.

Along with their validation as single photon emitters, recent work within our group has explored the intriguing possibility of producing etched quantum dot emitters which are self-aligned to photonic crystal cavities [270]. In 2D photonic crystal slabs and 1D photonic crystal nanobeams, the optimal cavity mode (with minimum mode volume and maximal overlap for an emitter embedded in the dielectric) is generally the lowest order acceptor mode. These states originate from propagating

modes within the lowest semiconductor band, and maintain similar symmetry and field patterns. For TE polarizations, structures consisting of connected regions of high dielectric material tend to produce the largest band gaps. This results in cavity field patterns which are concentrated near large dielectric areas, surrounded by air holes to produce the maximum dielectric contrast. See 3.2 for a more in-depth discussion.

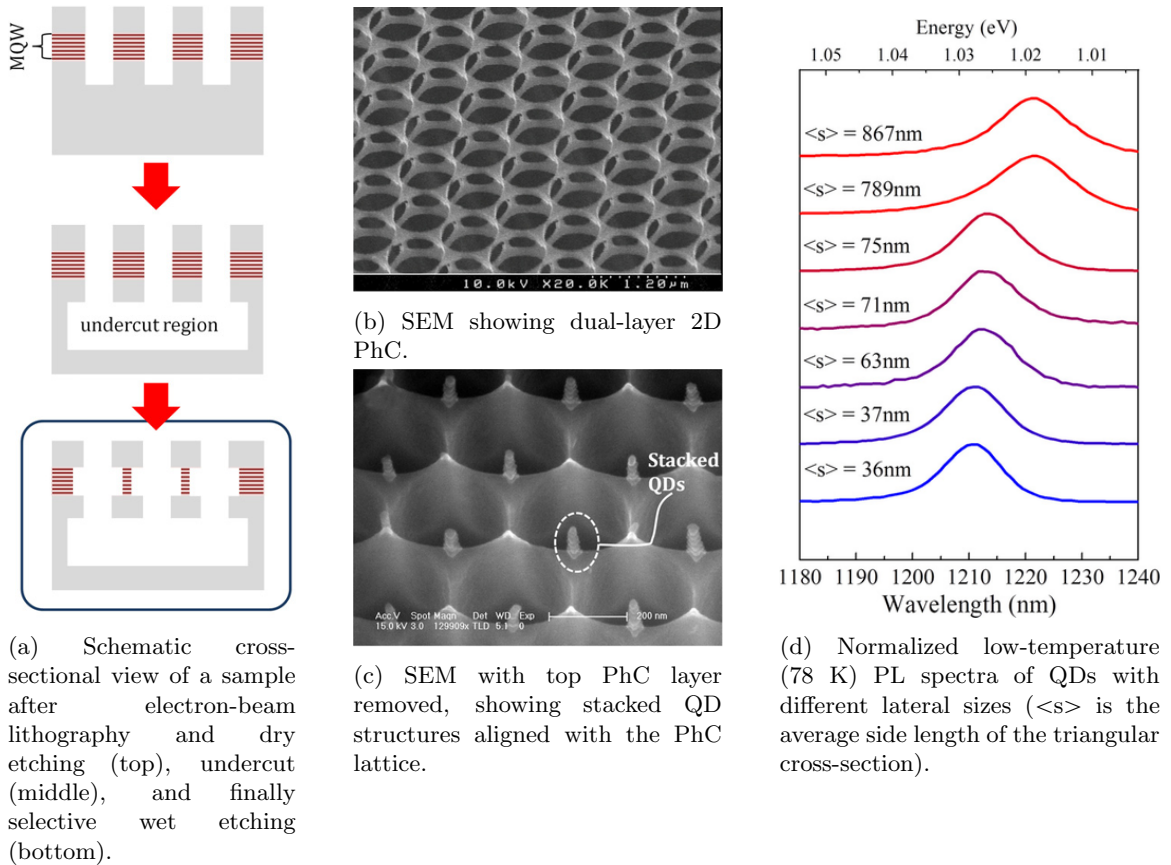


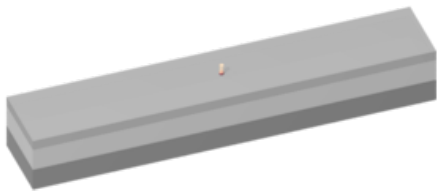
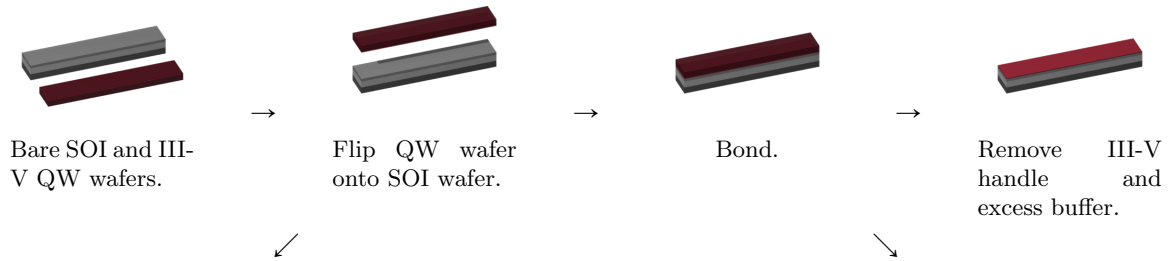
Figure 2.69: Self-aligned quantum nanostructures embedded in 2D PhCs by selective wet etching. From [270].

Using the photonic crystal itself as a mask, Oh *et al.* [270] used wet etching of planar  $\text{In}_{0.91}\text{Ga}_{0.09}\text{As}_{0.52}\text{P}_{0.6}$  MQWs to produce stacks of semiconductor quantum dots embedded inside a 2D photonic crystal slab. The photonic crystal consisted of a triangular lattice of circular holes. The design used a relatively large lattice constant of  $a=650$  nm - 850 nm with fairly small air holes,  $r = 0.25a - 0.35a$ . This left large dielectric regions between holes which would serve as the starting material for the quantum dots. For a mode with the E-field concentrated in the dielectric,

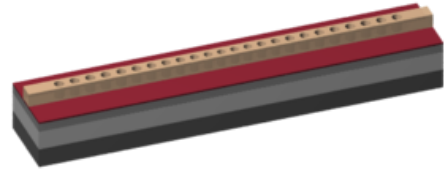
these features would be inherently aligned with the field maximum. Additionally, a moderately low etch selectivity between the QW and surrounding cladding layers required the large holes to ensure the structure would remain connected after wet etching, which enlarged the hole sizes to  $r \approx 0.45a - 0.48a$ . Finally, the minimal remaining dielectric material required the fairly large lattice constant to tune the final cavity resonance to 1200 nm - 1300 nm. The wet etch was performed at  $-1^\circ\text{C}$  to improve selectivity and reduce the QW etch rate to 6.5 nm/min, allowing exquisite control over the dot sizes. Studying dots with triangular edge lengths varying from 75 nm down to 36 nm, the authors reported a clear blue-shift of photoemission with decreasing sizes, with fairly broad spectra ( $\approx 10$  meV) and PL intensities around the same order of magnitude.

The final device from this process resembled a thin, two-layer cavity connected by a narrow stack of quantum dots. While this might not be ideal for our system, the structure is primarily a consequence of the MQW being embedded near the center of the cavity layer. If instead the wafer only had a single QW located near the surface, the emitter could be positioned just above the resonator, preserving a thicker device layer in which a high-quality cavity could reside. This also suggests an opportunity to isolate the material system for the cavity and emitter by using wafer bonding to integrate the two. Such a technique has received tremendous attention recently as a preferred method of integrating active photonic structures such as lasers into the SOI platform, yielding hybrid Si/III-V devices [83, 200, 202, 322, 335, 311]. Besides enabling optimal selection of the emitter and passive photonic components independently, these different material systems generally exhibit orthogonal etch chemistries, allowing greater flexibility in the fabrication process.

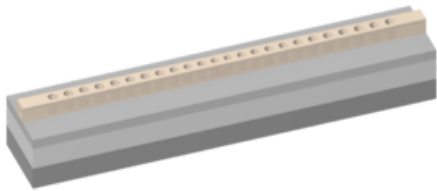
We therefore considered the integration of III-V QWs onto SOI photonics by wafer bonding, with the intention of using selective etching of the QW to produce a III-V QD directly on the cavity surface. Here, the technique would begin by bonding a III-V wafer with a QW very near the surface onto an unprocessed, SOI substrate. A wet etch could then remove the III-V substrate material, leaving only the QW and barrier layers atop the Si device layer. From this point, several potential schemes would be possible to mask the quantum dot and align it into the cavity; these are depicted schematically in Figure 2.70. In the first method, electron beam lithography would be used to define



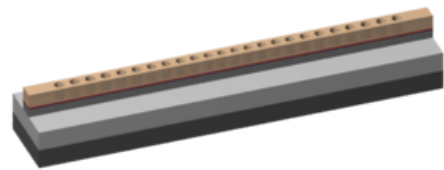
Perform e-beam lithography to define QD. Etch.



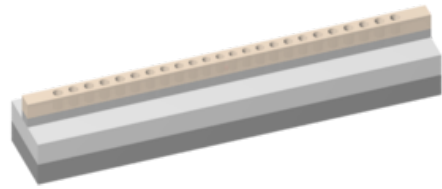
Perform e-beam lithography to define 1D nanobeam cavity.



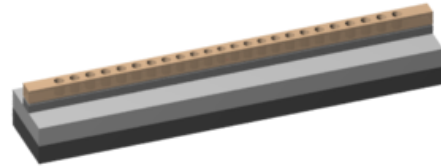
Perform *aligned* e-beam lithography to define 1D nanobeam cavity.



Etch 1D nanobeam cavity.



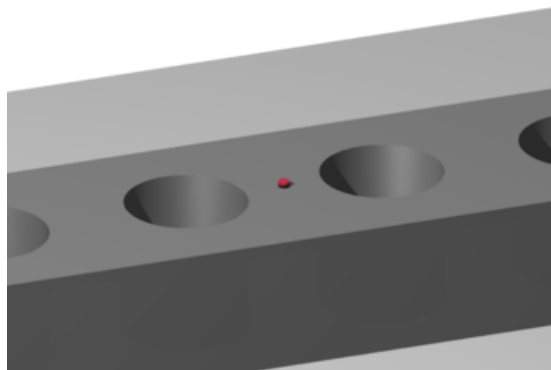
Etch 1D nanobeam cavity.



Leaving resist in place, use wet-etch to define QD in cavity.



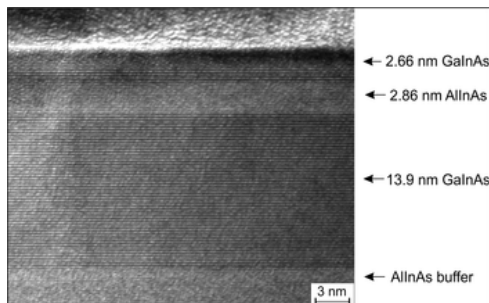
Remove resist.



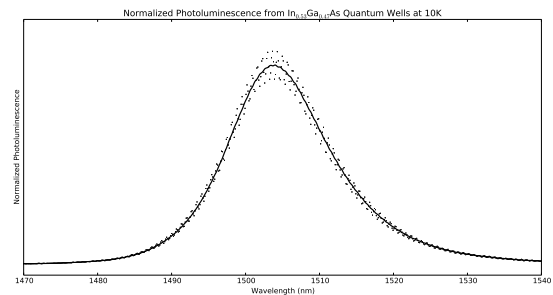
Detail of quantum dot in cavity.

Figure 2.70: Schematic of process flows for fabricating bonded/etched quantum dots in 1D photonic crystal nanobeams using aligned lithography (left) or self-aligned wet etching (right).

a quantum dot which would be etched from the planar QW material. A second, aligned lithographic step would then be used to create the resonator. Alternatively, electron beam lithography would be used to first define the cavity structure. After etching the cavity through both the III-V and Si device layers, the same polymer mask would be used to perform the wet etch which defines the quantum dot. This is similar to the technique developed by Oh *et al.* [270], but avoids the need to use III-V layers with highly selective etches, instead imposing this restriction on the silicon and polymer layer. The first method enjoys the most flexibility by isolating the dot creation from the cavity design, but requires a second, high-resolution, aligned lithographic step. By contrast, the second method couples the creation of the dot into the cavity design, requiring the cavity anti-node to exist at the largest region of dielectric. For a design meeting this constraint, however, this method has the distinct advantage of being inherently self-aligned, producing a quantum dot which is precisely located at the center of the largest dielectric region in the cavity. By careful command over the wet etch rate, the precise size (and therefore spectrum) of the emitter could also be readily controlled. Significantly, this could potentially occur after having measured the cavity spectrum, or gradually approached through a sequence of etch/measurement cycles.



(a) Cross-sectional TEM of a sample similar to the one we used. To ensure optimal coupling to the evanescent field, the stack-up was designed to keep the QW as close to the surface as possible.



(b) PL spectra of our QW sample at 10 K.

Figure 2.71: Characterization of our QW sample.

Before experimenting with patterning the QW layer, we attempted to bond the unpatterned material directly to 1D nanobeam resonators which had already been etched into the SOI substrate (the design and fabrication of these are described in Chapter 3). As with a patterned QW device, this

structure relies on evanescent coupling of the cavity mode into the III-V material, making it critical for the QW to be located as close to the surface as possible. We chose a sample containing a single, 12.6 nm  $\text{In}_{0.53}\text{Ga}_{0.47}\text{As}$  QW below a 4.2 nm  $\text{In}_{0.52}\text{Al}_{0.48}\text{As}$  buffer and 2.3 nm  $\text{In}_{0.53}\text{Ga}_{0.47}\text{As}$  cap. The QW rested on a 404 nm  $\text{In}_{0.52}\text{Al}_{0.48}\text{As}$  buffer layer. All layers were grown without interruptions directly on an InP substrate. A cross-section of a similar sample is presented in Figure 2.71a to illustrate the structure, along with the photoluminescence spectra of the bare sample recorded at 10K (Figure 2.71b). At room temperature, the peak shifted to  $\approx 1575$  nm - 1600 nm.

We began the integration by preparing both the SOI and III-V wafer for bonding. Appropriate surface preparation was critical to the success of the procedure. Many optimizations have been reported to assist in the bonding process, including the inclusion of vertical outgassing channels [200] and using straight aqueous HF rather than buffered HF, which tends to create pyramidal surface roughness on silicon due to anisotropic etch rates [210]. In our experience, the most significant factor influencing the bonding procedure was ensuring that both surfaces were free from debris. Since a significant amount of particulates can be created when cleaving wafers, we deposited a layer of AZ5214e photoresist to protect the front surfaces prior to any cleaving process; this layer was removed with acetone and IPA immediately before subsequent process steps. After the nanobeams had been processed (see 3.4), both the SOI and III-V were immersed in N-methylpyrrolidone (NMP) on a hotplate at  $65^\circ\text{C}$  for 10 min to remove any remaining organic material, then sprayed with IPA, acetone, and IPA to remove the NMP. Particulate removal continued using a 5 min ultrasonic bath in methanol and IPA spray. The nanobeams were then immersed for 30 s in Nanostrip (a stabilized solution of sulfuric acid and hydrogen peroxide) at  $70^\circ\text{C}$ , rinsed in DI, dipped in aqueous HF for 5 s, rinsed in DI, and dried; this last process was not conducted on the III-V sample as  $\text{H}_2\text{SO}_4:\text{H}_2\text{O}_2:\text{H}_2\text{O}$  etches InGaAs and InAlAs and would damage or remove the QW layer [58]. Surface cleanliness was verified using dark field microscopy to ensure adequate removal of particles, and additional cleaning performed if necessary. Immediately prior to bonding, the surfaces were activated in an 100 W  $\text{O}_2$  plasma at 300 mTorr for 5 min. The samples were then placed into contact and bonded in a Suss SB6L under vacuum (better than  $1 \times 10^{-3}$  mBar) using an applied force of  $\approx 510$  N at a temperature

of 150°C for 3 h, followed by 350°C for 1 h.

Once bonded, the InP substrate needed to be removed in order to expose the device. This is commonly done in an HCl solution, where the InP etch rate is known to vary greatly depending on the degree of HCl dissociation ( $> 15\mu\text{m}/\text{min}$  for 5:1 HCl:H<sub>2</sub>O to  $100\text{\AA}/\text{min}$  for a 1:1 mixture [257]). While even higher concentrations exhibit excellent selectivity against InGaAs etch stops [58], our sample only had the 404 nm InAlAs buffer layer, which would also be rapidly etched in these mixtures [130]. Following reports which suggest that dilutions  $< 3:1$  do not etch InAlAs [314], we used a 2:1 HCl:H<sub>2</sub>O mixture to remove the InP substrate, held at 4°C to further improve selectivity and controllability [367]. An alternative solution would have been a 1:1:2 HCl:H<sub>3</sub>PO<sub>4</sub>:CH<sub>3</sub>COOH mixture which exhibits a selectivity of 85 between InP and InAlAs, but only achieves modest InP etch rates ( $3000\text{\AA}/\text{min}$ ) [58].

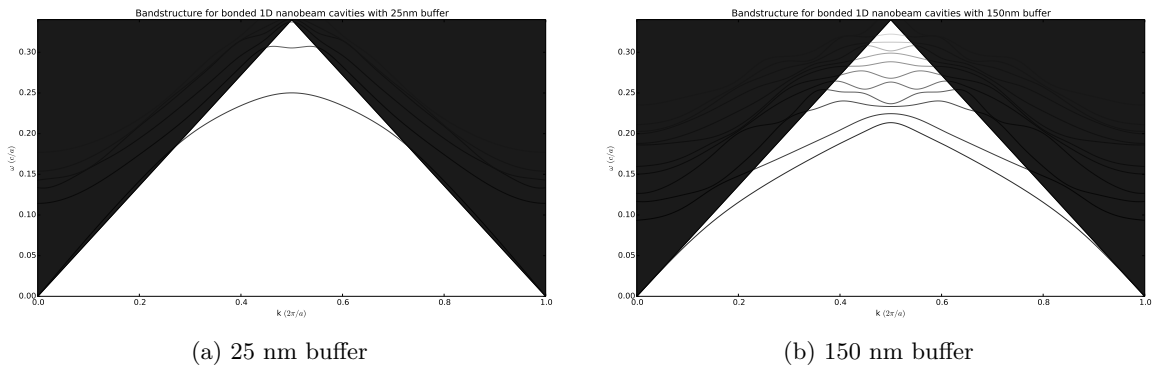


Figure 2.72: Photonic band structures of bonded 1D nanobeams, showing the collapse of the lowest-order band gap for thick buffers.

Following removal of the InP, we needed to thin the InAlAs buffer to avoid loading the photonic crystal with excessive dielectric material. For the SOI – III-V stack in our sample, photonic band structure simulations of the mirror region revealed that the incomplete band gap begins to collapse for a buffer thickness  $\gtrsim 35$  nm, and the lowest-order gap is essentially closed for thickness beyond  $\approx 150$  nm. However, complete removal of the buffer would destroy the electronic properties of the QW, as well as risk mechanical damage to the thin underlying layers. We chose to use a 3:1 HCl:H<sub>2</sub>O solution ( $\approx 108\text{\AA}/\text{s}$  etch rate, [314]) to thin the buffer to a target thickness of  $\approx 50$  nm.

Microphotoluminescence spectra of the completed device were measured at room temperature.

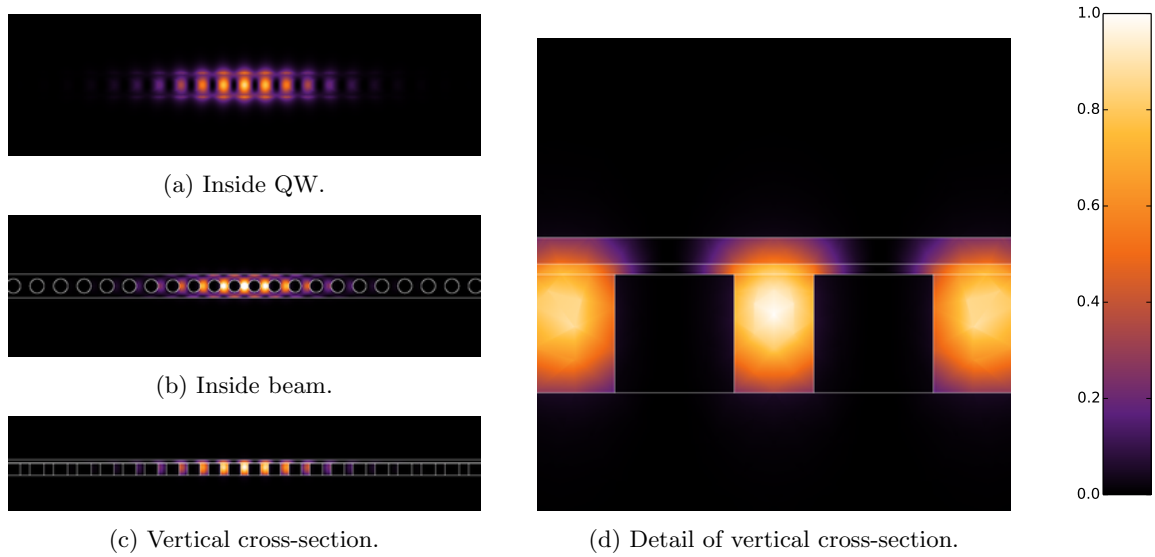


Figure 2.73: Electric-field energy ( $\epsilon|\vec{E}|^2$ ) for a bonded nanobeam cavity with 50 nm InAlAs buffer layer.

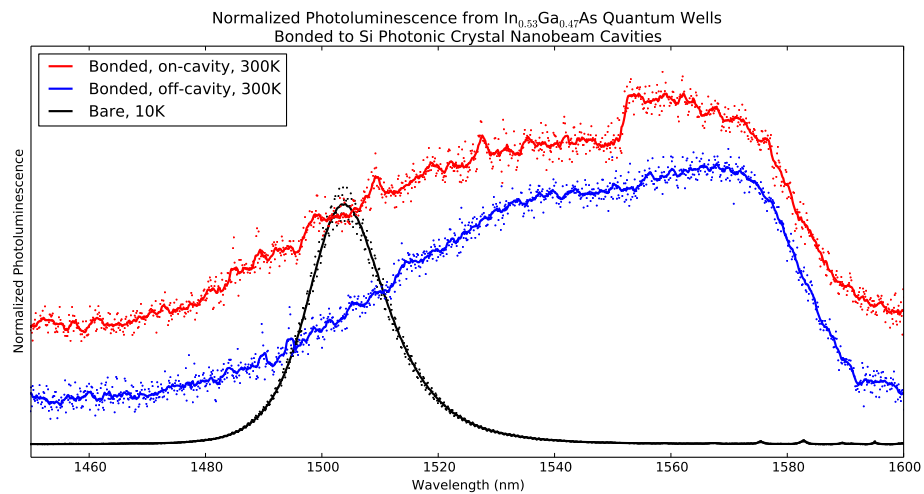


Figure 2.74: Comparison of normalized photoluminescence spectra from  $\text{In}_{0.53}\text{Ga}_{0.47}\text{As}$  QWs when coupled to a 1D nanobeam cavity, bonded, and unbonded. The peak unbonded PL was greater by a factor of  $\approx 700$ . The large red-shift between bonded and unbonded is due to measurements at different temperatures. The sharp edge and discrete peaks in the on-cavity spectrum are consistent with the semiconductor band-edge and presence of acceptor modes within the photonic band gap.

The system was pumped with a titanium-sapphire laser emitting at 821 nm, with a total power of 2270  $\mu\text{W}$  and a collection time of 5 s. To emphasize features corresponding to cavity coupled modes, the light was collected through a polarizer aligned to the cavity polarization. Comparative spectra over the cavity region were also recorded without the polarizer, as well as in adjacent regions away from the cavity; these were sampled for 1 s at an incident power of 4700  $\mu\text{W}$ .

Normalized  $\mu\text{PL}$  data for the cavity region (with polarizer), off-cavity background, and bare, pre-bonded sample are presented in Figure 2.74. We note that the bare spectra was recorded at 10K; the red shift at room temperatures was consistent with expectations. The overall luminescence efficiency of the on-cavity and off-cavity bonded spectra was essentially identical, but the curves exhibit several striking differences. While the off-cavity curve is mostly featureless, the data taken from the cavity region shows an abrupt transition near 1550 nm, as well as several smaller peaks between  $\approx 1500$  nm - 1530 nm. The abrupt rise in polarized photoluminescence beyond 1550 nm suggests the onset of the photonic crystal's semiconductor band and coupling to the continuum of lower-frequency guided modes; the shallow rise above 1550 nm in the off-cavity spectra is likely the result of an unintentional coupling to the nearby resonator, which was just beyond the excitation beam's focus. Similarly, the discrete peaks at higher energies are consistent with coupling to acceptor modes of the resonator within the photonic band gap of the mirror region; these features are not apparent in the off-cavity data. Both spectra show similar, broad, background luminescence. This is due to the use of an unpatterned QW layer in this device, enabling luminescence contributions from areas beyond the cavity. Greater suppression within the band gap is expected for devices where the QW layer has also been patterned. A more troubling result, however, is the relatively low luminescence efficiency. Although the data were taken at different temperatures, making precise, quantitative comparisons difficult, the original, unbonded data exhibited a peak intensity nearly 700 times greater than the measurements of the bonded sample. The decreased PL efficiency is possibly the result of having damaged the QW during the fabrication process, *e.g.*, through mechanical stress incurred during the bonding step or surface tension over the suspended regions following the InP substrate removal and InAlAs buffer thinning. Alternatively, the quantum well surface could have been inadvertently

exposed by chemical damage to the extremely thin cap layers during bonding prep, penetration of the HCl:H<sub>2</sub>O solutions under the suspended regions, or over etching of the InAlAs buffer, causing a loss of electron confinement and introduction of surface state defects. While many of these issues would likely be mitigated by bonding to a bare SOI substrate and patterning the QW, we decided to pursue other opportunities to achieve the desired emitter integration. Even so, these efforts have already demonstrated several critical features towards bonded emitter integration. Together, these data have shown that it is indeed possible to use wafer bonding to integrate III-V quantum wells onto silicon photonic crystal nanobeams, including evidence of PL spectral modification through evanescent coupling between the resonant mode and a shallow QW layer. We remain confident that there is great potential for this approach.

#### 2.4.4 Cavity-enhanced optical trapping

While the best characteristics of solid-state quantum emitters have generally come from quantum-confined, epitaxial III-V material, there still remains a number of barriers to scaling up their use in larger systems. Besides requiring low temperature operation, the spectral sensitivity to size and surface charges imposes extreme lithographic and process challenges in order to match emitter properties across the system. The optimization of these processes is generally unique to the substrate and emitter materials, restricting the range of possible cavity materials and requiring substantial efforts to explore each new combination.

By contrast, integration techniques capable of utilizing nanocrystal emitters — including colloidal quantum dots and color centers — could greatly relax or even eliminate these restrictions. Significantly, the use of discrete particles suggests an integration scheme which is not specific to the emitter itself. Besides completely separating the cavity and emitter material systems, such a method could be readily adapted to new emitters as they become available. The discrete nature of the sources also permits pre-screening of the emitters to match the emission wavelength or other properties, while a catch-and-release scheme could even incorporate *in situ* validation after assembly into the cavity.

To some extent, these objectives have been achieved by several groups — using fiber tapers [17], AFM [377], SEM nanomanipulators [313], and micropositioners [81] to assemble single NV centers onto photonic crystal cavities. Although none of these investigations reported strong coupling, the ability to pre-screen emitters, deterministically couple them to cavities, and maintain separation of the cavity and source all represent significant achievements towards producing larger cQED systems. Their future ultimate extensibility, however, is likely limited. A common feature amongst these techniques is the use of macroscopic devices to perform the assembly. While suitable for preparing a handful of systems, the need to pick-and-place each emitter individually limits their greater scalability, especially as alignment tolerances shrink below 20 nm.

An interesting alternative to macroscopic mechanical manipulation is to exploit optical gradient forces. In this case, *the cavity field itself* is used to integrate the particle. Because high-dielectric particles are naturally attracted to field maxima, this method is inherently self-aligned, drawing the particle towards the cavity anti-node where the maximum coupling is achieved. For non-spherical particles, the dipoles generally occur along the major axes. Because the particle orientation tends to align parallel to the cavity field, this serves to correctly yield the preferred dipole orientation as well [267].

Given this potential, we explored the use of optical trapping as a means to achieve deterministic integration of nanoparticle emitters into optical cavities. Although the experiments were hindered by optical nonlinearities — and ultimately unsuccessful — we believe these challenges could be resolved using different material systems, and a significant opportunity remains with the technique. Here, we present our general theoretical analysis of cavity-enhanced optical trapping, including derivations of significant figures-of-merit, relevant system characteristics, detailed calculations for our cavity design, and comparisons with existing reports in the literature. The cavity design itself, as well as experimental optimization and testing, can be found in Chapter 3.

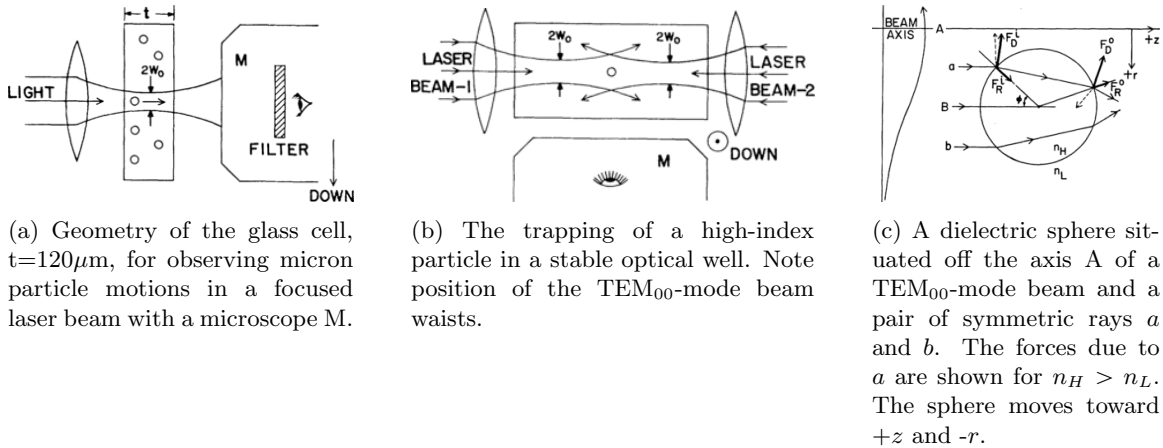


Figure 2.75: Illustrations of the optical trapping setup and diagram of the proposed model from Ashkin's first demonstration in 1970 [8].

#### 2.4.4.1 Optical trapping, gradient forces and cavity enhancement

The first optical trap was reported by Arthur Ashkin in 1970 [8] (see Figure 2.75). Observing 590 nm - 2.68  $\mu\text{m}$  latex spheres suspended in water within a thin glass cell, Ashkin demonstrated that a single laser beam would draw particles into the beam axis while accelerating them in the direction of the light, eventually capturing them against the glass surface. Completely trapping a particle was shown using two counter-propagating laser beams, whose opposing axial forces would balance each other. Ashkin also observed that size discrimination was possible, with smaller particles requiring higher laser powers to achieve comparable velocities. Additionally, applying the technique to low-index particles (air bubbles) produced the opposite effect, accelerating them away from the laser focus. This macroscopic trapping behavior was explained using a ray optics approach, where the recoil of reflected photons produced a net force along the direction of propagation (radiation pressure), while refracted photons – which were stronger near the optical axis – tended to draw the particle towards the focus.

As the technique improved, it was eventually shown that complete trapping is possible with a *single* laser beam [10]. Now known as optical tweezing, this method exploits the *optical gradient force*, which produces an effect proportional to  $\nabla|\vec{E}|^2$ . Not only is this responsible for drawing particles into the beam, Ashkin *et al.* [10] proved that a sufficiently tight focus produces a gradient *along* the optical axis which is capable of balancing the opposing radiation pressure and trapping

the particle in three dimensions. Significantly, this has the effect of directing particles towards the electric field maximum, precisely where optimal coupling would be achieved.

To quantify the limits of the technique, we consider the forces produced on a given particle. In general, this involves decomposing the incoming field into spherical harmonics, applying Mie theory to calculate the scattering properties of the particle (potentially using complex wave vectors to handle evanescent fields, *cf.* [28] and references therein), and integrating the Maxwell stress tensor over a surface enclosing the particle to calculate the force. As the nanocrystal emitters suitable for cQED systems have dimensions  $r \ll \lambda$ , however, we can obtain more intuitive results by focusing on the gradient forces produced within the Rayleigh regime. Here, we approximate the particle as a dipole with complex amplitude  $\vec{p} = \alpha \vec{E}$ , and only include the first terms in the Mie series expansion. Assuming real permittivities, this results in a complex particle polarizability  $\alpha = \alpha_0 / (1 - \frac{ik^3 \alpha_0}{6\pi\epsilon_0\epsilon_b}) \approx \alpha_0 + i \frac{k^3 \alpha_0^2}{6\pi\epsilon_0\epsilon_b}$ , where  $\alpha_0 = 4\pi\epsilon_0\epsilon_b r^3 \frac{\epsilon_p - \epsilon_b}{\epsilon_p + 2\epsilon_b}$  is the standard Clausius-Mossotti polarizability,  $k$  represents the magnitude of the wave vector in the medium,  $\epsilon_p$  and  $\epsilon_b$  represent the relative permittivities of the particle and background, and the denominator of  $\alpha$  provides a correction for the radiative reaction of the particle [70, 191]. Under the dipole approximation, the Lorentz force experienced by the particle will be [108]:

$$\vec{\mathcal{F}} = (\vec{p} \cdot \nabla) \vec{\mathcal{E}} + \frac{\partial \vec{p}}{\partial t} \times \vec{\mathcal{B}}$$

where, for clarity, we drop the time dependence  $e^{-i\omega t}$  and we use script characters to denote real values and block characters for complex amplitudes, *eg.*  $\vec{\mathcal{E}} = \text{Re}(\vec{E})$ . Inserting  $\vec{p} = \alpha \vec{E}$ , we find the time-averaged force  $\langle \vec{\mathcal{F}} \rangle$  by expanding the force vector and applying the rotating-wave approximation. Dropping terms  $\sim e^{-2i\omega t}$ , we find:

$$\begin{aligned}
\langle \vec{\mathcal{F}} \rangle &= \frac{1}{2} \operatorname{Re} \left( \alpha \left( \vec{E} \cdot \nabla \right) \vec{E}^* + \alpha \frac{\partial \vec{E}}{\partial t} \times \vec{B}^* \right) \\
&= \frac{1}{2} \operatorname{Re}(\alpha) \operatorname{Re} \left( \left( \vec{E} \cdot \nabla \right) \vec{E}^* + \frac{\partial \vec{E}}{\partial t} \times \vec{B}^* \right) \\
&\quad - \frac{1}{2} \operatorname{Im}(\alpha) \operatorname{Im} \left( \frac{\partial \vec{E}}{\partial t} \times \vec{B}^* \right) \\
&\quad - \frac{1}{2} \operatorname{Im}(\alpha) \operatorname{Im} \left( \left( \vec{E} \cdot \nabla \right) \vec{E}^* \right)
\end{aligned}$$

By Maxwell's equations, we can rewrite  $\partial \vec{E} / \partial t \times \vec{B}^* = -i\omega \vec{E} \times \vec{B}^* = \vec{E} \times (\nabla \times \vec{E}^*)$ . Expanding the  $\operatorname{Re}(\dots)$  and  $\operatorname{Im}(\dots)$  terms, and applying the vector identities:

$$\begin{aligned}
\nabla(\vec{A} \cdot \vec{B}) &= (\vec{A} \cdot \nabla) \vec{B} + (\vec{B} \cdot \nabla) \vec{A} + \vec{A} \times (\nabla \times \vec{B}) + \vec{B} \times (\nabla \times \vec{A}) \\
\nabla \times (\vec{A} \times \vec{B}) &= \vec{A}(\nabla \cdot \vec{B}) - \vec{B}(\nabla \cdot \vec{A}) + (\vec{B} \cdot \nabla) \vec{A} - (\vec{A} \cdot \nabla) \vec{B}
\end{aligned}$$

And some straight-forward algebraic manipulation yields:

$$\langle \vec{\mathcal{F}} \rangle = \frac{1}{4} \operatorname{Re}(\alpha) \nabla |\vec{E}|^2 + \frac{\omega \mu_0}{2} \operatorname{Im}(\alpha) \operatorname{Re} \left( \vec{E} \times \vec{H}^* \right) + \frac{1}{4} \operatorname{Im}(\alpha) \operatorname{Im} \left( \nabla \times \vec{E} \times \vec{E}^* \right)$$

Finally, we note that  $\operatorname{Im}(\alpha)$  is related to the *total* extinction cross-section  $\sigma_{ext}$ . Inserting  $\operatorname{Im}(\alpha) = \epsilon_0 \epsilon_b \sigma_{ext} / k = \sigma_{ext} / \omega \eta_b$ , where  $\eta_b = \sqrt{\mu_0 / \epsilon_0 \epsilon_b}$  is the characteristic impedance of the background, and  $n_b$  represents the refractive index of the surrounding medium, we arrive at our expression for the time-averaged force on a Rayleigh particle:

$$\langle \vec{\mathcal{F}} \rangle = \frac{1}{4} \operatorname{Re}(\alpha) \nabla |\vec{E}|^2 + \frac{\sigma_{ext} n_b}{2 c} \operatorname{Re} \left( \vec{E} \times \vec{H}^* \right) + \frac{\sigma_{ext}}{4 \omega \eta_b} \operatorname{Im} \left( \nabla \times \vec{E} \times \vec{E}^* \right)$$

These terms correspond to the gradient force, radiation pressure due to scattering, and the force due to polarization gradients, respectively.

In general, the primary challenge in optical tweezing is ensuring that the first term dominates the other two (in addition to Brownian motion). While transverse gradients are typically quite strong,

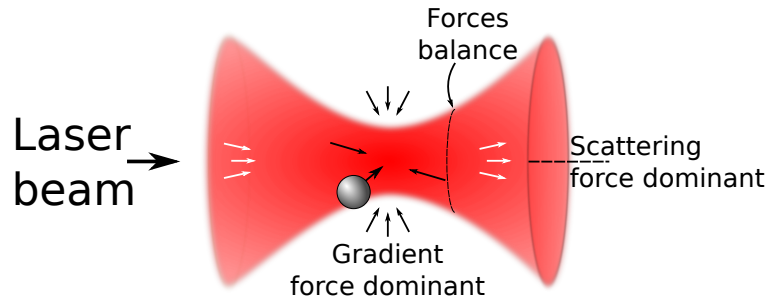


Figure 2.76: Schematic of a single Gaussian beam optical trap. Transverse gradient forces dominate near the focus and draw the particle towards the optical axis. Precisely at the focus, however, the symmetric axial profile results in a zero gradient force, but a net radiation pressure. Thus, a stable trapping position is found just beyond the focus, where the backwards-oriented axial gradient opposes the forward scattering forces. Far from the focus, the scattering forces again dominate.

achieving high axial gradients requires very high NA lenses and a tight focus. To circumvent this, the initial experiments used counter propagating beams to eliminate any net radiation pressure. As the particle size decreases, this requirement eases somewhat. Examining these further, we see that the gradient force, which is proportional to  $\text{Re}(\alpha)$ , acquires an  $r^3$  dependence on particle size from the polarizability. In comparison, the latter two follow  $r^6$  due to the  $\alpha_0^2$  dependence of  $\text{Im}(\alpha)$ . Thus, the realization of single-beam optical traps is somewhat easier for slightly smaller particles, and has become a common technique for the manipulation of small biological agents such as virii (dimensions  $\approx 100$  nm) bacteria [9] (few  $\mu\text{m}$ ), both demonstrated shortly after the first report of single-beam optical trapping [10], as well as polymer microspheres tethered to DNA.

Scaling this further into the nanometer regime, however, becomes increasingly difficult. While radiation pressure is minimal at these scales, the kinetic energy due to Brownian motion does *not* scale with size, resulting in an *increasing* velocity as the mass decreases. Simultaneously, the gradient force decreases as  $r^3$ , while diffraction effectively limits the achievable length scales of the field gradient. In order to trap a nanocrystal emitter — which typically have dimensions below 10 nm — the system must overcome the increased Brownian motion velocity of such a small particle, while producing only 1/1000th of the effective force it could yield against a 100 nm virus. For the initial report of a single-beam optical trap [10], the finite available laser power limited the minimum particle size to a 26 nm silica sphere. Using  $\lambda=514.5$  nm focused near the diffraction limit, this already required a 1.4 W beam; even higher powers would be required at longer wavelengths, which

cannot be focused as tightly. To our knowledge, there are few, if any, reports which surpass this size to capture smaller dielectric particles using a traditional optical trap<sup>1</sup>. At even smaller scales, Doppler cooling techniques are capable of slowing down atoms by exploiting the higher recoil momentum of blue-shifted photons. As these rely on the ultra narrow spectral lines exhibited by atomic species, however, they have yet to be scaled to the regime of nanocrystal emitters. These limits result in a mesoscopic regime between  $\approx 1$  nm and  $\approx 100$  nm, where scaling down optical gradient traps or scaling up atomic cooling methods has proven exceptionally difficult [231].

Unfortunately, nanocrystal emitters tend to have dimensions  $\approx 5 - 10$  nm, precisely where trapping is most difficult. While it might be technically possible to capture such particles by simply increasing the laser power, this faces a number of practical challenges. Besides obvious issues with laser availability and risk of damage to structures, even small levels of absorption in the surrounding media can cause a significant temperature rise, increasing Brownian motion and leading to thermophoresis (escape of the particle due to temperature gradients).

Instead, most approaches to capturing particles below 100 nm rely on trapping using the optical near-field around nanostructured objects, which can significantly enhance either the field gradient or energy density. Because evanescent field remains primarily confined to the higher dielectric material, the system experiences minimal absorption (in the surrounding medium) while exhibiting significantly sub-diffraction gradients. Many of the early suggestions for trapping sub-50 nm particles employed the optical hotspots near metallic structures. Following calculations showing the feasibility of trapping 10 nm diameter particles near a sharp metallic tip [267], a number of efforts have demonstrated experimental capture of Rayleigh particles using plasmonic tweezers (*cf.* [396, 179, 49, 231], as well as references therein). While this has led to the successful trapping of 20 nm polystyrene spheres [396], the use of metallic structures induces significant loss in the material itself. Although these losses might be tolerable for many biological trapping applications, their presence is unacceptable for cQED.

Alternatively, ultra-high  $Q/V$  dielectric resonators are capable of producing comparable gradient

---

<sup>1</sup>Jauffred *et al.* [150] claim to have trapped single CdSe/ZnS QDs with  $\approx 100$  mW at 1064 nm, but a simple calculation shows this to have a trapping depth below  $1 kT$ , and their own parameter fits required a beam radius of 100 nm, well below the diffraction limit

forces without incurring the losses associated with plasmonic structures. In this case, the enhancement primarily results from the intense electric field produced by recirculating photons, and will ultimately force the nanocrystal strongly towards the field maximum. As we will describe shortly, the cavity enhances the trapping force near the anti-node by a factor proportional to  $Q/V$ , identical to the figure-of-merit for maximizing light-matter interaction in the cQED system. An appropriately designed cavity is therefore inherently optimized for both purposes, making it an ideal platform for emitter integration and cQED operation.

We will consider a general dielectric cavity comprised of linear, dispersionless, isotropic material for simplicity, and a typical nanocrystal emitter with dimensions  $< 10$  nm. At this scale, the influence of the particle on the field profile is minimal, allowing us to determine the trapping behavior using only the bare field profile. Assuming the cavity mode parameters are known (through FDTD or FEM simulations, for example), this essentially entails calculating the derivatives from the normalized field, and applying correct field normalization. We note that this can be easily evaluated at any location within the cavity, or against different nanocrystal properties using the appropriate polarizability.

We begin by writing the complex magnitude of our physical electric field,  $\vec{E}$ , in terms of the normalized field from simulations,  $\vec{E}_N$ :

$$\vec{E} = \sqrt{\xi} \vec{E}_N$$

The normalization of  $\vec{E}_N$  can be selected arbitrarily, and is commonly chosen proportional to the field energy ( $\int \epsilon |\vec{E}_N|^2 d\vec{r}^3 = 1$ ), relative to a specific location ( $\vec{E}_N(\vec{r}_0) = 1$ ), or relative to the maximum field strength ( $\max(|\vec{E}_N|) = 1$ ). We will select the latter, for simplicity of analytic approximations, but carry the terms through the calculation for completeness.

In the case of a linear, dispersionless dielectric, it is straightforward to show that the energy carried by the electric and magnetic fields must be equal. Thus, the chosen normalization for  $\vec{E}_N$  automatically imposes a normalization on  $\vec{H}_N$  such that  $\int \epsilon |\vec{E}_N|^2 d\vec{r}^3 = \int \mu |\vec{H}_N|^2 d\vec{r}^3$ . This, in turn,

implies that  $\vec{H}$  shares the same scaling as  $\vec{E}$ :

$$\vec{H} = \sqrt{\xi} \vec{H}_N$$

The time-averaged energy in the resonator,  $U$ , is the sum of the electric and magnetic contributions. Since these are equal, we choose to write the energy in terms of the electric field:  $U = U_E + U_H = 2U_E$ . Again neglecting material dispersion, the time-averaged electric field energy is  $U_E = \langle \frac{1}{2} \int \epsilon |\vec{E}|^2 d\vec{r}^3 \rangle = \frac{1}{4} \int \epsilon |\vec{E}|^2 d\vec{r}^3$ . The total energy is then

$$U = \frac{1}{2} \int \epsilon |\vec{E}|^2 d\vec{r}^3$$

We recognize that this term is also related to the mode volume of the cavity,  $V$ , which can be calculated directly from the normalized mode profile:

$$\begin{aligned} V(\vec{r}_0) &= \frac{\int \epsilon |\vec{E}_N|^2 d\vec{r}^3}{\epsilon(\vec{r}_0) |\vec{E}_N(\vec{r}_0)|^2} \\ &= \frac{\int \epsilon |\vec{E}|^2 d\vec{r}^3}{\epsilon(\vec{r}_0) |\vec{E}(\vec{r}_0)|^2} \\ &= \frac{2U}{\epsilon(\vec{r}_0) |\vec{E}(\vec{r}_0)|^2} \end{aligned}$$

Rewriting  $V$  in terms of the normalized field profile, we can solve for  $\xi$ :

$$\begin{aligned} V &= \frac{U}{\xi} \frac{2}{\epsilon(\vec{r}_0) |\vec{E}_N(\vec{r}_0)|^2} \\ \xi &= \frac{U}{V} \frac{2}{\epsilon(\vec{r}_0) |\vec{E}_N(\vec{r}_0)|^2} \end{aligned}$$

We are free to choose the position  $\vec{r}_0$  arbitrarily, as it merely determines the location to which the electric field is normalized. Often,  $\vec{r}_0$  is selected to match the position of the emitter within the cavity, in which case  $V$  can be used to directly find the vacuum electric field strength and cavity coupling to the emitter. In order to maximize coupling, it is typically assumed that the emitter is located at the peak of the electric field. For cavity-enhanced optical trapping, however, the field maximum may reside deep within the dielectric, at a location which is inaccessible to the particle. While an excellent choice for  $\vec{r}_0$  might therefore be the peak field within the cladding (which is accessible to the particle), most cavity parameters are reported in relation to  $|\vec{E}|_{max}$ . For simplicity,

we will adopt this convention, accepting that the field at the emitter will be lower by some known factor (readily determined from the mode profile):

$$\vec{r}_0 : |\vec{E}_N(\vec{r}_0)| = |\vec{E}_N|_{max}$$

Besides confining the light (which minimizes the mode volume), the cavity enhances the field intensity by recirculating the energy. The quality factor,  $Q$ , is defined as the ratio of electromagnetic energy stored in the cavity to the energy lost per cycle:

$$Q = \omega_0 \frac{U}{P_{out}}$$

where  $\omega_0$  is the (potentially shifted) resonant frequency,  $U$  again represents the time-averaged energy and  $P_{out}$  is the loss rate. In equilibrium,  $\partial U / \partial t = 0$ , and the loss rate matches the power coupled into the cavity:  $P_{in} = P_{out}$ . In general, only a fraction of the total excitation power will couple into the cavity due to detuning or modal mismatch. Letting  $P$  represent the total excitation power, and  $C$  the fractional coupling coefficient, we have  $P_{in} = PC$ . We note that the presence of the particle will cause the resonance to shift, so that  $C$  is a function of the intrinsic cavity properties, particle location and polarizability, and excitation wavelength [136]. For an ideal, critically-coupled cavity which is excited on resonance,  $C$  will still approach 1. Solving for the stored energy  $U$ , we find:

$$U = \frac{Q P C}{\omega_0}$$

which finally yields the scale to convert our normalized field profile into physical units:

$$\begin{aligned} \xi &= \frac{U}{V} \frac{2}{\epsilon(\vec{r}_0) |\vec{E}_N(\vec{r}_0)|^2} \\ &= \frac{Q P C}{V \omega_0} \frac{2}{\epsilon(\vec{r}_0) |\vec{E}_N(\vec{r}_0)|^2} \end{aligned}$$

Rewriting our time-averaged force equation in terms of the normalized field profile shows:

$$\begin{aligned} \langle \vec{\mathcal{F}} \rangle &= \frac{1}{4} \text{Re}(\alpha) \nabla |\vec{E}|^2 + \frac{\sigma_{ext} n_b}{2 c} \text{Re}(\vec{E} \times \vec{H}^*) + \frac{\sigma_{ext}}{4 \omega \eta_b} \text{Im}(\nabla \times \vec{E} \times \vec{E}^*) \\ &= \xi \left( \frac{1}{4} \text{Re}(\alpha) \nabla |\vec{E}_N|^2 + \frac{\sigma_{ext} n_b}{2 c} \text{Re}(\vec{E}_N \times \vec{H}_N^*) + \frac{\sigma_{ext}}{4 \omega \eta_b} \text{Im}(\nabla \times \vec{E}_N \times \vec{E}_N^*) \right) \end{aligned}$$

and we arrive at the complete expression for the cavity-enhanced optical force:

$$\langle \vec{\mathcal{F}} \rangle = \frac{Q}{V} \frac{P}{\omega_0} \frac{C}{\epsilon(\vec{r}_0)} \frac{2}{|\vec{E}_N(\vec{r}_0)|^2} \left( \frac{1}{4} \text{Re}(\alpha) \nabla |\vec{E}_N|^2 + \frac{\sigma_{ext} n_b}{2 c} \text{Re} \left( \vec{E}_N \times \vec{H}_N^* \right) + \frac{\sigma_{ext}}{4 \omega \eta_b} \text{Im} \left( \nabla \times \vec{E}_N \times \vec{E}_N^* \right) \right)$$

The third term, corresponding to forces arising from polarization gradients, is nearly always insignificant compared to the field gradient and may be freely ignored. Additionally, the  $\vec{E}$  and  $\vec{H}$  fields are out-of-phase in standing-wave modes, so often  $\text{Re} \left( \vec{E} \times \vec{H}^* \right) \approx 0$  in the second term (there is essentially no radiation pressure in the cavity due to the absence of traveling waves). Moreover,  $\text{Re}(\alpha) \propto r^3$  while  $\sigma_{ext} \propto r^6$ . Thus, the optical force on Rayleigh particles is generally dominated by the gradient force (corresponding to the first term).

Dropping the second two terms and providing more explicit dependence on the coordinates for calculating mode volume ( $\vec{r}_0$ ) and particle position ( $\vec{r}$ ), we arrive at our final equation for the cavity-enhanced optical force:

$$\langle \vec{\mathcal{F}}(\vec{r}) \rangle \simeq \frac{Q}{V(\vec{r}_0)} \frac{P}{\omega_0} \frac{C}{\epsilon_0 \epsilon_R(\vec{r}_0)} \frac{2}{|\vec{E}_N(\vec{r}_0)|^2} \left( \frac{1}{4} \text{Re}(\alpha) \nabla |\vec{E}_N(\vec{r})|^2 \right)$$

This expression shows that the maximum achievable force is proportional to the standard gradient force ( $\nabla |\vec{E}_N|^2$ ), the cavity enhancement factor ( $Q/V$ ), the excitation power ( $P$ ), and penalty terms for incomplete coupling to the resonator ( $C$ ), and off-peak trapping, depending on where  $V$  is evaluated ( $|\vec{E}_N(\vec{r})|^2/|\vec{E}_N(\vec{r}_0)|^2$ ).

#### 2.4.4.2 Optical trapping metrics - depth, stiffness and sensitivity

While understanding the forces produced by optical traps provides valuable insight into the mechanism and optimization of the system, the actual value of the forces is not especially useful in an of itself. In particular, one can easily see that the gradient force becomes zero at an anti-node, or at least zero in tangential directions when trapped against a structure by an evanescent field. Instead, most traps are characterized by two additional metrics which better reflect their potential

for capturing particles. After defining these here, we will use them to analyze our cavity design in the next section.

The *depth* or *stability* of an optical trap refers to the potential barrier experienced by the particle, and is a measure of the energy difference in the system due to the presence of the particle. Once captured, the particle must obtain this quantity of energy to fully escape the trap. By convention, the depth is normally reported as a positive value (the additional energy required to escape) rather than a negative value (the potential energy of the particle in the trap). Considering the relationship  $\vec{f} = -\nabla U$ , we can find the potential barrier by integrating the force experienced by the particle as it is taken from the peak of the trap ( $\vec{r}_{trap}$ ) to a point infinitely far away:

$$\begin{aligned} U &= - \int_{\vec{r}_{trap}}^{\infty} \vec{f} \cdot d\vec{l} \\ &= - \frac{Q P C}{V \omega_0 \epsilon_0 \epsilon(\vec{r}_0)} \frac{2}{|\vec{E}_N(\vec{r}_0)|^2} \frac{\text{Re}(\alpha)}{4} \int_{\vec{r}_{trap}}^{\infty} \nabla |\vec{E}_N|^2 \cdot d\vec{l} \\ &= - \frac{Q P C}{V \omega_0 \epsilon_0 \epsilon(\vec{r}_0)} \frac{2}{|\vec{E}_N(\vec{r}_0)|^2} \frac{\text{Re}(\alpha)}{4} |\vec{E}_N|^2 \Big|_{\vec{r}_{trap}}^{\infty} \end{aligned}$$

Any realistic field must have finite energy, and must decay to 0 at infinity. Using  $\lim_{r \rightarrow \infty} \vec{E}_N(\vec{r}) = 0$  we get:

$$U = \frac{Q P C}{V \omega_0} \frac{\text{Re}(\alpha)}{2\epsilon_0 \epsilon(\vec{r}_0)} \frac{|\vec{E}_N(\vec{r}_{trap})|^2}{|\vec{E}_N(\vec{r}_0)|^2}$$

We note that the same result is found by considering the particle as a perturbation, and integrating the electric field energy within the particle's volume as the dielectric changes from  $\epsilon_b$  to  $\epsilon_p$  (while appropriately including the particle's effect on the electric field).

To maintain stability, the trap must be able to overcome Brownian motion, requiring a depth which is significantly greater than the thermal energy. For this reason, stability is commonly expressed in units of  $k_B T$  or may be defined as  $S = U/k_B T$ . A threshold of  $U \geq 10 k_B T$  ( $S \geq 10$ ) was suggested in the first report of single-beam capture [10] and has been generally adopted to define the onset of stable trapping.

We note that a standing wave optical trap will generally possess several significant field maxima.

Depending on the relative strength within these regions, it is possible for multiple anti-nodes to possess sufficient trapping stability, creating an ambiguity in the trapping location. While this can provide an interesting mechanism for assembling multiple nanoparticle structures or studying the flow- or Brownian motion-induced hopping between traps, it can also prevent an emitter from reaching the optimal coupling site and is generally a nuisance for a cQED platform. This ambiguity can be resolved by a sufficiently rapid taper in the field envelope such that only a single trap possesses sufficient stability to trap the particle. This strategy also results in a greater fraction of the energy residing within the primary anti-node. As this minimizes the mode volume and maximizes the coupling to the emitter, such a cavity design is preferred for cQED applications.

While the stability provides a threshold for capturing a particle, it does not place any restrictions on the movement of the particle within the trap. The trapping force addresses this to some extent, but at the peak of the trap, the tangential forces are necessarily zero; the lack of a clear position at which to evaluate the force makes it somewhat cumbersome to use. Instead, the strength of a trap is best characterized by its *stiffness* [337]. Within the vicinity of the stable position, we can essentially model the trap as a linear spring. The stiffness corresponds to the spring constant, and reflects the increasing force experienced by the particle as it is drawn away from equilibrium. We calculate the stiffness along each axis as the derivative of the restoring force, evaluated at the stable position:

$$k_i = - \left( \frac{d\vec{\mathcal{F}}_i}{d\vec{r}_i} \right) \Big|_{\text{trapping peak}}$$

In general, the gradients along different directions will not be equal. Since the trap is only as effective as its strength in the weakest direction, the *effective stiffness* is taken to be the limiting value:

$$k_{eff} = \min(k_i)$$

Approximating the system as a harmonic oscillator, we can estimate the variance in our position

using the equipartition theorem [320]:

$$k_{eff} \langle \Delta \vec{r}^2 \rangle = k_B T$$

Evaluating this explicitly, we find our expected displacement:

$$|\Delta \vec{r}| = \sqrt{\frac{k_B T}{\frac{Q}{V} \frac{P}{\omega_0} \frac{C}{2\epsilon_0 \epsilon(\vec{r}_0)} \frac{\text{Re}(\alpha)}{|\vec{E}_N(\vec{r}_0)|^2}}} \sqrt{\frac{1}{\min\left(\frac{d^2}{d\vec{r}_i^2} |\vec{E}_N|^2\right)}}$$

As with the other metrics, we see from the first term that the minimum displacement is achieved by maximizing  $Q/V$ . Additionally, the second term indicates that it is the *curvature* of  $|\vec{E}_N|^2$ , rather than merely the gradient, which must be maximized to ensure tight trapping.

Assuming the trap has sufficient *stability* to capture a particle, and a great enough *stiffness* to maintain its position accurately, the final quality we seek is the ability to discriminate between particle sizes. This feature is especially important for colloidal quantum dots, whose spectra depend heavily on nanocrystal dimensions. Although directly probing the nanocrystal optically might be possible during trapping, it is likely to be quite difficult to discriminate the nanocrystal's emission from the background due to the high laser powers required. Instead, we propose using the relative red-shift induced by the particle as a means of determining particle size. Compared to other integration techniques where the particle size is fixed from the beginning, this method enables a catch-and-release process to identify the particle and ensure it matches the cavity.

We therefore introduce the *sensitivity*, which we define as the relative change in the transmission (or reflection) of the cavity with respect to a change in nanocrystal diameter:

$$\zeta \equiv \left. \frac{dT}{d\varnothing} \right|_{\varnothing_0}$$

where  $\zeta$  is the sensitivity,  $\varnothing$  is the particle diameter,  $\varnothing_0$  is the target diameter, and  $T$  represents the normalized transmission (or reflection), such that  $T = 1$  when the laser is on resonance. The cavity spectrum can normally be fit to a Lorentzian, with a full-width at half-max (FWHM) related to the quality factor by  $\delta\omega = \omega_0/Q$ . Letting  $\omega_0$  represent the bare cavity resonance,  $\omega$  the laser frequency, and  $\Delta\omega(\varnothing)$  the diameter-dependent particle-induced resonance shift, we can write  $T$  as:

$$T = \frac{\left(\frac{\delta\omega}{2}\right)^2}{(\omega - (\omega_0 + \Delta\omega(\varnothing)))^2 + \left(\frac{\delta\omega}{2}\right)^2}$$

Using this, we can solve for  $\zeta$  as:

$$\begin{aligned}\zeta &= \left. \frac{dT}{d\varnothing} \right|_{\varnothing_0} \\ &= \left( \frac{2 \left(\frac{\delta\omega}{2}\right)^2 (\omega - \omega_0 - \Delta\omega(\varnothing_0))}{\left((\omega - \omega_0 - \Delta\omega(\varnothing_0))^2 + \left(\frac{\delta\omega}{2}\right)^2\right)^2} \right) \left. \frac{d}{d\varnothing} \Delta\omega(\varnothing) \right|_{\varnothing_0}\end{aligned}$$

To determine the effect of the particle on the cavity resonance, we apply the Hellmann-Feynman theorem to write [136]:

$$\frac{d\omega}{d\beta} = -\frac{\omega_0 \int \vec{E}^* \left(\frac{d\epsilon}{d\beta}\right) \vec{E} d\vec{r}^3}{\int \epsilon |\vec{E}|^2 d\vec{r}^3}$$

We wish to consider the change in resonance due to the change in particle dielectric. Using  $\epsilon_v$  to denote the dielectric within the particle volume, we insert  $\beta = \epsilon_v$  into the Hellmann-Feynman expression. In this case,  $\left(\frac{d\epsilon}{d\epsilon_v}\right) = 1$  within the particle volume, and 0 throughout the rest of the cavity. Thus, the integral in the numerator only needs to be carried out over the particle volume,  $V_p$ .

$$\frac{d\omega}{d\epsilon_v} = -\frac{\omega \int_{V_p} |\vec{E}_v|^2 d\vec{r}^3}{\int \epsilon |\vec{E}|^2 d\vec{r}^3}$$

We have now written  $E_v$  in the numerator to explicitly denote that this refers to the field *within a particle of permittivity  $\epsilon_v$* . In the Rayleigh approximation, this is related to the electric field in the bare cavity by:

$$\vec{E}_v = \frac{3\epsilon_b}{\epsilon_v + 2\epsilon_b} \vec{E}$$

where  $\epsilon_b$  refers to permittivity of the medium surrounding the particle. Additionally, we can approximate the field as constant over the particle volume. Simplifying the numerator, we get:

$$\frac{d\omega}{d\epsilon_v} = -\frac{\omega_0}{2} \frac{V_p}{\int \epsilon |\vec{E}|^2 d\vec{r}^3} \left( \frac{3\epsilon_b}{\epsilon_v + 2\epsilon_b} \right)^2 |\vec{E}|^2$$

Multiplying both sides by  $d\epsilon_v$ , we can find the total frequency shift by integrating the perturbation ( $\epsilon_v$ ) from the background dielectric ( $\epsilon_b$ ) to the actual particle dielectric ( $\epsilon_p$ ):

$$\begin{aligned}\Delta\omega &= \int d\omega \\ &= -\frac{\omega_0}{2} \frac{\epsilon_0 V_p |\vec{E}|^2}{\epsilon_0 \int \epsilon |\vec{E}|^2 d\vec{r}^3} \int_{\epsilon_b}^{\epsilon_p} \left( \frac{3\epsilon_b}{\epsilon_v + 2\epsilon_b} \right)^2 d\epsilon_v \\ &= -\frac{\omega_0}{2} \frac{|\vec{E}|^2}{\epsilon_0 \int \epsilon |\vec{E}|^2 d\vec{r}^3} \left( 3V_p \epsilon_0 \epsilon_b \frac{\epsilon_p - \epsilon_b}{\epsilon_p + 2\epsilon_b} \right)\end{aligned}$$

Inserting  $V_p = \frac{4}{3}\pi r^3$ , we see that the term in parentheses is exactly  $\text{Re}(\alpha)$ . Similarly, we recognize that the second term is related to the mode volume:  $\frac{|\vec{E}(\vec{r}_{trap})|^2}{\epsilon_0 \epsilon(\vec{r}_0) |\vec{E}(\vec{r}_0)|^2 V}$ . Performing these substitutions, writing in terms of the normalized electric field, and noting the implicit diameter dependence, we arrive at:

$$\Delta\omega = -\frac{\omega_0}{2V\epsilon_0\epsilon(\vec{r}_0)} \frac{|\vec{E}_N(\vec{r}_{trap})|^2}{|\vec{E}_N(\vec{r}_0)|^2} \text{Re}(\alpha)$$

Explicitly,  $\text{Re}(\alpha) = 4\pi\epsilon_0\epsilon_b \frac{\epsilon_p - \epsilon_b}{\epsilon_p + 2\epsilon_b} r^3 = \frac{\pi}{2}\epsilon_0\epsilon_b \frac{\epsilon_p - \epsilon_b}{\epsilon_p + 2\epsilon_b} \varnothing^3$ . Including this, we can expand the sensitivity in terms of the laser frequency and cavity parameters, as well as particle permittivity, diameter, and position:

$$\zeta = -\frac{2\left(\frac{\delta\omega}{2}\right)^2 \left(\omega - \omega_0 + \frac{\pi\omega_0\epsilon_b}{4V\epsilon(\vec{r}_0)} \frac{\epsilon_p - \epsilon_b}{\epsilon_p + 2\epsilon_b} \frac{|\vec{E}_N(\vec{r}_{trap})|^2}{|\vec{E}_N(\vec{r}_0)|^2} \varnothing_0^3\right) \left(\frac{3\pi\omega_0\epsilon_b}{4V\epsilon(\vec{r}_0)} \frac{\epsilon_p - \epsilon_b}{\epsilon_p + 2\epsilon_b} \frac{|\vec{E}_N(\vec{r}_{trap})|^2}{|\vec{E}_N(\vec{r}_0)|^2} \varnothing_0^2\right)}{\left(\left(\omega - \omega_0 + \frac{\pi\omega_0\epsilon_b}{4V\epsilon(\vec{r}_0)} \frac{\epsilon_p - \epsilon_b}{\epsilon_p + 2\epsilon_b} \frac{|\vec{E}_N(\vec{r}_{trap})|^2}{|\vec{E}_N(\vec{r}_0)|^2} \varnothing_0^3\right)^2 + \left(\frac{\delta\omega}{2}\right)^2\right)^2}$$

The optimal laser frequency to use for trapping depends on how marginal its power is. Intuitively, the maximum trapping forces are generated when the laser is exactly on resonance with the *detuned* system, *i.e.*,  $\omega = \omega_0 + \Delta\omega(\varnothing_0)$ . While the initial intensity in the bare cavity will be slightly diminished, the system will snap into resonance once the particle drifts into the cavity field. At this point, the field strength will be at its maximum, creating a strong trap for the particle and maintaining the resonant condition. However, this corresponds to operation at the peak of the Lorentzian — where  $\zeta = 0$  — implying that the particle size could not be detected by simply examining the transmitted (or reflected) power (one might still deduce the size by examining the noise spectrum due to Brownian motion).

Instead, if the laser is somewhat over-powered, we can choose to operate slightly off resonance and still maintain sufficient field strength to trap the particle. In this case, we would select the wavelength which produces the maximum sensitivity, which occurs by operating at the greatest

slope in the *detuned* system. Explicitly, we solve for  $\omega : \zeta = \zeta_{max}$ :

$$\begin{aligned} \frac{d\zeta}{d\omega} &= \left( \frac{2 \left(\frac{\delta\omega}{2}\right)^2 \frac{d}{d\varnothing} \Delta\omega(\varnothing) \Big|_{\varnothing_0}}{\left( (\omega - \omega_0 - \Delta\omega(\varnothing_0))^2 + \left(\frac{\delta\omega}{2}\right)^2 \right)^2} \right) \left( 1 - \frac{4(\omega - \omega_0 - \Delta\omega(\varnothing_0))}{(\omega - \omega_0 - \Delta\omega(\varnothing_0))^2 + \left(\frac{\delta\omega}{2}\right)^2} \right) \\ &= 0 \\ \omega &= \omega_0 + \Delta\omega(\varnothing_0) \pm \frac{\delta\omega}{2\sqrt{3}} \end{aligned}$$

Operating at these frequencies results in the maximum sensitivity of:

$$\begin{aligned} \zeta_{max} &= \pm \left( \frac{2 \left(\frac{\delta\omega}{2}\right)^2 \frac{\delta\omega}{2\sqrt{3}}}{\left( \left(\frac{\delta\omega}{2\sqrt{3}}\right)^2 + \left(\frac{\delta\omega}{2}\right)^2 \right)^2} \right) \frac{d}{d\varnothing} \Delta\omega(\varnothing) \Big|_{\varnothing_0} \\ &= \mp \frac{3\sqrt{3}}{4\delta\omega} \left( \frac{3\pi\omega_0\epsilon_b}{4V\epsilon(\vec{r}_0)} \frac{\epsilon_p - \epsilon_b}{\epsilon_p + 2\epsilon_b} \frac{|\vec{E}_N(\vec{r}_{trap})|^2}{|\vec{E}_N(\vec{r}_0)|^2} \varnothing_0^2 \right) \end{aligned}$$

Recognizing that  $Q = \frac{\omega_0}{\delta\omega}$ , we simplify to arrive at our optimal sensitivity:

$$\begin{aligned} \zeta_{max} &= \mp \frac{9\sqrt{3}\pi\epsilon_b}{16\epsilon(\vec{r}_0)} \frac{\epsilon_p - \epsilon_b}{\epsilon_p + 2\epsilon_b} \frac{Q}{V} \frac{|\vec{E}_N(\vec{r}_{trap})|^2}{|\vec{E}_N(\vec{r}_0)|^2} \varnothing_0^2 \\ &= \mp \frac{9\sqrt{3}}{8\epsilon_0\epsilon(\vec{r}_0)} \frac{Q}{V} \frac{|\vec{E}_N(\vec{r}_{trap})|^2}{|\vec{E}_N(\vec{r}_0)|^2} \frac{\text{Re}(\alpha_0)}{\varnothing_0} \end{aligned}$$

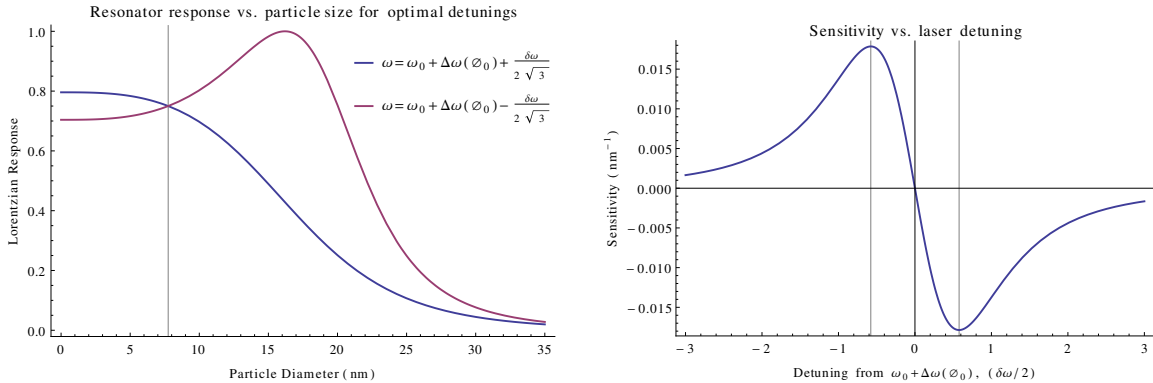
with

$$T = \frac{3}{4}$$

for  $\varnothing = \varnothing_0$

As with the other figures of merit — stability, force, stiffness, and mean displacement — we note that our ability to distinguish particle sizes based on the cavity output is directly related to  $Q/V$ . We also see that operating at the maximum sensitivity only degrades the peak trapping strength by a factor of  $\frac{3}{4}$ ; see Figure 2.77b. This nominal drop is well worth the particle distinguishability it enables.

We observe that there are two possible wavelengths with maximum sensitivity: either blue- or one red-detuned by  $\frac{\delta\omega}{2\sqrt{3}}$  relative to the perturbed cavity resonance. The two solutions correspond to equivalent points on each side of the Lorentzian; this behavior is shown in Figure 2.77a. Since



(a) Comparison of optimal laser detunings, showing the resonator response as a function of particle diameter. The detunings are selected to maximize the sensitivity at a specific particle diameter, marked here with a vertical line. The slope at this point is equivalent to the sensitivity. We observe that the two solutions have equal, but opposite, slopes in this region. For the negative detuning, we also note that multiple particle sizes could produce the same output.

(b) Plot showing the calculated sensitivity at a fixed particle size as a function of laser detuning. The detuning is reported in half-linewidths, relative to the red-shifted cavity resonance induced by the particle. We observe two peak detunings with opposite response, occurring at  $\omega_0 + \Delta\omega(\varnothing_0) \pm \frac{\delta\omega}{2\sqrt{3}}$ .

Figure 2.77: Expected trapping sensitivity for our system. Both plots correspond to trapping a  $\varnothing_0 = 7.75$  nm PbS quantum dot with our 1D nanobeam photonic crystal resonator, and are evaluated for  $Q = 1 \times 10^5$ .

the lineshape is mirrored, the cavity outputs for the two conditions undergo opposite changes as a function of particle size, resulting in slightly different behavior. For the blue-detuned frequency ( $\omega = \omega_0 + \Delta\omega(\varnothing_0) + \frac{\delta\omega}{2\sqrt{3}}$ ,  $\zeta -$ ), the cavity begins close to resonance and contains higher fields, but progressively detunes as the particles enter the field. This yields greater initial forces and favors smaller particles (which perturb it less), but creates an unstable trap — the forces flatten out as it gets closer to  $\vec{r}_{trap}$ , which could result in a larger  $|\Delta\vec{r}|$ . Moreover, this creates an ambiguity in the signal; the target signal threshold  $T = \frac{3}{4}$  could just as easily be the result of a large particle which is trapped off-peak as it is due to the intended  $\varnothing_0$  at the nominal trap position.

Conversely, with a red-detuned frequency ( $\omega = \omega_0 + \Delta\omega(\varnothing_0) - \frac{\delta\omega}{2\sqrt{3}}$ ,  $\zeta +$ ), the cavity begins further off-resonance. This yields smaller initial forces, but improves as the particle red-shifts the actual resonance. The ultimate behavior is a monotonically increasing force as the particle traverses the field until it reaches the trapping peak, which is *therefore preferred as it produces a stable resonance*. This comes at the expense of slightly favoring large particles, which are more likely to detune the

cavity all the way to the peak, although this effect is small compared to the inherent  $\varnothing_0^3$  dependence on the force. We note that there is also a potential ambiguity in  $T$  if the particle distribution contains significantly larger nanocrystals. Specifically, if a particle can red-shift the cavity enough so that the laser is blue-detuned relative to the perturbed peak, it is possible for a large particle to produce the same  $T = \frac{3}{4}$  signal as the intended  $\varnothing_0$ . This would occur when  $\Delta\omega(\varnothing) = \Delta\omega(\varnothing_0) - \frac{\delta\omega}{\sqrt{3}}$ , which happens when  $\varnothing = \left( \frac{4\epsilon(\vec{r}_0)}{\sqrt{3}\pi\epsilon_b} \frac{\epsilon_p + 2\epsilon_b}{\epsilon_p - \epsilon_b} \frac{|\vec{E}_N(\vec{r}_0)|^2}{|\vec{E}_N(\vec{r}_{trap})|^2} \frac{V}{Q} + \varnothing_0^3 \right)^{\frac{1}{3}}$ . Practically, this occurs for particles two- to three times bigger than  $\varnothing_0$ , which is unlikely to be a concern for reasonably well-controlled processes.

Besides inherent self-alignment, one of the primary benefits of using optical trapping to assemble cQED systems is the relative independence between the cavity and emitter. The technique is a platform for integration, and as long as the cavity operates at the correct wavelength and the trapping forces are sufficiently strong, the operation is agnostic to which emitter is chosen. This is not to say that any emitter can be trapped as effectively as any other — larger emitters and higher dielectrics are still preferred — but rather that the cavity does not need to be optimized for a specific emitter. Besides providing excellent flexibility in the choice of material systems, this also means that relative improvements to the cavity will have similar effects on either particle. Significantly, if we know the cavity performance for a given set of parameters, this allows us to calculate the cavity's behavior for a different emitter (size, material), as long as it operates in the Rayleigh regime. Thus, we can make quantitative comparisons between cavity designs or trapping systems, whether the reported values correspond to 50 nm beads or 5 nm quantum dots.

In order to facilitate such comparisons, we define *normalized performance metrics*, which are specific only to the cavity and not the trapped object or excitation. In particular, we can remove factors proportional to input power, emitter dimensions, or emitter permittivity, which can be adjusted for the different devices with equal flexibility. Factors that are specific to the cavity design are retained, including  $Q$ ,  $V$ , and  $\vec{E}_N$ . Relative coupling efficiency is somewhat more complicated, as literature often reports only the estimated power in the cavity, rather than the total excitation power. For this reason, we will generally remove the combined factor  $PC$ , rather than just  $P$ . We

also note that we preserve some factors of background permittivity, since the cavity parameters are generally specific to this value. Specifically,  $\text{Re}(\alpha)$  can be expanded into  $4\pi\epsilon_0\epsilon_b \frac{\epsilon_p - \epsilon_b}{\epsilon_p + 2\epsilon_b} r^3$ . We retain the factors of  $4\pi\epsilon_0\epsilon_b$ , while dropping  $\frac{\epsilon_p - \epsilon_b}{\epsilon_p + 2\epsilon_b} r^3$ .

With these adjustments, we find the following normalized performance metrics (and typical units):

Normalized depth  $\left(\frac{k_B T}{W nm^3}\right)$ :

$$\begin{aligned} U_N &\equiv U \left( P C \frac{\epsilon_p - \epsilon_b}{\epsilon_p + 2\epsilon_b} r^3 \right)^{-1} \\ &= \frac{Q}{V} \frac{2\pi}{\omega_0} \frac{\epsilon_b}{\epsilon(\vec{r}_0)} \frac{|\vec{E}_N(\vec{r}_{trap})|^2}{|\vec{E}_N(\vec{r}_0)|^2} \end{aligned}$$

Normalized stability  $\left(\frac{1}{W nm^3}\right)$ :

$$S_N \equiv \frac{U_N}{k_B T}$$

Normalized force  $\left(\frac{fN}{W nm^3}\right)$ :

$$\begin{aligned} \langle \vec{\mathcal{F}}_N \rangle &\equiv \langle \vec{\mathcal{F}} \rangle \left( P C \frac{\epsilon_p - \epsilon_b}{\epsilon_p + 2\epsilon_b} r^3 \right)^{-1} \\ &= \frac{Q}{V} \frac{2\pi}{\omega_0} \frac{\epsilon_b}{\epsilon(\vec{r}_0)} \frac{\nabla |\vec{E}_N(\vec{r})|^2}{|\vec{E}_N(\vec{r}_0)|^2} \end{aligned}$$

Normalized stiffness  $\left(\frac{fN}{W nm} \frac{1}{nm^3}\right)$ :

$$\begin{aligned} k_{i,N} &\equiv k_i \left( P C \frac{\epsilon_p - \epsilon_b}{\epsilon_p + 2\epsilon_b} r^3 \right)^{-1} \\ &= - \left( \frac{d\mathcal{F}_{i,N}}{d\vec{r}_i} \right) \Big|_{\vec{r}_{trap}} \end{aligned}$$

Normalized effective stiffness  $\left(\frac{fN}{W nm} \frac{1}{nm^3}\right)$ :

$$k_{eff,N} = \min(k_{i,N})$$

Normalizing  $\zeta$  gives a relationship proportional to  $U_N$ , so this does not offer any additional value as metric. Since the cavity-specific parameters can be readily derived from other values, we leave this term and will simply evaluate it for the desired nanocrystal.

For completeness, we consider the wavelength dependence of the trapping performance. Examining terms in the figures of merit, we see  $V \sim \omega_0^{-3}$ , while the scaling laws of Maxwell's equations (see 3.2.1) imply  $\nabla|\vec{E}|^2 \sim \omega_0$ . Thus, the stability, force and stiffness vary  $\sim \omega_0^2, \omega_0^3$ , and  $\omega_0^4$ , respectively. These suggest use of shorter wavelength systems to improve trapping. Conversely, the features of the resonator become smaller with decreasing wavelength, increasing sensitivity to defects and generally making the fabrication more difficult. To some extent, this can be mitigated by use of a lower index dielectric, for example using  $\text{Si}_3\text{N}_4$  instead of Si or GaAs. Overall, however, the frequency dependence of the trapping factors is unlikely to influence the wavelength selection significantly. As long as the system is capable of successfully trapping the particle, these differences are insignificant compared to considerations of emitter spectrum, cavity material system, or detector sensitivity.

#### 2.4.4.3 Cavity-enhanced optical trapping with silicon photonic crystal nanobeams

From the normalized metrics derived above, a general figure-of-merit for optimizing the trapping ability of a cavity is to maximize  $Q/V$ . Effectively, this serves to maximize the electric field intensity at the particle position for a given input power. It is therefore unsurprising that the same metric is commonly the figure-of-merit for cavities in cQED systems, and ends up being proportional to the Purcell enhancement, and similar to the factor controlling Rabi splitting ( $Q/\sqrt{V}$ ). The additional terms — corresponding to the permittivity and electric field energy — simply account for the spatial offset between the particle ( $\vec{r}_{trap}$ ) and mode volume's reference point ( $\vec{r}_0$ ). While primarily a matter of convenience (mode volume is generally reported relative to the peak E-field intensity, which may be inaccessible to the particle, rather than the particle location), they do suggest the importance of trapping near the E-field maximum; these serve as penalty factors if the field is lower at the trapping location.

In addition to the criteria for optimizing the cQED system, the use of the cavity to enhance the trapping performance warrants several other considerations. While both traveling wave and standing wave resonators can produce the necessary field enhancement to trap nanocrystal emitters,

traveling wave modes have a continuous field maximum rather than discrete anti-nodes. Not only does this tend to increase the mode volume, the absence of a longitudinal field gradient means the resonators only produce transverse forces and cannot control the particle position along the resonator. Moreover, the presence of multiple significant field maxima within the cavity mode can lead to an ambiguity in trapping location, potentially causing it to be trapped off-peak. Thus, beyond the desire to minimize the mode volume, we have additional motivation to use a geometry which provides a rapid taper in the field envelope. Photonic crystal nanobeams possess all of these features — ultra-high  $Q/V$ , standing wave resonances, rapid field decay, and maximum field gradients through tight confinement in all directions. Additionally, these devices may be naturally integrated with other passive optical devices and are compatible with large scale manufacturing techniques. Photonic crystal nanobeams are therefore an ideal platform for both cQED and cavity-enhanced optical trapping. Additional information about cavity geometries, nanobeam analysis, and optimization methods, as well as specific design parameters and performance characteristics, are discussed in detail in Chapter 3; experimental work, including fabrication, testing, and further optimization to maximize  $Q$ , is reviewed in 3.4.

Briefly, our resonator consisted of a 1D photonic crystal nanobeam fabricated in SOI with a 220nm device layer, and designed to operate near 1550 nm. This choice of material system provides high refractive index contrast (important for maximizing the photonic band gap, minimizing mode volume, and maximizing field gradients), extremely high material quality for low-loss resonators, and offers the potential to leverage mature CMOS processing technology for scalability or integration with electronic circuitry. The wavelength was chosen to operate within the telecommunications band, due to the wide availability of high-quality optical equipment in this range. We emphasize, however, that this is only one possible system configuration. Photonic crystal nanobeams are a general platform for optical trapping, and the same design optimization and analysis methods could readily be applied to alternative material systems or operating wavelengths.

The photonic crystal was composed of circular holes<sup>2</sup> etched into a silicon nanobeam, which

---

<sup>2</sup>Circular features are more easily resolved lithographically than sharp corners, and tend to produce higher-quality devices

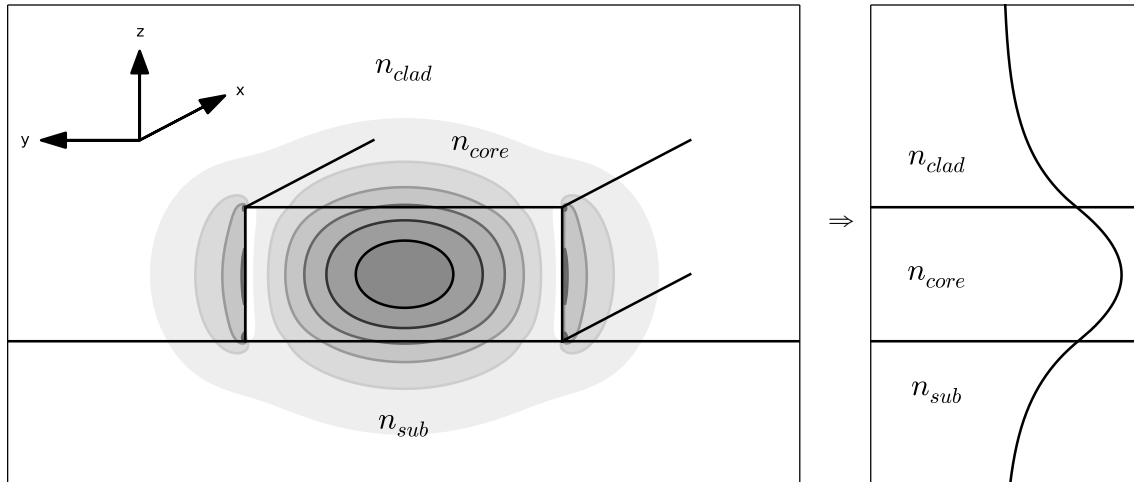
also served as the feeding waveguide. We left the substrate intact in order to prevent buckling of the beam due to surface tension when drying the emitter solvent. While significantly higher quality factors would be achieved by undercutting the device, we note that a post-trapping dry etch, such as a vapor phase HF etch, could later suspend the device and maximize the  $Q$  during cQED operation. For a typical device, the mirrors regions used a lattice constant of  $a_0 \approx 393$  nm, with holes of radius  $r = 0.25a_0 \approx 98$  nm. Throughout the device, the beam width and thickness were held constant at  $w = 1.2a_0 \approx 470$  nm and  $t \equiv 220$  nm  $\approx 0.56a_0$ . To define the cavity, the local lattice constant (hole spacing and radius) was reduced from  $a' = 1.0a_0$  to  $a' = 0.84a_0$  using a linear taper with steps of  $0.02a_0$ .

This design has a mode volume of  $V \approx 0.52 (\lambda/n_{Si})^3$  (in air) or  $\approx 0.55 (\lambda/n_{Si})^3$  (in solution) with a background index of 1.32. For a device with  $N = 15$  periods on either side of the cavity, the simulated quality factor can exceed  $10^6$ . Experimentally, we observed typical quality factors  $\approx 110,000$  (including beams with fewer mirror periods), as well as peak devices exceeding 250,000. While later designs with improved tapers may have potentially increased the quality factor, these have not been tested. As the adjustments only induce subtle changes in the field profile, the newer designs would have little effect on the mode volume or gradient calculation. We therefore used  $Q = 100k$  and  $Q = 250k$  to estimate our trapping forces, and evaluated the gradients using the original beam design.

The peak trapping forces occur just above the center of the cavity, where the electric field reaches its maximum within the cladding<sup>3</sup>. To accurately calculate the gradients from simulations (whose grid sizes are generally larger than a typical nanocrystal), we observed that the mode profile in the center of the cavity closely resembles the fundamental waveguide mode. An analytic form of this mode can be calculated using effective index theory<sup>4</sup> which decomposes the ridge waveguide into a TE-polarized, asymmetric vertical slab waveguide (substrate, silicon, cladding), followed by a TM-

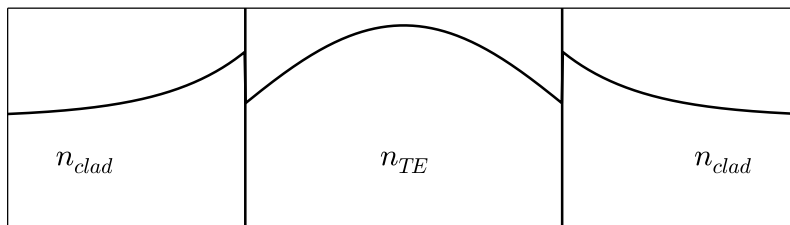
<sup>3</sup>Similar trapping forces occur halfway up the beam, along the vertical edges. The field is TE-polarized, allowing  $|\vec{E}|^2$  to benefit from a  $(n_{Si}/n_{clad})^4$  enhancement arising from the normal boundary between the beam and cladding. Because the beam is very close to a half-wavelength wide, however, the effective field at the edges is still lower than the unenhanced field along the top of the beam. Overall, each force component along the top surface is slightly higher than the corresponding force at the side.

<sup>4</sup>The numerical values for the  $k$  components and effective index will be somewhat off, but we only use this to reveal the form of the solution.



(a) Schematic of a ridge waveguide, overlaid with contours of the dominant electric-field component.

(b) The vertical field profile can be estimated by decomposing the 2D waveguide into a TE slab waveguide, corresponding to the vertical stack.



(c) The horizontal field profile can be estimated by decomposing the 2D waveguide into a TM slab waveguide. In this calculation, the effective index for the vertical stack (TE mode) is substituted for the core region.

Figure 2.78: Effective index method for estimating the effective index and field profile for a 2D waveguide. This method was used to determine the functional form of the trapping field, allowing more accurate estimation of trapping forces as well as informing ultimate limits which could be achieved in a dielectric 1D nanobeam cavity.

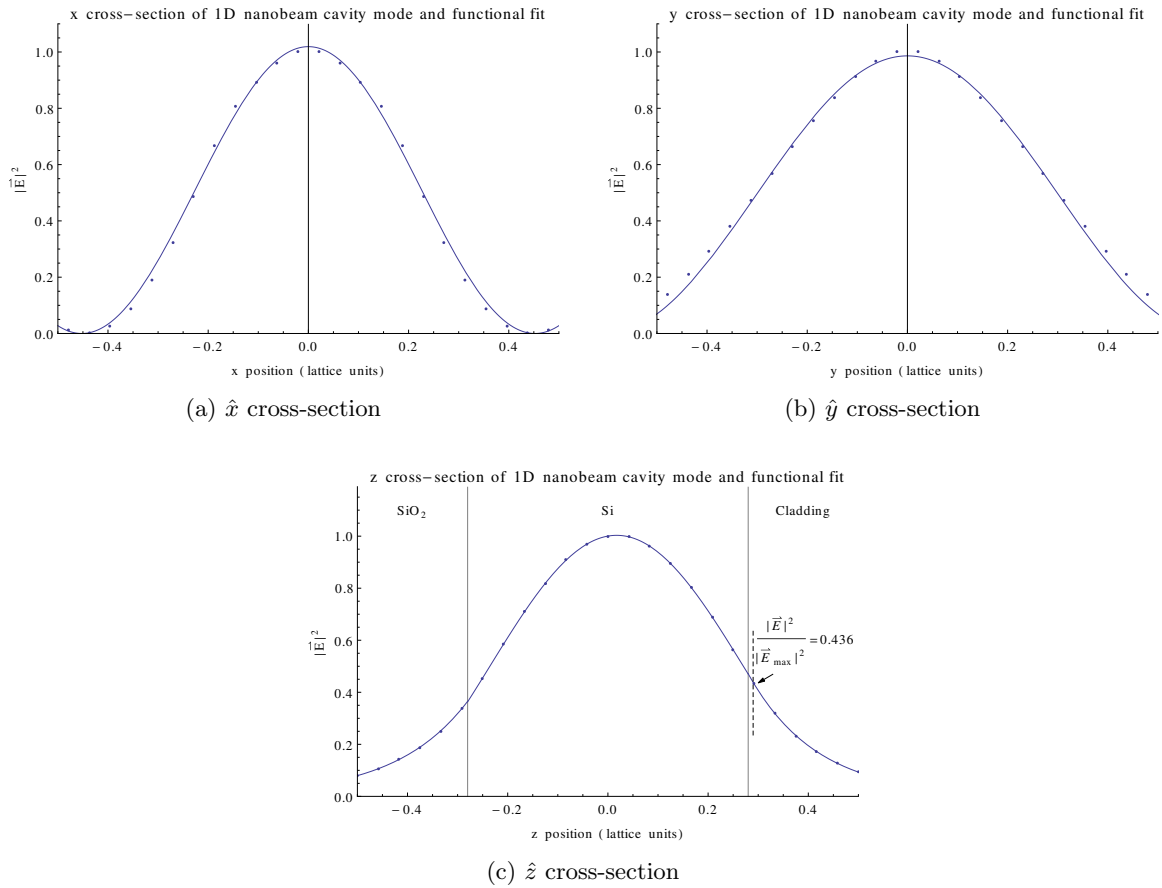


Figure 2.79: Cross-sections of the 1D nanobeam cavity mode from a 3D FDTD simulation, and fits to the functional forms derived from an effective index model of the 2D waveguide cross-section. Solid vertical lines in the  $\hat{z}$  cross-section show the material boundaries, while the dashed line shows the offset to the particle location. By this point, the field has decayed by a factor of 0.436 from its peak. The curvatures from these fits were used to calculate trapping metrics.

polarized, horizontal slab, where the silicon is replaced by the effective index found for the vertical stack; see Figure 2.78. For propagation in the  $\hat{x}$  with a dominant  $\hat{y}$  component (and  $\hat{z}$  the out-of-plane direction), this results in a separable mode profile of the form  $\vec{E}_{core}(x, y, z) \approx E_y(x, y, z) \approx X(x)Y(y)Z(z)$ . Within the waveguide core, this is simply  $\cos(k_x \cdot x)\cos(k_y \cdot y)\cos(k_z \cdot z + \phi)$ , where the  $x$  and  $y$  axes are centered on the cavity,  $z = 0$  is the substrate-silicon interface, and  $z = t$  is the top of the beam. Above the beam, the field is continuous over the interface and decays evanescently in the cladding. Within the trapping region (immediately above the cavity center), then, the field follows:

$$\vec{E}_{trap}(x, y, z) = \hat{y} \cos(k_x \cdot x)\cos(k_y \cdot y)\cos(k_z \cdot t + \phi)e^{-\kappa_c(z-t)}$$

This function is normalized to the peak electric field within the beam, consistent with our evaluation of  $V$ .

Using this form, we fit the parameters  $k_x, k_y, k_z, \kappa_c$  and  $\phi$  to the simulated  $|\vec{E}|^2$  for cavity field; these data and fitted curves are shown in Figure 2.79. With these values, we could quickly evaluate the cavity figures of merit. For trapping at a height  $r = \frac{1}{2}7.75 \text{ nm}$  above the beam surface (corresponding to typical nanocrystal dimensions, see 2.4.4.4) and inserting  $Q=100,000$  (to match our conservative experimental value), we found the following normalized parameters:

$$\begin{aligned} U_N &= \frac{Q}{V} \frac{2\pi}{\omega_0} \frac{\epsilon_b}{\epsilon_{r_0}} \frac{|\vec{E}_N(\vec{r}_{trap})|^2}{|\vec{E}_N(\vec{r}_0)|^2} \\ &= \frac{10^5}{0.55 \left(\frac{1550 \text{ nm}}{3.48}\right)^3} \frac{1550 \text{ nm}}{c} \left(\frac{1.32}{3.48}\right)^2 \cos(k_z \cdot t + \phi)^2 e^{-2\kappa_c \cdot r} \\ &= 157.064 \left(\frac{k_B T}{W \text{ nm}^3}\right) \\ k_{n, \{\hat{x}, \hat{y}\}} &= 2U_N (k_x^2, k_y^2) \\ &= (101.687, 60.845) \left(\frac{fN}{W \text{ nm}} \frac{1}{\text{nm}^3}\right) \end{aligned}$$

The factor  $\frac{|\vec{E}_N(\vec{r}_{trap})|^2}{|\vec{E}_N(\vec{r}_0)|^2} = \cos(k_z \cdot t + \phi)^2 e^{-2\kappa_c \cdot r}$  represents the drop in electric field intensity due to trapping off peak. This evaluated to 0.436 for our device, which is not a terrible penalty and indicates that the cavity-emitter interaction will remain quite strong at the surface.

We note the lack of a stiffness in the  $\hat{z}$  direction. Unlike forces in the  $\hat{x}$  and  $\hat{y}$  directions, whose

forces approach zero at the center of the trap, the evanescent gradient in the  $\hat{z}$  direction imposes its strongest force when the particle is at  $\vec{r}_{trap}$ . By its definition, this would result in a negative stiffness value. Because the particle is positively trapped against the beam surface, however, this is of little concern. In this geometry, we calculated the normalized force in the  $\hat{z}$  direction to be  $\mathcal{F}_{N,z}(\vec{r}_{trap}) = -2U_N\kappa_c = -12,079 \frac{fN}{Wnm^3}$ . This is already more than a factor of 4 - 8 greater than the forces in the  $\hat{x}$  or  $\hat{y}$  locations at for the expected displacement  $\Delta|\vec{r}| = 32.7$  nm ( $Q=100k$ ) and 20.7 nm ( $Q=250k$ ).

Examining both experimental and theoretical reports, we calculated the equivalent normalized trapping parameters for a variety of nanoscale optical traps<sup>5</sup>. These data are presented in table 2.2. We see that our cavity-enhanced optical trap performs extremely well as compared to other state-of-the-art nanoscale optical traps. For the conservative  $Q = 100,000$ , our effective stiffness is four times the closest alternative, while the stability exceeds that design by a factor of nearly forty. Compared to other devices, the margin is even greater.

---

<sup>5</sup>We only included reports which targeted  $\approx 50$  nm particles or smaller, as traps designed for larger particles are unlikely to perform well at nanocrystal size scales. Reports which did not contain sufficient detail were excluded, although none of these appeared to exceed the performance of the other devices. See also [289, 203, 136, 229, 320, 330, 159, 195, 243, 294, 49, 204, 211, 285, 51, 150, 149, 179, 293, 56, 152, 396, 22].

Design	Wavelength (nm)	Q	V $\left(\frac{\lambda^3}{n}\right)$	Normalized Stability $\left(\frac{k_B T}{W n m^3}\right)$	Normalized Stiffness $\left(\frac{f N}{W n m} \frac{1}{n m^3}\right)$		Reference <sup>6</sup>
					$\hat{x}$	$\hat{y}$	
Our 1D PhC nanobeam (SOI)	1,569.41	100,000	0.55	157.064	101.687	60.845	
		250,000	0.55	392.660	254.218	152.113	
1D PhC nanobeam with plasmonic bowtie (SOI/Au), tip radius = 10 nm	1,589.62	2,350	$1.35 \times 10^{-3}$	4.080	15.544	29.145	Ciminelli <i>et al.</i> [56]
1D PhC nanobeam with nanohole (SOI)	1,550	2,200		2.812	1.425	2.397	Serey <i>et al.</i> [320]
1D PhC nanobeam with nanohole (Si <sub>x</sub> N <sub>y</sub> )	1,064	5,000	4.4	1.902	0.907	0.583	Chen <i>et al.</i> [51]
1D PhC nanobeam (SOI)	1,548.15	2,500		2.125	0.307	0.211	Mandal <i>et al.</i> [229]
Ridge waveguide intersections (SOI)	1,550			0.0463	0.0311		Li <i>et al.</i> [197]
Gaussian beam, 500 nm waist	1,064			0.0170	0.000259	0.00113	Jauffred <i>et al.</i> [150]

Table 2.2: Comparison of normalized trapping parameters

<sup>6</sup>Many of these reports fail to include the factor of  $\frac{1}{2}$  resulting from time-averaging the field energy/forces, potentially resulting in over-reported values. We do not attempt to correct for this here.

To evaluate the feasibility of capturing a nanocrystal, we used these normalized values to calculate the absolute trapping performance for a typical emitter ( see 2.4.4.4). We considered a PbS colloidal quantum dot, with  $\varnothing = 7.75$  nm and a refractive index  $n = 4.2$  [145]. For the power coupled to the cavity, we used  $P = 1.454$  mW, corresponding to the threshold for stable trapping with our  $Q = 100k$  device. An illustration of the trapping depth and  $|\vec{E}|^2$  at the trapping surface are shown in Figure 2.80. Because none of the other devices are stable at this threshold, the expected  $|\Delta\vec{r}|$  is no longer strictly valid for these devices, but still provides a sense of scale. These data are presented in table 2.3.

### 1D nanobeam trapping stability and $|\vec{E}|^2$

$Q=100k$ ,  $P=1.454$  mW

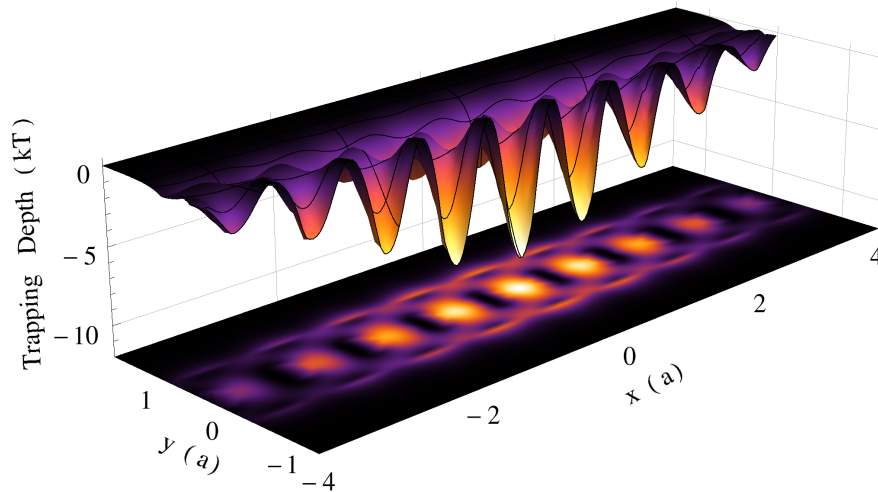


Figure 2.80: Illustration showing the expected trapping depth for our 1D nanobeam cavity, assuming  $Q = 100k$  and  $P = 1.454$  mW, matching the stable trapping threshold for this device.

Design	Trapping power required (mW)	P=1.454 mW				Expected Displacement (nm)	Sensitivity	Reference
		Stability ( $k_B T$ )	Stiffness ( $\frac{fN}{nm}$ )					
			$\hat{x}$	$\hat{y}$				
Our 1D PhC nanobeam (SOI)	Q=100k	1.454	10	6.474	3.874	32.698	0.0172	
	Q=250k	0.582	25	16.186	9.685	20.680	0.0430	
1D PhC nanobeam with plasmonic bowtie (SOI/Au)	21.322	0.682	2.598	4.871	39.929	0.00116	Ciminelli <i>et al.</i> [56]	
1D PhC nanobeam with nanohole (SOI)	81.200	0.179	0.0908	0.153	213.632	0.000312	Serey <i>et al.</i> [320]	
1D PhC nanobeam with nanohole (Si <sub>x</sub> N <sub>y</sub> )	120.079	0.121	0.0578	0.0371	333.989	0.000307	Chen <i>et al.</i> [51]	
1D PhC nanobeam (SOI)	107.481	0.135	0.0196	0.0134	555.343	0.000236	Mandal <i>et al.</i> [229]	
Ridge waveguide intersections (SOI)	4,932.870	0.00295	0.0198		457.284	0.00000513	Li <i>et al.</i> [197]	
Gaussian beam, 500 nm waist	13,426.649	0.00108	$1.646 \times 10^{-5}$	$7.177 \times 10^{-5}$	15,861.067	$2.746 \times 10^{-6}$	Jauffred <i>et al.</i> [150]	

Table 2.3: Absolute trapping performance for a 7.75 nm PbS quantum dot. The stability, stiffness, and displacement are evaluated at P=1.454 mW, corresponding to the stable trapping threshold for our  $Q = 100k$  device.

Our high- $Q/V$  1D photonic crystal nanobeam resonators outperformed these other devices on every trapping metric. Compared to the best alternative (1D nanobeam with plasmonic bowtie), our device showed a  $\approx 15\times$  improvement in trapping power and stability,  $1.5\times$  improvement in stability, and  $15\times$  in the ability to discriminate between particle sizes; our improvements over other approaches were even more drastic.

Although this device should be capable of capturing nanocrystal emitters with sufficient accuracy, we briefly consider opportunities to further enhance its performance and the ultimate limits of such approaches. Besides improving  $Q^7$ , there are two basic elements which can be addressed.

---

<sup>7</sup>Our more recent designs have simulated  $Q$ s approaching  $10^7$ , or approximately a 400% improvement over the current design. However, the measured quality factors of the current devices are still well below the simulated values. At this point, further improvements to quality factor are an experimental challenge, rather than a theoretical one. See 3.3.2.3.

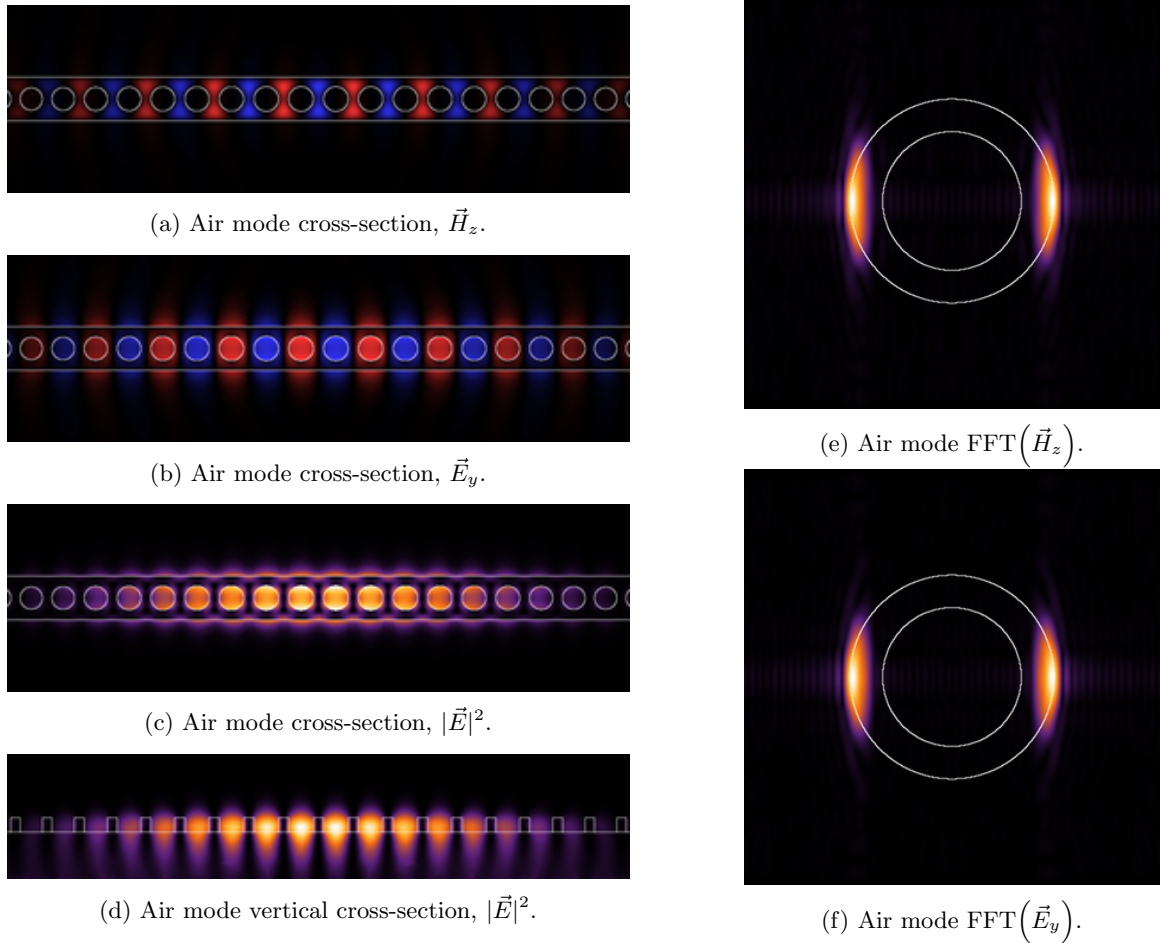


Figure 2.81: Cross-sections of air mode field (through center of beam) and corresponding FFTs ( $\lambda/4$  in substrate). Note that the  $\vec{E}$ -field confinement in the holes and the  $\vec{H}$  confinement within the dielectric are the opposite of what we find for the semiconductor mode (Figure 2.82). The FFT circles indicate the light cones for air (inner) and oxide (outer). The significant overlap within the oxide light-cone indicates heavy leakage for the mode, resulting in poor confinement and low  $Q$ . The extent of the mode into the cladding can also be readily seen in the vertical cross-section. Compare to the semiconductor mode shown in Figure 2.82.

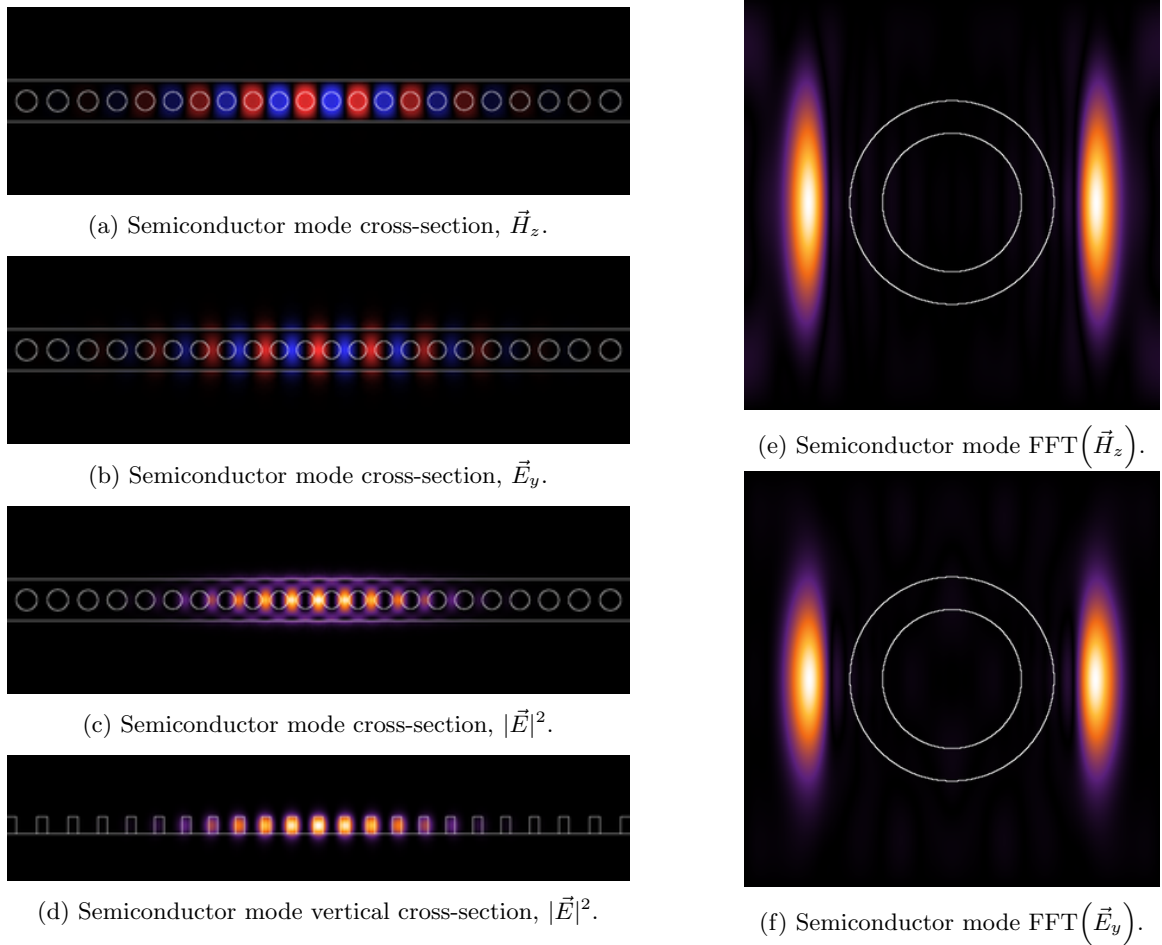


Figure 2.82: Cross-sections of semiconductor-mode field (through center of beam) and corresponding FFTs ( $\lambda/4$  in substrate). The FFT circles indicate the light cones for air (inner) and oxide (outer). Compared to the air mode resonance in Figure 2.81, the field here shows much tighter confinement (smaller  $V$ ) and significantly less overlap with the light cone (higher  $Q$ ).

First, we could seek enhancements to the electric field intensity. In our current device, the electric field maximum is recessed within the nanobeam core, at a location inaccessible to the particle. By the time it reaches the surface,  $|\vec{E}|^2$  has decayed by a factor of 0.436. It is tempting, therefore, to consider a donor (air) mode device, which inherently improves overlap in the cladding and enhances the *normalized* electric field near the particle. The  $|\vec{E}|^2$  and Fourier transform for air and semiconductor mode devices are compared in Figures 2.81 and 2.82. While we can see the electric field maximum is now accessible to the particle, these devices operate very close to the light line. This results in significant losses, as is evident from the Fourier transforms in Figure 2.82(e,f), and typical quality factors  $< 1,000$ . The high confinement offered by the semiconductor mode enables

higher quality factors and tighter gradients, and is therefore preferred.

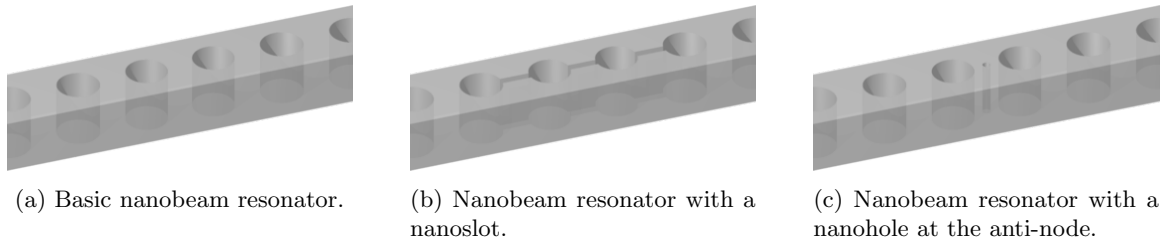


Figure 2.83: Introduction of nanoslots or nanoholes can reduce mode volume, enhance the electric field, and improve access to the field maximum.

A more sensible approach is the introduction of a nanohole [203, 320, 51] or nanoslot [298] (see Figure 2.83). Such structures maintain the tight confinement of the acceptor (dielectric) mode, while providing access to the true electric field maximum through an inclusion, eliminating the drop in the electric field at the surface. Moreover, continuity of  $\vec{D}_\perp$  across the interface can *further enhance* the electric field by a factor of  $\epsilon_{core}/\epsilon_{clad}$ .

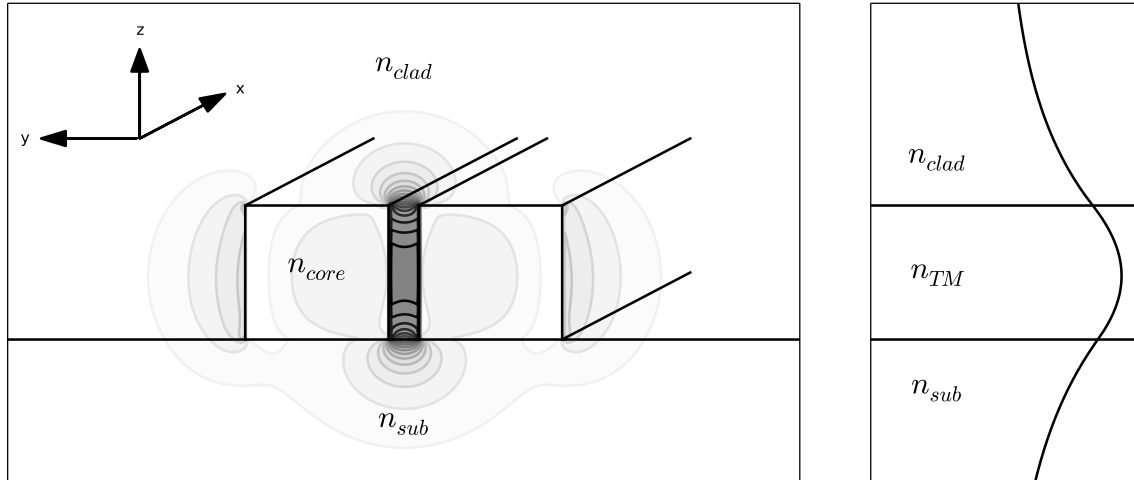
We considered the upper bounds we might expect by adding such an inclusion to our current device. Beginning with the normalized depth  $U_N$  for the unperturbed device:

$$U_N = \frac{Q}{V} \frac{2\pi}{\omega_0} \frac{\epsilon(\vec{r}_{trap})}{\epsilon(\vec{r}_0)} \frac{|\vec{E}_N(\vec{r}_{trap})|^2}{|\vec{E}(\vec{r}_0)|^2}$$

we calculated the enhancement factor,  $s = U'_N/U_N$ , where primed elements denote the equivalent perturbed variables. In the unperturbed geometry, the electric field maximum lies within the core, so  $\epsilon(\vec{r}_0) = \epsilon_{core}$ , while  $\epsilon(\vec{r}_{trap}) = \epsilon_{clad}$ . As the perturbation allows the particle to reach the  $\vec{E}$  field maximum, however,  $\vec{r}_0 = \vec{r}_{trap}$ , and  $\epsilon' = \epsilon_{clad}$  in both instances, while  $|\vec{E}'_N(\vec{r}_{trap})|^2 = |\vec{E}'_N(\vec{r}_0)|^2$ .

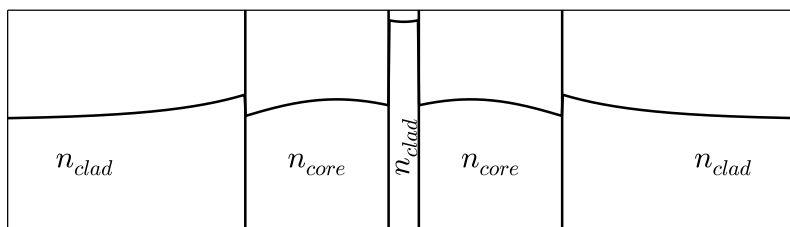
Together, these provide an enhancement of  $\frac{\epsilon_{core}}{\epsilon_{clad}} \frac{|\vec{E}_N(\vec{r}_0)|^2}{|\vec{E}_N(\vec{r}_{trap})|^2}$ .

Since the dominant electric field component is in the plane, a vertical nanoslot or nanohole at the anti-node will also result in a field enhancement within the inclusion. We recall that  $V = \frac{\int \epsilon |\vec{E}_N|^2 d\vec{r}}{\epsilon(\vec{r}_0) |\vec{E}_N(\vec{r}_0)|^2}$ . For a sufficiently small perturbation, very little energy will be contained in the inclusion and the numerator of  $V$  remains unchanged. In the case of a nanoslot, we can estimate  $\vec{E}'_N = \frac{\epsilon_{core}}{\epsilon_{clad}} \vec{E}_N$ . Similarly, the behavior of a sufficiently small nanohole can be approximated as a Mie cylinder, resulting in an enhancement  $\vec{E}'_N = \frac{2}{1 + \frac{\epsilon_{clad}}{\epsilon_{core}}} \vec{E}_N$ . As the contrast increases, this enhancement approaches 2, but will not exceed that of the nanoslot. At least from the perspective



(a) Schematic of a slotted waveguide, overlaid with contours of the dominant electric-field component.

(b) The vertical field profile can be estimated by decomposing the 2D waveguide into a TE slab waveguide, corresponding to the vertical stack. Here, the effective index for the horizontal stack (TM mode) is substituted for the core region.

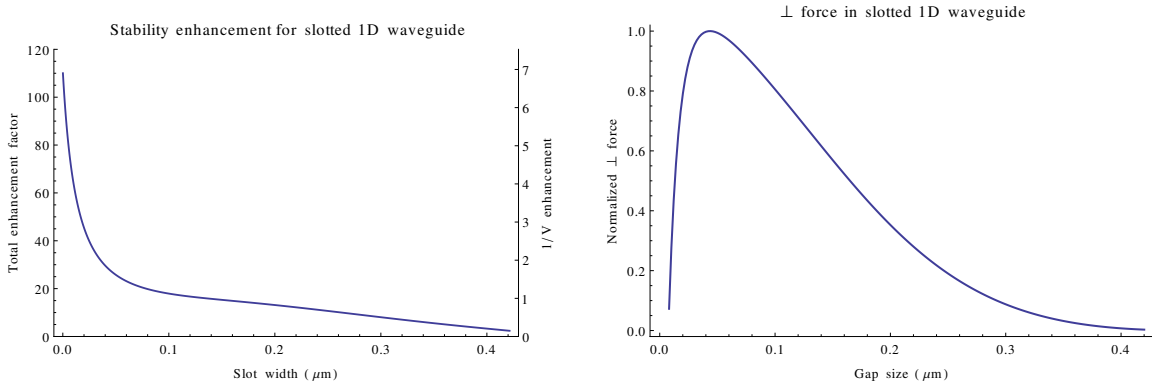


(c) The horizontal field profile can be estimated by decomposing the 2D waveguide into a TM slab waveguide.



Figure 2.84: Effective index method for estimating the effective index and field profile for a 2D slotted waveguide. A large field enhancement is observed within the slot region, but the gradient and curvature are relatively small due to the cosh functional form within this region.

of field enhancement, the nanoslot is the superior geometry. In both cases, the effect of the field enhancement on  $V$  is squared, but this is balanced by a decrease in the dielectric from  $\epsilon(\vec{r}_0) = \epsilon_{core}$  to  $\epsilon'(\vec{r}_0) = \epsilon_{clad}$ . For the nanoslot geometry, the combined effect *reduces*  $V$  as  $V' = \frac{\epsilon_{clad}}{\epsilon_{core}} V$ .



(a) Enhancement factor in 1D slotted vs. unslotted waveguides. The left axis includes a factor of  $\left(\frac{n_{core}}{n_{clad}}\right)^2 \frac{|\vec{E}(\vec{r}_0)|^2}{|\vec{E}(\vec{r}_{trap})|^2}$  to estimate how this translates to a 2D profile; the right axis shows the  $V^{-1}$  enhancement on its own. For the narrowest slot widths, the total enhancement approaches 110, as calculated analytically.

(b) Relative normal forces within the slot in 1D slot waveguide. Despite significantly greater enhancement for narrower gaps, the flat behavior of the cosh field dependence within the slot leads to maximum forces at a more moderate gap width  $\approx 44$  nm. A similar trend occurs for 2D waveguides.

Figure 2.85: Dependence of  $V^{-1}$  and force enhancement on gap width for a 1D slotted waveguide. These are calculated using an analytic solution for the field dependence, with numerical solutions for the characteristic equation to derive the propagation constant.

Including both the electric field enhancement and trapping at the maximum, we calculated the total enhancement for a sufficiently narrow nanoslot to be  $s = \frac{Q'}{Q} \left(\frac{\epsilon_{core}}{\epsilon_{clad}}\right)^2 \frac{|\vec{E}_N(\vec{r}_0)|^2}{|\vec{E}_N(\vec{r}_{trap})|^2} = \frac{Q'}{Q} \left(\frac{n_{core}}{n_{clad}}\right)^4 \frac{|\vec{E}_N(\vec{r}_0)|^2}{|\vec{E}_N(\vec{r}_{trap})|^2}$ . Given our values of  $n_{core} = 3.48$ ,  $n_{clad} = 1.32$  and  $\frac{|\vec{E}_N(\vec{r}_0)|^2}{|\vec{E}_N(\vec{r}_{trap})|^2} = \frac{1}{0.436} = 2.294$ , we found that a stability enhancement of up to  $s = 110.8$  would be possible for an infinitesimal slot, assuming  $Q$  could be maintained. As the gap size increases, energy confinement within the beam shifts away from the center and the field enhancement within the gap drops off rapidly. Beyond 135 nm, enough energy resides in the cladding to increase the mode volume beyond that for a plain waveguide, and the only stability enhancement comes from improved access to the anti-node. We calculated the dependence of  $V^{-1}$  and total enhancement on gap size using an analytic model for a 1D slotted waveguide; this trend is plotted in Figure 2.85a.

Despite the increase in field intensity within the slot, these structures can have a detrimental

effect on trapping normal to the surface. Within the gap, the dominant field component follows a cosh dependence, as opposed to the single exponential decay above a single-sided surface. Intuitively, this is equivalent to opposing evanescent forces from both boundaries of the slot. We calculated this effect using the same analytic model for the 1D slot; the data are presented in Figure 2.85b. For particularly narrow gaps, the magnitude of the opposing force is strong enough to significantly offset the primary trapping force, producing an overall weaker optical trap in spite of the greater field enhancement. This results in a peak perpendicular trapping force for a more moderate gap width of  $\approx 44$  nm. This behavior was verified with simulations of 2D slotted waveguides matching our nanobeam cross-section. The peak perpendicular trapping force occurred for a slot width around between 40 - 45 nm. Despite an overall stability enhancement of 29.2, the evanescent force in the slot (along  $\hat{y}$ ) exceeded the plain waveguide's surface trapping force (along  $\hat{z}$ ) by only  $3.85\times$ .

Overall, the stability enhancement is a more important metric than the trapping force. As long as it's possible to capture the particle, the precise magnitude of the force is not important, while the cQED cavity-emitter coupling follows the same enhancement trend as the stability. Practically, however, the 40 nm slot width is already approaching the limits of what could be readily fabricated. Thus, a peak enhancement of  $\approx 30$  is about the highest which could be expected by nanostructuring a dielectric nanobeam resonator such as our device.

Ultimately, we must also recognize that these values assume that the slot can be introduced without a commensurate loss in  $Q$ . The peak fields of the mode now exist along the etched surface of the slot, where they can be greatly affected by sidewall roughness or absorption from surface states present along the etched wall. Even with an ideal structure, the abrupt perturbation introduced by the slot will tend to extend Fourier components of the mode into the light cone, resulting in higher losses. While we have experimentally demonstrated cavities *on substrate* exhibiting  $Q > 250,000$  and  $V \approx 0.5 (\lambda/n)^3$ , there are no experimental demonstrations of slotted resonators with performance anywhere nearly as good, and typically several orders of magnitude lower. Thus, we have concluded that nanoslots offer little, if any, practical advantage, and efforts are better spent maintaining high experimental quality factors.

#### 2.4.4.4 Emitters

We developed the technique of cavity-enhanced optical trapping to be a general platform for emitter integration. As it can readily be applied to various combinations of cavity material systems and colloidal quantum dots or nanocrystal emitters — and is intended to render these choices as independent as possible<sup>8</sup> — we intentionally avoided concentrating on specific systems for either component of the system. For the sake of completeness, however, we briefly consider the choice of emitter here. Design of the cavity and its material system are the subject of Chapter 3.

Promising emitter candidates for optical trapping include II-VI core-shell quantum dots such as CdSe/ZnS for visible frequencies, metal-chalcogenides colloidal quantum dots PbS and PbSe for infrared applications, and impurity-related color centers in semiconductor nanocrystals, such as the nitrogen-vacancy center in diamond. Each of these systems are capable of producing single photons, with observations of photon anti-bunching in each case [245, 216, 61, 43]. Of these, diamond NV<sup>-</sup> centers have the distinct advantage in that they do not suffer from photobleaching. Additionally, the emission is not a function of the crystal size, but is a property of the defect itself. For integration via optical trapping, this permits the use of larger nanocrystals, greatly easing challenge of capturing the structure. Similarly, the improved photostability would prevent bleaching the emitter from the intense trapping field. However, the spectral width of the ZPL is  $\approx 50 \text{ cm}^{-1}$ , making these sources incapable of producing indistinguishable photons. While bulk colloidal quantum dots often show even broader distributions, these typically narrow to  $1 \text{ cm}^{-1}$  at cryogenic temperatures, and recent work has reported linewidths as low as  $0.013 \text{ cm}^{-1}$  [90].

Between the available colloidal quantum dots, those with CdSe cores are most widely studied and possess excellent emitter properties, including wide tunability and high brightness. As their emission spectra remain in the visible, however, these require photonic crystal devices with extremely small features, imposing severe fabrication challenges. Instead, we chose to pursue the use of PbS quantum dots, which can exhibit spectral peaks between  $\approx 850 \text{ nm} - 1650 \text{ nm}$ . Besides benefiting from larger feature sizes at these wavelengths, this enabled us to leverage the great availability of

---

<sup>8</sup>Despite completely independent material systems, the choice of emitter and cavity is inevitably coupled by the operating wavelength, as well as availability of other system components such as sources and detectors.

optical equipment designed for the telecommunications band, as well as the use of silicon-on-insulator for the cavity material system.

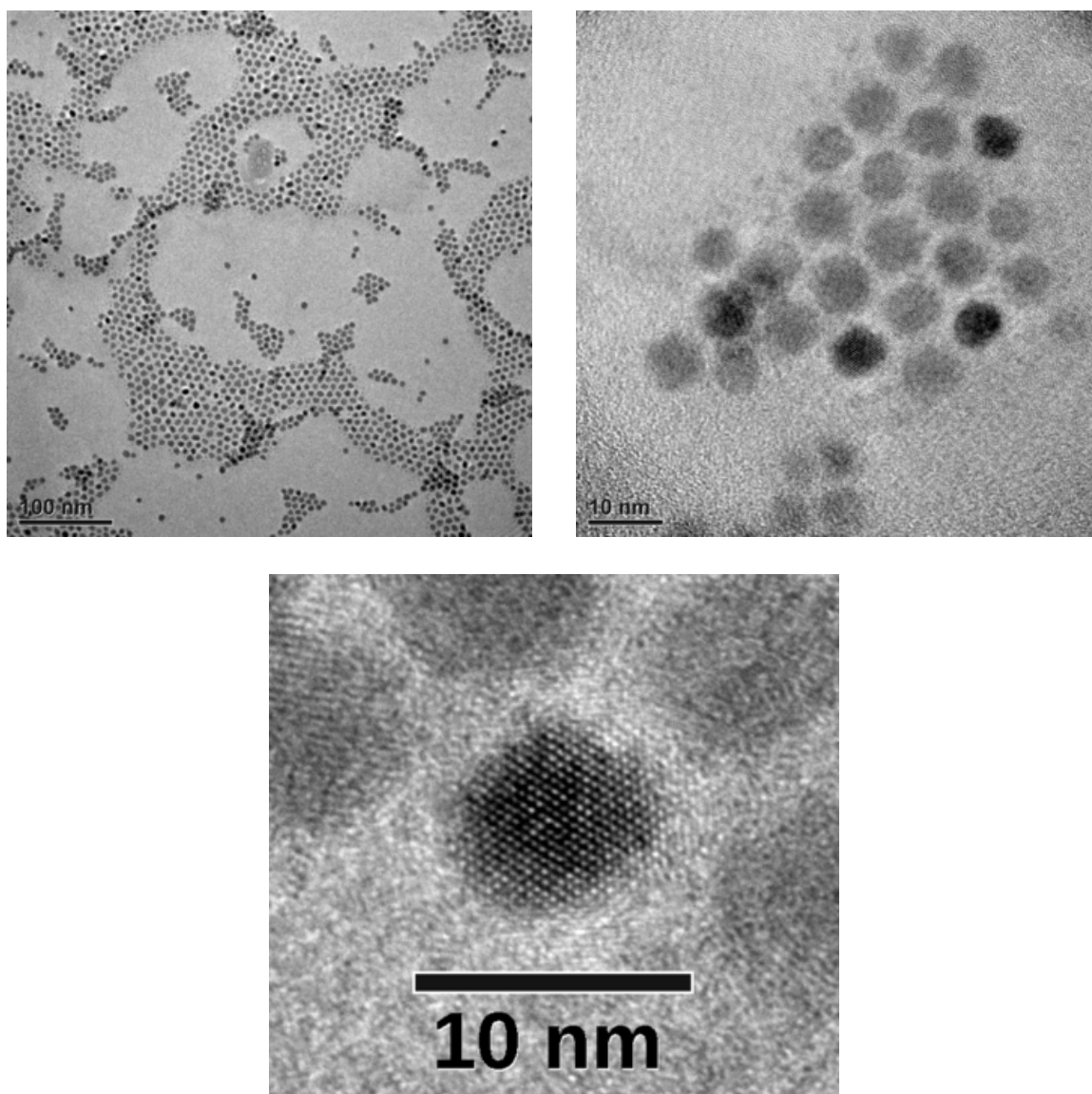


Figure 2.86: TEM images of the colloidal PbS QDs used in our studies, showing a typical diameter  $\approx 7.75$  nm.

We obtained colloidal PbS QDs from Evident Technologies (Troy, NY). These samples are suspended in toluene and are capped with oleic acid. TEM images of the dots are presented in Figure 2.86, showing a typical diameter  $\approx 7.75$  nm. This value was used to calculate the trapping metrics reported above. At room temperature, an ensemble measurement of these samples exhibited a broad Gaussian photoluminescence spectrum, with a center wavelength  $\approx 1473$  nm and a FWHM

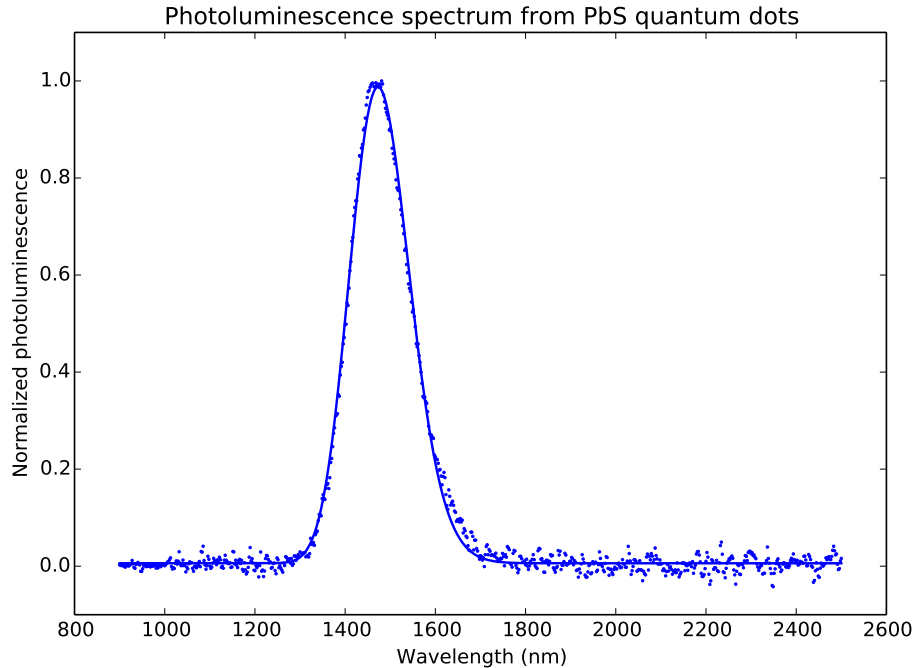


Figure 2.87: Room temperature photoluminescence spectrum for an ensemble of colloidal PbS QD dots, showing peak emission in the communications S band.

$\approx 156$  nm ( $\approx 719$   $\text{cm}^{-1}$ , or  $\approx 89.2$  meV); these data are shown in Figure 2.87.

While these emitters might still prove valuable as a single photon source, this spectral width is comparable to that for diamond  $\text{NV}^{-1}$  centers and far from lifetime limited, thus restricting their use to applications where indistinguishability is not a requirement. We note, however, that the wide energy spread could be due to a combination of inhomogeneous broadening (because it was an ensemble measurement), and rapid spectral diffusion. Peterson and Krauss [278] measured even greater spectral widths (240 meV) for PbS quantum dot ensembles, which narrowed by a factor of three for measurements on single quantum dots. In this study, the long integration times required to observe single quantum dots (300 s) precluded measurements of spectral diffusion. For similar measurements on CdSe quantum dots at 10K, however, emission maxima were known to shift by as much as 60 meV [76, 40, 78], resulting in spectral characteristics which depended on both integration time and excitation intensity. It thus remains an unconfirmed possibility that rapid spectral diffusion and inhomogeneous broadening could be dominant contributions to our broad spectra. Peterson and Krauss [278] also identified several other possible contributions which have been known to

cause significant broadening in other systems, including coupling to lattice vibrations of the capping ligands [306] and surface trapping at surface states or defect sites [252]. Further evidence of spectral modification due to trapped charges in the environment was reported by Turyanska *et al.* [351] for thiol-capped PbS quantum dots.

Long-term stability and photobleaching pose additional challenge for colloidal quantum dots, and are of particular concern with optical trapping given the high optical intensities used to capture the particles. Several recent studies have demonstrated excellent stability by isolating the quantum dots from the environment. Humer *et al.* [139] observed unaltered performance of colloidal suspensions after weeks of preparation by embedding the QDs in a polymer host (Novolak). Ihly *et al.* [143] noted the susceptibility of PbS and PbSe quantum dots to oxidative and photothermal degradation. Performing a comprehensive study on the origins of these effects, they found that the behavior could be effectively mitigated by encapsulating QD films using Al<sub>2</sub>O<sub>3</sub> films deposited by atomic layer deposition (ALD).

If surface charges are indeed the primary contributions to homogeneous broadening, there remains a possibility that the linewidth could also be improved through use of an encapsulating layer. Given recent reports of 400 MHz (1.65  $\mu\text{eV}$ , 0.013  $\text{cm}^{-1}$ ) linewidths measured for CdSe/CdZnS core/shell quantum using fast scanning systems [90], there might yet be a possibility of obtaining lifetime-limited linewidths from a system employing PbS quantum dots. If not, there could still be great potential for these materials as single photon sources, while the platform of cavity-enhanced optical trapping could be readily applied to other sources with the spectral characteristics necessary for indistinguishable photon emission. Although we were ultimately unable to capture PbS quantum dots with the current device to directly answer these questions, we remain optimistic about the potential of this system.

#### 2.4.4.5 Particle delivery, detection and fixation

To maximize the ease of testing multiple devices, our 1D nanobeams utilized gratings to couple light from a fiber array into SOI waveguides; the 1D nanobeam devices were then end-fire coupled from

the waveguides, allowing transmissive measurements to be taken through the cavity<sup>9</sup>. For optical trapping particles within a solution, we have to account for a potentially variable thickness of liquid above the devices, particularly as we intended to flush and dry the device *in situ* to fix the particle in place. Because this would change the effective focal point for an objective over the surface, coupling through a feeding waveguide was preferred over resonant scattering. Similarly, the use of grating couplers allowed many devices to be fabricated in a planar array, enabling large-scale automated testing by simply translating the substrate.

To deliver the particles, we designed a microfluidic device which could be bonded on top of the chip during emitter integration, and later removed for further processing or cQED testing. The device consisted of a single flow channel designed to cover cavity surface, which was fed by multiple input and dump ports. The channels were fabricated in PDMS using standard soft-lithography molding techniques, allowing it to seal over the feeding waveguide without obstructing the grating coupler region. This material also allowed the trapping process to be observed by an infrared camera above the surface, although it would become slightly defocused once the channel had been purged of solution. Throughout the trapping process, the Lorentzian response of the resonator could also be monitored to detect the presence of the particle and ensure the correct size particle was trapped (see discussion of sensitivity, above).

To trap a particle, a solution containing the PbS quantum dots could be flowed from the first input until a particle reached the vicinity of the cavity<sup>10</sup>. Once trapped, the second input containing only the pure solvent would be used to flush the channel of remaining particles while maintaining the trapping field. Based on calculations of Stokes drag, the traps would be able to withstand a flow velocity *at the surface* of nearly 2 mm/s without perturbing the particle beyond the mean trapping radius, easily adequate to handle any practical flow rate within the channel. Once the channel had been purged of excess quantum dots, an inert gas would be flowed over the channel to remove any

---

<sup>9</sup>This setup also permits reflective measurements and evanescently-coupled cavities, although these were not used here.

<sup>10</sup>For larger particles  $\approx 500$  nm, it is possible to use radiation pressure to draw particles into the waveguide's evanescent field and transport to the cavity [229]. For nanocrystal emitters in the  $\approx 10$  nm range, however, we must rely on fluid flow for particle transport. We also note that electro-osmotic flow would be preferred to the laminar flow profile within the microfluidic channel due to the greater velocity near the beam surface.

remaining solvent and fix the particle in place. After removing the channel, protective encapsulants such as an ALD  $\text{Al}_2\text{O}_3$  could be deposited to protect the particle from oxidative degradation. Finally, the oxide substrate could be optionally removed from underneath the beam using a vapor-phase HF etch [97] to further improve confinement and quality factor.

Although this system was perhaps the most simple method of delivering and fixating the particle, we would like to highlight several interesting alternatives suggested in the literature. Ropp *et al.* [299] suspended CdSe QDs in a custom water-based photoresist. Using a video-controlled feedback system, electro-osmotic flow was used to position to a given location. Once positioned, a UV laser exposed the photoresist to fix the particle in place. A similar active-trapping technique from the same authors measured photon anti-bunching from trapped single emitters, with  $g^{(2)}(0)=0.37$  [300]. While the trapping accuracy of the system was not quite as high as that predicted for our system, the two systems could be combined to deliver, capture, and fix the particle in place. Additionally, an appropriate host polymer could potentially be used to passivate the particle and prevent from oxidative degradation. Another interesting fixation technique was developed by Galloway *et al.* [102]. Rather than using optical trapping to capture the particle, local field enhancement near a plasmonic hotspot triggered the binding of proteins via three-photon absorption. These immobilized proteins were then able to chemically capture nanocrystals. A similar approach can be envisioned for sufficiently high  $Q/V$  dielectric cavities, and would enable self-aligned emitter-cavity integration similar to the cavity-enhanced optical trapping presented here.

### 2.4.5 Comparisons

Having explored the cavity-emitter integration techniques described above, we considered the ultimate potential of each one in terms of its overall scalability, practical challenge in fabrication and tuning, and general performance characteristics. A summary of these conclusions is presented in Table 2.4.

In terms of general scalability, the techniques utilizing the etched silicon nanopillars and quantum dots have the greatest potential. These processes were specifically designed with CMOS-

compatibility in mind, allowing them to inherently exploit the extensive fabrication infrastructure used for IC production. Because the heteroepitaxial structures utilize similar silicon growth templates, they too could benefit from the scalability of these processes. In particular, we note that the use of silicon wafers avoids several major scalability challenges traditionally faced active optical devices fabricated on III-V substrates. Besides significantly higher substrate cost, these wafers are generally limited to 4" in diameter due to the brittle nature of the material, while silicon foundries can already perform parallel fabrication over 300 mm (with 450 mm wafers in development). These considerations will likely limit the ultimate scalability of the bonded integration process. Cavity-enhanced optical trapping could potentially employ parallel cavity excitation and automated fluidic delivery, but will likely require a substantially manual process and is the least scalable of the techniques. While this could be capable of coupling several cQED systems together, its primary strength is the emitter-cavity material independence. The most important use of this technique may be for prototyping new devices, or characterizing new emitter material systems.

The relative fabrication challenges for each technique are essentially the reverse of their scalability. Optical trapping requires little processing beyond single-step lithography and etching, and will likely remain the most accessible technique. The bonded device rely on a similar process sequence for the cavity, but face slightly greater difficulties due to the bonding and time-sensitive etching steps. At the other extreme, the size scale required by the heteroepitaxial regrowth and SiQD approaches presents a significantly greater challenge than optical trapping or bonded techniques. The latter two also inherently include the cavity, whereas the regrowth and SiQD approaches are still faced with the alignment and fabrication of these onto the existing emitter structure. Finally, we note that significantly more work will be needed to improve the growth interface for heteroepitaxy, potentially through the use of chemical-mechanical polishing (CMP) and *in situ* oxidation removal in the growth chamber.

Given the ability of the optical trapping technique to perform capture-and-release emitters during integration, this method also has the best spectral tunability. While etching the bonded layers, the spectra will blue-shift as the emitter dimensions shrink. While not as forgiving as optical trapping, *in*

*situ* monitoring during the etch offers some ability to ensure spectral alignment between the cavity and emitter. The remaining two methods offer few post-fabrication tuning options, as the basic emitter spectra will be fixed during initial fabrication. Spectral adjustment (of either the emitter or cavity) during operation may still be possible using temperature, electric or magnetic fields, strain, and gas condensation, but these apply equally to the trapping and bonding methods and do not offer any distinct advantage for the growth or SiQD processes.

Without complete experimental values for the epitaxially-grown emitters and SiQDs, is difficult to predict their performance. For the bonded and trapped devices, we can make reasonable estimates based on common dipole and emitter lifetime values and simulations for our existing photonic crystal cavities (see 3.3). The wide range of potential nanocrystal emitters is particularly interesting here, as high-efficiency, long-life sources would exhibit extremely low saturation photon numbers which could lead to substantially nonlinear behavior at the single photon level.

Overall, we have concluded that the heteroepitaxial growth and optical trapping methods offer the most intriguing potential. Regrowth would enable the greatest large-scale integration. Because the growth apertures can simultaneously act as current apertures, these offer interesting opportunities for detector integration or electrical pumping. At the other extreme, optically trapping may be the least scalable technology, but offers the greatest flexibility in material choice. This method does not require substantial resources to execute, and is ideally suited as a platform for emitter characterization and initial experimental demonstration of small coupled systems, rather than large-scale production.

	Heteroepitaxy	SiQD	QW bonding & dimensional reduction	Cavity-enhanced optical trapping
<b>Emitter</b>	Grown III-V QD	Si QD	Etched III-V QD	Nanoparticle, colloidal QD, or nanocrystal color center PbS or PbSe QD, diamond NV <sup>-</sup> center
<b>Alignment mechanism</b>	Aligned lithography	Aligned lithography	Self-aligned lithography	Inherently self-aligned to mode
<b>Scalability</b>	Excellent	Excellent	Moderate	Moderate-low
<b>Fabrication difficulty</b>	Very challenging	Challenging	Moderate	Low
<b>Spectral tunability</b>	Moderate-low	Moderate-low <sup>11</sup>	Moderate <sup>12</sup>	Excellent <sup>13</sup>
<b>Approximate carrier lifetime (<math>\tau = \gamma^{-1}</math>)</b>		200 ns	854 ps	300 ns[278]
<b>Approximate dipole (<math>\vec{\mu}</math>)</b>	30 D		30 D	17 D (PbS QD), 100 D (CdSe)[171]
<b>Approximate coupling strength (<math>g/2\pi</math>)<sup>14</sup></b>			$\approx 25$ GHz	$\approx 14$ GHz
<b>Approximate saturation photon number (<math>N_0</math>)<sup>15</sup></b>			$7 \times 10^{-3}$	$1 \times 10^{-7}$

Table 2.4: Comparison between emitter-cavity integration techniques

<sup>11</sup>Limited post-fabrication tuning (strain, Stark effect)

<sup>12</sup>Blue-shift only by continued etching; *in situ* verification could be challenging.

<sup>13</sup>Catch-and-release processing, inherent trapping sensitivity to particle dimension.

<sup>14</sup> The coupling strength follows  $g = \vec{\mu} \cdot \vec{E}/\hbar$ , where  $\vec{\mu}$  is the emitter dipole and  $\vec{E}(\vec{r}) = \sqrt{\frac{\hbar\omega}{2\epsilon_0\epsilon(\vec{r})V(\vec{r})}}$  is the vacuum field at the dipole location.

<sup>15</sup>The saturation photon number  $N_0 = \frac{\gamma^2}{2g^2}$  refers to the number of photons needed to saturate the coupled cQED system and begin observing nonlinear effects, potentially at the single quanta level.

# Chapter 3

## Cavity Design

### 3.1 Cavity Structures

Our system design begins by selecting a suitable structure for the optical cavity. As discussed previously, the ideal cavity not only maximizes coupling between the emitter and the optical field of the resonator, but also maintains this interaction as long as possible. These features require a cavity design which simultaneously exhibits a high quality factor,  $Q$ , while minimizing the mode volume,  $V$ , in order to localize the optical field around the emitter and maximize the coupling. Besides enhancing the radiative decay rate through the Purcell effect, maximizing the field overlap between the emitter and the cavity is also responsible for directing emission into the mode of interest. Additionally, a high cavity  $Q$  is responsible for supporting a coherent exchange of energy between the emitter and cavity field, before irreversible decay occurs.

Until recently [390, 291, 334] nearly all cavity QED experiments consisted of single atoms dropped through a cavity formed between two ultrahigh reflectivity mirrors. These high-finesse Fabry-Perot resonators are typically 10s of  $\mu m$  in dimensions, achieving quality factors exceeding  $10^7$  with mode volumes on order  $\approx 3 \times 10^4 (\lambda/n)^3$  [163]. Faced with extreme challenges in reducing cavity size or further improving the multilayer dielectric coatings [135], however, researchers have begun to explore alternative cavity architectures to realize further increases in cavity metrics. To date, whispering gallery modes in silica microspheres have exhibited the highest quality factors of any resonator, with experimental values  $\approx 10^{10}$  approaching the fundamental limits set by material absorption [109, 359].

Unfortunately, not only are these structures difficult to integrate, but their extreme quality factors cannot be fully appreciated; for  $Q \gtrsim 10^8$ , the dominant dissipative mechanism becomes the atom's radiative decay rate rather than cavity leakage [331]. In this regard, toroidal silica microresonators provide another interesting alternative. Although they typically have more modest  $Q$ s, these already approach the useful limit, while their smaller mode volume ( $\approx 200 (\lambda/n)^3$  at the emitter location, compared to  $\approx 5200 (\lambda/n)^3$  for the  $120\mu\text{m}$  diameter microsphere referenced above) and monolithic fabrication are clear advantages. Strong coupling has been observed between single cooled Cs atoms and a microtoroid with an experimental  $Q$  of  $6 \times 10^7$  [6]. Such a system could rival even the projected limits for a Fabry-Perot configuration, with toroids exhibiting  $Q \approx 10^8$  and  $Q \approx 4 \times 10^8$  shown at  $\lambda = 850 \text{ nm}$  and  $1550 \text{ nm}$ , respectively [169, 331].

Despite impressive figures of merit and consequently low atom/photon saturation numbers, these atomic cQED all systems suffer from the general problem of a useful lifetime which is limited by the transit of the atom through the cavity. In early experiments, this duration was only  $T \approx 0.4\mu\text{s}$  [292, 346], resulting in a loss channel comparable to the atomic dephasing. The brief transit time and related uncertainty in instantaneous atom-field coupling presents a severe restriction on the information available in these experiments [346, 348, 53, 44]. The situation was later improved to  $T \approx 100\mu\text{s}$  by first cooling the atoms in a magneto-optical trap (MOT) [134], and eventually to  $T \approx 50\text{ms}$  by creating an additional far-off resonant trap (FORT) to trap the cooled atom in the cavity itself [241] (it can be as long as  $3\text{s}$  in the absence of a driving field). These gains come at a significant price, however, both in terms of greater system complexity and an inevitable decrease in coupling strength as the mode volume increases to make room for the trap [163]. The extension to many-cavity systems is further complicated by the variable coupling strength of each atom due to its precise position within the cavity field, which decreases exponentially in whispering gallery resonators.

With this in mind, we reconsider the cavity design criteria. For the purpose of creating extensible systems, two additional requirements seem clear:

- The emitters must be permanently affixed to- or embedded in the cavity;

- Coupling to and from the cavities must be possible with on-chip photonic components to enable larger scale integration.

We must also consider that  $Q/V$  is not the only relevant figure-of-merit. For example, achieving a higher coupling rate,  $g \propto 1/\sqrt{V}$  – even at the expense of greater cavity loss – would enable faster operation while reducing the number of photons needed to saturate the transition, both of which are crucial characteristics for modulators or quantum gates [45].

Although they do not achieve nearly the same quality factors as their free-space cousins, strong coupling has also been observed in a variety of solid state structures, including photonic crystal cavities, microdisks, and micropillars [390, 291, 14, 128, 81, 313]. Such systems typically have significantly smaller mode volumes and can readily integrate quantum dots or other “artificial atoms.” These emitters may be already embedded in the cavity or permanently affixed and often exhibit larger transition dipole moments than their atomic counterparts. Of course, they also present their own challenges, which will be discussed in Chapter 2.

Of these remaining architectures, 1D nanobeam and 2D slab photonic crystal cavities have some of the highest  $Q$ s and lowest mode volumes available in the solid state. Additionally, being planar devices, these can more easily couple to waveguides, splitters, interferometers, and other planar photonic components. Finally, their fabrication is naturally transferable to a foundry process, permitting integration with circuitry to enable tuning via carrier dispersion, Stark effect, or thermally. These features make photonic crystal cavities a natural choice for large-scale integration of cQED systems.

## 3.2 Photonic Crystals

Photonic crystals are materials whose dielectric function exhibits periodic variation in one or more spatial dimensions. When the scale of the periodicity is on the order of the optical wavelength, multiple reflections at the interfaces can strongly couple the forward and backward propagating waves. As these waves interfere constructively and destructively, a complex dispersion relationship

emerges, resulting in optical properties that are vastly different than any of the constituent materials. For some structures, light of the correct frequency may propagate with a group velocity which is significantly lower than it would be in bulk. There can also exist gaps in the energy-momentum structure where light of certain frequencies cannot propagate in a particular direction, or for some instances, in any direction at all. As a result, incoming radiation whose frequency falls within these ranges will be completely reflected from the material.

One commonly used device which relies on this effect is the multilayer dielectric mirror mentioned previously. These structures are one-dimensional photonic crystals, with a periodic dielectric function along one direction and continuous symmetry in the other two. Often, these come in the form of quarter-wave stacks, consisting of alternating layers of dielectrics with different indexes of refraction. Clearly, when each layer thickness is equivalent to one quarter of the wavelength of light in it, the partially reflected wave will combine destructively with the incoming light, allowing only a fraction of the light to be transmitted. As additional layers are added, the transmission will continue to decrease geometrically. After an infinite series, the transmission eventually reduces to zero. In the case where there is no absorption, such a situation implies perfect reflection.

The first analysis of such a system was presented by Lord Rayleigh in 1887 [213], which he applied to reports of lamellar structures by Brewster and later to experimental observations by Stokes [214]. By considering a homogeneous medium as artificially periodic, Rayleigh examined the effects of a small perturbation to the potential. He concluded that any such periodic variation, regardless of magnitude, would result in the perfect reflection of a harmonic wave provided that the period of the structure was sufficiently close to the half-wavelength of the vibration. Essentially, Rayleigh showed that a band gap would open near the edge of the Brillouin zone in *any* 1D structure due to splitting of the accidental degeneracy between even and odd modes. Having come long before the work of Brillouin or Bloch, however, the correlation between photonic propagation in a periodic structure and the transport of electrons through a crystal was not made until a century later. Instead, a second treatment by Rayleigh in 1917 [215], based on an argument similar to that above utilizing combined Fresnel reflections, provided a more practical method to analyze optical propagation in

1D periodic structures. Although it cannot be readily generalized to periodic photonic structures of higher dimensions, the new method was easily extended to arbitrary 1D stacks using transmission matrices and became a primary tool for their design.

In 1987, two independent proposals by Eli Yablonovitch [381] and Sajeev John [154] realized the powerful connection between the behavior of electrons in the solid state and the response of light to a structured dielectric material. Just as the periodic atomic potential of a crystal result in forbidden energy bands for electrons, this analogy implied a possibility to engineer the photonic density of states, not just in one dimension, as had been done in the multilayer dielectric mirrors, but with full three-dimensional control. A few years earlier, Kleppner had suggested [172] that by reducing the photonic density of states, the Purcell effect could just as well inhibit spontaneous emission as enhance it. Although Kleppner had already demonstrated the behavior in the microwave regime [138], Yablonovitch realized there was yet an immense opportunity if this could be accomplished in the optical domain. This energy range corresponds to the electronic band gap of many semiconductors, where radiative recombination results in large energy losses and reduced device performance. If microstructured semiconductor devices could exhibit a photonic band gap – in which no propagating states exist – the radiative decay would be prevented, thus eliminating the energy wasted to spontaneous emission in lasers, transistors, and photovoltaic cells.

John considered a different possibility: the photonic equivalent of Anderson localization. Analogous to electrons becoming trapped in highly disordered solids, such as amorphous semiconductors, a properly structured dielectric medium could prevent photon transport through creation of a strongly localized pseudogap in the density of states. John suggested that photon localization could be utilized as an important mechanism in practical devices, such as a trigger for bistable or nonlinear optical response, as well as a significant platform for studying fundamental transport phenomenon without the influence of electron-electron or electron-phonon interactions [155].

The two proposals sparked a flurry of research into photonic crystals. Following a rocky start, theorists soon confirmed the existence of a complete photonic band gap in a diamond structure [131]. Yablonovitch conducted the first experimental demonstration of a 3D band gap in the microwave

regime [382], followed by the first report of a 2D photonic crystal at optical wavelengths by Krauss *et al.* [183] and the first photonic crystal fiber by Knight *et al.* [173]. Since then, photonic crystals have been used to create lasers, sensors, filters, and a full spectrum of other compact optical devices. More recently, the wavelength-scale manipulation of light afforded by photonic crystal cavities has been applied to cQED [390, 291, 14, 163, 334, 128, 17, 272, 84, 81, 378, 176, 124], as well as the burgeoning field of cavity opto-mechanics [71, 72, 303, 302].

### 3.2.1 Band structure computation

In order to understand the behavior of light inside periodic crystals, we now consider methods to model the structures and some important properties of the modes we can infer by symmetry. It should be noted that a completely analytic treatment of 1D structures is possible using scattering matrices, as suggested by Rayleigh's later work. While the resulting closed-form expressions yield valuable insight, the challenges involved in analyzing more complex structures warrant a different approach. We shall return to the scattering analysis later, but for now we seek to establish a more general formalism.

Having realized the similarity between the propagation of electrons through a periodic atomic potential and that of light in a periodic dielectric, we will apply the techniques developed by physicists in the early 20<sup>th</sup> century to model electron behavior in crystals. Just as physicists used the Schrödinger equation to find the natural modes of electrons in a semiconductor, we introduce Maxwell's equations to analyze photonic crystals:

$$\begin{aligned}\nabla \times \vec{E}(\vec{r}, t) &= -\frac{\partial \vec{B}(\vec{r}, t)}{\partial t} \\ \nabla \times \vec{H}(\vec{r}, t) &= \vec{J}(\vec{r}, t) + \frac{\partial \vec{D}(\vec{r}, t)}{\partial t} \\ \nabla \cdot \vec{D}(\vec{r}, t) &= \rho \\ \nabla \cdot \vec{B}(\vec{r}, t) &= 0\end{aligned}$$

as well as the constitutive relations:

$$\vec{D}(\vec{r}, t) = \epsilon_0 \vec{E}(\vec{r}, t) + \vec{P}(\vec{r}, t)$$

$$\vec{B}(\vec{r}, t) = \mu_0 \mu(\vec{r}) \vec{H}(\vec{r}, t)$$

where  $\vec{E}, \vec{D}, \vec{P}, \vec{H}, \vec{B}, \vec{J}, \rho, \epsilon_0, \mu_0, \mu_r, \vec{r}$  and  $t$  represent the electric field, electric displacement, polarization density, magnetic field, magnetic flux density, current density, charge density, permittivity of free space, permeability of free space, relative permeability, position vector, and time, respectively. For our purposes, we wish to consider purely dielectric materials at optical frequencies and will be exciting at low intensities. In this case, we are justified in making the following assumptions:

- charge-free, source-free media ( $\rho \rightarrow 0, \vec{J} \rightarrow 0$ )
- linear dielectric response ( $\vec{D} = \epsilon_0 \epsilon_r(\vec{r}) \vec{E}$ )
- $\epsilon_r$  purely real and positive everywhere
- no magnetic response at optical frequencies ( $\mu_r \rightarrow 1$ )

As we are concerned with the harmonic modes of the system, we further decompose the fields by Fourier analysis into independent spatial- and time-dependent components:

$$\vec{E}(\vec{r}, t) = \vec{E}(\vec{r}) e^{-i\omega t}$$

Although we are typically interested in operation over a narrow frequency band, we note that the relative permittivity may, in general, depend on frequency. After making these simplifications and dropping the spatial dependence for clarity, we find:

$$\nabla \times \vec{E} = i\omega \mu_0 \vec{H}$$

$$\nabla \times \vec{H} = -i\omega \epsilon_0 \epsilon_r \vec{E}$$

We multiply the second equation by  $\epsilon_r^{-1}$ , take the curl, and substitute the first to arrive at our

master equation:

$$\begin{aligned}\nabla \times \left( \frac{1}{\epsilon_r} \nabla \times \vec{H} \right) &= \left( \frac{\omega}{c} \right)^2 \vec{H} \\ \hat{\Theta} \vec{H} &= \left( \frac{\omega}{c} \right)^2 \vec{H}\end{aligned}$$

with  $c = 1/\sqrt{\epsilon_0\mu_0}$  is the speed of light in vacuum and our operator  $\hat{\Theta} \equiv \nabla \times (\frac{1}{\epsilon} \nabla \times)$  defines an eigenproblem for our harmonic modes, where the spatial patterns of our magnetic field  $\vec{H}$  serves as the eigenvectors and the eigenvalues are proportional to the square of the frequency  $(\omega/c)^2$ . Solutions to this equation, along with the transversality requirement  $\nabla \cdot \vec{H} = 0$ , will describe propagation within our structure.

Although we could have derived a similar equation for the electric field, the system either becomes a generalized eigenproblem or requires a non-Hermitian operator. Both situations become more difficult to solve numerically. In contrast, conditions permit a simple eigenproblem with a Hermitian operator, with continuity of all  $\vec{H}$  components (though not necessarily their derivatives) over dielectric interfaces and a simple, spatially-independent transversality requirement. The Hermitian nature of the operator allows us to immediately recognize several aspects of the solutions, namely orthogonality, and that they have real eigenvalues. Moreover, for  $\epsilon_r > 0$ , the operator  $\hat{\Theta}$  is positive semi-definite, meaning the frequencies  $\omega^2$  must be non-negative. These facts restrict  $\omega$  to real values, so that our solutions correspond to lossless harmonic modes. Finally, the set of all solutions forms a complete basis into which any field pattern can be decomposed.

It is worth noting the effect of spatial scale on our solutions. Consider a transformation where our dielectric gets stretched by a factor  $s$ :  $\epsilon'(\vec{r}) = \epsilon(\vec{r}/s)$ . Letting  $\vec{r}' = s\vec{r}$ , we have  $\frac{\partial}{\partial x'} = \frac{1}{s} \frac{\partial}{\partial x}$  and thus  $\nabla' = \frac{1}{s} \nabla$ . Making appropriate substitutions for  $\vec{r}$  in our original solution  $\vec{H}(\vec{r})$ :

$$\begin{aligned}\nabla \times \frac{1}{\epsilon(\vec{r})} \nabla \times \vec{H}(\vec{r}) &= \left( \frac{\omega}{c} \right)^2 \vec{H}(\vec{r}) \\ s \nabla' \times \frac{1}{\epsilon(\vec{r}'/s)} s \nabla' \times \vec{H}(\vec{r}'/s) &= \left( \frac{\omega}{c} \right)^2 \vec{H}(\vec{r}'/s) \\ \nabla' \times \frac{1}{\epsilon(\vec{r}'/s)} \nabla' \times \vec{H}(\vec{r}'/s) &= \left( \frac{\omega}{sc} \right)^2 \vec{H}(\vec{r}'/s)\end{aligned}$$

We can define a new solution vector  $\vec{H}'(\vec{r}') = \vec{H}(\vec{r}'/s)$  and a new frequency  $\omega' = \omega/s$  which are just scaled versions of the originals. Since  $\epsilon(\vec{r}'/s) = \epsilon'(\vec{r}')$ , we get an equivalent master equation:

$$\nabla' \times \frac{1}{\epsilon'(\vec{r}')} \nabla' \times \vec{H}'(\vec{r}') = \left(\frac{\omega'}{c}\right)^2 \vec{H}'(\vec{r}')$$

Our scaled system behaves identically to the original, but with an appropriately expanded (condensed) magnetic field and an equivalently stretched (shrunk) wavelength with reduced (increased) frequency. This explains the initial demonstrations of photonic crystals in the microwave regime, which permit easier fabrication than their optical equivalent. It also allows us to solve our master equation in whatever coordinates are convenient and simply scale the solution as needed.

If our structure has translational symmetry, where  $\epsilon(\vec{r})$  is invariant for some spatial displacement  $\vec{d}$ :

$$\begin{aligned} \hat{T}_{\vec{d}} \epsilon(\vec{r}) &= \epsilon(\vec{r} - \vec{d}) \\ &= \epsilon(\vec{r}) \end{aligned}$$

then the translation operator  $\hat{T}_{\vec{d}}$  commutes with our wave operator  $\hat{\Theta}$ :

$$[\hat{T}_{\vec{d}}, \hat{\Theta}] = 0$$

and our solutions for  $\hat{\Theta}$  can be chosen in such a way that they are also eigenfunctions of  $\hat{T}_{\vec{d}}$ . We readily note that exponentials are eigenfunctions of the translation operator:

$$\begin{aligned} \hat{T}_{\vec{d}} e^{i\vec{k}\cdot\vec{r}} &= e^{i\vec{k}\cdot(\vec{r}-\vec{d})} \\ &= \left(e^{-i\vec{k}\cdot\vec{d}}\right) e^{i\vec{k}\cdot\vec{r}} \end{aligned}$$

with eigenvalue  $e^{-i\vec{k}\cdot\vec{d}}$  for some wave vector  $\vec{k}$ . Although such functions merely represent plane waves, we note the potential for degeneracy. Explicitly, sets of solutions where  $\vec{k}\cdot\vec{d}$  is spaced by an

integer multiple of  $2\pi$  have identical eigenvalues. Let  $\vec{k} \cdot \vec{d} = \vec{k}_0 \cdot \vec{d} + 2\pi m$  for some integer  $m$ . Then:

$$\begin{aligned} \hat{T}_{\vec{d}} e^{i\vec{k} \cdot \vec{r}} &= \left( e^{-i\vec{k} \cdot \vec{d}} \right) e^{i\vec{k} \cdot \vec{r}} \\ &= \left( e^{-i\vec{k}_0 \cdot \vec{d}} e^{-2\pi i m} \right) e^{i\vec{k} \cdot \vec{r}} \\ &= \left( e^{-i\vec{k}_0 \cdot \vec{d}} \right) e^{i\vec{k} \cdot \vec{r}} \end{aligned}$$

Because  $\hat{T}_{\vec{d}}$  is a linear operator, these functions may be combined and their sum will also remain an eigenvector. In this way, it is possible to construct much more complicated solutions which satisfy the eigenequations for  $\hat{T}_{\vec{d}}$  and  $\hat{\Theta}$  simultaneously. For a given wave vector  $\vec{k}$ , we find a spectrum of solutions with increasing  $\omega$ . The set of these solutions over all wave vectors comprises the dispersion relation or band structure for our system, equivalent to the energy-momentum relationship describing electron transport. Depending on the structure, these spectrum of  $\omega$

Upon further consideration, we can uncover additional implications of the symmetry. Clearly, the system operator  $\hat{\Theta}$  must commute not only with the translation operator for a single shift, but with *all* of the translation operators which obey the symmetry. Intuitively, this makes sense. For any shift to which our structure is indistinguishable, our solutions must also be indistinguishable. They can vary by at most a phase shift, which must be consistent across the structure (or we would be able to uniquely identify where we are by the variance in the phase change). Essentially, the components of our propagation constant which lie along the directions of symmetry become conserved quantities.

In the case of continuous translational invariance, this implies that  $\hat{\Theta}$  commutes with  $\hat{T}_{\vec{d}}$  for *any*  $\vec{d}$  along our direction of symmetry. For example, in a stack of dielectric slabs arranged along the  $\hat{z}$ -axis, we have continuous translational symmetry along  $\hat{x}$  and  $\hat{y}$ . Our solution must be an eigenvector of the translation operator for any shift in either  $\hat{x}$  or  $\hat{y}$ :

$$\begin{aligned}
\hat{T}_{d_x \hat{x}} e^{ik_x x} &= e^{ik_x(x-d_x)} \\
&= (e^{-ik_x d_x}) e^{ik_x x} \\
\hat{T}_{d_y \hat{y}} e^{ik_y y} &= e^{ik_y(y-d_y)} \\
&= (e^{-ik_y d_y}) e^{ik_y y}
\end{aligned}$$

which allows us to write our solution in the form:

$$\vec{H}(\vec{r}) = \vec{H}(z) e^{ik_x x + ik_y y}$$

Within each  $\hat{z}$  layer with refractive index  $n$ , we can similarly decompose the solution into plane waves,  $\vec{H}_n(z) \propto \sum_m \vec{c}_m e^{ik_{z,n,m} z}$ . For a plane wave in bulk media,  $|\vec{k}| = \sqrt{k_x^2 + k_y^2 + k_{z,n}^2} = \frac{n\omega}{c}$ , or in spherical coordinates we could write  $\vec{k} = \frac{n\omega}{c} (\sin\theta_n \cos\phi, \sin\theta_n \sin\phi, \cos\theta_n)$ , where  $\theta_n$  is the angle between the wave vector and the interface normal ( $\hat{z}$  axis) and  $\phi$  is the angle within the  $\hat{x} - \hat{y}$  plane. Since  $k_x$  and  $k_y$  are both conserved quantities, we can equate these between layers to arrive at Snell's law:  $n_1 \sin\theta_1 = n_2 \sin\theta_2$ . Additionally, when  $k_x^2 + k_y^2 > (\frac{n\omega}{c})^2$ ,  $k_{z,n} = \pm \sqrt{(\frac{n\omega}{c})^2 - (k_x^2 + k_y^2)}$  becomes imaginary, resulting in evanescent decay in the layer. Essentially, Snell's law and total internal reflection are consequences of continuous translational symmetry.

When the system has discrete translational symmetry,  $\hat{\Theta}$  only commutes with  $\hat{T}_{\vec{d}}$  when  $\vec{d}$  is an integer multiple of the periodicity. As in atomic crystals, we refer to the smallest repeating unit of our structure as the *unit cell*, which has dimensions given by the lattice constant  $a$ . If we consider a structure which has period  $a$  in the  $\hat{x}$  direction, then  $\hat{\Theta}$  must commute with  $\hat{T}_{a\hat{x}}$ . Calling  $b = (2\pi/a)\hat{x}$  our *primitive reciprocal lattice vector*, we find a degenerate set of wave vectors  $k_x + mb$ . As previously discussed, we combine these to form our solution:

$$\begin{aligned}
\vec{H}_{k_x}(\vec{r}) &= \sum_m \vec{c}_{k_x, m}(y, z) e^{i(k_x + mb)x} \\
&= e^{ik_x x} \sum_m \vec{c}_{k_x, m}(y, z) e^{imbx} \\
&= e^{ik_x x} \vec{u}_{k_x}(x, y, z)
\end{aligned}$$

By examination, we recognize the sum as a Fourier decomposition and see that  $\vec{u}$  represents *any* function with period  $a$  in the  $\hat{x}$  direction:  $\vec{u}_{k_x}(x + ma, y, z) = \vec{u}_{k_x}(x, y, z)$ . We have arrived at Bloch's theorem. Analogous to the results in solid-state physics, we find that our photon can propagate without scattering as a Bloch wave, whose field profile is that of a plane wave modulated by a periodic function. This conclusion is also consistent with our previous intuition; the solutions are indistinguishable when shifted by a lattice period, except for a consistent phase change.

As in the solid-state, the formalism is easily applied to structures with periodicity in multiple dimensions. Rather than a single lattice constant, we use a basis of primitive lattice vectors,  $\vec{a}_i$ . These need not be orthogonal, but must form a complete basis such that any vector can be written as a unique linear combination of them. Any integer combination of these is a lattice vector,  $\vec{R} = \sum_i m_i \vec{a}_i$ , to which the dielectric is invariant,  $\epsilon(\vec{r} + \vec{R}) = \epsilon(\vec{r})$ . From the primitive lattice vectors, we can also derive the primitive reciprocal lattice vectors,  $\vec{b}_i$ , which span the space of the reciprocal lattice and satisfy the relation  $\vec{a}_i \cdot \vec{b}_j = 2\pi\delta_{ij}$ . Writing our Bloch wave vector as a combination of these,  $\vec{k} = \sum_i c_i \vec{b}_i$ , our final solution will be of the form  $\vec{H}_{\vec{k}}(\vec{r}) = e^{i\vec{k}\cdot\vec{r}} \vec{u}(\vec{r})$  where  $\vec{u}$  also follows the lattice periodicity,  $\vec{u}(\vec{r} + \vec{R}) = \vec{u}(\vec{r})$ .

A Bloch mode with wave vector  $\vec{k}$  is unchanged by the addition of a reciprocal lattice vector, which merely results in renumbering the coefficients in the Fourier expansion of  $\vec{u}$ . This region, where  $-\pi < \vec{k} \cdot \vec{a}_i \leq \pi$ , is known as the first Brillouin zone and contains all non-redundant wave vectors. Additionally, just as translational invariance of the dielectric function implies translational invariance of the solution, the presence of other symmetries in our structure will impose similar restrictions on our solution space. The application of rotational invariance or mirror symmetry, for example, will further limit the range of unique solutions. The resulting area is known as the irreducible Brillouin zone, defined as the smallest region of reciprocal space for which solutions cannot be related by symmetry. It is thus sufficient to examine only this space of wave vectors, as any other solution could be obtained by addition of a reciprocal lattice vector, or application of an appropriate rotation, mirror, etc.

Returning to our master equation, we now consider the operation of  $\hat{\Theta}$  on our Bloch waves:

$$\begin{aligned}\hat{\Theta}\vec{H}_{\vec{k}}(\vec{r}) &= \left(\frac{\omega(\vec{k})}{c}\right)^2 \vec{H}_{\vec{k}}(\vec{r}) \\ \nabla \times \left(\frac{1}{\epsilon(\vec{r})} \nabla \times \left(e^{i\vec{k}\cdot\vec{r}} \vec{u}_{\vec{k}}(\vec{r})\right)\right) &= \left(\frac{\omega(\vec{k})}{c}\right)^2 e^{i\vec{k}\cdot\vec{r}} \vec{u}_{\vec{k}}(\vec{r})\end{aligned}$$

Applying the chain rule to take the curl of the exponential term explicitly, we can move it outside of the operators and cancel from both sides:

$$\begin{aligned}(i\vec{k} + \nabla) \times \frac{1}{\epsilon(\vec{r})} (i\vec{k} + \nabla) \times \vec{u}_{\vec{k}}(\vec{r}) &= \left(\frac{\omega(\vec{k})}{c}\right)^2 \vec{u}_{\vec{k}} \\ \hat{\Theta}_{\vec{k}} \vec{u}_{\vec{k}} &= \left(\frac{\omega(\vec{k})}{c}\right)^2 \vec{u}_{\vec{k}}\end{aligned}$$

We arrive at a new Hermitian operator,  $\hat{\Theta}_{\vec{k}} \equiv (i\vec{k} + \nabla) \times \frac{1}{\epsilon} (i\vec{k} + \nabla) \times$ , which depends on the wave vector  $\vec{k}$  and operates on our periodic Bloch wave envelope,  $\vec{u}_{\vec{k}}(\vec{r})$ . After imposing the periodic constraint  $\vec{u}_{\vec{k}}(\vec{r} + \vec{R}) = \vec{u}_{\vec{k}}(\vec{r})$  and a modified transversality requirement  $(i\vec{k} + \nabla) \cdot \vec{u}_{\vec{k}}(\vec{r}) = 0$ , we can now solve for the modes of our photonic crystal by considering only a single unit cell.

As in quantum mechanics, the restriction to the finite volume of a unit cell results in quantization of the eigenvalues, yielding discrete frequency bands rather than a continuous spectrum. To construct the full dispersion diagram, one typically fixes the wave vector,  $\vec{k}$ , solves the eigenvalue equation for the lowest bands of interest, and extracts the frequencies from the eigenvalues. This process is repeated for wave vectors lying between points of high symmetry in the irreducible Brillouin zone, yielding a photonic band structure analogous to the energy-momentum diagrams for electrons in crystals.

There are a variety of methods available to discretize and solve the eigenvalue equation, including finite difference schemes (FDTD, FDFD), scattering matrix methods (such as the CAMFR implementation), and the finite element method (FEM). But considering the periodic nature of  $\vec{u}_{\vec{k}}$  and its original construction from a Fourier series, using a plane wave expansion (PWE) is perhaps the most natural choice. Here, the vector  $\vec{u}_{\vec{k}}$  is represented by its Fourier coefficients. The

periodic constraint is automatically satisfied, while transversality can be intrinsically enforced by an intelligent choice of unit vectors for the expansion [157]. Care must be taken when truncating the basis, however, to avoid artifacts and poor solution convergence resulting from abrupt changes in the dielectric function at interfaces. An effective solution is to apply an anisotropic averaging of the dielectric, based on the effective electromagnetic boundary conditions for each field component [156, 180].

Once discretized, standard linear algebra techniques may be used to perform the operator inversion. To avoid excessive memory consumption, a block-iterative method can be used to solve the eigenvalue equation by applying the  $\hat{\Theta}_{\vec{k}}$  operator rather than storing the full matrix and inverting directly [157]. Fortunately in the case of a plane wave expansion, the  $(i\vec{k} + \nabla) \times$  operations can be applied analytically as a simple multiplication. Along with a Fourier transform and its inverse, this is all that is required for evaluation of the  $\hat{\Theta}_{\vec{k}}$  operator. These steps can be readily accomplished by a typical workstation for moderately sized data sets. Although greater computational resources would be desirable to study parameter variations, this still enables band structure calculations on a desktop computer, including the simulation of three dimensional unit cells at modest resolution.

One significant disadvantage to the PWE method is the use of a uniform grid. Often, one wishes to study the effects of structural perturbations which are far sub-wavelength in magnitude and smaller than reasonable dimensions for a uniform voxel. Although careful averaging of the dielectric function can yield decent estimates, there are instances where the ability to precisely locate interfaces is desirable, such as accurately extracting the field around nanoparticles. Additionally, the uniform grid often dedicates excessive resources to low-index claddings, which would not otherwise require the same resolution as the core structure. For example, in order to simulate structures without symmetry in a transverse direction such as a 2D photonic crystal slab, the cladding regions must be large enough to allow the evanescent field to decay adequately before reaching the boundary. This typically increases the transverse dimensions by several lattice constants, exacerbating the trade-off between resolution and computational resources. In such instances, alternative discretization schemes which support more flexible meshes may be useful, such as the finite element method

(FEM). For any method, care must again be taken to enforce the transversality constraint and ensure periodicity.

The eigenproblem described above typically provides the easiest way to calculate the band structure, but there are notable exceptions. Because the operator is Hermitian, the purely real eigenvalue spectrum implies that the solutions represent guided modes. This is generally sufficient, providing the phase and group velocities in guided modes, the field profile, and the wavelength range over which a photonic crystal mirror is effective. In order to study the depth of penetration into the mirror, however, we need to solve for the decaying modes within the band gap. Clearly, optimizing this decay rate will be critical to minimizing the mode volume in a photonic crystal cavity. Highly dispersive materials pose other challenges under this formulation. Because the frequency is not known *a priori*, the operator must be constructed by first estimating the appropriate wavelength. This estimate is used to calculate an approximate permittivity at the given wave vector. After solving for the eigenvalue, the resulting frequency is used to reconstruct the operator with a new permittivity. Accurate solutions require iterating this process until one achieves sufficient frequency convergence.

We can address both problems by rearranging the eigenvalue equation. Instead of selecting the wave vector, we can choose to specify the frequency and the wave vector's direction (potentially with an offset). This immediately fixes our permittivity, regardless of dispersion, and allows us to solve for decaying modes by selecting a frequency within the photonic band gap. If we write our wave vector  $\vec{k} = \vec{k}_o + \kappa\vec{k}_d$ , where  $\vec{k}_o$  represents the offset wave vector,  $\vec{k}_d$  the unit vector in the direction of our search, and  $\kappa$  its magnitude:

$$\hat{\Theta}\vec{H} = \left(\frac{\omega}{c}\right)^2 \vec{H}$$

$$(i\vec{k}_o + i\kappa\vec{k}_d + \nabla) \times \frac{1}{\epsilon}(i\vec{k}_o + i\kappa\vec{k}_d + \nabla) \times \vec{u} = \left(\frac{\omega}{c}\right)^2 \vec{u}$$

$$\left( \begin{array}{c} (i\vec{k}_o + \nabla) \times \frac{1}{\epsilon}(i\vec{k}_o + \nabla) \times \\ - \left(\frac{\omega}{c}\right)^2 \end{array} \right) \vec{u} = \left( \begin{array}{c} -i \kappa \vec{k}_d \times \frac{1}{\epsilon}(i\vec{k}_o + \nabla) \times \\ -i \kappa (i\vec{k}_o + \nabla) \times \frac{1}{\epsilon}\vec{k}_d \times \\ + \kappa^2 \vec{k}_d \times \frac{1}{\epsilon}\vec{k}_d \times \end{array} \right) \vec{u}$$

The transformation comes at a price: our system is now a generalized eigenvalue problem, and the equation is quadratic rather than linear. One typically linearizes the equation by writing it in a companion form with expanded eigenvectors  $\vec{v} \equiv (\vec{u}, \kappa\vec{u})$ , which imposes slight additional computational requirements. Our eigenvalues are potentially complex now, with the imaginary components of  $\vec{k}$  representing exponential decay for modes within the band gap. The solutions to this formulation are also highly redundant. In the original formulation, each eigenvalue of  $\hat{\Theta}_{\vec{k}}$  corresponded to a different band. This allows the use of optimized solvers which can return multiple eigenvalue/eigenvector pairs at minimal additional cost. For the fixed- $\omega$  approach, however, additional solutions are merely duplicates in another Brillouin zone. To retrieve a full band structure, we now have to sweep both a large range of frequencies and the relevant set of  $\vec{k}$  vector offsets and directions to span the irreducible Brillouin zone. As such, the  $\hat{\Theta}_{\vec{k}}$  formulation is usually preferred.

To simulate the majority of our band structures, we use the freely-available MIT Photonics Band (MPB) package from Steven Johnson's group at MIT [157], which provides an excellent implementation of the PWE method with anisotropic smoothing, full use of symmetry, and is easily scripted. In cases where we require a different operator formulation, for example to examine evanescent modes within the gap, we have explored the use of custom weak-form FEM implementations in COMSOL [60] and the dealII libraries [16], scattering matrix analysis with CAMFR [36], as well as custom PWE solvers in Matlab and python. Due to the ease of structure modeling, solver selection, and post analysis, the COMSOL implementation has proven the most versatile.

### 3.2.2 Gap characteristics

Using the formalism described in the previous section, we can now calculate band diagrams, analyze mode patterns and determine the behavior of arbitrary photonic crystals. For all but the most basic bi-layer stack, however, we must resort to numerical solutions. It is therefore helpful to begin with this simple case. After examining the analytic results available for a 1D stack, we will extend our discussion to higher dimensions.

Consider a simple system with 1D periodicity in the  $\hat{x}$  direction. We have lattice constant  $a$ , reciprocal lattice constant  $b = 2\pi/a$ , wave vector  $\vec{k} = k_x = k$ , dielectric  $\epsilon_r(x + m * a) = \epsilon_r(x)$ , impermeability  $\eta = 1/\epsilon_r$ , and magnetic field  $\vec{H} = \hat{y}u(x)e^{ikx}$  with  $u(x + m * a) = u(x)$ . Since  $u$  and  $\eta$  are periodic on the lattice, we expand these as Fourier series and plug into our master equation:

$$\begin{aligned}
\left(\frac{\omega}{c}\right)^2 \hat{y} \left( \sum_{q=-\infty}^{\infty} C_q e^{iqbx} \right) e^{ikx} &= \nabla \times \left( \sum_{l=-\infty}^{\infty} \eta_l e^{ilbx} \right) \nabla \times \left( \hat{y} \sum_{m=-\infty}^{\infty} C_m e^{imbx} \right) e^{ikx} \\
&= i \nabla \times \left( \sum_{l=-\infty}^{\infty} \eta_l e^{ilbx} \right) \left( \hat{z} \sum_{m=-\infty}^{\infty} (mb + k) C_m e^{imbx} \right) e^{ikx} \\
&= i \nabla \times \left( \hat{z} \sum_{l=-\infty}^{\infty} \sum_{m=-\infty}^{\infty} (mb + k) \eta_l C_m e^{i(l+m)bx} \right) e^{ikx} \\
&= \hat{y} \left( \sum_{l,m=-\infty}^{\infty} (mb + k)((l+m)b + k) \eta_l C_m e^{i(l+m)bx} \right) e^{ikx}
\end{aligned}$$

We can now drop the  $e^{ikx}$  from both sides, and equate terms of the same periodic order to arrive at a set of algebraic equalities. With  $l = q - m$ :

$$\left(\frac{\omega}{c}\right)^2 C_q = \sum_{m=-\infty}^{\infty} (mb + k)(qb + k) \eta_{q-m} C_m$$

If we pull the  $m = q$  term out of the sum and move to the other side:

$$\left( \left(\frac{\omega}{c}\right)^2 - (qb + k)^2 \eta_0 \right) C_q = \sum_{m \neq q} (mb + k)(qb + k) \eta_{q-m} C_m$$

calling our average refractive index  $\bar{n} = 1/\sqrt{\eta_0}$  :

$$C_q = \sum_{m \neq q} \frac{(mb+k)(qb+k)}{\left(\frac{\bar{n}\omega}{c}\right)^2 - (qb+k)^2} \frac{\eta_{q-m}}{\eta_0} C_m$$

The coupling between different harmonics is large whenever  $\bar{n}\omega/c \approx |qb+k|$ . As an equality, this would be the dispersion relation for plane waves in a medium with refractive index  $\bar{n}$ , repeated every reciprocal lattice vector. The solutions for successive reciprocal lattice vectors enter the first Brillouin zone at progressively higher frequencies. Due to the equivalence of these solutions, this results in the appearance of the bands folding at the Brillouin zone edges. At precisely these points, the two solutions must be equal and the curves appear to cross. These intersections represent a strong interaction between modes of different spatial frequencies, coupled by the periodicity of the lattice. It is this mixing of forward and backward modes which results in the opening of a band gap. At precisely the Brillouin zone boundary, equal contributions of these modes will cause the field to resemble a standing wave, giving certain characteristics to the bands immediately above and below the band gap. We will return to discuss these shortly.

For the case of weak periodicity (either small dielectric contrast or only a thin perturbation), we can approximate our solution in the vicinity of an intersection by considering only two terms. For the lowest order band, we use the crossing of the forward-propagating  $q = 0$  mode and the backwards  $q = -1$  mode; higher band gaps yield similar results for  $q = 0, -N$ .

$$C_0 \approx \frac{(k-b)k}{\left(\frac{\bar{n}\omega}{c}\right)^2 - k^2} \frac{\eta_1}{\eta_0} C_{-1}$$

$$C_{-1} \approx \frac{k(k-b)}{\left(\frac{\bar{n}\omega}{c}\right)^2 - (k-b)^2} \frac{\eta_{-1}}{\eta_0} C_0$$

Because  $\epsilon$  is real,  $\eta_m = \eta_{-m}^*$ . Substituting  $C_{-1}$  and rearranging, we get:

$$\left( \left( \frac{\bar{n}\omega}{c} \right)^2 - (k-b)^2 \right) \left( \left( \frac{\bar{n}\omega}{c} \right)^2 - k^2 \right) = \frac{|\eta_1|^2}{\eta_0^2} k^2 (k-b)^2$$

The intersection occurs at the edge of the first Brillouin zone, where  $k = b/2$ . After plugging this

in, we can solve for  $\omega$  on either side of the band gap:

$$\begin{aligned} \left( \left( \frac{\bar{n}\omega}{c} \right)^2 - \left( \frac{b}{2} \right)^2 \right)^2 &= \frac{|\eta_1^2|^2}{\eta_0^2} \left( \frac{b}{2} \right)^4 \\ \left( \frac{\bar{n}\omega}{c} \right)^2 - \left( \frac{b}{2} \right)^2 &= \pm \frac{|\eta_1^2|}{\eta_0} \left( \frac{b}{2} \right)^2 \\ \omega_{\pm} &= \omega_B \sqrt{1 \pm \frac{|\eta_1|}{\eta_0}} \\ \text{with } \omega_B &= \frac{\pi c}{a \bar{n}} \end{aligned}$$

We find that our band gap is roughly centered about the Bragg frequency  $\omega_B$  for the average dielectric.

Since we can easily change this frequency by scaling our coordinates, the absolute difference  $\Delta\omega = \omega_+ - \omega_-$  is not particularly useful in quantifying the band gap. Instead, the “size” of the band gap is typically reported as the ratio between the gap itself and the midgap frequency,  $\Delta\omega/\omega_m$ . With this in mind, we see that our gap will vary as  $\Delta\omega/\omega_m \approx |\eta_1|/\eta_0$ . This represents the most important conclusion we can draw about designing photonic crystals: the size of the gap tends to grow with increasing dielectric contrast.

Our approximation of weak perturbations and the dependence of the result on Fourier coefficients present difficulties in obtaining further insight for arbitrary structures. Fortunately, however, it is easy to obtain general analytic results for the simple bi-layer stack using scattering matrix analysis. We consider light striking the interface between two media at normal incidence, for which we only need to account for the forward and backward propagating modes in each material. Let  $U_m^{\pm}$  represent the field amplitudes at a transverse plane  $m$ . We can expand the coupling between the fields at planes 1 and 2 using a scattering matrix  $\mathbf{S}$  as:

$$\begin{pmatrix} U_2^+ \\ U_1^- \end{pmatrix} = \begin{pmatrix} t_{12} & r_{21} \\ r_{12} & t_{21} \end{pmatrix} \begin{pmatrix} U_1^+ \\ U_2^- \end{pmatrix}$$

where  $t_{12}$  and  $r_{12}$  represent the (potentially complex) coefficients of transmission and reflection for a field originating at plane 1 and either exiting at plane 2, or reflecting from the system. While this form has intuitive appeal, it is cumbersome to apply to systems with multiple scattering. By rearranging so that  $U_2$  appears entirely on the left, however, we can cascade subsequent scattering

using simple matrix multiplication:

$$\begin{pmatrix} U_2^+ \\ U_2^- \end{pmatrix} = \mathbf{M} \begin{pmatrix} U_1^+ \\ U_1^- \end{pmatrix}$$

or in general:

$$\begin{pmatrix} U_{N+1}^+ \\ U_{N+1}^- \end{pmatrix} = \mathbf{M}_N \mathbf{M}_{N-1} \cdots \mathbf{M}_1 \begin{pmatrix} U_1^+ \\ U_1^- \end{pmatrix}$$

For scattering at an interface (or through a system in general), we find:

$$\begin{pmatrix} U_2^+ \\ U_2^- \end{pmatrix} = \frac{1}{t_{21}} \begin{pmatrix} t_{12}t_{21} - r_{12}r_{21} & r_{21} \\ -r_{12} & 1 \end{pmatrix} \begin{pmatrix} U_1^+ \\ U_1^- \end{pmatrix}$$

while propagation through a uniform dielectric simply acquires a phase difference:

$$\begin{pmatrix} U_2^+ \\ U_2^- \end{pmatrix} = \begin{pmatrix} e^{i\phi} & 0 \\ 0 & e^{-i\phi} \end{pmatrix} \begin{pmatrix} U_1^+ \\ U_1^- \end{pmatrix}$$

with  $\phi = n\omega d/c$  for index  $n$ , frequency  $\omega$  and distance  $d$ .

The powers at a given plane  $m$  will be proportional to  $|U_m^\pm|^2$ , where the proportionality depends on the dielectric constant. If we consider a single unit cell in our stack, the system begins and ends in media with the same refractive index, allowing these quantities to be compared directly. The restriction to real  $\epsilon$  implies that the system is lossless. Conservation of power then requires  $|U_1^+|^2 + |U_2^-|^2 = |U_2^+|^2 + |U_1^-|^2$ , or equivalently, a unitary  $\mathbf{S}$  matrix,  $\mathbf{S}^\dagger \mathbf{S} = \mathbf{1}$ . Additionally, we expect identical transmission and reflection for the forward and backward directions, due to the system's reciprocal symmetry. Combining these constraints, we find:

$$\begin{aligned} t_{12} = t_{21} &\equiv t & |t|^2 + |r|^2 &= 1 \\ r_{12} = r_{21} &\equiv r & t/t^* &= -r/r^* \end{aligned}$$

Inserting these relations  $\mathbf{M}$  yields:

$$\begin{pmatrix} U_2^+ \\ U_2^- \end{pmatrix} = \begin{pmatrix} \frac{1}{t^*} & r \\ r^* & \frac{1}{t} \end{pmatrix} \begin{pmatrix} U_1^+ \\ U_1^- \end{pmatrix}$$

Our natural modes will again be Bloch waves with wave vector  $k$ . Propagation through a unit cell of length  $a$  will reproduce the incoming envelope multiplied by the Bloch wave:  $U_{m+1}^\pm = e^{ika}U_m^\pm$ .

Using this, we arrive at an eigenvalue equation:

$$\begin{pmatrix} U^+ \\ U^- \end{pmatrix} \begin{pmatrix} \frac{1}{t^*} & r \\ r^* & \frac{1}{t} \end{pmatrix} = e^{ika} \begin{pmatrix} U^+ \\ U^- \end{pmatrix}$$

which we can be readily solved:

$$\begin{aligned} e^{ika} &= \operatorname{Re} \left[ \frac{1}{t} \right] \pm \sqrt{\operatorname{Re} \left[ \frac{1}{t} \right]^2 - 1} \\ &= \operatorname{Re} \left[ \frac{1}{t} \right] \pm i \sqrt{1 - \operatorname{Re} \left[ \frac{1}{t} \right]^2} \end{aligned}$$

When  $\operatorname{Re}[1/t]^2 \leq 1$ , the second term on the right is purely imaginary, and we get  $|e^{ika}|^2 = (\operatorname{Re}[1/t])^2 + (1 - \operatorname{Re}[1/t]^2) = 1$ . These solutions correspond to propagating modes, with a phase shift given by the purely real  $k$  and no attenuation. This yields our dispersion relation:

$$\cos(ka) = \operatorname{Re} \left[ \frac{1}{t} \right]$$

Let our bilayer stack consist of indices  $n_1$  and  $n_2$  with thicknesses  $d_1 + d_2 = a$ . Propagation through each material will accumulate a phase  $\phi_i = 2\pi n_i d_i / \lambda = n_i k_0 d_i = n_i \omega d_i / c$ , while Fresnel reflection at the interfaces will give  $t_{ij} = 2n_i / (n_i + n_j)$  and  $r_{ij} = (n_i - n_j) / (n_i + n_j)$ . Entering these into our sequence of  $\mathbf{M}$  matrices, the dispersion relation becomes:

$$\cos(ka) = \frac{(n_1 + n_2)^2 \cos(\phi_1 + \phi_2) - (n_1 - n_2)^2 \cos(\phi_1 - \phi_2)}{4n_1 n_2}$$

The second term represents a phase matching condition. In the special case where  $\phi_1 = \phi_2$ , the reflected waves at the midgap frequency are exactly out of phase after a round trip within each layer. As a result, perfect destructive interference occurs, which maximizes the band gap and rate

of decay within the crystal.

We can achieve this phase matching by selecting  $d_1 = n_2 a / (n_1 + n_2)$  and  $d_2 = n_1 a / (n_1 + n_2)$ . The average dielectric is then  $\bar{n} \equiv (n_1 d_1 + n_2 d_2) / a = 2n_1 n_2 / (n_1 + n_2)$ , yielding a midgap frequency at the Bragg frequency,  $\omega_B = \pi c / a \bar{n}$ . The equivalent free-space wavelength is  $\lambda = 4a n_1 n_2 / (n_1 + n_2)$ , corresponding to layer thicknesses which are exactly one quarter wave. Substituting  $\omega = \omega_B \pm \Delta\omega / 2$  and solving at the edge of the Brillouin zone ( $k = \pi / a$ ), we find

$$-1 = \frac{(n_1 + n_2)^2 \cos\left(\pi \pm \pi \frac{\Delta\omega}{2\omega_B}\right) - (n_1 - n_2)^2}{4n_1 n_2}$$

$$\cos\left(\pi \frac{\Delta\omega}{2\omega_B}\right) = \frac{8n_1 n_2}{(n_1 + n_2)^2} - 1$$

Using  $\sin^2 \theta = (1 - \cos 2\theta) / 2$ :

$$\sin^2\left(\frac{\pi \Delta\omega}{4 \omega_B}\right) = 1 - \frac{4n_1 n_2}{(n_1 + n_2)^2}$$

$$= \frac{(n_1 - n_2)^2}{(n_1 + n_2)^2}$$

$$\frac{\Delta\omega}{\omega_B} = \frac{4}{\pi} \sin^{-1}\left(\frac{|n_1 - n_2|}{n_1 + n_2}\right)$$

For the case of a quarter wave stack, we have now precisely quantified the band gap, and again find that it grows with increasing dielectric contrast. The maximum attenuation can be found when  $\omega = \omega_B$ . Plugging this in yields:

$$\begin{aligned}
\operatorname{Re} \left[ \frac{1}{t} \right] &= -\frac{n_1^2 + n_2^2}{2n_1n_2} \\
e^{ika} &= \operatorname{Re} \left[ \frac{1}{t} \right] \pm \sqrt{\operatorname{Re} \left[ \frac{1}{t} \right]^2 - 1} \\
&= -\frac{n_1^2 + n_2^2}{2n_1n_2} \pm \sqrt{\frac{(n_1^2 + n_2^2)^2}{4n_1^2n_2^2} - 1} \\
&= -\frac{n_1^2 + n_2^2}{2n_1n_2} \pm \sqrt{\frac{n_1^4 + n_2^4 - 2n_1^2n_2^2}{4n_1^2n_2^2}} \\
&= -\frac{n_1^2 + n_2^2}{2n_1n_2} \pm \sqrt{\frac{(n_1^2 - n_2^2)^2}{4n_1^2n_2^2}} \\
&= -\frac{n_1^2 + n_2^2 \mp |n_1^2 - n_2^2|}{2n_1n_2} \\
&= -\left(\frac{n_1}{n_2}\right)^{\mp 1}
\end{aligned}$$

The two eigenvalues correspond to forward and backward propagation; the correct choice of exponent yields a magnitude  $\leq 1$ . If we choose  $n_L \leq n_H$ , we conclude that:

$$k = \frac{\pi + i \log \left( \frac{n_H}{n_L} \right)}{a}$$

or simply that the amplitude of wave in the center of the band gap decays by a factor  $\frac{n_L}{n_H}$  every unit cell. The decay parameter is maximized near the center of the gap and decreases smoothly towards the edge of the band gap. The functional form is somewhat complicated and is often Taylor expanded as a quadratic, although this tends to underestimate the decay. Nevertheless, it is clear that our ability to use higher dielectric contrast and operate near the center of the gap will have a profound effect on field confinement, and is crucial to minimizing the mode volume.

In order to fully describe the structure, we need to examine off-axis propagation as well. Doing so, the degeneracy between polarizations is broken and we must treat the TE and TM modes separately. For the case of TM modes, we can quickly conclude that *some* propagating mode must exist in a 1D stack at all frequencies, given the lack of reflection at the Brewster angle. Even in the case of TE light, however, the structure lacks a complete band gap, where no propagating modes exist for all combinations of  $\vec{k}_{\parallel}$  and  $\vec{k}_{\perp}$ . Although all 1D stacks will support a band gap for normal propagation, it is only an *incomplete* band gap due to the lack of structures which can coherently scatter the light

at greater angles of incidence.

Despite this absence of a complete gap, it is worth noting that 1D stacks can still exhibit omnidirectional reflection. For light originating from outside the material, only  $\vec{k}$  vectors above the light line are accessible. As long as the stack is composed of materials with higher index than the surrounding medium, the Brewster angle between stack layers can exist below the light line and the band gap can extend throughout the light cone. Without any propagating modes to couple to, the light is perfectly reflected. Unfortunately, the same cannot be said for light originating within an incomplete band gap medium. For any frequency, radiating modes will always exist within the light cone to which the guided modes can couple. Consequently, any cavity designed within an incomplete band gap is inevitably leaky. This imposes limitations on how abruptly a cavity can be terminated, creating a fundamental trade-off between quality factor and mode volume which we will discuss later.

On a more general note, the independent behavior of the two polarizations must be considered with some care when designing a practical device. While higher-dimensional structures cannot usually be separated into purely TE and TM modes, additional symmetries such as a mirror plane can result in clearly dominant electric or magnetic components, with modes which can be classified by whether they exhibit positive or negative parity. Due to the orientation dependence of the boundary conditions, each polarization can experience a different amount of coherent scattering within the same structure. This generally results in unique band characteristics and gap ranges for each polarization, including cases where band gaps exist for one polarization but not the other. In an ideal structure, these polarizations cannot couple due to their different parity. However, any perturbations which break the symmetry — such as a mismatched substrate or fabrication anomalies — can cause the modes to mix. If the band gaps do not overlap, this results in an additional leakage channel. We will revisit this shortly.

### 3.2.3 Mode characteristics

We now examine some general properties of the guided modes. As in quantum mechanics, the eigenfunctions of our system operator correspond to the solutions which minimize the energy. Through the variational theorem, the fundamental mode will minimize the energy functional overall, with each higher order solution minimizing the successively remaining orthogonal subspace.

It is straightforward to show that eigenmodes of  $\hat{\Theta}$  will indeed minimize the normalized energy functional:

$$U(\vec{H}) = \frac{(\vec{H}, \hat{\Theta}\vec{H})}{(\vec{H}, \vec{H})}$$

where  $(a, b)$  represents the inner product between vectors  $a$  and  $b$ . Rewriting in terms of  $\vec{E}$ , we find:

$$\begin{aligned} U(\vec{E}) &= \frac{(\nabla \times \vec{E}, \nabla \times \vec{E})}{(\vec{E}, \epsilon \vec{E})} \\ &= \frac{\int |\nabla \times \vec{E}|^2 \partial r^3}{\int \epsilon |\vec{E}|^2 \partial r^3} \end{aligned}$$

Examining the energy functional further, we can determine several qualitative aspects of the mode profiles which are consistent with its minimization. Due to the  $\nabla \times$  terms in the numerator, the modes should exhibit minimal spatial fluctuations. This is analogous to trends in (quantum) mechanics, where successively higher modes contain additional nodes in the solution. From the denominator, we conclude that modes can lower their energy by maximizing the confinement in high- $\epsilon$  regions. The fundamental mode will thus reside primarily in the high index regions and be relatively smooth. Orthogonality of the solutions results in the appearance of additional nodes for higher bands, forcing the field out of the high index and increasing overlap with the cladding.

As previously discussed, one usually strives to maximize the band gap of a photonic crystal. This serves to minimize the mode volume in a cavity (by increasing the rate of evanescent decay within the crystal and thus spatial confinement) while increasing the range of operating frequencies

for devices like dielectric mirrors. To accomplish this, photonic crystals are typically fabricated in high-index semiconductors surrounded by air, which maximizes the dielectric contrast. Based on the energy confinement trends, the electric field shows greater confinement to the semiconductor for bands below the gap, while bands above the gap exhibit greater overlap with the cladding region. For this reason, these are often referred to as the semiconductor band and air band, respectively, analogous to the valence and conduction band in electronic band structures.

The degree to which energy is contained within the dielectric can be quantified by the confinement factor:

$$\frac{\int_{\text{dielectric}} \epsilon(\vec{r}) |\vec{E}(\vec{r})|^2 \partial^3 \vec{r}}{\int \epsilon(\vec{r}) |\vec{E}(\vec{r})|^2 \partial^3 \vec{r}}$$

For a given wave vector, comparing the confinement factor between consecutive bands gives an indication as to the energy splitting between the modes. Although a full band diagram is necessary to completely characterize the band gap, greater differences in confinement are commensurate with larger band gaps, providing a qualitative means for evaluating structures. This also yields intuition about why certain structures yield greater gaps, which is particularly useful in understanding the differences between TE and TM modes. An excellent discussion of TE/TM gaps in 2D structures may be found in [153], which concludes with the rule of thumb, “TM band gaps are favored in a lattice of isolated high- $\epsilon$  regions, and TE band gaps are favored in a connected lattice.”

### 3.2.4 Defects

The cavity itself is created by introducing a defect into the crystal. Due to the broken translational symmetry, the structure no longer exhibits a photonic band gap, allowing frequencies within the gap to propagate. Moving further away, however, the crystal appears to be essentially undisturbed. Intuitively, these surrounding regions should still support the coherent scattering which gives rise to the band gap. It follows that light within the band gap cannot propagate through the surrounding crystal, and remains trapped within the defect region. Although overly simplistic, this is analogous

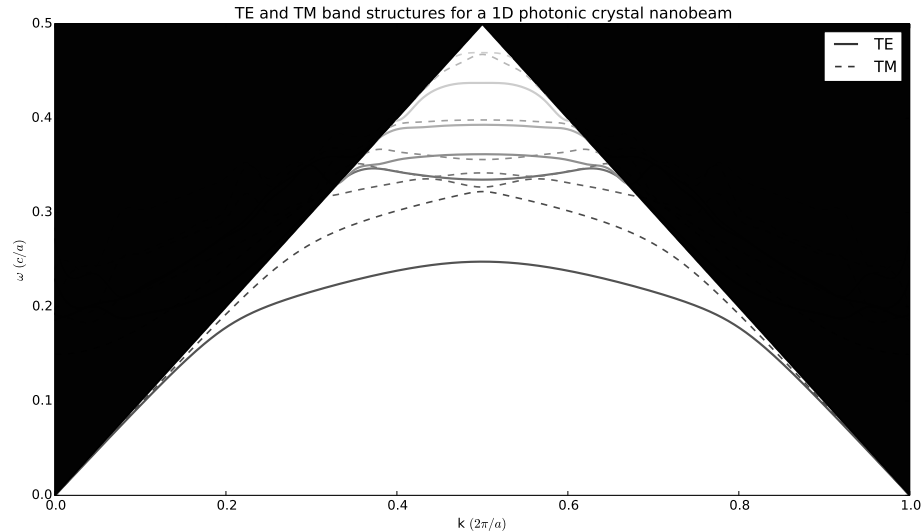


Figure 3.1: Comparison between TE and TM photonic band structures in a 1D nanobeam. A large (30%) band gap exists between the lowest TE bands, while a more complex TM band structure eliminates gaps between the lowest bands, and shows only small gaps between higher modes (with smaller  $k$ -space margin). The lowest TE bands have nearly twice the difference in E-field confinement factor as the lowest TM, indicative of the energy splitting between these pairs. The lack of large, overlapping band gaps makes TE-TM coupling (due to fabrication imperfections or asymmetries) a problem for maintaining confinement and quality factor.

to light being trapped between the reflectors in a Fabry-Perot resonator. In our case, the photonic crystal serves as a distributed mirror.

Any perturbation which disrupts the translational symmetry can act as a defect. This can be accomplished by merely shifting a feature, although it more frequently involves the addition or removal of dielectric material: changing the radius of a hole or rod, modifying a layer thickness, tapering a waveguide width, stretching the lattice constant or varying the local refractive index. For small changes, we may consider the disturbance perturbatively. Consider a slight variation in our permittivity,  $\epsilon'(\vec{r}) = \epsilon(\vec{r}) + \Delta\epsilon(\vec{r})$ , where  $\Delta\epsilon(\vec{r}) \ll \epsilon(\vec{r})$ . Applying perturbation theory to our wave equation and discarding second-order terms and higher, we find:

$$\frac{\Delta\omega}{\omega} = -\frac{1}{2} \frac{\int \Delta\epsilon(\vec{r}) |\vec{E}(\vec{r})|^2 \partial^3 \vec{r}}{\int \epsilon(\vec{r}) |\vec{E}(\vec{r})|^2 \partial^3 \vec{r}}$$

In the case of shifting boundaries between high-contrast regions, Johnson *et al.* emphasize the need to reformulate this slightly to accommodate the appropriate boundary conditions for each component

of the electric field [156].

For now, we'll consider a simple constant change in refractive index, which is  $\Delta n$  over a particular material and zero elsewhere. Expanding  $\epsilon' = (n + \Delta n)^2 \approx n^2 + 2n\Delta n$ , we can substitute  $\Delta\epsilon \approx 2n\Delta n = 2\epsilon\frac{\Delta n}{n}$ . Our frequency shift becomes:

$$\frac{\Delta\omega}{\omega} \approx -\frac{\Delta n}{n} \frac{\int_{\Delta} \epsilon(\vec{r}) |\vec{E}(\vec{r})|^2 \partial^3 \vec{r}}{\int \epsilon(\vec{r}) |\vec{E}(\vec{r})|^2 \partial^3 \vec{r}}$$

or simply that the fractional change in frequency is equal to the fractional change in index weighted by the energy confinement in the perturbed region, but opposite in sign. When the refractive index is lowered or we remove material, the wavelength in the material increases. To balance this, the frequency must therefore increase in order to maintain the same mode profile. Similarly, additional or higher dielectric material will reduce the frequency. We may use this result to quantify the response of refractive index sensors, include material nonlinearities, as well as understand the effects of small imaginary components of the refractive index, corresponding to material loss or gain.

The result also yields valuable insight into the characteristics of defect states. Removing dielectric material, for example by increasing a hole radius or decreasing the local lattice parameter, requires an increase in frequency. This tends to pull a state up from the semiconductor band, creating a localized state within the gap. Similarly, additional dielectric material — filling in a hole for example — will pull states down from the air band. In the process, the resulting defect states inherit their overall characteristics and symmetry from the bands of origin. For example, given a gap between the lowest two bands, a cavity formed by removing dielectric material will show monopole traits, while the addition of material will result in modes with an increasing number of nodal planes for larger perturbations. This is analogous to the introduction of impurities into semiconductors, where the ionization energy determines whether the dopant acts as an electron donor or acceptor. Cavity modes in photonic crystals are often referred to as donor or acceptor modes for precisely this reason [382]. Clearly, appropriate selection of the type of defect is critical in optimizing the energy confinement within the cavity.

Precise tuning of the resonance frequency can be accomplished by varying the amount of perturbation. In a Fabry-Perot resonator, for example, one adjusts the mirror separation, with the

resonant wavelengths varying in proportion to the cavity length. Due to the evanescent extent of the mode, distributed reflections, and complex field patterns, the relationship in photonic crystals is more complex and most easily verified by simulation. The general trends still follow the perturbative results above, however, with greater defects tending to push the mode further into the band gap.

When designing the defect, we have several important considerations. First, we must decide what type of defect to use, based on the desired field confinement. Acceptor modes concentrate most of the mode within the semiconductor core, exhibiting greater confinement. Perhaps most significantly, this results in a higher electric-field overlap with emitters contained within the core, such as embedded quantum dots or quantum well layers. For most structures, this also means the electric field maximum of acceptor modes is away from the interfaces. In realistic devices, rough surfaces due to lithographic line edge roughness or otherwise induced during the etching process can result in significant scattering, one of the primary losses responsible for low quality factors. Additional absorption due to unterminated surface states or adsorbed impurities can further degrade the cavity. By pulling the mode away from the edges, acceptor modes help minimize these loss channels. By contrast, donor modes tend to exhibit greater overlap with the cladding, which would be preferable for interaction with single gas-phase atoms or for use as refractive index sensors. Beyond the selection of donor and acceptor modes, the precise form of the defect may be used to break the symmetry between degenerate modes or optimize out coupling from the cavity [165].

The remaining major design choice lies in the strength of the perturbation. Because the field's decay rate into the surrounding crystal is greatest for frequencies near the center of the band gap, it is desirable to obtain a resonance as far from the band edges as possible. This encourages the use of a greater defect, in order to minimize the mode volume by pushing the cavity mode deep within the gap. Unfortunately, greater perturbations also induce significantly higher scattering, imposing a fundamental trade-off between the cavity quality factor and mode volume.

### 3.2.5 Tapers

So far, our analysis has essentially focused on how to minimize the mode volume. In short, high contrast materials and wavelength-scale periodicity serve to maximize the band gap, allowing a localized state near the middle of the gap to experience rapid decay within the crystal. However, we have mostly neglected to discuss the other major factor in our cavity's figure of merit. Although abrupt introduction of a defect can succeed in creating such a cavity, the quality factor will most likely be moderately low.

To understand this, we consider the potential sources of energy loss from the cavity. These include scattering losses ( $Q_{sc}$ ), material absorption ( $Q_{ab}$ ), leakage through the mirrors ( $Q_{\parallel}$ ), and potentially, coupling to radiation modes in the substrate and cladding ( $Q_{\perp}$ ). The total  $Q$  becomes  $Q^{-1} = Q_{sc}^{-1} + Q_{ab}^{-1} + Q_{\parallel}^{-1} + Q_{\perp}^{-1}$ . As the mode will decay exponentially in the mirror regions,  $Q_{\parallel}$  can be made arbitrarily high by adding additional photonic crystal layers, at least in theory (challenges in coupling and fabrication imperfections impose practical limits). Neglecting  $Q_{sc}$  and  $Q_{ab}$  for now, this leaves leakage into the cladding as the limiting factor on  $Q$ .

Because three-dimensional photonic crystals can support complete photonic band gaps, extending over wave vectors in *all* directions, the transverse coupling is only limited by fabrication imperfections. Due to fabrication and integration challenges, however, lower-dimensional structures are typically used, such as 2D photonic crystal slabs and 1D nanobeams. In these instances, confinement in the transverse directions relies on index guiding. Without periodic structures to provide coherent back reflections, the band gap is inevitably incomplete and permits radiation modes within the light cone defined by  $|\vec{k}_{\parallel}| \leq (n_{clad})\omega/c$ . By definition, guided modes must lie outside this region, so at first glance, this might not raise much concern. Certainly, there is incentive to remain as far away from this limit as possible. Waves with greater  $|\vec{k}_{\parallel}|$  will decay more rapidly into the cladding, for example. But even as modes approach the light line, they should not couple to radiation modes as long as  $|\vec{k}_{\parallel}| > (n_{clad})\omega/c$ .

The caveat is that the structure must remain unperturbed. Because the introduction of the defect breaks the translational symmetry, the cavity itself will scatter portions of the mode into

the light cone. In cases with negligible material absorption and perfect fabrication, this finite  $Q_{\perp}$  imposes a fundamental upper bound on the cavity quality. The degree to which the mode leaks into the cladding can be quantified by considering the mode pattern immediately above the cavity. By examining its Fourier transform, we can calculate these losses and determine the radiative limit on  $Q$  [361]. Explicitly,

$$P_{\hat{z}^+} = 2 \frac{\eta}{8\lambda^2 k_0^2} \int \int_{|\vec{k}_{\parallel}| \leq k_0} d\vec{k} \left( |FT_2(\vec{H}_{\hat{x}})|^2 + |FT_2(\vec{H}_{\hat{y}})|^2 + \frac{1}{\eta^2} |FT_2(\vec{E}_{\hat{x}})|^2 + \frac{1}{\eta^2} |FT_2(\vec{E}_{\hat{y}})|^2 \right)$$

$$Q_{\hat{z}^+} = \omega \frac{W_{\hat{z}^+}}{P_{\hat{z}^+}}$$

where  $\eta = \sqrt{\frac{\mu_0}{\epsilon_0}}$ ,  $k_0 = 2\pi/\lambda$ ,  $P_{\hat{z}^+}$ ,  $W_{\hat{z}^+}$ , and  $Q_{\hat{z}^+}$  represent the radiative power loss, total energy, and resulting quality factor in the upper half-plane for the  $\hat{z}$  direction, and  $FT_2$  is the two-dimensional Fourier transform of the given field component, taken just above the cavity in the  $\hat{x} - \hat{y}$  plane. Our total radiative  $Q_{\perp}$  would be the combination of the lower- and upper half-plane contributions:

$$Q_{\perp}^{-1} = Q_{\hat{z}^+}^{-1} + Q_{\hat{z}^-}^{-1}.$$

Having recognized this relationship, it was quickly realized that cavities could be optimized by suppressing modal components within the light cone. First proposed analytically [361, 333] and demonstrated experimentally shortly afterwards [2], this technique represents the most significant advancement in photonic crystal cavity design, enabling photonic crystal cavities with qualities exceeding 1,000,000 and leading to a number of direct design and optimization techniques. In essence, the field profile consists of a sinusoid modulated by an envelope function which is determined by the cavity structure. The Fourier transform of the mode represents the convolution of these two contributions. In order to minimize overlap with the light cone, two requirements should be met. First, the carrier wave should localize the wave far from the light cone by maximizing its spatial frequency. This corresponds to a  $\vec{k}_{\parallel}$  as far from the  $\Gamma$  point as possible [80], or intuitively, maximizing the guided mode's effective index. Equivalently, a larger  $|\vec{k}_{\parallel}|$  provides greater margin between the mode and the light cone, which tolerates additional dispersion by the modulating envelope before it couples to radiating modes. Ideally, we should utilize a gap between the lowest two bands, pulling

in a mode at the edge of the Brillouin zone.

Given this margin in Fourier space, the means to optimize the defect is fairly clear: minimize the high frequency components of the envelope in order to avoid smearing the mode into the light cone. Because rapid changes in the envelope require high spatial frequencies, we cannot abruptly introduce the defect. Instead, the crystal must be gradually modulated in order to produce a high-quality cavity [2]. The envelope is often designed to follow a Gaussian profile due to its minimal spread in Fourier space, although other spatial envelopes with localized frequencies, such as a sinc function, could be used. Practically, this can be implemented by appropriately choosing the imaginary component of the wave vector. The evanescent decay of the cavity mode into the crystal will be exponential,  $\propto e^{-qx}$ , where  $q = \text{Im}(\vec{k})$  is the imaginary part of the wave vector. In order to obtain a Gaussian field envelope  $\propto e^{-Bx^2}$ , for example, the crystal should be varied such that  $q = Bx$ . By finding the structural parameters that yield a given  $q$  at the cavity frequency, the tapering profile can be determined. Although the complex dispersion relation can be retrieved by proper formulation of the eigenproblem (see above), it is often easier to perform a Taylor expansion of the guided band near the Brillouin zone edge then use analytic continuation to extend to frequencies within the gap [343].

While a well-designed taper can almost completely avoid coupling to radiation modes, the gradual transition into the crystal allows the field to expand and increases the mode volume. This is an inevitable consequence of Fourier transforms, which implies that the spatial extent of the mode will be inversely proportional to its extent in  $k$  space. The design of the taper therefore represents a fundamental trade-off between the cavity's quality factor and mode volume. However, the effect of the taper is not balanced between the  $Q_{\perp}$  and  $V$ . For a Gaussian profile, a linear increase in  $V$  yields an exponential increase in  $Q_{\perp}$  [80]. Thus in order to maximize  $Q/V$ , one would typically choose a taper which sacrifices  $V$  until  $Q_{\perp}$  is pushed beyond limits imposed by roughness or absorption.

### 3.2.6 Coupling

Once the cavity itself is optimized, we must consider how to get light into and out of the resonator. In general, this can be accomplished by either coupling directly to the free-space emission from the

cavity or by utilizing a feeding waveguide, such as a nearby dielectric or photonic crystal waveguide, or a tapered fiber probe. For testing single cavities, the simplicity of free-space resonant scattering is particularly appealing. A typical implementation involves using a microscope with crossed polarizers to block the background reflected light, providing a strong signal only for light which couples to the cavity. Because no physical contact is involved, multiple devices on a chip can be easily tested by translating the stage. The cavities themselves do not need any additional optimization, although the radiation patterns can be engineered to achieve stronger coupling — at the expense of  $Q$  — if desired [165]. Perhaps most significantly, resonant scattering operates without introducing an additional loss channel, thus preserving the maximum possible quality factor for the cavity [295].

Fiber taper probes offer a similar ability to probe multiple cavities on a chip without modification or additional design work. Here, an optical fiber is heated and pulled to a diameter of  $\sim 1\mu m$ , then curved until a tight loop with a radius  $\sim 90\mu m$  is formed [18, 295]. By holding the loop in close proximity to the cavity (or a feeding waveguide), light can couple evanescently to the cavity. A unique benefit of fiber loops is the flexibility to dynamically control the coupling strength by varying the distance or contact length along the loop. And being naturally coupled to fiber systems, they are easily combined with other test instrumentations and directly address the problem of getting light on and off the chip, which must otherwise be handled separately.

Although both of these techniques are convenient for systems involving single cavities, their scalability is limited. As the number of cavities increases, accessing everything through on-chip dielectric waveguides seems imperative. Moreover, this enables integration with other passive photonic components, as well as electronic tuning, control, and amplification circuitry. Whether the waveguides are arranged to couple evanescently to the cavity or end-fired through the mirrors, efficient coupling requires two primary considerations: mode matching between the feeding waveguide and photonic crystal, and engineering the coupling rate. In the case of end-fire coupling, mode matching requires agreement not only between the effective indexes, but the spatial profiles as well. Generally, this involves an additional taper region between the feeding waveguide and the cavity which gradually adjusts the lattice parameter and feature size. Unlike the taper within the

cavity, this transition between the feeding waveguide and mirror region does not increase mode volume. Effectively, the mirror is turned on slowly to avoid spurious reflections, but the mode is still confined to the cavity itself.

A thorough analysis of the taper requires examining the mode at each point, performing a decomposition into the local eigenfunctions and calculating the scattering between these using coupled mode theory [156]. While this can be important to ensure no additional mirror regions are introduced (*e.g.*, between a strip and photonic crystal waveguide, which then feeds the cavity), the calculations can be somewhat involved and simple approximations are often adequate. For example, 1D nanobeam cavities are designed to operate near the  $X$  point in the Brillouin zone, where  $|\vec{k}| = \pi/a$ . The effective index in the mirror regions is therefore  $n_{eff} \approx \lambda/(2a)$ , which can be used to match the feeding waveguide's  $n_{eff}$  by tapering  $a$  in the mirror. Alternatively, efficient coupling has been demonstrated by fixing  $a$  throughout the device and only tapering feature size to optimize modal overlap [284].

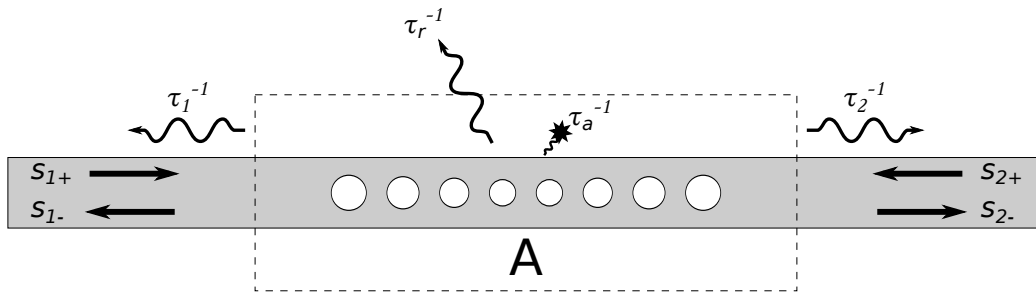


Figure 3.2: Loss mechanisms in temporal coupled mode theory.

Using temporal coupled mode theory, we can analyze the effect of coupling rate on the behavior of the resonator [388, 153], recovering the transmission/reflection spectra and quantifying the efficiency of energy transfer. Without any specific knowledge of the geometry, we can define simple parameters to describe the coupling rates into and out of the cavity. Consider a two-port cavity with decay lifetimes  $\tau_1$  and  $\tau_2$ , and external leakage  $\tau_x$  with  $1/\tau_x = 1/\tau_r + 1/\tau_a$  to accommodate radiation and absorption, resonant frequency  $\omega_0$ , incoming and outgoing field amplitudes  $s_{i\pm}$ , and field amplitude  $A$  within the resonator (see Figure 3.2). Assuming weak coupling, we can apply energy conservation and time reversal symmetry to yield [153]:

$$\frac{\partial A}{\partial t} = -i\omega_0 A - A/\tau_x - \sum_{l=1}^2 A/\tau_l + \sum_{l=1}^2 \sqrt{\frac{2}{\tau_l}} s_{l+}$$

with

$$s_{l-} = -s_{l+} + \sqrt{\frac{2}{\tau_l}} A$$

For a harmonic mode with time dependence  $e^{-i\omega t}$ ,  $\partial A/\partial t = -i\omega A$ . Our transmission and reflection are then:

$$\begin{aligned} T(\omega) &= \frac{|s_{2-}|^2}{|s_{1+}|^2} \\ &= \frac{\frac{4}{\tau_1 \tau_2}}{(\omega - \omega_0)^2 + \left(\frac{1}{\tau_x} + \frac{1}{\tau_1} + \frac{1}{\tau_2}\right)^2} \end{aligned}$$

$$\begin{aligned} R(\omega) &= \frac{|s_{1-}|^2}{|s_{1+}|^2} \\ &= \frac{(\omega - \omega_0)^2 + \left(\frac{1}{\tau_1} - \frac{1}{\tau_2} - \frac{1}{\tau_x}\right)^2}{(\omega - \omega_0)^2 + \left(\frac{1}{\tau_1} + \frac{1}{\tau_2} + \frac{1}{\tau_x}\right)^2} \end{aligned}$$

The spectrum shows a Lorentzian response, with full width at half max (FWHM) when  $\omega_0/\Delta\omega = \omega_0/(\frac{1}{\tau_x} + \frac{1}{\tau_1} + \frac{1}{\tau_2}) = Q$ . Peak transmission occurs when  $\tau_1 = \tau_2$ . This is similar to the condition for critical coupling to a traveling wave resonator, where the evanescent coupling rate must match the losses within the cavity to maximize the resonant dip [388]. When the incoming and outgoing waveguides are not matched, additional energy is lost to reflection (either due to partial cancellation of the energy reflected from the input port, or excessive reflection at the output). Assuming the waveguide rates are matched, on-resonance transmission only reaches unity in the limit of no external losses, where  $\tau_x \rightarrow \infty$ . Letting  $\tau_w^{-1} = \tau_1^{-1} + \tau_2^{-1} = 2\tau_1^{-1}$ , we can define quality factors representing the coupling to the waveguide and external losses:  $Q_x = \omega_0 \tau_x/2$ ,  $Q_w = \omega_0 \tau_w/2$  with  $Q^{-1} = Q_x^{-1} + Q_w^{-1}$ . In terms of these, we can write the transmission spectrum as:

$$T(\omega) = \frac{\frac{1}{Q_w^2}}{4 \left( \frac{\omega - \omega_0}{\omega_0} \right)^2 + \frac{1}{Q^2}}$$

On-resonance, we find:

$$\begin{aligned} T(\omega_0) &= \left( \frac{Q}{Q_w} \right)^2 \\ &= \frac{1}{\left( \frac{Q_w}{Q_x} + 1 \right)^2} \end{aligned}$$

Considering  $Q_x$  to be the fundamental limit due to intrinsic losses (often referred to as the *unloaded* quality factor), our relative *loaded* quality factor for a given peak transmission is:

$$\frac{Q}{Q_x} = 1 - \sqrt{T}$$

Having optimized the cavity and determined a maximum possible unloaded  $Q$ , we must make a trade-off between the loaded  $Q$  and transmission. Once this is determined, the coupling rate can be adjusted to achieve the desired parameters. In an end-fired geometry, we accomplish this by varying the number of lattice periods and potentially adjusting the taper, while the distance between the feeding waveguide (or fiber loop) controls this in the case of evanescent coupling.

However, this underscores another fundamental design challenge: the waveguides themselves represent significant loss channels, and in fact, efficient coupling to the cavity can only be achieved when these are relaxed enough to become the *dominant* loss mechanism. For example, achieving just a 25% transmission efficiency requires degrading  $Q$  by a factor of 2 compared to its intrinsic limit, while a 90% coupling efficiency degrades  $Q$  by a factor of nearly 20. Stated another way, after carefully engineering a cavity which could theoretically exhibit  $Q = 10^6$ , we must suffer  $Q = 50k$  in order to reach  $T=90\%$ . When possible, a reflective, end-fired geometry can provide a significant improvement [59]. Here, coupling to the outgoing waveguide is eliminated by using additional photonic crystal periods. Compared to a transmissive geometry, this allows  $\tau_2 \rightarrow \infty$ , removing half of the waveguide losses and avoiding the sensitivity of  $T$  to achieving  $\tau_1 = \tau_2$ . The reflective geometry allows a similar advancement over evanescent coupling. As standing wave resonators,

photonic crystal cavities couple equal amounts of light into both directions, losing half of the energy to backwards propagation. By avoiding the second direction altogether, reflective coupling recovers this lost energy. Whether or not the reflective geometry can be utilized, it remains critical to balance our ability to inject and extract photons with the desire to trap them effectively.

### 3.2.7 Design methodologies

Given a particular cavity structure, the process of evaluating its merit is straight-forward. Resonant frequencies and mode patterns may be directly obtained using either time or frequency domain methods. Once these are found, relevant design metrics, including quality factor, mode volume, and coupling rates may readily be extracted from the mode pattern, complex eigenvalues, and harmonic decay rate [230, 158]. The inverse problem of determining the ideal structure to optimize the metrics, however, is significantly more challenging. Given the resources required for each device simulation and extremely broad parameter space, obtaining a cavity design by direct search and parameter sweeps is computationally untenable.

Recently, researchers have begun exploring completely inverse methods for designing photonic devices. Rather than specifying a structure and solving for its eigenmodes, these techniques attempt to do the reverse: specify a field pattern [220] or merit function [219] ( $Q/V$ , for example), and invert the eigenvalue equation to solve for the corresponding dielectric function which maximizes the field similarity or figure of merit. While these strategies have yielded a variety of simulated devices, including resonators and splitters, these still face several significant challenges. Structural optimization towards a field pattern requires an accurate form of the final cavity mode, which generally is not known *a priori*, while formulating the inverse problem in terms of a merit function depends on an initial dielectric structure. In either case, the final results will depend greatly on these initialization vectors, effectively replacing the structural parameter sweep with a search over the starting field or dielectric. The extension to complete, three-dimensional optimization also poses extreme computational challenges, requiring solving large ( $10^7 \times 10^7$ ), ill-conditioned matrices; thus far, only optimization of 2D cross sections has been accomplished, with the extension to 3D

achieved using a pre-specified Bloch wavevector to model the extrusion [219]. Most significantly, however, the computed solutions are free to use a continuum of dielectric values, which does not reflect the essentially discrete values available in realistic material systems. Existing methods have included terms to minimize certain Fourier components of the dielectric and bound the dielectric to fixed ranges [220, 219], but the algorithms still produce unrealistic dielectric gradients. Later work has forced the resulting continuum into discrete values using a boundary parameterization and tuned with a steepest-descent method [221], but the resulting structures are composed of many small, irregular dielectric regions whose manufacturability and fabrication tolerance are clearly questionable. While the potential for inverse solutions is obviously desirable, their suitability for producing experimentally robust designs has yet to be demonstrated.

One can arrive at more practical devices using a hybrid approach between completely inverse methods and direct design. Here, a known photonic crystal structure with a large band gap provides a framework for the device. Using the bulk crystal modes as a basis, the cavity field is decomposed into a sum of these modes. From there, an inverse problem is solved to optimize the expansion coefficients, yielding the optimal cavity  $Q$  and field intensity which can be produced by the bulk cavity modes. As the bulk photonic crystal modes are already known, the dielectric structure is not directly involved in the computation. Instead, the dielectric defect which produced the optimal field is determined by inverting the Maxwell curl equation [106]. The ultimate success of the algorithm, however, depends heavily on the chosen photonic crystal basis and available parameter space. Introducing additional degrees of freedom (hole positions, sizes, shapes, etc) can potentially enable metrics, but these must be chosen carefully. Each new parameter imposes computational costs in evaluating the basis functions as well as requiring an increasing number of variables over which optimization must be performed. As with other optimization approaches, including genetic optimization or gradient descent [107, 309, 118, 251], the approach can be useful for final optimization over a small parameter space, but the bulk of the design still relies primarily on physical intuition.

Instead, we can use our insight from the preceding sections to develop targeted strategies for designing and optimizing photonic crystal cavities. Other similar recipes utilizing the same physical

principles can be readily found in the literature [80, 284, 286]. First, the desired resonance frequency must be selected based on the intended emitter. Once this has been determined, a suitable dielectric material system must be chosen which meets several criteria. Besides the availability of high-quality material and precise fabrication techniques, the most important features are that it should exhibit maximum dielectric contrast (to maximize the band gap) and possess minimum material absorption (to minimize losses and maintain a high quality factor). For the latter, it is important to consider both intrinsic absorption within the material as well as the effect of dangling surface bonds after processing. Dielectrics which can be chemically or physically passivated, for example by deposition of a capping layer or oxidation, are useful in this regard. Given these criteria, silicon-on-insulator and silicon nitride are excellent candidates, and provide the additional benefit of natural integration with CMOS electronics. While III-V materials have been widely used in photonic crystals due to their high dielectric contrast and compatibility with gain materials, they typically suffer from higher losses due to both unterminated surface bonds and higher intrinsic material absorption [201].

Following selection of a material system, one must decide on the type of structure itself, including the degree and type of periodicity. We will discuss the relative merits of 1D, 2D, and 3D structures a little more below, but in general, the robustness of the designs, tolerance to fabrication imperfections, and the ease of fabrication and integration with other components are of primary importance. For this reason, planar 1D and 2D structures, which can be readily fabricated using standard thin film processing techniques, are generally the best candidates. The periodicity itself must then be designed. Here, the goal is to maintain ease of fabrication while producing as large a band gap as possible and which is far away from the light cone. For this, we recognize that rounded features are more easily fabricated than sharp corners, for example, and recall that connected structures tend to produce TE gaps, while a disconnected lattice is more likely for TM operation. Often, the unit cell is simply chosen based on known structures, such as a triangular lattice of holes for 2D slabs or a linear array of circular holes in 1D nanobeams. The parameters themselves, such as slab thickness, hole radii, and lattice constant, are then chosen to maximize these qualities at the frequency of interest. This can often be accomplished by consulting existing gap maps, or readily obtained by a sweep of

the relevant parameters. Since only a single unit cell needs to be simulated, this requires significant fewer computational resources than a parameter sweep of the complete device. Along with this, there are often practical guidelines for these parameters. For example, the slab thickness is typically chosen based on available substrates, but generally will be around half an effective wavelength to prevent potential coupling to higher order waveguide modes. Greater perturbations typically yield greater band gaps, so hole radii are typically  $\sim 0.3a$ .

Once the design of the bulk crystal is complete, the type of defect is selected based on the intended field confinement. As detailed previously, removal of dielectric material will generally produce acceptor modes with high dielectric confinement and symmetry similar to the semiconductor mode, while additional dielectric material will pull states down from the air band. The actual defect may be created by changing hole sizes, shifting features, varying the lattice constant, or tapering the waveguide width, for example. [284] suggest utilizing a fixed lattice constant and tapering only the hole radius in nanobeam resonators, in order to ensure phase matching across the resonator and into the feeding waveguide. Similarly, [1] fixes both lattice constant and the hole radii, instead varying the waveguide width in a parabolic fashion to minimize scattering losses. The precise details of the defect and taper are the most critical elements for achieving a high quality factor, and offer the greatest opportunity for optimization methods such as genetic variation. However, excellent quality factors can be achieved using Fourier-domain analysis [333, 361, 2, 80, 343]. As described above, by designing the taper with a linear mirror strength vs. distance, a Gaussian field envelope is achieved within for the cavity mode. Due to its limited extent in momentum space, this minimizes scattering of the resonator energy into the light cone. As described above, the mirror strength as a function of taper parameters may be directly simulated using a complex Eigenvalue formulation, or estimated from a Taylor expansion of the band edge using analytic continuation. The rate of taper is inevitably a compromise; faster tapers achieve smaller mode volumes, but their greater extent in the Fourier domain results in increased scattering and lower  $Q$ , while the reverse is true for gradual tapers. While a linear increase in  $V$  can yield an exponential increase in  $Q$ , there remains a practical limit due to imperfect scattering and material losses. Realistically, the taper is selected to yield a

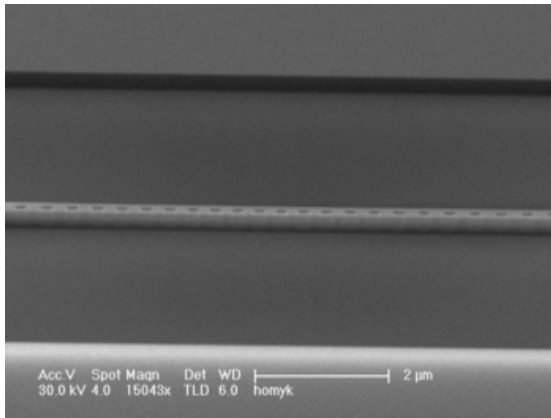
radiation-limited  $Q$  of perhaps  $10^6$ , which can preserve  $V$  under a cubic wavelength. For this, a simple linear taper of a given parameter (hole radius, lattice constant, etc.) is often adequate.

The final element of the cavity design is its coupling to external elements. This presents its own challenges, particularly in balancing the inevitable loss due to waveguide coupling with the desire to efficiently inject and extract photons. Once a suitable compromise has been made, the chosen coupling rate can be achieved by tailoring the distance to an evanescently-coupled waveguide, or the number of lattice periods in the mirror section for end-fired designs. In either case, attention must be paid to mode and phase matching between the cavity and feeding waveguide. An additional taper may be required to achieve the proper coupling, which itself should be carefully designed so as not to introduce additional gap regions [156]. Well engineered coupling schemes have demonstrated experimental values of 74.6% between the fiber and cavity mode, with a loaded  $Q$  approaching  $10^5$  [59], while other reports have achieved similar values, although only to the feeding waveguide [284].

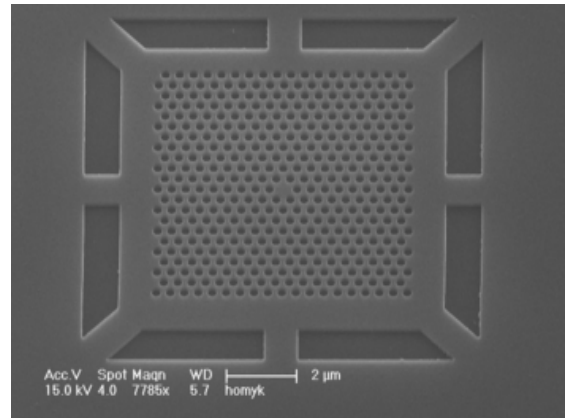
### 3.2.8 1D, 2D, 3D

Perfect 3D confinement requires a complete band gap in all directions. As discussed earlier, only a 3D photonic crystal — with coherent scattering structures arranged in all dimensions — can achieve such control of the light field. Unlike all other dielectric resonators, including both lower-dimensional photonic crystals cavities as well as ring resonators or other traditional structures, 3D photonic crystals eliminate the possibility of coupling to radiation modes. This unique feature allows the use of abrupt cavities, without needing to introduce tapers or make trade-offs between  $Q$  and  $V$ .

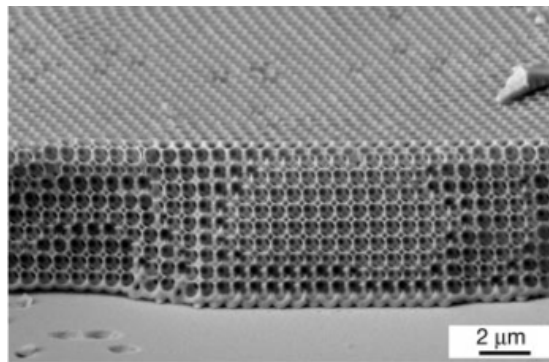
Complete photonic band gaps, as well as behavior such as spontaneous emission enhancement and suppression, have been experimentally demonstrated in a variety of structures including woodpile stacks [205, 269], inverse opal [360], and a lattice of drilled air holes in dielectric, known as Yablonoite [382]. Despite these successes, however, challenges in crystal fabrication and controlled introduction of the defect have prevented these structures from enjoying wider use. Geometries which are compatible with 2D lithography and thin-film fabrication techniques offer greater appeal,



(a) 1D photonic crystal nanobeam.



(b) 2D photonic crystal slab.



(c) 3D inverse opal photonic crystal (from [360]).

Figure 3.3: Examples of photonic crystals with 1D, 2D, and 3D periodicity.

and the majority of studies have focused on these devices. Besides utilizing established processing technology, these offer the opportunity for integration with waveguides, filters, and other passive photonic components and the promise of larger-scale integration.

The most common planar photonic crystals are 2D slab devices. These typically consist of a triangular or square lattice of holes etched in a thin semiconductor membrane (several hundred nm) on top of a sacrificial layer. The cavity is formed by omitting one or more of the holes, locally changing the lattice spacing, hole sizes or positions, or some combination of these. Finally, the membrane is suspended by etching away the sacrificial layer under the cavity. The resulting device has two-dimensional periodicity, relying on a two-dimensional band gap for in-plane confinement and index guiding in the out-of-plane direction. Using these techniques, experimental quality factors approaching 100,000 with mode volumes below a cubic wavelength are regularly reported, with  $Q$ s over 1,000,000 and volumes under a third cubic wavelength possible [261, 302].

Although proposed over ten years ago [93], one-dimensional (nanobeam) photonic crystals have only recently gained significant attention. These have periodicity only along the axis of propagation, and rely on total internal reflection for confinement in the vertical and transverse directions. In spite of this, recent work has reported the presence of ultrahigh  $Q/V$  cavities in nanobeam photonic crystals with experimental quality factors over 750,000 and mode volumes around half a cubic wavelength [357, 242, 264, 69, 127]. High performance cavities on substrates [127, 188, 357, 242] along with direct coupling of nanobeams to passive waveguides with an experimental transmission of  $T = 73\%$  [284] suggest the feasibility of dense integrated photonic systems. Lasers and switches have been demonstrated, while picogram masses and nanometer dimensions make 1D nanobeam cavities uniquely advantageous for optomechanical devices [71, 72, 277, 397, 94, 302].

In addition to having cavity parameters comparable to 2D photonic crystal slabs, nanobeam resonators have several important advantages. It was recently theorized [398] and subsequently demonstrated [237] that nanobeam cavities can support *overlapping* transverse electric (TE, electric field parallel to the substrate) and transverse magnetic (TM, magnetic field in the plane of the substrate) band gaps, whereas common 2D photonic crystal hole (rod) structures typically exhibit

only a TE (TM) gap but no TM (TE). Not only does an overlapping gap have important applications, such as single photon generation and frequency conversion [236], it has significant implications for maintaining cavity quality factors. In a suspended structure, the existence of vertical and transverse mirror symmetry results in TE-like and TM-like modes. Disturbances which break this symmetry can cause TE-TM coupling. For 2D holey slabs, the lack of a TM band gap results in leakage into the slab. For example, a sidewall taper of only  $2^\circ$  can cause  $Q$  to drop by an order of magnitude in 2D photonic crystal slab cavities due to this effect [164]. Similarly, the presence of a substrate can result in vertical symmetry breaking and TE-TM coupling, along with potentially greater radiation loss due to the lower light line. Tanaka *et al.* [342] fabricated 2D photonic crystal slab cavities in silicon-on-insulator (SOI), and reported losses due to TE-TM coupling which are comparable to radiative losses in the  $\text{SiO}_2$  substrate; together these dropped the theoretical  $Q$  to 760, an order of magnitude lower than the air suspended structure.

In general, the severity of these issues is significantly reduced in 1D nanobeam cavities due to the lack of a transverse slab mode and greater TE-TM band gap overlaps. The dual-polarization nanobeam cavity designed by McCutcheon *et al.* [237] had theoretical  $Q$  factors of  $7 \times 10^6$  and  $1.2 \times 10^5$  for TE and TM, respectively; the fabricated structure was intentionally detuned, but produced  $Q > 10^4$  for both polarizations. Although 2D photonic crystal slab structures with low-dimensional symmetry have shown overlapping TE and TM band gaps [340], to our knowledge, no cavities with high simultaneous TE- and TM- resonances have been reported in these.

### 3.3 Photonic Crystal Nanobeam Cavities

In this work, we explored the use of 1D photonic crystal nanobeams as a platform for scalable cQED systems. Our devices have exhibited experimental  $Q$ s over 300,000 *on substrate*, with mode volumes  $\sim 0.5(\lambda/n)^3$ . Given these ultrahigh quality factors and sub-wavelength mode volumes, 1D nanobeams are already ideal candidates for achieving strong coupling in the solid state. Additionally, their improved resilience to TE-TM coupling provides improved fabrication tolerance when compared to 2D slab devices, as well as the opportunity to function while still on a substrate, without the use

of matched cladding layers. Not only does this permit easier large-scale integration with dielectric waveguides and other passive photonic components, it extends their utility to sensing applications in fluid, as well as enables one of the emitter integration techniques to be described in 2.4.4. Combined with CMOS-compatible fabrication, these features will enable scalable, deterministic production of integrated cQED systems.

### 3.3.1 Mirror optimization

Using the intuition and design procedure outlined above, we began our cavity design and optimization. Typically, the selection of the emitter is an integral step in the process of formulating the complete cQED system. Unlike most previous efforts at creating cQED systems in the solid state [390, 291, 14, 334, 128, 272, 84, 176, 124], however, we abstracted the emitter integration from the cavity design. Doing so enabled us to perform independent selection of these material systems and resolved the challenge of meeting somewhat conflicting requirements.

For now, let it suffice to say that we targeted operation roughly in the communications C band (corresponding to wavelengths in the range 1530 nm - 1565 nm), and will assume an operating wavelength of  $\lambda = 1550$  nm throughout this discussion. Besides the wide availability of tunable lasers, amplifiers, detectors, fibers, and other passive components which are optimized for the C band, a primary motivation for operation in this region is the suitability of silicon-on-insulator (SOI) as the material system. At these wavelengths, silicon possesses a high refractive index  $n \approx 3.48$ , providing excellent contrast even against the oxide substrate. By comparison, most earlier efforts to produce cQED systems in the solid state were fabricated in III-V material systems in order to utilize embedded quantum dots [390, 291, 14, 334, 128, 272, 176]. While these typically show similar index contrasts, silicon exhibits lower absorption due to the lack of an active layer (our designs only integrated the active material where we want it, rather than throughout the device), as well as lower defect density and improved fabrication technology. Chemical treatments and thermal oxidation can be used to reduce roughness and remove etch damage [42, 41], while thermal oxide or nitride capping layers can provide further passivation of the surface [321]. Together, these features enable

an order of magnitude improvement in typical propagation losses for photonic devices fabricated in SOI as compared to those compound semiconductors [201, 199, 321, 42, 41]. Additionally, silicon photonics can leverage the tremendous fabrication resources of the IC industry, providing a natural path to large scale production as well as monolithic integration with electronics [15, 192].

The appropriate form of periodicity will depend on the intended polarization. For typical waveguide dimensions, the effective index for the lowest TE-like mode is generally higher than that of the fundamental TM mode. Consequently, a TE design will exhibit greater  $\vec{k}$ -space margin from the light cone, tighter confinement within the cavity, and lower bending losses in the passive dielectrics, and is thus preferred over TM structures.

As mentioned previously, a TE-like mode will benefit from a connected dielectric structure. For a 1D nanobeam waveguide, this generally takes the form of a perforated waveguide, often with either circular or rectangular holes. These structures can be readily coupled to ridge waveguides and easily suspended by removing the substrate under the cavity. We chose to make the holes circular due to the ease of fabricating rounded structures, although we note that rectangular holes can be useful for optomechanical devices [71, 72].

Before undergoing a parameter sweep to optimize the geometry, we roughly estimated appropriate values for the dimensions. For the waveguide thickness, the optimal value should be roughly half an *effective* wavelength of the mode. This is large enough to yield tight vertical confinement of the fundamental mode without introducing higher-order vertical modes which could serve as loss channels [153]. Assuming an effective index  $\approx 2.15$ , this would give an ideal thickness  $\approx 360$  nm. Practically, this value was determined by substrate availability as well as fabrication considerations. Device layers of 220 nm are common in SOI, so we selected this thickness. Because we intended for the cavity to operate around the edge of the Brillouin zone, we estimated  $k = 2\pi n_{eff}/\lambda = \pi/a$ , so  $a \approx \lambda/2n_{eff}$ . For the same effective index  $n_{eff} = 2.15$ , this yields  $a \approx 360$  nm. This effective index also corresponds to a ridge waveguide of width  $w \approx 410$  nm operating on top of the SiO<sub>2</sub> substrate, so we adopted this as the width estimate. Normalizing these values to the lattice constant, we found  $t \approx 0.6a$  and  $w \approx 1.4a$ . We chose  $r_0 \approx 0.3a$  for the hole radius, which is large enough to introduce

a strong perturbation while preserving a connected dielectric region to contain the field.

The optimal mirror geometry will be one which maximizes the band gap. As discussed previously, this provides the greatest reflectivity in the mirror region and serves to minimize the mode volume. Although the exact mirror parameters which optimize the cavity might differ slightly from this peak, calculation of the band structure involves a Hermitian operator and only requires simulation of a single lattice period. This requires significantly fewer computational resources than simulation of the entire cavity, allowing us to perform rapid evaluation of potential mirror geometries using broad parameter sweeps. Once an optimal range is found, the cavity optimization can be explored over a substantially reduced parameter range.

Band diagrams were calculated via PWE method using MPB [157]. Before conducting the full parameter sweep, convergence studies were performed to determine the necessary resolution and cladding dimensions. Subsequent simulations were performed using a resolution of 24 points per lattice period ( $a$ ) over a computational domain extending one lattice vector in the propagation direction ( $\hat{x}$ ), four laterally ( $\hat{y}$ ), and five vertically ( $\hat{z}$ ), with the interface between substrate and cladding in the middle of the region. MPB's default anisotropic dielectric averaging was applied to improve convergence. Mirror symmetry was used to reduce computational load and select TE-like modes. Because we were optimizing the device for operation on substrate (to be discussed in 2.4.4), we only applied odd symmetry to the  $y = 0$  plane, but note that an additional even symmetry condition could be applied to  $z = 0$  for vertically-symmetric devices. As we were primarily concerned with narrowband operation around a fixed frequency, we were free to ignore material dispersion and fixed our refractive indexes to  $n = 3.48$  for the silicon and  $n = 1.47$  for the oxide substrate. For each band structure, we swept the wave vector  $\vec{k}$  from  $0\hat{x}$  to  $\pi/a\hat{x}$  in increments of  $\pi/10a$ , then utilized a cubic spline interpolation to estimate frequencies between these points. The lowest three bands were simulated. Because the structure inevitably exhibits an *incomplete* band gap, only solutions below the light-cone in the *substrate* ( $\omega < |\vec{k}|c/n_{ox}$ ) were considered. Having applied this restriction, we calculated the band gap between the first and second bands. In cases where the second band remained entirely outside of the light cone, the peak of the light cone ( $\omega = \pi c/n_{ox}a$ ) was used for

the upper frequency.

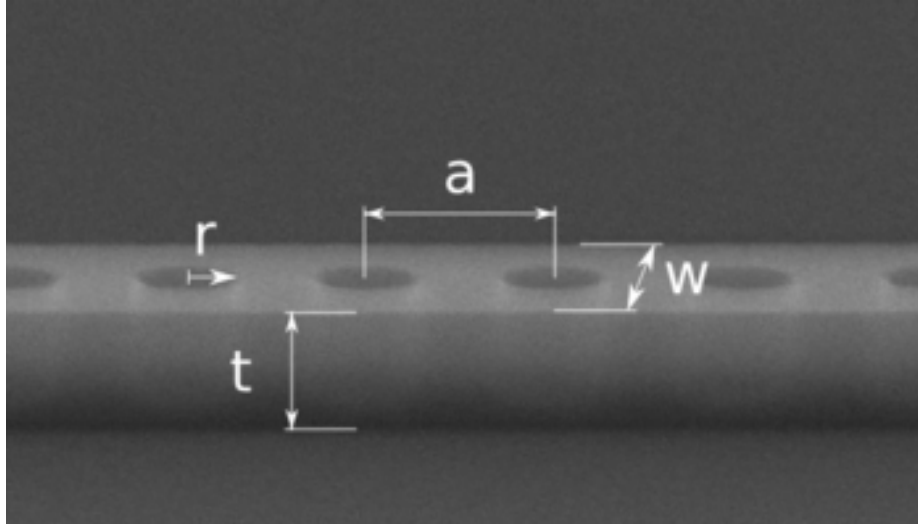


Figure 3.4: SEM of a 1D nanobeam cavity fabricated in SOI, illustrating the geometric parameters used to describe the device.

Using our estimated parameters as guidelines, we conducted a sweep over three structural parameters: beam width, beam thickness, and hole radius. For each set of parameters, dispersion diagrams and band gaps were calculated as described above. Due to the scale invariance of Maxwell's equations, the simulations were performed using parameters normalized to a lattice constant, after which the solutions were scaled to physically meaningful units. Our design had two constraints to which this could be performed: choosing the band gap's center wavelength to match our target wavelength of 1550 nm, or fixing the device thickness to match our SOI's 220 nm device layer. We opted for the latter method.

Having thus determined our lattice constant  $a = 220 \text{ nm}/t$ , we used the target frequency to impose a constraint on the other parameters. Because the precise location of the resonance within the gap was not known *a priori*, the original mirror optimization was based on the gap's center frequency, which shows the maximum decay rate in the mirror. Later work incorporated this constraint into the cavity design itself, using the semiconductor band edge of the innermost taper as the target frequency. The distinction is fairly minor, and the same method of calculation was used in both cases. Sweeping over the range of normalized beam thicknesses (or equivalently, lattice constant), we analyzed the band gap's target frequency (either band center of the mirror or semiconductor edge

of the taper) as a function of beam width and hole radius. Contours could then be extracted for combinations of beam width, beam thickness, and hole radius, which yielded a band gap optimized for our target frequency.

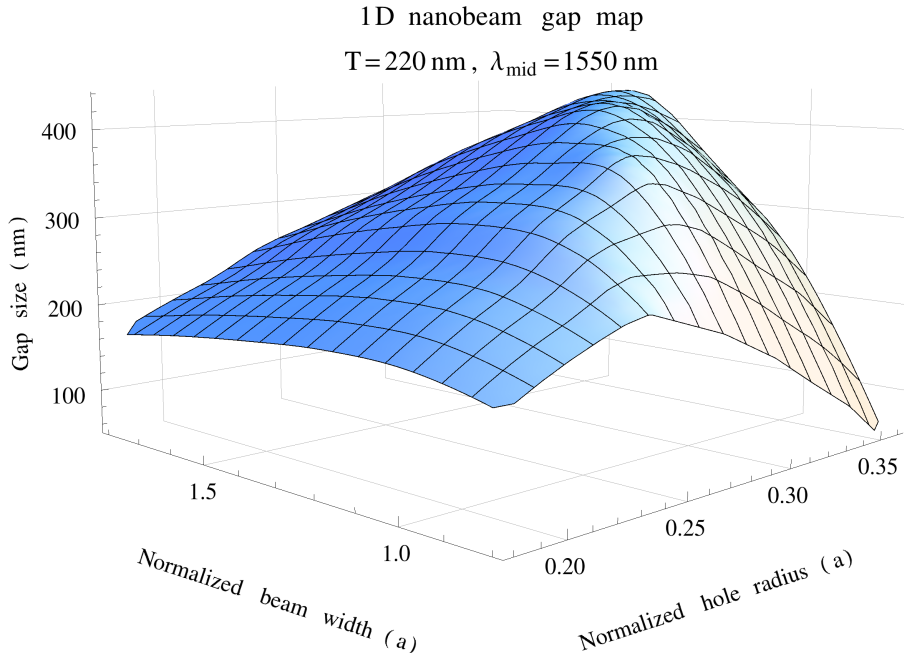


Figure 3.5: Dependence of TE band gap dependence 1D nanobeam geometry parameters. The thickness has been fixed to 220 nm to match the SOI substrate, while geometric combinations have been constrained to yield a mid-gap wavelength of  $\lambda = 1550 \text{ nm}$ . A peak gap of  $\approx 435 \text{ nm}$  occurs for  $w = 1.42a \approx 645 \text{ nm}$ ,  $r = 0.35a \approx 160 \text{ nm}$ , and  $t = 0.48a$ .

The results are plotted in Figure 3.5. Under the constraints of  $t = 220 \text{ nm}$  and a gap center with  $\lambda = 1550 \text{ nm}$ , we found the optimal nanobeam parameters to be  $w = 1.42a \approx 645 \text{ nm}$  and  $r = 0.35a \approx 160 \text{ nm}$  for  $t = 0.48a$  yielding  $a \approx 453 \text{ nm}$ . This set of parameters yields a gap-midgap ratio of  $\approx 28\%$ , corresponding to a band gap of  $\approx 435 \text{ nm}$ .

In addition to maximization of the band gap, the margin in  $\vec{k}$  space is important for loss optimization, as mentioned previously. The scaling performed here will shift the substrate's light cone commensurately with the gap frequencies. Designs with lower normalized frequencies which are further below the light cone will therefore sustain greater  $\vec{k}$  space margins. Intuitively, this will favor designs with more dielectric material, which tend to exhibit higher degrees of confinement and lower frequencies. We calculated the margin as the distance from the edge of the Brillouin zone

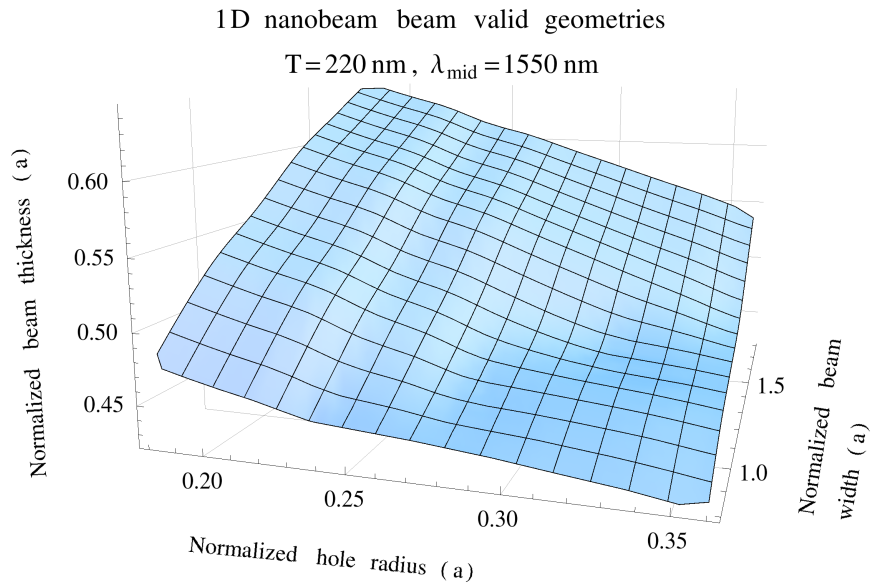


Figure 3.6: Combinations of normalized mirror geometry parameters which produce a mid-gap wavelength of  $\lambda = 1550 \text{ nm}$  and match a  $220 \text{ nm}$  SOI device layer.

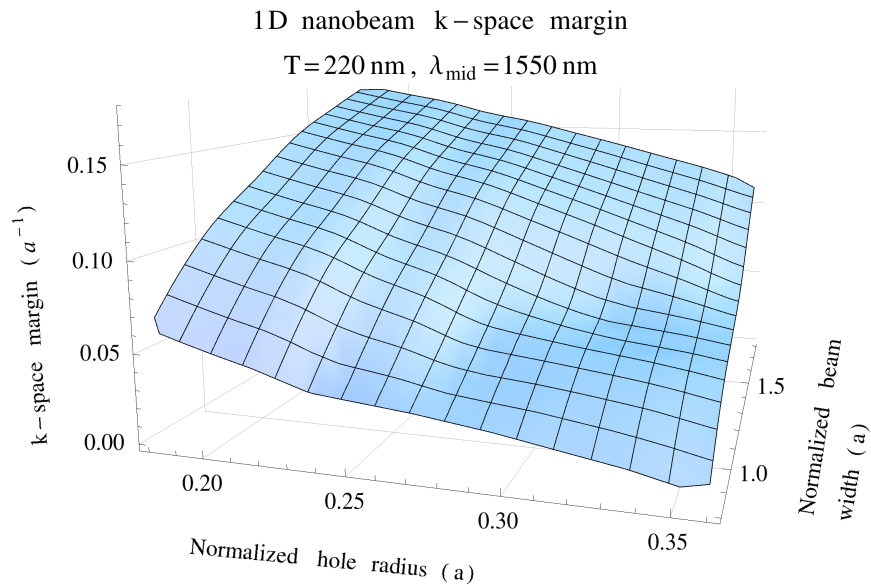


Figure 3.7: Extent of the band gap at in  $k$ -space at the mid-gap wavelength of  $\lambda = 1550 \text{ nm}$ . Thickness has been constrained to  $220 \text{ nm}$ , to match the substrate.

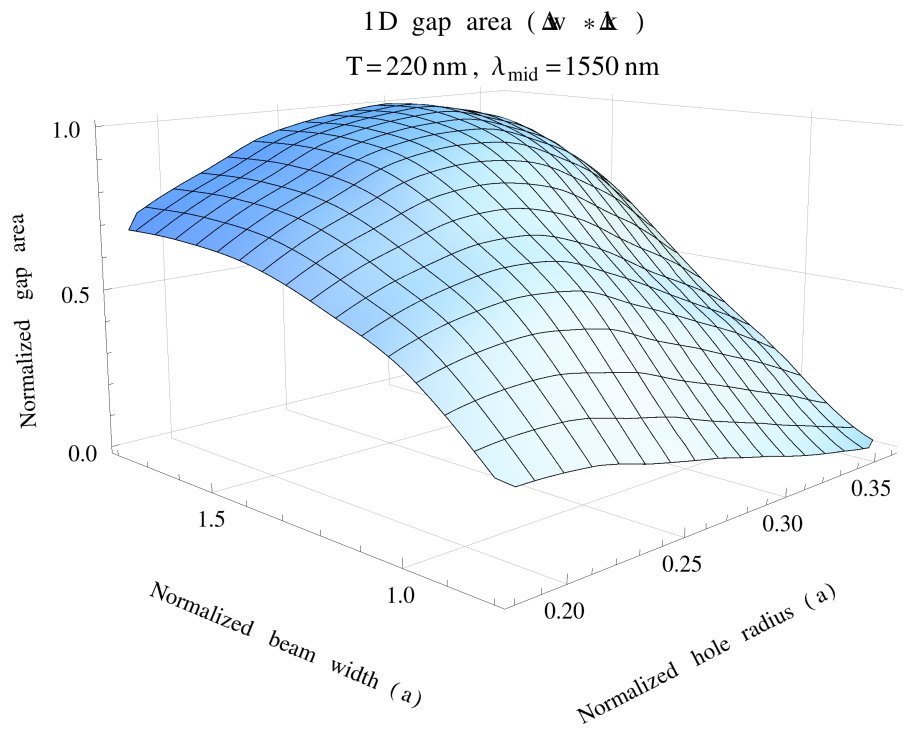


Figure 3.8: Combined metric showing the gap area for a 1D nanobeam geometry, defined as the product of the size of the energy gap ( $\Delta\omega$ ) and the extent in  $k$ -space ( $\Delta k$ ). Values have been normalized to the peak. The thickness is fixed to 220 nm; geometry combinations yield a mid-gap wavelength of  $\lambda = 1550 \text{ nm}$ .

( $|\vec{k}| = \pi/a$ ) to the oxide light cone  $|\vec{k}| = n_{ox}\omega/c$  and show the results in Figure 3.7. Consistent with expectations, we found greater margins for designs with larger widths, higher thickness, and smaller holes. This encouraged slightly more moderate parameters than those for a maximum band gap. Defining a merit function  $\Delta\omega\Delta k$  which equals the product of gap size and  $\vec{k}$  margin, we found the optimal parameters  $w = 1.60a \approx 640$  nm and  $r = 0.30a \approx 120$  nm for  $t \equiv 220$  nm =  $0.55a$ , corresponding to a lattice constant  $a \approx 400$  nm. The results may be seen in Figure 3.8. Finally, we note again that the cavity resonance could eventually fall closer to the band edge than the center of the gap. Although the exact location within the gap was not known *a priori*, the difference in scaling would have little effect on the mirror optimization and would only serve to improve  $\vec{k}$  margin for acceptor modes.

### 3.3.2 Defects, tapers, losses

As discussed previously, the type of defect will determine the properties of the cavity field. In most previous photonic crystal cQED systems, the clear choice has been to use acceptor modes. These inherit the field profiles from the semiconductor band, which exhibit strong confinement within the semiconductor core. Because the emitters have generally been quantum dots embedded within this region, acceptor modes maximize field overlap with the emitters and thus serve to minimize the mode volume.

In our case, the emitter is likely to remain on the surface of the nanobeam rather than embedded in the core. Although this might initially suggest a preference for an air mode cavity, the acceptor mode's electric field at the surface is still  $\approx 65\%$  of the peak field within the beam, resulting in only a modest increase in mode volume. Additionally, acceptor modes are typically further from the light cone than corresponding donor modes, due to operation closer to the semiconductor band. This provides greater margins in  $k$ -space, resulting in higher quality factors which can readily offset the increase in mode volume. Finally, the introduction of small holes or slots near the anti-node can further reduce the mode volumes in acceptor modes, if desired [298, 203, 320, 51].

To create the cavity, one needs to pull a localized state into the band gap from a neighboring

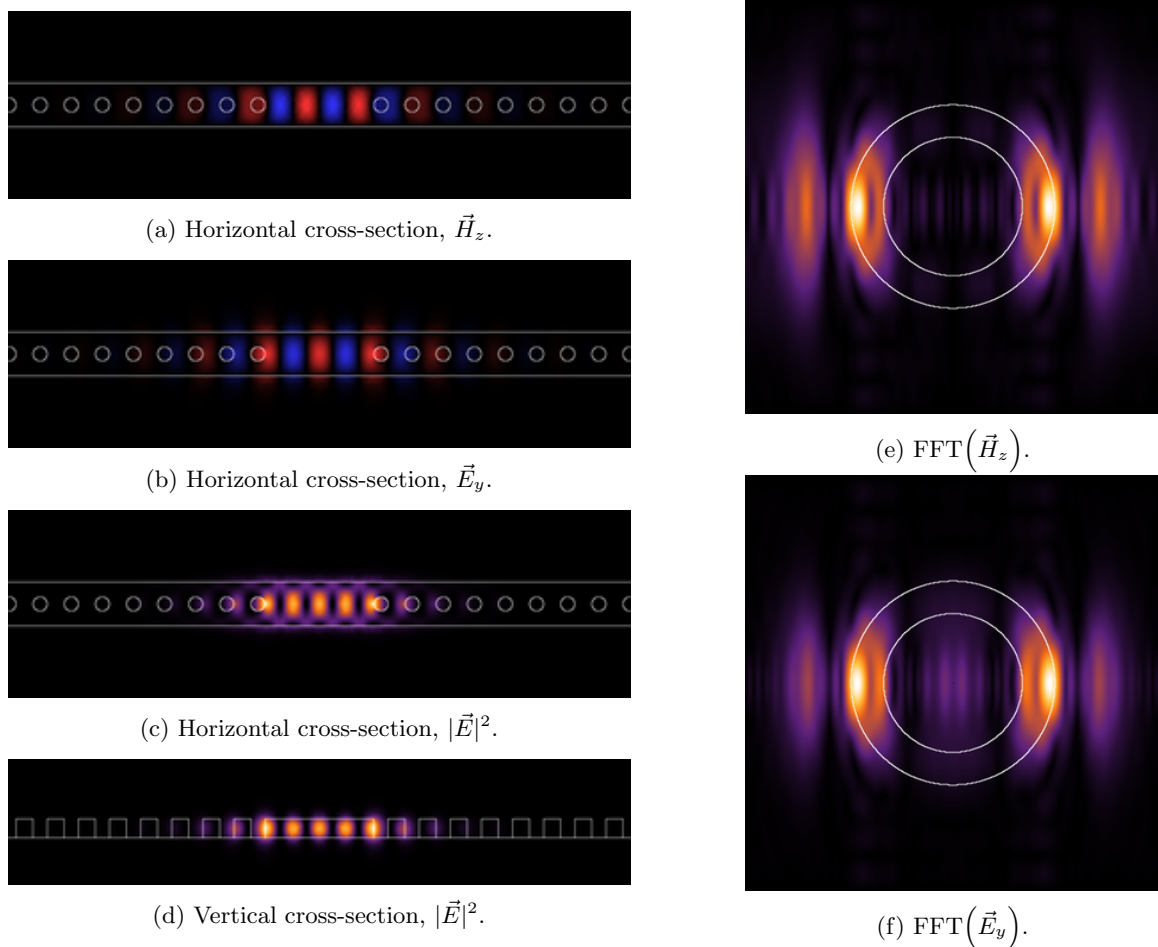


Figure 3.9: FEM simulations an abrupt cavity, showing cross-sections of the fields (through center of beam) and corresponding FFTs ( $\lambda/4$  in substrate). The FFT circles indicate the light cones for air (inner) and oxide (outer). Geometry parameters were selected to be similar to our nanobeam devices and produce a resonance near 1550 nm, but the cavity is constructed by abruptly introducing the mirror section, without a taper region. Although the light appears to be well-confined, FFTs reveal significant scattering into radiative modes.

band. Considering the structure as a Fabry-Perot, it is possible to simply draw the mirror sections apart until the cavity length supports a resonance at the desired wavelength. The L3 defect, where 3 holes are removed in a line, is an example of this method which is commonly used in 2D photonic crystal slabs. This approach is rather inefficient for creating an acceptor mode, however. Since the introduction of material tends to decrease frequencies, this method operates by pulling modes down from the air band. A fairly large defect is therefore required to achieve an acceptor-like resonance near the semiconductor edge, resulting in an excessively large mode volume. Additionally, the abrupt transition between the cavity and mirror regions will inevitably result in only a modest  $Q$ .

Conversely, acceptor modes which pull states up from the semiconductor band require much smaller perturbations and will typically minimize the mode volume. The optimal defect is essentially an L0 cavity, where no gap is introduced between the mirrors [284]. Instead, the defect operates by removing dielectric material, which serves to increase the frequency. In 1D nanobeam resonators, this is commonly accomplished by reducing the hole spacing and size in the cavity region; however, alternative methods exist. Quan *et al.* [284] advocate only modulating the hole size — using larger holes in the cavity region — while maintaining a fixed lattice constant throughout the device in order to preserve the real part of the wave vector. By selecting this to match the effective index of the feeding waveguide, the coupling between the cavity and feeding waveguide can be readily achieved. Ahn *et al.* [1] developed a cavity design where the spacing and size are both fixed, instead choosing to taper the waveguide width in a parabolic manner. Compared to variations of hole size and position — which are inevitably discrete in nature — the modulation of the width is continuous. This smoother perturbation could serve to minimize scattering losses [1, 315].

Both of these tapering methods rely on very precise control of feature size and geometry. Unfortunately, nm-scale precision can be difficult to achieve during fabrication due to a variety of factors, including proximity error during electron beam exposure, fracturing irregularities, variations in resist thickness, incomplete solvent removal, resist swelling, other effects due to ambient humidity, local developer saturation, temperature dependence of development, and sidewall conditions in etching chambers. These effects yield offsets which are not simply proportional to dose or feature size, and moreover may not even produce uniform variation across a single sample. Together, this makes the fabrication tuning effort much more involved than merely producing a dose array, and which might need to be repeated regularly due to inevitable drift in the processes.

By comparison, feature *location* is unaffected by these factors, and can be controlled with exquisite accuracy and precision by modern electron beam lithography systems. For this reason, we chose to rely on perturbing the hole spacing, rather than using beam width or only hole size, to introduce the defect and control the transition into to the mirror region. In our initial cavity design, the holes sizes were also tapered; at each location, the local radius was decreased by the

same proportion as the spacing. Theoretically, this feature serves to ease the transition within the taper and thus reduce scattering losses. Unfortunately, the reliance on accurate hole sizes made this design quite vulnerable to fabrication errors. Experimentally, we found that nanobeams employing fixed hole radii and beam widths were more robust to fabrication errors, consistently yielding higher quality factors. Subsequent work further refined the taper profile, but has not yet been verified experimentally. Here, we will present the initial design using tapered holes for completeness, as well as the revised design process. The experimental data and fabrication tolerant design process will be reserved for a later section (see 3.4.5).

### 3.3.2.1 Initial design

During our initial design phase, cavity simulations were performed using a freely-available finite-difference time-domain (FDTD) package [273]. With this technique, a preliminary simulation is required to identify a resonance with a wideband source (followed by a second long simulation to excite only that mode using a narrowband source), allow transients to decay, and continue long enough to accurately extract the frequency, field pattern, and quality factor. Given the computational resources available at the time, this process would take several hours for simulation of a single cavity, precluding large, multi-dimensional parameter sweeps.

Consequently, we decided to fix the beam width and hole radius for the mirror region, and then use thickness to tune the resonance. Based on the gap simulations described above, we had determined the maximum  $\Delta\omega\Delta k$  occurs with  $w = 1.60a \approx 640$  nm,  $r = 0.3a \approx 120$  nm, and  $t = 220$  nm =  $0.55a$ . For widths  $\gtrsim 625$  nm, however, the waveguide supports a higher order transverse mode. To avoid potential losses and complications arising from coupling to this mode, we decided to reduce the width to  $w = 1.0a$  while maintaining  $r = 0.3a$ . Although larger radii would possess greater band gaps which support smaller mode volumes, the additional dielectric material helps lower the resonant frequency, yielding increased margin in k-space to enable higher  $Q$ s.

For the cavity and taper region, we adopted a linear scaling of the local lattice constant<sup>1</sup>. This scale was applied to both the hole spacing and radius, while the beam thickness and width were

---

<sup>1</sup>This is not ideal, and will be discussed further in 3.3.2.3.

held constant throughout the device. In the innermost taper periods, the frequencies at the top of the semiconductor band extend into the band gap of the mirror section. This region of propagating modes forms the cavity. Because it is a natural consequence of the taper itself, no additional spatial gap needs to be introduced (L0 cavity). We chose to design the cavity with dielectric material at the center, yielding an electric field profile with even symmetry, rather than locating a hole there, which produces odd symmetry. Although the latter is often preferred since odd symmetry precludes any Fourier components at  $k = 0$  and could yield higher  $Q$ s [333, 165], the even symmetry produces only a single dominant anti-node which we preferred for coupling to the emitter.

To define the taper profile, one needs to specify both the depth, or minimum scale factor which occurs at the center, and the rate of rise back to the mirror region (or equivalently, number of taper periods). In general, a steeper taper will push the mode into the band gap more quickly. This tends to provide a rapid decay of the field and small mode volume, but because the abrupt modulation of the field results in greater scattering, this comes at the expense of lower quality factors. The resonance wavelength, although affected by the taper rate, is primarily controlled by the depth and will approximately follow the semiconductor band edge of innermost cavity period. A deeper cavity will therefore yield a resonance which is further into the mirror region's band gap, which determines the eventual decay rate within the mirror. Although this affects the in-plane leakage rate and therefore  $Q$ , this is a minor consequence. The total quality factor is ultimately determined by scattering since we are free to apply additional periods. Similarly, the decay rate within the mirror only has a minor affect on mode volume because the field will have almost entirely decayed within the taper itself. Instead, this depth helps determine the total number of periods required (and thus physical device footprint), as well as the sensitivity of coupling efficiency to each additional period. We settled on a taper progressing from  $0.84a$  at the cavity center up to  $1.0a$  in the mirror region, in steps of  $0.02a$ .

After choosing the mirror geometry and taper parameters, we swept the beam thickness to tune the resonance. With  $w = a$ ,  $r = 0.3a$  and the taper described above, we found that  $t \approx 0.5a$  yields a normalized resonance frequency of  $f \sim 0.284/a$ . Under the constraint that  $t = 220$  nm, this equates

to  $a \approx 440$  nm and  $\lambda \approx 1550$  nm. We note that these values correspond to a nanobeam on substrate; if the beam with the same geometry is undercut, the resonance will drop to  $\approx 1525$  nm. The electric and magnetic field profiles can be seen in Figure 3.10, as well as the Fourier transform of the fields at  $\lambda/4$  below the nanobeam (greater leakage occurs into the substrate than cladding due to its higher index).

Our first fabricated nanobeams utilized this design [295]. For a beam with 15 lattice periods in each half (including the taper), the device achieves a theoretical  $Q \approx 3.78 \times 10^5$ ,  $V \approx 0.5(\lambda/n)^3$ , and  $Q/V \approx 7.52 \times 10^5(\lambda/n)^{-3}$ .

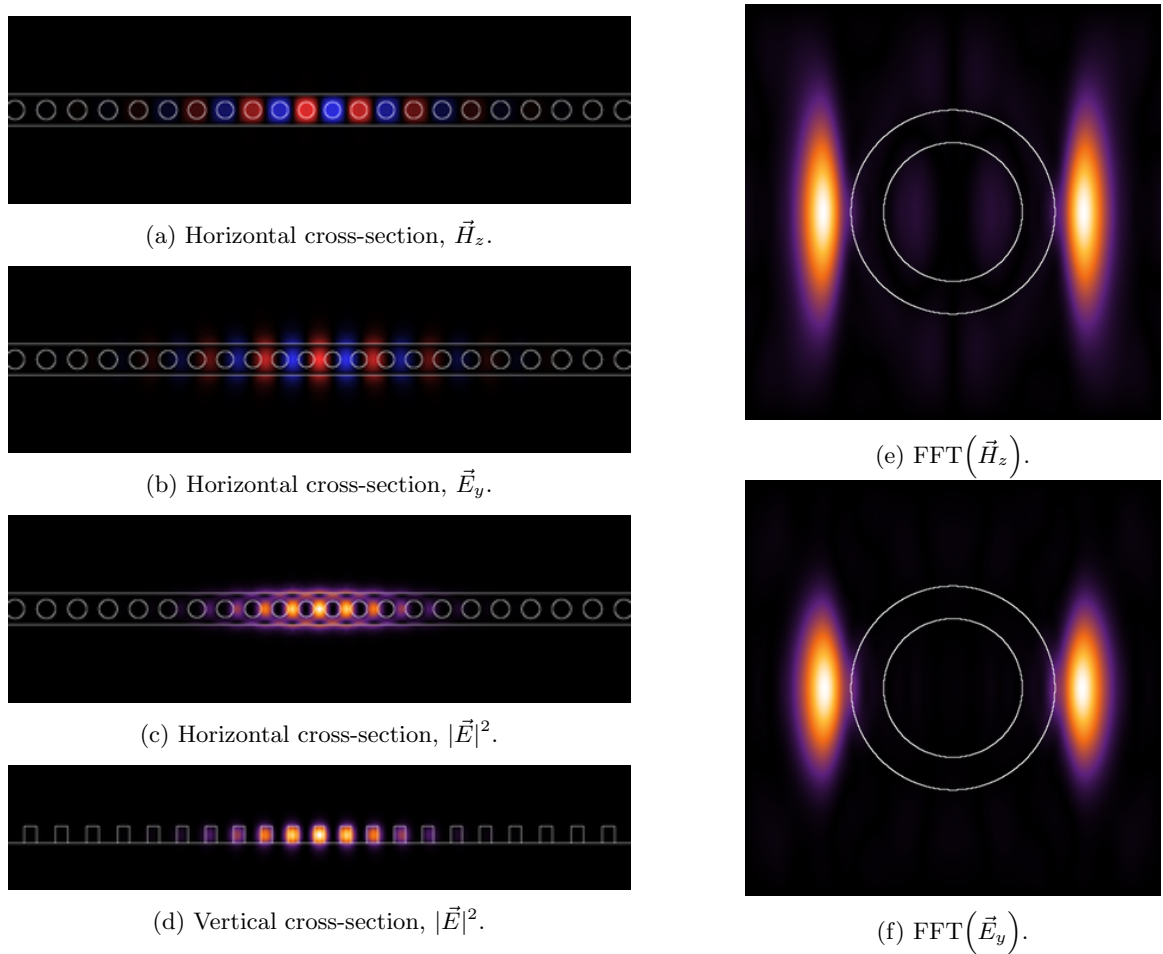


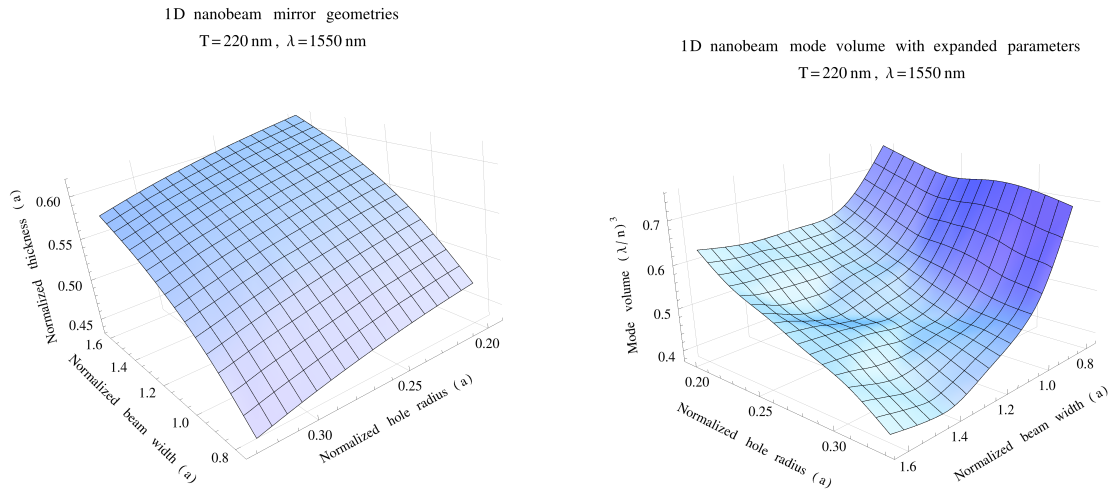
Figure 3.10: FEM simulations of our initial beam design, showing cross-sections of the fields (through center of beam) and corresponding FFTs ( $\lambda/4$  in substrate). The FFT circles indicate the light cones for air (inner) and oxide (outer).

### 3.3.2.2 Expanded parameter design

As greater computational resources became available, we revisited the mirror geometry in order to improve the quality factors. Using a commercial tool employing the finite element method [60], we were able to perform full cavity simulations in  $\approx 4$  min, rather than hours. This improvement enabled us to simulate cavities over an array of potential beam widths, thicknesses, and hole radii, covering a parameter range similar to that used in the band diagrams. Since the solutions have mirror symmetry along the in-plane directions, we reduced the computational region to cover only one quarter of the beam and applied perfect electrical and perfect magnetic boundary conditions in the longitudinal and transverse directions, respectively. All simulations used the same linear taper profile and 15 lattice periods within the quadrant. Although higher quality factors could be simulated using more lattice periods, this is sufficient to obtain quantitative comparisons between designs. Experimentally, the quality factor would likely be limited by imperfections and scattering before this point and additional periods would only serve to decrease coupling efficiency.

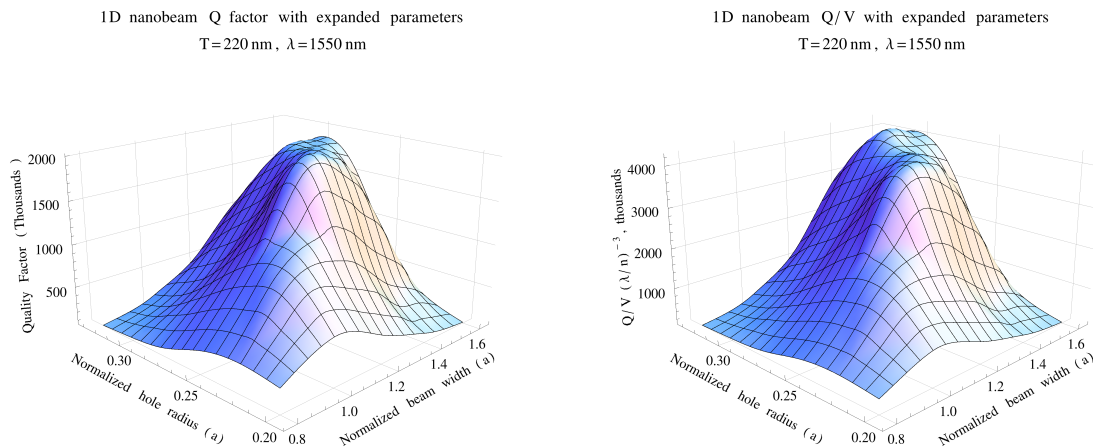
For each set of parameters, we constructed the geometry, performed the simulation, identified the eigensolution corresponding to the fundamental resonance, calculated the wavelength and quality factor from the complex eigenvalue, and extracted the field pattern from the eigenvector to obtain the mode volume. After tabulating the data, we imposed the restrictions  $t = 220$  nm and  $\lambda = 1550$  nm in a manner similar to that used to analyze the potential mirror geometries from their band diagrams. At each combination of relative beam width and hole radius, we found the corresponding thickness that would yield a resonant frequency at  $\lambda = 1550$  nm when the device was scaled to  $t = 220$  nm. The corresponding quality factors and mode volumes were then used to compare the devices and select the optimal geometry.

The results of the parameter sweep are shown in Figure 3.11. As a function of normalized beam width and hole radius, Figure 3.11a presents the normalized beam thickness which yields a resonance at  $\lambda = 1550$  nm. This relationship was utilized to maintain fixed resonant frequencies resonance when sweeping beam parameters during experimental tests. We found that the normalized thickness is typically in the range of  $0.5a$ , and consistent with expectations, the thickness *increases*



(a) Combinations of mirror geometry parameters which result in a *cavity* resonance at  $\lambda = 1550\text{ nm}$  with  $T=220\text{ nm}$ . Note that this is distinct from Figure 3.6, which presents a similar trend for the mirror section alone, and is related to the *mid-gap* frequency rather than resonance.

(b) Dependence of the mode volume on geometry parameters for a 1D nanobeam cavity.



(c) Dependence of quality factor on geometry parameters for a 1D nanobeam cavity.

(d) Dependence of the combined figure-of-merit,  $Q/V$ , for a 1D nanobeam cavity.

Figure 3.11: Results of FEM simulations used to optimize the 1D nanobeam geometry with an expanded parameter range. These values correspond to a device layer thickness of  $T = 220\text{ nm}$ , with a resonance wavelength of  $\lambda = 1550\text{ nm}$ .

with increasing beam width and decreasing hole radius. As both of these factors would tend to increase the amount of dielectric material, which would tend to lower resonant frequencies, it may seem counter-intuitive for the beam thickness to also increase. However, this behavior is readily explained by the inverse relationship between beam thickness and lattice constant. While increasing beam thickness would also tend to lower normalized frequencies, it also serves to decrease the normalization constant.

For mode volume, we found an opposite trend as compared to thickness; the results are presented in Figure 3.11b. As a function of increasing beam width or radius (and therefore, thickness as well), the mode volume decreased. This is due to the increasing volume of dielectric material, which tends to provide improved confinement within the core, and therefore lower mode volumes.

Unlike the trends for thickness and mode volume, which exhibited monotonic relationships with beam width and hole radius, our simulations yielded a peak quality factor of  $Q \approx 2 \times 10^6$  at  $w = 1.26a$ ,  $r = 0.253a$ , and  $t = 0.565a$ ; see Figure 3.11c. At larger beam widths and smaller hole radii, the greater beam thickness corresponds to a smaller lattice constant. In these regions, the drop in quality factor is due to the relatively aggressive spatial modulation of the mode, resulting in a broader spread in momentum space and a consequently higher coupling to radiation modes. These quality factors are therefore closer to their fundamental limit of  $Q \perp$ . At the other extreme, the less aggressive spatial modulation results in larger mode volumes. While this should also correspond to increasing quality factors, we recall that all of the simulations used  $N = 15$  periods. In this case, the limitation on quality factor is due to longitudinal coupling through the mirrors, and therefore a reflection of  $Q \parallel$  as well.

Combining the data for  $Q$  and  $V$ , we find an optimal  $Q/V \approx 4.3 \times 10^6(\lambda/n)^{-3}$ , corresponding to  $Q = 1.8 \times 10^6$  and  $V = 0.43(\lambda/n)^3$  for  $w = 1.46a$ ,  $r = 0.3a$ ,  $t = 0.57a$ ; the data is plotted in Figure 3.11d. By comparison, our point of maximum quality factor,  $Q_{max}$ , had  $V = 0.5(\lambda/n)^3$  and  $Q/V = 4.0 \times 10^6(\lambda/n)^{-3}$ . While the maximum  $Q/V$  is slightly higher than the figure-of-merit at  $Q_{max}$ , we note again that the quality factors are *loaded* by the finite mirror region. The *unloaded*  $Q$  at our  $Q_{max}$  parameters should be even greater than the unloaded  $Q$  here, which might yield an

even greater  $Q/V$  overall. Between the two, it is much preferable to err on the side of  $Q_{max}$ , which would enjoy both greater coupling efficiency (due to higher loading for a given  $N$ ) and fabrication tolerance (due to a less aggressive taper).

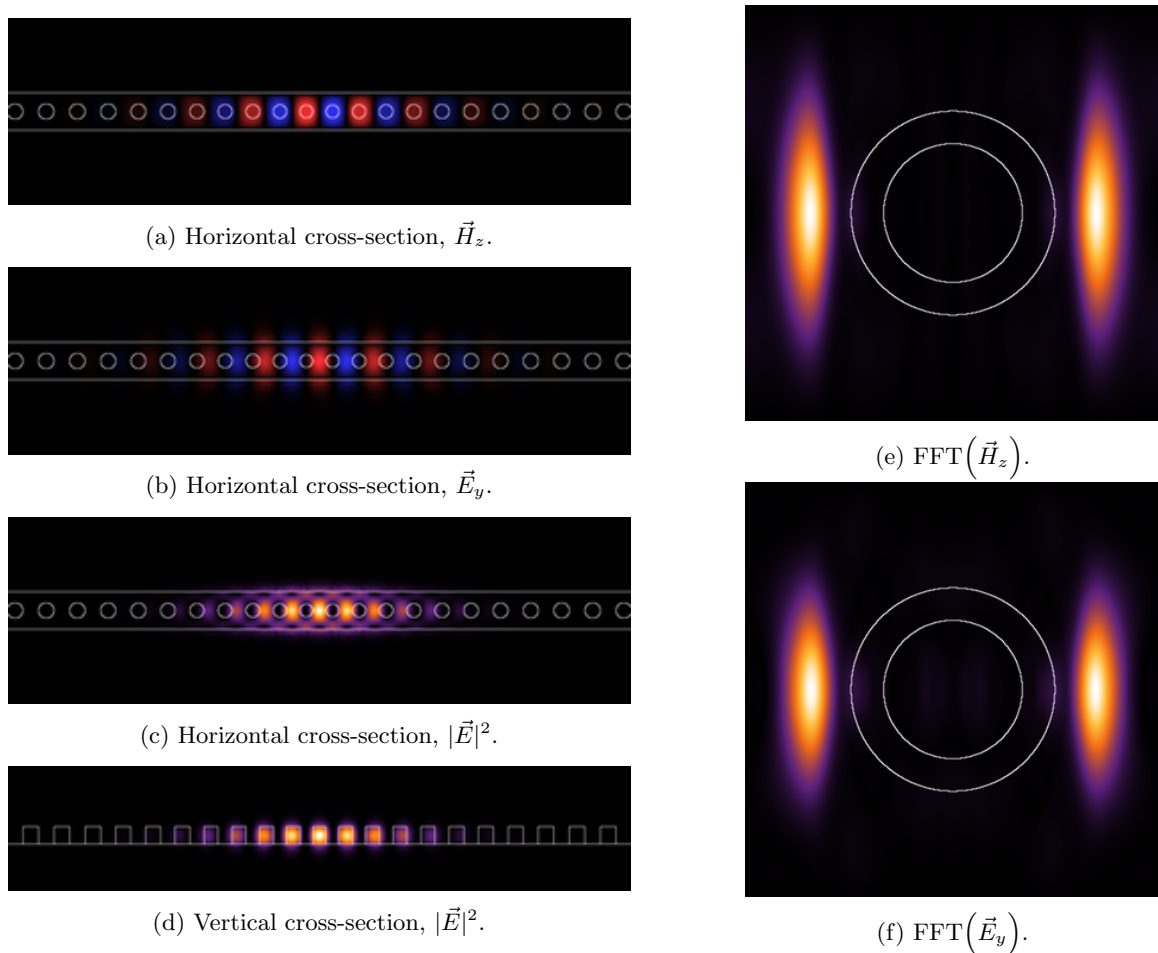


Figure 3.12: FEM simulations of our expanded beam design, showing cross-sections of the fields (through center of beam) and corresponding FFTs ( $\lambda/4$  in substrate). The FFT circles indicate the light cones for air (inner) and oxide (outer). Although the overall pattern appears similar, we note the use of *smaller* holes and a wider beam. While this decreases the mirror strength and results in a somewhat larger mode volume, this is outweighed by the  $Q$  improvement resulting from a more gentle confinement. Practically, the wider beam also results in less field interaction with edge roughness.

The  $Q_{max}$  solution represents our initial design revision, with  $w = 1.26a \approx 490$  nm,  $t = 0.565a \equiv 220$  nm, and  $r = 0.253a \approx 98$  nm, where  $a \approx 389$  nm, using a taper from  $a' = 0.84a$  to  $1.0a$  in steps of  $0.02a$ . Compared to the initial design, the new cavity provides a  $\approx 530\%$  improvement in quality factor while maintaining a comparable mode volume.

### 3.3.2.3 Analytic design

After experimental investigations using the previous nanobeam designs (and subsequent variants optimized for fabrication tolerance; see later section 3.4.5), we revisited the beam design once more. In particular, we realized that scattering losses could be drastically reduced by considering the taper profile in momentum space [333, 2]. Moreover, an opportunity existed for the process to yield deterministic resonances (within a few nm, or roughly several tenths of a percent) while simultaneously satisfying the fabrication constraints on the beam thickness. Not only would this eliminate the unnecessary simulation of beams with the wrong resonance, but it would enable automatic selection of the optimal mirror geometry and further restrict the parameter space. Together, these features would drastically reduce the computational burden while providing significantly improved designs. Finally, the technique can easily be adapted to donor mode cavities or applied to new material systems and mirror geometries, should the system requirements change.

To begin, a complete gap map was obtained over all possible mirror parameters, as described above. Rather than the combined set of all parameters, this separated the sweeps into parameters required to describe the mirror geometry and the remaining two needed to specify the taper. Not only did this greatly reduce the overall design space, it allows the majority of parameters to be simulated over only a single lattice period, rather than the complete cavity geometry.

With these data, we only needed to specify the two taper parameters in order to design the cavity: the depth and number of periods. As discussed previously, the cavity itself is merely a consequence of the taper, formed by the existence of a propagating mode in the semiconductor band of the innermost cavity period. The peak of this band occurs at the very edge of the Brillouin zone, where  $|\vec{k}| = \pi/a'$ . Within subsequent taper periods, this frequency will lie within the band gap. These periods will maintain a similar real component for the wave vector, albeit with a slightly modified  $a'$ . More importantly, the imaginary component of the wave vector indicates that these will begin to act as a mirror. To a reasonable approximation<sup>2</sup>, the band edge frequency will undergo a  $\pi$  phase shift within the innermost period and maintain a similar phase within the subsequent taper.

---

<sup>2</sup>Due to the broken symmetry, we technically cannot apply any concepts from the band structure analysis, nor do we have a clearly defined local lattice constant due to the taper.

By designing our cavity to use a single period before the decay begins, this results in a resonance at the band edge. It is therefore the taper depth which determines the resonance, which can be determined directly from the band structure. Although a more detailed treatment is required to analyze the coupling between mirror sections and the account for the finite depth of the mirror [156, 148], this description gives results which are accurate to within a few percent, and which we can correct later.

Applying these ideas, we used the band data to simultaneously impose  $t = 220$  nm, find the structure needed to yield  $\lambda = 1550$  nm, and determine the optimal mirror geometry. Specifically, we considered the inner taper with  $a' = sa$ , where  $s$  is the scaling factor (in this case, equal to the taper depth),  $a$  is the lattice constant in the mirror region, and the prime denotes a scaled parameter. For each combination of  $w', r'$  and  $t'$ , we extracted the normalized frequency,  $f'$ , at the top of the semiconductor band. Using the thickness constraint to find a lattice constant, these frequencies were scaled by  $a' = 220$  nm/ $t'$  to yield  $f = f'/a'$ . This enabled us to find  $t'(w', r')$  by solving  $f(w', r', t') = 1/1550$  nm. Thus, for each combination of  $w'$  and  $r'$ , we had a unique value for  $t'$  which would both meet the constraint  $t = 220$  nm and provide a semiconductor band maximum at  $\lambda = 1550$  nm for the innermost taper.

To determine the optimal mirror parameters, we considered the band gap of the mirror segment. For each possible set of  $(w', r', t')$  at the innermost taper ( $a' = sa$ , where  $s$  is the taper depth), we examined the corresponding geometry in the mirror region:  $(w, r, t) = (sw', r, st')$ . We note that the normalized beam width and thickness are *smaller* in the mirror region, since these are normalized to a larger lattice and we wish to maintain a constant absolute width and thickness throughout the beam, while  $r$  remains relative to the local lattice constant. For each set of  $(w, r, t)$ , we determined the band gap by identifying the semiconductor band maximum and air band minimum (or light cone in the substrate, if the air band lay entirely above this). These frequencies were again adjusted for the absolute lattice constant  $a = 220$  nm/ $t$ , after which the band gaps could be quantitatively compared. From this, we selected the maximum band gap as the optimal mirror geometry, although one could easily select a different metric (in particular, we might choose to evaluate the decay rate

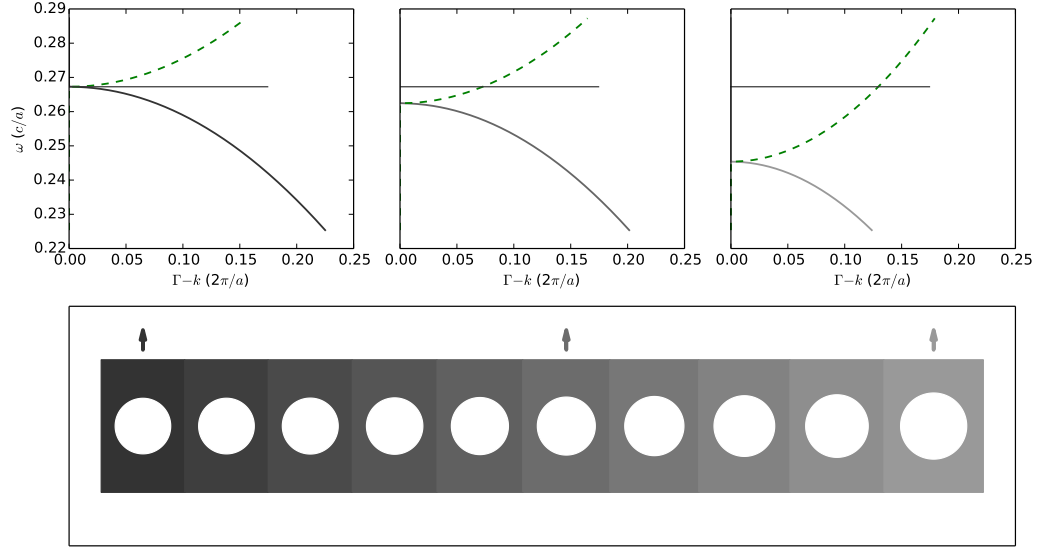
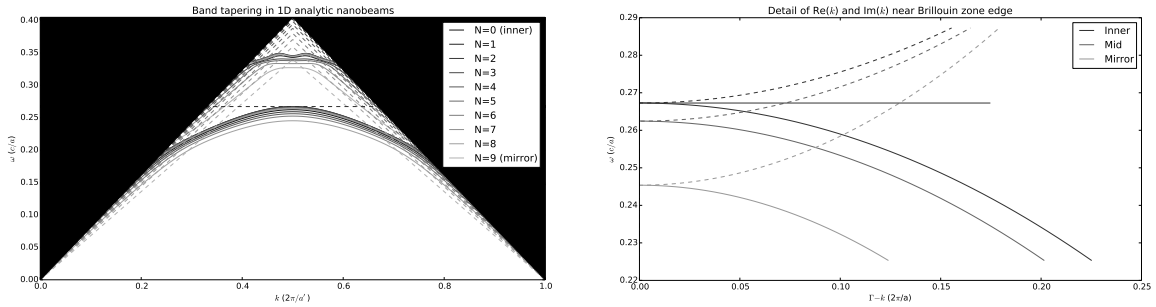


Figure 3.13: Schematic illustrating the analytic design process. Solid and dashed curves correspond to real and imaginary  $k$  components from the Brillouin zone edge; the solid black line highlights the resonance frequency, which matches the semiconductor band edge of the inner-most taper. Combinations of beam are chosen such that this resonance occurs at  $\lambda = 1550$  nm. These parameters are scaled up by  $[taperdepth]^{-1}$  to reveal the outer mirror segments. Geometry parameters yielding the maximum band gap are selected.

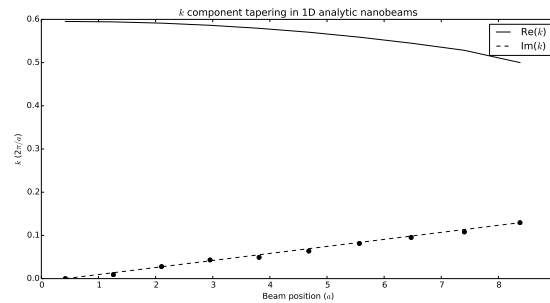
for the cavity resonance within the band gap, and select the corresponding maximum).

To design the taper, we adapted the analytic design technique reported by [343]. This method achieves a high quality factor by reducing the extent of the field in Fourier space, thereby minimizing scattering into the light cone. To accomplish this, the taper is designed to yield a Gaussian field envelope  $\propto e^{-Bx^2}$ . Since the evanescent decay of the cavity mode will itself be exponential ( $\propto e^{-q|x|}$  where  $q = \text{Im}(\vec{k})$ ), the taper should be constructed such that  $q = Bx$ . This requires knowledge of the decay rate at the cavity frequency for a given scaling factor,  $q(s)$ . While complex band structure simulations can reveal these rates, this would require an additional simulation for each tapered period at the cavity frequency. Instead, we applied the property of analytic continuation to extract this from our existing dispersion data. Using our optimized mirror geometry,  $(w, r, t)$ , we swept the scaling factor from  $s = [taper\ depth]$  to  $s = 1$  and extracted the semiconductor band  $\omega'_s(k')$  for each possible taper scaling,  $(w/s, r, t/s)$ . Examining the dispersion around the edge of the Brillouin zone, we fit a parabola of the form  $\omega'_s(k') = \alpha'_s - \beta'_s(k' - \pi)^2$ . Solving for  $k'$ , we then found  $q'_s(s, \omega'_s) = \text{Im}\left(\sqrt{(\alpha'_s - \omega'_s)/\beta'_s} + \pi\right)$ . For frequencies within the band gap,  $\omega'_s > \alpha'_s$ , resulting in



(a) Overlapping photonic structure showing the semiconductor and air bands for each of the taper segments. The dashed lines show the corresponding light cones (in oxide) for each segment. Note that  $k$  is plotted relative to the *scaled* lattice constant, while frequency is shown in normalized units (relative to the mirror segment, with  $a = 1$ ).

(b) Detailed view of the semiconductor band edge near the edge of the Brillouin zone ( $k$  values are relative to the  $\Gamma$  point), for mirror periods corresponding to the inner most taper segment, mid point, and mirror edge. Solid lines show real  $k$  components, corresponding to guided modes, while the dashed lines show imaginary components of the wave vector within the band gap. The horizontal black line highlights the cavity resonance frequency,  $\omega_0$ . The  $k(\omega) = \omega_0$  intercept determines the mirror strength along each segment.



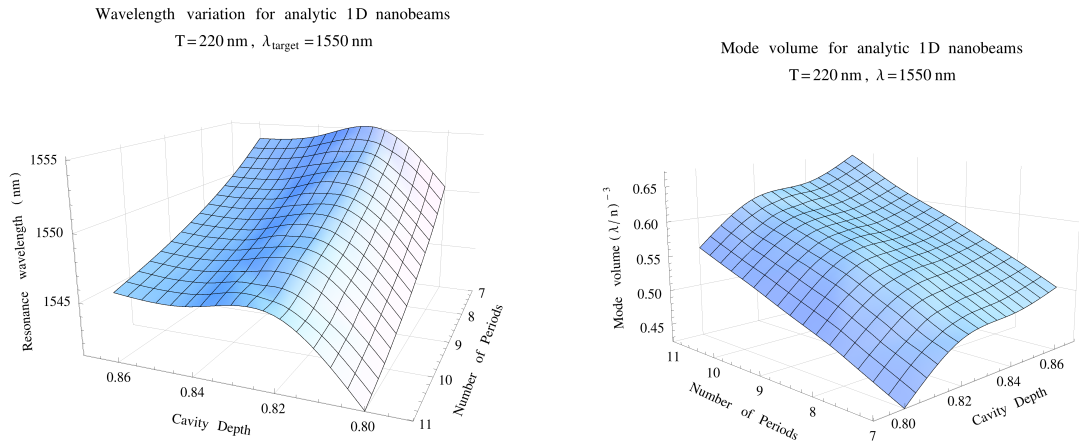
(c) Real and imaginary  $k$  components shown as a function of distance along the taper. The solid curve shows the real  $k$  component. Dots show the discrete  $\text{Im}(k)$  for each period, along with a dashed fit, revealing the linear  $k(x)$  relationship.

Figure 3.14: Analytic design band structures and corresponding  $k$  components along the taper.

a non-zero value for  $q'_s(s)$ . After scaling our resonant frequency to match a given taper scaling, these functions were evaluated to reveal the normalized decay rate at a given scale. Finally, these decay rates were adjusted to match the scaled lattice constants, yielding the absolute relationship  $q_s(s)$  for our cavity resonance, with  $q_{min} = q_s(\text{[taper depth]}) = 0$  and  $q_{max} = q_s(1)$ . For a taper with utilizing  $m$  periods, our target decay rate along the beam was  $\hat{q}_x(x) = q_{max} * x / (m - 1)$ . Beginning with the innermost taper  $s_0 = \text{[taper depth]}$ , we selected each subsequent period to satisfy  $q_s(s_i) = \hat{q}_x\left(\left(\sum_{n=0}^{i-1} s_n\right) - s_0/2 + s_i/2\right)$ , where the offset  $-s_0/2$  accounts for the existence of a propagating mode in the innermost period, and the term  $+s_i/2$  reflects the placement of the hole in the center of each period and selection of the total period length based on the target decay rate at this location.

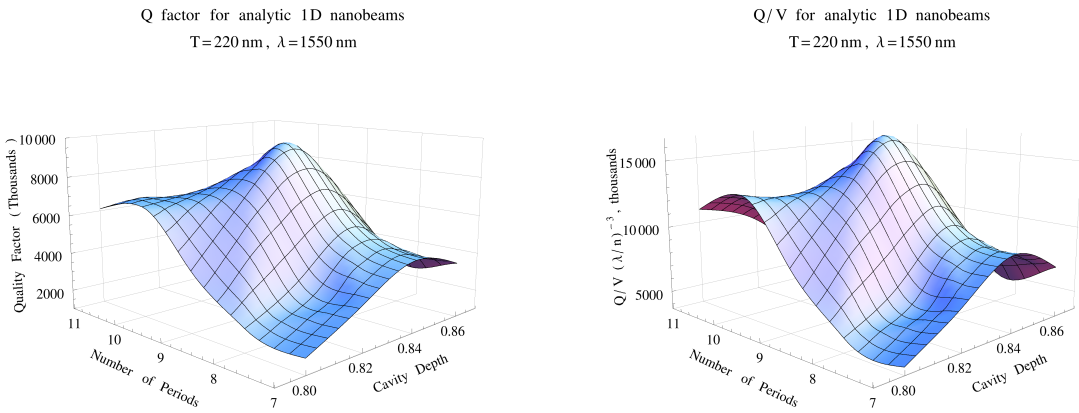
Using this algorithm and the band data obtained previously, we could design optimized cavities nearly instantaneously for a given number of taper periods,  $m$ , and taper depth,  $s_{min}$ . We began by simulating a cavity with a target wavelength of  $\lambda = 1550$  nm, thickness  $t = 220$  nm, taper rate  $m = 10$ , and depth  $s_{min} = 0.82$  using FEM [60]. As with previous simulations, we appended additional  $s = 1$  mirror periods to the beam until a total  $N = 15$  periods were included. Although our approximations were quite close, this yielded a resonance at a slightly longer wavelength than designed,  $\lambda = 1580.23$  nm, due to the finite depth of the mirror. To achieve closer resonances, we used this to calculate a correction factor and designed subsequent beams with a revised input wavelength  $\lambda' = (1550/1580.23) * \lambda$ .

Applying this correction, we swept the taper parameters and simulated cavities for  $m = 7..11$  and  $s_{min} = 0.80..0.86$ . The results are presented in Figure 3.15. Figure 3.15a displays the resonant wavelengths. For  $s_{min} \geq 0.82$ , these remained within  $\pm \approx 5$  nm or  $\approx 3\%$ , demonstrating the ability of the technique to provide deterministic resonances (further refinement would be possible by cascading additional correction factors). The mode volume, shown in Figure 3.15b, follows expected trends. Due to their higher decay rates, greater taper depths (low  $s_{min}$ ) are capable of producing smaller mode volumes. Similarly, steeper tapers (low  $m$ ) encourage a more rapid onset of the mirror, enabling a similar result.



(a) Wavelength variation of the cavity resonance using the analytic design procedure, showing the ability of the algorithm to perform deterministic design. The target wavelength was  $\lambda_{target} = 1550$  nm. Additional feedback cycles could further tighten this range.

(b) Dependence of the mode volume on taper length and depth for 1D nanobeams designed with the analytic process.



(c) Dependence of the quality factor on taper length and depth for 1D nanobeams designed with the analytic process.

(d) Dependence of the combined figure-of-merit,  $Q/V$ , on taper length and depth for 1D nanobeams designed with the analytic process.

Figure 3.15: Results of FEM simulations characterizing analytically-designed 1D nanobeam cavities. The quality factor and  $Q/V$  show >400% improvement over the expanded design results. Due to the deterministic design process, each depth and period combination produces a single, optimized cavity geometry which operates at the intended wavelength without excessive parameter sweeps to simultaneously tune resonance, quality, and mode volume.

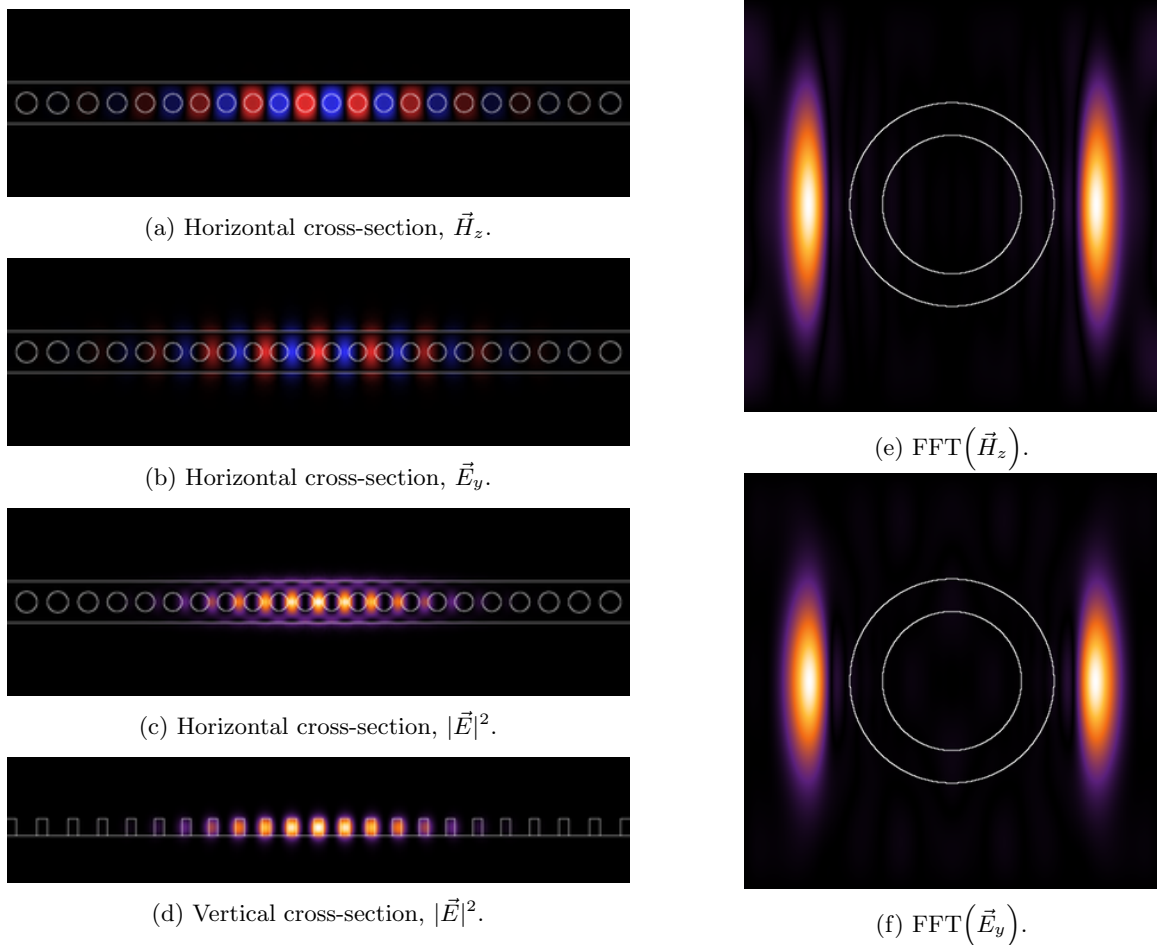


Figure 3.16: FEM simulations of our analytic beam design, showing cross-sections of the fields (through center of beam) and corresponding FFTs ( $\lambda/4$  in substrate). The FFT circles indicate the light cones for air (inner) and oxide (outer). This design has a slightly more gentle confinement than the expanded design, resulting in a marginally higher  $V$  but significant  $Q$  improvements.

The data for  $Q$  and  $Q/V$  are presented in Figure 3.15c and d, respectively. A similar explanation as before can be supplied for the  $Q$  maximum, with tighter confinement due to abrupt tapers or significant depth (low  $m$ ,  $s_{min}$ ) resulting in greater scattering, while cavities with more gentle confinement (high  $m$ ,  $s_{min}$ ) eventually suffer lateral leakage through the mirrors. Here, the maximum  $Q$  and  $Q/V$  both occurred for  $m = 9$  and  $s_{min} = 0.84$ . For this design, we found  $Q = 9.27 \times 10^6$  and  $V = 0.57(\lambda/n)^3$ , corresponding to a  $Q/V = 1.62 \times 10^7(\lambda/n)^{-3}$ . This represents a  $\approx 460\%$  improvement in  $Q$  and  $\approx 400\%$  improvement in  $Q/V$  over the previous  $Q_{max}$  design.

The preceding analysis was undertaken after fabrication work had concluded, and therefore has not been experimentally verified. Although the final designs presented here showed impressive

theoretical improvements in quality factor compared to the previous optimized beam, it is entirely possible, if not likely, that these gains would not be experimentally realizable due to scattering losses or other fabrication anomalies.

In spite of this, we believe the new process has merit for several reasons. First, while the fabrication tolerant variants discussed in a later section (see 3.4.5) consistently produced higher experimental quality factors than the design presented above, their theoretical  $Q$  was only  $\approx 4 \times 10^5$ , or nearly 400% *lower*. Improvements to the fabrication tolerant design variants therefore have immense potential to produce experimental success. Combined with the revised analysis here, the fabrication tolerant version retained nearly all of the gains of the regular, producing a theoretical  $Q \approx 7.8 \times 10^6$ . Even a fraction of this increase would be a tremendous improvement.

Along with the potential  $Q$  improvements, particularly for the fabrication-tolerant design, the new process was far more deterministic. In the previous design cycle, full-cavity parameter sweeps needed to be performed over all aspects of the mirror geometry and taper profile, after which solutions with the appropriate resonance could be identified and compared. Here, however, the process inherently produced a cavity with the given resonance (within a few nm, or roughly a few tenths of a percent). For a given taper depth and rate, optimal mirror parameters were automatically selected from gap maps. This eliminated unnecessary simulation of full cavities which were mistuned or inherently lower in  $Q$ , while reducing the dimensions of the parameter space to only two values for the taper. The drastic improvement in computation enabled a more complete exploration of the optimal taper parameters. Finally, the process can easily be applied to different material systems or mirror parameters.

### 3.3.3 Comparison

The designs and performance metrics are presented in Table 3.1 for an abrupt cavity (with no taper), our initial design, the revised design using an expanded parameter set, and the final analytic design. In each case, the dimensions were selected to provide a resonance near  $\lambda = 1550$  nm for a thickness of 220 nm (consistent with our SOI device layer thickness). All of the values were retrieved from

FEM simulations for  $N=15$  mirror periods (including the taper region) on either side of the cavity. Due to slow increase in mirror strength within the taper region, the mode volume is progressively higher as we go from the unrefined abrupt cavity to the analytic design. However, this increase is more than compensated for by the increase in cavity quality factor. Table 3.2 shows field patterns, field confinement, and Fourier transforms for the different designs. While the field patterns reveal only subtle differences between the structures, the Fourier transforms clearly exhibit a significant decrease in field components within the light cone, consistent with the large increase in quality.

	Normalized Width (a)	Normalized Thickness (a)	Normalized Mirror Radius (a)	Quality Factor	Mode Volume $(\frac{\lambda}{n})^3$	$Q/V$ $(\frac{\lambda}{n})^{-3}$
<b>Abrupt</b>	1.4	0.6	0.225	1,061	0.455	2,331
<b>Initial</b>	1.0	0.537	0.3	668,666	0.491	1,363,170
<b>Expanded</b>	1.2	0.56	0.25	1,859,130	0.520	3,572,430
<b>Analytic</b>	1.334	0.532	0.333	9,264,960	0.571	16,235,800

Table 3.1: Geometric parameters and performance metrics for different cavity designs. All devices used 15 mirror periods (including taper region) on each side of the cavity center.

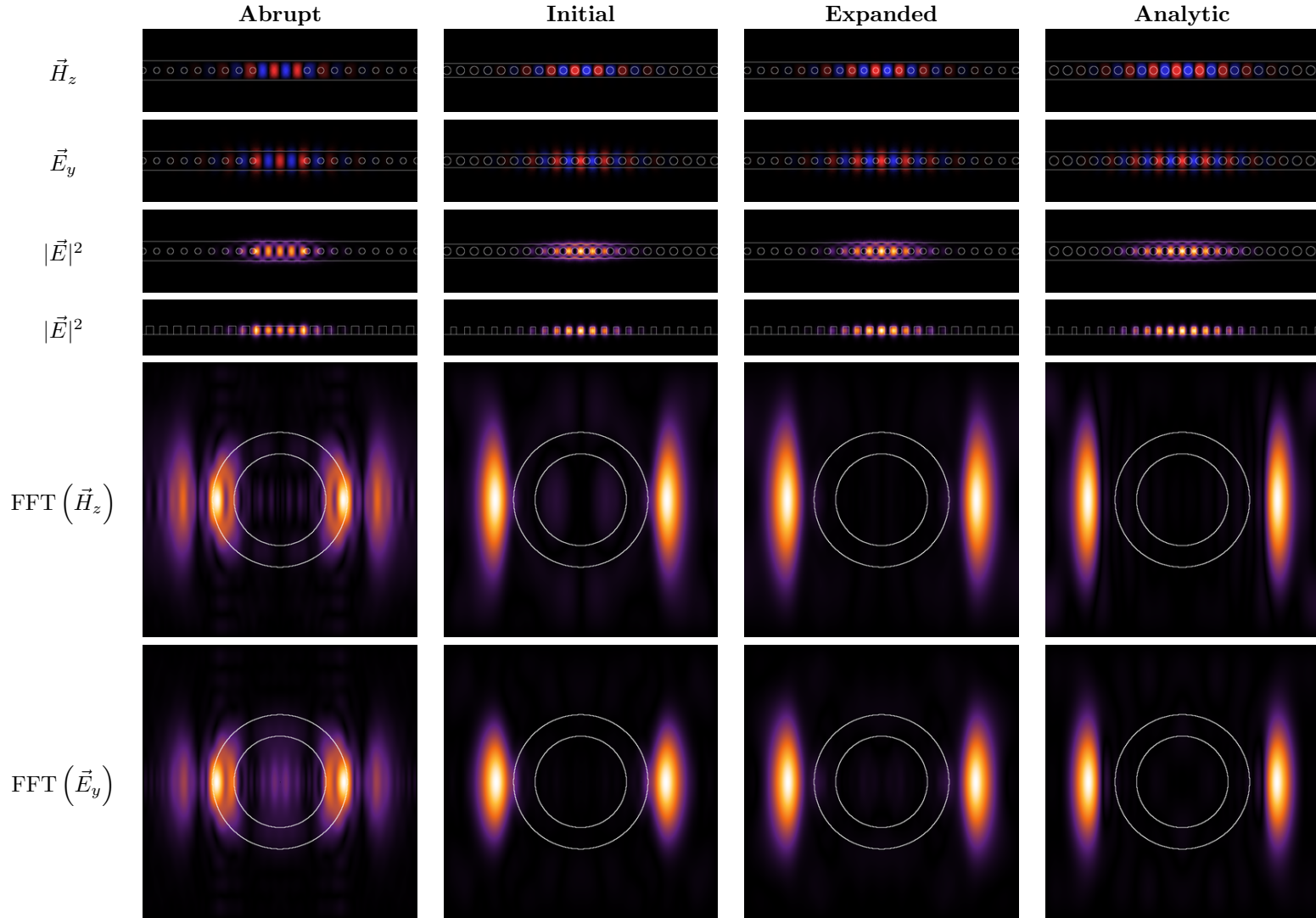


Table 3.2: Comparisons of electric and magnetic fields for different cavity designs. Horizontal sections are taken through the beam center, and FFTs are taken  $\lambda/4$  below the beam (in the substrate). The FFT circles indicate the light cones for air (inner) and oxide (outer). While the field patterns between the three tapered cavities reveal only subtle differences, the energy content within the light cones shows a dramatic reduction at each stage, explaining the progressive improvement in quality factor.

### 3.3.4 Coupling

Experimentally, we tested a number of coupling methods, including fiber taper, resonant scattering [295, 296] and end-fire coupling from a feeding waveguide. The first two methods did not require any additional design work, although we note that both techniques will benefit from a large number of mirror periods, to eliminate lateral losses and maximize coupling efficiency. In the case of fiber taper probes, the coupling rate and cavity loading were dynamically controlled during the course of the experiment based on proximity and placement of the fiber loop relative to the cavity, while resonant scattering provided minimal loading, albeit with a fixed coupling rate.

In order to end-fire couple efficiently, however, we needed to construct an additional coupling region. As described above, this section should adapt both the field pattern and effective index in order to achieve mode matching between the waveguide and mirror region. Quan *et al.* [284] encourage the use of a fixed photonic crystal period throughout the cavity, with the explicit purpose of optimizing coupling efficiency by matching the effective index between the mirror and waveguide. While this method naturally eliminates one of the concerns, the need for a transition region remains in order to achieve optimal field overlap. Moreover, current fabrication techniques achieve significantly more precise control over feature placement than absolute size. Due the relative energy density within the resonator itself as compared to the taper, the quality of a device is extraordinarily sensitive to fabrication accuracy of the cavity, whereas slight manufacturing variances in the coupling section will only have a minor impact on the device, primarily affecting the coupling. Given the minimal benefits from utilizing a fixed lattice, we chose to exploit experimental control over feature location as the primary feature in the cavity taper. Consequently, our coupling section needed to manipulate both the field pattern and effective index to achieve efficient energy transfer between the waveguide and cavity.

By expanding the electromagnetic mode in the basis of the individual coupling periods and performing transmission matrix calculations, it is technically possible to model the transition of the mode from the waveguide into the mirror region [156, 36, 209]. As with the cavity taper, however, a reasonable selection of intermediate periods is adequate to achieve an essentially adiabatic transition

between the waveguide and cavity. For a mode within the band gap, the complex wave vector lies at the edge of the Brillouin zone. This results in a wave vector with  $\text{Re}[k] = \pi/a$ . A sophisticated solution might match the propagation constants for the intermediate periods based on band data. For devices where we included tapers, we calculated the lattice period which would to match the propagation constant within the waveguide. We then applied a linear taper over  $N$  periods (typically 5) between this lattice constant and that of the waveguide mirror, while simultaneously tapering the hole radius between a minimum of  $\approx 60$  nm (based on fabrication control) and that of the mirror.

## 3.4 Cavity Fabrication, Testing, and Optimization

### 3.4.1 Fabrication

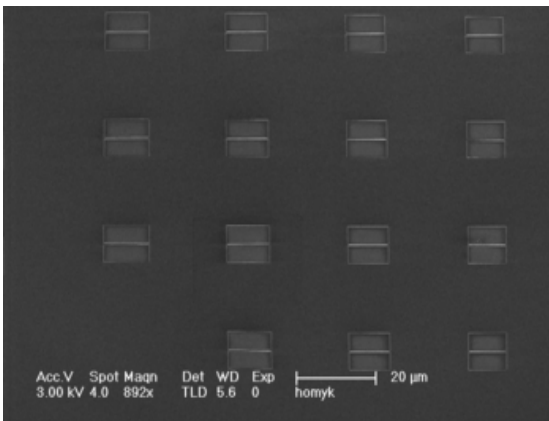
All of our 1D photonic crystal nanobeam devices were fabricated using pieces scribed from identical 8" SOI wafers purchased from SOITEC (Bernin, France), with a standard 220 nm device layer and nominal oxide thickness of 2  $\mu\text{m}$ . These substrates were produced using the SmartCut process, which uses ion implantation and layer exfoliation to transfer a single-crystal (100) silicon device layer onto a silicon handle wafer capped with a thick thermal oxide. This enables a thicker buried oxide than SIMOX for increased optical isolation from the substrate, and yields extremely high-quality device layers with excellent uniformity. Throughout our fabrication, we observed  $< \pm 2$  nm deviation in the device layer thickness (both across a given wafer and between wafers), as measured by reflectometry.

Our standard fabrication process began by cleaving a piece (typically  $\approx 15$  mm  $\times$  15 mm) from the source wafer and cleaning with acetone and IPA. Samples were left uncovered on a 180° hotplate for 5 min to dehydrate the surface prior to resist application. For the mask, our earliest devices used 2% PMMA 950k diluted in chlorobenzene from Microchem (Westborough, MA). We quickly transitioned to ZEP-520A (Zeon Corporation, Tokyo, Japan), which has improved etch resistance<sup>3</sup> and tended to produce higher-quality devices. The ZEP was initially used at full concentration, and later

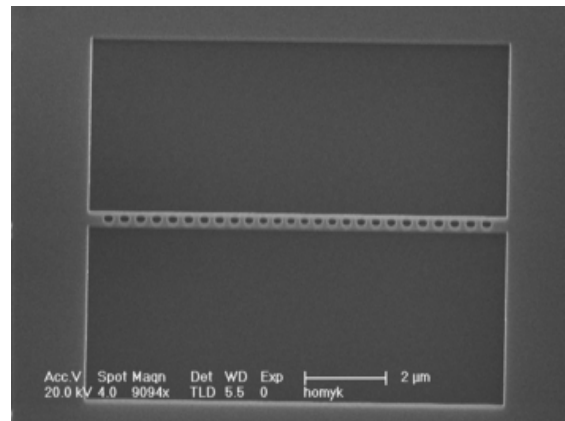
---

<sup>3</sup>We also tried a negative hydrogen silsequioxane resist (XR-1541, Dow Corning, Midland, MI), which is also known to have excellent resolution and etch resilience, but this resist tends to be extremely susceptible to contamination and degradation, and we found it often resulted in excess particulate deposition. The Al<sub>2</sub>O<sub>3</sub> hardmask utilized for pillar fabrication is unsuitable for photonic devices due to the potential edge roughness induced during the liftoff process.

diluted 1:1 in anisole to produce thinner layers which further improved resolution and repeatability. In each case, the wafer was loaded into a spin coating system, covered in the appropriate resist, and spun at a speed of 4000 rpm (PMMA) or 5000 rpm (ZEP) for 60 s, with an acceleration of 1330 rpm/s. After spin coating, samples were baked for 3 min at  $180^\circ$  to remove excess solvents. Film thickness was characterized using a reflectometer, with typical measurements of 110 nm (PMMA), 350 nm (full ZEP), and 120 nm (diluted ZEP).



(a) SEM showing array of 1D nanobeam devices.



(b) SEM showing a close-up of single 1D nanobeam device.

Figure 3.17: SEMs of our initial nanobeam devices, showing an array with different lattice constants and a single device. The hole tapering is visible at the center of the cavity. These devices were designed to be tested by tapered fiber loops and cross-polarized resonant scattering setups. Large buffer regions were included to avoid coupling to slab modes.

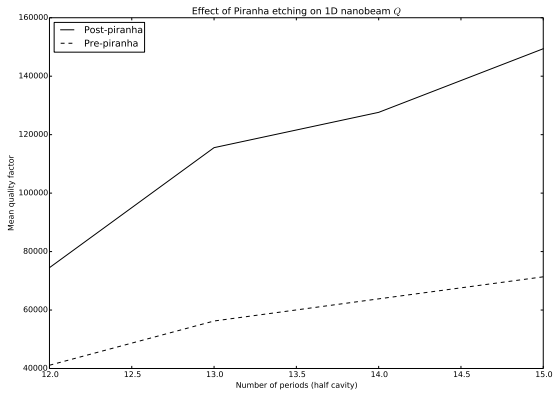
Because both PMMA and ZEP are positive resists, device lithography required exposing the holes and area surrounding the nanobeam, rather than the nanobeam itself. For the early devices which were coupled by fiber taper or resonant scattering, a simple inverted mask was developed, fractured using a 2.5 nm step size, and written with a single low-current beam. Subsequent waveguide-coupled masks were made by defining an  $8\ \mu\text{m}$  buffer region beyond the waveguide (large enough to prevent leakage into slab waveguide modes), and subtracting the device shape from the buffer to invert the pattern. To avoid excess lithography time exposing the bulk of the buffer region, this pattern was split into a fine-resolution region for all areas within  $1\ \mu\text{m}$  of the device, and a coarse-resolution region for areas beyond that (with a 100 nm overlap, to ensure alignment between the region). The fine region was fractured at 2.5 nm and written with a low current, while the buffer area was

fractured at 10 nm - 20 nm and written at much higher currents.

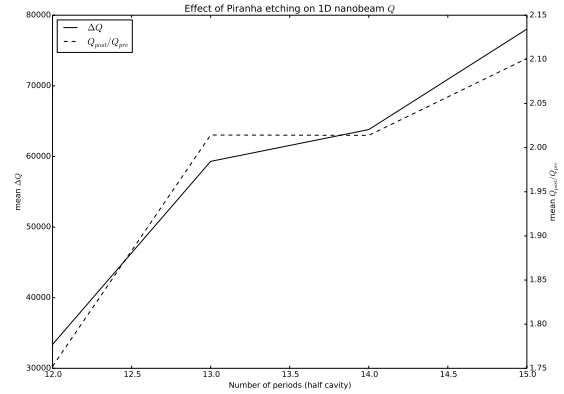
Electron beam lithography was performed in a Leica EBPG 5000+ operating at 100 kV. For the PMMA, fine patterns were exposed with a dose of  $\approx 1,000 \text{ } \mu\text{C}/\text{cm}^2$  using a  $\approx 700 \text{ pA}$  beam. ZEP layers were written with beam currents of  $\approx 300 \text{ pA}$  (fine patterns) and  $\approx 5 \text{ nA}$  (coarse patterns), using doses of  $\approx 220 \text{ } \mu\text{C}/\text{cm}^2$ . Once exposed, devices with PMMA were developed in 1:3 MIBK:IPA for 30 s, rinsed with IPA for 5 s, and dried with  $\text{N}_2$ . ZEP masks were developed in ZED-n50 (Zeon Corporation, Tokyo, Japan) for 90 s, rinsed with IPA for 30 s, and dried with  $\text{N}_2$ .

Etching was performed in an Oxford Plasmalab System100 ICP380. Samples were first affixed to a 6" silicon carrier wafer by applying a thin coating of Fomblin oil (Solvay, Brussels, Belgium) to the back of the sample with a cleanroom swab. The carrier wafer both provided mechanical support for the small sample pieces, and also served to load the chamber with excess silicon in order to slow the process and eliminate pattern-dependent etch rates, thus improving process repeatability and control. During etching, the sample table and sidewalls temperatures were actively controlled with PID-driven thermostats and held at  $15^\circ\text{C}$  and  $40^\circ\text{C}$ , respectively; these temperatures ensure adequate sample passivation while prevent excess contamination of the chamber sidewalls. During the process, the carrier wafer was held in place by an  $\text{Al}_2\text{O}_3$  clamp and backed by 10 Torr He pressure to ensure adequate thermal transfer between the table and sample. We used a mixed-mode gas chemistry consisting of  $\text{SF}_6$  and  $\text{C}_4\text{F}_8$  to simultaneously etch and passivate in order to achieve highly anisotropic sidewalls. For a typical process, the chamber pressure was regulated to 10 mTorr and gas flows were set to 32 sccm ( $\text{SF}_6$ ) and 52 sccm ( $\text{C}_4\text{F}_8$ ) using mass flow controllers. Once the flows and pressure had stabilized, a 3 s strike process was used to establish the plasma. Etching proceeded for 70 s using an ICP power of 1,200 W and a capacitively-coupled power of 23 W. Once the primary etch had finished, a 30 s  $\text{O}_2$  plasma at 2,500 W/25 W/100 sccm/10 mTorr was used to remove excess passivation developed during the etch.

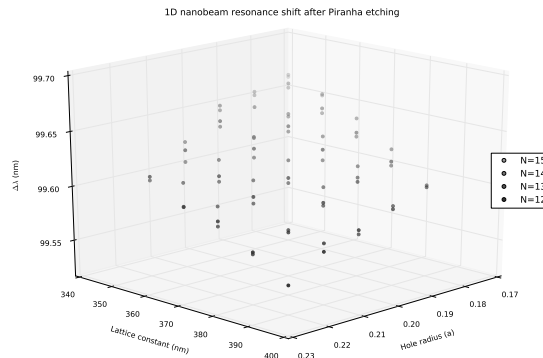
While not used for the initial devices, a post-etch chemical treatment using piranha/HF etch cycles [41] was found to improve quality factors by  $\approx 2.75\times$  (with a greater effect on devices with more mirror periods and higher quality factors; see Figure 3.18). We used a fresh 3:1 solution of



(a) 1D nanobeam quality factors before and after piranha treatment.



(b) Absolute and relative change in 1D nanobeam quality factor after piranha treatment.

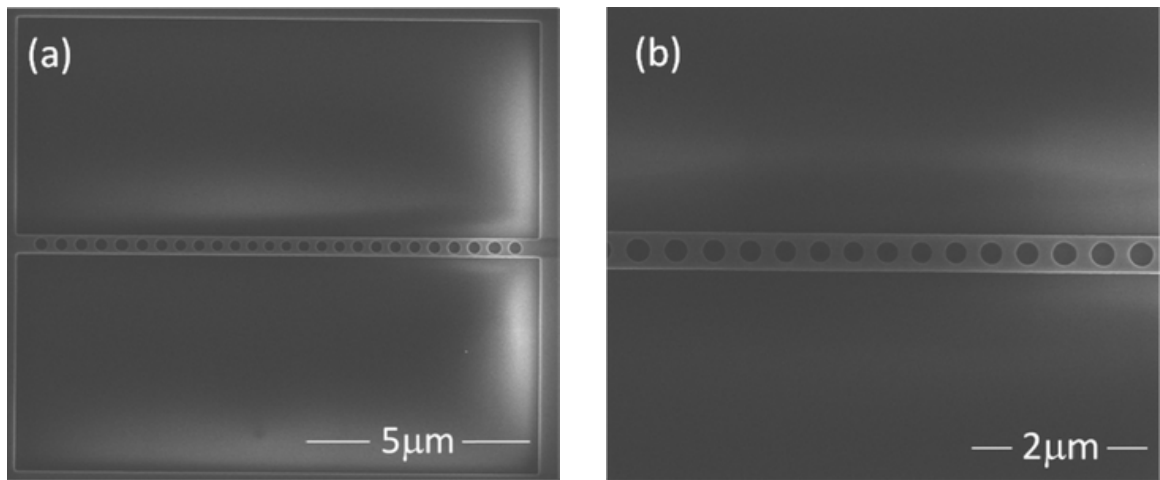


(c) Resonance shift of 1D nanobeam cavities due to piranha treatment.

Figure 3.18: Effect of piranha treatment on 1D photonic crystal nanobeam cavities. All devices showed a significant increase in  $Q$  after treatment. A more pronounced effect (in both relative and absolute change) is observed as the number of cavity periods increased, due to the greater sensitivity of high- $Q$  devices to surface quality. Over the entire set, the mean  $Q$  increased by a factor of 2.75. Devices also blue-shifted by an average of 5.45 nm. Despite similar resonant wavelengths across devices, clear trends in resonance *shift* are observed for the geometries due to differences in their field components at the surface.

$\text{H}_2\text{SO}_4:\text{H}_2\text{O}_2$ . A beaker containing  $\text{H}_2\text{SO}_4$  was first placed on a hotplate and heated to  $65^\circ\text{C}$ . Once the temperature had stabilized,  $\text{H}_2\text{O}_2$  was added to the beaker and mixed. Samples were then immersed in the piranha solution for 10 min, after which they were immersed and rinsed in several successive DI baths to wash off the acid. Following the piranha treatment, the resulting chemical oxide was removed by a 10 s dip in 1:6 dilution of buffered HF in DI, successively rinsed with DI, and dried with  $\text{N}_2$ .

### 3.4.2 Fiber loop and resonant scattering



(a) SEM image of a 1D nanobeam cavity.

(b) SEM image of the center of a nanobeam, showing a region of tapered holes surrounding the cavity anti-node.

Figure 3.19: The first generation of our nanobeam devices, which were tested using a tapered fiber loop and resonant scattering.

Our first 1D photonic crystal nanobeam cavities used the initial design parameters, with a normalized width of  $w = 1a$ , normalized hole radius of  $r_0 = 0.3a'$ , which varied with the *local* lattice constant, and a linear cavity taper from  $a' = 0.84a$  at the cavity center to  $a' = 1a$  in steps of  $0.02a$ . Arrays of the nanobeams were fabricated using a PMMA mask, where the dose and lattice constant were swept to vary the wavelength.

We tested the devices by coupling to the cavities using a tapered fiber loop [332, 141], consisting of a Corning SMF-28 optical fiber which had been heated and stretched to produce a tapered region with a  $1 \mu\text{m}$  diameter, then bent to produce a loop with a  $200 \mu\text{m}$  radius of curvature. Once affixed

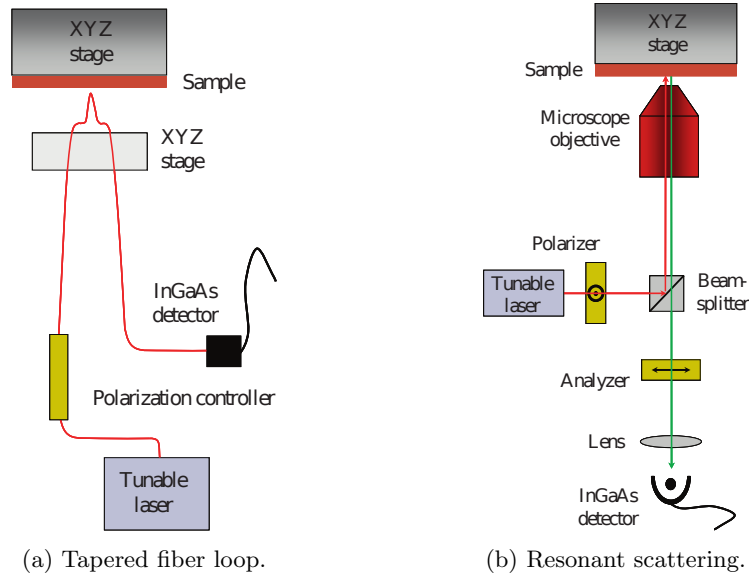


Figure 3.20: Schematics describing the experimental setups for characterizing our 1D nanobeams.

to a glass slide, the fiber position was manipulated on a computer-controlled x,y,z stage. Samples were also mounted on a movable stage, allowing adjustment of both the relative position and angular orientation of the fiber and nanobeam axes. The output from an Agilent 81682A tunable laser was fed into a polarization controller, through the fiber loop, and collected by an InGaAs photodiode at the output. A schematic of this setup is shown in Figure 3.20a.

Using this apparatus, we characterized the transmission spectra as a function of the contact length between the fiber and cavity, contact position, and angle. These results were compared to crossed-polarized resonant scattering measurements, and reported in [295, 296]. To test each device, the fiber loop was aligned to the cavity using the motorized stage. As the loop came near to the surface of the sample, electrostatic and van der Waals forces pulled the fiber into the sample, causing it to stick to the nanobeam. Once the taper was touching the surface, the contact length could be adjusted by advancing or retracting the actuators. Once in place, the laser wavelength was scanned in order to sample the cavity spectrum. Sample transmission spectra taken from the center and edge of the beam are compared in Figure 3.21.

The presence of the fiber taper created an additional loss mechanism for the cavity, commensurate with the coupling strength. As expected, longer contact lengths resulted in greater coupling,

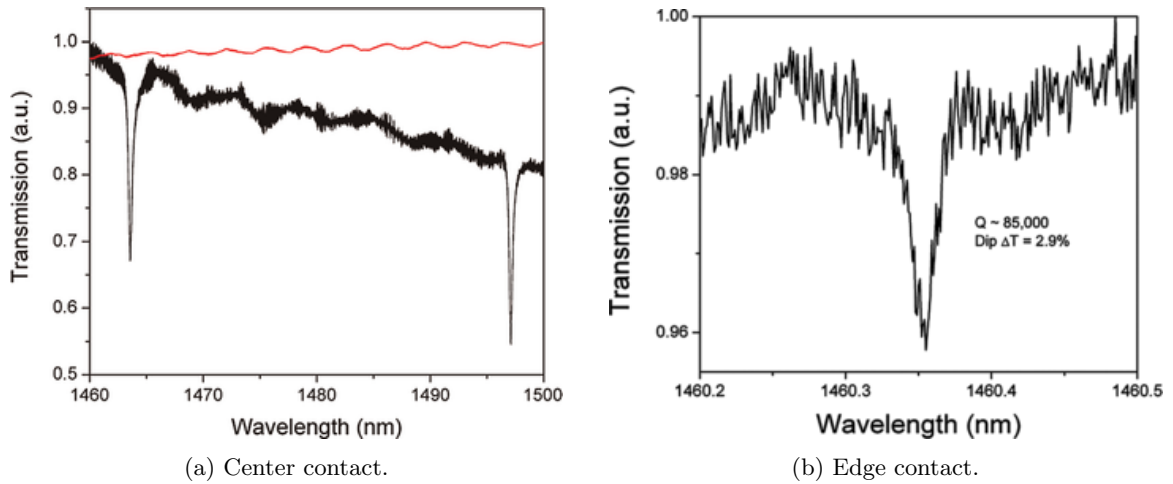


Figure 3.21: Fiber loop transmission spectra of a typical nanobeam cavity at  $45^\circ$ , comparing the effects for center and edge contact positions. The red curve in (a) shows the spectrum directly from the laser. Note the red-shift induced for the center contact position due to higher dielectric loading, as well as the deeper resonant dip. In contrast, the spectra taken from the edge exhibits a higher quality factor.

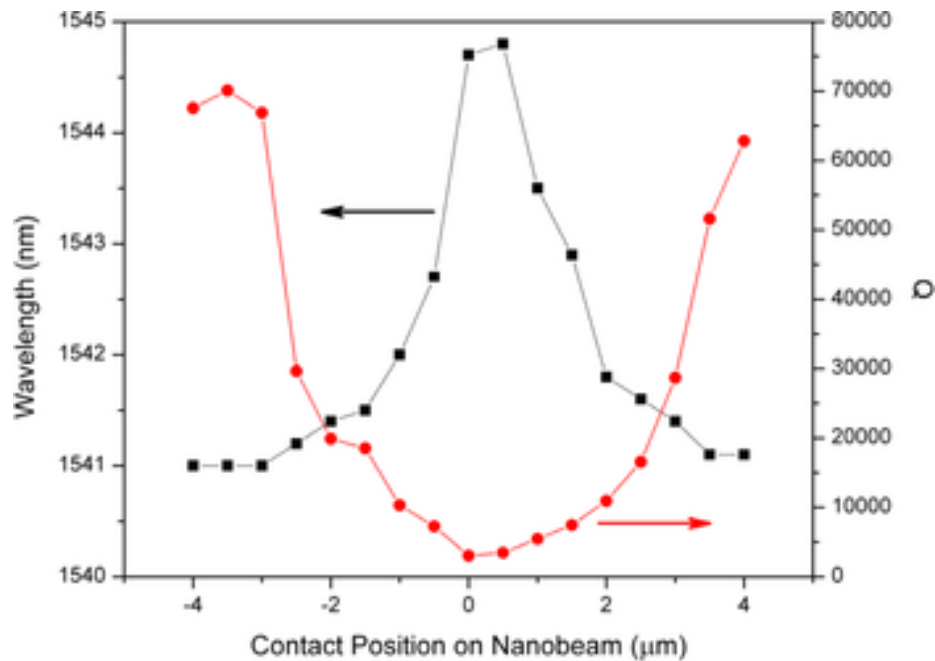


Figure 3.22: Fiber loop transmission measurements as a function of position on a typical nanobeam cavity at  $45^\circ$  (center of the nanobeam corresponds to  $0 \mu\text{m}$  and the attached edges to  $\pm 6 \mu\text{m}$ ), showing cavity resonant wavelength (black squares) and  $Q$  (red circles).

producing deeper resonance dips with lower  $Q$ s. Particularly for positions near the center of the cavity, the dielectric loading from the fiber also red shifted the resonant wavelength by several nm. Conversely, the highest quality factors observed with the tapered fiber loop corresponded to the weakest coupling, where the fiber rested near the edge of the cavity with minimal coupling length. In this scenario, the presence of the fiber produces only a minimal change in the resonant wavelength. This behavior can be seen in Figures 3.21 and 3.22. For fiber positions beyond  $\pm 4 \mu\text{m}$  from the center of the cavity, coupling was too low to continue observing the resonant dip.

The effects of fiber angle were also studied. When the fiber angle was aligned with the cavity, deep resonant dips were observed, consistent with a high degree of coupling. This behavior was still observed for positions near the edge of the cavity, due to the extension of the fiber above the anti-node. When aligned perpendicular to the cavity, no coupling was observed, as the cavity and fiber polarizations no longer overlapped. Peak quality factors were measured for contact positions near the edge of the device, minimal contact length, and angles of  $20^\circ - 60^\circ$  between the fiber and cavity axes. From these devices,  $Q$ s as high as 85,000 were measured using the fiber apparatus, although the average quality factor was only 20,000.

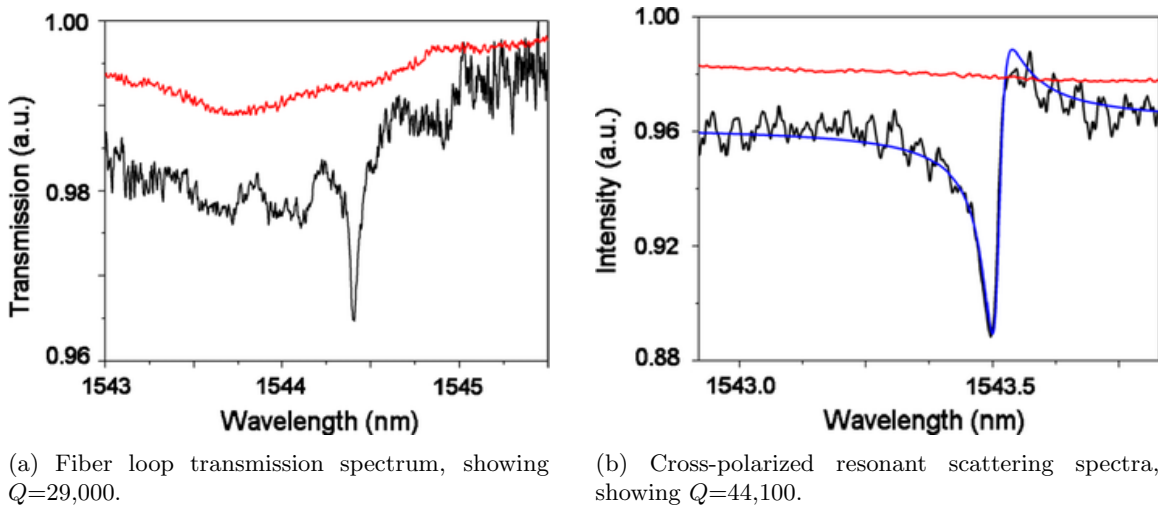


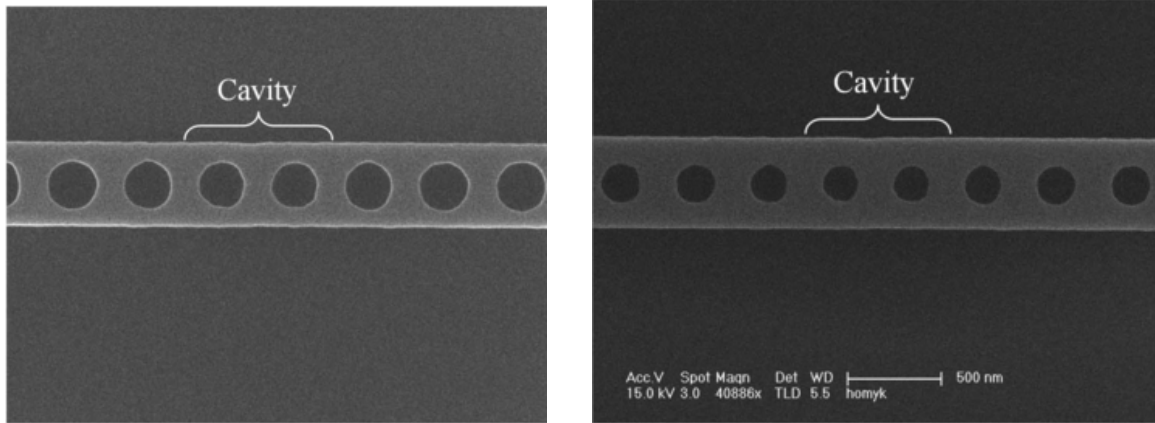
Figure 3.23: Comparison of spectra recorded from the same cavity using the fiber loop setup and cross-polarized resonant scattering technique. Black curves show raw data for the cavity; red curves show laser spectra; the blue curve in (b) shows the fitted Fano lineshape. Note the red-shift and drop in  $Q$  induced by the fiber loop due to dielectric loading and the introduction of an additional loss channel.

The devices were also characterized using a resonant scattering setup [238, 79]; a schematic of this arrangement is presented in Figure 3.20b. Here, normally incident light was directed at the cavity center, with an incoming polarization which was rotated  $45^\circ$  relative to that of the cavity. Due to the partial overlap in polarization, this excitation was still able to couple to the cavity, which scattered light at its own polarization. This scattered light also exhibited a partial overlap with a polarization which was orthogonal to the incoming energy. By collecting the scattered light through a crossed polarizer (rotated  $90^\circ$  relative to the excitation beam), it was possible to selectively measure scattered components which had coupled to the cavity, while rejecting pure reflections from the surface. Measured with this technique, the cavity spectra exhibited a Fano resonance [100]; an example resonance is shown in Figure 3.23, and compared to a fiber loop measurement of the same device. Because the resonant scattering technique coupled to an already-existing loss channel, it was possible to characterize the cavities without further degradation in  $Q$  or a change in resonance, while the fiber loop represented a significant load, inducing substantial losses and red-shifts. On average, we observed that  $Q$ s measured using the fiber loop were 38% lower than those measured through the crossed polarizers.

### 3.4.3 ALD passivation

While the highest-performing devices from the initial testing were approaching levels needed for optical trapping, the average quality factors were still quite low and additional improvements were needed. As a potential solution, we explored the effects of atomic layer deposition (ALD) on the nanobeam cavities; this work was reported in [104]. In this process, thin-film deposition occurs through sequential application of two or more gas phase chemicals. The growth takes place as a chemical reaction at the sample surfaces. Because the reaction is self-limiting, the technique enables extremely accurate control of film thickness by simply by counting the number of cycles. Additionally, the nature of the deposition results in extremely conformal films, which tend to reduce surface roughness. Previous work has reported significantly lower propagation losses in silicon strip and slot waveguides through the use of ALD-grown  $\text{Al}_2\text{O}_3$  and  $\text{TiO}_2$  films [3, 316]. Moreover, the

atomic-level control over growth could be used to tune cavity resonances to match emitter spectra, while it is also possible to incorporate active materials directly, for example by doping  $\text{Al}_2\text{O}_3$  layers with erbium during deposition [326]



(a) Cavity before ALD deposition.

(b) Cavity after deposition of 20 nm  $\text{Al}_2\text{O}_3$  by ALD.

Figure 3.24: SEM images comparing the cavity region of a silicon nanobeam before and after ALD.

The device geometry and fabrication followed the initial design. Devices were characterized using the resonant scattering setup to avoid loading the cavities with the fiber taper. The quality factor of each device was measured prior to deposition in order to establish a baseline. Following initial characterization, samples were coated with 20 nm of either  $\text{TiO}_2$  ( $n = 2.27$  at  $\lambda = 1.55 \mu\text{m}$ ) or  $\text{Al}_2\text{O}_3$  ( $n = 1.62$  at  $\lambda = 1.55 \mu\text{m}$ ). The  $\text{TiO}_2$  deposition occurred at  $120^\circ\text{C}$  using titanium tetrachloride ( $\text{TiCl}_4$ ) and water as precursors [4].  $\text{Al}_2\text{O}_3$  was deposited at  $200^\circ\text{C}$  using trimethylaluminum ( $\text{Al}_2(\text{CH}_3)_6$ ) and water as precursors [282]. Figure 3.24 presents SEM images of a cavity before and after the deposition of 20 nm of  $\text{Al}_2\text{O}_3$ , showing a clear reduction in hole size due to the thin film.

After growth, cavities were again characterized using the resonant scattering technique. The sample coated with  $\text{TiO}_2$  showed an average red-shift in the cavity resonance of  $59.2 \pm 0.7$  nm, while resonances for the  $\text{Al}_2\text{O}_3$ -coated sample red-shifted by an average of  $30.3 \pm 0.8$  nm. The results of the  $Q$  measurements are shown in Figure 3.25. While on  $\text{TiO}_2$ -coated cavity showed an  $Q$  increase of 29%, the average change in  $Q$  over all cavities was  $-1.3 \pm 16\%$ . In contrast, every  $\text{Al}_2\text{O}_3$  coated cavity showed an increase in quality factor, with an average improvement of  $38 \pm 31\%$  and a maximum

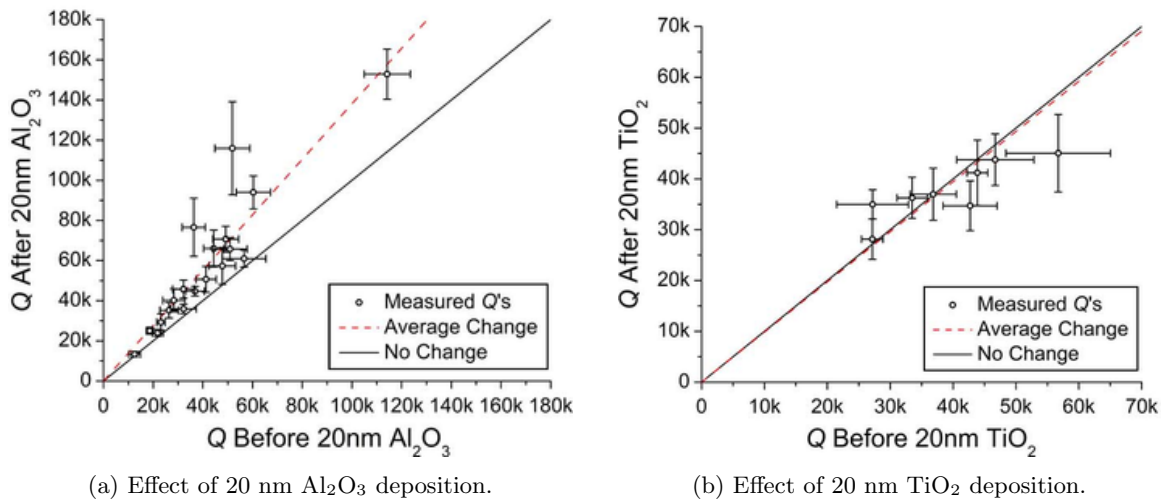


Figure 3.25: Comparison of cavity  $Q$ s before and after ALD. The solid lines have a slope of 1 and represent no change in  $Q$ , while the dotted lines represent the average change. For  $\text{Al}_2\text{O}_3$  deposition, cavity quality increased by an average of 38%, while  $\text{TiO}_2$  deposition led to an average decrease of 1.3%.

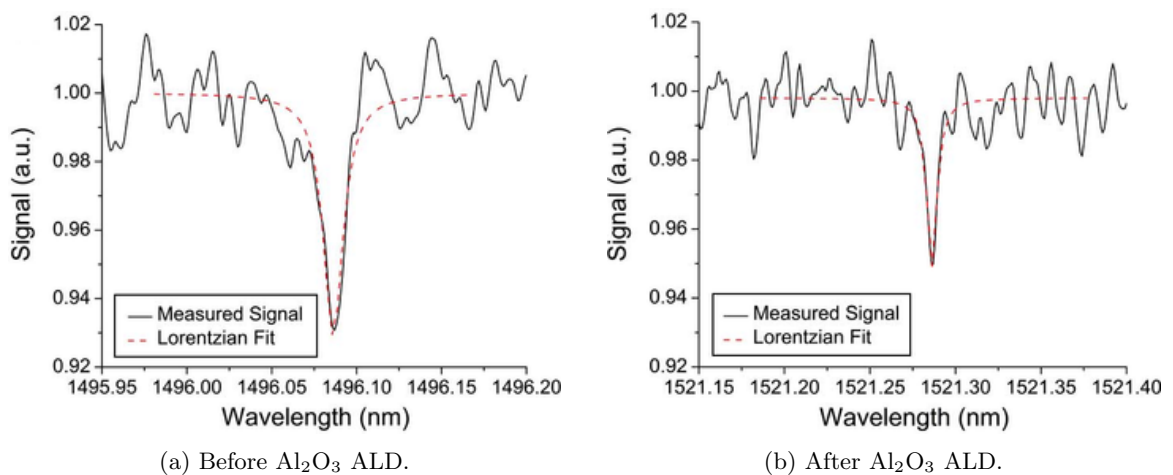
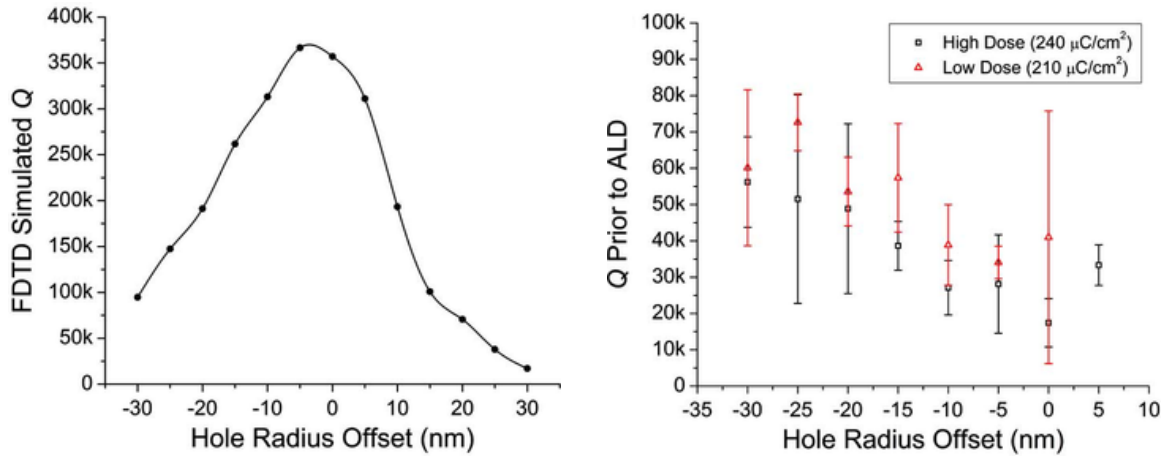


Figure 3.26: Crossed polarizer resonant scattering measurements of a cavity before and after 20 nm  $\text{Al}_2\text{O}_3$  ALD. Before the deposition, the cavity resonance exhibited a  $Q$  of 107,000; this increased to 212,000 after ALD.

increase of 124%. Figure 3.26 presents cavity spectra from the  $\text{Al}_2\text{O}_3$ -coated sample before and after deposition, showing an increase in  $Q$  from 107,000 to 212,000.



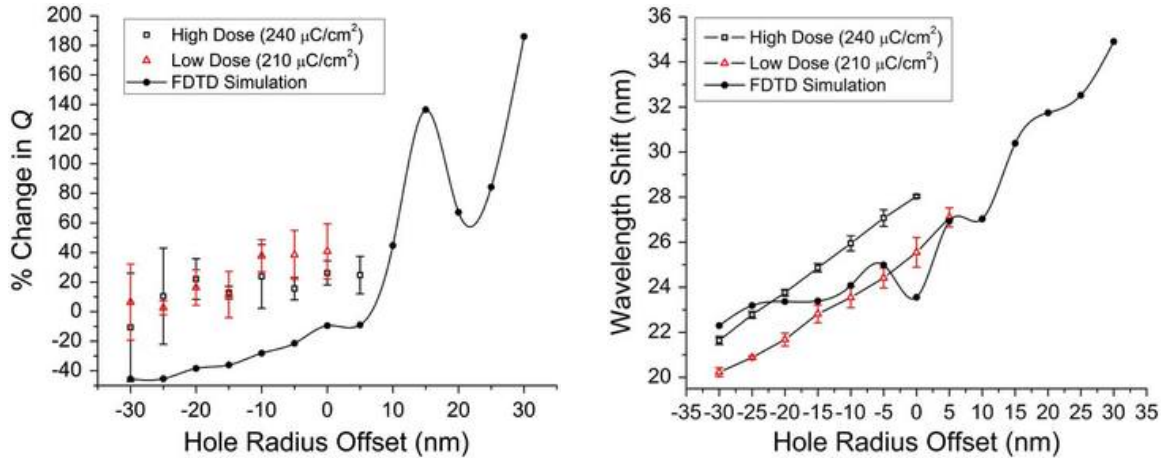
(a) FDTD simulation of the  $Q$  as a function of hole radius offset, prior to ALD coating. As expected, a peak is found for the designed hole radius, corresponding to a 0 nm offset.

(b) Plot showing the average measured  $Q$  of several cavities prior to ALD coating versus the hole radius offset. A trend of higher  $Q$  is observed for cavities with smaller holes (negative offset).

Figure 3.27: Dependence of nanobeam quality on hole radius offset. Based on FDTD simulations, a peak is expected for an offset of 0 nm. Experimentally, we did not observe the peak, but rather a consistent trend indicating the starting holes were too large.

While the deposition of 20 nm of  $\text{Al}_2\text{O}_3$  resulted in a clear increase in the cavity  $Q$ , from these initial tests it was not clear what factors contributed to the improvement. The fact that the sample coated with  $\text{TiO}_2$  did not show the same increase suggests that the effect is not exclusively due to a decrease in surface roughness. FDTD simulations of the silicon nanobeam  $Q$  (see Figure 3.27a) indicate that the  $Q$  is highly dependent on the hole radius, with a peak  $Q$  near the nominal radius of  $r_0 = 0.3a$ . To explore this further, an additional sample was fabricated with the same basic geometry, but where a fixed offset was added to the hole radii. For each lattice constant, 13 cavities were defined with offsets ranging from -30 nm to 30 nm in 5 nm steps.

This sample was characterized, coated with 20 nm of  $\text{Al}_2\text{O}_3$ , and recharacterized as before. Fifty-three of the sixty cavities that were characterized on the sample showed increases in the  $Q$ , with the average increase being  $20 \pm 19\%$ . Figure 3.27b shows a plot of the measured  $Q$  prior to ALD coating as a function of hole radius offset. Unlike the simulation, there was not a clear peak in the  $Q$ . This suggests that our range of hole sizes did not cover the designed range. From the percent increase in



(a) Average change in  $Q$  of cavities after the ALD process, as a function of the initial hole radius offset.

(b) Average red-shift in cavity resonance after the ALD process, as a function of the initial hole radius offset.

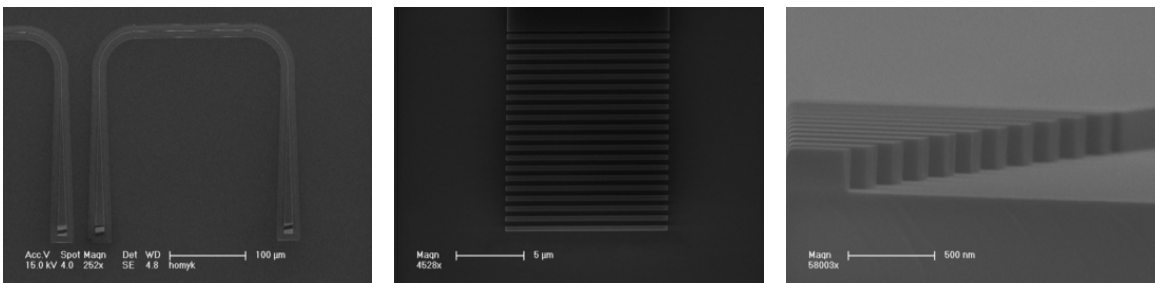
Figure 3.28: Plots showing the changes in cavity behavior due to the ALD process as a function of the hole radius.

$Q$  as a function of the hole radius offset (Figure 3.28a), there was also a clear trend showing greater  $Q$  increases for cavities with larger holes. Following ALD, these cavities had hole sizes closer to those of the cavities that showed the highest  $Q$ s prior to ALD. This is consistent with the notion that the increase in  $Q$  was due to the shift of hole size closer to the optimal (highest  $Q$ ) design. We will revisit this conclusion in 3.4.5.

Figure 3.28b shows a plot of the shift in the cavity mode wavelength as a result of the deposition of 20 nm of  $\text{Al}_2\text{O}_3$ , along with FDTD simulation results. While the wavelength shift showed very little dependence on the lattice constant, it showed a strong dependence on the initial hole radius offset. The shift also showed some dependence on the dosage used during electron beam lithography, consistent with larger holes and narrower beams being expected for higher exposures. The higher dose array showed wavelength shifts in the range of  $21.6 \pm 0.2$  nm for the smallest holes to  $28.0 \pm 0.1$  nm for the largest holes. The lower dose array showed wavelength shifts in the range of  $20.2 \pm 0.2$  nm for the smallest holes to  $27.1 \pm 0.4$  nm for the largest. FDTD simulations predicted a similar range of wavelength shifts.

### 3.4.4 Further improvements - expanded parameters, fracturing, PEC

Following the experiments with atomic layer deposition, we modified our design to use grating couplers and be fed from waveguides, rather than relying on fiber loop or resonant scattering measurements. A fiber array holding polarization-maintaining single mode fibers at a fixed spacing of  $250\ \mu\text{m}$  was used to couple into and out of the feeding waveguides. Using a computer-controlled stage platform, this enabled rapid, automatic characterization of hundreds of devices on a sample. SEMs of a complete grating-coupled device loop, as well as close-ups of the grating, are shown in Figure 3.29. While we considered the use of evanescently-coupled nanobeams, we primarily worked with end-fired devices due to the relative ease with which the coupling strength can be controlled; see Figure 3.30.



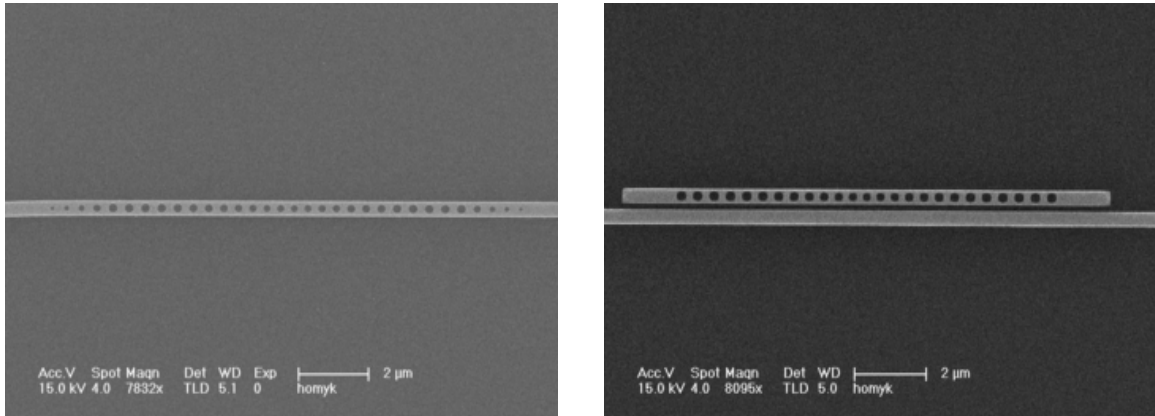
(a) SEM showing a complete grating loop, including input and output gratings at the bottom, tapered sections to couple the grating mode into the single mode waveguide, and the device loop at the top. Although difficult to resolve at this scale, the nanobeam device is at the center of the flat section at the top. Due to the use of positive resist, wide buffer regions must be defined, surrounding the entire device, to avoid coupling into slab modes.

(b) SEM showing a close-up view of the grating coupler.

(c) SEM examining a side view of a grating. Devices were often cleaved after optical testing in order to examine the sidewalls. The highly anisotropic etch profile of the grating can be seen.

Figure 3.29: SEMs showing a complete grating-coupled 1D nanobeam device, as well as detailed views of the grating region.

Although we found numerous standout devices with  $Q$ s exceeding 100k, typical quality factors remained  $\approx 20\text{k}$ . After characterizing hundreds of such devices using the original geometry, we began exploring a larger design space with the hopes of reliably increasing the quality factor. A larger parameter sweep was performed using FEM, yielding an improved design, and featuring a



(a) SEM of an end-fired 1D nanobeam device. The tapered holes at the ends perform mode matching between the waveguide and photonic crystal modes. The coupling strength is controlled by the number of mirror periods.

(b) SEM of an evanescently-coupled 1D nanobeam device. The coupling strength is controlled by the gap distance between the waveguide and photonic crystal.

Figure 3.30: SEMs comparing end-fired and evanescently-coupled nanobeams.

wider beam, smaller holes, and a more gentle confinement (see the expanded design described in `refchap:cav.nanobeam.design.expanded`).

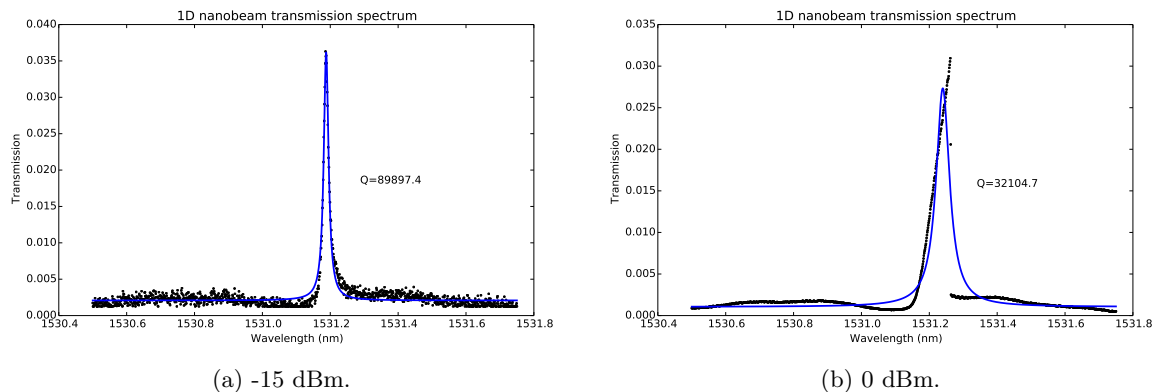


Figure 3.31: Typical transmission spectral for an expanded parameter 1D nanobeam at low and high excitation. The same device is represented in both curves, with black dots corresponding to experimental data and the blue line showing a Lorentzian fit. The powers listed correspond to output from the laser; powers coupled into the nanobeam were lower due to additional propagation and coupling losses. At high powers, the lineshape no longer follows a Lorentzian profile, but instead exhibits a triangular profile with a sudden, sharp drop, characteristic of optical bistability.

The expanded parameter devices were similarly characterized. At low excitation (laser powers below -15 dBm, before losses in the grating couplers) these devices indeed showed fairly significant gains, with typical  $Q$ s falling between 70k - 100k (see Figure 3.31a); by comparison, low-power wavelength sweeps of devices with the original geometry revealed typically quality factors between

40k - 60k. At higher powers, however, the resonance qualities of the new devices dropped significantly due to an optical bistability (to be discussed shortly, in 3.4.6). At a standard excitation power of 0 dBm, the average  $Q$  had fallen to  $\approx 25k$  (see Figure 3.31b).

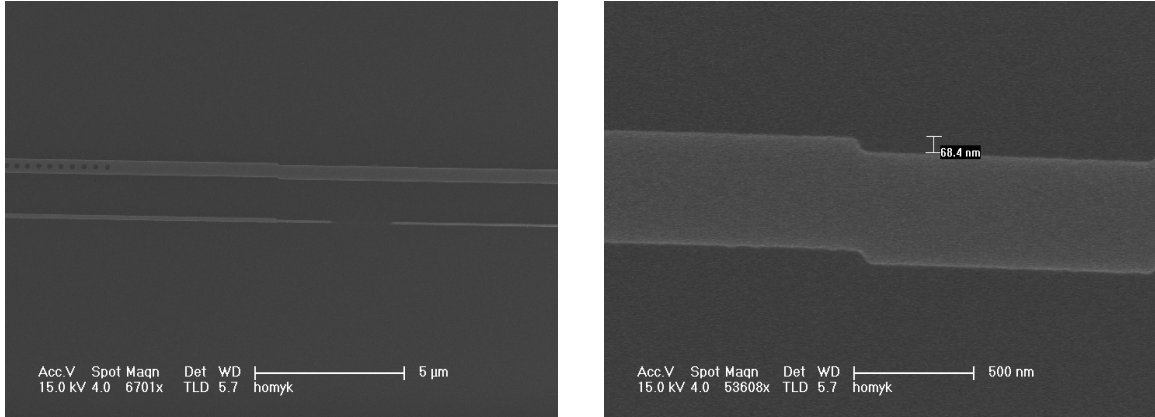


Figure 3.32: SEMs showing a stitching error at the field boundary between a manual cavity field and the connecting waveguide. The thin line below the cavity is due to a misalignment between the low- and high-current beams.

Using the same design, we explored a variety of modifications to the fracturing process<sup>4</sup> in an attempt to improve the fabricated device quality. A new algorithm for fracturing circles had recently been introduced into the fracturing software (Layout Beamer, GeniSys, Munich, Germany) which produced more symmetric trapezia and slightly more consistent results between geometries. For completeness, we also note that compaction<sup>5</sup> is not recommended for photonic crystals.

The software also allows the ability to manually specify the locations of write fields and their order. While we had previously utilized this feature to ensure field boundaries did not occur over the cavity, we had neglected to set the write order. This resulted in having all manual fields (cavities and grating couplers) being written first, before returning to fill in the remaining area (long waveguides). In some instances, we found that tool drift between the time a cavity was written and when it returned to write the waveguide could result in a stitching error, resulting in a misalignment between

<sup>4</sup>Fracturing converts the geometric beam design into a format suitable for electron-beam lithography, which includes discretizing the objects into trapezoidal shapes which can be raster-scanned by the electron beam, defining the write order of shapes, and setting beam step sizes and dwell times. For our process, this also entailed defining the buffer region and inverting the design to make it compatible with a positive resist, and separating it into detailed and bulk regions to be written at different currents.

<sup>5</sup>Compaction is a feature of the fracturing software which identifies similar features and writes them as an array, rather than individual, unique elements. This can cause issues for photonic crystals, as minute differences between holes can be inadvertently lost, while also causing each hole to be written piecemeal, rather than all at once.

the cavity and coupling waveguide; an example of this, as well as a misalignment between low- and high-current beams, is shown in Figure 3.32. By interlacing the manual and automatic fields, this slow drift and associated stitching errors were mitigated. Figure 3.32 also reveals a misalignment between the low- and high-current beams, which we used to define fine features while rapidly filling in the large buffer around the beam. Moving the interface further from the beam, increasing the overlap region, and ensuring the buffer was written at a slightly higher dose (even when performing dose arrays of the beam itself) were effective at eliminating this problem.

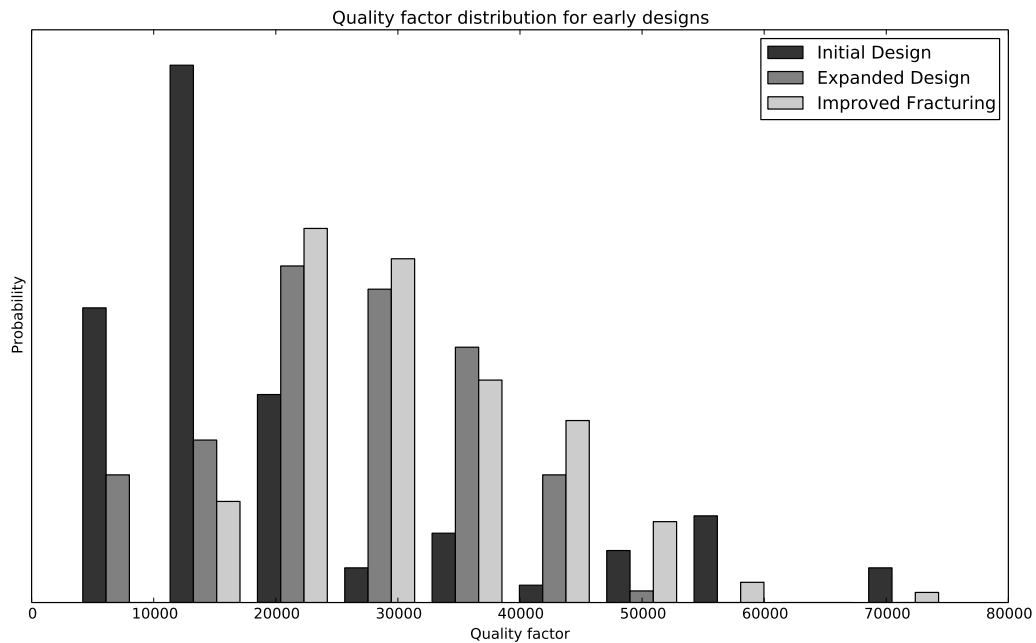
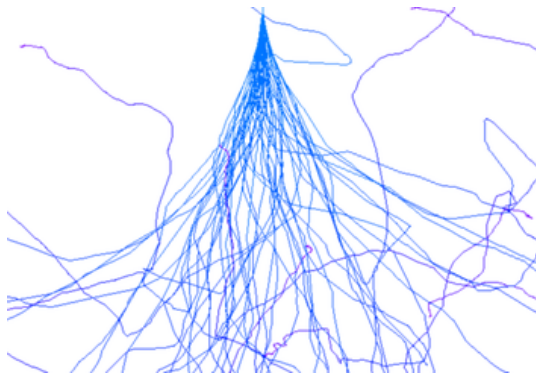


Figure 3.33: Distributions of the quality factors for several design iterations, sampled at a laser power of 0 dBm. The averages for the initial, expanded, and improved fracturing were 21,187.1, 25,674.8, and 30,823.3, respectively. Both the expanded and revised fracturing showed consistent improvements over the initial design. While higher  $Q$ s were observed at lower power, the data for earlier devices was more complete at moderate powers. Note that the expanded design and revised fracturing used identical device geometries, and show similar distributions. In this case, the gains came primarily from an increase in fabrication reliability, including a few higher quality beams and the elimination of low-quality devices.

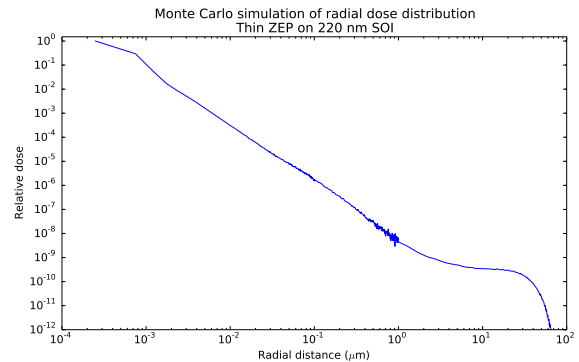
Distributions of the quality factors for the initial design, expanded design, and results after fracturing improvements are shown in Figure 3.33. Combined, these improvements to the fracturing process resulted in a modest increase in  $Q$  over the expanded design, raising the average at 0 dBm from  $\approx 26$ k to  $\approx 31$ k. We note that these distributions appear quite similar; the gains are most likely due to slight improvements in reliability, yielding a few higher-quality resonances but primarily by

the elimination of low-performing devices.

We also investigated the use of the proximity error correction (PEC) to improve the fidelity of lithographic features. Due to a variety of scattering mechanisms, the electrons impinging on the sample during e-beam lithography can result in exposure far from the intended location. This results in a pattern- and location-dependent background exposure, known as proximity error. Generally, these can be separated into a low, long-range ( $\approx 30 \mu\text{m}$ ) contribution which gradually changes base exposure level (in a pattern-dependent manner), a more severe mid-range interaction ( $\approx 100 \text{ nm}$ ) which perturbs neighboring patterns, and a short-range beam spreading ( $< 30 \text{ nm}$ ). Although the feature location will remain well-defined, this spatially varying dose offset can cause certain regions to become over- or under-exposed, making precise control of feature size and shape challenging on the nm scale. For photonic crystals, variation of hole diameter within the cavity poses a severe challenge to controlling the resonance frequency and maintaining a high quality factor.



(a) Simulated electron paths in PMMA.



(b) Simulated electron dose at 100 kV for ZEP on SOI, used for proximity error correction. Dose is measured at center of resist.

Figure 3.34: Monte Carlo simulations of electron propagation and resist exposure, calculated using PENELOPE[21].

If the profile of the electron scattering is known, it is possible to mitigate this issue by deconvolving the point spread function of the beam from the pattern. This results in a spatially-varying dose modifier, which can be incorporated in the process during fracturing. Previously, we had tried (and eventually abandoned) an electron dose distribution based on PMMA on Si, which does not quite match our material stack. To improve this, we explored PEC profiles derived in two

manners. First, we performed Monte Carlo simulations for our material stack using PENELOPE, a published code to calculate electron, photon, and positron scattering and energy loss [21]. A sample electron shower and the radial dose distribution for our device layers are shown in Figure 3.34. This program has been widely used for generating PEC profiles (including the generation of the original distribution for PMMA-on-Si). Although often reduced to a sum of Gaussians (corresponding to long-, short- and mid-range interactions), this method has the advantage of providing a complete distribution and assuming any analytic form if desired.

We also experimented with an empirical method for deriving the back-scattered electron distributions [353]. Here, a simple checkerboard pattern is written at a large range of doses, surrounded by patterns at varying distances and densities. By examining the doses and patterns which yield optimal exposure, it is possible to determine the ideal base dose, long- and mid-range contributions, and scattering range. While the final output is reduced to the simplified sum-of-Gaussians, this form tends to provide an adequate fit for most purposes. The most significant advantage of this technique, however, is that the empirical results inherently include effects specific to the actual process, including resist development or layer composition, and do not require any assumptions about the material stack, electron scattering behavior, or dose-to-clear. Several images of the dose sensors used are presented in Figure 3.35. This technique resulted in long- and mid-range scattering lengths of  $\approx 33.3 \mu\text{m}$  and  $\approx 150 \text{ nm}$ , respectively. These compare reasonably well with the values of  $\approx 30.4 \mu\text{m}$  and  $\approx 93 \text{ nm}$  derived from fits to the Monte Carlo distribution.

We tried a variety of different PEC conditions when fracturing, including the numeric Monte Carlo distribution, multi-Gaussian fits to the Monte Carlo data, empirically-derived parameters and no PEC. When applied, PEC was calculated for the combined low- and high-beam patterns (to ensure both contributions were taken into account), prior to separating these into different patterns. Somewhat surprisingly, the addition of PEC to the process *lowered* the quality factors to  $\approx 20\text{k} - 30\text{k}$ . The highest quality beams were consistently produced by the PEC-free process. While we never determined the root cause of this behavior, it is possible that the e-beam pattern generator showed difficulty when switching clocks (which is how it applies the dose variations) and did not properly

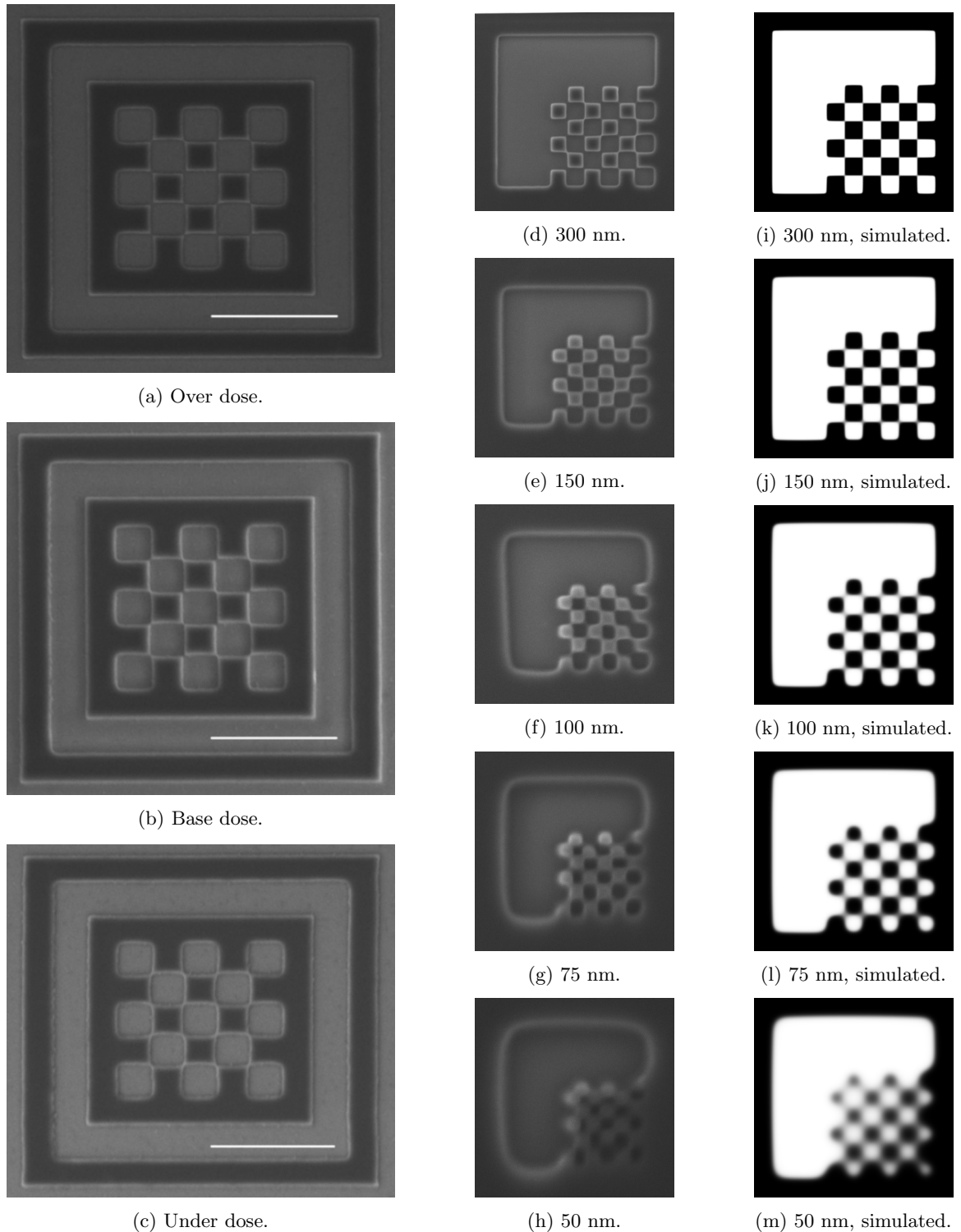


Figure 3.35: Empirical derivation of exposure parameters and proximity effects using dose sensors. Images in the left column show base dose patterns, surrounded by 50% filled patterns to determine optimal exposure level. Scale bars are  $2\ \mu\text{m}$ . Note the disconnected corners in the over-dosed pattern, the connected corners and channel debris in the under-exposed pattern, and the square features in the base dose. The right columns show mid-range dose sensors used to determine proximity effects from nearby features, and their simulated equivalents. Sizes denote checkerboard square lengths. Note the similarity of corner rounding and feature blurring between the measured and simulated patterns.

write all trapezia in areas where the doses varied significantly<sup>6</sup> such as the cavity locations. We therefore continued all further exposure with PEC disabled.

### 3.4.5 SEM feedback, fabrication robustness, and constant radius designs

After our experiments with proximity error correction indicated the quality factor's sensitivity to hole fabrication, we attempted to quantify the fabrication accuracy in the hopes of further improving  $Q$ , or at least process reliability. Along with conclusions from the ALD study that the hole dimensions were over-sized, it seemed plausible that refining the fabricated geometry was necessary to achieving optimal device performance.

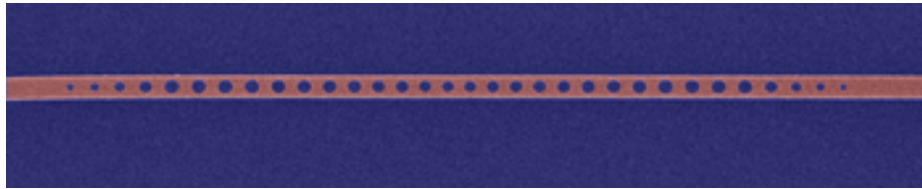


Figure 3.36: 1D photonic crystal nanobeam which has been segmented to identify the device regions (Si, red) and etched areas ( $\text{SiO}_2$ , blue). These regions could then be further analyzed to extract device geometry, including beam width, hole location, and radius. This geometry utilized local hole tapering, which tracked the tapering of the lattice constant.

To extract quantitative measurements of the device dimensions, we developed a script in Matlab to automatically analyze SEM images, measure critical dimensions, and compare to the nominal geometry<sup>7</sup>. The routine performed the following steps:

1. Image clean-up and segmentation (see Figure 3.36)

Crop off scale bars; center beam within image and eliminate excess border area; perform Canny edge extract to locate device borders; separate into device and etched areas.

2. Initial hole fit and correction

Identify hole regions, calculate  $\hat{x}$  and  $\hat{y}$  centroids; fit line to center locations; rotate coordinate

<sup>6</sup>We had previously observed that the nanopillars wrote more reliably with PEC disabled, and later found other issues related including dropped trapezia due to misconfigured parameters for beam settling and dwell times when moving. It is unclear if these contributed to problems with the PEC, although possible.

<sup>7</sup>Our SEM analysis routines also produced a CAD drawing of the device geometry which could be imported into Comsol or FDTD software to match simulations to the actual device, although we did not find this to be particularly insightful for  $Q$ s beyond  $\approx 30k$ .

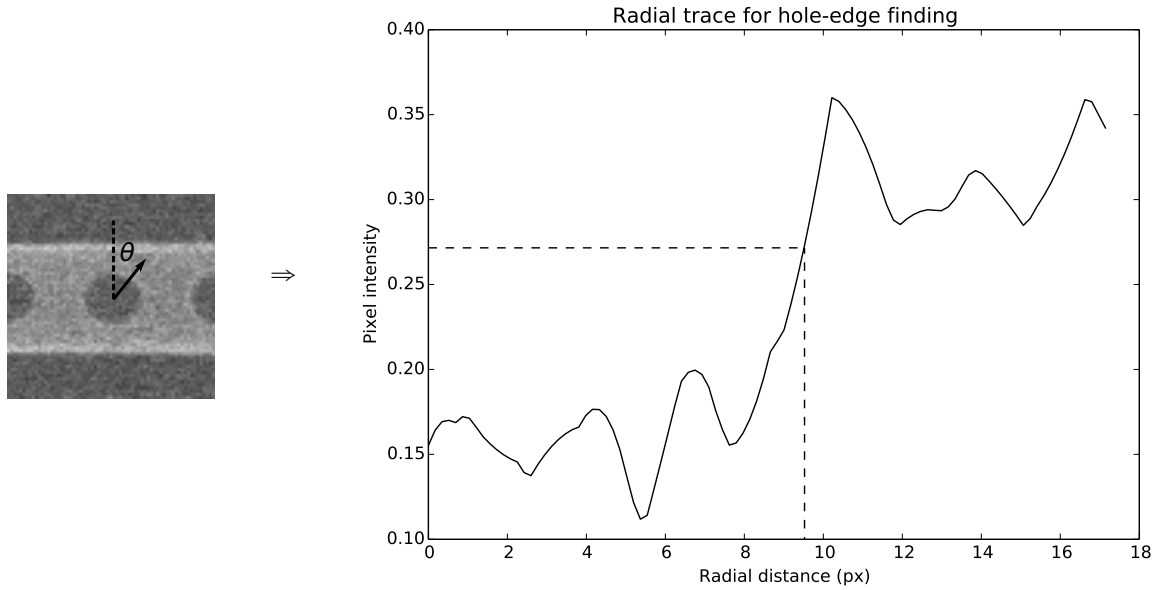


Figure 3.37: Illustration of sub-pixel hole-edge finding. Beginning from the centroid of each hole, radial traces are examined as a function of angle. The location of the hole-edge can be found from intersection with the mid-point intensity.

system to align device axis to image  $\hat{x}$  coordinates

### 3. Sub-pixel hole tracing (see Figure 3.37)

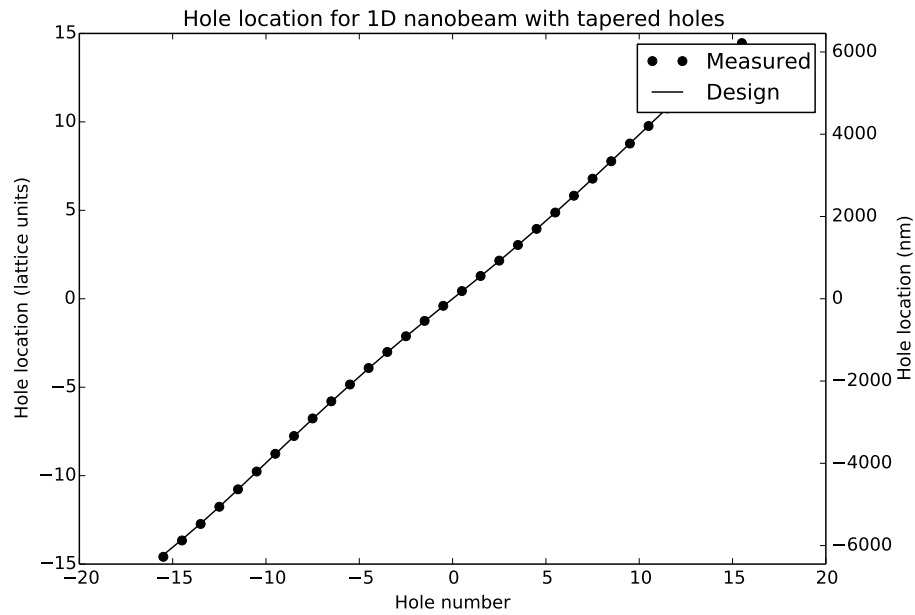
For a given hole, the intensity is examined along a ray projecting from the centroid. The location of the hole-edge is determined by finding the intersection with the mid-point intensity<sup>8</sup> (normalized over the full image). This procedure is performed for a multitude of angles to determine the radial distance as a function of angle around the circle, and then repeated for all holes. Non-inverted inclusions or other edge anomalies are naturally included.

### 4. Normalization and analysis

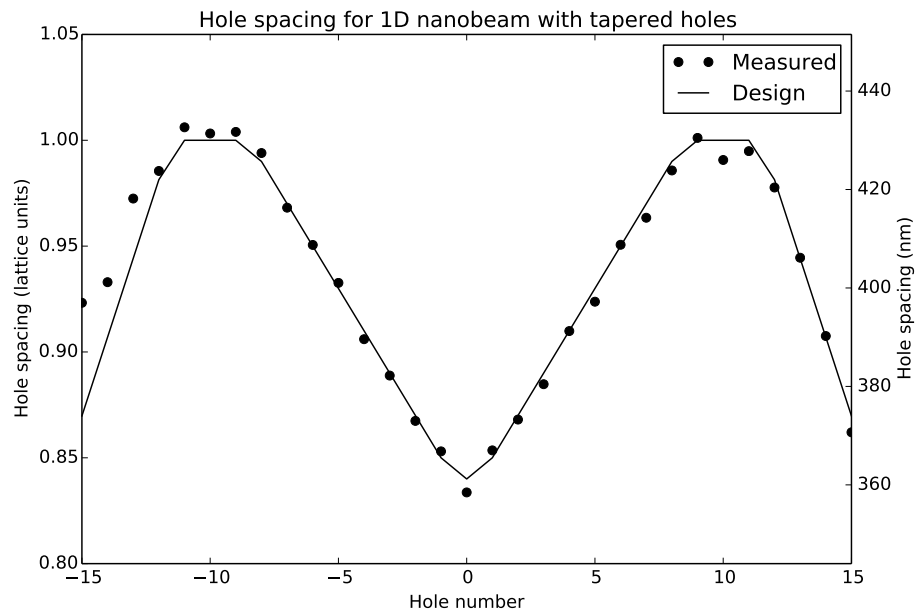
Determine the local lattice constant<sup>9</sup> (in px); use to scale extracted dimensions into lattice units (a) or physical (nm); compare to design parameters.

<sup>8</sup>This can be easily adapted to curve fit an expected profile, for example an erf, although we did not notice any appreciable difference doing so.

<sup>9</sup>Although hole size can vary due to a number of causes, the position accuracy by e-beam lithography is extremely tight. Rather than relying on the SEM scale bars, we determined lattice constant by averaging the hole spacing in the mirror (non-tapered) sections.



(a) Hole locations.



(b) Hole spacing (local lattice constant).

Figure 3.38: Comparison of the designed and measured location and spacing of holes in a 1D photonic crystal nanobeam with tapered holes. Hole number is relative to the cavity center. The solid line shows the expected position, while circular points show the position as determined from SEM analysis. The spacing reflects the difference between neighboring hole locations, corresponding to the cavity taper and local lattice constant. Excellent agreement is observed over both short- and long-range, reflecting the ability to achieve extremely high positional accuracy with electron-beam lithography.

Results for hole positions extracted from an SEM are presented as points in Figure 3.38; these are compared to the designed geometry, presented as solid lines. Excellent agreement is observed over both short- and long-range. We found a standard deviation of  $\approx 1.2\%$  in expected hole spacings (limited by the resolution of the SEM), reflecting the ability to achieve extremely high positional accuracy with electron-beam lithography. The profile of the cavity taper is clearly observed in the hole spacings, as well as the coupling tapers on the outside.

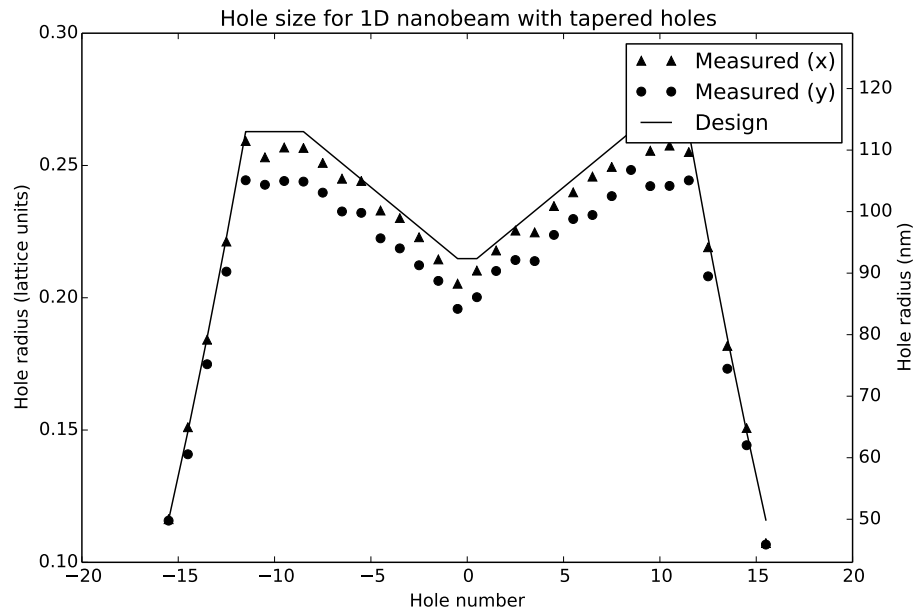


Figure 3.39: Comparison of designed and measured hole sizes for a 1D photonic crystal nanobeam with tapered holes. Hole number is relative to the cavity center. Here, the complete hole-edge profiles have been fit to ellipses, with  $\hat{x}$  corresponding to the cavity axis and  $\hat{y}$  the transverse direction.

A comparison between the designed hole sizes and those measured from the SEM image is presented in Figure 3.39. Here, the full hole profiles were reduced to ellipses for clarity. We observed reasonable agreement between the geometric dimensions in the design file and the experimentally-observed values, with the overall size trend following the taper profile as expected. However, an offset was revealed between the intended and fabricated dimensions. For this device, we measured average *diameter* errors along the  $\hat{x}$  and  $\hat{y}$  directions of  $-3.7$  nm ( $-0.00865a$ ) and  $-12.7$  nm ( $-0.0296a$ ), respectively. After subtracting out the design dimensions (to account for intended variation), we found the standard deviation of hole sizes to be  $2.63$  nm ( $0.006a$ , or  $\approx 1.4\%$ ) and  $3.96$  nm ( $0.009a$ , or  $\approx 2.0\%$ ) along the  $\hat{x}$  and  $\hat{y}$  axes. These accuracies are quite comparable to state-of-the-art positional

and diameter resolutions of  $<1\%$  and  $<5\%$  reported elsewhere in literature [266].

While the size discrepancy could be due to the precise intensity threshold for the holes in the SEM (at least in part), we note that the original design called for  $r_0 = 0.3a$ , which had been adjusted with a fixed offset of -16 nm in the CAD file in an attempt to correct for the over-sized holes observed in the ALD experiment (the data in Figure 3.39 corresponds to the CAD file, not original design). Despite the fact that the final dimensions were closer to the intended dimensions than previously observed, the variation between runs is a testament to the difficulty of precisely controlling feature dimensions. Quite a variety of factors can contribute to dimensional variation, including PEC, exact dose, fracturing irregularities, variations in resist thickness, incomplete solvent removal, resist swelling, effects due to ambient humidity, local developer saturation, temperature dependence of development, and sidewall conditions in etching chambers. Unfortunately, these effects can yield offsets which are not simply proportional to dose or feature size, and moreover, may not even produce uniform variation across a single sample. Even with fabrication processes approaching nm resolution, previous studies have concluded that variations as small as 1 nm can drop  $Q$  factors of high-quality resonators by a factor of 15[120, 339].

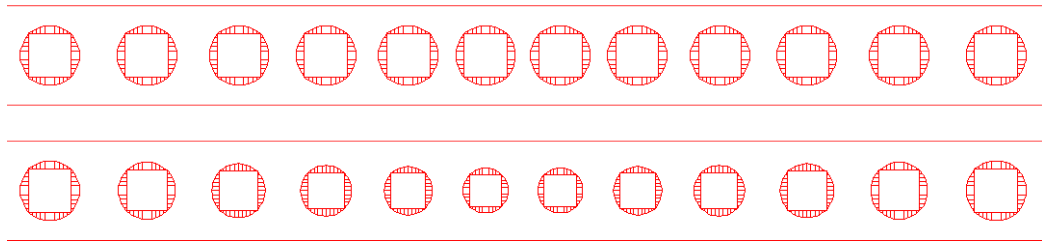


Figure 3.40: Fracturing results for fixed-radius and tapered-hole nanobeam cavities. Note the slight differences in patterns between the larger edge holes and tapered center holes. These changes can inadvertently introduce non-systematic errors in hole dimensions, whereas the fixed-radius holes have nominally identical write processes.

Given the susceptibility of photonic crystal devices to hole diameter variation and the inherent difficulties in controlling these dimensions, we performed a redesign of the cavities which relied exclusively on positional control to establish the taper. This designed employed fixed-radius holes

throughout the device, which did not follow the cavity taper, as well as a fixed beam width. Modulation of the mirror strength was accomplished by varying only the hole location, allowing us to exploit the high positional accuracy of e-beam lithography while avoiding any explicit reliance on local dimensions for the beam width or individual holes. Additionally, the use of identical hole features avoids the introduction of non-systematic errors through differences in how each hole size is fractured (see Figure 3.40).

The initial design of the fixed-radius design followed essentially the same process as that used for the expanded parameter design (see 3.3.2.2). The results of the parameter sweeps are presented in Figure 3.41, with field patterns shown in Figure 3.42. Due to the non-ideal linear taper profile — which is further exacerbated by the fixed holes — a higher degree of radiative leakage can be observed in the FFTs. The final device design uses a beam width  $w = 1.25a$ , fixed hole radius  $r = 0.225a$ , and device thickness of  $0.6a$ . This results in a mode volume of  $V = 0.469(\lambda/n)^3$  and simulated  $Q$  of 502k, in comparison to  $\approx 1,800k$  for the equivalent design with tapered holes.

Despite substantially lower simulated  $Q$ s, we found the experimental  $Q$  performance for these devices to be greatly superior to the previous design. A comparison between  $Q$  distributions for the original expanded devices (with revised fracturing) and the fixed-radius beams is presented in Figure 3.43. The improvements can be primarily attributed to fabrication tolerance; for an ideally-tuned fabrication, the tapered devices are still expected to perform better. For sets of both tapered-hole and fixed-radius devices fabricated on the same chip, we did occasionally observe improved performance of the tapered devices (when all of the fabrication processes were very well-tuned), but the performance was inconsistent at best and never substantially out-performed the fixed-radius devices. As with the expanded parameter devices, we observed significantly higher  $Q$ s at lower excitation powers (see Figure 3.44), which became blurred out at higher powers due to an optical bistability. Although some of the data is noisier for the highest  $Q$ s<sup>10</sup>, we observed clear resonances over 250k, with several noisier spectra showing quality factors over 300k. While Kuramochi *et al.* [188] reported a higher  $Q$  of  $3.6 \times 10^5$  for a 1D nanobeam cavity with oxide over- and under-

<sup>10</sup>To observe the highest  $Q$ s, we had to measure devices at extremely low input powers in order to avoid spectral smearing due to optical nonlinearities; these are difficult to distinguish clearly due to receiver noise.

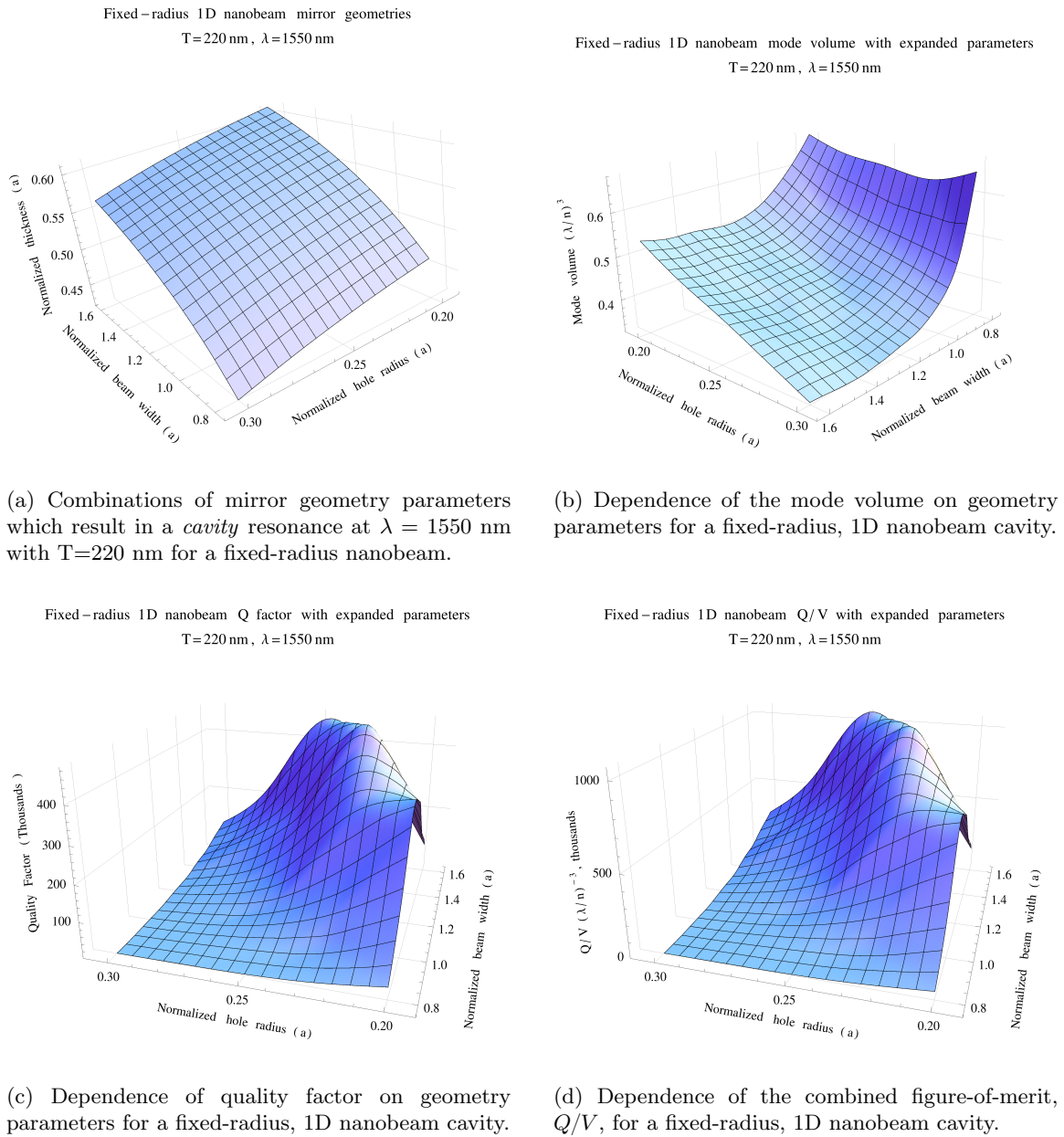


Figure 3.41: Results of FEM simulations used to optimize the fixed-radius 1D nanobeam geometry. The design followed a similar process to the one used for the expanded parameter range devices. These values correspond to a device layer thickness of  $T = 220$  nm, with a resonance wavelength of  $\lambda = 1550$  nm.

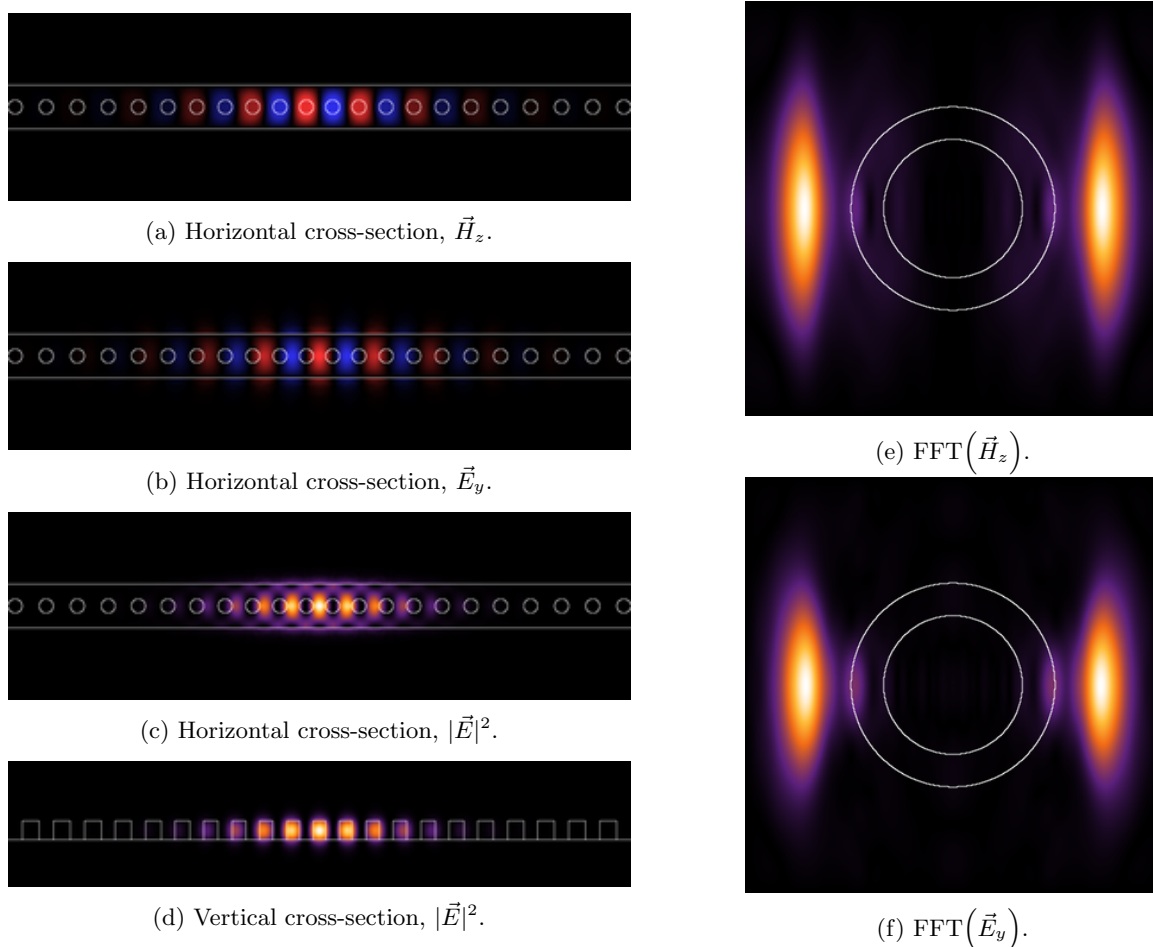


Figure 3.42: FEM simulations of our fixed-radius beam design, showing cross-sections of the fields (through center of beam) and corresponding FFTs ( $\lambda/4$  in substrate). The FFT circles indicate the light cones for air (inner) and oxide (outer). Although this design shows slightly more theoretical leakage than the equivalent design with tapered holes, the fabrication tolerance outweighs this from a practical standpoint.

cladding (which eases TE-TM coupling, and is expected to have higher  $Q$ ), their mode volume was substantially larger at  $0.78(\lambda/n)^3$ , resulting in a  $Q/V$  of  $4.6 \times 10^5(\lambda/n)^3$ . By comparison, our devices have a mode volume of  $0.469(\lambda/n)$ , resulting in a  $Q/V$  of  $5.3 \times 10^5(\lambda/n)^3$  (for  $Q = 250k$ ). To our knowledge, this represent the highest  $Q/V$  ever reported for a cavity on substrate.

We also performed a similar SEM analysis of the devices. These data are presented in Figures 3.45, 3.46, and 3.47. As expected, the hole positions and spacing track the expected locations extremely tightly. The hole radius is again slightly elliptical, and in this case slightly over-developed from that of the design. The mean hole radius errors were  $+8.9$  nm and  $+2.9$  nm along  $\hat{x}$  and  $\hat{y}$ , respectively. The hole sizes also showed a tighter distribution, with standard deviations of 1.85 nm

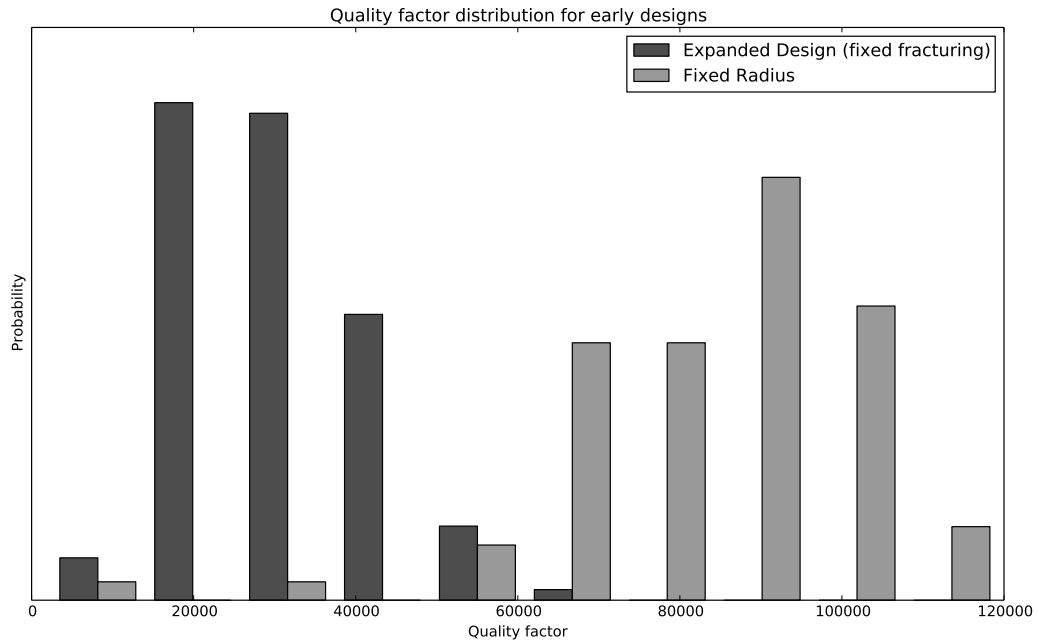


Figure 3.43: Comparison between  $Q$  distributions for the expanded parameter design (with fixed fracturing) and fixed-radius devices. Both sets correspond to devices sampled at a laser power of 0 dBm. Despite significantly lower theoretical quality factors, the fixed-radius devices significantly out-performed the tapered devices.

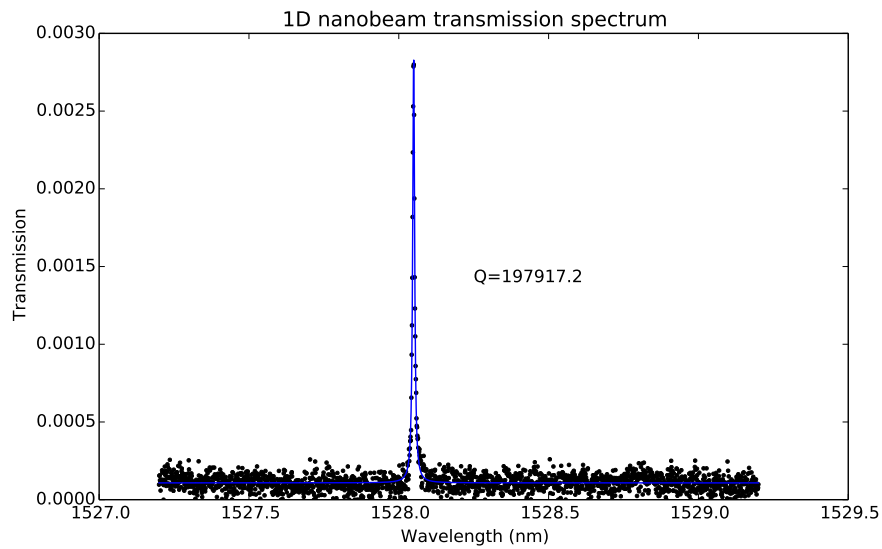


Figure 3.44: Ultra-high  $Q$  spectrum from a fixed-radius, 1D photonic crystal nanobeam on substrate.

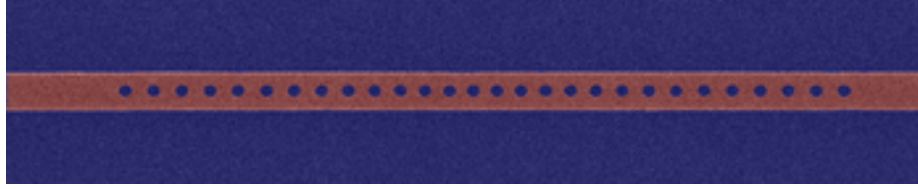
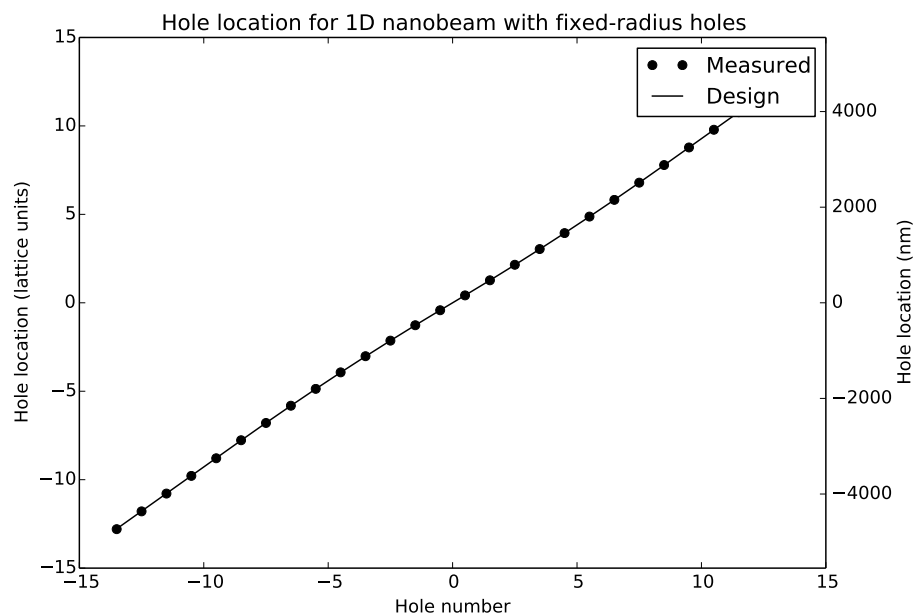


Figure 3.45: Fixed-radius, 1D photonic crystal nanobeam which has been segmented to identify the device regions (Si, red) and etched areas ( $\text{SiO}_2$ , blue).

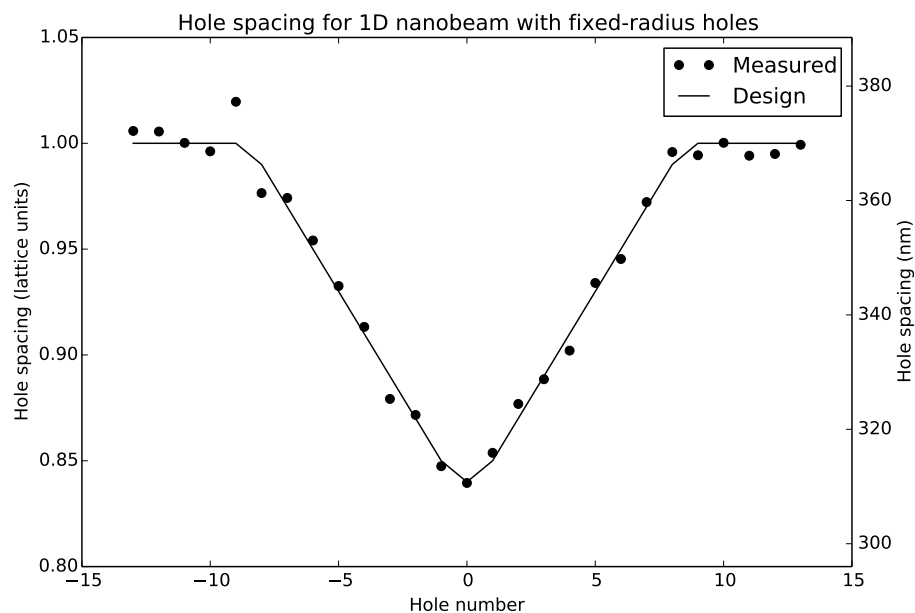
and 1.92 nm in  $\hat{x}$  and  $\hat{y}$ , respectively — approximately half of the variation seen for the tapered holes. While further work would be required to fully characterize the improvement, it is possible that this results, at least in part, from a more consistent lithographic process due to identical fractured output (see Figure 3.40).

Although we believe the primary benefit of the fixed-radius nanobeams stems from the enhanced ease of fabrication — specifically an improved resilience to *systematic* errors, or a reduction in their occurrence — we also studied the performance of both devices which had been perturbed by *random* errors. Using FEM, we simulated nanobeam cavities of each type which had undergone random perturbations to the beam width, hole positions (in both  $\hat{x}$  and  $\hat{y}$ ), and hole radii. These elements were simultaneously varied by a normalized error magnitude (uniformly distributed rather than Gaussian, and proportional to the lattice constant), where each hole was moved and resized independently, and the beam had a fixed (but potentially offset) width. For a given error rate, we simulated 8 - 10 beams of each type and analyzed the resonance properties.

These data are presented in Figure 3.48. The performances track extremely closely for perturbations  $>0.5\%a$ , and are nearly indistinguishable beyond 1% errors. Interestingly, we note that the magnitude of disorder observed in our SEM analysis, and associated  $Q$ s from optical measurements, tend to fall near these values. Beyond this point, disorder-induced losses tend to make performance design-independent. Similar conclusions have been reported by other authors. Asano *et al.* [7] concluded that experimental cavity quality factors are essentially determined by disorder, rather than cavity design. Amongst the mechanisms they studied, these authors found the dominant loss mechanisms to be due to variation of air-hole radii, as well as surface roughness and tilt of the holes (a  $3^\circ$  etch angle can result in  $Q$  degradation by a factor of 5). Minkov *et al.*



(a) Hole locations.



(b) Hole spacing (local lattice constant).

Figure 3.46: Comparison of the designed and measured location and spacing of holes in a fixed-radius, 1D photonic crystal nanobeam. Hole number is relative to the cavity center. The solid line shows the expected position, while circular points show the position as determined from SEM analysis. The spacing reflects the difference between neighboring hole locations, corresponding to the cavity taper and local lattice constant. Excellent agreement is observed over both short- and long-range, reflecting the ability to achieve extremely high positional accuracy with electron-beam lithography.

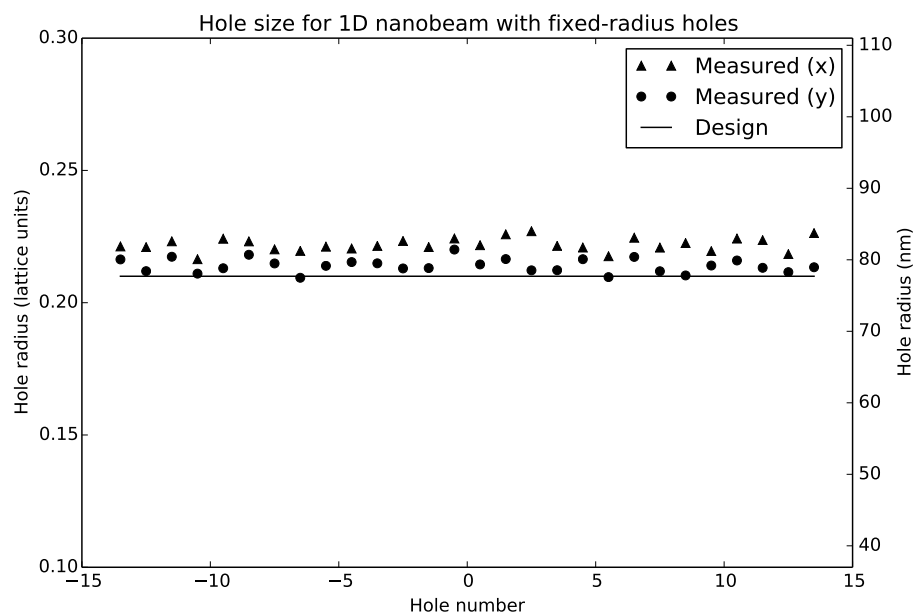


Figure 3.47: Comparison of designed and measured hole sizes for a fixed-radius, 1D photonic crystal nanobeam. Hole number is relative to the cavity center. Here, the complete hole-edge profiles have been fit to ellipses, with  $\hat{x}$  corresponding to the cavity axis and  $\hat{y}$  the transverse direction.

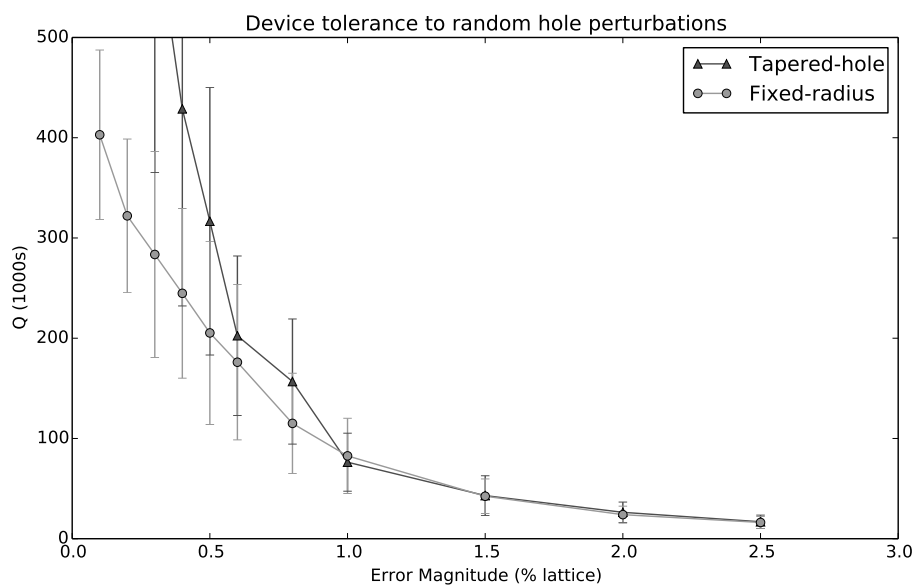


Figure 3.48: Tolerance of tapered-hole and fixed-radius nanobeam cavities to random perturbations in beam width, hole position, and hole radius.

[249] studied disorder-induced losses for a similar range (0.1% - 1.5%), and found that degradation of quality associated with disorder follows the disorder squared:  $Q_d^{-1} \propto \sigma^2$ . Significantly, the same group also concluded that most important contribution comes from fluctuations in the hole area [250]. Although the SEM analysis might not have the resolution to probe this further, these conclusions that hole radius perturbations are one of the most dominant factors determining experimental  $Q$  could further support the notion of using fixed-radius devices to eliminate radius error due to anomalous lithographic effects.

Finally, we also performed a similar analytic design process using the fixed-radius constraint. Performance trends and field profiles are presented in Figures 3.49 and 3.50. This process resulted in a significantly improved design with a  $V = 0.50(\lambda/n)^3$  and  $Q = 7.84 \times 10^6$ . This represents a 1500% improvement when compared to the expanded parameter, fixed-radius design, and nearly achieves the performance of the analytic tapered design. We note that this represents nearly  $4\times$  the improvement between the analytic-tapered-hole and linear-tapered-hole designs. This substantial increase in gains offered by analytic design are likely due to the more abrupt mirror created by using fixed holes. Even with the reduced degrees of freedom by restricting hole radius, the analytic process is capable of creating a smooth field envelope. Although we have not had an opportunity to fabricate and test these devices, we believe these could show significant performance improvements over previous designs.

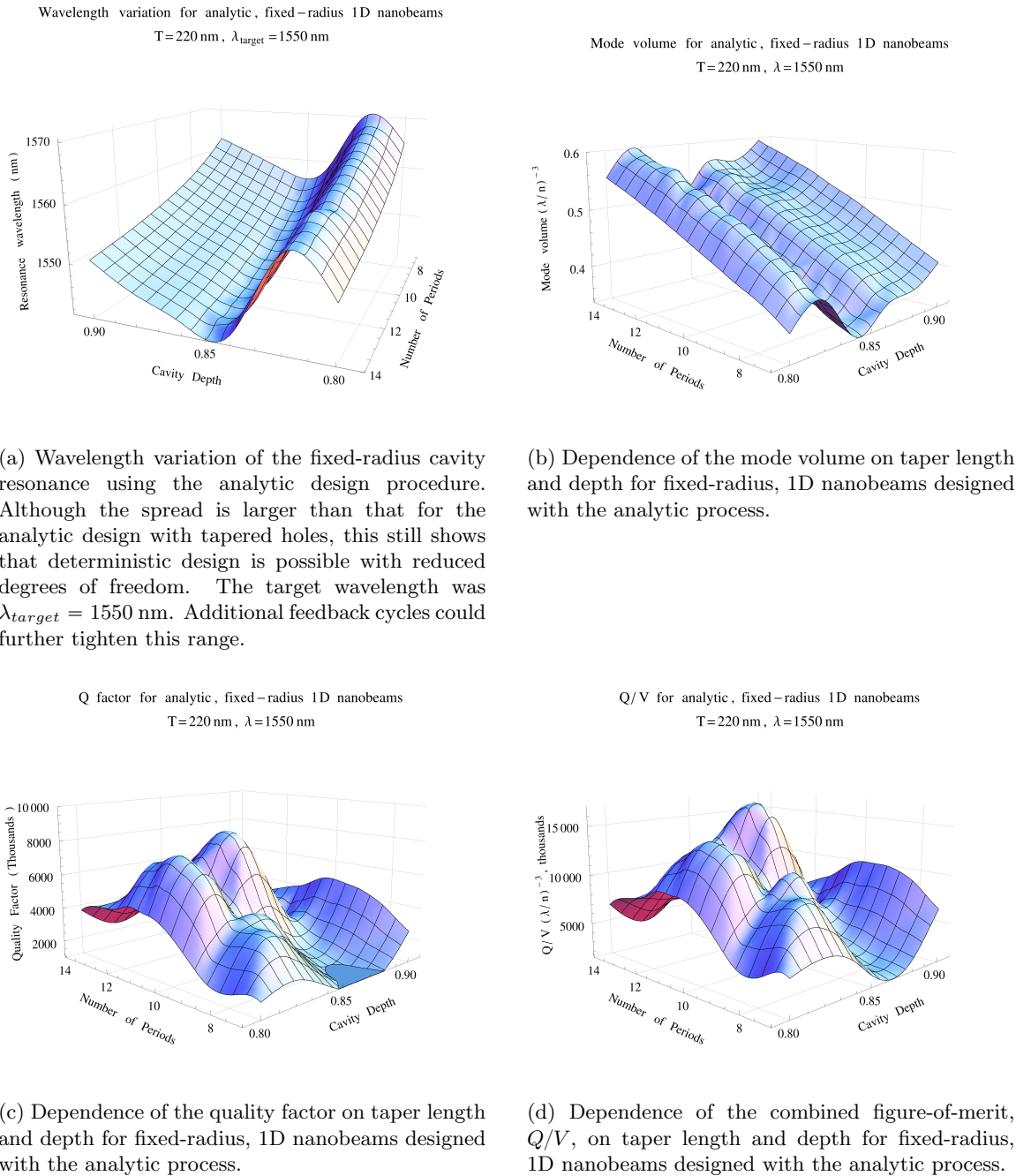


Figure 3.49: Results of FEM simulations characterizing fixed-radius, analytically-designed 1D nanobeam cavities. The quality factor and  $Q/V$  show remarkable improvements over the basic fixed-radius design, including a theoretical  $Q$  of  $7.8 \times 10^6$  which is nearly as high as that for the tapered radius cavities. Due to the deterministic design process, each depth and period combination produces a single, optimized cavity geometry which operates at the intended wavelength without excessive parameter sweeps to simultaneously tune resonance, quality, and mode volume.

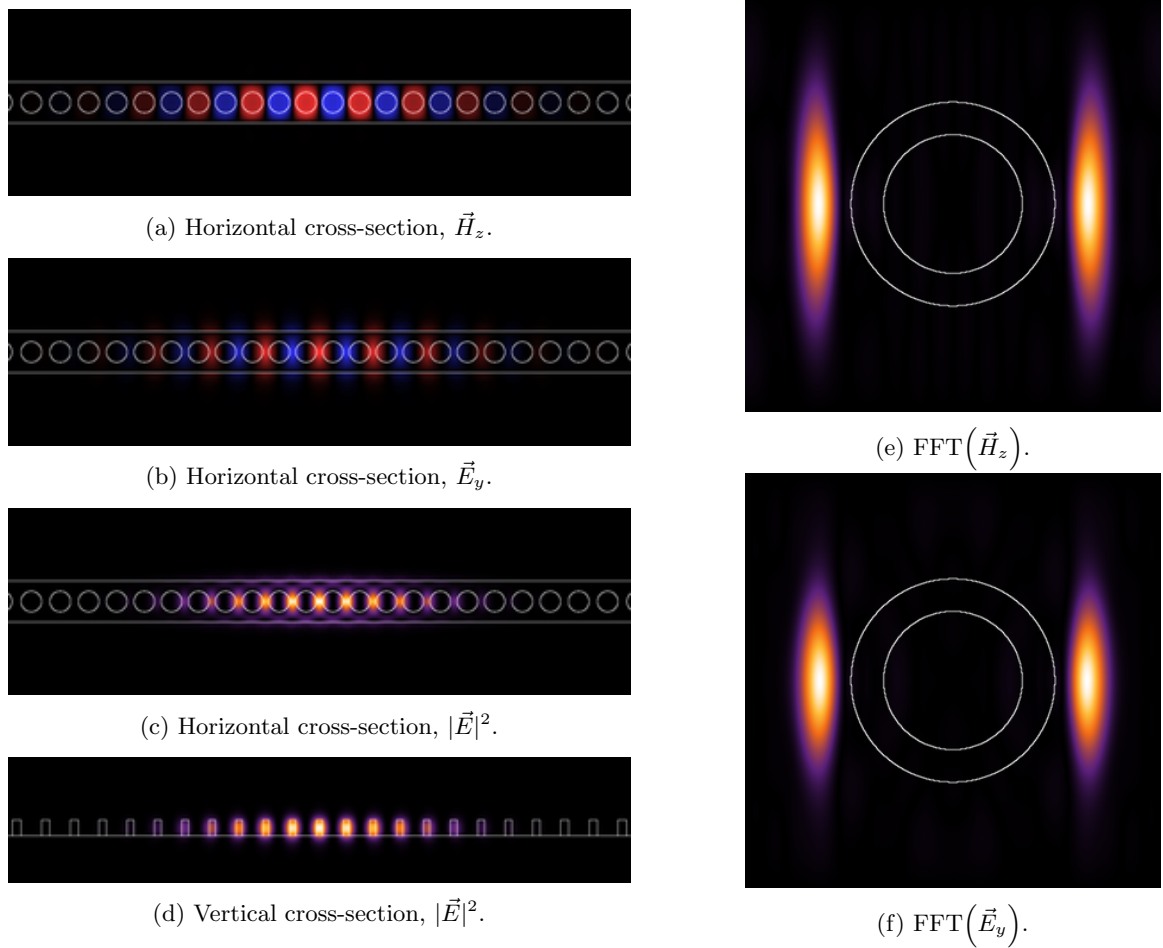
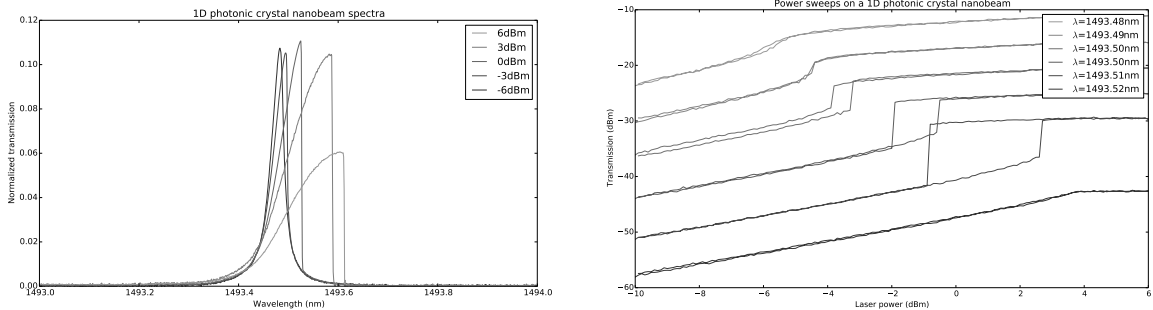


Figure 3.50: FEM simulations of our fixed-radius, analytic beam design, showing cross-sections of the fields (through center of beam) and corresponding FFTs ( $\lambda/4$  in substrate). The FFT circles indicate the light cones for air (inner) and oxide (outer). This device represents a significant improvement over the fixed-radius, expanded beam design with a much more appropriately designed taper. Although the theoretical performance does not quite reach that of the tapered design, practical improvements in fabrication tolerance would likely significantly outweigh these concerns.

### 3.4.6 Optical bistability

While measuring the nanobeam cavities, we noticed that significantly different quality factors would be measured for a given device, depending on the laser power used. Examining these at even higher excitation powers, we observed drastic modifications to the resonance lineshape (Figure 3.51a), beginning with a red-shift<sup>11</sup> of the peak and general smearing of the Lorentzian profile, followed by an abrupt drop beyond a certain point. Performing a bidirectional power-sweep at various red-detuned wavelengths resulted in a hysteretic response (Figure 3.51b), whose width depended on the magnitude of the detuning and input power. Data from a typical set of scans are shown in Figure 3.51.



(a) Normalized transmission spectra for a 1D nanobeam cavity over a range of input powers.

(b) Bidirectional power sweeps at several wavelengths, all of which are red-shifted from the nominal (cold-cavity) resonance. Curves are offset for clarity.

Figure 3.51: Wavelength and power sweeps of a 1D photonic crystal nanobeam exhibiting bistable characteristics. At higher powers, the lineshape changes dramatically, exhibiting a red-shift of the peak and an abrupt drop for long wavelengths. Higher excitation powers also show a decrease in the normalized power transmitted through the device, as increasing energy is lost to nonlinear absorptive effects. In the power sweeps, the bistability results in a hysteretic response.

This behavior is characteristic of an optical bistability, which arises due to optical nonlinearities which become significant at high energy densities. At sufficient intensities, several of these effects — including the optical Kerr effect, free-carrier dispersion, and thermo-optic detuning — can modify the refractive index of the nanobeam (through dependence on intensity, local concentration of free electrons or holes, and local temperature) enough to substantially shift the resonance (see 3.2.4).

Simultaneously, these effects couple through absorptive processes, including linear absorption (both

<sup>11</sup>Due to the method used to tune the laser, scans are performed from blue to red, resulting in the lineshape we observed in the curves. A somewhat more stunted response would be recorded for a red-to-blue scan.

inherent to the material and at surface states), two-photon absorption, and free-carrier absorption, which not only modify the relative amplitude for the device, but result in extremely complex spectral responses for the device.

Due to the extremely high  $Q/V$  for our cavities, the local electric field density can be exceptionally high at even moderate input power. Such effects have been previously reported in a number of photonic crystal geometries [385, 268, 341, 19, 321, 123, 265, 352, 386, 287]. Many authors exploit the behavior for applications in optical switching [341, 268, 123, 265, 386], as well as sensing [287], where the ultimate sensitivity becomes primarily based on laser linewidth and stability, rather than cavity  $Q$ . They also provide important mechanisms for tuning the resonance, which are critical to reliable operation of the cQED system.

Unfortunately, these effects were extremely detrimental for our application. The nonlinear drop in power coupled to the cavity and resonance shifts created significant challenges to trapping quantum dots using the cavity field (see 2.4.4). After observing the behavior, we sought to quantify the contributing factors in order to understand if trapping sub-10 nm objects would indeed be possible with our system.

We adapted the model developed by Barclay *et al.* [19] for evanescently-coupled cavities (measuring reflectance) to one suitable for an end-fired geometry (measuring transmission). For a general cavity with a Lorentzian transmission spectrum (see 3.2.6), the normalized transmitted follows:

$$T(\omega) = \frac{4\gamma_{in}\gamma_{out}}{(\omega - \omega_0)^2 + (\gamma_{in} + \gamma_{out} + \gamma_0)^2}$$

where  $\gamma_{in}$  and  $\gamma_{out}$  represent the coupling rates into- and out-of the cavity,  $\gamma_0$  represents other inherent losses (radiative or absorptive), and  $\omega_0$  the resonance frequency. In the limit that  $\gamma_0 \rightarrow 0$  and  $\gamma_{in} = \gamma_{out}$ , the transmission approaches unity when on resonance.

In the case of nonlinear optical behavior, we expect additional frequency shifts and loss terms

which depend on the energy within the cavity. Letting  $U$  represent the stored energy:

$$T(\omega, U) = \frac{4\gamma_{in}\gamma_{out}}{(\omega - \omega_0 - \Delta\omega_0(U))^2 + (\gamma_{in} + \gamma_{out} + \gamma_0 + \gamma'(U))^2}$$

Following Barclay *et al.* [19], we expect additional loss-terms arising from two-photon absorption (TPA) and free-carrier absorption (FCA):  $\gamma'(U) = \bar{\gamma}_{TPA}(U) + \bar{\gamma}_{FCA}(U)$ , where the bar denotes quantities which are normalized over the mode profile. As derived earlier using perturbation theory, the resonance frequency will shift proportional to changes in the refractive index, weighted by their modal energy confinement:

$$\begin{aligned} \frac{\Delta\omega_0(U)}{\omega_0} &= \frac{\int \left( \frac{\Delta n(\vec{r})}{n(\vec{r})} \right) n^2(\vec{r}) |\vec{E}(\vec{r})|^2 d\vec{r}^3}{\int n^2(\vec{r}) |\vec{E}(\vec{r})|^2 d\vec{r}^3} \\ &= -\Delta\bar{n}(U) \end{aligned}$$

We expect the refractive index of the core<sup>12</sup> to shift due to the Kerr effect, free-carrier dispersion (FCD) and thermo-optic effects:  $\Delta\bar{n}(U) = \Delta\bar{n}_{Kerr}(U) + \Delta\bar{n}_{FCD}(U) + \Delta\bar{n}_{th}(U)$ .

These expressions can be expanded and written in terms of modal-averaged parameters:

$$\begin{aligned} \bar{\gamma}_{TPA}(U) &= \Gamma_{TPA} \beta'_{Si} \frac{U}{V_{TPA}} \\ \bar{\gamma}_{FCA}(U) &= \Gamma_{FCA} \left( \frac{\tau \sigma'_{Si} \beta'_{Si}}{2\hbar\omega_0} \frac{U^2}{V_{FCA}^2} \right) \\ \Delta\bar{n}_{Kerr}(U) &= \frac{\Gamma_{Kerr}}{n_{Si}} \left( n'_{2,Si} \frac{U}{V_{Kerr}} \right) \\ \Delta\bar{n}_{FCD}(U) &= -\frac{\Gamma_{FCD}}{n_{Si}} \left( \frac{\tau \zeta_{Si} \beta'_{Si}}{2\hbar\omega_0} \frac{U^2}{V_{FCD}^2} \right) \\ \Delta\bar{n}_{th}(U) &= \frac{\Gamma_{th}}{n_{Si}} \left( \frac{dn_{Si}}{dT} \frac{dT}{dP_{abs}} P_{abs}(U) \right) \end{aligned}$$

where the total *absorbed* power,  $P_{abs}(U) = (\gamma_{lin} + \bar{\gamma}_{TPA}(U) + \bar{\gamma}_{FCA}(U))U$ . Here, we also note that the intrinsic cavity losses have been separated into radiative and absorptive components,  $\gamma_0 =$

$\gamma_{lin} + \gamma_{rad}$ .

<sup>12</sup>Due to the minimal modal energy in the cladding and substrate, these are unlikely to undergo significant shifts in refractive index, and the mode would be similarly less effected by such changes. We therefore neglect these terms, although they could be incorporated in principle.

Expressions for the modal-weighting terms,  $\Gamma_-$ , and effective volumes,  $V_-$  are given explicitly in [19]. These will not be repeated here, but can be readily evaluated from mode profiles extracted by FDTD or FEM simulations. The material parameters,  $\beta'_{Si} = \beta_{Si}(c/n_g)^2$ ,  $\sigma'_{Si} = \sigma_{Si}(c/n_g)$ ,  $n'_{2,Si} = (c/n_g)n_{2,Si}$ ,  $\zeta_{Si}$ <sup>13</sup> and  $\frac{dn_{Si}}{dT}$ , corresponding to the material-dependent two-photon absorption strength, free-carrier cross-section, Kerr coefficient, a free-carrier dispersion coefficient, and thermo-optic coefficient<sup>14</sup> are related to material constants found in the literature. For these parameters, we used:

Parameter	Value	Units	Source
$V_{TPA}$	2.0650	$(\lambda/n_{Si})^3$	FEM
$V_{FCA}$	1.5732	$(\lambda/n_{Si})^3$	FEM
$\Gamma_{TPA}$	0.9967		FEM
$\Gamma_{FCA}$	0.9998		FEM
$\Gamma_{th}$	0.9114		FEM
$V_{FCD}$	$V_{FCA}$		
$\Gamma_{FCD}$	$\Gamma_{FCA}$		
$n_{Si}$	3.48		
$\sigma_{Si}$	$14.5 \times 10^{-22}$	$m^2$	[19]
$\zeta_{Si}^e$	$8.8 \times 10^{-28}$	$m^3$	[19]
$\zeta_{Si}^h$	$4.6 \times 10^{-28}$	$m^3$	[19]
$n_{2,Si}$	$4.4 \times 10^{-18}$	$m^2 \cdot W^{-1}$	[19]
$\beta_{Si}$	$8.4 \times 10^{-12}$	$m \cdot W^{-1}$	[19]
$\frac{dn_{Si}}{dT}$	$1.86 \times 10^{-4}$	$K^{-1}$	[19]

Table 3.3: Material and computed constants for calculating bistable optical response of our 1D photonic crystal nanobeams.

In our system, we also needed to consider fixed coupling losses due to the grating couplers, propagation losses in the waveguides, fiber facets, etc.:  $P_{meas} = P_{laser} * \eta_{in} * T * \eta_{out}$ . For these, we first estimated the combined  $\eta_{in} * \eta_{out}$  spectrum based on average measurements over several grating-coupler loopbacks (straight waveguide without a cavity), which accounts for typical losses in all of these components, and then used them as free parameters in the system, allowing them to account for non-ideal cavity coupling from the waveguide.

Although the energy coupled into the resonator cannot be easily determined from the input power of the laser (due to spectral and non-linear dependence), the *transmitted* power is directly

<sup>13</sup>We make the same substitution when using  $\zeta$  as Barclay *et al.* [19],  $\Delta n_{FCD,Si} = -(\zeta_{Si}^e N_e + (\zeta_{Si}^h N_h)^{0.8})$  to account for relative electron- and hole- contributions to free carrier dispersion in silicon.

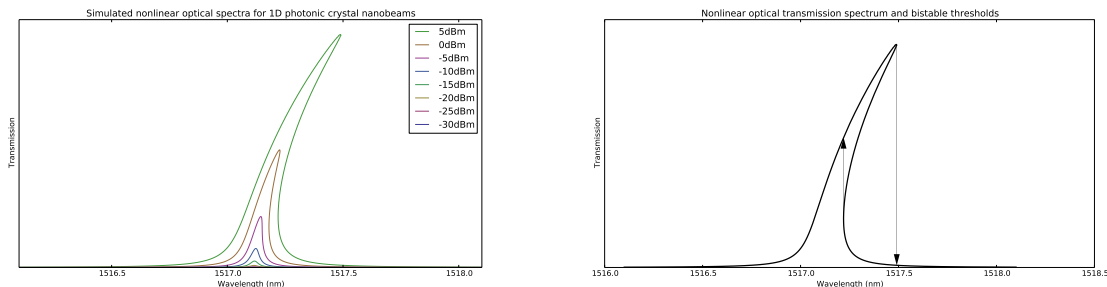
<sup>14</sup>Measurements of resonances shifts where the stage temperature was varied led to almost exactly the resonance shift predicted using perturbation theory with the  $\Gamma_{th}$  and  $dn_{Si}/dT$  values here.

proportional to this through the loss rate out of the cavity:

$$U = \frac{P_{out}}{2\gamma_{out}}$$

$$= \frac{P_{meas}}{2\gamma_{out} \eta_{out}}$$

The remaining unknowns include the temperature rise for a given power absorption ( $\frac{dT}{dP_{abs}}$ ) and the free-carrier lifetime,  $\tau$ , which is itself dependent on free-carrier density (and thus,  $U$ ); we followed the suggestion in [19] and fit  $\tau$  to the form  $\tau^{-1}(U) = A + BN(U)^\alpha$ . In total, then, our unknowns consist of  $\gamma_{in}$ ,  $\gamma_{out}$ ,  $\eta_{in}$ ,  $\eta_{out}$ ,  $\gamma_{lin}$ ,  $\gamma_{rad}$ ,  $dT/dP_{abs}$ , and  $\tau(U)$ , which we desired to fit to our data set,  $P_{meas}(P_{in}, \omega_0)$ .



(a) Simulated nonlinear optical transmission spectra, showing progressive deformation of the Lorentzian response with increasing power.

(b) Nonlinear optical transmission spectrum with bistable thresholds marked. Arrows indicate direction of hysteresis loop which would be observed during wavelength sweeps.

Figure 3.52: Nonlinear optical transmission spectra.

We began the parameter fitting in a manner similar to Barclay *et al.* [19]. At the lowest excitation power, nonlinear effects can be neglected ( $\Delta\bar{n}(U), \gamma'(U) = 0$ ). This allowed us to measure  $\gamma_0$  directly by fitting a Lorentzian to the cold-cavity spectrum, and use a ratiometric parameter,  $\rho$ , to control the radiative- and absorptive components:  $\gamma_{lin} = \rho\gamma_0$ ,  $\gamma_{rad} = (1 - \rho)\gamma_0$ .  $\eta_{\{in,out\}}$  was initialized as described above, allowing  $\gamma_{\{in,out\}}$  to be fit based on overall cavity transmission.

Once these initial parameter estimates had been made, we extracted the locations of the critical points in each spectra, obtaining estimates of  $\Delta\bar{n}(U)$  and  $\gamma'(U)$ . With these data (examining just the critical points, for now), we performed several nonlinear Nelder-Mead error minimizations over the entire set of parameters, refining the combined set in a self-consistent manner. A process variable was used to control the relative weight of wavelength- vs. magnitude error in the minimization.

Up to this point, our parameter fitting was essentially equivalent to that reported in [19]. While this process was fairly successful at reconstructing the critical points, we found that intermediate points on the spectra were only partially representative of the data<sup>15</sup>. To produce a more exact representation, we performed several alternating Nelder-Mead optimizations, first between *complete*  $P_{meas}(P_{in}, \omega)$  data and simulated bistable curves, followed by only the critical points. This combination of both techniques was crucial to achieving an acceptable reconstruction of the full curve. Using only full spectra, for example, tended to follow the curves well but could significantly over- or undershoot the bistable threshold, while fits using only the critical points would stray from the spectral shapes in the middle.

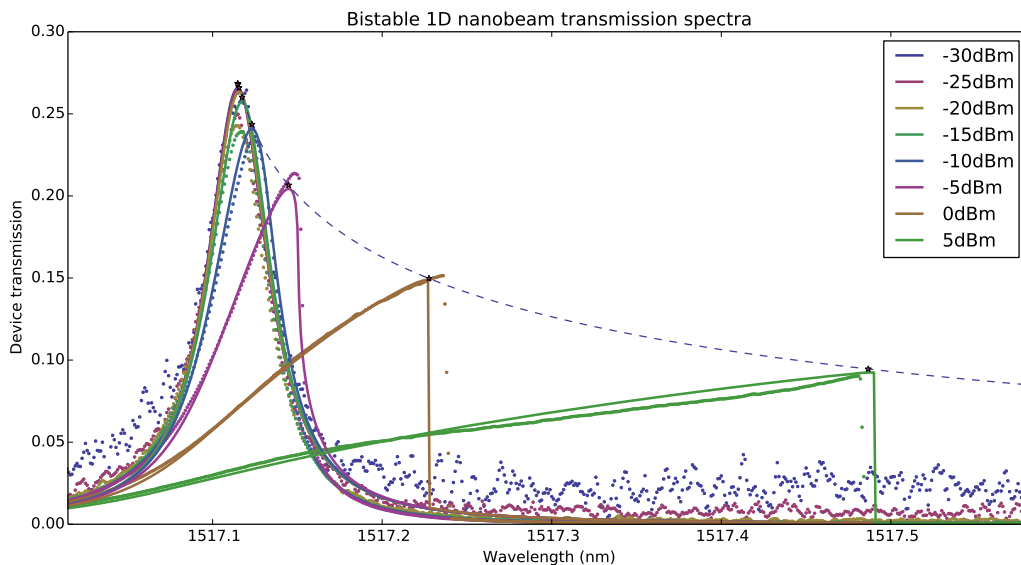


Figure 3.53: Normalized transmission spectra for a fixed-radius, 1D nanobeam cavity (colored dots) and corresponding simulated spectra (solid lines). Labeled powers correspond to the laser output, before coupling and propagation losses. Excellent agreement for both the lineshape variation and bistable thresholds are reproduced over a wide range of input powers. The dashed line shows the simulated  $(\Delta\omega_0, \Delta T)$  trend of the critical point, with star symbols to mark the values corresponding to the laser inputs.

Results of the optimization are presented in Figure 3.53; derived parameters are shown in Table 3.4. Excellent agreement over the entire spectral line was achieved for a wide range of input powers, suggesting that this serves as a fairly realistic model of the device performance. The numeric values for the carrier lifetime  $\tau$  fell between 38 ns (at small carrier concentrations) and 1 ps (at

<sup>15</sup>We note that Barclay *et al.* [19] only reported the critical points, and may have had significant errors across the complete cavity spectra.

Parameter	Value	Units
$\lambda_0$	1517.11	nm
$\gamma_{in}/2\pi$	1.19015	GHz
$\gamma_{out}/2\pi$	0.45462	GHz
$\eta_{in}$	0.52028	
$\eta_{out}$	0.00695	
$\gamma_{lin}/2\pi$	1.19284	GHz
$\gamma_{rad}/2\pi$	0	GHz
$dT/dP_{abs}$	13.1162	K/mW

Table 3.4: Parameters to model optical bistability in 1D nanobeam, extracted from nonlinear optimization.

nearly degenerate free-carrier levels). The value for  $dT/dP_{abs}$  also fell close to the range reported by Barclay *et al.* [19], suggesting these results are physically reasonable. We do note that all of the cold-cavity performance was allocated to absorption (rather than radiative losses), while the input grating efficiency ( $\eta_{in}$ ) was also estimated to be significantly higher than the output ( $\eta_{out}$ ). The former suggests a high degree of nonlinearity was required to fit the data, while the latter results in a substantial amount of energy being coupled into the resonator (also leading to large nonlinearities). This could indicate that the nonlinearities extended below our cold-cavity measurements (limited by our detector sensitivity), and readily confirm the significantly nonlinear behavior of the devices.

From the calculations in 2.4.4.3, a device with  $Q = 100k$  would require 1.454 mW coupled into the cavity in order to trap our quantum dot. Using  $Q = \omega_0 \frac{U}{P}$ , this corresponds to a trapped energy of 119.6 fJ<sup>16</sup>. Assuming the parameters are close enough to extrapolate this far, trapping a PbS QD with this device would have required a laser power of 94.7 mW, and would have undergone a nonlinearity-induced red-shift to 1524.3 nm ( $\Delta\lambda = 7.2$  nm). Although such a power is perfectly realistic with other lasers or EDFAs (and still lower than that required for trapping by Gaussian beam), it was quite beyond the range of our experimental setup.

Beyond merely detuning the resonance, coupling this much power into the cavity would induce severe parasitic losses through extremely high two-photon and free-carrier absorption. At this level, the combined loss rate would have reached  $\gamma/2\pi=12.49$  GHz, lowering the  $Q$  by an order of magnitude over its intrinsic value (15,820.6, vs. 165,660 for this device). Simultaneously, the total normalized

<sup>16</sup>A lower  $Q$  cavity with non-ideal coupling, but which used the same design (and thus, field gradients and mode volume) would require the same energy; it would just take more power to get there.

transmission through the cavity would drop from 0.269 to 0.013. Given that the sensitivity also follows  $Q/V$  (and does not scale for power, unlike trapping stability of stiffness) and relies on transmission for sensing, this could render particle detection almost impossible.

Experimentally, there are several potential means to remedy these issues. Reports in the mid-IR[321] revealed that adsorbed water or surface Si-H bonds contributed significantly to the bistable response, and could be at least partially mitigated through similar piranha/HF treatments, immediately transferring to an  $N_2$ -purged environment for testing, or attempting to anneal off adsorbed  $H_2O$  in an  $N_2$ -purged environment. Although the absorption of  $H_2O$  is significantly higher at their wavelength of  $4.5 \mu\text{m}$  than at  $1550 \text{ nm}$ , this does suggest an opportunity to improve performance by annealing, or potentially working at another wavelength range (water absorption drops significantly at shorter wavelengths). Surface coatings might also reduce the performance sensitivity to surface adsorbates. As we did not have an  $N_2$  purged environment available, we did attempt to immediately encapsulate using a post-piranha oxidation in a rapid thermal annealer (RTA). No reduction in bistability was observed; however, a proper coating with  $Si_3N_4$  might be effective (although the thickness of such a layer would need to be carefully balanced; thicker layers might reduce interaction with unwanted surface contamination, but they would also reduce trapping performance and coupling strength to the emitter).

Finally, we note that many of these challenges could be inherently solved in another material system. The significant losses at higher powers largely originate from two-photon absorption, whose effect is compounded as it induces greater free-carrier absorption as well. By using a larger band gap material, such as  $Si_3N_4$ , it could be possible to circumvent many of these issues entirely. Although the lower index contrast would hurt performance somewhat, the ability to operate at shorter wavelengths inherently provides tighter gradients for trapping and would also enable use of more sensitive single photon detectors. Very high-quality photonic crystal cavities devices have been demonstrated in  $Si_3N_4$ , and new geometries could be readily designed with the analytic algorithm we developed above.

## Chapter 4

# Conclusions and Outlook

We investigated four unique methods for achieving scalable, deterministic integration of quantum emitters into ultra-high  $Q/V$  photonic crystal cavities, including selective area heteroepitaxy, engineered photoemission from silicon nanostructures, wafer bonding and dimensional reduction of III-V quantum wells, and cavity-enhanced optical trapping. In these areas, we were able to demonstrate site-selective heteroepitaxy, size-tunable photoluminescence from silicon nanostructures, Purcell modification of QW emission spectra, and limits of cavity-enhanced optical trapping designs which exceed any reports in the literature and suggest the feasibility of capturing and detecting nanostructures with dimensions below 10 nm. In addition to process scalability and the requirement for achieving accurate spectral and spatial overlap between the emitter and cavity, these techniques paid specific attention to the ability to separate the cavity and emitter material systems in order to allow optimal selection of these independently, and eventually enable monolithic integration with other photonic and electronic circuitry.

We also developed an analytic photonic crystal design process yielding optimized cavity tapers with minimal computational effort, and reported on a general cavity modification which exhibits improved fabrication tolerance by relying exclusively on positional rather than dimensional tapering. We compared several experimental coupling techniques for device characterization. Significant efforts were devoted to optimizing cavity fabrication (including the use of atomic layer deposition to improve surface quality), exploration into factors affecting the design fracturing, and automated analysis of SEM images. Using optimized fabrication procedures, we experimentally demonstrated 1D photonic

crystal nanobeam cavities exhibiting the highest  $Q/V$  reported on substrate. Finally, we analyzed the bistable behavior of the devices to quantify the nonlinear optical response of our cavities. These results are immediately transferable to other photonic crystal devices. In addition to experimentally testing the analytically designed cavities described here, future work should examine the application of our design and fabrication processes to other applications. The reliability of other devices might be significantly improved by exclusive use of feature location, rather than dimensional control, to develop photonic crystal tapers. Similarly, the design process could be greatly assisted by using the analytic design technique, which can be generally applied to other material systems, design features, and tapering parameters.

From the investigations on emitter integration, we have concluded that the selective-area epitaxy holds the greatest potential for large-scale cQED system development. Future work in this area should consider opportunities for improving the growth interface quality and reliability, perhaps through the use of chemical-mechanical polishing and *in situ* oxidation removal in the growth chamber. Challenges will also remain to defining the cavity over the emitter structure.

Cavity enhanced optical trapping enables the greatest independence between cavity and emitter material systems, and could be suitable for early experiments up to several coupled cavities; we believe that it remains especially interesting as a platform for probing novel nanocrystal emitters or colloidal quantum dots, without imposing significant material constraints between the cavity and emitter. While optical bistability ultimately prevented us from capturing a nanocrystal emitter with our system, realistic calculations using experimentally-derived parameters show that it should be quite possible. Future work should examine other cavity material systems and spectral ranges where two-photon absorption and other nonlinearities are less problematic, as well as integrated techniques emitter delivery and fixation.

We found that persistent phonon-mediated transitions hampered the efficiency of silicon light emission, while the presence of surface-related defects might ultimately limit the usability of dimensionally-reduced QW emitters. While these features make these systems unsuitable as quantum emitters, we believe that these technologies might still find use as classical light sources.

Through these efforts, we reported several other notable achievements, including the reliable fabrication of structures down to 2.5 nm in silicon and an etching technique to help circumvent lithographic size limitations, development of an extremely selective silicon etch mask and ultra-high aspect ratio silicon nanostructures, a dry etching process for producing undercut and suspended structures in a single step, geometric engineering of the silicon band gap, and the fabrication and characterization of low-noise SiGe quantum dot photodetectors. In addition to our original goal to assemble cQED systems, the devices and techniques described here could hold great potential as on-chip light sources for integrated optics systems, geometrically-engineered quantum electron devices, or cavity-based biochemical sensing and detection.

# Bibliography

- [1] Ahn B H, Kang J H, Kim M K, Song J H, Min B, Kim K S and Lee Y H (2010). ‘One-dimensional parabolic-beam photonic crystal laser’. *Optics Express*, 18(6), 5654.
- [2] Akahane Y, Asano T, Song B S and Noda S (2003). ‘High-Q photonic nanocavity in a two-dimensional photonic crystal.’ *Nature*, 425(6961), 944–7.
- [3] Alasaarela T, Korn D, Alloatti L, Säynätjoki A, Tervonen A, Palmer R, Leuthold J, Freude W and Honkanen S (2011). ‘Reduced propagation loss in silicon strip and slot waveguides coated by atomic layer deposition.’ *Optics express*, 19(12), 11529–11538.
- [4] Alasaarela T, Saastamoinen T, Hiltunen J, Säynätjoki A, Tervonen A, Stenberg P, Kuittinen M and Honkanen S (2010). ‘Atomic layer deposited titanium dioxide and its application in resonant waveguide grating.’ *Applied optics*, 49(22), 4321–4325.
- [5] Alivisatos A P (1996). ‘Semiconductor clusters, nanocrystals, and quantum dots’. *Science*, 271(5251), 933–937.
- [6] Aoki T, Dayan B, Wilcut E, Bowen W P, Parkins A S, Kippenberg T J, Vahala K J and Kimble H J (2006). ‘Observation of strong coupling between one atom and a monolithic microresonator.’ *Nature*, 443(7112), 671–4.
- [7] Asano T, Song B S and Noda S (2006). ‘Analysis of the experimental Q factors ( $\sim 1$  million) of photonic crystal nanocavities.’ *Optics express*, 14(5), 1996–2002.
- [8] Ashkin A (1970). ‘Acceleration and Trapping of Particles by Radiation Pressure’. *Physical Review Letters*, 24(4), 156–159.

- [9] Ashkin A and Dziedzic J (1987). ‘Optical trapping and manipulation of viruses and bacteria’. *Science*, 235(4795), 1517–1520.
- [10] Ashkin A, Dziedzic J M, Bjorkholm J E and Chu S (1986). ‘Observation of a single-beam gradient force optical trap for dielectric particles’. *Optics Letters*, 11(5), 288.
- [11] Aspect A, Grangier P and Roger G (1981). ‘Experimental tests of realistic local theories via Bell’s theorem’. *Physical Review Letters*, 47(7), 460–463.
- [12] Atkinson P, Ward M B, Bremner S P, Anderson D, Farrow T, Jones G a C, Shields a J and Ritchie D a (2006). ‘Site-Control of InAs Quantum Dots using Ex-Situ Electron-Beam Lithographic Patterning of GaAs Substrates’. *Japanese Journal of Applied Physics*, 45(4A), 2519–2521.
- [13] Audoit G, Mhuirheartaigh E N, Lipson S M, Morris M A, Blau W J and Holmes J D (2005). ‘Strain induced photoluminescence from silicon and germanium nanowire arrays’. *Journal of Materials Chemistry*, 15(45), 4809.
- [14] Badolato A, Hennessy K, Atatüre M, Dreiser J, Hu E, Petroff P M and Imamoglu A (2005). ‘Deterministic coupling of single quantum dots to single nanocavity modes.’ *Science (New York, NY)*, 308(5725), 1158–61.
- [15] Baehr-Jones T, Pinguet T, Guo-Qiang P L, Danziger S, Prather D and Hochberg M (2012). ‘Myths and rumours of silicon photonics’. *Nature Photonics*, 6(April), 6–8.
- [16] Bangerth W, Hartmann R and Kanschat G (2007). ‘deal.II—A general-purpose object-oriented finite element library’. *ACM Transactions on Mathematical Software*, 33(4), 24–es.
- [17] Barclay P E, Santori C, Fu K M, Beausoleil R G and Painter O (2009). ‘Coherent interference effects in a nano-assembled diamond NV center cavity-QED system’. *Optics Express*, 17(10), 8081.
- [18] Barclay P E, Srinivasan K and Painter O (2003). ‘Design of photonic crystal waveguides for

- evanescent coupling to optical fiber tapers and integration with high-Q cavities'. *Journal of the Optical Society of America B*, 20(11), 2274.
- [19] Barclay P E, Srinivasan K and Painter O (2005). 'Nonlinear response of silicon photonic crystal micresonators excited via an integrated waveguide and fiber taper'. *Optics Express*, 13(3), 801.
- [20] Baribeau J M, Jackman T E, Houghton D C, Maigné P and Denhoff M W (1988). 'Growth and characterization of Si<sub>1-x</sub>Ge<sub>x</sub> and Ge epilayers on (100) Si'. *Journal of Applied Physics*, 63(12), 5738–5746.
- [21] Baró J, Sempau J, Fernández-Varea J and Salvat F (1995). 'PENELOPE: An algorithm for Monte Carlo simulation of the penetration and energy loss of electrons and positrons in matter'. *Nuclear Instruments and Methods in Physics Research Section B: Beam Interactions with Materials and Atoms*, 100(1), 31–46.
- [22] Barth M and Benson O (2006). 'Manipulation of dielectric particles using photonic crystal cavities'. *Applied Physics Letters*, 89(2006), 9–12.
- [23] Basche T, Moerner W E, Orrit M and Talon H (1992). 'Photon antibunching in the fluorescence of a single dye molecule trapped in a solid'. *Physical Review Letters*, 69(10), 1516–1519.
- [24] Batson P (1993). 'Distortion of the core exciton by the swift electron and plasmon wake in spatially resolved electron-energy-loss scattering'. *Physical Review B*, 47(12).
- [25] Batson P and Bruley J (1991). 'Dynamic screening of the core exciton by swift electrons in electron-energy-loss scattering'. *Physical Review Letters*, 67(3), 350–353.
- [26] Batson P and Heath J (1993). 'Electron energy loss spectroscopy of single silicon nanocrystals: The conduction band'. *Physical Review Letters*, 71(6), 911–914.
- [27] Beard M C, Knutsen K P, Yu P, Luther J M, Song Q, Metzger W K, Ellingson R J and Nozik A J (2007). 'Multiple exciton generation in colloidal silicon nanocrystals.' *Nano letters*, 7(8), 2506–12.

- [28] Bekshaev A Y, Bliokh K Y and Nori F (2013). ‘Mie scattering and optical forces from evanescent fields: a complex-angle approach.’ *Optics express*, 21(6), 7082–95.
- [29] Bennett A, Unitt D, Atkinson P, Ritchie D and Shields A (2005). ‘High performance single photon sources from photolithographically defined pillar microcavities.’ *Optics express*, 13(1), 50–55.
- [30] Bennett A, Unitt D, Shields A, Atkinson P and Ritchie D (2005). ‘Influence of exciton dynamics on the interference of two photons from a microcavity single-photon source.’ *Optics express*, 13(20), 7772–7778.
- [31] Benson O, Santori C, Pelton M and Yamamoto Y (2000). ‘Regulated and Entangled Photons from a Single Quantum Dot’. *Physical Review Letters*, 84(11), 2513–2516.
- [32] Benyoucef M and Reithmaier J P (2013). ‘Direct growth of IIIV quantum dots on silicon substrates: structural and optical properties’. *Semiconductor Science and Technology*, 28(9), 094004.
- [33] Benyoucef M, Usman M and Reithmaier J P (2013). ‘Bright light emissions with narrow spectral linewidths from single InAs/GaAs quantum dots directly grown on silicon substrates’. *Applied Physics Letters*, 102(13), 132101.
- [34] Beveratos A, Kühn S, Brouri R, Gacoin T, Poizat J P and Grangier P (2002). ‘Room temperature stable single-photon source’. *European Physical Journal D*, 18(2), 191–196.
- [35] Beyer V, Schmidt B, Heinig K H and Stegemann K H (2009). ‘Light emitting field effect transistor with two self-aligned Si nanocrystal layers’. *Applied Physics Letters*, 95(19).
- [36] Bienstman P (2012). ‘CAMFR - CAvity Modeling FRamework’.
- [37] Birnbaum K M, Boca A, Miller R, Boozer A D, Northup T E and Kimble H J (2005). ‘Photon blockade in an optical cavity with one trapped atom’. *Nature*, 436(7047), 87–90.

- [38] Birudavolu S, Luong S, Nuntawong N, Xin Y, Hains C and Huffaker D (2005). 'In-situ mask removal in selective area epitaxy using metal organic chemical vapor deposition'. *Journal of Crystal Growth*, 277(1-4), 97–103.
- [39] Birudavolu S, Nuntawong N, Balakrishnan G, Xin Y C, Huang S, Lee S C, Brueck S R J, Hains C P and Huffaker D L (2004). 'Selective area growth of InAs quantum dots formed on a patterned GaAs substrate'. *Applied Physics Letters*, 85(12), 2337.
- [40] Blanton S A, Hines M A and Guyot-Sionnest P (1996). 'Photoluminescence wandering in single CdSe nanocrystals'. *Applied Physics Letters*, 69(25), 3905–3907.
- [41] Borselli M, Johnson T J and Painter O (2006). 'Measuring the role of surface chemistry in silicon microphotronics'. *Applied Physics Letters*, 88(13), 131114.
- [42] Borselli M, Srinivasan K, Barclay P E and Painter O (2004). 'Rayleigh scattering, mode coupling, and optical loss in silicon microdisks'. *Applied Physics Letters*, 85(17), 3693–3695.
- [43] Brouri R, Beveratos A, Poizat J P and Grangier P (2000). 'Photon antibunching in the fluorescence of individual color centers in diamond.' *Optics letters*, 25(17), 1294–1296.
- [44] Brune M, Schmidt-Kaler F, Maali A, Dreyer J, Hagley E, Raimond J and Haroche S (1996). 'Quantum Rabi Oscillation: A Direct Test of Field Quantization in a Cavity'. *Phys Rev Lett*, 76(11), 1800.
- [45] Buckley S, Rivoire K and Vučković J (2012). 'Engineered quantum dot single-photon sources.' *Reports on progress in physics Physical Society (Great Britain)*, 75(12), 126503.
- [46] Canham L T (1990). 'Silicon quantum wire array fabrication by electrochemical and chemical dissolution of wafers'. *Applied Physics Letters*, 57(10), 1046.
- [47] Cavigli L, Bietti S, Accanto N, Minari S, Abbarchi M, Isella G, Frigeri C, Vinattieri A, Gurioli M and Sanguinetti S (2012). 'High temperature single photon emitter monolithically integrated on silicon'. *Applied Physics Letters*, 100(23), 231112.

- [48] Chance R R, Prock A and Sibley R (1974). ‘Lifetime of an emitting molecule near a partially reflecting surface’. *The Journal of Chemical Physics*, 60(7), 2744.
- [49] Chen K Y, Lee A T, Hung C C, Huang J S and Yang Y T (2013). ‘Transport and trapping in two-dimensional nanoscale plasmonic optical lattice.’ *Nano letters*, 13(9), 4118–22.
- [50] Chen R, Tran T T D, Ng K W, Ko W S, Chuang L C, Sedgwick F G and Chang-Hasnain C (2011). ‘Nanolasers grown on silicon’. *Nature Photonics*, 5(3), 170–175.
- [51] Chen Y F, Serey X, Sarkar R, Chen P and Erickson D (2012). ‘Controlled photonic manipulation of proteins and other nanomaterials’. *Nano Letters*, 12, 1633–1637.
- [52] Cheng S F, Gao L, Woo R L, Pangan A, Malouf G, Goorsky M S, Wang K L and Hicks R F (2008). ‘Selective area metalorganic vapor-phase epitaxy of gallium arsenide on silicon’. *Journal of Crystal Growth*, 310(3), 562–569.
- [53] Childs J, An K, Otteson M, Dasari R and Feld M (1996). ‘Normal-Mode Line Shapes for Atoms in Standing-Wave Optical Resonators’. *Physical Review Letters*, 77(14), 2901–2904.
- [54] Choi D, Ge Y, Harris J S, Cagnon J and Stemmer S (2008). ‘Low surface roughness and threading dislocation density Ge growth on Si (0 0 1)’. *Journal of Crystal Growth*, 310(18), 4273–4279.
- [55] Chuang L C, Moewe M, Chase C, Kobayashi N P, Chang-Hasnain C and Crankshaw S (2007). ‘Critical diameter for III-V nanowires grown on lattice-mismatched substrates’. *Applied Physics Letters*, 90(4), 043115.
- [56] Ciminelli C, Conteduca D, Dell’Olio F and Armenise M N (2014). ‘Design of an Optical Trapping Device Based on an Ultra-High Q/V Resonant Structure’. *IEEE Photonics Journal*, 6(6), 1–16.
- [57] Clauser J F and Shimony A (1978). ‘Bell’s theorem. Experimental tests and implications’. *Reports on Progress in Physics*, 41(12), 1881–1927.

- [58] Clawson A (2001). ‘Guide to references on IIIIV semiconductor chemical etching’. *Materials Science and Engineering: R: Reports*, 31(1-6), 1–438.
- [59] Cohen J D, Meenehan S M and Painter O (2013). ‘Optical coupling to nanoscale optomechanical cavities for near quantum-limited motion transduction’. *Optics Express*, 21(9), 11227–11236.
- [60] Comsol (2015). ‘COMSOL Multiphysics Modeling Software’.
- [61] Correa R E, Dauler E A, Nair G, Pan S H, Rosenberg D, Kerman A J, Molnar R J, Hu X, Marsili F, Anant V, Berggren K K and Bawendi M G (2012). ‘Single photon counting from individual nanocrystals in the infrared’. *Nano Letters*, 12(6), 2953–2958.
- [62] Cui H, Wang C X and Yang G W (2008). ‘Origin of self-limiting oxidation of Si nanowires.’ *Nano letters*, 8(9), 2731–7.
- [63] Cullis A and Canham L (1991). ‘Visible light emission due to quantum size effects in highly porous crystalline silicon’. *Nature*, 353(26), 335–338.
- [64] Currie M T, Samavedam S B, Langdo T A, Leitz C W and Fitzgerald E A (1998). ‘Controlling threading dislocation densities in Ge on Si using graded SiGe layers and chemical-mechanical polishing’. *Applied Physics Letters*, 72(14), 1718–1720.
- [65] De la Torre J, Souifi A, Lemiti M, Poncet A, Buseret C, Guillot G, Bremond G, Gonzalez O, Garrido B and Morante J (2003). ‘Optical and electrical transport mechanisms in Si-nanocrystal-based LEDs’. *Physica E: Low-dimensional Systems and Nanostructures*, 17, 604–606.
- [66] Deal B E and Grove A S (1965). ‘General Relationship for the Thermal Oxidation of Silicon’. *Journal of Applied Physics*, 36(12), 3770.
- [67] Delerue C, Allan G and Lannoo M (1993). ‘Theoretical aspects of the luminescence of porous silicon’. *Physical Review B*, 48(15), 11024–11036.

- [68] Demichel O, Oehler F, Calvo V, Noé P, Pauc N, Gentile P, Ferret P, Baron T and Magnea N (2009). ‘Photoluminescence of silicon nanowires obtained by epitaxial chemical vapor deposition’. *Physica E: Low-Dimensional Systems and Nanostructures*, 41(6), 963–965.
- [69] Deotare P B, McCutcheon M W, Frank I W, Khan M and Loncar M (2009). ‘High quality factor photonic crystal nanobeam cavities’. *Applied Physics Letters*, 94(12), 121106.
- [70] Draine B T (1988). ‘The Discrete Dipole Approximation and Its Applications to Interstellar Graphite Grains’. *The Astrophysical Journal*, 333, 848–872.
- [71] Eichenfield M, Camacho R, Chan J, Vahala K J and Painter O (2009). ‘A picogram- and nanometre-scale photonic-crystal optomechanical cavity.’ *Nature*, 459(7246), 550–5.
- [72] Eichenfield M, Chan J, Camacho R M, Vahala K J and Painter O (2009). ‘Optomechanical crystals.’ *Nature*, 462(7269), 78–82.
- [73] Elarde V, Yeoh T, Rangarajan R and Coleman J (2004). ‘Controlled fabrication of InGaAs quantum dots by selective area epitaxy MOCVD growth’. *Journal of Crystal Growth*, 272(1-4), 148–153.
- [74] Ellis D J P, Bennett A J, Dewhurst S J, Atkinson P, Nicoll C a, Ritchie D a and Shields A J (2008). ‘Oxide-apertured microcavity single-photon-emitting diodesimultaneous confinement of current and light’. *Journal of Physics: Condensed Matter*, 20(45), 454212.
- [75] Ellis D J P, Bennett A J, Shields A J, Atkinson P and Ritchie D A (2006). ‘Electrically addressing a single self-assembled quantum dot’. *Applied Physics Letters*, 88(13), 133509.
- [76] Empedocles S, Norris D and Bawendi M (1996). ‘Photoluminescence Spectroscopy of Single CdSe Nanocrystallite Quantum Dots’. *Physical Review Letters*, 77(18), 3873–3876.
- [77] Empedocles S A (1997). ‘Quantum-Confined Stark Effect in Single CdSe Nanocrystallite Quantum Dots’. *Science*, 278(5346), 2114–2117.

- [78] Empedocles S a and Bawendi M G (1999). ‘Influence of Spectral Diffusion on the Line Shapes of Single CdSe Nanocrystallite Quantum Dots’. *The Journal of Physical Chemistry B*, 103(11), 1826–1830.
- [79] Englund D, Faraon A, Fushman I, Stoltz N, Petroff P and Vucković J (2007). ‘Controlling cavity reflectivity with a single quantum dot.’ *Nature*, 450(7171), 857–861.
- [80] Englund D, Fushman I and Vučković J (2005). ‘General recipe for designing photonic crystal cavities’. *Optics Express*, 13(16), 5961.
- [81] Englund D, Shields B, Rivoire K, Hatami F, Vuckovic J, Park H and Lukin M D (2010). ‘Deterministic Coupling of a Single Nitrogen Vacancy Center to a Photonic Crystal Cavity.’ *Nano letters*, 10(10), 3922–3926.
- [82] Ertekin E, Greaney P a, Chrzan D C and Sands T D (2005). ‘Equilibrium limits of coherency in strained nanowire heterostructures’. *Journal of Applied Physics*, 97(11), 114325.
- [83] Fang A W, Park H, Cohen O, Jones R, Paniccia M J and Bowers J E (2006). ‘Electrically pumped hybrid AlGaInAs-silicon evanescent laser’. *Optics Express*, 14(20), 9203.
- [84] Faraon A, Barclay P E, Santori C, Fu K M C and Beausoleil R G (2011). ‘Resonant enhancement of the zero-phonon emission from a colour centre in a diamond cavity’. *Nature Photonics*, 5(5), 301–305.
- [85] Faraon A, Englund D, Bulla D, Luther-Davies B, Eggleton B J, Stoltz N, Petroff P and Vučković J (2008). ‘Local tuning of photonic crystal cavities using chalcogenide glasses’. *Applied Physics Letters*, 92(4), 043123.
- [86] Faraon A, Englund D, Fushman I, Vučković J, Stoltz N and Petroff P (2007). ‘Local quantum dot tuning on photonic crystal chips’. *Applied Physics Letters*, 90(21).
- [87] Faraon A, Majumdar A, Kim H, Petroff P and Vučković J (2010). ‘Fast electrical control of a quantum dot strongly coupled to a photonic-crystal cavity’. *Physical Review Letters*, 104(4).

- [88] Fauchet P M (2005). ‘Light emission from Si quantum dots’. *Materials Today*, 8(1), 26–33.
- [89] Fedorych O, Kruse C, Ruban A, Hommel D, Bacher G and Kümmell T (2012). ‘Room temperature single photon emission from an epitaxially grown quantum dot’. *Applied Physics Letters*, 100(6).
- [90] Fernée M J, Sinito C, Louyer Y, Tamarat P and Lounis B (2013). ‘The ultimate limit to the emission linewidth of single nanocrystals.’ *Nanotechnology*, 24(46), 465703.
- [91] Flagg E B, Muller A, Polyakov S V, Ling A, Migdall A and Solomon G S (2010). ‘Interference of single photons from two separate semiconductor quantum dots’. *Physical Review Letters*, 104(13).
- [92] Fleury L, Sick B, Zumofen G, Hecht B and Wild U P (1998). ‘High photo-stability of single molecules in an organic crystal at room temperature observed by scanning confocal optical microscopy’. *Molecular Physics*, 95(6), 1333–1338.
- [93] Foresi J S, Villeneuve P R, Ferrera J, Thoen E R, Steinmeyer G, Fan S, Joannopoulos J D, Kimerling L C, Smith H I and Ippen E P (1997). ‘Photonic-bandgap microcavities in optical waveguides’. *Nature*, 390(6656), 143–145.
- [94] Frank I W, Deotare P B, McCutcheon M W and Lončar M (2010). ‘Programmable photonic crystal nanobeam cavities’. *Optics Express*, 18(8), 8705.
- [95] Freedman S J and Clauser J F (1972). ‘Experimental test of local hidden-variable theories’. *Physical Review Letters*, 28(14), 938–941.
- [96] Fry P W, Itskevich I E, Mowbray D J, Skolnick M S, Finley J J, Barker J A, O’Reilly E P, Wilson L R, Larkin I A, Maksym P A, Hopkinson M, Al-Khafaji M, David J P, Cullis A G, Hill G and Clark J C (2000). ‘Inverted electron-hole alignment in InAs-GaAs self-assembled quantum dots.’ *Physical review letters*, 84(4), 733–736.
- [97] Fukuta Y, Fujita H and Toshiyoshi H (2003). ‘Vapor hydrofluoric acid sacrificial release

- technique for micro electro mechanical systems using labware'. *Japanese Journal of Applied Physics, Part 1: Regular Papers and Short Notes and Review Papers*, 42(6 A), 3690–3694.
- [98] Fushman I, Englund D and Vuckovic J (2005). 'Coupling of PbS quantum dots to photonic crystal cavities at room temperature'. *Applied Physics Letters*, 87(24), 241102.
- [99] Fushman I, Waks E, Englund D, Stoltz N, Petroff P and Vučković J (2007). 'Ultrafast nonlinear optical tuning of photonic crystal cavities'. *Applied Physics Letters*, 90(9).
- [100] Galli M, Portalupi S L, Belotti M, Andreani L C, O'Faolain L and Krauss T F (2009). 'Light scattering and Fano resonances in high-Q photonic crystal nanocavities'. *Applied Physics Letters*, 94(7).
- [101] Gallo P, Felici M, Dwir B, Atlasov K A, Karlsson K F, Rudra A, Mohan A, Biasiol G, Sorba L and Kapon E (2008). 'Integration of site-controlled pyramidal quantum dots and photonic crystal membrane cavities'. *Applied Physics Letters*, 92(26), 263101.
- [102] Galloway C M, Kreuzer M P, Aćimović S S, Volpe G, Correia M, Petersen S B, Neves-Petersen M T and Quidant R (2013). 'Plasmon-assisted delivery of single nano-objects in an optical hot spot.' *Nano letters*, 13(9), 4299–304.
- [103] Garoufalis C S, Zdetsis A D and Grimme S (2001). 'High level ab initio calculations of the optical gap of small silicon quantum dots.' *Physical review letters*, 87(27 Pt 1), 276402.
- [104] Gehl M, Gibson R, Hendrickson J, Homyk A, Säynätjoki A, Alasaarela T, Karvonen L, Tervonen A, Honkanen S, Zandbergen S, Richards B C, Olitzky J D, Scherer A, Khitrova G, Gibbs H M, Kim J Y and Lee Y H (2012). 'Effect of atomic layer deposition on the quality factor of silicon nanobeam cavities'. *Journal of the Optical Society of America B*, 29(2), A55.
- [105] Gérard J, Sermage B, Gayral B, Legrand B, Costard E and Thierry-Mieg V (1998). 'Enhanced Spontaneous Emission by Quantum Boxes in a Monolithic Optical Microcavity'. *Physical Review Letters*, 81(5), 1110–1113.

- [106] Geremia J, Williams J and Mabuchi H (2002). ‘Inverse-problem approach to designing photonic crystals for cavity QED experiments’. *Physical Review E*, 66(6), 066606.
- [107] Goh J, Fushman I, Englund D and Vucković J (2007). ‘Genetic optimization of photonic bandgap structures.’ *Optics express*, 15(13), 8218–30.
- [108] Gordon J P (1973). ‘Radiation forces and momenta in dielectric media’. *Physical Review A*, 8, 14–21.
- [109] Gorodetsky M L, Savchenkov A A and Ilchenko V S (1996). ‘Ultimate Q of optical microsphere resonators.’ *Optics letters*, 21(7), 453–455.
- [110] Goy P, Raimond J M, Gross M and Haroche S (1983). ‘Observation of cavity-enhanced single-atom spontaneous emission’. *Physical Review Letters*, 50(24), 1903–1906.
- [111] Gomez D E, van Embden J and Mulvaney P (2006). ‘Spectral diffusion of single semiconductor nanocrystals: The influence of the dielectric environment’. *Applied Physics Letters*, 88(15), 154106.
- [112] Green M, Zhao J, Wang A, Reece P and Gal M (2001). ‘Efficient silicon light-emitting diodes’. *Nature*, 412(August), 805–808.
- [113] Griscom D L (1991). ‘Optical Properties and Structure of Defects in Silica Glass’. *Journal of the Ceramic Society of Japan*, 99(1154), 923–942.
- [114] Grom G, Lockwood D and McCaffrey J (2000). ‘Ordering and self-organization in nanocrystalline silicon’. *Nature*, 407(September).
- [115] Gruber A (1997). ‘Scanning Confocal Optical Microscopy and Magnetic Resonance on Single Defect Centers’. *Science*, 276(5321), 2012–2014.
- [116] Guichard A R, Barsic D N, Sharma S, Kamins T I and Brongersma M L (2006). ‘Tunable light emission from quantum-confined excitons in TiSi<sub>2</sub>-catalyzed silicon nanowires’. *Nano Letters*, 6(9), 2140–2144.

- [117] Guichard A R, Kekatpure R D, Brongersma M L and Kamins T I (2008). ‘Temperature-dependent Auger recombination dynamics in luminescent silicon nanowires’. *Physical Review B - Condensed Matter and Materials Physics*, 78(23).
- [118] Hafner C, Xudong C, Smajic J and Vahldieck R (2007). ‘Efficient procedures for the optimization of defects in photonic crystal structures.’ *Journal of the Optical Society of America A, Optics, image science, and vision*, 24(4), 1177–1188.
- [119] Haft D, Schulhauser C, Govorov A O, Warburton R J, Karrai K, Garcia J M, Schoenfeld W and Petroff P M (2002). ‘Magneto-optical properties of ring-shaped self-assembled InGaAs quantum dots’. *Physica E: Low-dimensional Systems and Nanostructures*, 13(2-4), 165–169.
- [120] Hagino H, Takahashi Y, Tanaka Y, Asano T and Noda S (2009). ‘Effects of fluctuation in air hole radii and positions on optical characteristics in photonic crystal heterostructure nanocavities’. *Physical Review B*, 79(8), 085112.
- [121] Hanbury Brown R and Twiss R Q (1956). ‘A Test of a New Type of Stellar Interferometer on Sirius’. *Nature*, 178(4541), 1046–1048.
- [122] Hansen L, Bensing F and Waag A (2000). ‘InAs quantum dots embedded in silicon’. *Thin Solid Films*, 367(1-2), 85–88.
- [123] Haret L D, Tanabe T, Kuramochi E and Notomi M (2009). ‘Extremely low power optical bistability in silicon demonstrated using 1D photonic crystal nanocavity’. *Optics Express*, 17(23), 21108.
- [124] Hausmann B J M, Shields B J, Quan Q, Chu Y, de Leon N P, Evans R, Burek M J, Zibrov A S, Markham M, Twitchen D J, Park H, Lukin M D and Lonc R M (2013). ‘Coupling of NV Centers to Photonic Crystal Nanobeams in Diamond.’ *Nano letters*.
- [125] He J, Yadavalli K, Zhao Z, Li N, Hao Z, Wang K L and Jacob A P (2008). ‘InAs/GaAs nanostructures grown on patterned Si(001) by molecular beam epitaxy.’ *Nanotechnology*, 19(45), 455607.

- [126] Heitz R, Ledentsov N N, Bimberg D, Egorov a Y, Maximov M V, Ustinov V M, Zhukov a E, Alferov Z I, Cirilin G E, Soshnikov I P, Zakharov N D, Werner P and Gosele U (1999). ‘Optical properties of InAs quantum dots in a Si matrix’. *Applied Physics Letters*, 74(12), 1701.
- [127] Hendrickson J, Gehl M, Gibson R, Richards B C, Olitzky J D, Zandbergen S, Khitrova G, Gibbs H M, Alasaarela T, Saynatjoki A, Tervonen A, Honkanen S, Homyk A, Scherer A, Kim J Y and Lee Y H (2011). ‘Increased quality factor of silicon nanobeam cavities by atomic layer deposition of Al<sub>2</sub>O<sub>3</sub>’. *In preparation*.
- [128] Hennessy K, Badolato A, Winger M, Gerace D, Atatüre M, Gulde S, Fält S, Hu E L and Imamolu A (2007). ‘Quantum nature of a strongly coupled single quantum dot-cavity system.’ *Nature*, 445(7130), 896–9.
- [129] Henry M D, Walavalkar S, Homyk A and Scherer A (2009). ‘Alumina etch masks for fabrication of high-aspect-ratio silicon micropillars and nanopillars.’ *Nanotechnology*, 20(25), 255305.
- [130] Hjort K (1996). ‘Sacrificial etching of III - V compounds for micromechanical devices’. *Journal of Micromechanics and Microengineering*, 6(4), 370–375.
- [131] Ho K, Chan C and Soukoulis C (1990). ‘Existence of a photonic gap in periodic dielectric structures’. *Physical Review Letters*, 65(25), 3152–3155.
- [132] Hong C K, Ou Z Y and Mandel L (1987). ‘Measurement of subpicosecond time intervals between two photons by interference’. *Physical Review Letters*, 59(18), 2044–2046.
- [133] Hong S, Loehr J, Goswami S, Bhattacharya P and Singh J (1990). ‘Photocurrent and intrinsic modulation speeds in P-I(MQW)-N GaAs/AlGaAs stark effect modulators’.
- [134] Hood C, Chapman M S, Lynn T W and Kimble H (1998). ‘Real-Time Cavity QED with Single Atoms’. *Physical Review Letters*, 80(19), 4157–4160.
- [135] Hood C J, Kimble H J and Ye J (2001). ‘Characterization of high finesse mirrors: loss, phase shifts and mode structure in an optical cavity’. *Physical Review A*, 64(3), 8.

- [136] Hu J, Lin S, Kimerling L and Crozier K (2010). ‘Optical trapping of dielectric nanoparticles in resonant cavities’. *Physical Review A*, 82(5), 1–8.
- [137] Hu Z and Kimble H J (1994). ‘Observation of a single atom in a magneto-optical trap.’ *Optics letters*, 19(22), 1888.
- [138] Hulet R G, Hilfer E S and Kleppner D (1985). ‘Inhibited spontaneous emission by a Rydberg atom’. *Physical Review Letters*, 55(20), 2137–2140.
- [139] Humer M, Guider R, Jantsch W and Fromherz T (2013). ‘Integration, photostability and spontaneous emission rate enhancement of colloidal PbS nanocrystals for Si-based photonics at telecom wavelengths’. *Optics Express*, 21(16), 18680.
- [140] Hung C L, Meenehan S M, Chang D E, Painter O and Kimble H J (2013). ‘Trapped atoms in one-dimensional photonic crystals’. *New Journal of Physics*, 15(8), 083026.
- [141] Hwang I K, Kim G H and Lee Y H (2006). ‘Optimization of coupling between photonic crystal resonator and curved microfiber’. *IEEE Journal of Quantum Electronics*, 42(2), 131–136.
- [142] Hybertsen M (1994). ‘Absorption and emission of light in nanoscale silicon structures’. *Physical Review Letters*, 72(10), 1514–1517.
- [143] Ihly R, Tolentino J, Liu Y, Gibbs M and Law M (2011). ‘The photothermal stability of PbS quantum dot solids.’ *ACS nano*, 5(10), 8175–86.
- [144] Intallura P M, Ward M B, Karimov O Z, Yuan Z L, See P, Shields A J, Atkinson P and Ritchie D A (2007). ‘Quantum key distribution using a triggered quantum dot source emitting near 1.3  $\mu\text{m}$ ’. *Applied Physics Letters*, 91(16).
- [145] Ioffe (2015). ‘NSM Archive - Physical Properties of Semiconductors’.
- [146] Ishikawa T, Kohmoto S and Asakawa K (1998). ‘Site control of self-organized InAs dots on GaAs substrates by in situ electron-beam lithography and molecular-beam epitaxy’. *Applied Physics Letters*, 73(12), 1712.

- [147] Ishikawa T, Nishimura T, Kohmoto S and Asakawa K (2000). ‘Site-controlled InAs single quantum-dot structures on GaAs surfaces patterned by in situ electron-beam lithography’. *Applied Physics Letters*, 76(2), 167.
- [148] Istrate E, Green A and Sargent E (2005). ‘Behavior of light at photonic crystal interfaces’. *Physical Review B*, 71(19), 195122.
- [149] Jaquay E, Martínez L J, Mejia C a and Povinelli M L (2013). ‘Light-assisted, templated self-assembly using a photonic-crystal slab.’ *Nano letters*, 13(5), 2290–4.
- [150] Jauffred L, Richardson A C and Oddershede L B (2008). ‘Three-dimensional optical control of individual quantum dots.’ *Nano letters*, 8(10), 3376–80.
- [151] Jewell J, Harbison J, Scherer A, Lee Y and Florez L (1991). ‘Vertical-cavity surface-emitting lasers: Design, growth, fabrication, characterization’. *IEEE Journal of Quantum Electronics*, 27(6), 1332–1346.
- [152] Jing P, Wu J and Lin L Y (2014). ‘Patterned Optical Trapping with Two-Dimensional Photonic Crystals’. *ACS Photonics*, 1(5), 398–402.
- [153] Joannopoulos J D, Johnson S G, Winn J N and Meade R D (2008). *Photonic crystals: molding the flow of light*. Second edition. Princeton University Press, Princeton, NJ.
- [154] John S (1987). ‘Strong localization of photons in certain disordered dielectric superlattices’. *Physical Review Letters*, 58(23), 2486–2489.
- [155] John S (1991). ‘Localization of light’. *Phys Today*, May, 32–40.
- [156] Johnson S, Bienstman P, Skorobogatiy M, Ibanescu M, Lidorikis E and Joannopoulos J (2002). ‘Adiabatic theorem and continuous coupled-mode theory for efficient taper transitions in photonic crystals’. *Physical Review E*, 66(6).
- [157] Johnson S and Joannopoulos J (2001). ‘Block-iterative frequency-domain methods for Maxwell’s equations in a planewave basis’. *Optics Express*, 8(3), 173.

- [158] Johnson S G (2006). 'Harminv - Harmonic Inversion Software'.
- [159] Kang P, Serey X, Chen Y F and Erickson D (2012). 'Angular orientation of nanorods using nanophotonic tweezers.' *Nano letters*, 12(12), 6400–7.
- [160] Kao D B, McVittie J P, Nix W D and Saraswat K C (1988). 'Two-dimensional thermal oxidation of silicon - II: modeling stress effects in wet oxides'. *IEEE Transactions on Electron Devices*, 35(1), 25–37.
- [161] Kash K, Scherer A, Worlock J M, Craighead H G and Tamargo M C (1986). 'Optical spectroscopy of ultrasmall structures etched from quantum wells'. *Applied Physics Letters*, 49(16), 1043–1045.
- [162] Kawaguchi Y, Honda Y, Matsushima H, Yamaguchi M, Hiramatsu K and Sawaki N (1998). 'Selective Area Growth of GaN on Si Substrate Using SiO<sub>2</sub> Mask by Metalorganic Vapor Phase Epitaxy'. *Japanese Journal of Applied Physics*, 37(Part 2, No. 8B), L966–L969.
- [163] Khitrova G, Gibbs H M, Kira M, Koch S W and Scherer A (2006). 'Vacuum Rabi splitting in semiconductors'. *Nature Physics*, 2(2), 81–90.
- [164] Kim M K, Yang J K, Lee Y H and Hwang I K (2007). 'Influence on etching slope of two-dimensional photonic crystal slab resonators'. *Journal of the Korean Physical Society*, 50(4), 1027.
- [165] Kim S H, Kim S K and Lee Y H (2006). 'Vertical beaming of wavelength-scale photonic crystal resonators'. *Physical Review B - Condensed Matter and Materials Physics*, 73(23).
- [166] Kim T W, Cho C H, Kim B H and Park S J (2006). 'Quantum confinement effect in crystalline silicon quantum dots in silicon nitride grown using SiH<sub>4</sub> and NH<sub>3</sub>'. *Applied Physics Letters*, 88(12), 123102.
- [167] Kim T Y, Park N M, Kim K H, Sung G Y, Ok Y W, Seong T Y and Choi C J (2004). 'Quantum confinement effect of silicon nanocrystals in situ grown in silicon nitride films'. *Applied Physics Letters*, 85(22), 5355.

- [168] Kimble H, Dagenais M and Mandel L (1977). ‘Photon antibunching in resonance fluorescence’. *Physical Review Letters*, 39(11).
- [169] Kippenberg T J, Spillane S M and Vahala K J (2004). ‘Demonstration of ultra-high- Q small mode volume toroid microcavities on a chip’. *Applied Physics Letters*, 85(25), 6113–6115.
- [170] Kiraz A, Atatüre M and Imamolu A (2004). ‘Quantum-dot single-photon sources: Prospects for applications in linear optics quantum-information processing’. *Physical Review A - Atomic, Molecular, and Optical Physics*, 69(3), 032305–1.
- [171] Klem E J D, Levina L and Sargent E H (2005). ‘PbS quantum dot electroabsorption modulation across the extended communications band 1200-1700 nm’. *Applied Physics Letters*, 87(5).
- [172] Kleppner D (1981). ‘Inhibited Spontaneous Emission’. *Physical Review Letters*, 47(4), 233–236.
- [173] Knight J C, Broeng J, Birks T A and Russell P S J (1998). ‘Photonic Band Gap Guidance in Optical Fibers’. *Science*, 282(5393), 1476–1478.
- [174] Koehl W F, Buckley B B, Heremans F J, Calusine G and Awschalom D D (2011). ‘Room temperature coherent control of defect spin qubits in silicon carbide’. *Nature*, 479(7371), 84–87.
- [175] Kohmoto S, Nakamura H, Ishikawa T and Asakawa K (1999). ‘Site-controlled self-organization of individual InAs quantum dots by scanning tunneling probe-assisted nanolithography’. *Applied Physics Letters*, 75(22), 3488.
- [176] Kojima T, Kojima K, Asano T and Noda S (2013). ‘Accurate alignment of a photonic crystal nanocavity with an embedded quantum dot based on optical microscopic photoluminescence imaging’. *Applied Physics Letters*, 102(1), 011110.
- [177] Kolasinski K W, Wellner A, Neuendorf R, Pedersen C X and Palmer R E (2001). ‘Photoluminescence from silicon nanostructures’. Technical report, University of Birmingham.
- [178] Koski K, Hölsä J and Juliet P (1999). ‘Properties of aluminium oxide thin films deposited by reactive magnetron sputtering’. *Thin Solid Films*, 339(1-2), 240–248.

- [179] Kotnala A, DePaoli D and Gordon R (2013). ‘Sensing nanoparticles using a double nanohole optical trap.’ *Lab on a chip*, 13(20), 4142–6.
- [180] Kottke C, Farjadpour A and Johnson S G (2008). ‘Perturbation theory for anisotropic dielectric interfaces, and application to subpixel smoothing of discretized numerical methods’. *Physical Review E*, 77(3), 036611.
- [181] Kovalev D, Heckler H, Ben-Chorin M, Polisski G, Schwartzkopff M and Koch F (1998). ‘Breakdown of the k-Conservation Rule in Si Nanocrystals’. *Physical Review Letters*, 81(13), 2803–2806.
- [182] Kozłowski G, Zaumseil P, Schubert M a, Yamamoto Y, Bauer J, Matejova J, Schulli T, Tillack B and Schroeder T (2011). ‘Compliant substrate versus plastic relaxation effects in Ge nanoheteroepitaxy on free-standing Si(001) nanopillars’. *Applied Physics Letters*, 99(14), 141901.
- [183] Krauss T F, Rue D L, M R and Brand S (1996). ‘Two-dimensional photonic-bandgap structures operating at near-infrared wavelengths’. *Nature*, 383(6602), 699–702.
- [184] Kuhn A, Henrich M and Rempe G (2002). ‘Deterministic Single-Photon Source for Distributed Quantum Networking’. *Physical Review Letters*, 89(6), 067901.
- [185] Kuhn H (1970). ‘Classical aspects of energy transfer in molecular systems’. *Journal of Chemical Physics*, 53(1), 101–108.
- [186] Kulzer F, Koberling F, Christ T, Mews A and Basché T (1999). ‘Terrylene in p-terphenyl: single-molecule experiments at room temperature’. *Chemical Physics*, 247(1), 23–34.
- [187] Kundmann M, Thomas P, Twesten R D, Hunt J and Barfels M (2008). ‘EELS Imaging and Analysis School’. Technical report, Gatan, Pleasanton, CA.
- [188] Kuramochi E, Taniyama H, Tanabe T, Kawasaki K, Roh Y G and Notomi M (2010). ‘Ultra-high-Q one-dimensional photonic crystal nanocavities with modulated mode-gap barriers on SiO<sub>2</sub> claddings and on air claddings’. *Optics Express*, 18(15), 15859.

- [189] Lai W t, Liao P h, Homyk A P, Scherer A and Li P W (2013). ‘SiGe Quantum Dots Over Si Pillars for Visible to Near-Infrared Broadband Photodetection’. *IEEE Photonics Technology Letters*, 25(15), 1520–1523.
- [190] Laurent S, Varoutsis S, Le Gratiet L, Lemàtre A, Sagnes I, Raineri F, Levenson A, Robert-Philip I and Abram I (2005). ‘Indistinguishable single photons from a single-quantum dot in a two-dimensional photonic crystal cavity’. *Applied Physics Letters*, 87(16), 1–3.
- [191] Le Ru E C, Somerville W R C and Augu   B (2013). ‘Radiative correction in approximate treatments of electromagnetic scattering by point and body scatterers’. *Physical Review A - Atomic, Molecular, and Optical Physics*, 87(1), 1–13.
- [192] Lee B G, Rylyakov A V, Green W M J, Assefa S, Baks C W, Rimolo-Donadio R, Kuchta D M, Khater M H, Barwicz T, Reinholm C, Kiewra E, Shank S M, Schow C L and Vlasov Y A (2014). ‘Monolithic silicon integration of scaled photonic switch fabrics, CMOS logic, and device driver circuits’. *Journal of Lightwave Technology*, 32(4), 743–751.
- [193] Lee T H, Kumar P, Mehta A, Xu K, Dickson R M and Barnes M D (2004). ‘Oriented semiconducting polymer nanostructures as on-demand room-temperature single-photon sources’. *Applied Physics Letters*, 85(1), 100–102.
- [194] Lewis P A and Ahmed H (1999). ‘Patterning of silicon nanopillars formed with a colloidal gold etch mask’. *Journal of Vacuum Science & Technology B: Microelectronics and Nanometer Structures*, 17(6), 3239.
- [195] Li H, Yu X, Wu X, Shi W, Chen M, Liu L and Xu L (2012). ‘All-optically-controlled nanoparticle transporting and manipulating at SOI waveguide intersections’. *Optics Express*, 20(22), 24160.
- [196] Li R R, Dapkus P D, Thompson M E, Jeong W G, Harrison C, Chaikin P M, Register R a and Adamson D H (2000). ‘Dense arrays of ordered GaAs nanostructures by selective area growth

- on substrates patterned by block copolymer lithography'. *Applied Physics Letters*, 76(13), 1689.
- [197] Li Y, Zheng J, Gao J, Shu J, Aras M S and Wong C W (2010). 'Design of dispersive optomechanical coupling and cooling in ultrahigh-Q/V slot-type photonic crystal cavities'. *Optics Express*, 18(23), 23844.
- [198] Liang B L, Wong P S, Nuntawong N, Albrecht A R, Tatebayashi J, Rotter T J, Balakrishnan G and Huffaker D L (2007). 'Optical properties of patterned InAs quantum dot ensembles grown on GaAs nanopylamids'. *Applied Physics Letters*, 91(24), 243106.
- [199] Liang D and Bowers J (2009). 'Photonic integration: Si or InP substrates?' *Electronics Letters*, 45(12), 578.
- [200] Liang D and Bowers J E (2008). 'Highly efficient vertical outgassing channels for low-temperature InP-to-silicon direct wafer bonding on the silicon-on-insulator substrate'. *Journal of Vacuum Science & Technology B: Microelectronics and Nanometer Structures*, 26(4), 1560.
- [201] Liang D and Bowers J E (2010). 'Recent progress in lasers on silicon'. *Nature Photonics*, 4(8), 511–517.
- [202] Liang D, Fang A W, Park H, Reynolds T E, Warner K, Oakley D C and Bowers J E (2008). 'Low-Temperature, Strong SiO<sub>2</sub>-SiO<sub>2</sub> Covalent Wafer Bonding for IIIV Compound Semiconductors-to-Silicon Photonic Integrated Circuits'. *Journal of Electronic Materials*, 37(10), 1552–1559.
- [203] Lin S, Hu J, Kimerling L and Crozier K (2009). 'Design of nanoslotted photonic crystal waveguide cavities for single nanoparticle trapping and detection.' *Optics letters*, 34(21), 3451–3.
- [204] Lin S, Zhu W, Jin Y and Crozier K B (2013). 'Surface-enhanced Raman scattering with Ag nanoparticles optically trapped by a photonic crystal cavity.' *Nano letters*, 13(2), 559–63.

- [205] Lin S Y, Fleming J G, Hetherington D L, Smith B K, Biswas R, Ho K M, Sigalas M M, Zubrzycki W, Kurtz S R and Bur J (1998). ‘A three-dimensional photonic crystal operating at infrared wavelengths’. *Nature*, 394(6690), 251–253.
- [206] Littleton B N, Fernee M J, Gomez D E, Mulvaney P and Rubinsztein-Dunlop H (2009). ‘High-Resolution Line Width Measurement of Single CdSe Nanocrystals at Long Time Scales’. *The Journal of Physical Chemistry C*, 113(14), 5345–5348.
- [207] Liu H I, Biegelsen D K, Ponce F A, Johnson N M and Pease R F W (1994). ‘Self-limiting oxidation for fabricating sub-5 nm silicon nanowires’. *Applied Physics Letters*, 64(11), 1383.
- [208] Liu J, Michel J, Giziewicz W, Pan D, Wada K, Cannon D D, Jongthammanurak S, Danielson D T, Kimerling L C, Chen J, Ilday F O, Kärtner F X and Yasaitis J (2005). ‘High-performance, tensile-strained Ge p-i-n photodetectors on a Si platform’. *Applied Physics Letters*, 87(10).
- [209] Liu V and Fan S (2012). ‘S 4: A free electromagnetic solver for layered periodic structures’. *Computer Physics Communications*, 183(10), 2233–2244.
- [210] Ljungberg K, Soderbarg A and Backlund Y (1993). ‘Spontaneous bonding of hydrophobic silicon surfaces’. *Applied Physics Letters*, 62(12), 1362.
- [211] Lø vhaugen P I, Ahluwalia B S, Huser T R and Hellesø O G (2013). ‘Serial Raman spectroscopy of particles trapped on a waveguide’. *Optics Express*, 21(3), 2964–2970.
- [212] Lochmann A, Stock E, Schulz O, Hopfer F, Bimberg D, Haisler V, Toropov A, Bakarov A and Kalagin A (2006). ‘Electrically driven single quantum dot polarised single photon emitter’. *Electronics Letters*, 42(13), 774.
- [213] Lord Rayleigh (1887). ‘On the maintenance of vibrations by forces of double frequency, and on the propagation of waves through a medium endowed with a periodic structure’. *Philosophical Magazine*, 24(147), 145–159.
- [214] Lord Rayleigh (1888). ‘On the remarkable phenomenon of crystalline reflexion described by Professor Stokes’. *Philosophical Magazine*, 26(160), 256–265.

- [215] Lord Rayleigh (1917). ‘On the reflection of light from a regularly stratified medium’. *Proceedings of the Royal Society A: Mathematical, Physical and Engineering Sciences*, 93(655), 565–577.
- [216] Lounis B, Bechtel H, Gerion D, Alivisatos P and Moerner W (2000). ‘Photon antibunching in single CdSe/ZnS quantum dot fluorescence’. *Chemical Physics Letters*, 329(5-6), 399–404.
- [217] Lounis B and Moerner W E (2000). ‘Single photons on demand from a single molecule at room temperature.’ *Nature*, 407(6803), 491–493.
- [218] Lounis B and Orrit M (2005). ‘Single-photon sources’. *Reports on Progress in Physics*, 68(5), 1129–1179.
- [219] Lu J, Boyd S and Vučković J (2011). ‘Inverse design of a three-dimensional nanophotonic resonator’. *Optics Express*, 19(11), 10563.
- [220] Lu J and Vuckovic J (2010). ‘Inverse design of nanophotonic structures using complementary convex optimization’. *Optics Express*, 18(4), 3793.
- [221] Lu J and Vučković J (2013). ‘Nanophotonic computational design’. *Optics Express*, 21(11), 13351.
- [222] Luan H C, Lim D R, Lee K K, Chen K M, Sandland J G, Wada K and Kimerling L C (1999). ‘High-quality Ge epilayers on Si with low threading-dislocation densities’. *Applied Physics Letters*, 75(19), 2909.
- [223] Luppi M and Ossicini S (2005). ‘Ab initio study on oxidized silicon clusters and silicon nanocrystals embedded in SiO<sub>2</sub>: Beyond the quantum confinement effect’. *Physical Review B*, 71(3).
- [224] Luryi S, Kastalsky A and Bean J (1984). ‘New infrared detector on a silicon chip’. *IEEE Transactions on Electron Devices*, 31(9), 1135–1139.

- [225] Luxmoore I J, Toro R, Del Pozo-Zamudio O, Wasley N A, Chekhovich E A, Sanchez a M, Beanland R, Fox a M, Skolnick M S, Liu H Y and Tartakovskii a I (2013). ‘III-V quantum light source and cavity-QED on silicon.’ *Scientific reports*, 3, 1239.
- [226] Mårtensson T, Carlberg P, Borgström M, Montelius L, Seifert W and Samuelson L (2004). ‘Nanowire Arrays Defined by Nanoimprint Lithography’. *Nano Letters*, 4(4), 699–702.
- [227] Mabuchi H, Turchette Q A, Chapman M S and Kimble H J (1996). ‘Real-time detection of individual atoms falling through a high-finesse optical cavity.’ *Optics letters*, 21(17), 1393–5.
- [228] Mahler B, Spinicelli P, Buil S, Quelin X, Hermier J P and Dubertret B (2008). ‘Towards non-blinking colloidal quantum dots.’ *Nature materials*, 7(8), 659–664.
- [229] Mandal S, Serey X and Erickson D (2010). ‘Nanomanipulation using silicon photonic crystal resonators.’ *Nano letters*, 10(1), 99–104.
- [230] Mandelshtam V A and Taylor H S (1997). ‘Harmonic inversion of semiclassical short time signals’. *Chemical Physics Letters*, 107(17), 675606769.
- [231] Maragò O M, Jones P H, Gucciardi P G, Volpe G and Ferrari A C (2013). ‘Optical trapping and manipulation of nanostructures’. *Nature Nanotechnology*, 8(11), 807–819.
- [232] Massoud H Z and Plummer J D (1987). ‘Analytical relationship for the oxidation of silicon in dry oxygen in the thin-film regime’. *Journal of Applied Physics*, 62(8), 3416.
- [233] Massoud H Z, Plummer J D and Irene E A (1985). ‘Thermal Oxidation of Silicon in Dry Oxygen’. *Journal of The Electrochemical Society*, 132(7), 1745.
- [234] Massoud H Z, Plummer J D and Irene E A (1985). ‘Thermal Oxidation of Silicon in Dry Oxygen Growth-Rate Enhancement in the Thin Regime I. Experimental Results’. *Journal of The Electrochemical Society*, 132(11), 2685.
- [235] Massoud H Z, Plummer J D and Irene E A (1985). ‘Thermal Oxidation of Silicon in Dry Oxygen: Growth-Rate Enhancement in the Thin Regime II. Physical Mechanisms’. *Journal of The Electrochemical Society*, 132(11), 2693.

- [236] McCutcheon M W, Chang D E, Zhang Y, Lukin M D and Loncar M (2009). ‘Broadband frequency conversion and shaping of single photons emitted from a nonlinear cavity’. *Optics Express*, 17(25), 22689.
- [237] McCutcheon M W, Deotare P B, Zhang Y and Loncar M (2011). ‘High-Q transverse-electric/transverse-magnetic photonic crystal nanobeam cavities’. *Applied Physics Letters*, 98(11), 111117.
- [238] McCutcheon M W, Rieger G W, Cheung I W, Young J F, Dalacu D, Fdrick S, Poole P J, Aers G C and Williams R L (2005). ‘Resonant scattering and second-harmonic spectroscopy of planar photonic crystal microcavities’. *Applied Physics Letters*, 87(22), 1–3.
- [239] McKeever J, Boca A, Boozer A D, Buck J R and Kimble H J (2003). ‘Experimental realization of a one-atom laser in the regime of strong coupling.’ *Nature*, 425(6955), 268–71.
- [240] McKeever J, Boca A, Boozer A D, Miller R, Buck J R, Kuzmich A and Kimble H J (2004). ‘Deterministic generation of single photons from one atom trapped in a cavity.’ *Science (New York, NY)*, 303(5666), 1992–4.
- [241] McKeever J, Buck J R, Boozer A D, Kuzmich A, Nägerl H C, Stamper-Kurn D M and Kimble H J (2003). ‘State-Insensitive Cooling and Trapping of Single Atoms in an Optical Cavity’. *Physical Review Letters*, 90(13), 133602.
- [242] Md Zain A R, Johnson N P, Sorel M and De La Rue R M (2008). ‘Ultra high quality factor one dimensional photonic crystal/photonic wire micro-cavities in silicon-on-insulator (SOI)’. *Optics Express*, 16(16), 12084.
- [243] Mejia C A, Huang N and Povinelli M L (2012). ‘Optical trapping of metal-dielectric nanoparticle clusters near photonic crystal microcavities’. *Optics Letters*, 37(17), 3690–3692.
- [244] Michler P (editor) (2003). *Single quantum dots: fundamentals, applications and new concepts*. First edition. Springer-Verlag, Berlin.

- [245] Michler P, Imamoglu A, Mason M, Carson P, Strouse G and Buratto S (2000). ‘Quantum correlation among photons from a single quantum dot at room temperature’. *Nature*, 406(6799), 968–70.
- [246] Michler P, Kiraz A, Becher C, Schoenfeld W V, Petroff P M, Zhang L, Hu E and Imamoglu A (2000). ‘A quantum dot single-photon turnstile device.’ *Science (New York, NY)*, 290(5500), 2282–2285.
- [247] Miller J D, Cline R A and Heinzen D J (1993). ‘Far-off-resonance optical trapping of atoms’. *Physical Review A*, 47(6).
- [248] Min K, Shcheglov K, Yang C, Atwater H A, Brongersma M L and Polman A (1996). ‘Defect-related versus excitonic visible light emission from ion beam synthesized Si nanocrystals in SiO<sub>2</sub>’. *Applied Physics . . .*, 69(14), 2033–2035.
- [249] Minkov M, Dharanipathy U P, Houdré R and Savona V (2013). ‘Statistics of the disorder-induced losses of high-Q photonic crystal cavities’. *Optics Express*, 21(23), 28233.
- [250] Minkov M and Savona V (2012). ‘Effect of hole-shape irregularities on photonic crystal waveguides’. *Optics Letters*, 37(15), 3108–3110.
- [251] Minkov M and Savona V (2014). ‘Automated optimization of photonic crystal slab cavities.’ *Scientific reports*, 4, 5124.
- [252] Mittleman D M, Schoenlein R W, Shiang J J, Colvin V L, Alivisatos A P and Shank C V (1994). ‘Quantum size dependence of femtosecond electronic dephasing and vibrational dynamics in CdSe nanocrystals’. *Physical Review B*, 49(20), 14435–14447.
- [253] Moewe M, Chuang L C, Dubrovskii V G and Chang-Hasnain C (2008). ‘Growth mechanisms and crystallographic structure of InP nanowires on lattice-mismatched substrates’. *Journal of Applied Physics*, 104(4), 044313.
- [254] Monte A F G, Finley J J, Whittaker D M, Itskevitch I, Mowbray D J, Skolnick M S, Sales

- F V and Hopkins M (2003). ‘Non-linear effects on the power dependent photocurrent of self-assembled InAs/GaAs quantum dots’. *Microelectronics Journal*, 34(5-8), 667–669.
- [255] Monte A F G and Qu F (2011). ‘Nonlinear effects of the photocurrent in self-assembled InAs/GaAs quantum dots’. *Journal of Applied Physics*, 109(5).
- [256] Mosor S, Hendrickson J, Richards B C, Sweet J, Khitrova G, Gibbs H M, Yoshie T, Scherer A, Shchekin O B and Deppe D G (2005). ‘Scanning a photonic crystal slab nanocavity by condensation of xenon’. *Applied Physics Letters*, 87(14), 141105.
- [257] Mounaix P, Delobelle P, Mélique X, Bornier L and Lippens D (1998). ‘Micromachining and mechanical properties of GaInAs/InP microcantilevers’. *Materials Science and Engineering: B*, 51(1-3), 258–262.
- [258] Mukherjee S, Paul A, Neophytou N, Kim R, Geng J, Povolotskyi M, Kubis T C, Ajoy A, Novakovic B, Fonseca J, Steiger S, McLennan M, Lundstrom M and Klimeck G (2014). ‘nanoHUB Band Structure Lab’.
- [259] Nassiopoulos A G, Grigoropoulos S and Papadimitriou D (1996). ‘Electroluminescent device based on silicon nanopillars’. *Applied Physics Letters*, 69(15), 2267–2269.
- [260] Nayfeh A, Chui C O, Saraswat K C and Yonehara T (2004). ‘Effects of hydrogen annealing on heteroepitaxial-Ge layers on Si: Surface roughness and electrical quality’. *Applied Physics Letters*, 85(14), 2815–2817.
- [261] Noda S, Fujita M and Asano T (2007). ‘Spontaneous-emission control by photonic crystals and nanocavities’. *Nature Photonics*, 1(8), 449–458.
- [262] Noé P, Guignard J, Gentile P, Delamadeleine E, Calvo V, Ferret P, Dhalluin F and Baron T (2007). ‘Enhancement of the photoluminescence of silicon oxide defect states by combining silicon oxide with silicon nanowires’. *Journal of Applied Physics*, 102(1).
- [263] Nomura M, Kumagai N, Iwamoto S, Ota Y and Arakawa Y (2010). ‘Laser oscillation in a strongly coupled single quantum dot-nanocavity system’. *Nature Physics*, 6(4), 12.

- [264] Notomi M, Kuramochi E and Taniyama H (2008). ‘Ultra-high-Q Nanocavity with 1D Photonic Gap’. *Optics Express*, 16(15), 11095.
- [265] Notomi M, Shinya A, Mitsugi S, Kira G, Kuramochi E and Tanabe T (2005). ‘Optical bistable switching action of Si high-Q photonic-crystal nanocavities’. *Optics Express*, 13(7), 2678.
- [266] Notomi M, Yamada K, Shinya A, Takahashi J, Takahashi C and Yokohama I (2001). ‘Extremely Large Group-Velocity Dispersion of Line-Defect Waveguides in Photonic Crystal Slabs’. *Physical Review Letters*, 87(25), 253902.
- [267] Novotny L, Bian R and Xie X (1997). ‘Theory of Nanometric Optical Tweezers’. *Physical Review Letters*, 79, 645–648.
- [268] Nozaki K, Tanabe T, Shinya A, Matsuo S, Sato T, Taniyama H and Notomi M (2010). ‘Sub-femtojoule all-optical switching using a photonic-crystal nanocavity’. *Nature Photonics*, 4(7), 477–483.
- [269] Ogawa S, Imada M, Yoshimoto S, Okano M and Noda S (2004). ‘Control of light emission by 3D photonic crystals.’ *Science (New York, NY)*, 305(5681), 227–9.
- [270] Oh D Y, Kim S H, Huang J, Scofield A, Huffaker D and Scherer A (2013). ‘Self-aligned active quantum nanostructures in photonic crystals via selective wet-chemical etching.’ *Nanotechnology*, 24(26), 265201.
- [271] Ohta H, Watanabe T and Ohdomari I (2007). ‘Strain Distribution around SiO<sub>2</sub>/Si Interface in Si Nanowires: A Molecular Dynamics Study’. *Japanese Journal of Applied Physics*, 46(5B), 3277–3282.
- [272] Ohta R, Ota Y, Nomura M, Kumagai N, Ishida S, Iwamoto S and Arakawa Y (2011). ‘Strong coupling between a photonic crystal nanobeam cavity and a single quantum dot’. *Applied Physics Letters*, 98(17), 173104.
- [273] Oskooi A F, Roundy D, Ibanescu M, Bermel P, Joannopoulos J D and Johnson S G (2010).

- ‘Meep: A flexible free-software package for electromagnetic simulations by the FDTD method’. *Computer Physics Communications*, 181(3), 687–702.
- [274] Patel R B, Bennett A J, Farrer I, Nicoll C A, Ritchie D A and Shields A J (2010). ‘Two-photon interference of the emission from electrically tunable remote quantum dots’. *Nature Photonics*, 4(9), 632–635.
- [275] Pelton M, Santori C, Vucković J, Zhang B, Solomon G, Plant J and Yamamoto Y (2002). ‘Efficient Source of Single Photons: A Single Quantum Dot in a Micropost Microcavity’. *Physical Review Letters*, 89(23), 233602.
- [276] Peng X H, Alizadeh A, Bhate N, Varanasi K K, Kumar S K and Nayak S K (2007). ‘First-principles investigation of strain effects on the energy gaps in silicon nanoclusters.’ *Journal of physics Condensed matter : an Institute of Physics journal*, 19(26), 266212.
- [277] Perahia R, Cohen J D, Meenehan S, Alegre T P M and Painter O (2010). ‘Electrostatically tunable optomechanical zipper cavity laser’. *Applied Physics Letters*, 97(19), 191112.
- [278] Peterson J J and Krauss T D (2006). ‘Fluorescence spectroscopy of single lead sulfide quantum dots.’ *Nano letters*, 6(3), 510–4.
- [279] Pinkse P W H, Fischer T, Maunz P and Rempe G (2000). ‘Trapping an atom with single photons’. *Nature*, 404(6776), 365–368.
- [280] PlasmaChem (2015). ‘ZnCdSeS alloyed quantum dots’.
- [281] Prokes S, Glembocki O, Bermudez V, Kaplan R, Friedersdorf L and Searson P (1992). ‘SiHx excitation: An alternate mechanism for porous Si photoluminescence’. *Physical Review B*, 45(23), 13788–13791.
- [282] Puurunen R L (2005). ‘Surface chemistry of atomic layer deposition: A case study for the trimethylaluminum/water process’. *Journal of Applied Physics*, 97(12), 121301.
- [283] Qi J, Belcher A M and White J M (2003). ‘Spectroscopy of individual silicon nanowires’. *Applied Physics Letters*, 82(16), 2616–2618.

- [284] Quan Q, Deotare P B and Loncar M (2010). ‘Photonic crystal nanobeam cavity strongly coupled to the feeding waveguide’. *Applied Physics Letters*, 96(20), 203102.
- [285] Quan Q, Floyd D L, Burgess I B, Deotare P B, Frank I W, Tang S K Y, Ilic R and Loncar M (2013). ‘Single particle detection in CMOS compatible photonic crystal nanobeam cavities’. *Optics Express*, 21(26), 32225.
- [286] Quan Q and Loncar M (2011). ‘Deterministic design of wavelength scale, ultra-high Q photonic crystal nanobeam cavities’. *Optics Express*, 19(19), 18529.
- [287] Quan Q, Vollmer F, Burgess I B, Deotare P B, Frank I W, Sindy, Tang K Y, Ilic R and Loncar M (2011). ‘Ultrasensitive on-chip photonic crystal nanobeam sensor using optical bistability’. *CLEO: 2011 - Laser Science to Photonic Applications*, 1–2.
- [288] Raab E L, Prentiss M, Cable A, Chu S and Pritchard D E (1987). ‘Trapping of Neutral Sodium Atoms with Radiation Pressure’. *Physical Review Letters*, 59(23), 2631–2634.
- [289] Rahmani A and Chaumet P C (2006). ‘Optical trapping near a photonic crystal.’ *Optics express*, 14(13), 6353–8.
- [290] Reischle M, Beirne G J, Schulz W M, Eichfelder M, Rossbach R, Jetter M and Michler P (2008). ‘Electrically pumped single-photon emission in the visible spectral range up to 80 K.’ *Optics express*, 16(17), 12771–12776.
- [291] Reithmaier J P, Sek G, Löffler A, Hofmann C, Kuhn S, Reitzenstein S, Keldysh L V, Kulakovskii V D, Reinecke T L and Forchel A (2004). ‘Strong coupling in a single quantum dot-semiconductor microcavity system.’ *Nature*, 432(7014), 197–200.
- [292] Rempe G, Thompson R J, Brecha R J, Lee W D and Kimble H J (1991). ‘Optical bistability and photon statistics in cavity quantum electrodynamics’. *Physical Review Letters*, 67(13), 1727–1730.
- [293] Renaut C, Cluzel B, Dellinger J, Lalouat L, Picard E, Peyrade D, Hadji E and de Fornel F (2013). ‘On chip shapeable optical tweezers.’ *Scientific reports*, 3, 2290.

- [294] Renaut C, Dellinger J, Cluzel B, Honegger T, Peyrade D, Picard E, de Fornel F and Hadji E (2012). ‘Assembly of microparticles by optical trapping with a photonic crystal nanocavity’. *Applied Physics Letters*, 100(10), 101103.
- [295] Richards B C, Hendrickson J, Olitzky J D, Gibson R, Gehl M, Kieu K, Khankhoje U K, Homyk A, Scherer A, Kim J Y, Lee Y H, Khitrova G and Gibbs H M (2010). ‘Characterization of 1D photonic crystal nanobeam cavities using curved microfiber’. *Optics Express*, 18(20), 20558.
- [296] Richards B C, Hendrickson J, Olitzky J D, Gibson R, Gehl M, Kieu K, Polynkin P, Khitrova G, Gibbs H M, Khankhoje U K, Homyk A, Scherer A, Kim J Y and Lee Y H (2011). ‘Progress in growth, fabrication, and characterization of semiconductor photonic crystal nanocavities’. *Physica Status Solidi (B)*, 248(4), 892–896.
- [297] Rivoire K, Kinkhabwala A, Hatami F, Masselink W T, Avlasevich Y, Mullen K, Moerner W E and Vuckovic J (2009). ‘Lithographic positioning of fluorescent molecules on high-Q photonic crystal cavities’. *Applied Physics Letters*, 95(12), 123113.
- [298] Robinson J, Manolatou C, Chen L and Lipson M (2005). ‘Ultrasmall Mode Volumes in Dielectric Optical Microcavities’. *Physical Review Letters*, 95(14), 143901.
- [299] Ropp C, Cummins Z, Probst R, Qin S, Fourkas J T, Shapiro B and Waks E (2010). ‘Positioning and immobilization of individual quantum dots with nanoscale precision.’ *Nano letters*, 10(11), 4673–9.
- [300] Ropp C, Probst R, Cummins Z, Kumar R, Berglund A J, Raghavan S R, Waks E and Shapiro B (2010). ‘Manipulating quantum dots to nanometer precision by control of flow.’ *Nano letters*, 10(7), 2525–30.
- [301] Sadamitsu S, Umeno S, Koike Y, Hourai M, Sumita S and Shigematsu T (1993). ‘Dependence of the grown-in defect distribution on growth rates in Czochralski silicon’. *Japanese Journal of Applied Physics, Part 1: Regular Papers and Short Notes and Review Papers*, 32(9 A), 3675–3681.

- [302] Safavi-Naeini A H, Alegre T P M, Chan J, Eichenfield M, Winger M, Lin Q, Hill J T, Chang D E and Painter O (2011). ‘Electromagnetically induced transparency and slow light with optomechanics’. *Nature*, 472(7341), 69–73.
- [303] Safavi-Naeini A H, Alegre T P M, Winger M and Painter O (2010). ‘Optomechanics in an ultrahigh-Q two-dimensional photonic crystal cavity’. *Applied Physics Letters*, 97(18), 181106.
- [304] Saifullah M, Boothroyd C, Botton G and Humphreys C (1998). ‘Electron energy loss spectroscopy of silicon nanostructures fabricated in a scanning transmission electron microscope’. *Electron Microscopy*, 2(96), 123–124.
- [305] Salhi B, Gelloz B, Koshida N, Patriarche G and Boukherroub R (2007). ‘Synthesis and photoluminescence properties of silicon nanowires treated by high-pressure water vapor annealing’. *Physica Status Solidi (a)*, 204(5), 1302–1306.
- [306] Salvador M R, Hines M A and Scholes G D (2003). ‘Exciton-bath coupling and inhomogeneous broadening in the optical spectroscopy of semiconductor quantum dots’. *Journal of Chemical Physics*, 118(20), 9380–9388.
- [307] Samavedam S B, Currie M T, Langdo T A and Fitzgerald E A (1998). ‘High-quality germanium photodiodes integrated on silicon substrates using optimized relaxed graded buffers’. *Applied Physics Letters*, 73(15), 2125–2127.
- [308] Sanaka K, Pawlis A, Ladd T, Lischka K and Yamamoto Y (2009). ‘Indistinguishable Photons from Independent Semiconductor Nanostructures’. *Physical Review Letters*, 103(5), 053601.
- [309] Sanchis L, Cryan M J, Pozo J, Craddock I J and Rarity J G (2007). ‘Ultrahigh Purcell factor in photonic crystal slab microcavities’. *Physical Review B - Condensed Matter and Materials Physics*, 76(4).
- [310] Sangouard N and Zbinden H (2012). ‘What are single photons good for?’ *Journal of Modern Optics*, 59(17), 1458–1464.

- [311] Santis C T, Steger S T, Vilenchik Y, Vasilyev A and Yariv A (2014). ‘High-coherence semiconductor lasers based on integral high-Q resonators in hybrid Si/III-V platforms.’ *Proceedings of the National Academy of Sciences of the United States of America*, 111(8), 2879–84.
- [312] Santori C, Fattal D, Vucković J, Solomon G S and Yamamoto Y (2002). ‘Indistinguishable photons from a single-photon device.’ *Nature*, 419(6907), 594–597.
- [313] van der Sar T, Hagemeyer J, Pfaff W, Heeres E C, Thon S M, Kim H, Petroff P M, Oosterkamp T H, Bouwmeester D and Hanson R (2011). ‘Deterministic nanoassembly of a coupled quantum emitter photonic crystal cavity system’. *Applied Physics Letters*, 98(19), 193103.
- [314] Sauer N J and Chough K (1992). ‘A Selective Etch for InAlAs over InGaAs and for Different InGaAlAs Quaternaries’. *Journal of The Electrochemical Society*, 139(1), L10.
- [315] Sauvan C, Hugonin J P, Maksymov I S and Lalanne P (2013). ‘Theory of the Spontaneous Optical Emission of Nanosize Photonic and Plasmon Resonators’. *Physical Review Letters*, 110(23), 237401–.
- [316] Säynätjoki A, Karvonen L, Alasaarela T, Tu X, Liow T Y, Hiltunen M, Tervonen A, Lo G Q and Honkanen S (2011). ‘Low-loss silicon slot waveguides and couplers fabricated with optical lithography and atomic layer deposition’. *Optics Express*, 19(27), 26275.
- [317] Scherer A and Craighead H G (1986). ‘Fabrication of small laterally patterned multiple quantum wells’. *Applied Physics Letters*, 49(19), 1284.
- [318] Scofield A C, Kim S H, Shapiro J N, Lin A, Liang B, Scherer A and Huffaker D L (2011). ‘Bottom-up photonic crystal lasers.’ *Nano letters*, 11(12), 5387–90.
- [319] Seidl S, Kroner M, Hogele A, Karrai K, Warburton R J, Badolato A and Petroff P M (2006). ‘Effect of uniaxial stress on excitons in a self-assembled quantum dot’. *Applied Physics Letters*, 88(20), 203113.

- [320] Serey X, Mandal S and Erickson D (2010). ‘Comparison of silicon photonic crystal resonator designs for optical trapping of nanomaterials.’ *Nanotechnology*, 21(30), 305202.
- [321] Shankar R, Bulu I, Leijssen R and Lončar M (2011). ‘Study of thermally-induced optical bistability and the role of surface treatments in Si-based mid-infrared photonic crystal cavities’. *Optics Express*, 19(24), 24828.
- [322] Shearn M, Diest K, Sun X, Zadok A, Atwater H, Yariv A and Scherer A (2009). ‘Advanced silicon processing for active planar photonic devices’. *Journal of Vacuum Science & Technology B: Microelectronics and Nanometer Structures*, 27(6), 3180.
- [323] Shen Y R (2002). *The Principles of Nonlinear Optics*. First edition. Wiley-Interscience.
- [324] Shields A (2007). ‘Semiconductor quantum light sources’. *Nature photonics*, 215–223.
- [325] Singh J (2003). *Electronic and optoelectronic properties of semiconductor structures*, volume 1. First edition. Cambridge University Press, New York.
- [326] Solehmainen K, Kapulainen M, Heimala P and Polamo K (2004). ‘Erbium-Doped Waveguides Fabricated with Atomic Layer Deposition Method’. *IEEE Photonics Technology Letters*, 16(1), 194–196.
- [327] Solomon G, Pelton M and Yamamoto Y (2001). ‘Single-mode Spontaneous Emission from a Single Quantum Dot in a Three-Dimensional Microcavity’. *Physical Review Letters*, 86(17), 3903–3906.
- [328] Solomon G S, Pelton M and Yamamoto Y (2000). ‘Modification of spontaneous emission of a single quantum dot’. *Physica Status Solidi (A) Applied Research*, 178(1), 341–344.
- [329] Song H Z, Usuki T, Hirose S, Takemoto K, Nakata Y, Yokoyama N and Sakuma Y (2005). ‘Site-controlled photoluminescence at telecommunication wavelength from InAsInP quantum dots’. *Applied Physics Letters*, 86(11), 113118.
- [330] Song Y, Liu M, Zhang Y, Wang X and Jin C (2011). ‘High-Q photonic crystal slab nanocavity with an asymmetric nanohole in the center for QED’. *JOSA B*, 28(2), 265–274.

- [331] Spillane S M, Kippenberg T J and Vahala K J (2005). ‘Ultra-high-Q toroidal microresonators for cavity quantum electrodynamics’. *Physical Review A*, 71(1), 013817.
- [332] Srinivasan K, Barclay P E, Borselli M and Painter O (2004). ‘Optical-fiber-based measurement of an ultrasmall volume high-Q photonic crystal microcavity’. *Physical Review B - Condensed Matter and Materials Physics*, 70(8).
- [333] Srinivasan K and Painter O (2002). ‘Momentum space design of high-Q photonic crystal optical cavities’. *Optics Express*, 10(15), 670–684.
- [334] Srinivasan K and Painter O (2007). ‘Linear and nonlinear optical spectroscopy of a strongly coupled microdisk-quantum dot system.’ *Nature*, 450(7171), 862–5.
- [335] Sun X, Zadok A, Shearn M J, Diest K A, Ghaffari A, Atwater H A, Scherer A and Yariv A (2009). ‘Electrically pumped hybrid evanescent Si/InGaAsP lasers’. *Optics Letters*, 34(9), 1345.
- [336] Sutter E, Camino F and Sutter P (2009). ‘One-step synthesis of GeSiO<sub>2</sub> core-shell nanowires’. *Applied Physics Letters*, 94(8), 083109.
- [337] Svoboda K and Block S M (1994). ‘Biological applications of optical forces.’ *Annual review of biophysics and biomolecular structure*, 23, 247–285.
- [338] Sychugov I, Juhasz R, Valenta J and Linnros J (2005). ‘Narrow Luminescence Linewidth of a Silicon Quantum Dot’. *Physical Review Letters*, 94(8), 087405.
- [339] Taguchi Y, Takahashi Y, Sato Y, Asano T and Noda S (2011). ‘Statistical studies of photonic heterostructure nanocavities with an average Q factor of three million.’ *Optics express*, 19(12), 11916–21.
- [340] Takayama S i, Kitagawa H, Tanaka Y, Asano T and Noda S (2005). ‘Experimental demonstration of complete photonic band gap in two-dimensional photonic crystal slabs’. *Applied Physics Letters*, 87(6), 061107.

- [341] Tanabe T, Notomi M, Mitsugi S, Shinya A and Kuramochi E (2005). ‘Fast bistable all-optical switch and memory on a silicon photonic crystal on-chip’. *Optics Letters*, 30(19), 2575.
- [342] Tanaka Y, Asano T, Hatsuta R and Noda S (2006). ‘Investigation of point-defect cavity formed in two-dimensional photonic crystal slab with one-sided dielectric cladding’. *Applied Physics Letters*, 88(1), 011112.
- [343] Tanaka Y, Asano T and Noda S (2008). ‘Design of Photonic Crystal Nanocavity With Q-Factor of  $\sim 10^9$ ’. *Journal of Lightwave Technology*, 26(11), 1532–1539.
- [344] Tatebayashi J, Mariani G, Lin A, Hicks R F and Huffaker D L (2010). ‘Optical characteristics of GaInP/GaP double-heterostructure core-shell nanowires embedded in polydimethylsiloxane membranes’. *Applied Physics Letters*, 96(25), 253101.
- [345] Tatebayashi J, Ota Y, Ishida S, Nishioka M, Iwamoto S and Arakawa Y (2012). ‘Site-controlled formation of InAs/GaAs quantum-dot-in-nanowires for single photon emitters’. *Applied Physics Letters*, 100(26), 263101.
- [346] Thompson R, Rempe G and Kimble H (1992). ‘Observation of normal-mode splitting for an atom in an optical cavity’. *Physical Review Letters*, 68(8), 1132–1135.
- [347] Thompson R, Stevenson R, Shields A, Farrer I, Lobo C, Ritchie D, Leadbeater M and Pepper M (2001). ‘Single-photon emission from exciton complexes in individual quantum dots’. *Physical Review B*, 64(20), 201302.
- [348] Thompson R, Turchette Q, Carnal O and Kimble H (1998). ‘Nonlinear spectroscopy in the strong-coupling regime of cavity QED’. *Physical Review A*, 57(4), 3084–3104.
- [349] Tsybeskov L, Hirschman K D, Duttagupta S P, Zacharias M, Fauchet P M, McCaffrey J P and Lockwood D J (1998). ‘Nanocrystalline-silicon superlattice produced by controlled recrystallization’. *Applied Physics Letters*, 72(1), 43–45.
- [350] Tuovinen C, Malinin A, Ovchinnikov V and Toivola T (2002). ‘Properties of Silicon Nanopillar Structures’. *Physica Scripta*, 101(1), 125.

- [351] Turyanska L, Patane A, Henini M, Hennequin B and Thomas N R (2007). ‘Temperature dependence of the photoluminescence emission from thiol-capped PbS quantum dots’. *Applied Physics Letters*, 90(10), 101913.
- [352] Uesugi T, Song B S, Asano T and Noda S (2006). ‘Investigation of optical nonlinearities in an ultra-high-Q Si nanocavity in a two-dimensional photonic crystal slab’. *Optics Express*, 14(1), 377.
- [353] Unal N, Charlton M D, Wang Y, Waizmann U, Reindl T and Hofmann U (2011). ‘Easy to adapt electron beam proximity effect correction parameter calibration based on visual inspection of a Best Dose Sensor’. *Microelectronic Engineering*, 88(8), 2158–2162.
- [354] Valenta J, Juhasz R and Linnros J (2002). ‘Photoluminescence spectroscopy of single silicon quantum dots’. *Applied Physics Letters*, 80(6), 1070.
- [355] Varnava M, Browne D E and Rudolph T (2008). ‘How good must single photon sources and detectors be for efficient linear optical quantum computation?’ *Physical Review Letters*, 100(6).
- [356] Varoutsis S, Laurent S, Kramper P, Lemaître A, Sagnes I, Robert-Philip I and Abram I (2005). ‘Restoration of photon indistinguishability in the emission of a semiconductor quantum dot’. *Physical Review B - Condensed Matter and Materials Physics*, 72(4).
- [357] Velha P, Picard E, Charvolin T, Hadji E, Rodier J, Lalanne P and Peyrade D (2007). ‘Ultra-High Q/V Fabry-Perot microcavity on SOI substrate’. *Optics Express*, 15(24), 16090.
- [358] Verma V B, Stevens M J, Silverman K L, Dias N L, Garg A, Coleman J J and Mirin R P (2011). ‘Photon antibunching from a single lithographically defined InGaAs/GaAs quantum dot’. *Optics Express*, 19(5), 4182.
- [359] Vernooy D W, Ilchenko V S, Mabuchi H, Streed E W and Kimble H J (1998). ‘High-Q measurements of fused-silica microspheres in the near infrared.’ *Optics letters*, 23(4), 247–249.

- [360] Vlasov Y A, Bo X Z, Sturm J C and Norris D J (2001). ‘On-chip natural assembly of silicon photonic bandgap crystals.’ *Nature*, 414(6861), 289–293.
- [361] Vuckovic J, Loncar M, Mabuchi H and Scherer A (2002). ‘Optimization of the Q factor in photonic crystal microcavities’. *IEEE Journal of Quantum Electronics*, 38(7), 850–856.
- [362] Vučković J, Fattal D, Santori C, Solomon G S and Yamamoto Y (2003). ‘Enhanced single-photon emission from a quantum dot in a micropost microcavity’. *Applied Physics Letters*, 82(21), 3596–3598.
- [363] Walavalkar S, Latawiec P and Scherer A (2013). ‘Coulomb blockade in vertical, bandgap engineered silicon nanopillars’. *Applied Physics Letters*, 102(18), 183101.
- [364] Walavalkar S S, Hofmann C E, Homyk A P, Henry M D, Atwater H a and Scherer A (2010). ‘Tunable visible and near-IR emission from sub-10 nm etched single-crystal Si nanopillars.’ *Nano letters*, 10(11), 4423–8.
- [365] Walavalkar S S, Homyk A P, Henry M D and Scherer A (2013). ‘Three-dimensional etching of silicon for the fabrication of low-dimensional and suspended devices.’ *Nanoscale*, 5(3), 927–31.
- [366] Walavalkar S S, Homyk A P, Hofmann C E, Henry M D, Shin C, Atwater H A and Scherer A (2011). ‘Size tunable visible and near-infrared photoluminescence from vertically etched silicon quantum dots’. *Applied Physics Letters*, 98(15), 153114.
- [367] Wallin J, Landgren G, Streubel K, Nilsson S and Öberg M (1992). ‘Selective area regrowth of butt-joint coupled waveguides in multi-section DBR lasers’. *Journal of Crystal Growth*, 124(1-4), 741–746.
- [368] Walters R J, Bourianoff G I and Atwater H a (2005). ‘Field-effect electroluminescence in silicon nanocrystals.’ *Nature materials*, 4(2), 143–6.
- [369] Wang J W J, Rahman A, Klimeck G and Lundstrom M (2005). ‘Bandstructure and orientation effects in ballistic Si and Ge nanowire FETs’. In ‘IEEE International Electron Devices Meeting, 2005. IEDM Technical Digest.’, IEEE, Washington, D.C., 533–536.

- [370] Wang T, Liu H, Lee A, Pozzi F and Seeds A (2011). '1.3- $\mu\text{m}$  InAs/GaAs quantum-dot lasers monolithically grown on Si substrates.' *Optics express*, 19(12), 11381–6.
- [371] Wang Y, Zou J, Zhao Z M, Hao Z and Wang K L (2009). 'High quality InAs quantum dots grown on patterned Si with a GaAs buffer layer.' *Nanotechnology*, 20(30), 305301.
- [372] Wen X, Dao L V and Hannaford P (2007). 'Temperature dependence of photoluminescence in silicon quantum dots'. *Journal of Physics D: Applied Physics*, 40(12), 3573–3578.
- [373] Wilcoxon J, Samara G and Provencio P (1999). 'Optical and electronic properties of Si nanoclusters synthesized in inverse micelles'. *Physical Review B*, 60(4), 2704–2714.
- [374] Windl W, Liang T, Lopatin S and Duscher G (2004). 'Modeling and characterization of atomically sharp perfect Ge/SiO<sub>2</sub> interfaces'. *Materials Science and Engineering: B*, 114–115, 156–161.
- [375] Witt W P and Barrow R F (1959). 'The heat of sublimation of aluminium trifluoride and the heat of formation of aluminium monofluoride'. *Transactions of the Faraday Society*, 55(i), 730.
- [376] Wolkin M, Jorne J, Fauchet P, Allan G and Delerue C (1999). 'Electronic States and Luminescence in Porous Silicon Quantum Dots: The Role of Oxygen'. *Physical Review Letters*, 82(1), 197–200.
- [377] Wolters J, Schell A W, Kewes G, Nusse N, Schoengen M, Doscher H, Hannappel T, Lochel B, Barth M and Benson O (2010). 'Enhancement of the zero phonon line emission from a single nitrogen vacancy center in a nanodiamond via coupling to a photonic crystal cavity'. *Applied Physics Letters*, 97(14), 141108.
- [378] Wolters J, Schell A W, Kewes G, Nusse N, Schoengen M, Doscher H, Hannappel T, Lochel B, Barth M and Benson O (2010). 'Enhancement of the zero phonon line emission from a single nitrogen vacancy center in a nanodiamond via coupling to a photonic crystal cavity'. *Applied Physics Letters*, 97(14), 141108.

- [379] Wong P S, Balakrishnan G, Nuntawong N, Tatebayashi J and Huffaker D L (2007). ‘Controlled InAs quantum dot nucleation on faceted nanopatterned pyramids’. *Applied Physics Letters*, 90(18), 183103.
- [380] Wu Y, Cui Y, Huynh L, Barrelet C J, Bell D C and Lieber C M (2004). ‘Controlled Growth and Structures of Molecular-Scale Silicon Nanowires’. *Nano Letters*, 4(3), 433–436.
- [381] Yablonovitch E (1987). ‘Inhibited Spontaneous Emission in Solid-State Physics and Electronics’. *Physical Review Letters*, 58(20), 2059–2062.
- [382] Yablonovitch E, Gmitter T, Meade R, Rappe A, Brommer K and Joannopoulos J (1991). ‘Donor and acceptor modes in photonic band structure’. *Physical Review Letters*, 67(24), 3380–3383.
- [383] Yamamoto Y, Machida S, Igeta K and Horikoshi Y (1989). ‘Enhanced and inhibited spontaneous emission of free excitons in GaAs quantum wells in a microcavity’. In Eberly J H, Mandel L and Wolf E (editors), ‘Coherence and Quantum Optics VI’, Springer US, 1949–1257.
- [384] Yang L, Motohisa J, Takeda J, Tomioka K and Fukui T (2007). ‘Selective-area growth of hexagonal nanopillars with single InGaAs/GaAs quantum wells on GaAs(111)B substrate and their temperature-dependent photoluminescence’. *Nanotechnology*, 18(10), 105302.
- [385] Yang X, Husko C, Wong C W, Yu M and Kwong D L (2007). ‘Observation of femtojoule optical bistability involving Fano resonances in high-QV[<sub>sub m</sub>] silicon photonic crystal nanocavities’. *Applied Physics Letters*, 91(5), 051113.
- [386] Yanik M F, Fan S and Soljacic M (2003). ‘High-contrast all-optical bistable switching in photonic crystal microcavities’. *Applied Physics Letters*, 83(14), 2739.
- [387] Yao X c, Wang T x, Xu P, Lu H, Pan G S, Bao X h, Peng C z, Lu C y, Chen Y a and Pan J w (2012). ‘Observation of eight-photon entanglement’. *Nature Photonics*, 6(4), 225–228.

- [388] Yariv A (2000). ‘Universal relations for coupling of optical power between microresonators and dielectric waveguides’. *Electronics Letters*, 36(4), 321–322.
- [389] Ye J, Vernooy D and Kimble H (1999). ‘Trapping of Single Atoms in Cavity QED’. *Physical Review Letters*, 83(24), 4987–4990.
- [390] Yoshie T, Scherer A, Hendrickson J, Khitrova G, Gibbs H M, Rupper G, Ell C, Shchekin O B and Deppe D G (2004). ‘Vacuum Rabi splitting with a single quantum dot in a photonic crystal nanocavity.’ *Nature*, 432(7014), 200–3.
- [391] Yu S P, Hood J D, Muniz J A, Martin M J, Norte R, Hung C L, Meenehan S M, Cohen J D, Painter O and Kimble H J (2014). ‘Nanowire photonic crystal waveguides for single-atom trapping and strong light-matter interactions’. *Applied Physics Letters*, 104(11), 111103.
- [392] Yurtsever A and Muller D (2015). ‘Silicon in Si<sub>3</sub>N<sub>4</sub> and SiO<sub>2</sub>’.
- [393] Zacharias M, Heitmann J, Scholz R, Kahler U, Schmidt M and Blasing J (2002). ‘Size-controlled highly luminescent silicon nanocrystals: A SiO/SiO<sub>2</sub> superlattice approach’. *Applied Physics Letters*, 80(4), 661.
- [394] Zaitsev A (2000). ‘Vibronic spectra of impurity-related optical centers in diamond’. *Physical Review B*, 61(19), 909–922.
- [395] Zakharov N D, Werner P, Gosele U, Heitz R, Bimberg D, Ledentsov N N, Ustinov V M, Volovik B V, Alferov Z I, Polyakov N K, Petrov V N, Egorov V a and Cirlin G E (2000). ‘Structure and optical properties of Si/InAs/Si layers grown by molecular beam epitaxy on Si substrate’. *Applied Physics Letters*, 76(19), 2677.
- [396] Zehtabi-Oskuie A, Bergeron J G and Gordon R (2012). ‘Flow-dependent double-nanohole optical trapping of 20 nm polystyrene nanospheres.’ *Scientific reports*, 2, 966.
- [397] Zhang Y, Khan M, Huang Y, Ryou J, Deotare P, Dupuis R and Loncar M (2010). ‘Photonic crystal nanobeam lasers’. *Applied Physics Letters*, 97(5), 051104.

- [398] Zhang Y, McCutcheon M W, Burgess I B and Loncar M (2009). ‘Ultra-high-Q TE/TM dual-polarized photonic crystal nanocavities’. *Optics Letters*, 34(17), 2694.
- [399] Zhao Z, Hao Z, Yadavalli K, Wang K L and Jacob A P (2008). ‘Optical properties of InAs quantum dots grown on patterned Si with a thin GaAs buffer layer’. *Applied Physics Letters*, 92(8), 083111.
- [400] Zhao Z, Hulko O, Kim H, Liu J, Sugahari T, Shi B and Xie Y (2004). ‘Growth and characterization of InAs quantum dots on Si(001) substrates’. *Journal of Crystal Growth*, 271(3-4), 450–455.
- [401] Zondervan R, Kulzer F, Orlinskii S B and Orrit M (2003). ‘Photoblinking of rhodamine 6G in poly(vinyl alcohol): Radical dark state formed through the triplet’. *Journal of Physical Chemistry A*, 107(35), 6770–6776.
- [402] Zubia D and Hersee S D (1999). ‘Nanoheteroepitaxy: The Application of nanostructuring and substrate compliance to the heteroepitaxy of mismatched semiconductor materials’. *Journal of Applied Physics*, 85(9), 6492.
- [403] Zwiller V, Jonsson P, Blom H, Jeppesen S, Pistol M E, Samuelson L, Katznelson A, Kotelnikov E, Evtikhiev V and Björk G (2002). ‘Correlation spectroscopy of excitons and biexcitons on a single quantum dot’. *Physical Review A*, 66(5).